

**Porous and Cellular Materials  
for Structural Applications**

19990303 050

Preceding Page <sup>S</sup> Blank

---

**MATERIALS RESEARCH SOCIETY**  
**SYMPOSIUM PROCEEDINGS VOLUME 521**

# **Porous and Cellular Materials for Structural Applications**

Symposium held April 13-15, 1998, San Francisco, California, U.S.A.

**EDITORS:**

**Daniel S. Schwartz**  
*The Boeing Company*  
*St. Louis, Missouri, U.S.A.*

**Donald S. Shih**  
*The Boeing Company*  
*St. Louis, Missouri, U.S.A.*

**Anthony G. Evans**  
*Harvard University*  
*Cambridge, Massachusetts, U.S.A.*

**Haydn N.G. Wadley**  
*University of Virginia*  
*Charlottesville, Virginia, U.S.A.*



**Materials Research Society**  
Warrendale, Pennsylvania

**DISTRIBUTION STATEMENT A**  
**Approved for public release**  
**Distribution Unlimited**

This work relates to Department of Navy Grant N00014-98-1-0479 issued by the Office of Naval Research. The United States Government has a royalty-free license throughout the world in all copyrightable material contained herein.

Support was furnished by the U.S. Army Research Office, Contract #DAAG55-98-1-9223. The views, opinions, and/or findings contained in this report are those of the authors and should not be construed as an official Department of the Army position, policy, or decision, unless so designated by other documentation.

Single article reprints from this publication are available through University Microfilms Inc., 300 North Zeeb Road, Ann Arbor, Michigan 48106

CODEN: MRSPDH

Copyright 1998 by Materials Research Society.  
All rights reserved.

This book has been registered with Copyright Clearance Center, Inc. For further information, please contact the Copyright Clearance Center, Salem, Massachusetts.

Published by:

Materials Research Society  
506 Keystone Drive  
Warrendale, PA 15086  
Telephone (724) 779-3003  
Fax (724) 779-8313  
Website: <http://www.mrs.org/>

Library of Congress Cataloging in Publication Data

Porous and cellular materials for structural applications : symposium held April 13-15, 1998, San Francisco, California, U.S.A. / editors, Daniel S. Schwartz, Donald S. Shih, Anthony G. Evans and Haydn N.G. Wadley  
p. cm. -- (Materials Research Society symposium proceedings ; v. 521)  
Includes bibliographical references and index.  
ISSN 0272-9172  
ISBN 1-55899-427-0

1. Porous materials--Congresses. I. Schwartz, Daniel S. II. Shih, Donald S. III. Evans, Anthony G. IV. Wadley, Haydn N.G. V. Series : Materials Research Society symposium proceedings ; v. 521.

TA418.9.P6P62 1998  
620.1'16--dc21

98--37975  
CIP

Manufactured in the United States of America

---

## CONTENTS

Preface .....	ix
Acknowledgments .....	xi
Materials Research Society Symposium Proceedings .....	xii

### **PART I: MECHANICAL BEHAVIOR OF SOLID FOAMS: THEORY AND GENERAL OBSERVATIONS**

<b>*Influence of Imperfections on Effective Properties of Cellular Solids .....</b>	<b>3</b>
<i>Joachim L. Grenestedt</i>	
<b>Mechanical Properties of a Structural Polyurethane Foam and the Effect of Particulate Loading .....</b>	<b>15</b>
<i>S.H. Goods, C.L. Neuschwanger, and L.L. Whinnery</i>	
<b>Numerical Modeling of the Strength of Highly Porous Aerated Autoclaved Concrete .....</b>	<b>21</b>
<i>Thomas Schneider, Georg Schober, and Peter Grell</i>	
<b>Modeling of Fatigue for Cellular Materials .....</b>	<b>27</b>
<i>J.S. Huang and J.Y. Lin</i>	
<b>Analysis of Deformation of Porous Metals .....</b>	<b>33</b>
<i>Dong Nyung Lee, Heung Nam Han, Kyu Hwan Oh, and Hyoung Seop Kim</i>	
<b>A Continuum Plasticity Model for the Constitutive Behavior of Foamed Metals .....</b>	<b>39</b>
<i>Ronald E. Miller and John W. Hutchinson</i>	
<b>Elastic Properties of Porous Structural Ceramics Produced by Plasma Spraying .....</b>	<b>45</b>
<i>A. Wanner</i>	

### **PART II: MECHANICAL PROPERTIES OF METALLIC FOAMS**

<b>*Reduction in Young's Modulus of Aluminum Foams Due to Cell Wall Curvature and Corrugation .....</b>	<b>53</b>
<i>W. Sanders and L.J. Gibson</i>	
<b>Compressive, Tensile, and Shear Testing of Melt-Foamed Aluminum .....</b>	<b>59</b>
<i>H. von Hagen and W. Bleck</i>	

\*Invited Paper

<b>Effects of Thermomechanical Processing on the Resulting Mechanical Properties of 6101 Aluminum Foam</b> .....	65
<i>R.W. Margevicius, P.W. Stanek, and L.A. Jacobson</i>	
<b>*Compressive Deformation and Yielding Mechanisms in Cellular Al Alloys Determined Using X-ray Tomography and Surface Strain Mapping</b> .....	71
<i>H. Bart-Smith, A.F. Bastawros, D.R. Mumm, A.G. Evans, D.J. Sypeck, and H.N.G. Wadley</i>	
<b>Shear Properties on Aluminum Metal Foams Prepared by the Melt Route</b> .....	83
<i>E. Saenz, P.S. Baranda, and J. Bonhomme</i>	
<b>Bending Properties of Foamed Aluminum Panels and Sandwiches</b> .....	91
<i>F. Šimančík, J. Kováčik, and N. Mináriková</i>	
<b>High Cycle Fatigue Properties of Aluminum Foams</b> .....	97
<i>B.E. Zettl, S.E. Stanzl-Tschegg, R. Gradinger, and H.P. Degischer</i>	
<b>Strain Rate Effects in Porous Materials</b> .....	103
<i>J. Lankford, Jr. and K.A. Dannemann</i>	
<b>The Effect of Parent Metal Properties on the Performance of Lattice Block Material™</b> .....	109
<i>M.L. Renauld, A.F. Giannel, M.S. Thompson, and J. Priluck</i>	

### **PART III: MANUFACTURE OF SOLID FOAMS**

<b>*Production Methods for Metallic Foams</b> .....	121
<i>J. Banhart and J. Baumeister</i>	
<b>Aluminum Foam, "ALPORAS": The Production Process, Properties, and Applications</b> .....	133
<i>T. Miyoshi, M. Itoh, S. Akiyama, and A. Kitahara</i>	
<b>The Effect of Oxide Layers on Gas-Generating Hydride Particles During Production of Aluminum Foams</b> .....	139
<i>V. Gergely and T.W. Clyne</i>	
<b>Investigation for the Selection of Foaming Agents to Produce Steel Foams</b> .....	145
<i>C.J. Yu, H.H. Eifert, M. Knuewer, M. Weber, and J. Baumeister</i>	
<b>Complex Foamed Aluminum Parts as Permanent Cores in Aluminum Castings</b> .....	151
<i>F. Šimančík and F. Schoerghuber</i>	
<b>Joining of Aluminum Structures With Aluminum Foams</b> .....	159
<i>J. Burzer, T. Bernard, and H.W. Bergmann</i>	

\*Invited Paper

<b>Lyophilic Liquid Porosimetry and a New Liquid Autoporosimeter</b> .....	165
<i>I. Tyomkin</i>	

<b>Eddy-Current Characterization of Metal Foams</b> .....	171
<i>K.P. Dharmasena and H.N.G. Wadley</i>	

**PART IV: OTHER FOAM MATERIALS AND PROCESSES**

<b>Applications for Silica-Based Aerogel Products on an Industrial Scale</b> .....	179
<i>M. Schmidt and F. Schwertfeger</i>	

<b>Structural Graphitic Carbon Foams</b> .....	185
<i>Kristen M. Kearns, David P. Anderson, and Heather J. Anderson</i>	

<b>*Steel and Titanium Hollow Sphere Foams</b> .....	191
<i>K.M. Hurysz, J.L. Clark, A.R. Nagel, C.U. Hardwicke, K.J. Lee, J.K. Cochran, and T.H. Sanders, Jr.</i>	

<b>Novel Hollow Powder Porous Structures</b> .....	205
<i>David J. Sypeck, Phillip A. Parrish, and Haydn N.G. Wadley</i>	

<b>Fabrication and Properties of Syntactic Magnesium Foams</b> .....	211
<i>M. Hartmann, K. Reindel, and R.F. Singer</i>	

<b>Porous Al Alloys by Local Melting and Diffusion of Metal Powders</b> .....	217
<i>N. Wang, E.A. Starke, Jr., and H.N.G. Wadley</i>	

**PART V: HICE-BASED MATERIALS**

<b>Development and Scale-up of the Low-Density-Core Process for Ti-64</b> .....	225
<i>D.S. Schwartz, D.S. Shih, R.J. Lederich, R.L. Martin, and D.A. Deuser</i>	

<b>Superplastic Foaming of Titanium and Ti-6Al-4V</b> .....	231
<i>D.C. Dunand and J. Teisen</i>	

<b>Elastic Properties of Low Density Core (LDC) Ti-6Al-4V Sandwich Cores</b> .....	237
<i>D.T. Queheillalt, H.N.G. Wadley, and D.S. Schwartz</i>	

<b><i>In Situ</i> Sensing of the Expansion of Low-Density-Core (LDC) Ti-6Al-4V Sandwich Structures</b> .....	243
<i>D.T. Queheillalt, B.W. Choi, H.N.G. Wadley, and D.S. Schwartz</i>	

<b>Process Modeling of Ti-6Al-4V SPM Materials</b> .....	249
<i>S.S. Ahmed, G. Huang, H. Gegel, and D. Barker</i>	

\*Invited Paper

<b>The Influence of Internal Pore Pressure During Roll Forming of Structurally Porous Metals</b> .....	<b>257</b>
<i>D.M. Elzey and H.N.G. Wadley</i>	

**PART VI: APPLICATION AND DESIGN PRINCIPLES**

<b>Parameters of Construction for Applications of Metal Foams</b> .....	<b>265</b>
<i>R. Neugebauer and Th. Hipke</i>	
<b>Lightweight Products With Metal Foam - Properties and Methods of Processing</b> .....	<b>271</b>
<i>R. Neugebauer, H. Bräunlich, and U. Wagner</i>	

**PART VII: GASAR MATERIALS**

<b>*Formation of Ordered Gas-Solid Structures Via Solidification in Metal-Hydrogen Systems</b> .....	<b>281</b>
<i>V.I. Shapovalov</i>	
<b>GASAR Porous Metals Process Control</b> .....	<b>291</b>
<i>J.M. Apprill, D.R. Poirier, M.C. Maguire, and T.C. Gutsch</i>	
<b>The Effect of GASAR Processing Parameters on Porosity and Properties in Aluminum Alloy</b> .....	<b>297</b>
<i>C.J. Paradies, A. Tobin, and Jeff Wolla</i>	
<b>*Characterization of Porous GASAR Aluminum</b> .....	<b>303</b>
<i>R.J. Bonenberger, A.J. Kee, R.K. Everett, and P. Matic</i>	
<b>Metallographic Study of GASAR Porous Magnesium</b> .....	<b>315</b>
<i>Chanman Park and Steven R. Nutt</i>	
<b>Author Index</b> .....	<b>321</b>
<b>Subject Index</b> .....	<b>323</b>

\*Invited Paper

---

## PREFACE

This volume is a record of the "Porous and Cellular Materials for Structural Applications" symposium, held from April 13-15, at the 1998 MRS Spring Meeting in San Francisco. A diverse and international group of experts was brought together to present and discuss recent developments in the area of porous and cellular materials, including polymer-, ceramic- and metal-based materials. The general focus of the symposium was on porous materials that are being developed, at least in part, for structural applications. Theoretical aspects of the mechanical behavior of porous and cellular materials were discussed, as well as the specific mechanical properties of a wide variety of solid foam materials. Design principles for the use of solid foams in structures were presented, and a number of promising applications for porous and cellular materials were shown. Papers on the manufacture of solid foams and the production of parts containing solid foams were presented. A significant portion of the symposium was devoted to new porous materials that cannot be classified as foams, such as hollow spheres, hot isostatically compacted and expanded (HICE) materials and GASAR materials. Papers delivered on these novel materials covered their manufacture, properties and prospective uses. The symposium demonstrated that the development and understanding of porous and cellular materials has advanced significantly in the past decade, particularly in the area of porous metallic materials.

The organizers would like to take this opportunity to thank the following people and agencies for funding the symposium:

Office of Naval Research (Drs. G. Yoder and S. Fishman)  
Materials Division of NASA/Langley Research Center  
Materials Science Division of the Army Research Office (Dr. W. Simmons)

The organizers are grateful for the financial assistance and the high level of interest in this research area. We would also like to thank K. Frazier for help with preparing the proceedings, and D. Queheillalt for help in running the technical sessions.

Daniel S. Schwartz  
Donald S. Shih  
Anthony G. Evans  
Haydn N.G. Wadley

June 1998

---

## ACKNOWLEDGEMENTS

The organizers would like to thank the following people for their help with the manuscript peer-review process and/or for acting as chairs of the technical sessions. We are grateful to them for volunteering their time and expertise, which contributed significantly to the quality of these proceedings.

J. Banhart  
A. F. Bastawros  
R. J. Bonenberger  
W. Choi  
J. K. Cochran  
K. A. Dannemann  
A. Giamei  
L. J. Gibson  
J. L. Grenestedt  
J. W. Hutchinson  
M. Knuewer  
G. London  
A. G. Tobin  
A. Wanner

## MATERIALS RESEARCH SOCIETY SYMPOSIUM PROCEEDINGS

- Volume 481— Phase Transformation and Systems Driven Far From Equilibrium, E. Ma, P. Bellon, M. Atzmon, R. Trivedi, 1998, ISBN: 1-55899-386-X
- Volume 482— Nitride Semiconductors, F.A. Ponce, S.P. DenBaars, B.K. Meyer, S. Nakamura, S. Strite, 1998, ISBN: 1-55899-387-8
- Volume 483— Power Semiconductor Materials and Devices, S.J. Pearton, R.J. Shul, E. Wolfgang, F. Ren, S. Tenconi, 1998, ISBN: 1-55899-388-6
- Volume 484— Infrared Applications of Semiconductors II, S. Sivananthan, M.O. Manasreh, R.H. Miles, D.L. McDaniel, Jr., 1998, ISBN: 1-55899-389-4
- Volume 485— Thin-Film Structures for Photovoltaics, E.D. Jones, R. Noufi, B.L. Sopori, J. Kalejs, 1998, ISBN: 1-55899-390-8
- Volume 486— Materials and Devices for Silicon-Based Optoelectronics, J.E. Cunningham, S. Coffa, A. Polman, R. Soref, 1998, ISBN: 1-55899-391-6
- Volume 487— Semiconductors for Room-Temperature Radiation Detector Applications II, R.B. James, T.E. Schlesinger, P. Siffert, M. Cuzin, M. Squillante, W. Dusi, 1998, ISBN: 1-55899-392-4
- Volume 488— Electrical, Optical, and Magnetic Properties of Organic Solid-State Materials IV, J.R. Reynolds, A.K-Y. Jen, L.R. Dalton, M.F. Rubner, L.Y. Chiang, 1998, ISBN: 1-55899-393-2
- Volume 489— Materials Science of the Cell, B. Mulder, V. Vogel, C. Schmidt, 1998, ISBN: 1-55899-394-0
- Volume 490— Semiconductor Process and Device Performance Modeling, J.S. Nelson, C.D. Wilson, S.T. Dunham, 1998, ISBN: 1-55899-395-9
- Volume 491— Tight-Binding Approach to Computational Materials Science, P.E.A. Turchi, A. Gonis, L. Colombo, 1998, ISBN: 1-55899-396-7
- Volume 492— Microscopic Simulation of Interfacial Phenomena in Solids and Liquids, S.R. Phillpot, P.D. Bristowe, D.G. Stroud, J.R. Smith, 1998, ISBN: 1-55899-397-5
- Volume 493— Ferroelectric Thin Films VI, R.E. Treece, R.E. Jones, S.B. Desu, C.M. Foster, I.K. Yoo, 1998, ISBN: 1-55899-398-3
- Volume 494— Science and Technology of Magnetic Oxides, M. Hundley, J. Nickel, R. Ramesh, Y. Tokura, 1998, ISBN: 1-55899-399-1
- Volume 495— Chemical Aspects of Electronic Ceramics Processing, P.N. Kumta, A.F. Hepp, D.B. Beach, J.J. Sullivan, B. Arkles, 1998, ISBN: 1-55899-400-9
- Volume 496— Materials for Electrochemical Energy Storage and Conversion II—Batteries, Capacitors and Fuel Cells, D.S. Ginley, D.H. Doughty, T. Takamura, Z. Zhang, B. Scrosati, 1998, ISBN: 1-55899-401-7
- Volume 497— Recent Advances in Catalytic Materials, N.M. Rodriguez, S.L. Soled, J. Hrbek, 1998, ISBN: 1-55899-402-5
- Volume 498— Covalently Bonded Disordered Thin-Film Materials, M.P. Siegal, J.E. Jaskie, W. Milne, D. McKenzie, 1998, ISBN: 1-55899-403-3
- Volume 499— High-Pressure Materials Research, R.M. Wentzocovitch, R.J. Hemley, W.J. Nellis, P.Y. Yu, 1998, ISBN: 1-55899-404-1
- Volume 500— Electrically Based Microstructural Characterization II, R.A. Gerhardt, M.A. Alim, S.R. Taylor, 1998, ISBN: 1-55899-405-X
- Volume 501— Surface-Controlled Nanoscale Materials for High-Added-Value Applications, K.E. Gonsalves, M-I. Baraton, J.X. Chen, J.A. Akkara, 1998, ISBN: 1-55899-406-8
- Volume 502— *In Situ* Process Diagnostics and Intelligent Materials Processing, P.A. Rosenthal, W.M. Duncan, J.A. Woollam, 1998, ISBN: 1-55899-407-6
- Volume 503— Nondestructive Characterization of Materials in Aging Systems, R.L. Crane, S.P. Shah, R. Gilmore, J.D. Achenbach, P.T. Khuri-Yakub, T.E. Matikas, 1998, ISBN: 1-55899-408-4
- Volume 504— Atomistic Mechanisms in Beam Synthesis and Irradiation of Materials, J.C. Barbour, S. Roorda, D. Ila, 1998, ISBN: 1-55899-409-2
- Volume 505— Thin-Films—Stresses and Mechanical Properties VII, R.C. Cammarata, E.P. Busso, M. Nastasi, W.C. Oliver, 1998, ISBN: 1-55899-410-6
- Volume 506— Scientific Basis for Nuclear Waste Management XX, I.G. McKinley, C. McComble, 1998, ISBN: 1-55899-411-4
- Volume 507— Amorphous and Microcrystalline Silicon Technology—1998, S. Wagner, M. Hack, H.M. Branz, R. Schropp, I. Shimizu, 1998, ISBN: 1-55899-413-0

---

## MATERIALS RESEARCH SOCIETY SYMPOSIUM PROCEEDINGS

- Volume 508—Flat-Panel Display Materials—1998, G. Parsons, T.S. Fahlen, S. Morozumi, C. Seager, C-C. Tsai, 1998, ISBN: 1-55899-414-9
- Volume 509—Materials Issues in Vacuum Microelectronics, W. Zhu, L.S. Pan, T.E. Felter, C. Holland, 1998, ISBN: 1-55899-415-7
- Volume 510—Defect and Impurity Engineered Semiconductors and Devices II, S. Ashok, J. Chevallier, K. Sumino, B.L. Soporl, W. Goetz, 1998, ISBN: 1-55899-416-5
- Volume 511—Low-Dielectric Constant Materials IV, C. Chiang, J.T. Wetzal, T-M. Lu, P.S. Ho, 1998, ISBN: 1-55899-417-3
- Volume 512—Wide-Bandgap Semiconductors for High Power, High Frequency and High Temperature, S. DenBaars, M.S. Shur, J. Palmour, M. Spencer, 1998, ISBN: 1-55899-418-1
- Volume 513—Hydrogen in Semiconductors and Metals, N.H. Nickel, W.B. Jackson, R.C. Bowman, 1998, ISBN: 1-55899-419-X
- Volume 514—Advanced Interconnects and Contact Materials and Processes for Future Integrated Circuits, S.P. Murarka, D.B. Fraser, M. Eizenberg, R. Tung, R. Madar, 1998, ISBN: 1-55899-420-3
- Volume 515—Electronic Packaging Materials Science X, D.J. Belton, R. Pearson, M. Gaynes, E.G. Jacobs, 1998, ISBN: 1-55899-421-1
- Volume 516—Materials Reliability in Microelectronics VIII, T. Marieb, J. Bravman, M.A. Korhonen, J.R. Lloyd, 1998, ISBN: 1-55899-422-X
- Volume 517—High-Density Magnetic Recording and Integrated Magneto-Optics: Materials and Devices, K. Rubin, J.A. Bain, T. Nolan, D. Bogy, B.J.H. Stadler, M. Levy, J.P. Lorenzo, M. Mansuripur, Y. Okamura, R. Wolfe, 1998, ISBN: 1-55899-423-8
- Volume 518—Microelectromechanical Structures for Materials Research, S.B. Brown, C. Muhlstein, P. Krulevitch, G.C. Johnston, R.T. Howe, J.R. Gilbert, 1998, ISBN: 1-55899-424-6
- Volume 519—Organic/Inorganic Hybrid Materials, R.M. Laine, C. Sanchez, E. Giannelis, C.J. Brinker, 1998, ISBN: 1-55899-425-4
- Volume 520—Nanostructured Powders and Their Industrial Application, G. Beaucage, J.E. Mark, G. Burns, H. Duen-Wu, 1998, ISBN: 1-55899-426-2
- Volume 521—Porous and Cellular Materials for Structural Applications, D.S. Schwartz, D.S. Shih, H.N.G. Wadley, A.G. Evans, 1998, ISBN: 1-55899-427-0
- Volume 522—Fundamentals of Nanoindentation and Nanotribology, N.R. Moody, W.W. Gerberich, S.P. Baker, N. Burnham, 1998, ISBN: 1-55899-428-9
- Volume 523—Electron Microscopy of Semiconducting Materials and ULSI Devices, C. Hayzelden, F.M. Ross, C.J.D. Hetherington, 1998, ISBN: 1-55899-429-7
- Volume 524—Application of Synchrotron Radiation Techniques to Materials Science IV, S.M. Mini, D.L. Pery, S.R. Stock, L.J. Terminello, ISBN: 1-55899-430-0
- Volume 525—Rapid Thermal and Integrated Processing VII, M.C. Öztürk, F. Roozeboom, P.J. Timans, S.H. Pas, 1998, ISBN: 1-55899-431-9
- Volume 526—Advances in Laser Ablation of Materials, R.K. Singh, D.H. Lowndes, D.B. Chrisey, J. Narayan, T. Kawai, E. Fogarassy, 1998, ISBN: 1-55899-432-7
- Volume 527—Diffusion Mechanisms in Crystalline Materials, Y. Mishin, N.E.B. Cowern, C.R.A. Catlow, D. Farkas, G. Vogl, 1998, ISBN: 1-55899-433-5
- Volume 528—Mechanisms and Principles of Epitaxial Growth in Metallic Systems, L.T. Wille, C.P. Burmester, K. Terakura, G. Comsa, E.D. Williams, 1998, ISBN: 1-55899-434-3
- Volume 529—Computational and Mathematical Models of Microstructural Evolution, J.W. Bullard, R. Kalia, M. Stoneham, L-Q. Chen, 1998, ISBN: 1-55899-435-1
- Volume 530—Biomaterials Regulating Cell Function and Tissue Development, D. Mooney, A.G. Mikos, K.E. Healy, Y. Ikada, R.C. Thomson, 1998, ISBN: 1-55899-436-X
- Volume 531—Reliability of Photonics Materials and Structures, E. Suhir, M. Fukuda, C.R. Kurkjian, 1998, ISBN: 1-55899-437-8
- Volume 532—Silicon Front-End Technology—Materials Processing and Modelling, N.E.B. Cowern, D. Jacobson, P. Griffin, P. Packan, R. Webb, 1998, ISBN: 1-55899-438-6
- Volume 533—Epitaxy and Applications of Si-Based Heterostructures, E.A. Fitzgerald, P.M. Mooney, D.C. Houghton, 1998, ISBN: 1-55899-439-4

---

**Part I**

**Mechanical Behavior of Solid Foams:  
Theory and General Observations**

---

## Influence of Imperfections on Effective Properties of Cellular Solids

JOACHIM L. GRENESTEDT

Department of Aeronautics, Division of Lightweight Structures  
Kungl Tekniska Högskolan (Royal Institute of Technology)  
S-100 44 Stockholm, Sweden  
joachim@flyg.kth.se

### ABSTRACT

The mechanical properties of cellular solids, or solid foams, is affected by "imperfections" such as wavy distortions of cell walls, variations in cell wall thickness, non-uniform cell shape, etc. The present paper is focused mainly on elastic stiffnesses of closed cell cellular solids. A "perfect" model is first discussed and shown to predict the behavior of PVC foams well. However, this model over-estimates the stiffnesses of aluminum foams. The relatively poor properties of the aluminum foam are believed to be caused by imperfections in the cells. The main body of the paper focuses on modeling different kinds of imperfections, and analyzing their impact on foam properties.

### I. INTRODUCTION

Cellular solids are used among other things as core materials in sandwich structures. The micro structures of most cellular solids are typically rather disordered, see Fig. 1, as opposed to being uniform, perfectly ordered and periodic. A number of deviations, or imperfections, from a perfectly ordered foam can be identified. These include e.g. wavy distortions of the cell walls, cell wall thickness variations, and non-uniform shape of the cells. The influence of wavy distortions on stiffness has been studied by Grenestedt [1] and Simone and Gibson [2]. The influence of thickness variations has been studied by Grenestedt and Bassinet [3]. Regarding foams with non-uniform cell shapes, Van der Burg et al. [4] analyzed open cell foams, and Grenestedt and Tanaka [5] analyzed closed cell foams. Silva and Gibson [6] studied the influence of cell wall removal in 2D foams. The present paper mainly discusses the results of the projects which the present author has been involved in.

The paper is organized as follows: In Section II some concepts of effective properties of cellular solids are briefly reviewed, and in Section III some scaling laws (how stiffnesses scale with density) are discussed. In Section IV a 3D perfect closed cell reference model – without imperfections – is introduced. The following three sections each deal with one kind of imperfection:

wavy distortions (Section V), thickness variations (Section VI), and non-uniform cell shapes (Section VII).

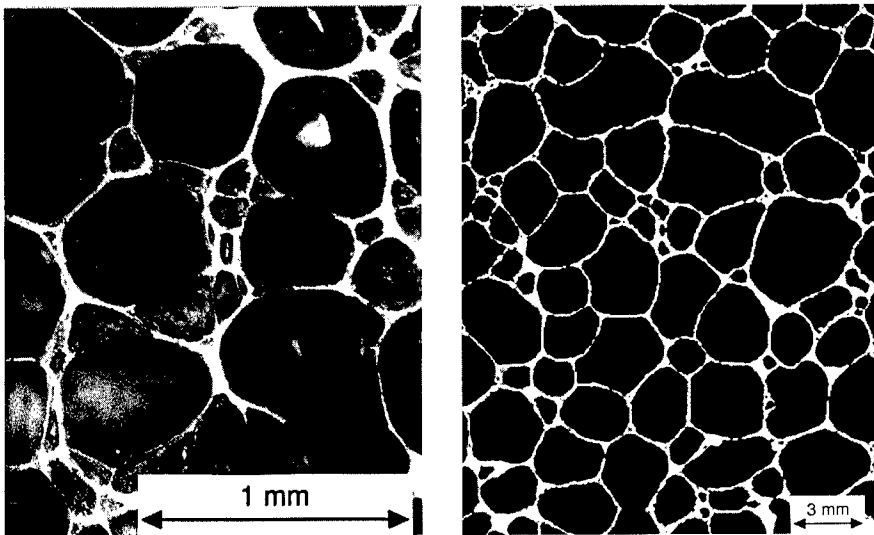


**Fig. 1.** Micro graphs of Divinycell [7] H130 expanded PVC (left) and Alporas [8] aluminum foam (right). Both materials have approximately the same relative densities.

## II. EFFECTIVE PROPERTIES OF CELLULAR SOLIDS, AND AN ASSUMPTION OF PERIODICITY

The size of a single cell is typically orders of magnitude smaller than the size of the cellular solids used for example as sandwich cores in many engineering structures. For example, the diameter of a single cell in expanded PVC is in the order of 1 mm, whereas the core thickness in a ship is typically in the order 10 or 100 mm, and the in-plane dimensions are typically some meters. On a large scale, the cellular solid can thus be considered to be homogeneous, and effective material properties such as Young's modulus and Poisson's ratio can be introduced. Such effective properties will presently be calculated by using different models of cellular solids. Macroscopic stress  $\bar{\sigma}_{ij}$  and strain  $\bar{\epsilon}_{kl}$  are introduced as volume averages over many cells. Over head bars are throughout the paper used for macroscopic foam quantities, while the absence of a bar is used for a cell wall quantity (fully dense material). Effective elastic stiffnesses are introduced as the quantities relating macroscopic stress  $\bar{\sigma}_{ij}$  to macroscopic strain  $\bar{\epsilon}_{kl}$ ,

$$\bar{\sigma}_{ij} = \bar{C}_{ijkl} \bar{\epsilon}_{kl} \Leftrightarrow \bar{\epsilon}_{ij} = \bar{S}_{ijkl} \bar{\sigma}_{kl} \quad (1)$$

It is not reasonable to model all the millions of cells in a structure like a ship, so some kind of restriction is introduced in the modeling. A simplification which seems justifiable is to assume that the cellular solid has some periodicity. This is assumed in the present analysis. It is also assumed that the deformation is periodic.

### III. SCALING OF STIFFNESSES WITH DENSITY

Cellular solids of higher densities usually have higher stiffnesses than cellular solids of lower densities. How the stiffnesses scale with density depends on the cell morphology, and in particular in which way the cell walls or struts deform when the cellular solid is deformed. The scaling of stiffness with density is easily calculated by assuming a local deformation mechanism (e.g. bending, or stretching, of the cell walls) and using dimensional considerations and linearity. Below is a summary of scaling between a stiffness (denoted  $\bar{E}$ , but the formula applies as well for shear stiffness  $\bar{G}$  and bulk modulus  $\bar{K}$ ) and relative density  $\bar{\rho} / \rho$ ,

$$\bar{E} \propto E \left( \frac{\bar{\rho}}{\rho} \right)^m \quad (2)$$

where

in 2D:  $m = 1$  for stretching controlled micro structures

$m = 3$  for bending controlled micro structures

in 3D:  $m = 1$  for stretching controlled rod and plate like micro structures

$m = 2$  for bending or twisting controlled rod like micro structures

$m = 3$  for bending controlled plate like micro structures

It has been assumed that the cell wall members are plate or rod like, such that beam and plate theories with Kirchhoff kinematics well describe their deformations. We observe that stiffnesses scale cubically ( $m=3$ ) with density for closed cell bending controlled (plate like) micro structures.

Most models for cellular solids deform by a combination of mechanisms, so the scaling may be hard to determine *a priori* for a given model. *A posteriori* we can determine whether the model deformed for example mainly by stretching or by bending by studying the scaling.

#### IV. PERFECTLY ORDERED KELVIN BASE MODEL

The presently used 3D perfect closed cell reference model consists of flat faced 14-hedra (tetrakaidecahedra) as depicted in Fig. 2. These 14-hedra pack in a bcc arrangement, and completely fill space. Kelvin [9] used this model, but with slightly curved faces, to model liquid foams. All 14-hedra have the same size, and have cubic symmetry. The stiffness of the resulting cellular solid thus has cubic symmetry, but is not isotropic. As it turns out, the anisotropy is though very slight. We will thus for this model present isotropic stiffnesses such as Young's modulus and bulk modulus without further discussion. For cellular solids which are not isotropic, we will present isotropic stiffness which are obtained by averaging stiffnesses over all directions. For a full discussion, see Kröner [10] and Grenestedt [11].

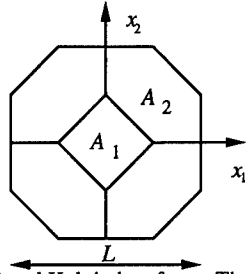


Fig. 2. A 14-hedron of the flat faced Kelvin bcc foam. The projections in the three different coordinate directions are identical. 14-hedra of this shape packed in a bcc fashion fill space.

The Young's modulus and bulk modulus of this foam scale virtually linearly with density. The bulk modulus is very close to the theoretical maximum limit, provided by the Hashin-Shtrikman [12] upper bound,

$$\bar{K} = \frac{4GK(\bar{\rho} / \rho)}{4G + 3K(1 - \bar{\rho} / \rho)} \xrightarrow{\bar{\rho} \rightarrow 0} \frac{\bar{\rho}}{\rho} \frac{4GK}{4G + 3K} = \frac{\bar{\rho}}{\rho} \frac{2E}{9(1 - \nu)} \quad (3)$$

The low density asymptote is of particular interest for the presently considered low density cellular solids. The Young's modulus is for the flat-faced Kelvin cellular solid

$$\frac{\bar{E}}{E} \approx 0.35 \frac{\bar{\rho}}{\rho} \quad (4)$$

when Poisson's ratio for the solid is  $\nu=0.3$ . The low density asymptote of the Hashin-Shtrikman upper bound on Young's modulus is

$$\bar{E} = \frac{9\bar{K}\bar{G}}{3\bar{K} + \bar{G}} = \frac{\bar{\rho}}{\rho} \frac{2(7-5\nu)E}{3(1-\nu)(9+5\nu)} \quad (5)$$

For  $\nu=0.3$ , this becomes  $\bar{E} \approx 0.50E(\bar{\rho} / \rho)$ . The reference model thus has almost the highest possible bulk modulus, and a Young's modulus which is 30% lower than the maximum possible Young's modulus.

The elastic properties which this model predicts very well match the experimentally measured properties of expanded PVC (Divinycell ([7,13,14]) of three different grades and with densities ranging from 36 to 400 kg/m<sup>3</sup>, see Grenestedt [11]. The good correlation with experiments was the main reason for selecting this model as our reference model. However, the experimentally measured stiffnesses of metal foams such as Alporas is considerably lower than that predicted by the present model, see e.g. Sugimura et al. [15]. We believe that the low stiffnesses are due to geometric imperfections when compared with the perfect reference model. In the following three Sections, three different types of imperfections are independently studied.

## V. INFLUENCE OF WAVY DISTORTIONS

In this Section, the study by Grenestedt [1] on influence of wavy distortions of the cell walls is discussed. The cell walls are assumed to have constant thickness, and a kind of upper bound stiffnesses can be derived. Details of the derivation are omitted.

For open cell materials, wavy distortions of the cell struts can reduce the stiffness immensely. The reason is that the axial stiffness of a wavy strut, which has an amplitude of the waviness equal to the thickness of the strut, is only a seventh of that of a straight strut\*. Much bending occurs in an axially loaded wavy strut, and this is the reason for the low stiffness. However, if the struts in the open foam are such arranged, that the struts deform by bending even if they are straight, then waviness in the struts may have very little influence on stiffness.

We now turn to closed cell 3D models. The only geometry considered in the present model is the shape of a single cell wall. All cell walls in the model are assumed to be made of the same material and have the same shape, but they may have different sizes. This simplification, which of

\* It has here been assumed that the strut is slender, that the ends are constrained against rotation, that the strut has a rectangular cross section, is made of isotropic material, and that the wavy imperfections are shallow and have the shape  $\hat{w}_0[1 - \cos(2m\pi x / a)]$  where  $x$  is the axial coordinate,  $\hat{w}_0$  is the amplitude of the waviness,  $a$  is the length of the strut, and  $m$  any integer.

course is a gross simplification, allows us to derive upper bounds and we need only analyze a single cell wall. A real foam usually consists of cell walls of many different shapes. For the model, we select one cell wall shape which in some sense should be representative for all cell walls in the foam. With this single representative cell wall we develop a simple model which hopefully can provide us with relevant quantitative information about foams with wavy cell walls.

The shape of a representative cell wall naturally depends on the foam. We assume that a square plate with side  $a$ , uniform thickness  $t$ , and with the wavy imperfections

$$w_0(x, y) = \hat{w}_0 \sin \frac{m\pi x}{a} \sin \frac{n\pi y}{a} \quad (6)$$

is a representative cell wall shape. Here,  $x$  and  $y$  are coordinates,  $\hat{w}_0$  is the amplitude of the waviness, and  $m$  and  $n$  integers. We refer to Grenestedt [1] for the derivation of the stiffnesses of this model, and here only present some results. The shear moduli for the cases  $m=n=1$  and  $m=n=2$  are given in Fig. 3.

For vanishing waviness amplitude,  $\hat{w}_0 = 0$ , the present model predicts the same stiffnesses as the low density asymptotes of the Hashin-Shtrikman upper bounds, i.e.  $\bar{K} / E \approx 0.32(\bar{\rho} / \rho)$ ,  $\bar{G} / E \approx 0.20(\bar{\rho} / \rho)$  and  $\bar{E} / E \approx 0.50(\bar{\rho} / \rho)$  when  $\nu=0.3$ . For the aluminum foam, experiments gave  $(\bar{E} / E) / (\bar{\rho} / \rho) = 0.23$ , which is 64% of the Young's modulus of the Kelvin foam. The present model predicts the Young's modulus  $(\bar{E} / E) / (\bar{\rho} / \rho) = 0.31$  for  $\hat{w}_0 / t = 5$ ,  $m=n=1$ , and  $t / a = 0.003$ , which is 62% of the upper bound, and  $(\bar{E} / E) / (\bar{\rho} / \rho) = 0.28$  for  $\hat{w}_0 / t = 2$ ,  $m=n=2$ , and  $t / a = 0.003$ , which is 56% of the upper bound; both appear to be fair estimates of the wavy imperfections in the Alporas foam, Fig. 1.

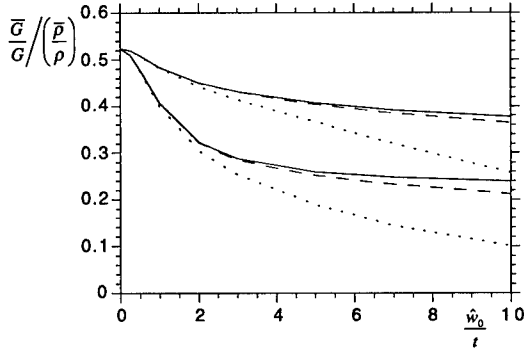


**Fig. 3.** Normalized shear modulus  $(\bar{G} / G) / (\bar{\rho} / \rho)$  versus normalized amplitude of wavy imperfections  $\hat{w}_0 / t$  for the closed cell model foam with  $\nu=0.3$ . Solid line is for  $t/a=0.003$ , dashed

line for  $t/a=0.009$ , and dotted line for  $t/a=0.03$ . The curves with  $m=n=1$  (and  $t/a=0.003, 0.009, 0.03$ ), are above the curves with  $m=n=2$  (and the same  $t/a$ ).

## VI. KELVIN MODEL WITH THICKNESS VARIATIONS

In this Section, the influence of cell wall thickness variations as obtained by Grenstedt and Bassinet [3] are discussed. The model presented in Section IV is used as a reference, and cell wall thickness variations are introduced in this model. The resulting stiffnesses have no bounding properties.

A model as depicted in Fig. 4, which has the volume of 16 of the 14-hedra introduced in Section IV, was chosen as a unit cell for all analysis. This model is then repeated periodically (in three dimensions). There are 112 different cell walls in the unit cell. Each wall has constant thickness  $t_i$ , but all walls may have different thicknesses. The 112 walls were allocated thicknesses randomly, as

$$t_i = t_0(1 + \alpha\varphi_i)c, \quad i = 1, 2, \dots, 112 \quad (7)$$

where the amplitude of the cell wall thickness variation  $\alpha \in (0,1)$  is a real number,  $\varphi_i \in (-1,1)$  is a random number with a uniform distribution, and  $t_0$  is the cell wall thickness of the perfect structure, i.e. when  $\alpha=0$ . Since a random distribution may change the density of the cellular solid (the amount of material within the unit cell), all cell walls were multiplied with a normalizing factor  $c$  to keep the density of the cellular solid constant, independent of the thickness variations.

We omit the details of the analysis, but present the variation of shear modulus with thickness imperfection amplitude  $\alpha$  in Fig. 5. We see that the shear modulus is not very sensitive for cell wall thickness variations in this model. Even for  $\alpha=0.9$ , which means that the thickest cell wall can be 19 times as thick as the thinnest, the shear modulus has only decreased by less than 20%.

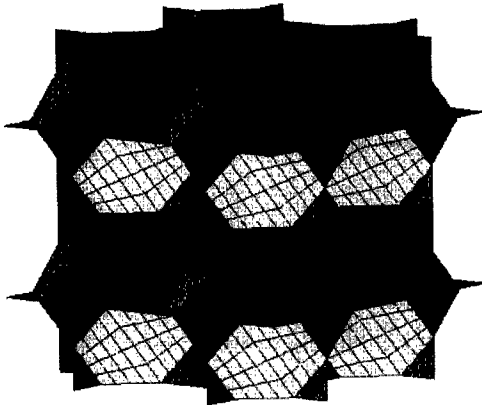


**Fig. 4.** The large flat faced Kelvin bcc foam model. The volume of this model is 16 times that of a single 14-hedron. The model contains 112 different cell walls, which in the imperfect case all have different thicknesses. The model repeats periodically in 3D.

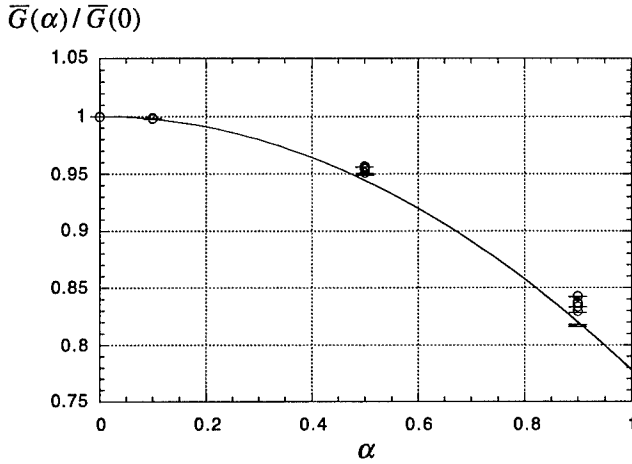


**Fig. 5.** Shear modulus of imperfect foam normalized by shear modulus of perfect foam  $[\bar{G}(\alpha)/\bar{G}(0)]$ . The relative density of the foam is  $\bar{\rho}/\rho = 0.01$ . The solid line is a curve fit,  $\bar{G}(\alpha)/\bar{G}(0) = 1 - (2/9)\alpha^2$ .

## VII. KELVIN MODEL WITH CELL SHAPE VARIATIONS

In this Section, the influence of cell shape variations as obtained by Grenestedt and Tanaka [5] are discussed. The model presented in Section IV is again used as a reference. The cell walls of that model coincide with the boundaries of the Voronoi sets<sup>†</sup> made from points, or "kernels", arranged in a bcc fashion. The non-uniform models were created by moving the kernels in a random fashion, but not letting the movement be more than  $\alpha L$ , where  $\alpha$  is an amplitude of the cell shape non-uniformity, and  $2L$  is the length of the side of the perfect unit cell ( $L$  is also the "diameter" of the perfect 14-hedron, see Fig. 2). Just as in the last Section, periodicity was assumed with 16 cells in the unit cell. In Fig. 6, a 2D cellular solid is generated as a means of demonstrating the procedure. Observe that  $\alpha$  and  $-\alpha$  in general make different cellular solids.

We again omit the details of the analysis, but present the variation of shear modulus with amplitude of the cell shape non-uniformity  $\alpha$  in Fig. 7. We see that the shear modulus is not very sensitive for cell shape variations in this model. Even for  $\alpha=0.5$ , the shear modulus has only decreased by less than 10%.

<sup>†</sup> The Voronoi set  $V^k$  of kernel  $p^k$  is the set of points in space which are closer to  $p^k$  than to any other kernel  $p^l$ , where  $k \neq l$ . Each Voronoi set  $V^k$  (which here is a volume) is convex and encloses only one kernel,  $p^k$ . The boundaries of the Voronoi sets are flat.

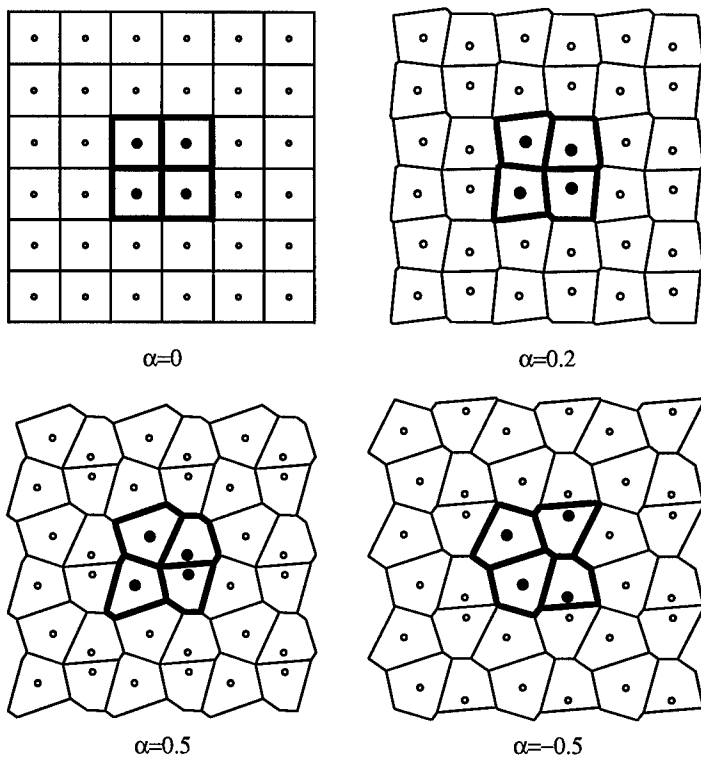


**Fig. 6.** A sequence of 2D cellular solids generated from perturbed kernels. The kernels are marked with circles. The length of a side of a cell is  $L$  in the perfect case ( $\alpha=0$ ). The unit cell contains four cells which are marked with bold lines; its kernels are marked by filled circles. The statistical distribution is the same for all figures, but the amplitude of the cell shape non-uniformity  $\alpha$  varies. In the top row  $\alpha=0$  and  $\alpha=0.2$ , and in the bottom row  $\alpha=0.5$  and  $\alpha=-0.5$ .

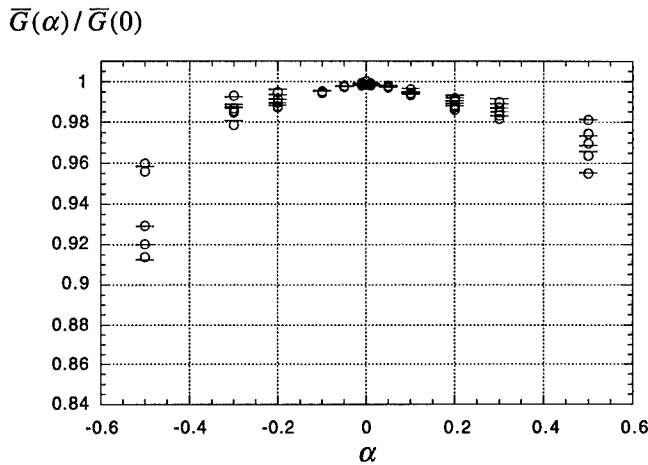


Fig. 7. Shear modulus of imperfect foam normalized by shear modulus of perfect foam  $[\bar{G}(\alpha) / \bar{G}(0)]$ . The relative density of the foam is  $\bar{\rho} / \rho = 0.01$ .

### VIII. CONCLUSIONS

In this paper, the influence of three different kinds of imperfections in the micro geometry of cellular solids were studied. The imperfections were: waviness of cell walls, thickness variations of cell walls, and shape variations of cells. The results from these studies suggest that stiffnesses are most sensitive to cell wall waviness. Cell walls with only moderate wavy imperfections may lead to a knock down by 50% of the stiffnesses of the cellular solid. The insensitivity of stiffnesses to even quite large cell wall thickness variations and cell shape variations is rather remarkable. From micro graphs of Divinycell H130 expanded PVC (which is very stiff) and Alporas aluminum foam (which is much more compliant) it appears that the main difference is cell wall waviness. The cell walls of the PVC foam are more straight than those of the aluminum foam.

### ACKNOWLEDGMENTS

The author gratefully wishes to acknowledge his colleagues who have contributed to the research behind this article. These include, in alphabetical order, Franck Bassinet, Bernard Budiansky, Anthony G. Evans, John W. Hutchinson, Yuki Sugimura, and Kazuto Tanaka.

## REFERENCES

1. Grenestedt, J.L., "Influence of Wavy Imperfections in Cell Walls on Elastic Stiffness of Cellular Solids," *J.Mech.Phys.Solids*, Vol. 46, No. 1, pp. 29-50, 1998.
2. Simone, A.E., Gibson, L.J., "The Effects of Cell Face Curvature and Corrugations on the Stiffness and Strength of Metallic Foams," Dept. of Materials Science and Engineering, MIT, Cambridge, MA 02139, USA, 1997 (*submitted*).
3. Grenestedt, J.L., Bassinet, F., "Influence of Cell Wall Thickness Variations on Elastic Stiffness of Closed Cell Cellular Solids," Dept. of Aeronautics, Royal Institute of Technology, S-100 44 Stockholm, Sweden, 1998 (*submitted*).
4. Van der Burg, M.W.D., Shulmeister, V., Van der Giessen, E., Marissen, R., "On the linear Elastic Properties of Regular and Random Open-Cell Foam Models," *Journal of Cellular Plastics*, Vol. 33, pp. 31-54, 1997.
5. Grenestedt, J.L., Tanaka, K., "Influence of Cell Shape Variations on Elastic Stiffness of Closed Cell Cellular Solids," Dept. of Aeronautics, Royal Institute of Technology, S-100 44 Stockholm, Sweden, 1998 (*in preparation*).
6. Silva, M.J., Gibson, L.J., "The Effects of Non-periodic Microstructure and Defects on the Compressive Strength of Two-dimensional Cellular Solids," *Int. J. Mech. Sci.*, Vol. 39, No. 5, pp. 549-563, 1997.
7. Divinycell, *Technical Manual H Grade*, DIAB, Box 201, S-312 22 Laholm, Sweden, 1995.
8. Akiyama, S., et al., U.S. Patent 4,713,277, Dec. 15, 1987.
9. Thomson, W. (Lord Kelvin), "On the Division of Space with Minimum Partitional Area," *Phil.Mag.*, Vol. 24, No. 151, pp. 503-514, 1887.
10. Kröner, E., "Berechnung der elastischen Konstanten des Vielkristalls aus den Konstanten des Einkristalls," *Zeitschrift für Physik*, Vol. 151, pp. 504-518, 1958.
11. Grenestedt, J.L., "Effective Elastic Behavior of Some Models for "Perfect" Cellular Solids," 1998 (*to appear in Int. J. Solids Struct.*).
12. Hashin, Z., Shtrikman, S., "A Variational Approach to the Theory of the Elastic Behaviour of Multiphase Materials," *J. Mech. Phys. Solids*, Vol. 11, pp. 127-140, 1963.
13. Divinycell, *Technical Manual HT Grade*, DIAB, Box 201, S-312 22 Laholm, Sweden, 1992.
14. Divinycell, *Technical Manual HCP Grade*, DIAB, Box 201, S-312 22 Laholm, Sweden, 1992.
15. Sugimura, Y., Meyer, J., He, M.Y., Bart-Smith, H., Grenestedt, J., Evans, A.G., "On the Mechanical Performance of Closed Cell Al Alloy Foams," *Acta mater.*, Vol. 45, No. 12, pp. 5245-5259, 1997.

## MECHANICAL PROPERTIES OF A STRUCTURAL POLYURETHANE FOAM AND THE EFFECT OF PARTICULATE LOADING

S.H. GOODS\*, C.L. NEUSCHWANGER\* and L.L. WHINNERY\*

\*Sandia National Laboratories, Livermore, CA, 94550

### ABSTRACT

The room temperature mechanical properties of a closed-cell, polyurethane encapsulant foam have been measured as a function of foam density. Tests were performed on both unfilled and filler reinforced specimens. Over the range of densities examined, the modulus of the unloaded foam could be described by a power-law relationship with respect to density. This power-law relationship could be explained in terms of the elastic compliance of the cellular structure of the foam using a simple geometric model found in the literature. The collapse stress of the foam was also found to exhibit a power-law relationship with respect to density. Additions of an aluminum powder filler increased the modulus relative to the unfilled foam.

### INTRODUCTION

Polyurethane foams are used as encapsulants to provide environmental isolation and to mitigate harsh thermal and mechanical shock environments. For the latter application it is necessary to fully characterize the tension and compression properties of the chosen foam system. Historically, a principal constituent of many polyurethane foam systems has been toluene diisocyanate (TDI), a suspect human carcinogen. It is desirable, therefore, to replace such potentially hazardous constituents. To that end, the CRETE foam system (1), which uses non-TDI components was developed and is the subject of the work reported here. The purpose of the current work was three-fold. Our first goal was to measure "quasi-static" tensile and compressive mechanical properties of CRETE, specifically, elastic modulus and compressive collapse stress. A second goal was to relate certain of these properties to the microstructure and density of the foam through simple microstructural models based on cell strut flexure and buckling. Lastly, the effect of a metal powder additive on the modulus of foam was measured and compared to the unloaded foam formulation.

### EXPERIMENTAL

#### Formulation of CRETE Foam System

CRETE is a rigid, closed cell, water blown polyurethane foam. As with other polyurethane foams, reaction of the water with isocyanate produces carbon dioxide that expands the foam so that no physical blowing agents are needed. The density of CRETE foam is varied by changing the amount of added water, thereby controlling the amount of rise in the foam (through the evolution of CO<sub>2</sub>). The amount of catalyst and surfactant can also be varied slightly to optimize processing and foam properties.

CRETE is formulated from the following constituents:

- Voranol 490: A polyether polyol
- Isonate 143L: A modified methylene diisocyanate (MMDI)
- DC193: A silicone glycol copolymer surfactant.
- Polycat 17: A tertiary amine catalyst.
- Distilled water: Added as a chemical blowing agent producing carbon dioxide.

Foam was also processed with additions of a gas-atomized aluminum powder. The powder particles were spherical in shape and had mean diameters in the 2-4  $\mu\text{m}$  range. The powder was added to the polyol and diisocyanate constituents of the foam and then all of the components were mixed together in the usual fashion. SEM revealed that the powder particles were well incorporated into the cell wall and strut structure of the foam.

## Mechanical Testing

Room temperature uniaxial tension and compression mechanical properties were evaluated as a function of foam density. Right circular cylinders, 50.8 mm long and 28.7 mm in diameter, were cored from 20 cm diameter pours of the foam with the cylinder axis parallel to the direction of the foam rise. None of the cored samples included the foam skin or any material from within 3 mm of the surface. These simple right circular cylinders served as the compression specimens. For tension testing, the cylinders were bonded to pull studs. Gauge sections measuring 25.4 mm long and 19.0 mm in diameter were then machined into the foam cylinders. All specimens were instrumented with a mechanically attached extensometer for displacement measurement. The reduced gauge section in the tension specimens insured that failure occurred within the specimen between the attachment points of the extensometer and not at the bondline between the foam and the pull studs. Tests were conducted on specimens having densities between 0.1 g/cm<sup>3</sup> and approximately 0.8 g/cm<sup>3</sup> at an initial strain rate of  $1.7 \times 10^{-4} \text{ s}^{-1}$ .

Modulus,  $E^*$ , as a function of foam density was determined for specimens tested in both tension and compression. An additional parameter for compression testing, the collapse stress,  $\sigma_c^*$ , a broad plateau region subsequent to linear loading, was also determined as a function of density.

## RESULTS AND DISCUSSION

### Modulus and Strength of Foam

The modulus as a function of foam density is shown in Figure 1 for both tension and compression testing. Mechanical properties during the early stages of compression (up to the onset of collapse) are essentially identical to those observed in tension. The modulus of the foam exhibits a power-law dependence with respect to foam density as:

$$E^* \propto (\rho^*)^n \quad (1)$$

where  $E^*$  is the modulus of the foam,  $\rho^*$  is the foam density and  $n$  is the density exponent. Over the range of density shown in Figure 1, the data are well fit for a density exponent of  $n = 1.6$ .

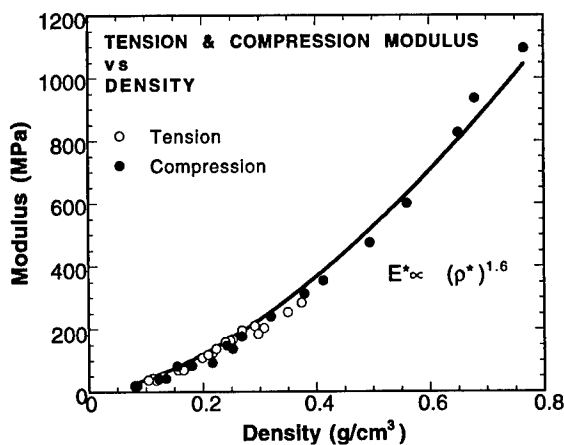


Figure 1. Foam modulus follows a power law behavior with respect to density.

Foam specimens tested in compression show a relatively abrupt change in the initial slope of the loading curve followed by a sustained plateau region. At the lower densities (up to approximately 0.3 g/cm<sup>3</sup>), the stress after the plateau actually drops slightly, giving rise to a yield

point-like behavior. The inset in Figure 2 is typical of this behavior. The broad plateau region results from the collapse or cell wall buckling of the foam (2). The stress begins to increase subsequent to this plateau region as the foam begins to densify. Unlike the tests performed in tension, fracture is inhibited by the absence of tensile stresses and as a result, engineering strains in excess of 90% have been measured with little observable indication of fracture. Figure 2 shows the plateau stress for the foam specimens as a function of density. This plateau stress, also called the collapse stress,  $\sigma_c^*$ , is important in the design of cushions for shock or impact mitigation as it represents the onset of the mechanical instability of the foam microstructure (2). It too, exhibits a power-law dependence with respect to foam density.

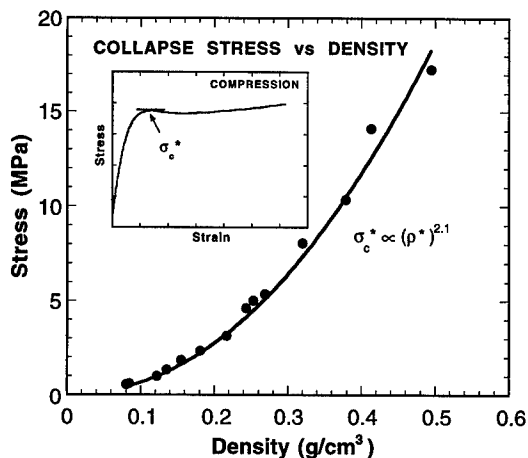


Figure 2. Collapse stress for foam with respect to foam density.

#### Prediction of Modulus and Strength

The dependence of both the modulus and the collapse stress of a cellular foam on density can be understood in terms of the mechanical properties of the polymer material from which the cell struts (and for a closed-cell foam, the cell walls) are made and the deformation mechanics of the cellular structure itself. Elastic moduli are related principally to the bending stiffness of the members comprising the cellular structure while the collapse is caused by the buckling of these same members.

The important cell strut/wall properties are the solid polymer density,  $\rho_s$ , and its modulus,  $E_s$ . The important structural features for the analysis of the modulus and the collapse stress are the relative density of the foam,  $\rho^*/\rho_s$ , (as before,  $\rho^*$  is the density of the foam) and whether or not the cells are open or closed. In this regard a parameter,  $\phi$ , is defined as the fraction of material in the cell struts (2). For an open cell foam,  $\phi = 1$ , while for a closed cell foam, where some of the polymer is in the cell walls, it is less than 1.

The principal mechanism of linear-elastic deformation for foams was first identified correctly by Menges and Knipschild as cell wall bending (3). They also pointed out that open and closed cell foams have similar stiffness because it is the cell wall edges or struts, rather than the thin cell wall membranes, that carry the majority of an imposed load. Ko also identified cell wall bending as the controlling factor in the determination of the modulus but the model presented in that work was complicated by the extremely complex cell geometry (4). Similarly, Patel and Finnie report in great detail the geometrical requirements necessary for various three dimensional structures to fill space (5). They describe how no regular polyhedra can meet all of the requirements for mutually shared edges while satisfying compatibility. The analysis of the mechanics of the cell structures based upon rigorous compatibility leads to intractable mathematics.

A much simplified model of an open cell foam has been put forth by Gibson and Ashby (2,6) in which the foam is modeled as an array of cubic cells which are staggered so that corners of one cell rest upon the midpoint of adjacent cells. Such a structure corresponds neither to the actual geometric characteristics of a real foam nor can it be reproduced to fill space. This "unit cell" does, however, capture the critical physical processes that govern the deformation and structural stability of a cellular structure. In the original analysis, the elastic modulus is found to be governed by the flexure of cell struts normal to an applied load and follows the relationship:

$$\frac{E^*}{E_s} \approx \phi^2 \left( \frac{\rho^*}{\rho_s} \right)^2 + (1-\phi) \frac{\rho^*}{\rho_s} \quad (2)$$

The quadratic term describes the contribution of the cell struts to the modulus and is the same for open cell foams. The linear term accounts for the cell walls. Note that an additional term accounting for internal (atmospheric) gas pressure within the cells is ignored in Equation 2.

The data shown in Figure 1 can be directly compared to Equation 2 using known values for  $\rho_s$ ,  $E_s$  and  $\phi$ . For the density of the solid we use a value of 1.2 g/cm<sup>3</sup> (7). The value for the

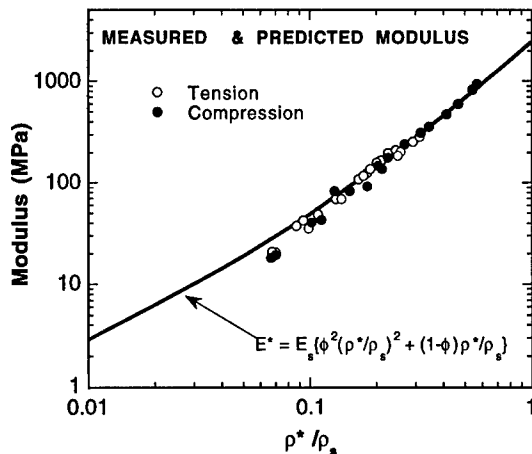


Figure 3. Comparison of modulus measurements to Eq. 2. Note that density is normalized by the density of the solid polymer.

modulus of solid polyurethane is less well established and varies considerably depending on the precise formulation, processing conditions and product form. We use a value within the range of those reported, 2.7 GPa (6,7,8). The last term,  $\phi$ , has been measured for polyurethane foams and found to equal approximately 0.9 (9). Note that in keeping with the form of Eq. 2, the abscissa is now the normalized density,  $\rho^*/\rho_s$ . It is clear from Figure 3 that the model well represents the data over the range of densities examined experimentally, predicting both the absolute values of the modulus as well as its density dependence.

The dependence of the collapse stress on foam density can be examined in a similar fashion. When an axial load is small, the compressed columns that comprise the cell struts parallel to the applied load are laterally stable. However, as the load is increased, these columns become unstable and lateral displacements tend to remain. This instability is termed "lateral buckling" and the applied load necessary to cause it is called the "Euler buckling load". The derivation of the Euler buckling load is a well known problem in mechanics (10) and its application to a foam structure yields a prediction of collapse as (2,6):

$$\frac{\sigma_c^*}{E_s} = C \left( \frac{\rho^*}{\rho_s} \right)^2 \left( 1 + \left( \frac{\rho^*}{\rho_s} \right)^{1/2} \right)^2 \quad (3)$$

The constant  $C$  contains all of the geometric constants and from a comprehensive analysis of the data in the literature, Gibson and Ashby (2,6) have determined that  $C = 0.03$ . Using this value and the same values for  $\rho_s$  and  $E_s$  as used before, we compare the collapse stress measurements in Figure 2 to Equation 3. The results are shown in Figure 4. Notwithstanding the uncertainty in some of the parameters, the agreement between the measured and predicted collapse stress is quite good. As with the modulus, Equation 3 predicts the density dependence of  $\sigma_c^*$  quite well. In this instance, though, the absolute values of the collapse stress are somewhat overestimated by Equation 3.

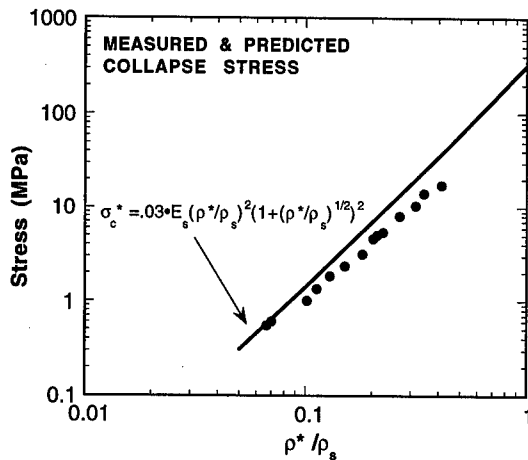


Figure 4. Comparison between the measured collapse stress and Equation 3.

#### Effect of Particle Loading on Modulus

The influence of a rigid filler phase on the modulus of the foam is shown in Figure 5. This Figure compares the original modulus data for CRETE shown in Figure 1 to specimens containing controlled additions of the aluminum powder filler. Note that the original CRETE data is presented as the bold solid line representing the best fit through the data and that the individual data points have been omitted for clarity. The measured moduli for the specimens containing 10 wt.%, 30 wt.% and 50 wt.% are also shown in this Figure. The term,  $\rho^*/\rho_s$  continues to refer to the ratio of the density of the polymer within each specimen to that of solid polyurethane. In this way we can directly compare the effects of Al additions on the modulus at constant relative polymer density.

Because the aluminum powder is well dispersed within the polymer, the foam struts and walls should act as particle-reinforced structural elements. The modulus of such "composite" structures typically depends on the volume fraction of the additive and its modulus relative to that of the host matrix (11,12). Since the modulus of aluminum is approximately 30-times greater than that of the polyurethane in which it is dispersed, we expect, that additions of Al powder would yield a foam with an increased overall modulus.

Figure 5 shows that additions of 10 wt. % or less of the Al filler have no measurable effect on the modulus of the foam. However, higher Al loading fractions do yield specimens with measurably increased moduli. At 30 wt.% loading, the modulus of the filled foam is as much as twice that of the unfilled CRETE. With increasing amounts of aluminum, the modulus continues to increase relative to that of the unmodified foam. At 50 wt. % loading, a three-fold increase in modulus can be realized.

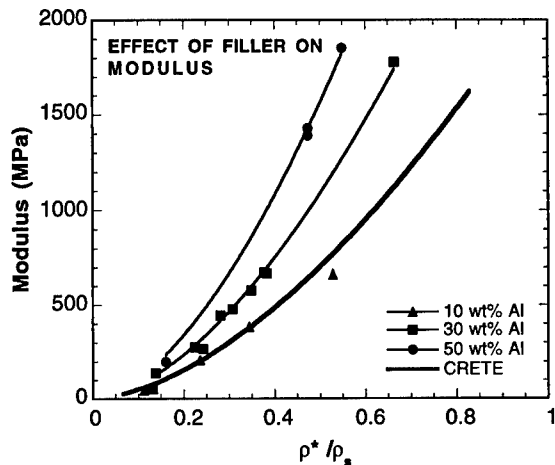


Figure 5. Effect of aluminum powder on modulus of CRETE foam.

## CONCLUSION

The agreement between the measured modulus and the collapse stress with those predicted by Equations 2 and 3 suggests that a model available in the literature (2,6) based on a simple, idealized cell geometry, can be useful in describing certain mechanical and physical properties of foams. The agreement is remarkable in light of the simple cubic unit cell geometry chosen as the basis of the model. While not physically realistic, this cell geometry captures the density dependence of cell strut bending upon which the modulus is dependent and the cell strut buckling upon which the collapse stress of the foam is dependent. Incorporation of a metal powder into the cell structure of the foam increases the overall modulus. This increase can be rationalized in terms of the expected effect of adding a rigid particulate filler phase to a compliant matrix.

## ACKNOWLEDGMENT

This work supported by DOE Contract DE-AC04-94AL85000. SEM analysis of the aluminum loaded foams was conducted by N. Y. C. Yang.

## REFERENCES

1. S. H. Goods, C. L. Neuschwanger, C. Henderson and D.M. Skala, "Mechanical Properties and Energy Absorption Characteristics of a Polyurethane Foam", SAND97-8490, Sandia National Laboratories, (1997)
2. L. J. Gibson and M. F. Ashby, *Proc. Roy. Soc.*, A382 (1982), p. 43
3. G. Menges and F. Knipschild, *Polymer Engineering Science*, 15 (1975), p. 623.
4. W. L. Ko, *J. Cell Plastics*, 1 (1965), p. 45.
5. M. R. Patel and I. Finnie, *J. Mater.*, 5 (1970), p. 909.
6. L. J. Gibson and M. F. Ashby, *Cellular Solids. Structure and Properties* (New York, N.Y., Pergamon Press, 1988).
7. D. W. Reitz, M. A. Schuetz and L. R. Glicksman, *J. Cell. Plast.*, 20 (1984), p. 104.
8. *PLASTICS DIGEST*, 10, (D.A.T.A. Business Publishing), p. 1301-1304.
9. W. F. Roff and J. R. Scott, *Fibres, Films, Plastics and Rubbers-A Handbook of Common Polymers*, (London, Butterworths, 1971), p. 455.
10. W. A. Nash, *Strength of Materials, 3rd Ed.*, Schaums Outline Series, (New York, N.Y., McGraw-Hill, Inc., 1994)
11. E. H. Kerner, *Proc. Phys. Soc. (B)*, 69, 808 (1956).
12. T. B. Lewis and L. E. Nielson, *J. Appl. Polymer Sci.*, 14, (1970), p.1449

---

## NUMERICAL MODELLING OF THE STRENGTH OF HIGHLY POROUS AERATED AUTOCLAVED CONCRETE

Thomas Schneider\*, Georg Schober\*\* and Peter Greil\*

\*University of Erlangen–Nuernberg, Department of Materials Science, Glass and Ceramics,  
Martensstraße 5, D-91058 Erlangen, Germany

\*\*Hebel AG, Materialtechnische Entwicklung, Postfach 1353, D-83343 Fürstfeldbruck, Ger-  
many

### Abstract

Highly porous building materials like aerated autoclaved concrete are characterized by low thermal conductivity and high mechanical strength, which both strongly depend on porosity. The influence of porosity distribution on the compressive strength of aerated autoclaved concrete was investigated by using finite element analysis and multiaxial Weibull theory. Calculations of failure probability of microstructures with ordered as well as random pore configurations show a dependence of compressive strength on the Weibull modulus of the matrix material and the size and arrangement of pores. The results of the calculations are compared to experimental data of aerated autoclaved concrete.

### 1 Introduction

The use of autoclaved aerated concrete (AAC) in constructions requires a high mechanical strength but thermal conductivity. In the production process of AAC a hierarchical pore structure is introduced [1]: i.) inter particle pores (IPP) with a pore size of  $10^{-8}$  to  $10^{-6}$ m, ii.) inter cluster pores (ICP) with a mean pore size of about  $10^{-5}$ m and iii.) artificial air pores (AAP) with a pore size of  $0.5 \cdot 10^{-3}$  to  $3 \cdot 10^{-3}$ m. The AAP are introduced by the formation of  $H_2$  by chemical reaction between Al and  $Ca(OH)_2$  within the mass during plastic state [2].

The geometrical density of AAC is controlled by the portion of AAP, which leaves the portion of IPP without a significant change and leads to a slight variation in the portion of ICP. The density of commercial AAC varies in a range of 200–1000 kg/m<sup>3</sup> [3], with compressive strength varying from 3 to 15 MPa in a density range from 400 to 800 kg/m<sup>3</sup>.

The microstructure of AAC should be considered on two levels: The first level represents the structure of the matrix material on a microscopic scale. The second level represents the arrangement of the AAP on a macroscopic scale. Taking this hierarchical microstructure of AAC into account, stress distribution in AAC under an external load is mainly dominated by the distribution of AAP. While IPP and ICP are more than two decades smaller than AAP, the short range stress field surrounding the IPP and ICP is supposed to be unperturbed compared to the long range stress field caused by the AAP. The matrix material is treated as homogeneous and isotropic referring to mechanical properties. Three point bending test data of the matrix material can be fitted using a Weibull distribution with the parameters  $m = 8.4$  and  $\sigma_0 = 6.1$ , figure 1.

It is the aim of the present work to investigate the strength porosity relationship in highly porous AAC materials. Stress distribution was calculated using a finite element approach.

The failure probability of the porous microstructure was analysed by the extended weakest link model developed by Batdorf et al. [4].

## 2 Calculations

The AAP in AAC can sufficiently be approximated by spherical pores. For random pore configurations with monomodal or multimodal pore radii the pores are distributed in a given area by generating random coordinates using a random number routine. Intersection of pores with other pores and the edge of the area are not allowed. Pore coordinates are generated until the appropriate pore volume fraction is reached. For calculations with random pore configuration and multimodal pore size a Gauss distribution is assumed for representing the AAP.

The finite element analysis code MARC is used for stress calculations, using six node two dimensional plain strain triangles. In consequence the models represent porous bodies containing parallel cylindrical holes. The kinematic constraints create repetitive unit cells. The material parameters used for the stress calculation are a Young's-modulus of 7250 MPa and a Poisson's ratio of 0.2, as it is found in commercially used AAC materials.

The failure probability is derived from the extended weakest-link model developed by Batdorf et al. [4, 5]. Using fracture mechanics an equivalent mode I stress intensity factor  $K_{Ieq}$  is introduced to summarize the effect of mixed-mode loading on flaws in a multiaxial stress field, with  $a$  as crack size,  $Y_I$  as the geometric correction factor and  $\sigma_{eq}$  as the equivalent stress:  $K_{Ieq} = \sigma_{eq} \cdot \sqrt{a} \cdot Y_I$ . In this investigation only mode I failure of volume flaws is assumed. Failure of the matrix material occurs if the size of a flaw exceeds a critical value  $a_c$  depending on the orientation  $\omega$  and the location  $\mathbf{x}$  of the flaw. Using Weibull theory, the probability  $P_a$  that the size of a given flaw exceeds the critical value  $a_c$  can be written as

$$\int_{a_c(\mathbf{x},\omega)}^{\infty} f_a(a) da = \left( \frac{\sigma_{eq}(\mathbf{x},\omega)}{\tau_0} \right)^m \quad (1)$$

where  $m$  and  $\tau_0$  depend on the strength and the statistical properties of the material.

The assumption that the matrix material of AAC is homogeneous and isotropic implies, that uniform distributions are used for the scatter of the location  $\mathbf{x}$  and orientation  $\omega$  of the flaw. The probability that a flaw has the location  $\mathbf{x}$  and the orientation  $\omega$  is  $P_{\mathbf{x}} = \frac{1}{V} dV$  and  $P_{\omega} = \frac{1}{4\pi} d\Omega$ , respectively. The probability that the size of one flaw exceeds the critical value  $a_c$  depending on  $\mathbf{x}$  and  $\omega$  is obtained by multiplying  $P_{\mathbf{x}}$ ,  $P_{\omega}$  and  $P_a$  and integrating over all possible locations and orientations.

As the number of flaws in  $V$  is a random variable described by a Poisson's distribution the failure probability can finally be obtained by [6]

$$P_f = 1 - \exp \left[ - \frac{1}{V_0} \int_V \frac{1}{4\pi} \int_{\Omega} \left( \frac{\sigma_{eq}}{\sigma_0} \right)^m d\Omega dV \right] \quad (2)$$

where  $\sigma_0$  and  $m$  are material parameters. In this investigation the characteristic strength of the porous material is characterized by the applied stress, which is needed to achieve an over all failure probability of  $P_f = 0.632$  ( $P_f = [1 - (1/e)]$ ).

The integration in equation 2 is done by using a post processor for calculation of the failure probability of multiaxial loaded ceramic components called STAU [7].

### 3 Results

The normalized strength  $\sigma^* = \sigma_D / \sigma_{D(d^*=1)}$  of a unit cell containing two pores as a function of the normalized center to center pore distance  $d^* = d_{C-C} / r_{\text{pore}}$  is shown in figure 2. The external load is tension in global y-direction.

The strength pore-distance relationship of the two pore configuration remains unaffected by  $m$  until a normalized pore distance of  $d^* = 4$  is reached. From  $d^* = 4$  to  $d^* = 2$  the strength decreases. The higher the Weibull parameter  $m$  the stronger the decrease of the strength. The corresponding increase of the normalized stress  $\sigma_y^* = \sigma_y / \sigma_{y(d^*=1)}$  (at point A) with decreasing pore distance  $d^*$  is shown in figure 2.

Pores with monomodal pore radii are used to calculate the influence of pore size on the strength of a multipore structure. Two pore volume fractions of  $f_p = 0.1$  and  $f_p = 0.4$  are considered, with the normalized pore radii  $r^* = r_{\text{pore}} / r_{\text{pore,min}}$  being varied from of 1 up to 6.7. While pore size was kept constant the Weibull parameter  $m$  was changed. The left plot in figure 3 shows the  $\sigma^* - r^*$  relationship for  $f_p = 0.1$  with  $\sigma^*$  remaining almost unaffected by increasing  $r^*$ . For all Weibull parameters used, the variation of  $\sigma^*$  is in a range of 0.05. A different behaviour, however, is observed at higher porosities. The right plot in figure 3 shows similar calculation for  $f_p = 0.4$  where  $\sigma^*$  increases with  $r^*$ .

Stereological analysis show a Gauss distribution for AAP in AAC [8]. A mean deviation of  $s = 0.2$  and a mean pore size of  $\bar{r}^* = 0.5$  are used for the calculation with random pore configurations. The pore radii vary in a range of  $\bar{r}^* = 0.1$ . Figure 4 shows the normalized strength  $\sigma^* = \sigma_D / \sigma_{D,f_p=0.18}$  plotted vs. pore volume fraction  $f_p$ . The dashed line in figure 4 gives an exponential function of the form  $\sigma = C \cdot e^{-B \cdot f_p}$  with  $C = 2.2$  and  $B = 4.5$ , which fits the calculated data. The experimental data (open circles) is derived from compression tests on 120x120x150mm specimens of AAC material with varying porosity.

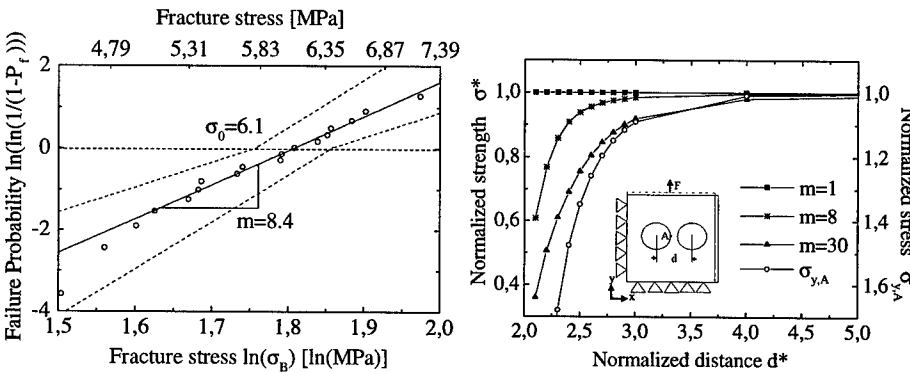


Figure 1: Three point bend test data of  $40 \times 40 \times 160 \text{ mm}^3$  specimens of the matrix material of AAC. The Weibull parameter is  $m = 8.4$  and  $\sigma_0 = 6.1$ . The dashed lines represent the 90% confidence interval.

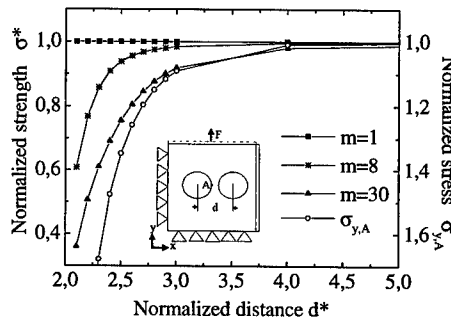


Figure 2: Normalized strength  $\sigma^*$  and normalized stress  $\sigma_{y,A}$  at point A of a two pore configuration vs. the normalized distance  $d^*$ . The external load is tension in global y-direction.

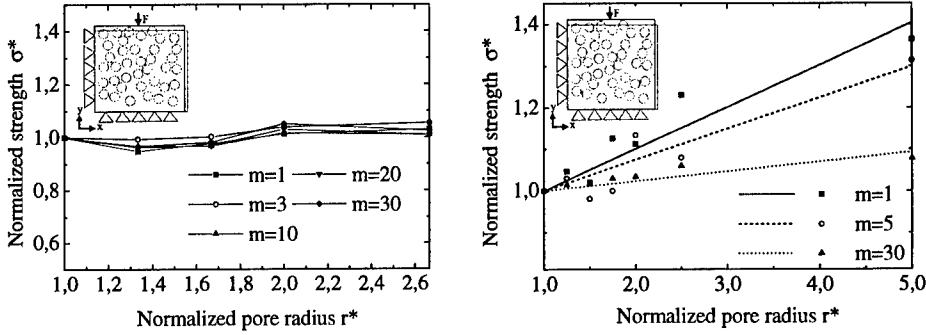


Figure 3: Normalized strength  $\sigma^*$  as a function of normalized pore radius  $r^*$  for a pore volume fraction of  $f_P = 0.1$  (left) and  $f_P = 0.4$  (right). The strength is normalized on the strength at  $r^* = 1$ . The lines in the right figure ( $m = 1$ : solid,  $m = 5$ : dashed,  $m = 30$ : dotted) give the linear regression of the calculated values (lines with symbols).

## 4 Discussion

The aim to predict the decrease with increasing porosity resulted in a variety of equations for the strength porosity relationships [9, 10]. Three typical equations to predict the strength  $\sigma_D$  as a function of porosity  $f_P$  are

$$\sigma_D = \sigma_{D_0}(1 - f_P)^A, \quad \sigma_D = \sigma_{D_0} \cdot e^{-B \cdot f_P} \quad \text{and} \quad \sigma_D = -\frac{\sigma_{D_0}}{n} \cdot \log \frac{f_P}{f_{P,cr}} \quad (3)$$

derived by Balshin [11], Ryshkewitch [12] and Schiller [13], respectively.  $\sigma_{D_0}$  is the strength of the fully dense material ( $f_P = 0$ ),  $A$ ,  $B$  and  $n$  are constants,  $f_{P,cr}$  is the porosity at which the strength completely disappears. The strength porosity relationship is predicted assuming the strength of the matrix material to be constant over the entire porous body. As Brezny and Green [10] pointed out, this only holds for non brittle materials.

The results of the calculations on the two pore model show that the stress concentration, and in consequence the strength, is a function of the inter pore distance and the Weibull parameter  $m$ . The  $\sigma^* - d^*$  relationship for the Weibull parameter  $m = 4.30$  of the two pore model can be expressed by the relation

$$\sigma^* = A_1 + A_2 \cdot e^{-k(m) \cdot d^*} \quad (4)$$

with  $k$  as a function of  $m$ ,  $A_1 = 1$  and  $A_2 = 50$ . The dependence of the  $k$ -value on  $m$  can be fitted by  $k = B_1 + B_2 \cdot e^{-l \cdot m}$  with  $B_1 = 2.1$ ,  $B_2 = 20$  and  $l = -0.5$ . The pore distances, which yield a decrease of normalized strength  $\Delta\sigma^*$  of  $\Delta\sigma^* = 0.1$ ,  $d_{0.1}^*$ , and  $\Delta\sigma^* = 0.01$ ,  $d_{0.01}^*$ , respectively, were calculated for varying Weibull parameter  $m$ , figure 5. For a Weibull parameter  $m = 8.4$  of the matrix material of AAC, a  $d_{0.1}^*$  of 2.6 and a  $d_{0.01}^*$  of 3.6 are obtained respectively. While the stressed volume increases with pore radius, the number of pores at a fixed porosity will decrease with increasing pore size. The equation used by Le Roy [14] to predict the porosity pore distance relationship can be solved for the porosity  $f_P$ :

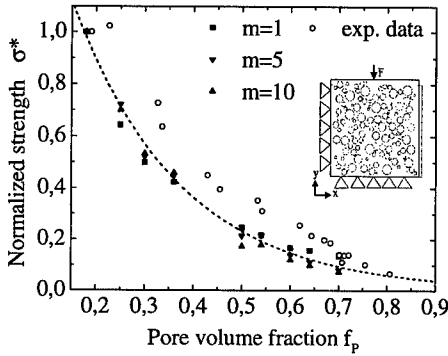


Figure 4: Exponential fit (dashed line) of calculated strength (filled symbols) compared to experimental data (open circles) of AAC.

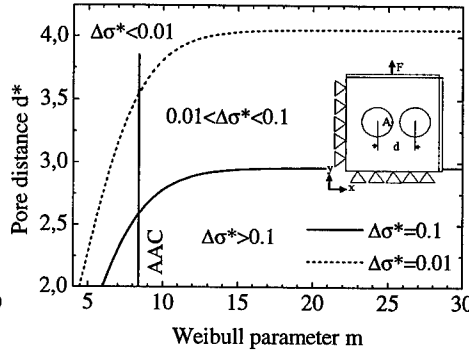


Figure 5: Normalized center to center pore distance  $d^*$  yielding a decrease of strength of the two pore model of 0.1 (solid line) and 0.01 (dashed line) depending on  $m$ .

$f_P = (1/d^*)^2 \cdot 3/2 \cdot \pi$ . Using  $d_{0.01}^*$  and  $d_{0.1}^*$  as calculated for the matrix material of AAC the corresponding porosities  $f_{P,0.1}$  and  $f_{P,0.01}$  are  $f_{P,0.1} = 0,69$  and  $f_{P,0.01} = 0,36$ .

In consequence a significant influence of the pore size distribution on strength will occur at a porosity higher than at least 0.36. For lower porosities the stress concentration is equivalent to that of isolated pores, what ever their size.

As porosity increases, the pores approach each other and the stress concentration factor and the stressed volume will depend on both, the pore radii and the center distance of the pores. The results in figure 3 for  $f_P = 0.4$  suggest a strong influence of the Weibull parameter  $m$  on the  $\sigma^* - r^*$  relationship. The corresponding normalized slopes  $a^* = a/a_{m=30}$  of the linear fits of the  $\sigma^* - r^*$  relationships for  $f_P = 0.4$  depend on the Weibull parameter  $m$ :  $a^* = e^{(-0.05 \cdot m + 1.5)}$ . The  $m$ -value of 8.4 of the matrix material of AAC yields a slope of  $a = 0.07$ . In consequence a five times greater pore radius yields an increase of normalized strength of 0.28 for AAC.

## 5 Conclusions

The finite element calculations show that interaction of stress field surrounding pores in loaded AAC is likely to occur at a porosity of about 0.3. For AAC with lower porosity the parameters of the pore size distribution are supposed to have no influence on the strength of AAC. In consequence, a higher  $\sigma_0$  value of the matrix material is of particular importance to improve the strength of AAC with low porosity. The calculations for highly porous AAC show that the strength of AAC can be improved by increasing the size of the AAP.

---

## References

- [1] Prim, P. and Wittmann, F.H.: Structure and Water Absorbition of Aerated Concrete. In *Autoclaved Aerated Concrete, Moisture and Properties*, eds. Wittmann, F.H. Elsevier, Amsterdam, 1983, P. 55–69.
- [2] Grundlach, H.: *Dampfgehärtete Baustoffe*, Bauverlag GmbH, Wiesbaden und Berlin, 1973.
- [3] Aroni, S., Groot, G.J., Robinson, M.J., Svanholm, G. and Wittman, F.H.: *Rilem Recommended Practice: Autoclaved Aerated Concrete, Properties, Testing and Design*, Chapman & Hall, London, 1993.
- [4] Batdorf, S.B. and Crose, J.G.: A Statistical Theory for the Fracture of Brittle Structures Subjected to Nonuniform Stress, *Journal of Applied Mechanics* 41 (1974) P. 459–461.
- [5] Batdorf, S.B.: Fundamentals of the Statistical Theory of Fracture. In *Proceedings of the International Symposium on Fracture Mechanics of Ceramics*, eds. Bradt, R.C., Hasselman, D.P.H and Lange, F.F. Plenum Press New York, 1989, P. 1–30.
- [6] Thiemeier, T., Brückner-Foit, A. and Kölker, H.: Influence of the Fracture Criterion on the Failure Prediction of Ceramics Loaded in Biaxial Flexure, *Journal of the American Ceramic Society* 74 (1991) P. 48–52.
- [7] Heger, A.: *Bewertung der Zuverlässigkeit mehrachsiger belasteter keramischer Bauteile*, Phd-thesis, University of Karlsruhe, 1993.
- [8] Schober, G.: Effect of Size Distribution of Air Pores in AAC on Compressive Strength. In *Proceedings of the 3rd Rilem International Symposium on Autoclaved Aerated Concrete, Zürich, Switzerland*, eds. Wittmann, F.H. A.A. Balkema Publishers Rotterdam, 1992, P. 77–80.
- [9] Rice, R.W. and Grace, W.R.: Evaluation and Extension of Physical Property-Porosity Models based on Minimum Solid Area, *Journal of Material Science* 31 (1996) P. 102–118.
- [10] Brezny, R. and Green, D.: Mechanical Behaviour of Cellular Ceramics, In *Materials Science and Technology*, eds. R.W. Cahn, P. Haasen, E.J. Kramer, vol. 11, Structure and Properties of Ceramics, volume editor: M.S. Swain, VCH Weinheim, 1994, P. 465–516.
- [11] Balshin, Y.: Relation of Mechanical Properties of Powder Metals and their Porosity and the Ultimate Properties of Porous Metal–Ceramic Materials, *Dokl. Akad. Nauk. SSSR* 67 (1949) P. 831–834.
- [12] Ryshkewitch, E.: Compression Strength of Porous Sintered Alumina and Zirconia, *Journal of the American Ceramic Society* 36, No.2 (1953) P. 65–68.
- [13] Schiller, K.K.: Porosity and Strength of Brittle Solids (with Particular Reference to Gypsum). In *Mechanical Properties of Non-Metallic Brittle Materials*, eds. Walton, W.H. Buittenworth Sc. Publ., London, 1958, P. 35–49.
- [14] Le Roy, G., Embury, J.D., Edwards, G. and Ashby, M.F.: A Model of Ductile Fracture Based on the Nucleation and Growth of Voids, *Acta Metall.* 29 (1981) P. 1509–1522.

---

## MODELING OF FATIGUE FOR CELLULAR MATERIALS

J. S. Huang\* and J. Y. Lin\*\*

\*Professor, \*\*Ph.D. candidate.

Dept. of Civil Engineering, National Cheng Kung University,  
Tainan, 70101 Taiwan.

### ABSTRACT

Dimensional arguments are used to analyze the fatigue of cellular materials. A modeling describing the fatigue of foams with or without macrocrack is derived and compared to the existing experimental data of cementitious foams and phenolic foams; agreement is good.

### INTRODUCTION

Cellular materials are increasingly being used as load-bearing components in lightweight structures. The fatigue failure of cellular materials might lead to a catastrophic fracture of the lightweight structures. The fatigue macrocrack propagation rate of rigid polyurethane foam was obtained by Noble [1,2]. Yau and Mayer [3] studied the fatigue resistance of a glass-reinforced rigid polycarbonate foam. Tsai and Ansell [4] gave a review of the wood fatigue literature and measured the flexural fatigue properties of various woods. Fatigue properties of laminated wood were presented by Bonfield and Ansell [5]. Elastic properties of foams were described well by a bending model of cell walls proposed by Gibson and Ashby [6]. In the paper, the expression for crack propagation rate of foams with a macrocrack is derived by using dimensional arguments analysis. It is assumed that the macrocrack advances one cell size when the first unbroken cell wall ruptures after some cycles of loading. Theoretical modeling of foams is compared to existing experimental data of phenolic foams [6]. Also, the modeling for foams without any macrocrack is presented and compared to experimental data of cementitious foams [7].

FOAMS WITHOUT MACROCRACK

The model used to study the fatigue of cellular materials without any macrocrack is shown in Figure 1. If the fatigue behavior of the solid cell wall material is governed by the Basquin law:

$$\Delta\sigma(N_f)^\alpha = C_1 \tag{1}$$

where  $N_f$  is the number of cycles to failure,  $\Delta\sigma$  is the cyclic stress range, and  $\alpha$  and  $C_1$  are material constants. Since the relative density of the foam (the ratio of its density  $\rho^*$

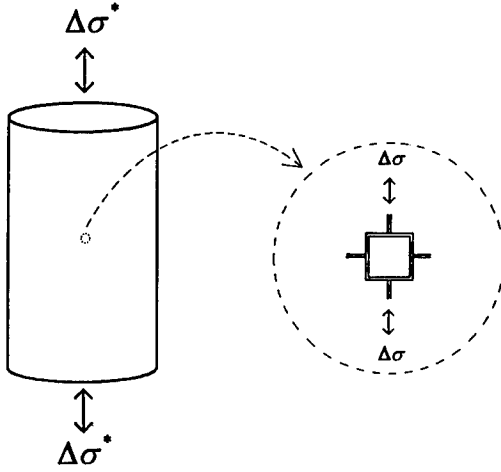


Fig. 1 Foams without macrocrack under a cyclic stress range.

to that of the cell wall materials  $\rho_s$ ) is proportional to  $(t/l)^2$ , the cyclic stress range applied on the foam  $\Delta\sigma^*$  is related to the cyclic stress range exerted on the solid cell walls:

$$\Delta\sigma^* \propto \Delta\sigma \left( \frac{\rho^*}{\rho_s} \right)^y \tag{2}$$

It is assumed that the foam will fail when one of the solid cell walls ruptures after some cycles of loading; that is  $N_f^*$

$=N_f$ . Then, the fatigue of foam without macrocrack is:

$$\Delta\sigma^* \left( N_f^* \right)^\alpha = g_0 \left( \frac{\rho^*}{\rho_s} \right)^\gamma \quad (3)$$

where  $g_0$  is a microstructure coefficient and can be determined experimentally.

#### FOAMS WITH MACROCRACK

A foam with a central macrocrack  $a^*$  is under a cyclic stress range  $\Delta\sigma^*$  as shown in Figure 2. The induced bending moment exerted at the first unbroken cell wall will cause fatigue failure. The number of cycles to failure of the first unbroken cell wall depends on the existence of microcracks within it and the magnitude of applied cyclic stress. Therefore, three cases of foams are of concern: microcrack propagation, high cycle fatigue and low cycle fatigue.

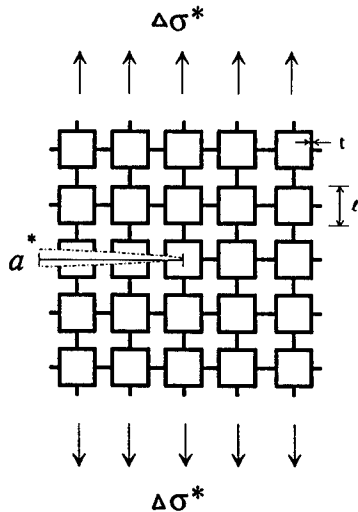


Fig. 2 Foams with a macrocrack under a cyclic stress range.

It is assumed that the microcrack propagation rate of the solid cell walls is described well by Paris law:

$$\frac{da}{dN} = A(\Delta K_I)^m \quad (4)$$

where A and m are material constants and  $\Delta K_I$  is the cyclic stress intensity range. By using dimensional arguments analysis, the cyclic concentrated force range per unit thickness of the first unbroken cell wall is found to be:

$$\Delta P \propto \Delta \sigma^* \left(\frac{\ell}{t}\right) \sqrt{a^*} \ell \quad (5)$$

Then, the macrocrack growth per cycle of the foam:

$$\frac{da^*}{dN^*} = \frac{\ell}{N_f} = g_1 A \ell (m-2) a^{m/2-1} \left[ \frac{1}{\sqrt{\pi \ell}} \left(\frac{\rho^*}{\rho_s}\right)^{-3/2} \right]^m (\Delta K_I^*)^m = A_1^* (\Delta K_I^*)^m \quad (6)$$

Here  $g_1$  is a microstructure coefficient of the foam and must be determined empirically.

When the first unbroken cell wall without any microcrack, the fatigue life of a foam can be derived from Basquin law for solid cell wall. The cyclic elastic stress range acting at the first unbroken cell wall is found to be:

$$\Delta \sigma \propto \frac{\Delta M}{t^3} \propto \frac{\Delta \sigma^* \ell^2 \sqrt{a^*} \ell}{t^3} \quad (7)$$

The number of cycles to failure of the first unbroken cell wall, at which the macrocrack advances one cell size, is given:

$$N_f \propto \left[ \frac{C_1 \sqrt{\pi \ell}}{\Delta K_I^*} \left(\frac{t}{\ell}\right)^3 \right]^{1/\alpha} \quad (8)$$

Hence, the macrocrack growth rate of the foam is:

$$\frac{da^*}{dN^*} = \frac{\ell}{N_f} = g_2 \ell \left[ \frac{1}{C_1 \sqrt{\pi \ell}} \left(\frac{\rho^*}{\rho_s}\right)^{-3/2} \right]^{1/\alpha} (\Delta K_I^*)^{1/\alpha} = A_2^* (\Delta K_I^*)^{1/\alpha} \quad (9)$$

where  $g_2$  is another microstructure coefficient of foams.

Under higher cyclic stresses, the first unbroken cell wall will deform plastically and eventually lead to low cycle fatigue. Coffin-Manson law is then employed to describe the fatigue of solid cell walls:

$$\Delta \varepsilon^P \ell (N_f)^\beta = C_2 \quad (10)$$

The stress-strain curve of solid cell walls can be represented by the equation of  $\sigma = k \varepsilon^n$ ;  $K$  and  $n$  are both material constants. Consequently, the cyclic plastic strain range acting at the first unbroken cell wall can be expressed as:

$$\Delta \varepsilon^P \ell = \left( \frac{\Delta \sigma}{k} \right)^{1/n} \propto \left( \frac{\Delta M}{k t^3} \right)^{1/n} \propto \left( \frac{\Delta \sigma^* \ell^3}{k t^3} \sqrt{\frac{a^*}{\ell}} \right)^{1/n} \quad (11)$$

The number of cycles to failure of the first unbroken cell wall is found to be:

$$N_f = \left( \frac{C_2}{\Delta \varepsilon^P \ell} \right)^{1/\beta} \propto \left[ \frac{C_2 \sqrt{\pi \ell}}{\Delta K_I^*} k \left( \frac{t}{\ell} \right)^3 \right]^{1/n\beta} \quad (12)$$

Then, the macrocrack growth rate of the foam is:

$$\frac{da^*}{dN^*} = \frac{\ell}{N_f} = g_3 \ell \left[ \frac{1}{C_2 k \sqrt{\pi \ell}} \left( \frac{\rho^*}{\rho_s} \right)^{-3/2} \right]^{1/n\beta} (\Delta K_I^*)^{1/n\beta} = A_3^* (\Delta K_I^*)^{1/n\beta} \quad (13)$$

Here  $g_3$  is also a microstructure coefficient of foams.

Based on the experimental result on fatigue of cementitious foams without any macrocrack presented by Huang [7], equation (3) describes well the fatigue of cementitious foams:

$$\Delta \sigma^* (N_f^*)^{0.034} = 118 \left( \frac{\rho^*}{\rho_s} \right)^{3.6} \quad (14)$$

Also, the experimental data on fatigue of phenolic foams [6]

are compared with the theoretical modeling. Equation (9) can be rearranged as:

$$\log(\Delta K_I^*) = \alpha \log\left(\frac{da^*}{dN^*}\right) + \frac{3}{2} \log\left(\frac{\rho^*}{\rho_s}\right) - \log\left(\frac{g_2 \alpha \ell^\alpha}{C_1 \sqrt{\pi \ell}}\right)^{1/\alpha} \quad (15)$$

The dependence of the cyclic stress intensity range, required to give the same macrocrack growth rate for three relative density phenolic foams, on relative density is 3/2 [8], coinciding with the exponent of the relative density term in equation (15).

The existing experimental data on cementitious foams and phenolic foams support the modeling we proposed.

#### CONCLUSIONS

A modeling describing the fatigue of cellular materials has been derived. Theoretical modeling of foams is compared to existing experimental data of cementitious foams and phenolic foams; the agreement is good. Results show that fatigue of cellular materials depends on the cyclic stress range, macrocrack size, the cell geometry and relative density of cellular materials, and the fatigue parameters of the solid materials from which they are made.

#### REFERENCES

1. F.W.Noble and J. Lilley, *J. Mater. Sci.* **16**, 1801 (1981).
2. F.W. Noble, *J. Mater. Sci.* **18**, 1827 (1983).
3. S. S. Yau and G. Mayer, *Mater. Sci. Engng.* **78**, 111 (1986).
4. K. T. Tsai and M. P. Ansell, *J. Mater. Sci.* **25**, 865 (1990).
5. P. W. Bonfield and M. P. Ansell, *J. Mater. Sci.* **26**, 4765 (1991).
6. L. J. Gibson and M. F. Ashby, *Cellular Solid: Structures and Properties*, Pergamon Press, Oxford (1988).
7. Z. H. Huang, MS thesis, Department of Civil Engineering, National Cheng Kung University, (1997).
8. J. S. Huang and J. Y. Lin, *Acta Mater.* **44**, 289 (1996).

## ANALYSIS OF DEFORMATION OF POROUS METALS

Dong Nyung Lee\*, Heung Nam Han\*\*, Kyu Hwan Oh\* and Hyoung Seop Kim\*\*\*

\*Division of Materials Science and Engineering, Seoul National University, Seoul 151-742, Korea, dnlee@snumfc.snu.ac.kr

\*\*Sheet Products & Process Research Team, Technical Research Laboratories, Pohang Iron & Steel Co., Ltd., Pohang P.O. Box 36, Kyungbuk, 790-785, Korea

\*\*\*Department of Metallurgical Engineering and Rapidly Solidified Material Research Center, Chungnam National University, Taejeon, 305-764, Korea

### ABSTRACT

The elasto-plastic finite element method using a yield criterion advanced by Lee and Kim was employed to analyze the effect of indenting geometry on the Brinell hardness of sintered porous copper specimens with various densities. The changes in geometry of porous iron rings with various initial relative densities were also calculated for various friction coefficients between the metal rings and compression platens. The calculated hardness values were in very good agreement with the measured data. The friction coefficient could be determined from the relationship between the change in the inner diameter and height reduction of porous metal rings with various initial relative densities.

### INTRODUCTION

The elastic-plastic deformation of porous metals is affected by the internal pores. Yield criteria which take the pore effect into account are necessary to analyze the elastic-plastic behavior of porous metals. Yield criteria for the porous metals have been advanced by many investigators[1-6]. Most of them [1-5] unreasonably suggested zero yield stress only at zero relative density. Lee and Kim [6] modified a yield equation suggested by Doraivelu *et al.* [4] so that it incorporated only one experimental parameter estimated from yield stress vs. initial relative density data. The modified yield condition for porous metals is given by

$$(2 + R^2)J_2' + (1 - R^2)J_1^2/3 = \eta Y_0^2 \quad (1)$$

where  $\eta = Y_R^2/Y_0^2 = [(R - R_c)/(1 - R_c)]^2$

$$J_2' = \frac{1}{6} [(\sigma_{11} - \sigma_{22})^2 + (\sigma_{22} - \sigma_{33})^2 + (\sigma_{33} - \sigma_{11})^2] + \sigma_{12}^2 + \sigma_{23}^2 + \sigma_{31}^2$$

$$J_1 = \sigma_{11} + \sigma_{22} + \sigma_{33}$$

$J_2'$  and  $J_1$  are the second deviatoric stress invariant and the first stress invariant, respectively.  $Y_R$  is the yield stress of the porous metal with the relative density  $R$ , and  $Y_0$  is the yield stress at  $R = 1$ . For work hardening metals,  $Y_R$  and  $Y_0$  are the flow stresses of the porous and non-porous metals, respectively.  $R_c$  is an experimental parameter and may be interpreted as a critical relative density at which the yield stress of porous metal becomes zero; that is,  $Y_R = 0$  at  $R = R_c$ . For non-porous metals,  $R = 1$  and  $Y_R = Y_0$ , Eqn. (1) becomes the von Mises yield criterion.

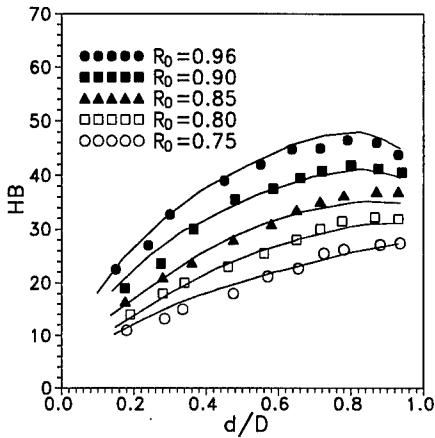


Fig. 1 Relationship between Brinell hardness and diameter ratio  $d/D$ . Symbols indicate measured data [12] and curves indicate calculated values.

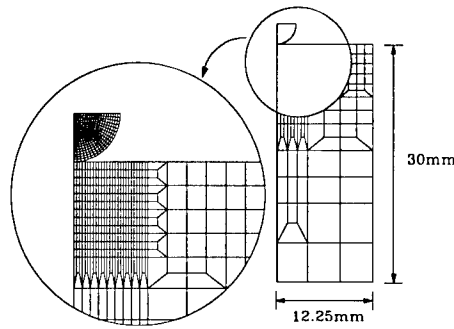


Fig. 2. Initial mesh for analysis of indenting.

Elasto-plastic and thermo-elasto-plastic finite element analyses using Eqn. (1) as a yield function have yielded very good results for various deformation behaviours of sintered porous metals [7-11]. In this paper, deformation behaviour in indenting and ring compression of porous metals have been discussed.

## DEFORMATION BEHAVIOUR

### Indenting

Tabata *et al.* [12] measured the Brinell hardnesses of sintered copper specimens as a function of  $d/D$ , with  $d$  and  $D$  being diameters of the indented mark and the indenter, respectively, and the results are shown in Fig. 1. The hardness increased with increasing  $d/D$ , except those of higher initial density specimens. It is to be expected that the hardness increases with increasing initial relative density. There is no theoretical explanation of the hardness data in their paper.

Here the finite element analysis has been made of a 2-dimensional axisymmetric frictionless indentation of the specimens of 24.5 mm in diameter and 30 mm in height by a 5 mm diameter hemispherical iron indenter. The dimension of the specimens and indenter are identical to those used in Tabata's experiment. The mechanical properties ( $\sigma_{eq}$  in MPa) of the non-porous copper specimens ( $\nu = 0.3$ ,  $E=117\text{GPa}$ ,  $\sigma_o=54\text{MPa}$ ) and  $Rc$  show the following relationships of  $\sigma_{eq} = 660 \epsilon_{eq}^{0.33}$  and  $Rc = 0.6541$  [12].

The initial mesh for analysis of indentation is shown in Fig 2. The Brinell hardness is load  $F$  divided by indented surface area.

$$HB = \frac{F}{\pi D/2 \{D - (D^2 - d^2)^{1/2}\}} = \frac{F}{\pi D t} \quad (2)$$

where  $F$ ,  $D$ ,  $d$  and  $t$  are applied load, diameter of indenter, diameter of indentation and depth of indentation, respectively. The calculated HB's as a function of  $d/D$  are shown in Fig. 1 along with the measured HB by Tabata *et al.* A very good agreement between the measured and calculated values can be seen.

The Brinell hardness is usually measured at constant  $F$  and  $D$ . For an indenting load of 2450 N, the usual Brinell hardness value is shown in Fig. 3 as a function of initial relative density. A linear relationship between the initial relative density and the hardness is seen within Tabata *et al.*'s experimental range.

Calculated grid distortions and relative density distributions in the specimens with initial relative densities of 0.8 and 0.9 during indentation are shown in Fig. 4. The shape of densification zone under the indenter is similar to that of the plastic zone of non-porous metal indented by a spherical indenter. It is interesting to note that the region next the indenter sinks rather than bulges.

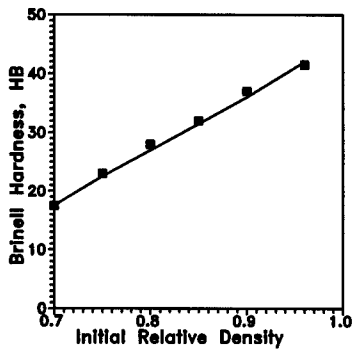


Fig. 3. Relationship between Brinell hardness (load=2450N) and initial relative density. Symbols indicate measured data [12] and curves indicate calculated values.

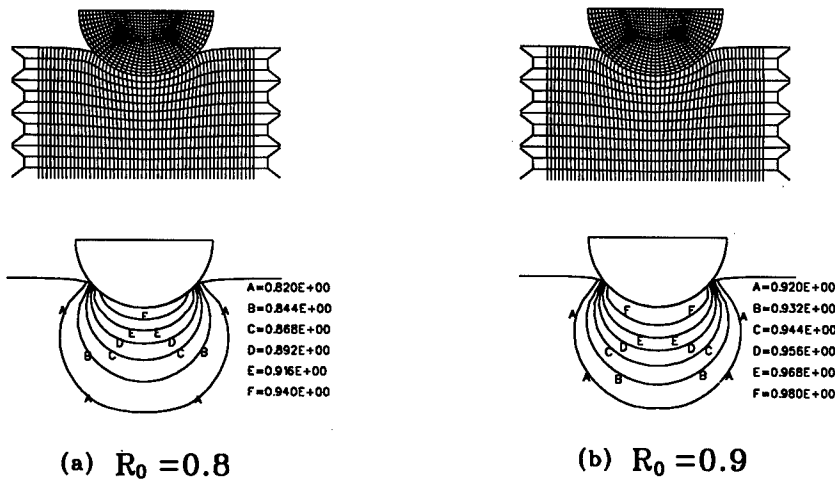


Fig. 4. Calculated grid distortions and relative density distributions in specimens with initial relative densities of (a) 0.8 and (b) 0.9, indented to  $d/D=0.63$ .

## Ring Compression

In the forming of sintered porous metals, the elastic-plastic deformation behavior is influenced by the internal pores, and the conditions of friction will be different from those in conventional forming of non-porous solid metals. In order to find a proper lubricant for the forming of sintered porous metals, a method for evaluation of lubricants must be established. The ring compression test is widely applicable to evaluate lubricants, because this method is easily used with only measurement of the change in geometry of a ring.

Oh and Mun [13] measured the average relative density and the change in the inner diameter of sintered iron rings which were subjected to compression under various friction conditions. They used specimens of two different sizes with dimensions of 28 mm in outer diameter, 14 mm in inner diameter, and 4.7 mm in height, namely, OD : ID : H = 6 : 3 : 1; and 24 mm in outer diameter, 12.5 mm in inner diameter and 6 mm in height, namely, OD : ID : H = 6 : 3.1 : 1.5. Their experimental results are shown in Fig. 5 (symbols). The mechanical properties ( $\sigma_{eq}$  in MPa) of nonporous iron ( $\nu=0.3$ ,  $E=209.5$  GPa) were taken to be  $\sigma_{eq} = 660 \epsilon_{eq}^{0.33}$  and  $R_c = 0.6541$  for the finite element calculation of grid distortions, and changes in geometry of porous rings. The initial grid for ring compression is shown in Fig. 6. The FEM calculation results are shown in Fig. 5 along with measured data. The friction coefficients in the calculation were set to best fit the measured data. Fig. 5 demonstrates that the elasto-plastic FEM using yield condition of Eqn. (1) simulates the deformation of the porous metal rings quite closely.

Figure 7 shows the grid distortions of porous iron rings (OD : ID : H = 6 : 3 : 1) with various relative densities of 0.85 reduced by 50% under various friction conditions. At lower levels of friction, the inner and outer surfaces flow outward, resulting in outward barrelling. As friction increases, a neutral flow point, where the radial velocity of the deforming material becomes zero, appears in the specimen, resulting in the inward barrelling of the inner surface and the outward barrelling of the outward surface. At lower levels of friction,  $\mu=0.02$  and  $0.05$ , no folding occurs, whereas at a high level of friction,  $\mu=0.2$ , folding occurs at the inner edge as well as the outer edge.

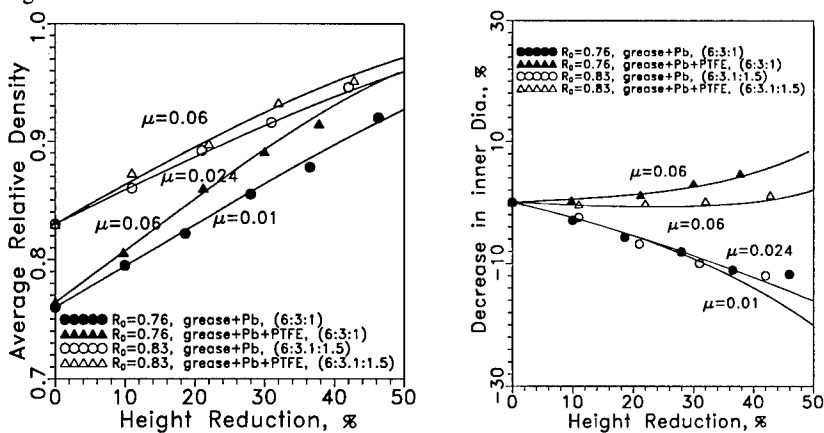


Fig. 5. (a) Average relative densities and (b) change of geometry of porous iron rings (OD : ID : H equal to 6 : 3 : 1 and 6 : 3.1 : 1.5) with initial relative densities of 0.76 and 0.83 as function of height reduction. Symbols indicate measured data [13] and curves indicate calculated values.

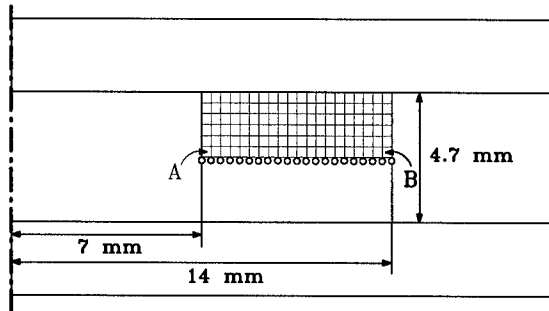


Fig. 6. Initial mesh for analysis of compression of porous metal ring (OD : ID : H = 6 : 3 : 1).

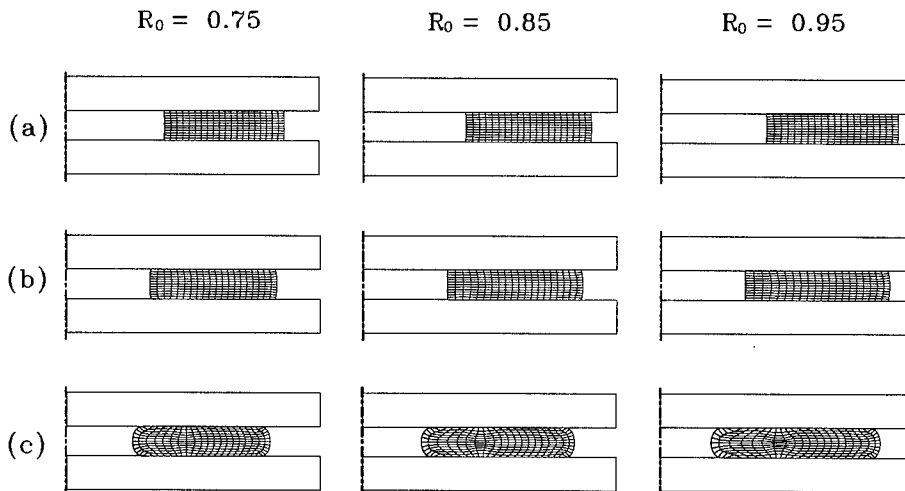


Fig. 7. Calculated grid distortions in porous iron rings (OD : ID : H = 6 : 3 : 1) with initial relative densities of 0.75, 0.85 and 0.95, reduced by 50% under friction coefficients of (a) 0.02, (b) 0.05, and (c) 0.2.

## CONCLUSIONS

1. The Brinell hardness calculated for a given load and indenter diameter increases linearly with the initial relative density of the specimen and correlates well with the measured data, although the measured hardness tends to increase with increasing ratio of indented mark to indenter diameter.

2. The analysis of ring compression of porous metals has enabled ring compression testing to be used as a method of determining the coefficient of friction in porous metal forming processes.

---

3. The average relative density during ring compression increases with increasing friction, and lubricants can be evaluated by measurement of the change of the average relative density and the change of inner diameter.

#### ACKNOWLEDGMENTS

This work has been supported by Korea Science and Engineering Foundation through Research Center for Thin Film Fabrication and Crystal Growing of Advanced Materials, Seoul National University.

#### REFERENCES

1. S. Shima and M. Oyane, *Int. J. Mech. Sci.* **18**, p. 285 (1976).
2. A.L. Gurson, *J. Engng. Mater. Tech. (Trans. ASME)* **99**, p. 2 (1977).
3. V. Tvergaard, *Int. J. Fracture* **18**, p. 237 (1982).
4. S.M. Doraivelu, H.L. Gegel, J.S. Gunasekera, J.C. Malas, J.T. Morgan and J.F. Thomas, *Int. J. Mech. Sci.* **26**, p. 527 (1984).
5. S.B. Biner and W.A. Spitzig, *Acta Metall. Mater.* **38**, p. 603 (1990).
6. D.N. Lee and K.S. Kim ; *Powder Metall.* **35**, p. 275 (1992).
7. H.N. Han, H.S. Kim, K.H. Oh and D.N. Lee, *Powder Metall.* **37**, p. 140 (1994).
8. H.N. Han, H.S. Kim, K.H. Oh and D.N. Lee, *Powder Metall.* **37**, p. 259 (1994).
9. H.N. Han, Y. Lee, K.H. Oh and D.N. Lee, *Mater. Sci. Eng.(A)* **206** p. 81 (1996).
10. H. N. Han, H. S. Kim and D. N. Lee, *Scr. Metall. Mater.* **29**, p. 1211 (1993).
11. H. N. Han, K. H. Oh and D. N. Lee, *Scr. Metall. Mater.* **32**, p. 1937 (1995).
12. T. Tabata and S. Masaki, *J. Eng. Mater. Tech. (Trans. ASME)* **112**, p. 95 (1990).
13. H.-K. Oh and J.-H. Mun, *J. Mech. Wkg. Tech.* **9**, p. 279 (1984).

## A CONTINUUM PLASTICITY MODEL FOR THE CONSTITUTIVE BEHAVIOUR OF FOAMED METALS

RONALD E. MILLER and JOHN W. HUTCHINSON

Division of Applied Science, Harvard University, Cambridge, MA 02138

### ABSTRACT

A yield surface is proposed that can be fit to the plastic flow properties of a broad class of solids which exhibit plastic compressibility and different yield points in tension and compression. The yield surface is proposed to describe cellular solids, including foamed metals, and designed to be fit to three simple experimental results: (1) the compressive stress-strain response (including densification), (2) the difference between the tensile and compressive yield points and (3) the degree of compressibility of the foam, as measured by the lateral expansion during a uniaxial compression test. The model is implemented using finite elements and used to study the effects of plastic compressibility on two problems: the compression of a doubly notched specimen and indentation by a spherical indenter.

### INTRODUCTION

Foamed metals have been proposed as a candidate for core material in sandwich panel and shell structures [1]. In order to use foamed metals in these structural applications, it is important that a reliable model of mechanical behaviour is developed to assist in the design process. This paper discusses the modelling of the plastic flow of foamed metals. The objective is to present a yield surface that can be used to describe foamed metals from within a continuum plasticity framework. More generally, the yield surface is such that it describes a broad class of materials exhibiting pressure dependent yield and a significant volume change during plastic flow.

Experimental data regarding plastic behaviour of metal foams have focussed largely on the uniaxial compression test [2, 3, 4, 5, 6]. The basic shape of the compressive stress-strain curves is an initial elastic regime, followed by a long plateau region during which the stress remains nearly constant and large strain develops, and finally a rapid increase in slope as the foam begins to densify. An interesting property of most cellular materials, and indeed foamed metals, is the unusually small degree of lateral expansion which takes place during the plateau region of the compression test. To quantify this behaviour, we define a "plastic expansion ratio" as  $\nu_{pl} = -\epsilon_{22}^{pl}/\epsilon_{11}^{pl}$ , where  $\epsilon_{22}^{pl}$  is the plastic strain perpendicular to the direction of compression and  $\epsilon_{11}^{pl}$  is the compressive plastic strain in the loading direction. For dense metals, this ratio is 0.5, as plastic flow is fully incompressible. By contrast, cellular solids can exhibit a value of  $\nu_{pl}$  as low as 0.02 for foamed polystyrene, while  $\nu_{pl}$  has been measured to be 0.17 for a typical closed cell aluminum foam [7]. The degree of compressibility of a material can significantly affect its response to loading, as we will demonstrate in the results section.

Unfortunately, there are only a few measurements of the yield behaviour of metal foams under loads other than simple compression. Some existing tensile measurements [3, 8, 9] suggest a slightly higher yield point in tension than in compression. The main contributions to the measurement of yield in multiaxial stress are those of references [8], [10] and [11], but difficulties with experimental scatter and the paucity of tensile loading states in this small handful of studies make it difficult to establish unambiguously the shape of these yield surfaces. On the theoretical side, Gibson, Ashby, Zhang and Triantafillou [12] proposed a yield surface based on the analysis of a single idealized cell in the foam structure. We shall see that this yield surface (which we refer to as the GAZT yield criterion) is a special case of the more general yield surface to be proposed here.

The contribution of this paper will be to present a theoretical yield surface for cellular materials. The specific goal is an accurate description of foamed metals, but in fact the model can be used to describe a broad class of materials which exhibit the following three characteristics: (1) compressibility during plastic deformation (indicated by a value of  $\nu_{pl}$  lower than 0.5), (2) a difference

between the yield points in uniaxial tension and compression, and (3) a compressive stress-strain curve which, after some general initial hardening and possibly a plateau region exhibits rapid hardening due to densification. Three adjustable parameters in the yield surface can be used to fit the model to simple tests without the need for detailed experimental knowledge of the shape of the yield surface. After describing the model, we use a finite element implementation to study two problems; the notch strengthening effect and indentation by a spherical indenter.

## THEORY

The yield behaviour of metal foams will be described within the classical framework of incremental plasticity with associated flow and isotropic hardening (for details see [13]). The key ingredient to this framework is the yield surface itself, a convex envelope in stress space, within which the material remains elastic, and on which plastic flow may take place. It is represented as  $f(\sigma, \kappa) = 0$  where  $\sigma$  is the stress tensor and  $\kappa$  represents some set of variables upon which the hardening of the material depends.

The simplest and most commonly used yield surface for dense metals is the Mises yield condition. This is expressed as  $f = \sigma_e - d$ , where  $d$  corresponds to the uniaxial strength of the material and  $\sigma_e$  is the *effective stress*:

$$\sigma_e = \sqrt{\frac{3}{2} s_{ij} s_{ij}}, \quad s_{ij} = \sigma_{ij} - \frac{\sigma_{kk}}{3} \delta_{ij}. \quad (1)$$

The lack of any dependence on the pressure,  $p = -\sigma_{kk}/3$ , in this yield surface means that such a material cannot deform plastically in hydrostatic compression or tension, and leads to incompressible plastic deformation during associated flow. The model of Drucker and Prager (DP) [14], originally proposed as a model for soil, incorporates a linear dependence on the pressure  $f = \sigma_e - \gamma p - d$  where a new material parameter  $\gamma$  is introduced. It is straightforward to verify that a DP material exhibits a yield point in tension,  $\sigma_t$ , different from that in compression,  $\sigma_c$ .

The DP model will exhibit a  $\nu_{pl}$  that is different from 0.5, but its value is fixed by  $\gamma$ , which is set to produce the correct tensile and compressive yield points. In order to allow for variation in  $\nu_{pl}$ , we include a quadratic dependence on the pressure, as inspired by the form of the GAZT yield surface mentioned in the introduction [12]. Thus we propose a yield surface of the form

$$f = \sigma_e - \gamma p + \frac{\alpha}{d} p^2 - d, \quad (2)$$

with two new material parameters  $\gamma$  and  $\alpha$ . It can be shown that convexity of the yield surface is satisfied as long as  $\alpha$  and  $d$  are positive. We now propose to obtain the parameters  $\gamma$ ,  $\alpha$  and  $d$  from a strictly empirical approach. Specifically, we will fit the yield surface to three values that can presumably be obtained from simple materials tests: the compressive yield strength,  $\sigma_c$ , the tensile yield strength,  $\sigma_t$ , and the plastic expansion ratio  $\nu_{pl}$ .

In uniaxial compression,  $\sigma_e = \sigma_c$  and  $p = \sigma_c/3$ . Consequently, we can set  $f = 0$  in equation (2) and solve for  $\sigma_c$ . Similarly in uniaxial tension,  $\sigma_e = \sigma_t$  and  $p = -\sigma_t/3$ . Thus we find

$$\sigma_c = \frac{2d}{1 - \gamma/3 + \sqrt{(1 - \gamma/3)^2 + 4\alpha/9}}, \quad \sigma_t = \frac{2d}{1 + \gamma/3 + \sqrt{(1 + \gamma/3)^2 + 4\alpha/9}}, \quad (3)$$

from which it follows that

$$r \equiv \frac{\sigma_c}{\sigma_t} = \frac{1 + \gamma/3 + \sqrt{(1 + \gamma/3)^2 + 4\alpha/9}}{1 - \gamma/3 + \sqrt{(1 - \gamma/3)^2 + 4\alpha/9}}, \quad (4)$$

where we have defined the ‘‘yield asymmetry ratio,’’  $r$ .

The plastic expansion ratio in uniaxial compression can be computed analytically for this yield surface. From the definition of  $\nu_{pl}$  given earlier, it can be shown that

$$\nu_{pl} = \frac{1/2 - \gamma/3 + 2\alpha/9d_o}{1 - \gamma/3 + 2\alpha/9d_o}, \quad d_o \equiv \frac{1}{2} \left( 1 - \gamma/3 + \sqrt{(1 - \gamma/3)^2 + 4\alpha/9} \right). \quad (5)$$

By solving equations (3),(4) and (5) for the free parameters in the yield surface expression, we have a simple means of characterizing our foamed metal plasticity behaviour in terms of  $\sigma_c$ ,  $\sigma_t$  and  $\nu_{pl}$ . The resulting yield surface parameters are

$$\gamma = \frac{6r^2 - 12r + 6 + 9(r^2 - 1)/(1 + \nu_{pl})}{2(r + 1)^2}, \quad (6)$$

$$\alpha = \frac{45 + 24\gamma - 4\gamma^2 + 4\nu_{pl}(2 + \nu_{pl})(-9 + 6\gamma + \gamma^2)}{16(1 + \nu_{pl})^2}, \quad (7)$$

$$d = d_o\sigma_c, \quad (8)$$

where we have assumed that  $\nu_{pl} > -1$ .

For simplicity, we will assume that  $r$  and  $\nu_{pl}$  (and therefore  $\alpha$  and  $\gamma$ ) remain constant as the material hardens. Hardening is incorporated strictly through  $d$ , by fitting  $\sigma_c(\epsilon)$  to an experimentally obtained uniaxial compression curve. Details will be published elsewhere [15].

In the introduction we mentioned that the GAZT yield surface for plastically deforming foams is a special case of our more general yield surface. The GAZT yield surface is obtained by setting  $\gamma = 0$ , while  $\alpha$  is a function of the relative density of the foam. In order to discuss the behaviour of the GAZT yield surface in the remaining sections, we will choose the GAZT surface for a foam with relative density of 8% (and thus  $\alpha = 0.0648$ ). One interesting result of the GAZT yield surface is the value of  $\nu_{pl}$  derived from it, which we find to be  $\nu_{pl} = 0.47$  from equation (5). This suggests that the GAZT material is nearly incompressible in uniaxial compression, and will demonstrate considerable lateral expansion. Finally, because  $\gamma = 0$ , the asymmetry ratio for the GAZT model is  $r = 1.0$ .

## RESULTS

### Notch Strengthening

A problem that has been well analysed using conventional plasticity models is the compressive loading of a doubly notched specimen in plane strain, as shown schematically in the inset of figure 1b. A simple estimate for the lower bound of the load per unit depth  $P$  can be made by assuming that the stress state across the ligament is uniaxial compression, and hence the limit state is reached when  $P = P^* \equiv c\sigma_c$ . In fact, much greater values of  $P$  can be obtained for moderately deep notches in a Mises material. Even more counterintuitive is that the limiting value of  $P$  will *increase* with increasing notch depth  $a$  and fixed ligament width  $c$ . In the limit of very deep notches it can be shown that  $P$  approaches an upper bound of  $2.96P^*$  when a rigid, perfectly plastic Mises material is assumed [13]. This apparent strengthening is a consequence of the constraint effect brought about by incompressible plastic flow. As the degree of compressibility in a material increases, the amount of strengthening will decrease.

We systematically vary the compressibility of the material, as measured through  $\nu_{pl}$ , by defining a class of materials for which the material properties  $r$  and  $\nu_{pl}$  are linearly related. This relationship is given by

$$r = r_0 - 2(r_0 - 1)\nu_{pl}, \quad 0.0 < \nu_{pl} < 0.5, \quad (9)$$

so that in the limit  $\nu_{pl} = 0.5$  we recover a Mises material with  $r = 1$ , while for  $\nu_{pl} = 0.0$  we find  $r = r_0$ , the asymmetry ratio for a typical metal foam. For concreteness, we take  $r_0 = 0.765$ , as reported in [3]. We now choose a set of six materials, parametrically spanning the space of  $0.0 < \nu_{pl} < 0.5$  and  $r_0 > r > 0.0$  through the constants  $\gamma$  and  $\alpha$  as shown in the table inset to figure 1.

In figure 1, we present the results of a finite element study of the notch strengthening effect. The ratios  $a/w = 0.6$  and  $h/w = 2.73$  were chosen for the calculation. Because the strains are small relative to the densification strain, the model is essentially elastic-perfectly plastic. In frame (a), we show the load versus total strain for various values of  $\nu_{pl}$ . Also included for comparison

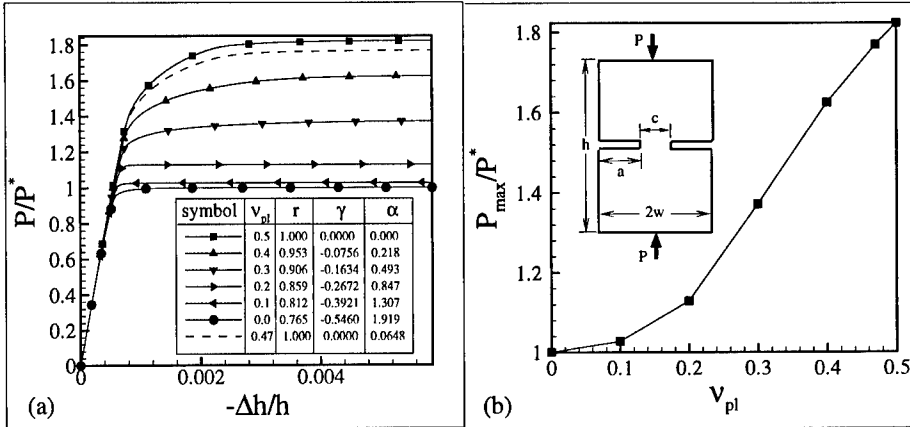


Figure 1: Finite element calculations of the notch strengthening effect with  $a/w = 0.6$ . (a) Load versus strain for various values of  $\nu_{pl}$ . The dashed line in shows the GAZT material for comparison. The table shows the values of the parameters used to define the family of materials with varying properties. (b) Limit load as a function of  $\nu_{pl}$ . The inset shows the model geometry.

in this figure is the curve for the GAZT material. In frame (b) we plot the limiting load  $P_{max}$ , as a function of the lateral expansion ratio. For the incompressible Mises material ( $\nu_{pl} = 0.5$ ), the effect of the notch is an apparent strengthening such that  $P_{max} = 1.82P^*$ . Note that this is lower than the result mentioned at the start of this section for two main reasons. First, the geometry studied here does not satisfy the requirement of a “very deep crack” assumed in the previous result. Second, the finite element model is not rigid-plastic, but elastic-plastic, and the elastic compliance of the material will reduce its constraining effect. The importance of the Mises limit in this set of results is as a benchmark against which to compare the compressible foam models. As  $\nu_{pl}$  decreases, the notch strengthening effect also decreases rapidly, and for  $\nu_{pl}$  less than about 0.17, the notch strengthening falls to below about 10% of  $P^*$ .

### Indentation

A widely used means to determine the yield strength of materials is the indentation hardness measurement (see [16] for details). One such test, the Brinell hardness test, uses a spherical indenter whose size can be adapted depending on the material being considered. The Brinell hardness,  $H$ , is defined as the load divided by the projected indentation area ( $H = P/\pi a^2$  in the inset of figure 2b). In fully dense metals which do not appreciably work harden,  $H$  is found to be equal to approximately 3 times the compressive yield strength of the material<sup>1</sup>. This “constraint factor” of 3 is a direct consequence of the incompressibility of dense metals during plastic flow, whereby the flowing material beneath the indenter is constrained by the surrounding metal. Indentation experiments [5, 7, 10, 18] have demonstrated that the constraint factor for cellular solids tends to be much lower than 3, and approaches unity for some materials.

In figure 2a, we present finite element calculations of Brinell hardness tests for the same materials as were considered in figure 1. The materials are elastic-perfectly plastic up to a densification strain, after which rapid hardening ensues. As was the case in notch strengthening, the fairly weak dependence of the GAZT yield surface on pressure means that its behaviour is close to that

<sup>1</sup>It was reported by Tabor [16] that  $H = 2.8\sigma_c$  for perfectly plastic metals based on experimental results, while Biwa and Storåkers [17] have found a value of  $H = 3.07\sigma_c$  from numerical analysis.

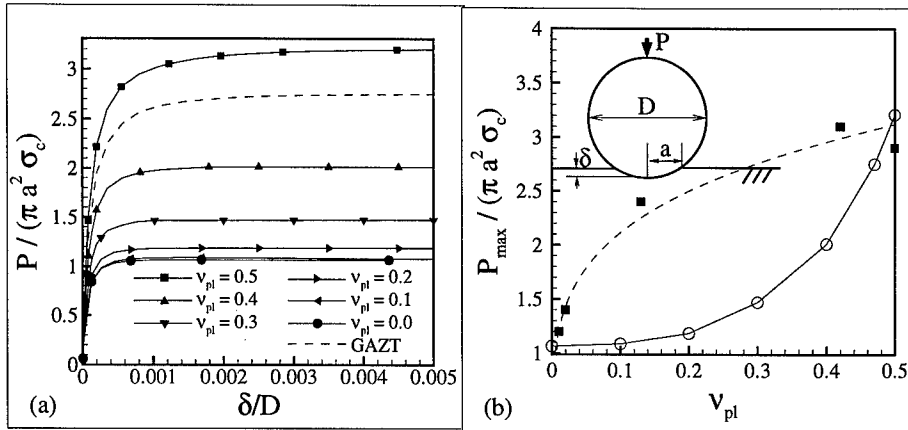


Figure 2: Finite element calculations of the Brinell indentation test. (a) Brinell hardness versus indentation depth for various values of  $\nu_{pl}$ . The dashed line shows the GAZT material for comparison. (b) Limiting hardness as a function of  $\nu_{pl}$  (circles and solid line) compared to experimental data from [7] (squares and dashed line). The inset shows the model geometry.

of a standard Mises material. In frame b, the limiting hardness is plotted as a function of the lateral expansion coefficient. The hardness of these materials is a strong function of their ability to laterally expand. In the Mises limit of  $\nu_{pl} = 0.5$ , we see the limiting hardness is  $H = 3.2\sigma_c$ , in good agreement with the results of previous studies [17]. As well, the experimental data points from reference [7] are included for comparison in the figure. The simulations and experiments suggest two very different dependencies of  $H$  on  $\nu_{pl}$ . It is possible that parameters other than  $\nu_{pl}$  influence the measured hardness level in cellular materials. For example, the effect of the asymmetry ratio,  $r$ , has not been fully explored.

In figure 3, we present axisymmetric cross-sections beneath the spherical indenter. We compare the deformations for a material with  $\nu_{pl} = 0.2$  with the GAZT material ( $\nu_{pl} = 0.47$ ). It is clear from frame (a) that the more compressible material fails very locally under the indenter by the compressive collapse of the elements. Elements a short distance from the indenter are completely undisturbed. The GAZT material, on the other hand, behaves much like an incompressible Mises

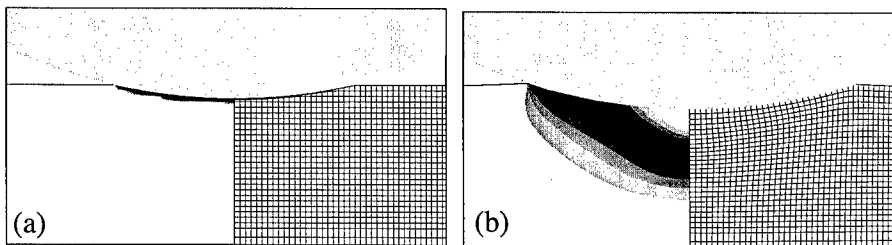


Figure 3: Region under the indenter for the material with  $\nu_{pl} = 0.2$  in (a) and the GAZT ( $\nu_{pl} = 0.47$ ) material in (b). On the left half of each figure are contours of equivalent plastic strain, on the right half is the deformed mesh which was originally a grid of perfect squares.

solid. There is a substantial plastic zone under the indenter, and some piling up of material that flows out to the sides. The element grid, which was a grid of perfect squares in the underformed state, can be compared to the experimental results in reference [7].

### SUMMARY

We have proposed a yield surface that can be used to describe the plastic deformation of a class of materials characterized by a tensile yield point different from that in compression and some degree of plastic compressibility. The model can be used to describe foamed metals, for example, by fitting the free parameters to three experimentally determined quantities: (1) the compressive stress-strain response, (2) the yield asymmetry ratio  $r = \sigma_c/\sigma_t$  and (3) the lateral expansion ratio  $\nu_{pl}$ .

The model was used to demonstrate the effect of material compressibility on the expected response in two mechanical tests, compression of a doubly notched specimen and indentation by a spherical indenter. In both cases, the limit load was a strong function of the plastic compressibility, implying that care must be taken when interpreting the results of indentation tests on cellular materials. At small values of  $\nu_{pl}$ , the deformation is mainly localized collapse of the material directly beneath the indenter, while as  $\nu_{pl}$  approaches 0.5, the deformation is accommodated by material flowing to the sides, as is typical of a fully incompressible Mises material.

### ACKNOWLEDGEMENTS

The finite element calculations in this work were performed using the commercial code ABAQUS. The authors would like to thank Lorna Gibson, Erik Andrews, Tim McCormack and Gael Gioux for access to their experimental data prior to publication. This work has been supported by the Department of the Navy, award number N00014-96-1-1028. RM also thanks the University of Saskatchewan for financial support.

### REFERENCES

- [1] A. G. Evans, J. W. Hutchinson, and M. F. Ashby. to appear in *Acta Mat.*, 1998.
- [2] L. J. Gibson and M. F. Ashby. *Cellular Solids: Structure and Properties*. Cambridge University Press, Cambridge, 2nd edition, 1997.
- [3] Y. Sugimura, J. Meyer, H. Bart-Smith, J. Grenstedt, and A. G. Evans. *Acta Mat.*, 45(12):5245–5259, 1997.
- [4] O. Prakash, H. Sang, and J. D. Embury. *Mat. Sci. Engng.*, A199:195–203, 1995.
- [5] D. J. Sypeck, H. N. G. Wadley, H. Bart-Smith, S. Koehler, and A. G. Evans. *Review of Progress in Quantitative Nondestructive Evaluation*, 17, 1998.
- [6] P. H. Thornton and C. L. Magee. *Metallurgical Trans. A*, 6:1801–1807, 1975.
- [7] M. C. Shaw and T. Sata. *Int. J. Mech. Sci.*, 8:469–478, 1966.
- [8] T. C. Triantafillou, J. Zhang, T. L. Shercliff, L. J. Gibson, and M. F. Ashby. *Int. J. Mech. Sci.*, 31(9):665–678, 1989.
- [9] E. Andrews and L. J. Gibson. unpublished results.
- [10] G. Gioux and L. J. Gibson. unpublished results.
- [11] T. McCormack and L. J. Gibson. unpublished results.
- [12] L. J. Gibson, M. F. Ashby, J. Zhang, and T. C. Triantafillou. *Int. J. Mech. Sci.*, 31(9):635–663, 1989.
- [13] L. M. Kachanov. *Foundations of the Theory of Plasticity*. North-Holland, Amsterdam, 1971.
- [14] D. C. Drucker and W. Prager. *Q. Appl. Math.*, 10:157–165, 1952.
- [15] R. E. Miller. unpublished.
- [16] D. Tabor. *The Hardness of Metals*. Clarendon Press, Oxford, 1951.
- [17] S. Biwa and B. Storåkers. *J. Mech. Phys. Sol.*, 43(8):1303–1333, 1995.
- [18] M. Wilsea, K. L. Johnson, and M. F. Ashby. *Int. J. Mech. Sci.*, 17:457–460, 1975.

---

## ELASTIC PROPERTIES OF POROUS STRUCTURAL CERAMICS PRODUCED BY PLASMA-SPRAYING

A. WANNER

Universität Stuttgart, Institut für Metallkunde, Seestr. 71, D-70174 Stuttgart, Germany

E-Mail: alexander.wanner@po.uni-stuttgart.de

currently with Dept. of Materials Science and Engineering, Northwestern University, Evanston, IL., USA

### ABSTRACT

This study focuses on the relationship between porosity and elastic stiffness of structural ceramic materials produced by plasma-spraying. Mg-Al-spinel was chosen as a model material and studied in as-sprayed condition as well as upon annealing to increasingly higher temperatures up to 1650°C. The detailed analysis of the stiffness and mass density evolution offers a deep insight into the initial microstructural state of the material and into the morphological changes that occur upon heat treatment.

### INTRODUCTION

Like many other ceramic materials of engineering interest, plasma-sprayed ceramics are typically not fully dense, i.e. they exhibit a certain amount of porosity, by which the mass density and the effective elastic moduli are reduced. In thick-walled, free-standing ceramic materials produced by plasma-spraying, the porosity-induced modulus reduction is highly desired, as it diminishes internal stresses evolved during processing and service from thermal gradients within the material or from thermal expansion mismatch to adjacent materials. It has been shown that the effective Young's moduli of as-sprayed, intentionally porous plasma ceramics, estimated from static tests on components assuming isotropic elasticity, can be more than one order of magnitude lower than those of the corresponding fully-dense materials [1]. Recently it has also been shown that these materials are clearly anisotropic, as they exhibit a considerably lower stiffness when loaded perpendicular to the substrate plane than in directions parallel to that plane [2]. From these observations it has been concluded that the anisotropy of these plasma-sprayed materials is primarily governed by the presence and the alignment of slit-like pores in the microstructure, which are formed during the deposition process and are preferentially oriented parallel to the former substrate interface. The stiffness enhancement [1] and anisotropy reduction [2] observed upon high-temperature annealing can readily be explained as being a result of sintering, by which these pores shrink and, on average, adopt a more spherical shape.

In the present study, the evolution of elastic properties of such a material upon high-temperature annealing is investigated in detail and quantitatively correlated to the porosity. Spinel ( $MgAl_2O_4$ ) was chosen as a model material because it has been shown that this oxide exhibits its thermodynamically stable cubic *spinel* structure even upon rapid solidification (i.e. in as-sprayed condition) [1,3] and also does not exhibit any phase transformations below the melting temperature. This allows for calculating the porosity on base of mass density measurements and for attributing the observed elastic modulus changes directly to the changes in pore content and morphology.

### MATERIAL

The plasma-sprayed spinel studied in this work is a commercial material manufactured by the company LWK-Plasmakeramik GmbH (Wiehl, Germany) using an atmospheric plasma-spraying technique [4]. Slightly off-stoichiometric spinel powder with chemical composition 74.4 wt.%  $Al_2O_3$  + 25.6 wt.% MgO and particle sizes ranging from 60 to 120  $\mu m$  was spray-deposited onto a flat steel substrate, and subsequently removed by cooling [5]. Figures 1 and 2 show the typical microstructures in as-sprayed and in high-temperature annealed conditions, respectively. The as-sprayed material consists of lamellar grains which are not continuously bonded to each other, forming slit-like intergranular pores.

Upon annealing at 1650°C for 2 hours, these slit-pores almost vanish. On average, the residual pores have more spherical shapes and are less aligned. As will be shown in the following, these microstructural changes give rise to dramatic changes in the elastic behavior.

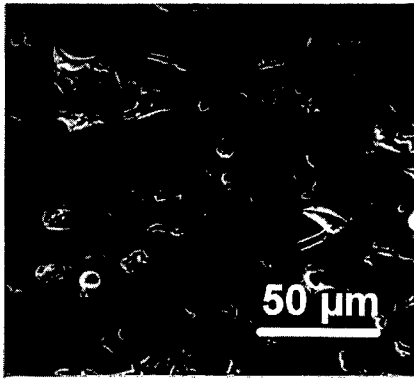


Figure 1. Typical microstructure of the as-sprayed material (SEM micrograph of polished cross-section; Spraying direction is vertical)

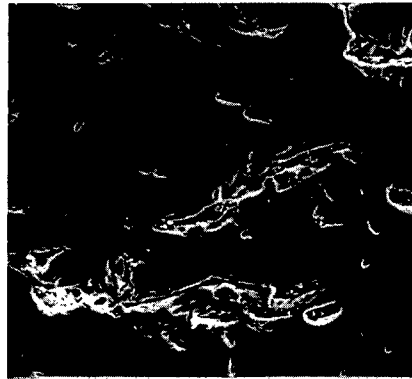


Figure 2. Typical microstructure upon annealing at 1650°C for 2 hours (Same orientation and scale as Figure 1).

## EXPERIMENTAL

The velocities of longitudinal elastic waves propagating in the directions of the principal specimen axes were measured using an ultrasonic phase spectroscopy technique, which recently has been demonstrated to be a viable method to measure wave velocities in porous ceramic materials along relative short pathlengths [6,7]. For these experiments, cube-shaped samples with nominal dimensions  $8 \times 8 \times 8 \text{ mm}^3$  and edges parallel and perpendicular to the former substrate interface were machined from 10 mm thick, as-sprayed material by cutting and grinding. Velocity measurements were carried out by attaching a pair of identical broadband ultrasonic transducers on opposite sides of the specimen. One transducer was used to transmit a *continuous*, harmonic elastic wave into the specimen, the other one to receive the signal transmitted through the specimen. While sweeping the frequency  $f$  of the signal from 100 kHz upwards, the phase shift  $\Delta\phi$  between the incident and transmitted waves was measured continuously. It is important to note that there always exists an upper frequency limit above which the attenuation due to scattering and absorption in the specimen is beyond the dynamic range of the measurement system [6]. In the most extreme case of the present study, this upper frequency limit was as low as 2.4 MHz. It is the great advantage of this continuous-wave phase spectroscopy technique over ultrasonic pulse propagation methods that it allows for accurate wave velocity measurements on relatively small samples despite this constraint to relatively low frequencies. A detailed description of the technique and the experimental set-up has already been reported elsewhere [6].

The wave velocity,  $v$ , is readily determined from the slope of the resulting  $\Delta\phi(f)$  function (“phase spectrum”) according to the equation [6,7]

$$v = -2\pi L \left( \frac{d\Delta\phi}{df} \right)^{-1} \quad (\text{Eq. 1})$$

in which  $L$  is specimen thickness in the direction of wave propagation. In the present study, the slope  $d\Delta\phi/df$  turned out to always be fairly constant in the frequency range covered by the measurements, indicating that dispersion (i.e. dependence of velocity on frequency) plays no significant role. The

velocities of longitudinal waves propagating in the directions parallel to the principal specimen axes are further denoted  $v_1$ ,  $v_2$ , and  $v_3$ , where direction 1 is perpendicular and directions 2 and 3 are parallel to the substrate surface. The evolution of these velocities upon sintering was studied by annealing the same specimen in air at successively higher temperatures. All velocity measurements were performed at room temperature between these 2-hour anneals, which ranged from room temperature to 1650°C in steps of 150K to 250K. Simultaneously, the evolution of the mass density was studied by repeatedly measuring specimen mass and dimensions. Under the assumption that the material is transversely isotropic and that the specimen axes coincide with the principal axes of the material, the elastic stiffness coefficients  $C_{ij}$  can be calculated from the longitudinal wave velocities  $v_i$  according to

$$C_{ii} = \rho v_i^2 \quad (\text{Eq. 2})$$

where  $\rho$  is the mass density of the material and the subscript  $i$  denotes the direction.

## RESULTS AND DISCUSSION

In Figure 3, the stiffness coefficients of the plasma-sprayed spinel are plotted against the maximum annealing temperature. As expected, there is no significant difference between the results obtained for  $C_{22}$  and  $C_{33}$ , and it can be assumed that this free-standing plasma-sprayed is isotropic in the plane parallel to the substrate interface (2-3-plane). The coefficient  $C_{11}$  is considerably lower than the coefficient  $C_{22,33}$ , i.e. the material is less stiff when loaded perpendicular to the plane of isotropy than when loaded in any direction parallel to that plane. This result coincides with results of earlier measurements on four other oxide ceramic materials produced the same way [2]. Upon annealing at increasingly higher temperatures, both  $C_{11}$  and  $C_{22,33}$  first go through a broad minimum and then increase steeply by more than one order of magnitude. Due to the logarithmic scaling, the width of the gap between the  $C_{11}$  and  $C_{22,33}$  scales with the logarithm of the ratio  $C_{22,33}/C_{11}$  and is therefore a direct measure for the degree of anisotropy. This gap is widest at the point of minimum stiffness, where  $C_{22,33}/C_{11}$  is as high as 7.2. As the stiffness increases steeply upon anneals above 900°C (i.e.  $T/T_M > 0.5$ ), the two curves converge, which indicates that the material turns more and more isotropic.

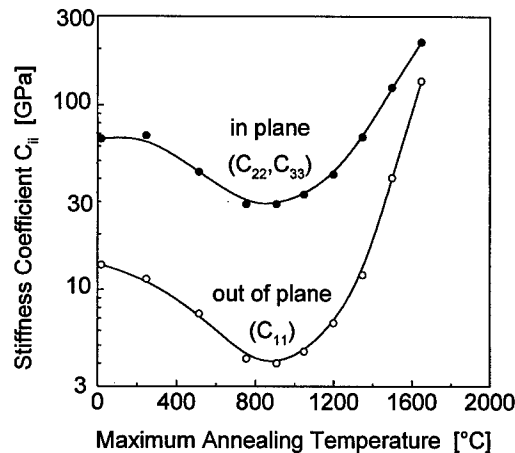


**Figure 3.** In-plane and out-of-plane stiffness coefficients of the intentionally porous plasma-sprayed spinel as a function of maximum annealing temperature. Upon annealing above  $\sim 900^\circ\text{C}$  ( $\cong 0.5 T_M$ ), the stiffness increases dramatically and approaches the corresponding stiffness coefficient of fully dense, polycrystalline spinel (347 GPa). Note that the two curves converge as the stiffness increases, indicating that the material becomes more isotropic. As will be discussed in the main text, the stiffness drop upon annealing at moderate temperatures is probably a result of intergranular microcracking.

In order to analyze the effect of porosity on the elastic stiffness it is useful work with the *relative* densities and stiffness coefficients, i.e. with data that are normalized by the corresponding values of fully dense, polycrystalline (quasi-isotropic) spinel. While the mass density of fully-dense spinel is well

known ( $\rho_0 = 3.6 \text{ g/cm}^3$  [8]), it requires some effort to obtain a reliable value of  $C_{11}^0$ . For the further analysis, this coefficient was derived from the Young's and shear moduli measured by Porter *et al.* [9] on conventional, hot-pressed spinel materials exhibiting porosities in the range  $0.02 < P < 0.4$ . Porter *et al.* published their results in shape of a modulus-porosity plot (Fig. 4a). By plotting their results versus  $1-P$  rather than versus  $P$  and also using logarithmic scales (Fig. 4b), it becomes obvious that, at  $P \leq 0.3$ , their data can be well described by a simple power-law expression

$$\frac{M}{M_0} = (1-P)^n = \left(\frac{\rho}{\rho_0}\right)^n \quad (3)$$

where  $M$  is the modulus of interest and the subscript  $o$  denotes properties of the fully dense material. By extrapolation (dashed lines in Fig. 4b), the moduli of fully dense, quasi-isotropic spinel are obtained, which can be used to calculate  $C_{11}^0$ . The results are  $E_0 = 286 \text{ GPa}$ ,  $G_0 = 114 \text{ GPa}$ , and  $C_{11}^0 = 347 \text{ GPa}$ .

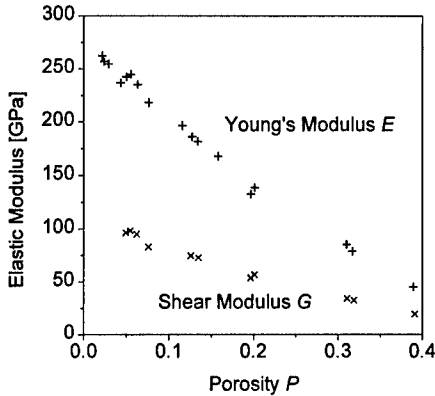


**Figure 4a.** Young's and shear moduli of hot-pressed spinel samples exhibiting different porosities as reported by Porter *et al.* [9].

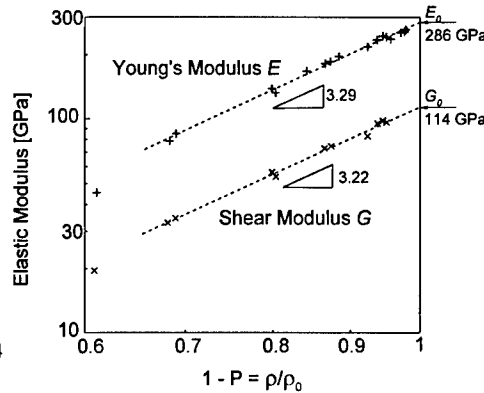


**Figure 4b.** After plotting the data of Porter *et al.* in a different fashion it becomes obvious that the modulus-porosity relationship is according to a power-law (Eq. 3) with  $n \approx 3.25$  for  $P \leq 0.3$ .

In the diagram shown in Figure 5a, the relative stiffness coefficients of the plasma-sprayed spinel in as-sprayed or annealed conditions are plotted against the relative density (again in log-log fashion). It turns out that the stiffness-porosity relationship observed on this material is entirely different from that of the conventionally processed material and cannot be described by the simple power-law (Eq. 3) with a constant exponent  $n$ .

The power  $n$  as defined by Eq. 3 can be regarded as a measure of the efficiency with which the pores reduce the effective stiffness. This efficiency depends on the (average) shape of the pores and on their orientational distribution. By comparing Eq. 3 to theoretically derived equations valid for materials with simple pore shapes, arrangements, and orientations (e.g. foams with equiaxed cells [10] or materials with dilute, randomly oriented ellipsoidal pores [11]), it can be shown that  $n$  is around 2 in the case of equiaxed pores and can achieve high values for other shapes. In the extreme case, the pores degenerate to closed cracks and  $n$  goes to infinity, since cracks have no volume but still reduce the stiffness.

In Figure 5b, the  $n$ -values obtained by applying Eq.3 to the individual data points of Figure 5a are plotted against the annealing temperature. At first sight, this plot looks like a horizontally flipped version of the  $C_{ij}$ -vs.-temperature diagram shown in Figure 3, which illustrates that the considerable stiffness changes observed upon annealing are primarily caused by changes in pore morphology, while the change of the total volume fraction of the pores plays only a minor role.

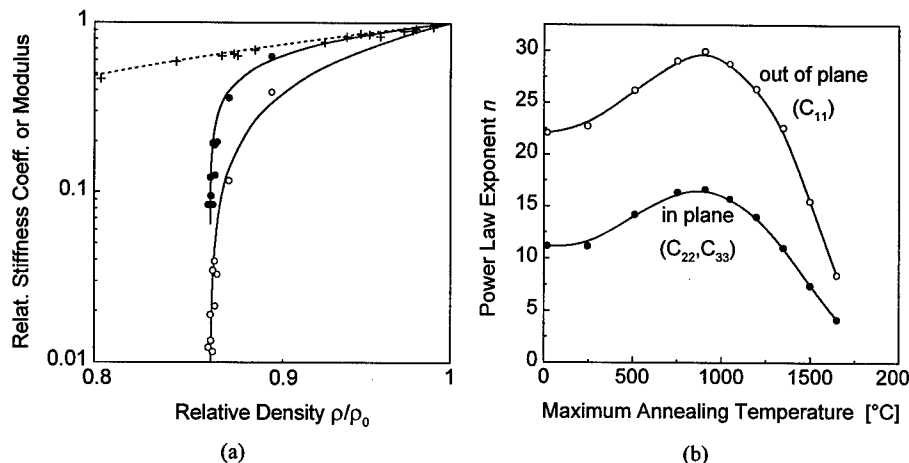


**Figure 5 a.** log-log plot of relative stiffness vs. relative density; (•) in-plane and (o) out-of-plane stiffness coefficients of the *plasma-sprayed* spinel in different conditions, (+) relative Young's moduli of various *hot-pressed* spinels [9], (---) simple power-law with  $n = 3.25$ , (—) modified power-laws with  $P_{crit} = 0.140$  and  $m = 0.35$  or  $m = 0.75$ . **b.** Power  $n$  as a function of annealing temperature, as obtained by applying the simple power-law to the stiffness-density data of plasma-sprayed spinel.

Other than in a cellular material, the stiffness of a plasma-sprayed ceramic material vanishes at a *finite* relative density. As can be seen from the  $C_{ii}/C_{11}^0 - \rho/\rho_0$  plot shown in Figure 5a, the critical  $\rho/\rho_0$  -value of the plasma-sprayed material investigated in the present study is 0.86, which corresponds to a critical porosity of  $P_{crit} = 0.14$ . The existence of this kind of microstructural situation has already been observed in studies on conventional powder-metallurgical materials, however at much larger porosities. Wang [12] has established a theoretical model for the modulus-porosity correlation of sintering spheres, showing that the stiffness vanishes if the spheres merely touch each other but do not form any load-bearing contact areas. In the case of the simple-cubic arrangement studied by Wang, this critical situation corresponds to a porosity of  $P_{crit} \approx 0.48$ . Conversely, the flat, irregularly-shaped particles formed during a spray-deposition process fit together like the pieces of a jigsaw-puzzle and hence fill the space much better than equiaxed particles in any thinkable 3D-arrangement. Phani and Niyogi [13] have proposed to use a modified, two-parameter equation to describe the modulus-porosity correlation of a powder-metallurgical material.

$$\frac{M}{M_0} = \left(1 - \frac{P}{P_{crit}}\right)^m \quad (4)$$

This modified power-law is purely empirical, but is attractive due to its mathematical simplicity and fulfillment of the boundary conditions of  $M = 0$  at  $P = P_{crit}$  and  $M = M_0$  at  $P = 0$ . As shown in Figure 5a, the data of the plasma-sprayed spinel can be described quite well with  $P_{crit} = 0.140$  and  $m = 0.35$  (in-plane) or  $m = 0.75$  (out of plane).

From the experimental results of the present study we can conclude that the particles in the as-sprayed spinel fill the space almost perfectly but are only discontinuously bonded to each other. The stiffness drop observed upon annealing at increasingly higher temperatures below 900°C, where sintering processes are too slow to become effective, is probably due to microfracture events that weaken or

loosen part of these vulnerable inter-particle bonds, caused by recovery processes that go on in the rapidly solidified particles already at moderate temperatures. The dramatic stiffness increase observed upon annealing above 900°C is the impressive result of the transition from a very early to an intermediate state of powder consolidation, which to this extent can only be observed if the sintering grains fit almost perfectly together in the first place.

## CONCLUSIONS

Plasma-sprayed ceramic materials may be extremely compliant compared to the corresponding fully dense materials, even if they exhibit only moderate porosities. The reason for this effect is that, even if the spray-deposited grains fill the space to a large degree, these grains may be bonded only locally to each other, forming intergranular slit-pores which strongly decrease the elastic moduli but possess only a small volume fraction. Annealing treatments at moderate homologous temperatures may reduce the stiffness even further. Due to the brittleness of the material, these local intergranular bonds are highly sensitive to small shape changes of the adjacent grains, caused, e.g., by recovery processes. As this study shows, such fracture processes can have a considerable effect on the stiffness, while no porosity increase is observed within the error of measurement. Upon annealing at high homologous temperatures, the grains sinter together and the slit-pores spheroidize and vanish, which gives rise to a dramatic stiffness increase. It should be noted, however, that a large fraction of this increase again is observed at virtually constant porosity, indicating that the change of average pore shape is much more important than the change of volume fraction. These results show that modulus-porosity correlations established for conventionally processed ceramic materials do not apply to plasma-sprayed materials and that it is generally not possible to estimate the elastic moduli of these plasma-sprayed materials with acceptable accuracy based only on density measurements. On the other hand, this study also shows that by relating the experimentally measured elastic properties and mass densities to the corresponding data of fully dense material, it is possible to get a deep insight into the microstructure of the material and into the morphological changes that occur upon heat treatment.

## ACKNOWLEDGEMENTS

The author thanks Dr. Ekkehard H. Lutz (formerly with LWK Plasmakeramik, Gummersbach, Germany) for provision of specimen materials and for helpful discussions, as well as Dagmar Vogt and Uschi Sattler (Max-Planck-Institut für Metallforschung, Stuttgart) for ceramographic preparation of specimens.

## REFERENCES

1. E.H. Lutz, *J. Am. Ceram. Soc.* **77**, 1274 (1994).
2. A. Wanner and E.H. Lutz, "Elastic anisotropy of plasma-sprayed, free-standing ceramic materials," *J. Am. Ceram. Soc.* (submitted 1998).
3. H.G. Wang and H. Herman, *Ceramic Bulletin* **68** (1), 97 (1989).
4. S. Schindler and W. Schultze, *Interceram* **37**, 39-32 (1988).
5. E.H. Lutz, LWK-Plasmakeramik GmbH, Wiehl, Germany (private communication, 1997/98).
6. A. Wanner, "Elastic Modulus Measurements of Extremely Porous Ceramic Materials by Ultrasonic Phase Spectroscopy," *Mater. Sci. and Engg. A*. (1998) *accepted for publication*.
7. L.C. Lynnworth, W.R. Rea, and E.P. Papadakis, *J. Acoust. Soc. Am.* **70**, 1699 (1981).
8. CRC Handbook of Chemistry and Physics, edited by R.C. Weast, 65<sup>th</sup> Edition (CRC-Press, Boca Raton, FL, 1984).
9. D.F. Porter, J.S. Reed, and D. Lewis III, *J. Am. Ceram. Soc.* **60**, 345 (1977).
10. L.J. Gibson and M.F. Ashby, *Proc. R. Soc. London A* **382A**, 43 (1982).
11. M. Kachanov, I. Tsukov, and B. Shafiro, *Appl. Mech. Rev.* **47** (1), S151 (1994).
12. J.C. Wang, *J. Mater. Sci.* **19**, 801 (1984).
13. K.K. Phani and S.K. Niyogi, *J. Mater. Sci.* **22**, 257 (1987).

---

**Part II**  
**Mechanical Properties of  
Metallic Foams**

## Reduction In Young's Modulus Of Aluminum Foams Due To Cell Wall Curvature And Corrugation

W. Sanders, L. J. Gibson

Department of Materials Science and Engineering, Massachusetts Institute of  
Technology, Cambridge, MA 02139, ljgibson@mit.edu

### ABSTRACT

Measurements of the Young's modulus and compressive strength of several closed-cell aluminum foams indicate that they are lower than expected from models for foam behaviour. Microstructural characterization has revealed that there are a number of defects in the cell structure which may contribute to the reduction in mechanical properties. These include: cell wall curvature, cell wall corrugations, density variations and non-equiaxed cell shape. Finite element analysis of a closed-cell tetrakaidecahedral unit cell with idealized curved or corrugated cell walls indicates that these two types of defects can reduce the Young's modulus and compressive strength by up to 70%. In this paper we report the results of measurements of the curvature of the cell walls and of the amplitude and frequency of corrugations in the cell walls and use simple bounds to estimate the reduction in modulus that they are responsible for.

### INTRODUCTION

Measurements [1] of the Young's modulus and compressive strength of several closed-cell aluminum foams indicate that they are lower than expected from various models [2-4]. The moduli and strength are found to vary roughly as the square of the relative density, as one might expect for an open-cell foam [2]. Models for closed-cell foams suggest that both the Young's modulus and the compressive strength should vary almost linearly with relative density. Microstructural characterization has revealed that there are a number of defects in the cell structure which may contribute to the reduction in mechanical properties [1, 5]. These include: cell wall curvature, cell wall corrugations, density variations and non-equiaxed cell shape. Finite element analysis of a closed cell tetrakaidecahedral unit cell with curved or corrugated cell walls indicates that these two types of defects may be responsible for reductions in modulus and strength of up to 70% relative to the values for cells with planar cell walls. In this study we report measurements of the curvature and of the amplitude and frequency of corrugations in the cell walls of closed-cell foams manufactured by Alcan, [Kingston, Ontario, Canada, now produced by Cymat, Mississauga, Ontario, Canada], Shinko Wire [Amagasaki, Japan, trade name Alporas] and Mepura [Ranshofen, Austria, trade name Alulight].

### MATERIALS AND METHODS

Specimens of closed-cell aluminum foam were obtained from each manufacturer. The relative densities of the specimens were: Alporas ( $\rho^*/\rho_s = 0.08$ ), Alulight ( $\rho^*/\rho_s = 0.14$ ) and Alcan ( $\rho^*/\rho_s = 0.06, 0.14$ ). Surfaces were cut using an electric discharge machine (EDM). The contrast of the cell edges was improved by painting the outer layer of cells with matte black spray paint and then grinding the paint off the edges at the surface. The image of the surface of each specimen was then digitized using an Apple Color OneScanner 600/27 and improved by manipulating the contrast with NIH Image version 1.59. The curvature and corrugations measurements were made using Canvas version 5.0. Curvature measurements were made on horizontal slices of each foam. A single horizontal slice was examined in the Alporas and Alulight foams. Three horizontal slices, in the top, middle and bottom sections of the Alcan foams were

examined corresponding to the sections of Alcan foam characterized by Simone [1]. Between 300 and 1200 cell walls were examined on each type of foam. Cell wall curvature was characterized by the enclosed angle  $\theta$  which was determined by measuring the length  $L$  and area  $A$  of the triangle shown in Fig. 1a. Assuming constant radius of curvature, the enclosed angle,  $\theta$ , is found from:

$$\theta = 4 \tan^{-1} \left( \frac{4A}{L^2} \right) \quad (1)$$

Note that the angle  $\theta$  is related to the normalized curvature parameter  $L/2R$  used by Simone and Gibson [3] by  $L/2R = \tan(\theta/2)$  where  $R$  is the radius of curvature. The data for enclosed angle for each specimen was plotted as a histogram with  $10^\circ$  increments in  $\theta$ .

Cell wall corrugations were observed only in the 6% dense Alcan foam, and only in vertical planes. The corrugations are thought to be the result of cell wall buckling during processing, while the cell wall material is cooling; it is thought that the cell walls in the denser foam are more resistant to buckling. For each cell wall the length  $L$ , amplitude  $\alpha$ , and number of corrugations were measured (Fig. 1b). Average values of the normalized amplitude ( $\alpha/L$ ) and normalized frequency ( $L/\lambda$ ) were calculated.

The reduction in Young's modulus due to the curvature was estimated using simple upper and lower bounds:

$$E_{upper} = \sum_i E_i V_i \quad (2)$$

and

$$E_{lower} = \frac{1}{\sum_i \frac{V_i}{E_i}} \quad (3)$$

where  $E_i$  is the Young's modulus of a unit tetrakaidecahedral cell with the curvature  $i$  [3] and  $V_i$  is the volume fraction of cell walls with curvature  $i$ . The reduction in Young's modulus due to cell wall corrugation was estimated from the Young's modulus of a unit tetrakaidecahedral cell with the measured average values of normalized amplitude ( $\alpha/L$ ) and normalized frequency ( $L/\lambda$ ) [3]. The combined effect of both curvature and corrugations for the 6% dense Alcan foam was obtained by multiplying the modulus reduction for each effect.

## RESULTS AND DISCUSSION

Histograms of the curvature of the cell walls of each of the foams are shown in Fig. 2. The cell walls in the Alporas foam have the lowest curvatures, with 80% of the cells with enclosed angles of less than  $40^\circ$ . The Alulight foam had an almost uniform distribution of enclosed angles. There was little difference in the histograms of the enclosed angle for horizontal slices taken from the top, middle and bottom sections of the Alcan foams. The average values of the normalized amplitude and normalized frequency of the 6% dense Alcan foam are  $\alpha/L = 0.058$  and  $L/\lambda = 1.14$ , respectively.

Previously obtained data for the relative modulus is plotted against relative density in Fig. 3 along with lines indicating the predictions of Gibson and Ashby's models for open- and closed-cell foams and Simone and Gibson's finite element estimates for the unit tetrakaidecahedral cell with planar faces. The data for the closed cell foams studied here lie near the line for open-cell foams and well below those for closed-cell foams. The discrepancy between the measured modulus and the closed-cell model prediction is a factor of between 3 for the higher density foams and 10 for the lower density foams.

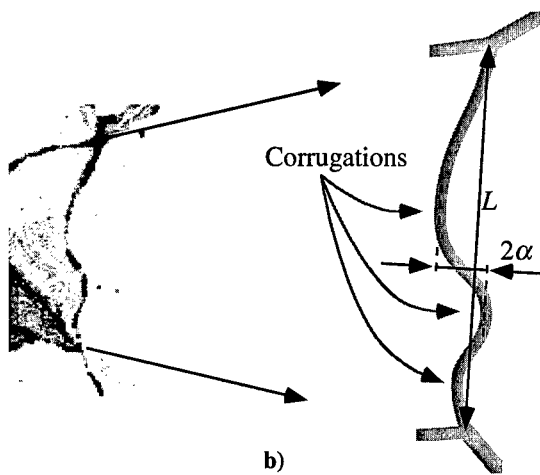
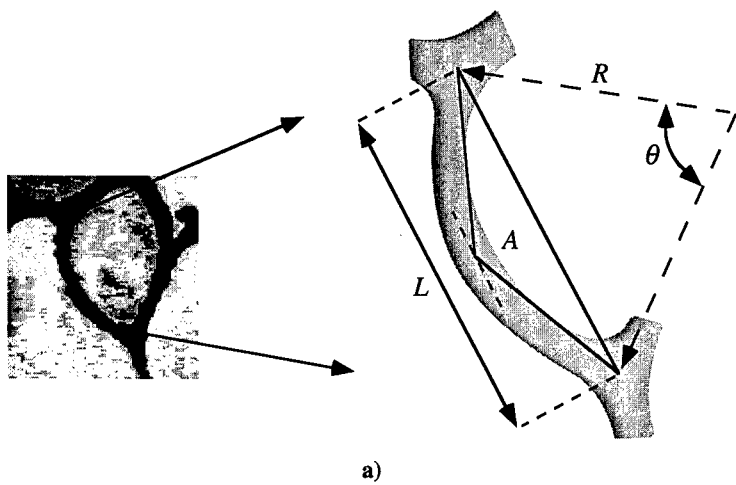


**Figure 1.** Illustration of measurement of a) cell wall curvature and b) cell wall corrugation in foam.

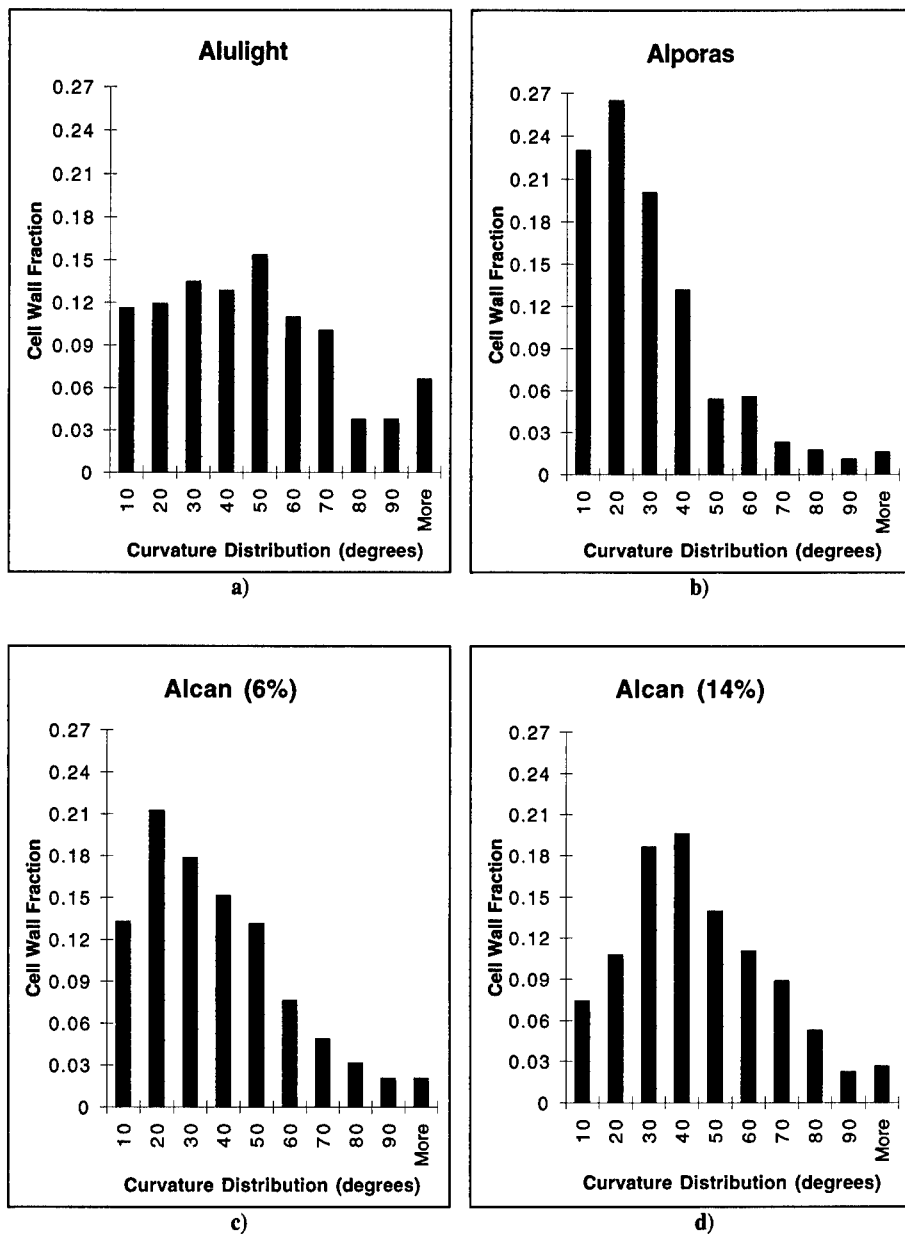
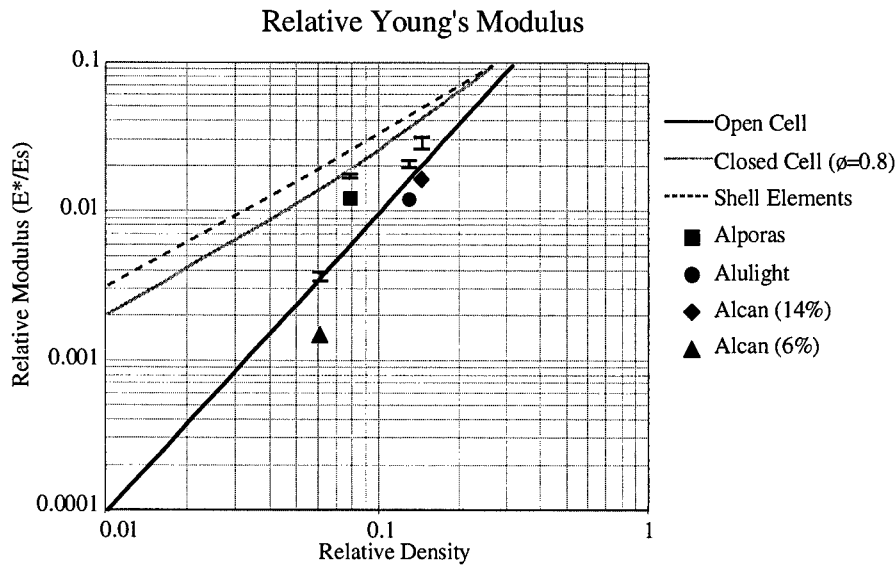


Figure 2. Curvature distribution for a) Alulight, b) Alporas, c) Alcan (6%), and d) Alcan (14%).



**Figure 3.** Relative Young's Modulus versus relative density for several foams including corrections for curvature and corrugation.

The estimated increases in the values of Young's modulus that could be expected if the cell wall curvature and corrugations were not present are indicated on the figure. The curvature and corrugations appear to be responsible for a reduction in the Young's modulus by a factor of roughly 2-3.

### CONCLUSIONS

The curvature and corrugations in the closed cell foams studied here appear to be responsible for a reduction in the Young's modulus by a factor of 2-3. The measured values of Young's modulus are lower than those predicted by models for closed-cell foams by even larger factors.

### REFERENCES

1. Simone, A. E. and Gibson, L. J., *Acta Mater.*, 1998a, in press.
2. Gibson, L. J and Ashby, M. F., *Cellular Solids: Structure and Properties*, 2nd Ed. (Cambridge University Press, 1997)
3. Simone, A. E. and Gibson, L. J., *Acta Mater.*, 1998b, in press.
4. Grenestedt, J., "Influence of cell wall wiggles on stiffness of cellular solids", (Internal report) Mech 295, Harvard University (1996).
5. Sugimura, Y., Meyer, J., He, M. Y., Bart-Smith, H., Grenestedt, J. L. and Evans, A. G., *Acta Mater.*, 1998, in press.

## COMPRESSIVE, TENSILE AND SHEAR TESTING OF MELT-FOAMED ALUMINIUM

H. VON HAGEN, W. BLECK

Institute of Ferrous Metallurgy (IEHK), Aachen University of Technology, Intzestr.1, 52072  
Aachen, Germany

### ABSTRACT

For construction purposes it is utterly important to get detailed information on the possible influence of the foam thickness on the mechanical properties and on the deformation behaviour of metallic foams. The effect of compressive, tensile and shear loads on aluminium foam samples has been examined with the testing methods for sandwich material as described in German and ASTM-standards. The aim is to provide more data on these mechanical properties varying the sample density and thickness. Regarding the results the most reliable material parameters as well as steps towards a relationship between the different strength parameters can be obtained.

### INTRODUCTION

At the IEHK the test procedures according to German standards (DIN), that are similar to ASTM-standards, have been established for the testing of sandwich material (steel facesheets and aluminium foam core) under compression, tension and shear<sup>1</sup>. As under ideal conditions these tests should only affect the foam core, a number of melt-foamed aluminium samples has been tested to obtain mechanical properties according to the variation of their density and thickness.

### EXPERIMENT

#### Chemical Composition and structure of tested materials

**Table I:** Chemical composition (mass-%) of the tested aluminium foams (alloyed silicon and silicon carbide contents calculated from analyzed silicon and carbon contents).

Foam	C	Si total	Si sol.	SiC	Mn	Cu	Ti	Ca	Mg	Fe	Zn
I	0,014	0,05	0,05	-	<0,005	<0,005	1,51	1,33	<0,001	0,11	0,002
II	3,36	14,39	6,53	11,22	0,03	0,082	0,083	0,0041	0,518	0,22	0,073

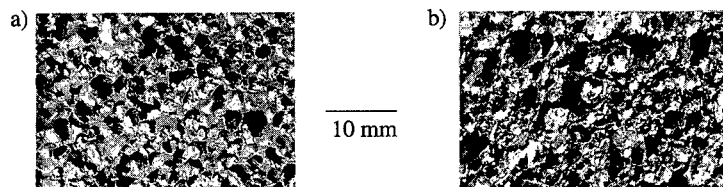


**Fig. 1:** Porous structure of a) foam I (density 0,35 g/cm<sup>3</sup>) and b) foam II (density 0,21 g/cm<sup>3</sup>).

**Table I** shows the chemical compositions of the two tested foams. A discontinuous process is used for foam I (Alporas). Its structure is shown in **Fig. 1a**. After melting aluminium in a mould

calcium is alloyed to increase the viscosity.  $\text{TiH}_2$  is injected as a blowing agent expanding the melt and forming the cells. Foam slabs are obtained after cooling showing a characteristic density profile between 0,2 and 0,43  $\text{g/cm}^3$  parallel to the foaming direction<sup>2</sup>. A principally continuous process (foam II, Alcan) is based on the application of particles (SiC) to increase the viscosity and stabilize the gas bubbles. The blowing gas is injected directly forming a liquid foam at the melt surface. This foam is taken away by a transportation belt<sup>3</sup>. The structure is depicted in Fig. 1b. The densities range between 0,18-0,36  $\text{g/cm}^3$ . The test samples (15 mm thick) are taken vertically with regard to the density profile.

### Compression Test

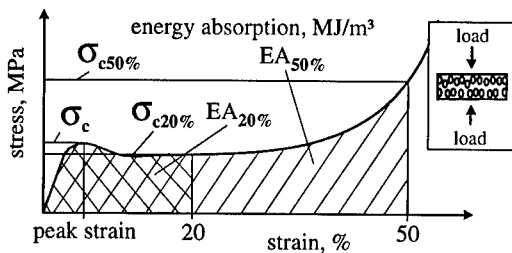


Fig. 2: Compression test, schematic test set-up and stress-strain curve.

The flatwise compression test (DIN 53291/ASTM C365) is performed on small samples (50 by 50 mm), the compressive load is applied vertically to the surfaces with a constant rate of motion. The stress-strain curve shows the typical course for foams with three stages, Fig. 2<sup>1</sup>. The compressive strength  $\sigma_c$  at peak strain, if it exists, can be determined by this test as well as the stress at 20 or 50% deformation ( $\sigma_{c20\%}$  or  $\sigma_{c50\%}$ ). The energy absorption ability of the foam is measured as the area below the curve for 20 or 50% strain ( $EA_{20\%}$  or  $EA_{50\%}$ ).

### Tensile Test

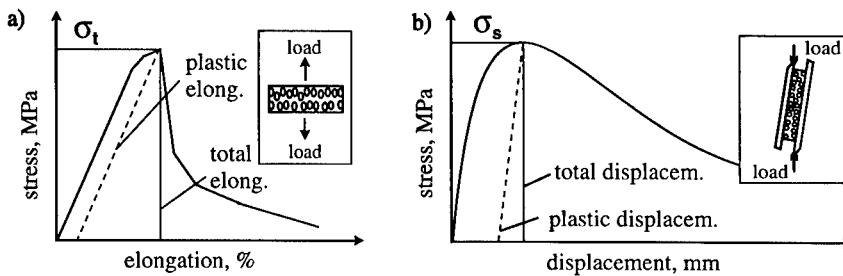


Fig. 3: Schematic test set-ups and stress-deformation curves, a) tensile test and b) shear test.

With this method (DIN 53292/ASTM C297) samples (50 by 50 mm) glued to loading fixtures by an epoxy resin are tested under a tensile load at a constant rate of motion as shown in Fig. 3a<sup>1</sup>. At the first stage the stress-elongation curve indicates a linear-elastic elongation behaviour. After a short plastic elongation a crack starts cutting the foam core. From then on the load decreases very fast. This test gives information on the tensile strength and demonstrates a small plastic deformation and energy absorption even for ductile foams.

## Shear Test

The determination of the shear properties of an aluminium foam sample is of special interest because the foam has to transmit the shear loads used as a core for sandwich construction. The shear test (DIN 53294/ASTM C273) is demonstrated in Fig. 3b<sup>1</sup>. A compressive load is introduced so that the sample (200 by 40-50 mm) is diagonally under a shear load. The deformation of the sample is measured as the displacement of the load plates against each other. The resulting stress-displacement curve demonstrates an almost linear-elastic beginning that changes into plastic deformation. The maximum load defines the failure visible as a crack cutting the whole sample. After that the load decreases fast, the further load is based on the cracked cell walls clinging against one another. The maximum load determines the shear strength  $\sigma_s$  of the foam.

## RESULTS

### Compression Test

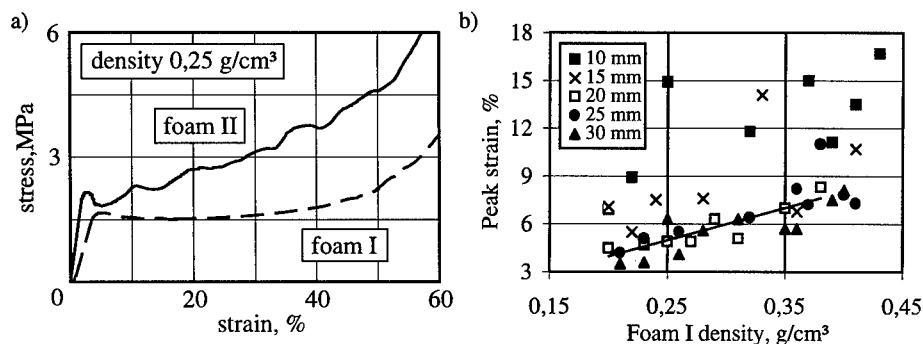


Fig. 4: a) Comparison of stress-strain curves of foam I and II (thickness 15 mm, density 0,25 g/cm<sup>3</sup>) and b) peak strain for different thicknesses (foam I).

The Foam II material shows a higher compressive strength and energy absorption due to its chemical composition with high contents of SiC and soluble silicon, Fig. 4a. But this composition results in a higher brittleness of foam II with a rising second stage and oscillations in stress during the compression. Foam I has a slow, smooth rising of stress during the second stage. The peak strain of foam I is affected by the sample thickness, Fig. 4b. At 10 and 15 mm the results display a rather high scatter (5 to 19% strain). The thicker samples show low peak strain values with a slow, approximately linear increase corresponding to the foam density.

In Fig. 5a the compressive stress of foam I at 20% and 50% strain over the density for five different sample thicknesses can be observed. As the scatter of the compressive strength  $\sigma_c$  is higher than that of the stress at 20% strain with their almost congruent parabolic compensation curves, the latter should be used as reliable data for foam I. A higher scatter with increasing density can be observed presumably caused by material clusters with a higher density, that increase the sample mass without rising the stress. Low densities are only obtained in samples without clusters explaining this effect starting at a density of 0,26 g/cm<sup>3</sup>. A significant influence of the sample thickness on the compressive stress is not visible. The energy absorption is shown in

Fig. 5b. It is also not distinctively dependent on the sample thickness and it grows with increasing density. The energy absorption increases faster at 50% strain due to the rising stress.

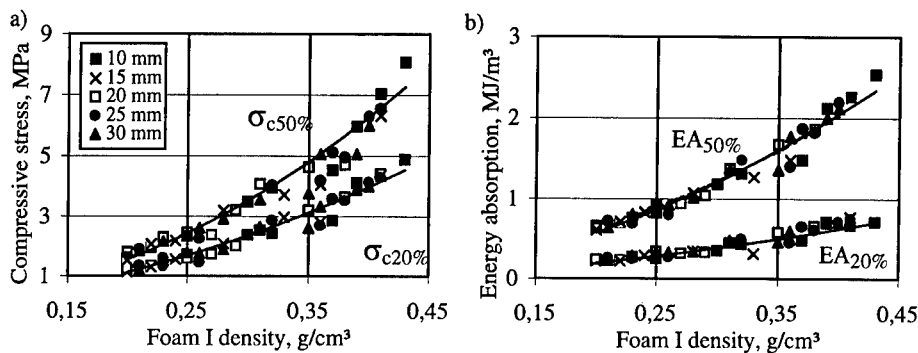


Fig. 5: a) Compressive stress and b) energy absorption at 20% and 50% strain for different sample thicknesses (foam I).

#### Tensile Test

The tensile testing effects a rather high scatter of the tensile strength values, Fig. 6a. It seems that this test is especially critical to inhomogeneities of the foam samples. With decreasing sample thickness and increasing density the total elongation grows for foam I, Fig. 6b, while foam II shows an almost constant elongation level. Regarding the behaviour of foam I the important role of elastic deformation during the tensile test becomes visible.

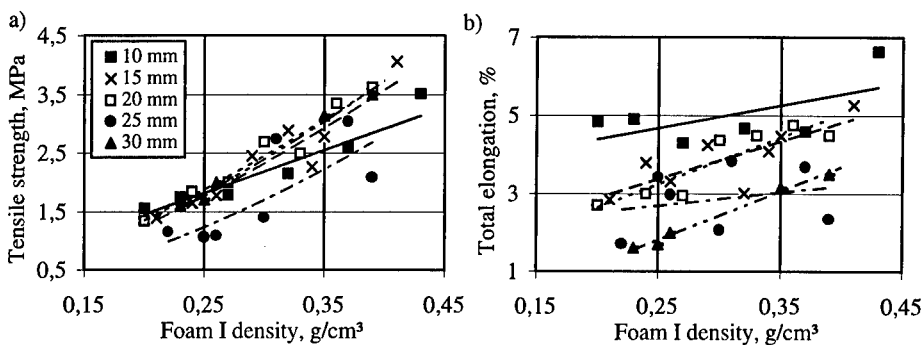


Fig. 6: a) Tensile strength and b) total elongation for different sample thicknesses (foam I).

#### Shear Testing

The shear tests, Fig. 7a, result in a lower scatter of the strength values than the tensile tests. Parabolic compensation curves fit the shear strength with growing foam density. An influence of the sample thickness cannot be observed. The displacement grows with increasing density and rising sample thickness, Fig. 7b.

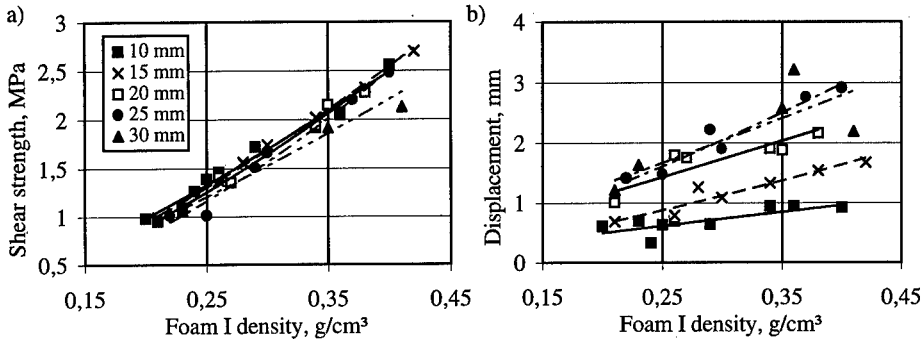


Fig. 7: a) Shear strength and b) displacement for different sample thicknesses (foam I).

Comparison of compressive, tensile and shear testing results

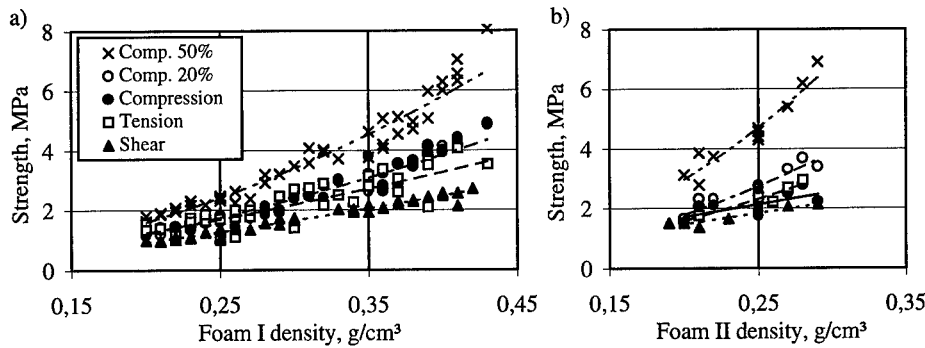


Fig. 8: a) Comparison of compressive, tensile and shear strength a) foam I (all thicknesses) and b) foam II (sample thickness 15 mm).

Fig. 8a demonstrates the relationship between the strength properties of foam I, obtained by the different tests neglecting the difference in thickness, Fig. 8b that of foam II (thickness 15 mm). Shear is the most critical load, therefore it should be used as a criterion in sandwich construction. Ashby et al. have determined a dependence of the compressive strength  $\sigma_c$  on the relative density  $\rho_f/\rho_s$  (foam)/ $\rho_s$  (solid) and the yield strength  $\sigma_{ys}$  (solid) in MPa, in its simplest form matching an open-cell foam written as equation (1)<sup>4</sup>, generalized for strength in equation (2):

$$\sigma_c = \sigma_{ys} \cdot 0,3 \cdot \left(\frac{\rho_f}{\rho_s}\right)^{3/2} \quad (1) \quad \Rightarrow \quad \sigma = \sigma_{ys} \cdot const. \cdot \left(\frac{\rho_f}{\rho_s}\right)^{exp} \quad (2)$$

If we apply this model (equation (2)) to all the strength/stress results, the parameters in Table II are obtained. There has been only a smaller number of foam II samples in comparison to foam I, so these results are somewhat uncertain.

**Table II:** Resulting parabolic compensation curves written as parameters of equation (2).

foam parameters	I (more ductile)		II (more brittle)	
	const. $\cdot \sigma_{ys}$	exponent	const. $\cdot \sigma_{ys}$	exponent
compr. stress at 50% strain	200	1,85	610,6	2,05
compr. stress at 20% strain	123,1	1,81	260,3	1,92
compressive strength $\sigma_c$	93,0	1,67	21,3	0,97
tensile strength $\sigma_t$	47,3	1,40	138,9	1,72
shear strength $\sigma_s$	35,4	1,40	19,4	0,99

The parabolic compensation curves match the results in an acceptable way showing some significant differences between the two materials. The higher exponent ( $> 3/2$ ) for foam I at compressive strength is based on the foam's material distribution that doesn't exactly fit the assumption of an open-cell foam. The values for the compressive stress at 20% strain don't differ much from that of the compressive strength. The curve for the compressive stress at 50% strain has the highest gradient. The lower coefficients of tension and shear show the more critical load forms. It seems that an equitation for the strength difference between compression, tension and shear has to consider an additional density influence. Regarding the differences between the more ductile foam I and the more brittle foam II the higher stress properties at 20 and 50% strain as well as the bigger differences in the gradient of the compensation curves of the latter are clearly to be observed. In contrast to foam I the results of foam II fit the simple assumption of  $\sigma_t = 1,1 \cdot \sigma_c$  better, but also with an additional density influence<sup>4</sup>. The rather low values for the compressive strength especially in comparison to the stress results at 20% strain are interesting. The materials deformation characteristics visible in the course of the stress-strain curve seem to play an important role on the relationship of the strength/stress values under different loads.

## CONCLUSIONS

The behaviour of aluminium foam samples under compressive, tensile and shear loads has been examined according to German standards, that are similar to that of the ASTM. Visualizing the strength properties no distinct influence of the sample thickness can be observed, in contrast there is one onto the strain properties. The strength results can be described with the Gibson/Ashby model, obtaining a relationship between the different strength and stress parameters. The uncritical load usually is compression, the most critical one is shear. Higher strength values, but lower deformation are obtained for the more brittle foam compared to the more ductile one.

## REFERENCES

1. H. v. Hagen, D. Nicklas, W. Bleck, in Proceedings of the 5th European Conference on Advanced Materials, Processes and Applications, Vol.1, edited and published by the Netherlands Society for Materials Science (Zwijndrecht, 1997), p. 415-418.
2. S. Akiyama et al., European Patent EP 0 210 803 B1 (20 September 1989).
3. H. Sang and L.D. Kenny, European Patent EP 0 587 619 B1, (10 July 1996).
4. M.F. Ashby, C.J. Seymour, D. Cebon, in Metallschäume, edited by J. Banhart (MIT Publishers, Bremen, 1997), p. 199-216.

---

## Effects of Thermomechanical Processing on the Resulting Mechanical Properties of 6101 Aluminum Foam

R. W. Margevicius, P. W. Stanek, and L. A. Jacobson  
Los Alamos National Laboratory, Los Alamos, NM 87545

### Abstract

High porosity aluminum was fabricated in a number of ways. The starting material was a cast 6101 aluminum that had a relative density of 9.8%. The cast aluminum block was compressed by uniaxial, biaxial, and triaxial densification. Uniaxial compression was done at room temperature and 200°C. Biaxial compression was achieved by unidirectional rolling at room temperature and 200°C. Triaxial compression was done by cold isostatic pressing at 3.4, 6.7, and 34 MPa (0.5, 1.0, and 5.0 ksi). Metallography and mechanical test specimens were machined from the processed bars. The mechanical properties showed that the relative yield strength depended both on relative density and processing temperature.

### Introduction

It has been long realized that foaming materials is an effective means for improving some properties while not dramatically affecting others. For example, an obvious driving force for using porous materials is a reduction in density, however, thermal conductivity can remain fairly high in foamed materials (see, for example, Figure 1.3 in reference [1]).

The goal of the program being pursued at Los Alamos is the production of a 30-60% relative density beryllium aluminum foamed material. The principal production path being pursued at Los Alamos is the consolidation of powder by hot isostatic pressure (HIP) where the powder is not evacuated under vacuum, but rather the trapped interparticle spacing is under pressure. This powder/pressurized gas compact, now at about 80-90% relative density, would be heated at ambient pressure to allow the argon to swell the compact by creep mechanisms. The resultant foam would be closed pore with approximately 30-60% relative density.

An alternate processing route to the production of a 30-60% relative density porous material is the densification of a less dense, e.g., 10% relative density, material. It is the purpose of the work detailed here to examine how different processing routes would affect the density achieved as well as the resulting mechanical properties. Since beryllium processing imposes daunting fabrication as well as safety issues, an aluminum was chosen first as a surrogate for the beryllium. Ultimately, beryllium and beryllium/aluminum porous structures are the goal.

### Materials and Methods

#### Cast Aluminum Foam

A 10% relative density foam was obtained from ERG, Inc. The block was approximately 100x300x300 mm (4x12x12 in.) with a pore size of ~0.8 mm (20 pores per inch). The foam is nominally an aluminum 6101 alloy (Al-0.6Mg-0.5Si) with an as cast microstructure.

#### Processing

The cast aluminum foam was subject to three main processing routes, corresponding approximately to uniaxial, biaxial, and triaxial compression. Samples for densification had a minimum dimension any given direction of 25.4 mm (1 inch). Samples were compressed uniaxially in a universal testing machine at two strain rates and two temperatures. The strain rates tested were 0.001/sec and 0.1/sec and the temperatures tested were 25 and 200°C. The foams compressed at 200°C were not tested in a furnace, but rather were put in a furnace at about 225°C, quickly transferred to the testing machine, and the compression test was completed in six seconds.

Samples were rolled using a standard rolling mill at 25 and 200°C. Here again, the foam was in a furnace at about 250°C, it was removed from the furnace, taken to the rolls, and rolled in about five seconds. The rolls were preheated to about 175-200°C. Samples for CIPping were sealed in a polyethylene envelope and subjected to at 3.4, 6.7, and 34 MPa (0.5, 1.0, and 5.0 ksi) isostatic pressure at room temperature. To discern the effect of densification on the resulting mechanical properties, bend tests were performed on selected foams. Samples approximately 8x8x40 mm were cut from densified foams and tested in four-point bending. While it was realize *a priori* that this was likely to be too small of a cross section to adequately test a foam, since all the samples would have these dimensions, we felt some qualitative comparisons might be made.

## Results and Discussion

### Compression of As-cast Foam

The two properties of interest when looking at the foams at lower magnification are the relative density and uniformity of densification. The relative densities for all the foams processed are given in Table below.

The densification of the as-cast foam by uniaxial compression is shown in Figure 1. The three conditions shown are room temperature 0.001 and 0.1/sec and 200°C 0.1/sec. Increasing the strain rate from 0.001 to 0.1/sec increases the yield stress,  $\sigma_{pl}^*$ , from about 1.2 to 1.8 MPa. The effect of increasing the temperature from 25 to 200°C at constant strain rate lowers the yield stress from about 1.2 to 1.0 MPa. The yield stress is approximately 1-1.5 MPa for the conditions tested here. A calculation of the theoretical yield stress based on the relative density [1]

$$\frac{\sigma_{pl}^*}{\sigma_{ys}} \approx 0.3 \left( \frac{\rho^*}{\rho_s} \right)^{1.5}$$

with  $\sigma_{ys}$  equaling approximately 55 MPa for 6101 Al in an overaged condition [2] would give  $\sigma_{pl}^*/\sigma_{ys}$  of about 0.55 MPa. The yield stresses here are about two times higher. However, the exact condition of the as-cast foam has not been determined and is the subject of continuing research: an overaged condition is assumed, however, something between peak aged and overaged is certainly possible. The densification strain (not shown in Figure 1) was approximately 50-60%.

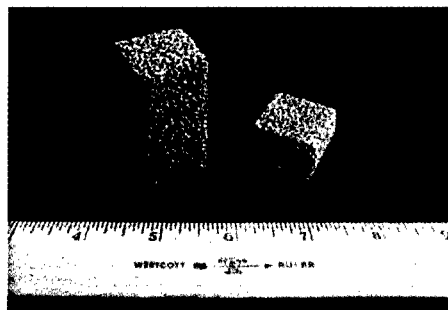
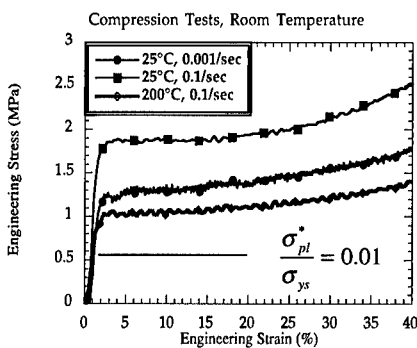


Figure 1. Compression tests of as-cast foamed aluminum.

Figure 2. As-cast and compressed foams.

Table. Resulting relative densities from the various processing paths.

Process	Conditions	Process Temperature (°C)	Relative Density (percent)
Uniaxial Compression	0.001/sec	25	23
	0.1/sec	25	27
	0.1/sec	200	29
Rolling	30% reduction, one pass	25	11
	30% reduction, six passes	25	11
	65% reduction, two passes	25	18
	65% reduction, six passes	25	19
	65% reduction, one pass	200	23
CIP	3.4 MPa	25	20
	6.7 MPa	25	31
	34 MPa	25	50

Occasionally compression of the foams from 50.8 mm to 18 mm caused a slight buckling, Figure 2. Although all three foams were compressed the same amount, slight differences in the relative densities were measured. We have not determined whether this is due to a sampling error or whether the effect is genuine. The desiccation of the foams was rather uniform, Figure 3. Although slight differences in densities were measured, this difference is likely due to sampling error rather than an intrinsic difference.

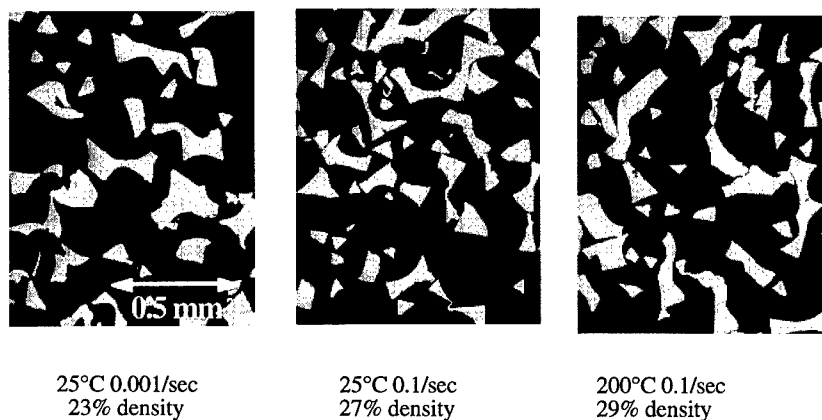


Figure 3. Densification microstructures of the uniaxially compressed foams.

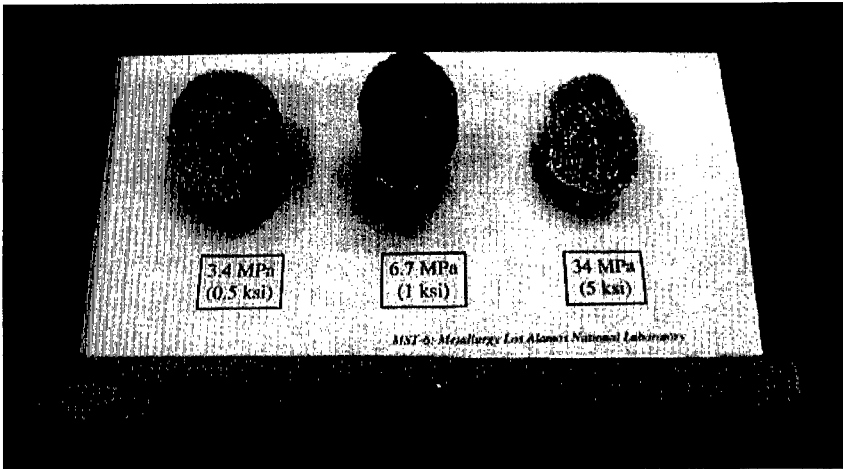
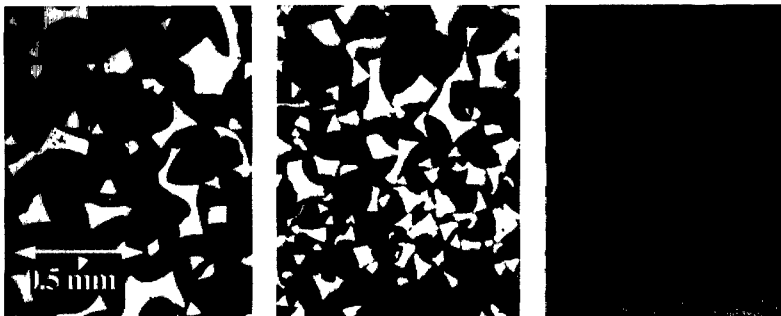


Figure 4. Anisotropic compaction of CIPped foams at 3.4, 6.7, and 34 MPa.

### **Cold Isostatic Pressing (CIPping)**

Cold isostatic pressing of the foam did not isotropically compact the foam, Figure 4. Independent of CIP pressure, the resulting shape of the once cylindrical piece was an elliptical cylinder. This may indicate some natural anisotropy present in the foam. To date, we have not kept track of the original thin dimension of the cast plate, but samples were taken such that the original cylindrical axes were parallel to one long direction of the cast block (*viz.*, the short direction of the cast block is parallel to the diameter of the cylinder).

CIPping did compact the foams, Figure 5. The lowest pressure we were able to produce, 3.4 MPa, compacted the originally 9.8% relative density foams to 20%. Increases in pressure produced correspondingly higher densities, Figures 5 and 6. Relative density increases dramatically at lower pressures and begins to saturate at the highest pressure, 34 MPa. This would be expected from the way in which foams densify; that is, at low densities, the large volume fraction of porosity does not interfere with the cell walls that are coming closer to each other. Once cell walls begin to impinge, correspondingly higher pressures are required to continue densification of the foam.



3.4 Mpa, 20% density

6.7 MPa, 31% density

34 MPa, 50% density

Figure 5. Compaction of CIPped foams

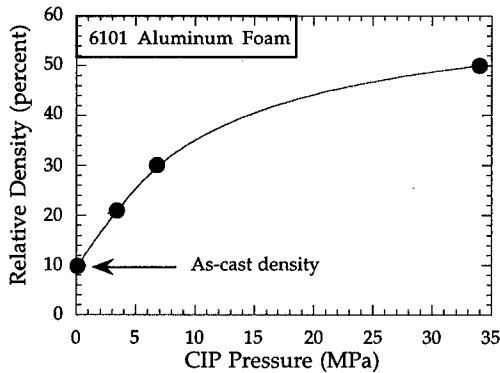


Figure 6. Density vs. CIP pressure for as-cast aluminum foam

### Rolling

The densification of the rolled foamed occurred qualitatively in the same fashion as the CIPped samples, that is, at 30 % reduction it increased from 9.8% to 11% dense, while at 65% reduction, the density increased to about 20%, Table. One concern was that the rolling process would densify the surfaces of the foams more and the inner part less. This did not apparently happen, Figure 7. The black strips on the top and bottoms of the left two micrographs represent the top and bottoms of the rolled foams. No higher density at the surfaces is readily apparent. Qualitatively, no difference in the microstructure between the samples rolled at 25°C and 200°C, Figure 7.

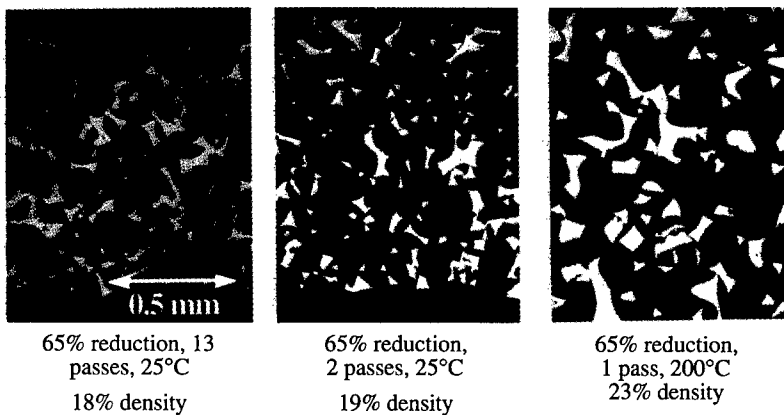


Figure 7. Densification of rolled foams.

### Bend Tests

Bend samples compressed at room temperature, (i.e., rolled at 25°C in two and 13 passes and CIPped at 6.7 MPa) with approximately the same density all had very similar stress displacement traces, Figure 8. The sample that had been machined from the bar rolled at 200°C had an appreciably lower curve, while that taken from the CIP 34 MPa material had a much higher curve.

The CIP 34 MPa sample can be understood in terms of its dramatically higher 50% relative density. The rolled 200°C curve was an interesting observation; while the relative density was similar to the room temperature samples, it is clear that the higher temperature processing did allow for some recovery to take place.

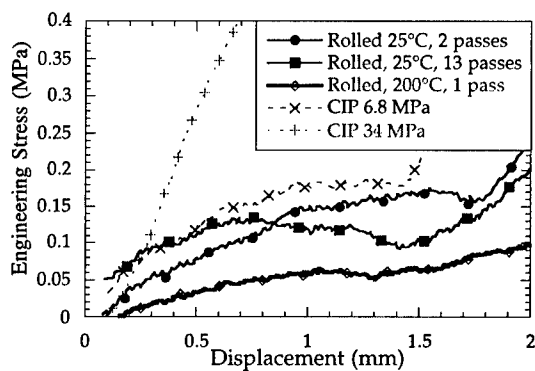


Figure 8. Room temperature bend tests of foams compacted by various methods.

## Acknowledgments

We would like to acknowledge DARPA for financial support. We would also like to thank D. Sandoval and D. Rodella for helping with the mechanical testing and J. Montoya and A. Kelly for the help with metallography.

## References

1. *Cellular Solids, Structure and Properties, second edition*, L. J. Gibson and M. F. Ashby, Cambridge University Press, Cambridge, UK, 1997.
2. *ASM Handbook*, vol. 2, ASM International, 104-5, 1990.

---

**COMPRESSIVE DEFORMATION AND YIELDING MECHANISMS  
IN CELLULAR Al ALLOYS DETERMINED USING  
X-RAY TOMOGRAPHY AND SURFACE STRAIN MAPPING**

H. BART-SMITH \*, A. -F. BASTAWROS \*, D.R. MUMM \*, A.G. EVANS \*,  
D.J. SYPECK \*\*, H.N.G. WADLEY \*\*

\* Division of Engineering and Applied Sciences, Harvard University, Cambridge, MA 02138

\*\* School of Engineering and Applied Science, University of Virginia, Charlottesville, VA 22903

**ABSTRACT**

The mechanisms of compressive deformation that occur in closed cell Al alloys have been established. This has been achieved by using x-ray computed tomography (CT) and surface strain mapping to determine the deformation modes and the cell morphologies that control the onset of yielding. The deformation is found to localize in narrow bands having width of order of a cell diameter. Outside the bands, the material remains elastic. The cells within the bands that experience large permanent strains are primarily elliptical. A group of cells work collectively to allow large localized deformation. Size does not appear to be the initiator of the deformation bands. Equiaxed cells remain elastic. The implications for manufacturing materials with superior mechanical properties are discussed. Visualization of internal deformation of a closed cell Al alloy core, as part of a sandwich panel construction, is also possible using x-ray tomography. Preliminary results for a punch indentation test are presented.

**INTRODUCTION**

Cellular metals have compressive stress/strain characteristics that enhance the mechanical performance of buckling or bending limited structures [1-3]. In order to attain these mechanical attributes, the cellular alloy must have stiffness and yield strength approaching theoretically achievable levels. The levels for closed cell solids with planar walls at low relative densities, (exemplified by the Kelvin solid) are expected to have stiffnesses represented by [4-8]:

$$\frac{E}{E_s} = 0.35\rho \quad (1a)$$

where  $E$  is the Young's modulus,  $E_s$  the modulus of the cell wall material and  $\rho$  the relative density. A similar relationship exists for the yield strength,  $\sigma_o$ , at low density [5,7,8]:

$$\frac{\sigma_o}{\sigma_s} \approx 0.3\rho \quad (1b)$$

where  $\sigma_s$  is the yield strength of the cell wall material.

The corresponding results for open cell solids are [8]:

$$\frac{E}{E_s} \approx \rho^2 \quad (2a)$$

and [10]:

$$\frac{\sigma}{\sigma_s} = 0.3\rho^{3/2} \quad (2b)$$

The difference between closed and open cell systems is that the deformations of the former are controlled by membrane stretching and the latter by beam bending [8].

Compression and tensile testing of various closed cell Al alloys [5,7,9,10] have revealed (Fig. 1) that their stiffnesses and yield strengths are in a range from a factor 2 to 100 lower than (1). This relatively inferior performance has been attributed to morphological defects, particularly non-planarities in the walls, such as curves and wiggles [4,6]. Numerical simulations [5-7] have affirmed the substantial influence of such defects on the properties. But, direct correlations between cell morphology and mechanical behavior have yet to be established. The purpose of this investigation is to observe the local deformations by methods that interconnect the properties with the cell morphologies. Both x-ray computed tomography (CT) [11-13] and optical methods are used. The former provides images of the interior cells and the latter of the surface features. These methods yield complementary information about the material deformations.

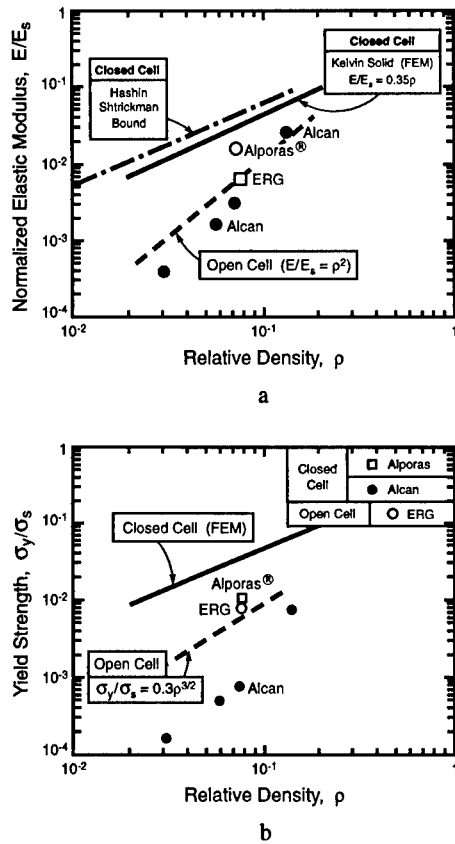


Fig. 1. The mechanical properties of cellular Al alloys compared with expected values for open and closed cell solids [7,9]: (a) Young's modulus, (b) yield strength.

## MATERIALS

One material is focused upon for this study.

It is a closed cell material with relative density,  $\rho = 0.07$ , having the cell morphology described elsewhere [9]. It has the trade name ALPORAS<sup>®</sup> [14]. The cells are about 3–4mm in diameter. The compressive stress/strain characteristics are illustrated on Fig. 2. In the plateau deformation domain there are distinct and quite regular stress oscillations, related to the number of deformation bands capable of forming. The compressive Young's modulus is:  $E \approx 1GPa$ . The nominal "yield strength", designated as the first peak in the stress/strain curve is:  $\sigma_o \approx 1.0 - 1.2MPa$  [5,7,9]. Local yielding occurs at much lower stresses, resulting in an initial loading modulus of only 200 MPa [6,7,9]. This material has about 1/3 the stiffness and yield strength expected from (1). But, it is stiffer than an open cell solid (2) at the equivalent density.

Surface strain measurements and x-ray studies were performed on ALPORAS<sup>®</sup>.

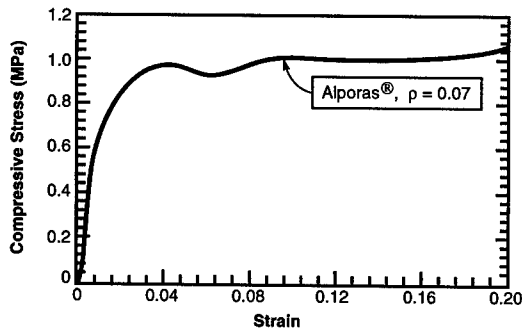


Fig. 2. Compressive stress/strain curve for ALPORAS.

## MEASUREMENT PROTOCOL

### Surface Strain Mapping

Commercial, digital speckle interferometry software [15] has been used for in situ surface deformation mapping. The method relies on comparison of pairs of images taken by optical microscopy during the deformation history sequence [16,17,23,24]. Two methods were implemented in order to define a continuum planar strain tensor on the surface, comprising cell walls, as well as cell cavities. (i) The surface was imaged directly. (ii) It was covered with a thin latex film epoxy-bonded to the surface with a substantial pre-stretch. In both cases, the specimen surface was sprayed with a krylon paint to enhance the speckle pattern.

The ALPORAS<sup>®</sup> specimens had dimensions, 30x30x50mm, such that the cross section was no less than 8 cells wide. Each specimen was compressed in a servohydraulic testing machine (Instron 8501) under displacement control at 50 $\mu$ m/s. Imaging was carried out with a CCD array of 640x480 pixels. Consecutive images were captured for later analysis. The principal in-plane incremental strains were obtained through post-processing of the displacement maps, employing a central difference scheme.

## X-Ray Computed Tomography

Compression tests with x-ray computed tomography were performed on the ALPORAS® material in order to quantify the yielding and deformation mechanisms. Initial testing was carried out externally from the imaging system. It was determined that the first stress minimum, beyond the initial peak, occurred at a strain ~6%, (Fig. 2). In subsequent tests, the cell deformation was characterized by this level of strain.

Before straining, the internal structure was imaged using a Picker (Cleveland, OH) PQ-2000 CT Imaging System. The specimen was tested using an electromechanical test frame and then removed to the CT machine. Repeated scans were taken to match those of the unconstrained configuration.

In situ compression testing was performed using a specially designed loading stage. This was placed directly into the CT machine and the specimen compressed incrementally. After each strain increment an image was taken, yielding a two dimensional projection of the middle cross section of the specimen. Compression was carried out to ~15% strain.

Features within the cellular material which determine the deformation characteristics, were highlighted. *These images capture the internal deformation fully constrained by all of the surrounding cells.*

## SURFACE STRAINS

Maps of the incremental principal strain, chosen to emphasize deformation banding, are displayed as a false color (Fig. 3), with the principal direction indicated by superimposed vectors. The ALPORAS® material deforms heterogeneously, by deformation banding, at loadings well below the peak stress ( $\sigma/\sigma_{\text{peak}} \approx 0.3$ ). Typically, at these loads, a band having width about one-cell diameter (3mm) initiates. It then propagates across the specimen as the load increases. At the load peak, the band has extended across the entire specimen (with local densification) and, thereafter, the stress decreases upon further straining. The band normals are usually within ~20° of the loading axis. In some cases, several bands (two or more) may initiate within the gauge length. In others, the band initiates at one of the loading platens. This happens primarily in specimens with relatively high peak stresses.

In all cases, the principal strain directions are normal to the band plane (Fig. 3), indicative of a crushing mode of deformation. There is a large strain discontinuity across each of the bands. Outside the bands, the average strains are small and in the elastic range. Within the bands, strain increments exceed the average by a factor of 10, indicative of cell collapse and local densification. Such behavior is typical of that found in the transverse compression of honeycombs [8], bonded cylinders [18], etc.

These surface measurements provide a vivid visualization of the importance of band formation in plastic deformation. However, they do not identify the cells that initiate the bands and, therefore, are unable to provide a morphological explanation for the relatively low yield strength. The following x-ray measurements provide some of the missing information.

## INTERNAL DEFORMATIONS

Images of interior cells before and after axial straining (Fig. 4) elucidate the cell morphologies that yield prematurely, as well as those that resist yielding. These images comprise two dimensional sections through the foam, each ~0.5mm thick. The displacements of locations within the cell walls obtained from comparisons before and after straining (Figs. 5a-c), provide an explicit visualization. The cells outside the deformation bands deform elastically and retain their original shape (Fig. 5c). Conversely, the cells exhibiting permanent deformations within the bands

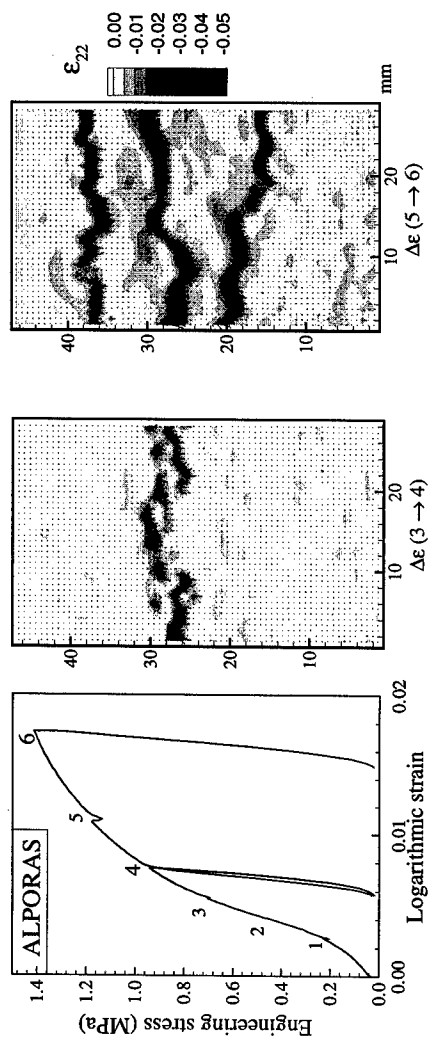


Fig. 3. Surface maps of the incremental principal strain. Principal directions are indicated by superimposed vectors. Stress-strain curves are also indicated

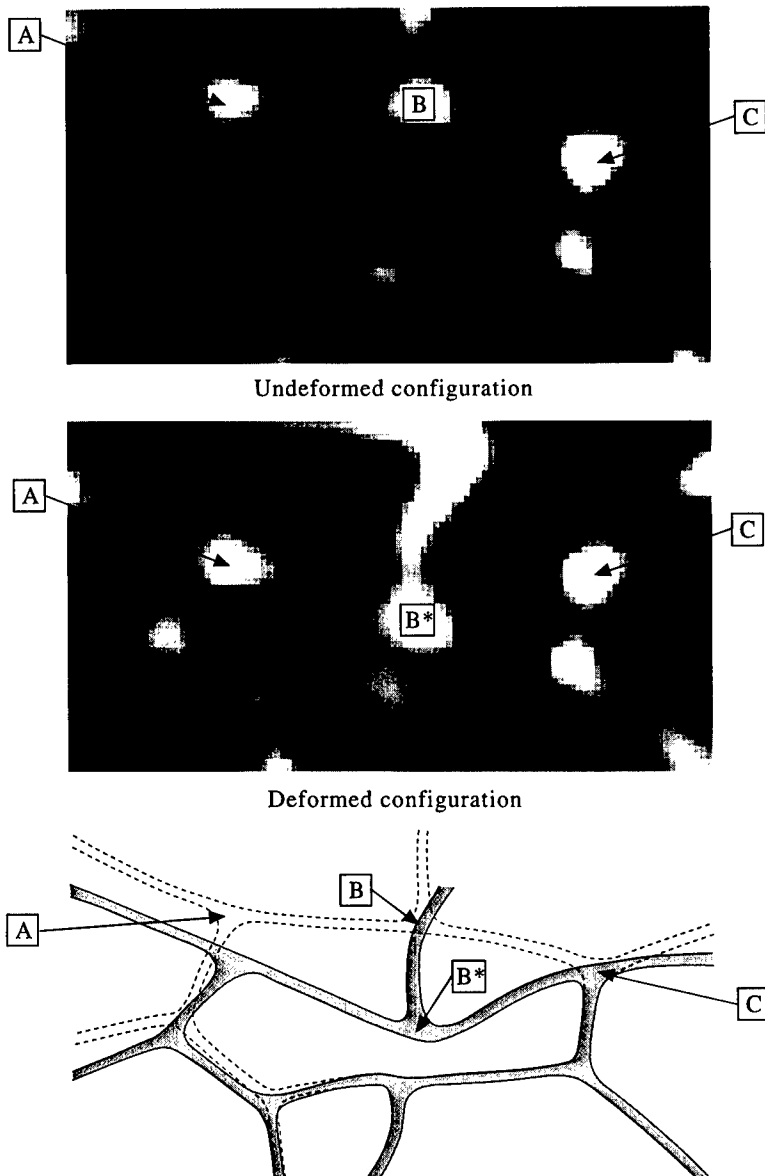


Fig. 4. X-ray tomographic images of a plane through the center of the test specimen before and after straining by 6%, highlighting a critical cell. Because of the image depth (1mm) there is apparent overlap of the cell walls. The schematic of the deformed and undeformed gives a clearer indication of the associated cell geometries.

comprise one of the two morphologies indicated on Fig. 5a,b. (i) Ellipsoidal cells with T-shaped cell wall intersections. These wall intersections are approximately parallel with the load direction. (ii) Non-planar walls with appreciable curvature. It is clear that an interaction between cells is necessary for deformation to take place within narrow bands. This cooperation is emphasized when critical cells of the types described are present. Further inspection of these images reveals that there is no obvious preference for the larger cells to be more susceptible to permanent deformations. That is, large cells remain elastic provided that they have an "equiaxed" morphology with minimal ellipticity. The implication is that shape is more important than size in determining the yielding susceptibility of the cells. Examination of cells within the deformation band shows more ellipticity than those outside.

Comparison between two consecutive images, produced from the in situ compression testing, pinpoints the location where a deformation band starts, (Fig. 6). The increment in strain between the two images is  $\sim 1.3\%$ . These cells show the ellipticity expected, combined with the necessary cell wall interactions. What is clear is that the deformation band is instigated at more than one location and that these "hot-spots" meet as straining is increased.

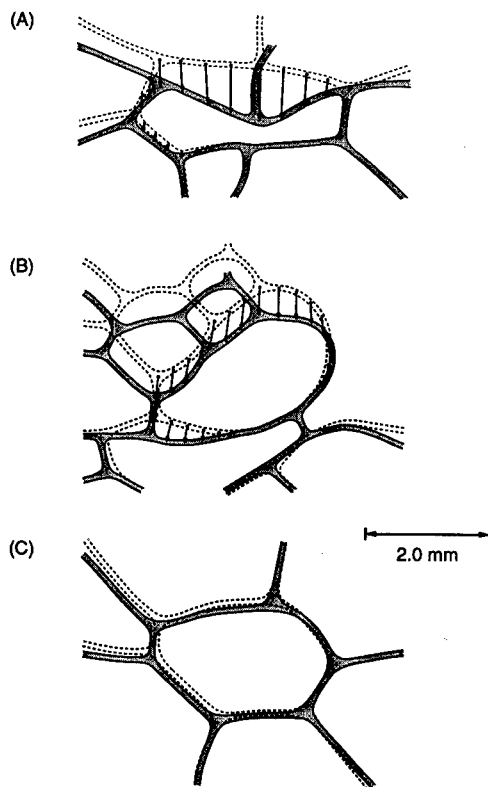


Fig. 5. Schematics of three typical cells indicating their shapes before and after testing to 6% strain: (a) and (b) represents cells within the deformation bands that experience appreciable permanent deformations, (c) represents a cell that experiences minimal change

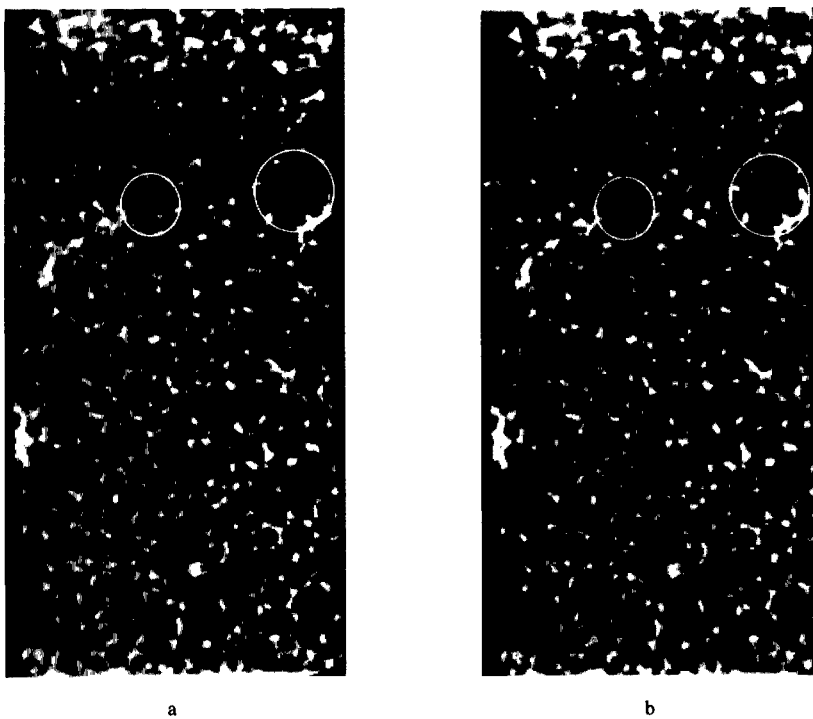


Fig. 6. Consecutive x-ray images from in situ compression test (~1.3% incremental strain). Critical cells for deformation band formation highlighted: (a) before straining, (b) after straining.

#### PUNCH INDENTATION OF SANDWICH PANEL WITH CLOSED CELL POROUS AL CORE

X-ray imaging has been used to analyze internal deformations of a sandwich panel. The panel is constructed using Al alloy 6061-T6 face sheets separated by a closed cell porous Al core, ALPORAS. The 5"\*5" panel has faces which are 0.03" thick and the core is 0.4" thick. Bonding between the core and face is achieved using a standard industrial epoxy adhesive.

After imaging the internal cell configuration, the panel was indented using a half inch diameter circular punch indenter. The indenter was displaced 3mm and the stress-displacement curve is presented, (Fig. 7). CT images were captured after deformation. Fig. 8 examines the internal structure of the core before and after indenting. Comparing these results with the compressive response of the core material alone, [9], it is clear that the face sheets have a significant influence on the mechanical response to straining.

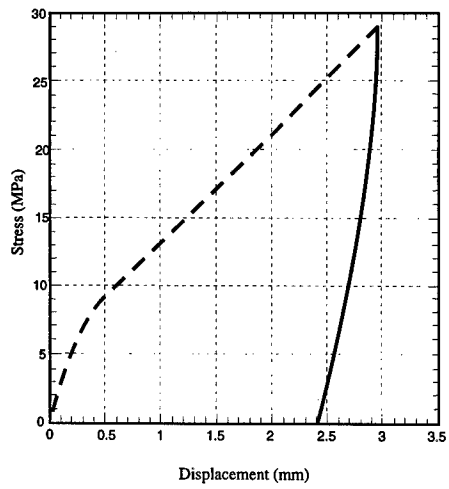
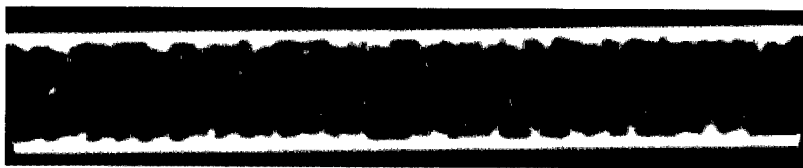
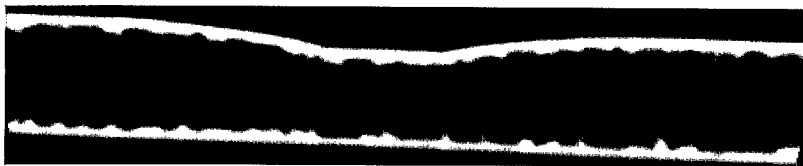


Fig. 7. Stress/displacement curve for punch indentation test of sandwich panel



a



b

Fig. 8. X-ray images showing internal deformation of a sandwich panel subjected punch indentation: (a) before indentation, (b) after indentation.

## CONCLUDING REMARKS

The cell morphologies that dictate yielding appear to be shape dominated. That is, elliptical cells with cell wall junctions that experience bending initiate band formation and have an important influence on the yield strength. Highly curved cell walls also have a detrimental influence. The former finding is consistent with calculations that demonstrate a diminished strength upon removal of cell walls [22,23], which serves to convert equiaxed cells into elliptical morphologies. The presence of large cells, provided that they are relatively equiaxed, appears to be of secondary performance.

Given the role of cell shape, improvement of the mechanical properties through control of the cells during manufacture appears to be particularly challenging. That is, while the elimination of large cells is tractable, approaches for avoiding elliptical cells are less clear. One contribution to ellipticity derives from gravitational effects at high temperature, which cause distortions of the cells. Addressing these issues may be an avenue for controlling cell shape and enhancing performance.

It is now possible to track the internal deformation of sandwich panels. Further investigation is to be carried out to examine the effects of the face/core interface. The influence of face sheet thickness must also be quantified.

## ACKNOWLEDGMENTS

The authors recognize the assistance provided by Boeing in the supply of materials.

## REFERENCES

1. B. Budiansky, Harvard University, Mech 319, November 1997.
2. W. Abramowicz and T. Wierzbicki, *Int. J. Mech. Sci.*, **30**, 1988, 263-271.
3. M. Y. He and J. W. Hutchinson, unpublished research.
4. A. Kraynik, M. K. Neilsen, D.A. Reinelt and W. E. Warren in Foams, Emulsions, and Cellular Materials, edited by J-F Sadoc and N. Rivier (to appear in the Proceedings of the NATO Advanced Study Institute, 1997).
5. A. Simone, Ph.D. Thesis, Dept. Civil Eng., M.I.T, Aug. 1997.
6. J. Grenestedt, *J. Mech. Phys. Solids*, to be published.
7. A. Simone and L. Gibson, *Acta Mater.* to be published.
8. L. J. Gibson and M. F. Ashby, Cellular Solids: Structure and Properties, Pergamon Press, Oxford, 2nd Edition, (1997).
9. Y. Sugimura, J. Meyer, M. Y. He, H. Bart-Smith, J. Grenestedt and A. G. Evans, *Acta mater.*, Vol. 45, No. 12, 1997, 5245-5259.
10. R. C. Gradinger, R. Kretz, H. P. Degischer and F. G. Rammerstorfer, *Deformation Behavior of Aluminium Foam under Compressive Loading*, Junior Euromat, Lausanne, August 1997.
11. D. E. Bray and R. K. Stanley, *Nondestructive Evaluation*, McGraw-Hill, New York (1989).
12. M. Schmidt, *A Review of X-ray Computed Axial Tomography, Non-Destructive Testing - Australia Vol 26 No.2 March/April 1989*.

- 
13. The Physics of Medical Imaging, (edited by S. Webb), Adam Hilger, Bristol (1988).
  14. S. Akiyama, K. Imagawa, A. A. Kitahara, S. Nagata, K. Morimoto, T. Nishikawa, U.S. Patent No. 4 713 277 (15 December 1987).
  15. Instron, Surface Displacement Analysis User Manual, 1997.
  16. D. J. Chen, F. P. Chiang, Y. S. Tan and H. S. Don, H. S., *Applied Optics*, **32**, 1839-1849, (1993).
  17. F. P. Chiang, *Experimental Techniques in Fracture*, edited by J. S. Epstein (Society of Experimental Mechanics, Bethel, CT), (1993).
  18. S. D. Papka and S. Kyriakides, *J. Mech. Phys. Solids*, **42**, 1499-1532, (1994).
  19. B. Budiansky and N. A. Fleck, *J. Mech. Phys. Solids*, **41**, 183-211, (1994).
  20. M. J. Silva and L. J. Gibson, *Int. J. Mech. Sci.*, **39**, 549-563, (1997).
  21. O. Prakash, H. Sang and J. D. Embury, *Mater. Sci. Engng*, **A199**, 195-203, (1995).
  22. M. F. Ashby, Materials Selection in Mechanical Design, Pergamon Press, Oxford, (1995).
  23. D. L. Davidson, The observation and measurement of displacements and strain by stereomaging, *Scanning Electron Microscopy*, 1979, II, SEM Inc., AMF O'Hare, IL 60666, USA.
  24. M. R. James, W. L. Morris and B. N. Cox, A high accuracy automated strain field mapper, *Experimental Mechanics*, **60**, (1990).

## SHEAR PROPERTIES ON ALUMINUM METAL FOAMS PREPARED BY THE MELT ROUTE

E. SAENZ\*, P. S. BARANDA\*\*, J. BONHOMME \*\*\*

\*UTRC GmbH, Technologiezentrum, Am Europaplatz, D-52068 Aachen, Germany. SaenzE@ctaero.com

\*\*UTRC, S.L. c/o CTA Parque Tecnológico de Alava. 01510 Miñano (Alava). Spain. barandap@eng1.otis.com

\*\*\*ITMA, Parque Tecnológico de Asturias, 33 428 Coruña-Llanera, Spain. jbonhomme@itma.es

### ABSTRACT

The shear modulus and shear strength of AlSi7Mg aluminum foam with 15% (vol) of 13 $\mu$ m SiC particles were determined through shear testing. A foam slab with a density of 0.31 g/cm<sup>3</sup> was supplied by Hydro Aluminium.

Four samples were tested according to ASTM C 273-61. The specimens were bonded to steel load plates. The relative displacement of the plates was measured using two extensometers. In order to evaluate the effect of the cell size distribution on shear properties, cell size and material distribution analyses were carried out for the metal foam slab in areas close to those from which the shear specimens were extracted.

A fast failure was observed after the maximum shear load. The failure in the samples were located in the central section of the slab mainly because the lower density was located there.

### 1. INTRODUCTION

The concept of metallic foams is not new. Foamed aluminum was produced as early as 1951, since then the interesting combination of properties (light weight, good energy absorption, low thermal conductivity, recyclability, etc) of these materials have spurred new developments including cheaper fabrication methods, and increasing number of potential applications are continuing to emerge [1-7]. The large scale use of these materials appeared to be hampered mainly by their elevated cost.

Currently there are at least four relatively large development programs worldwide focused on Al foams. The main objectives of these projects include an improvement of the material processing and the evaluation of its potential industrial applications. As a result, it is expected that the material properties will be improved in the following years. A sector for which metal foams are of particular interest is the transportation industry, where the good combination of properties makes Al foams very appealing for future applications [8-9].

In recent times, the available data for Al foam properties has increased significantly [10-12], but there is not enough information on the material's shear properties. In this paper the shear properties of AlSi7Mg foam were obtained according to the ASTM C 273-61 [13].

### 2. EXPERIMENTAL METHOD

#### 2.1. Aluminum foam

The aluminum foam slab was prepared by Hydro Aluminium following the melt route. This process has been described by Hydro Aluminium Researchers [4]. The base alloy used was AlSi7Mg with 15 vol. % of 13 $\mu$ m SiC particles. The foam slab was supplied in a density of 0.31 g/cm<sup>3</sup>, coded as HAL 176. The original foam slab dimensions were 1500 mm x 700 mm with a thickness ( $e$ ) of 90-100 mm

The main macro-characteristics of the Al foams obtained by the melt route are:

- Closed cells
- Continuous skin covering all the slab. Due to the manufacturing process, the bottom skin, in contact with the conveyor belt, has a smooth surface while the upper and lateral skins have more irregular surfaces.

## 2.2. Shear test (ASTM C 273-61)

Rectangular specimens 125x700 mm of Al foams were cut out of the slab using a diamond impregnated disk. These rectangular specimens were milled to a final thickness of 60 mm, removing the upper skin of the slab. The bottom skin was not removed. After the machining process, the surface flatness and parallelism of the samples were checked.

Given the final dimensions of the specimens (60x125x700 mm), it should be noted that the length was less than twelve times the thickness as required by ASTM C 273 because a geometrical limitation in the testing machine used. The specimens were not heat treated and the density was determined individually for each test specimen before the shear test.

Initial tests were carried out using Al load plates (15 mm thickness), however, the excessive bending observed proved these plates to be inadequate for this test. As a result, steel load plates of the same thickness were used for all the tests reported here. The specimens were bonded to the load plates using a structural two component epoxy adhesive (Krafft KAIEP A12/B9 [14]). The adhesive was cured at room temperature for 24 h. The surface of the specimens and load plates were cleaned with acetone and dried with hot air before the adhesive was applied.

Four specimens were tested. The tests were carried out on an Instron 5583 universal testing machine. The relative displacement of the load plates was measured by two extensometers, models Instron 2630-119 and 2630-118, situated on the middle of opposite load plates in order to obtain an average shear modulus and to compensate possible extensometer misalignments. Figure 1 shows the shear test set-up. A tensile load was applied to the ends of the load plates through a universal joint so as to distribute the load uniformly across the width of the specimen. The load was applied using constant crosshead speed. The speed was set to 0.5 mm/min based on preliminary test results in order to reach the maximum loads within 3 to 6 minutes as recommended by the standard. Using this speed, the time obtained to reach the maximum load was between 3 to 7 minutes for all the tests reported here.

During each test the load and strain were recorded continuously to failure. Moreover, the position of the failure plane relative to the bottom skin was determined as follows. The distance between the bottom skin and the fracture surface was measured at several locations in order to obtain an average measurement ( $H_a$ ) and the relative location of the failure surface ( $H_a/e \times 100\%$ , where  $e$  is the slab thickness). These results were then correlated with the millistructure results. Figure 2 illustrates where the height measurements were done.

## 2.3. Millistructure characterization (Cell structure characterization)

In order to correlate the material shear behavior and the cell structure characteristics, a millistructural analysis was carried out. The cell size distribution along two perpendicular cross-sections (TS and LS on Figure 3) through the foam slab were obtained. Four samples of “*exe*” dimensions obtained from different locations in the slab were analyzed. The study was carried out on the complete sample (100%) and also on three equal horizontal band sections (33.3%), which were named Upper, Middle and Lower according to their relative position on the sample as shown in Figure 5. Samples were cut by spark erosion in order to avoid cell wall damage and embedded in black resin. These mounted specimens were then ground and polished. The image of the polished cross-section was acquired by a TV camera and later processed to obtain an enhanced image (fig. 5).

The parameters obtained were Cell Density (NC/cm<sup>2</sup>) or number of cells per unit area, Linear Cell Density (NL/cm) or the number of cells intercepted at 9 different levels in the cross-section (0.1  $e$ , 0.2  $e$ , 0.3  $e$ .....0.9  $e$ ), the average cell size ( $m$ ) and the cell size standard deviation ( $\sigma$ ). The software used to analyze the images was Optimas 6.1 [15].

As described in the previous section, the height of the shear specimens was between 0.6  $e$  and 0.7  $e$ . Therefore, the shear specimens include only the lower and middle sections of the slab (fig. 5).

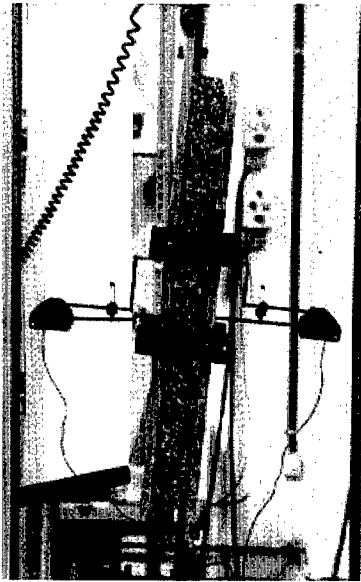


Figure 1: Tension shear test set-up. One extensometer where situated on each load plate

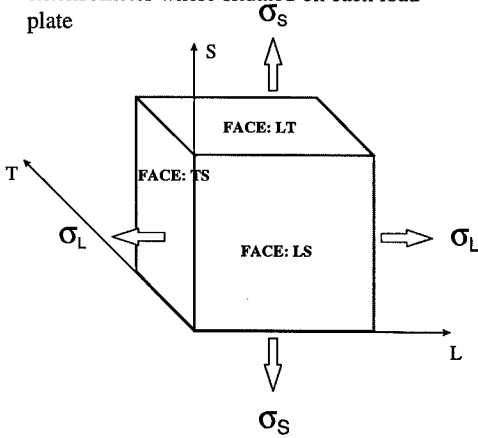


Figure 3: Planes and directions defined on HAL foams. L direction corresponds to the foam extraction direction. LT plane correspond to the conveyor plane surface (base)

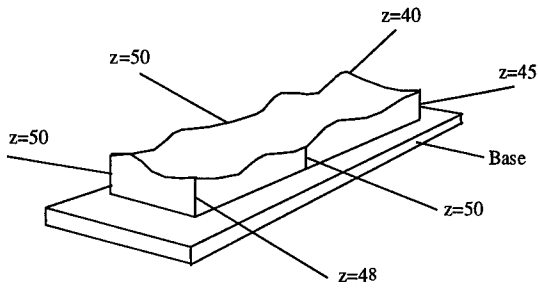


Figure 2: Height measurements obtained between the failure plane and the bottom skin (base) on HAL 176 L. (Measurements are in mm)

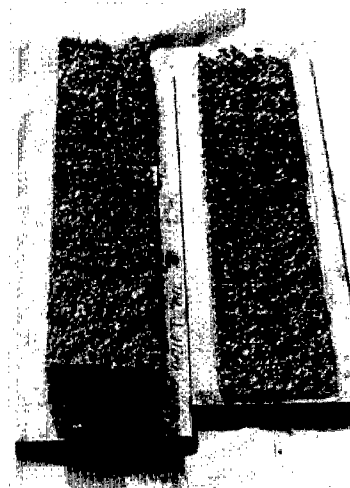


Figure 4: Typical surface of the failure located in the core of the foam

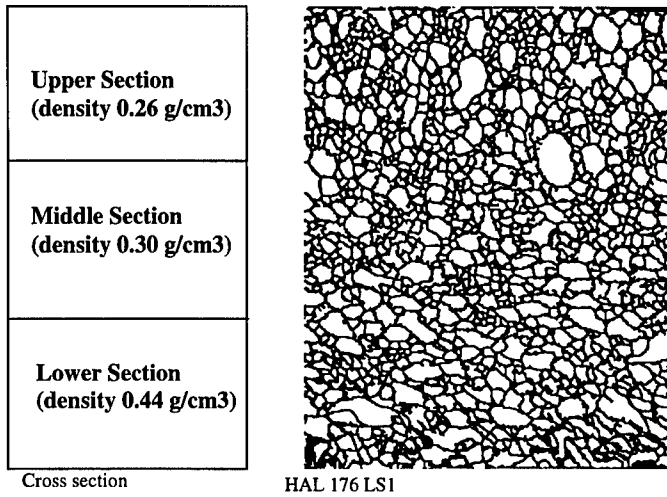


Figure 5: Typical millistructure of HAL 176 LS cross section. The Upper, Middle and Lower sections of studied and the average density per section are indicated

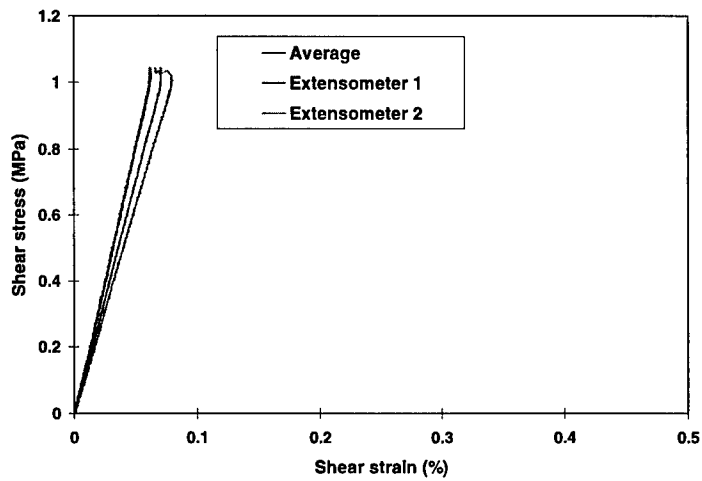


Figure 6: Typical shear stress-strain curve on HAL 176 samples. A backward movement was observed after the maximum load. Nominal foam slab density was 0.31 g/cm<sup>3</sup>.

### 3. RESULTS AND DISCUSSION:

The shear test results are shown in Table I, and Figures 2, 4 and 6 show typical results obtained on the tested samples. The following is a summary of the main results:

- The average failure surface was located in the middle section of the original foam slab, within the 48% to 54% band measured from the bottom skin. The failure surface was always located in the Al foam, no bonding or interface failures occurred.
- The material's failure was produced instantaneously after the maximum shear load. After it a backward movement was produced on the shear stress-strain curve, at the moment there is not a clear explanation on this behavior.
- The shear failure strain was lower than 0.1%, thus the material had a brittle behavior.
- The shear properties had a small scatter for both L and T directions.
- The time necessary to get the maximum load was within 3 to 7 minutes, so it was assumed that a good shear loads distribution was applied over all the samples.

Table II shows the results of the millistructure analysis and Figure 5 shows a typical millistructure of the material studied and the sections distribution in the cross section. In order to obtain the average density at each section some samples were cut by spark erosion and their skins were removed. The main results are:

- The cells in the lower section are distorted. They appear elongated in the L (longitudinal) direction. This may be as result of shear stresses introduced by the conveyor during the extraction process. In the middle and upper section an equiaxial shape was observed.
- A high cell density per area (NC/cm<sup>2</sup>) and a low average cell size (m) were obtained. The maximum average cell size tends to be located in the upper section and the highest cell density was located in the middle section. Nevertheless the differences in average cell size and cell density between the sections are small.
- The minimum cell density per length (NL/cm) was obtained both in the lower and middle area. This information seems to be contradictory with the cell density per area, but it can be justified by the cell shape distortion mentioned before.
- The lower section has the highest density whereas the lowest density was obtained in the upper section (drainage effect [16]). Since the upper section was removed, the shear specimens had the lower and middle section of the initial slab.

According to the Gibson-Ashby models the maximum stress that the metal foam can support depends on their density. Thus if the density increases the maximum stress also increases, thus in a foam with a non uniform density distribution its failure is expected to be produced in the section with the lowest density. This analysis is in agreement with the obtained results where the fracture surface was located in the section with the lowest density on the shear samples studied.

In order to estimate the percent of material located in the cell wall faces equation 1 [11] was used. Table III shows the results obtained and a comparison with the open cell model ( $\phi=1$ ). It is observed that the shear modulus increases if the material located on the cell walls (faces) increases. According to the obtained results the foam studied could be represented by a close cell model with  $\phi=0.78$  or 22% of solid which is contained on the cell faces.

$$\frac{G^*}{E_s} \approx \frac{3}{8} \left\{ \phi^2 \cdot \left( \frac{\rho^*}{\rho_s} \right)^2 + (1 - \phi) \cdot \frac{\rho^*}{\rho_s} \right\} \quad (1)$$

**Table I: Shear test results on HAL samples**

Direction	Slab density (g/cm <sup>3</sup> )	Sample density $\rho^*$ (g/cm <sup>3</sup> )	Average shear Modulus G* (MPa)	Specific shear modulus (MPa/Kg. m <sup>3</sup> )	Average Strain at Pmax (%)	Shear Strength (MPa)	Specific shear strength (MPa/Kg. m <sup>3</sup> )	Time to Pmax (min)	Average Failure plane position (%)
L	0.31	0.36	1365	3.79	0.07	1.04	0.0029	7.3	49%
L	0.31	0.38	1365	3.59	0.07	1.01	0.0027	6.9	51%
T	0.31	0.35	1272	3.63	0.09	1.03	0.0029	6.7	54%
T	0.31	0.35	1273	3.64	0.08	1.03	0.0029	6.7	48%

Average values	1319	3.66	0.08	1.03	0.0029
Std. Deviation	53	0.09	0.01	0.01	0.0001
Max. Deviation (%)	7.05	5.45	12.90	2.92	6.58

**Table II: Millistructure results on HAL samples**

Sample	m (mm)	$\sigma$ (mm)	NC/cm <sup>2</sup>	Min. NL/cm (at height)
<b>176 LS1</b>	1.53	0.98	19.46	2.281 (0.3 e)
176 LS1_upper	1.42	0.96	21.51	
176 LS1_middle	1.46	0.87	21.53	
176 LS1_lower	1.63	0.97	17.31	
<b>176 LS2</b>	1.57	1.06	18.37	2.396 (0.1 e, 0.2 e)
176 LS2_upper	1.63	1.01	18.91	
176 LS2_middle	1.43	0.93	20.84	
176 LS2_lower	1.52	1.11	16.99	
<b>176 TS1</b>	1.41	0.96	21.94	2.72 (0.1 e, 0.3 e, 0.5e)
176 TS1_upper	1.48	1.05	20.7	
176 TS1_middle	1.26	0.86	25.24	
176 TS1_lower	1.41	0.88	21.85	
<b>176 TS2</b>	1.63	1.08	16.86	2.566 (0.4 e, 0.6 e)
176 TS2_upper	1.71	1.14	16.3	
176 TS2_middle	1.51	1.03	18.15	
176 TS2_lower	1.58	0.98	17.66	

**Table III: Comparison between the shear results and the Gibson-Ashby model for foams (2.76 g/cm<sup>3</sup> and 90 GPa are the density and the E modulus of the solid material [17])**

MATERIAL HAL 176				Average shear Modulus obtained (G*) (MPa)	G* calculated Close cell $\phi=70\%$ (30% on faces) (MPa)	G* calculated Close cell $\phi=78\%$ (22% on faces) (MPa)	G* calculated for Open cells (MPa)
Bottom Skin	Direction	$\rho^*$ (g/cm <sup>3</sup> )	$\rho^* / \rho_s$				
Yes	L	0.36	0.13	1365	1602	1318	574
Yes	L	0.38	0.14	1365	1708	1412	640
Yes	T	0.35	0.13	1272	1550	1272	543
Yes	T	0.35	0.13	1273	1550	1272	543

---

where:  $G^*$ : shear modulus of the metal foam  
 $\rho^*$ : density of the metal foam  
 $E_s$ : Young's modulus of the solid material  
 $\rho_s$ : density of the solid material  
 $\phi$ : fraction of solid which is contained in the cell edges

#### 4. CONCLUSIONS

The cell structure of the material shows that the material studied has a rather homogeneous cell size and cell density distribution. The average cell size and cell density were 1.5 mm and 19.2 cells per cm<sup>2</sup>, respectively.

The material had an instantaneous failure which was located in the middle section of the initial slab because in this section the lowest density was obtained on the tested samples.

#### ACKNOWLEDGMENTS

The authors gratefully acknowledge the review and comments of Petter Asholt of Hydro Aluminium.

The research work has been carried out within the framework of the European Commission's "Industrial and Materials Technologies" (or B/E II) multiannual (94-98) program for R&D. The authors gratefully acknowledge the collaboration of all partners of the METEOR project "Light-weight Metal Foam Components for the Transport Industry" (Contract BRPR-CT96-0215 - BriteEuRam project BE96-3018).

#### 5. REFERENCES

1. G.J. Davies; S. Zhen. *J. Mat. Sci.* **18**, 1899 (1983).
2. Jin et al. US Patent No. 4 973 358 (27 November 1990)
3. S. Akiyama et al. US Patent No. 4 713 277 (15 December 1987)
4. Wolfgang Ruch,; Walter and Kirkevag Bjorn. European Patent No. 0 483 184 (6 May 1992)
5. J. Baumeister. US Patent 5 151 246 (1992). European Patent No. 0460392\*1 (1996)
6. Kenny et al. US Patent No. 5 281 251 (25 January 1994)
7. H.D. Kunze, J. Baumeister, J. Banhart, M. Weber. *PMI*, **25** (4), 183 (1993).
8. J. Banhart, J. Baumeister, M. Weber in Symposium on Automotive Technology & Automotive. Paper No. 96NM006. Florence, June, 1996
9. L. Lorenzi, A. Fuganti, E. Todaro, E. Fossat in Symposium on Automotive Technology & Automotive. Paper No. 970015. Florence, June, 1996
10. M. Ashby et al. *Foams database* (Granta design 1996)
11. L. Gibson and M. Ashby, Cellular Solids, 2<sup>nd</sup> ed. (Cambridge University Press, Cambridge 1977) p. 197.
12. A. Simone. Porous Metals and Metallic Foams. (Massachusetts Institute of Technology, 1997). PhD Thesis.
13. ASTM C-273-61 standard. Test Method for Shear Properties in flatwise plane of flat sandwich constructions or sandwich cores
14. Krafft Technical Document No. TT5089. 1995
15. Optimas 6.1 software. Optimas Corporation. Washington, 1996.
16. J.T. Beals; M.S. Thompson. UTRC internal report. October 1996
17. P. Asholt (Hydro Aluminium private communication). March 1998.

## BENDING PROPERTIES OF FOAMED ALUMINUM PANELS AND SANDWICHES

F. Simančík, J. Kováčik, N. Mináriková

Institute of Materials & Machine Mechanics, Račianska 75, 830 08 Bratislava 38, Slovakia

### ABSTRACT

The foamed panels and sandwiches were prepared by powder metallurgical route using various matrix alloys. The effect of the apparent density, geometry and structure of the foam on its bending stiffness was studied with respect to the results of the four-point-bending. It has been shown that the modulus of elasticity of the foam cannot be related only to its apparent density, because the distribution of the cell-wall material along the thickness of the foamed panel is not uniform. Therefore the real moment of inertia of the foam's cross-section should be used for the calculation of bending stiffness. This moment can be determined from the square weight of the foamed sample.

### INTRODUCTION

A new technique for foaming of aluminum panels and sandwiches has been recently developed at the Institute of Materials and Machine Mechanics for the Austrian company MEPURA GmbH [1]. For the process a foamable wire-shaped precursor prepared via the powder metallurgical route is used. Foamed aluminum panels up to 1 m<sup>2</sup> with the thickness of 5-50 mm can be manufactured (Fig. 1). The foamed panels are always covered by a dense aluminum skin which improves their mechanical properties and appearance. Sandwiches with bulk aluminum coversheets can be prepared as well by foaming of the precursor between two face plates which are inserted together with the precursor into the mold prior to foaming. During the process, the face plates are diffusion bonded to the foamed core. This type of bonding provides a certain formability of the sandwich plate and results in a significant improvement of the mechanical properties and the thermal stability in comparison with glued or brazed sandwiches.

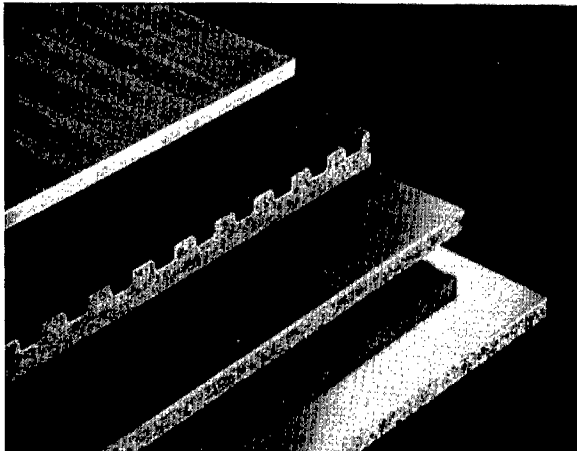


Fig. 1 Various foamed aluminum panels and sandwiches.

The foamed aluminum panels and sandwiches are assumed to be used in the various structural applications, where the high bending stiffness at a low weight is essential. The bending stiffness characterizes the resistance of the sample towards the elastic deformation: the higher the stiffness, the higher the loading necessary to obtain a given deformation. The bending stiffness  $B$  is generally computed according to the following equation:

$$B = E.J \quad (1)$$

where  $E$  refers to the elasticity modulus of the material and  $J$  is the cross sectional moment of inertia. The elasticity modulus of aluminum foam is usually represented as a function of the foam's density [2] considering the aluminum foam as a macroscopically homogeneous material with certain outer dimensions which can be used for calculation of  $J$ :

$$J = \frac{bh^3}{12} \quad (2)$$

where  $b$  refers to the width and  $h$  to the thickness of the test sample.

The bending stiffness can be computed also in a different manner, by considering the aluminum foam as an aluminum profile (isotropic) with the elasticity modulus of an used aluminum alloy. In this case the actual cross sectional moment of inertia should be applied. This depends significantly on the distribution of cell walls along the thickness of foamed sample.

The aim of this study is to investigate the influence of various structural parameters such as pore size, distribution of the pores, apparent density and thickness of the foam on the actual cross sectional moment of inertia of foamed panels and sandwiches.

## EXPERIMENT

Experimental foam samples with a typical density of 0.5-0.9 g/cm<sup>3</sup> were made of AlSi12, AlMg1Si0.6 or Al99.96 aluminum alloys. The sandwich samples were prepared with a foamed core of AlSi12 alloy and Al-coversheet with a thickness of 1 or 2 mm on both sides. The thickness of the foamed samples was 5, 10, 15 and 20 mm, thickness of the foamed cores in sandwiches was 10, 25 and 40 mm. At least 10 samples with various densities were prepared for each combination. All samples had the same width (50 mm) and length (400 mm) in order to study the effect of the density and the thickness on the stiffness-to-weight ratio. The cross sections of some samples were subjected to the computer image analysis in order to estimate an actual moment of inertia with respect to the cell-wall distribution along the thickness of the sample.

The apparent density of the foams was determined from the weight and the volume of the sample. The bending stiffness  $B$  was calculated from the slope of the load-deflection curve recorded during four-point-bending test according to:

$$B = EJ = \frac{1}{48} \frac{Fc}{y_\epsilon} (3l^2 - 4c^2) \quad (3)$$

where  $F$  is the load causing the deflection  $y_\epsilon$ ,  $l$  and  $c$  refer to the span between the supports and to the distance between the bending force and the supports, respectively ( $l=300$  and  $c=75$  mm in this study). In order to obtain a linear part of the load-deflection curve the short unloading was applied at the strain of  $\epsilon \approx 0.1$ . The deflection was measured in the center of the specimen by electronic extensometer, ram speed was kept constant at 0.01 m.min<sup>-1</sup>.

## RESULTS AND DISCUSSION

The results experimentally obtained for bending stiffness were used for the calculation of the apparent modulus of elasticity  $E$  according to (1) applying the moment of inertia  $J$  according to (2). The trendlines based on power law function [2] were computed for each of the series in order to see the important differences. It can be seen in Fig. 2 that the apparent modulus of elasticity, calculated for samples with comparable densities, decreases with increasing thickness of the samples. Although there is no significant difference between Young's moduli of both matrix alloys, the wrought aluminum alloy foams exhibit slightly higher apparent modulus of elasticity than the cast aluminum foams with the same apparent density.

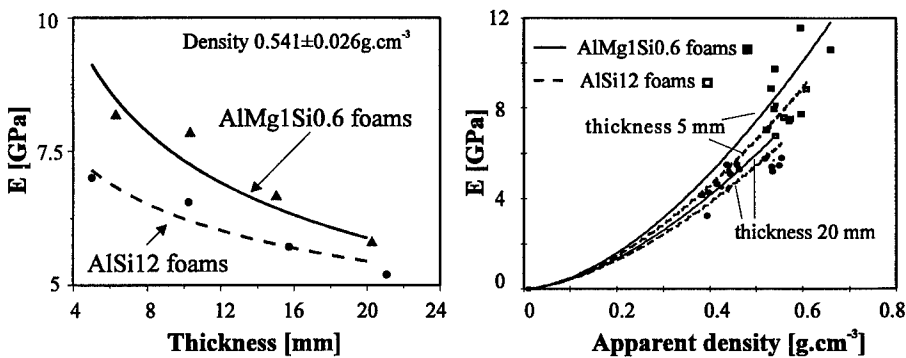


Fig. 2 Effect of the thickness, matrix alloy and density on the apparent modulus of elasticity of the foamed aluminum panels.

This behavior can be explained by computer image analysis of the cross sections of foamed samples (see Fig. 3 and Table I). All analyzed foams exhibit the non-uniform distribution of the cell-wall material along the thickness; higher portion of the material is collected near the surface and creates the dense skin. Such samples will be stiffer than the more homogeneous samples with the same overall apparent density. The contribution of the skin to the actual moment of inertia of the cross section increases when the sample becomes thinner. Therefore thinner samples will exhibit higher apparent modulus of elasticity than thicker ones with equal apparent density. This analysis shows that the use of the apparent modulus of elasticity in the case of the samples with a surface skin (above all for samples with little thickness, e.g. plates) is not correct because the foamed panel is not macroscopically homogeneous body. It would be more correct to consider the aluminum foam with a surface skin as a sandwich. Thus the properties of the foamed panels cannot be related only to the apparent density, the thickness must also be taken into account.

The pore size and the thickness of the pore-walls and surface skin are mostly affected by the fluidity of the matrix alloy during foaming. Therefore the minimum thickness has been observed for cast AlSi12-alloy, maximum for wrought AlMg1Si0.6-alloy. Because of the surface skin, the apparent density of the sample is much higher than an actual foam's density, especially in a case of AlMg1Si0.6 foams (see Table I). These foams exhibit also considerably higher contribution of the surface skin to the actual moment of inertia (more than 70 %) than the more homogeneous cast aluminum foams. Despite of this, the effect of matrix alloy on the

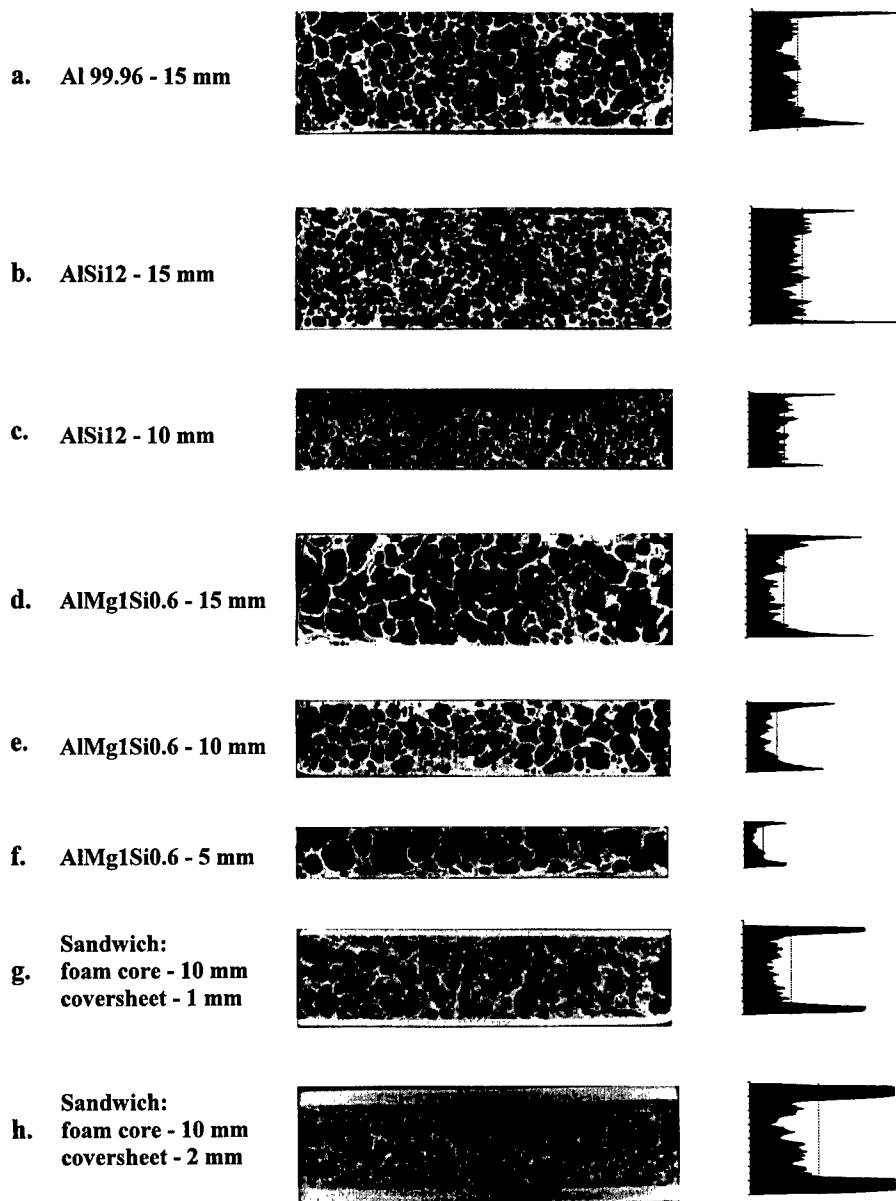


Fig. 3 Structures of the foamed aluminum panels and sandwiches and distributions of the cell-wall material along their thickness (see also Table I)

**Table I** Structural parameters and cross-sectional moments of inertia of foamed aluminum panels and sandwiches (see Fig. 3) according to a computer image analysis.

$\rho_f$  - density of the foam without skin,  $\rho_s$  - apparent density of the sample,  
 $J_{SS}/J_s$  - contribution of the surface skin to the moment of inertia (image value)

Sample	Mean pore size	Sample thickness	Surface skin thickness	Apparent density $\rho_s$	$\rho_f/\rho_s$	Weight	Moment of inertia $J_s$	$J_{SS}/J_s$
	[mm <sup>2</sup> ]	[mm]	[mm]	[g.cm <sup>-3</sup> ]	[%]	[g]	[cm <sup>4</sup> ]	[%]
a Al 99.96	7.68	16.0	1.10	0.49	89%	157	0.68	48%
b AlSi12	5.87	16.3	0.62	0.50	96%	163	0.68	28%
c AlSi12	2.74	10.6	0.52	0.47	96%	99	0.21	37%
d AlMg1Si0.6	13.78	15.0	1.79	0.45	76%	134	0.55	51%
e AlMg1Si0.6	6.87	10.0	1.51	0.46	70%	92	0.21	71%
f AlMg1Si0.6	12.22	6.7	0.92	0.54	72%	72	0.06	72%
g sandwich 1 mm	5.77	13.0	1.46	0.81	69%	211	0.54	76%
h sandwich 2 mm	5.81	15.3	2.26	1.15	63%	352	1.14	86%

moment of inertia obtained for foamed samples with similar apparent density and thickness was relatively low (see also Fig. 4). It appears that the effect of pore size and shape on the stiffness of the material is negligible when compared with the effect of density and thickness of the sample. The higher contribution of the surface skin in a case of wrought aluminum foams has probably been offset by much lower actual density of the foam core.

Aluminum foam can also be considered as an aluminum profile, with walls having the modulus of elasticity of aluminum, and whose cross-sectional moment of inertia  $J$  is a function of the distribution of the cell-wall material ( $J$  is almost constant in all directions). The actual moment of inertia of the aluminum foam with respect to the arbitrary distribution of the pores and to the scatter in their size cannot be calculated from the geometry and density of the sample. However, it can be determined from the bending stiffness according to (1), considering the Young's modulus of aluminum (i.e.  $E = 69$  GPa). From the practical point of view, the apparent density of the foam is not of the great importance, more significant is the weight of the component for a given property. The suitable parameter for the characterization of the foamed panels which combines the weight, density and thickness of the sample could be the square weight, i.e. the weight per unit area of the material, supposing the relative density of the foam does not exceed 0.4.

Fig. 4 illustrates the actual moment of inertia calculated from experimentally obtained bending stiffness in a dependence of the square weight of various foamed panels and sandwiches. It can be seen, that the bending stiffness increases with increasing square weight, what could be expected as well. However it is of interest, that from the point of view of the designer (stiffness versus weight) the difference between particular types of the samples almost disappears; the scatter of the moment of inertia at a given square weight is relatively low. For a given weight the bending stiffness of the samples decreases in a following sequence: foams → sandwiches with 1 mm coversheet (compare also samples in Fig. 3d and 3g) → sandwiches with 2 mm coversheet → bulk Al-sheet. The potential of the foamed aluminum panels and sandwiches for lightweight stiff structures is obvious.

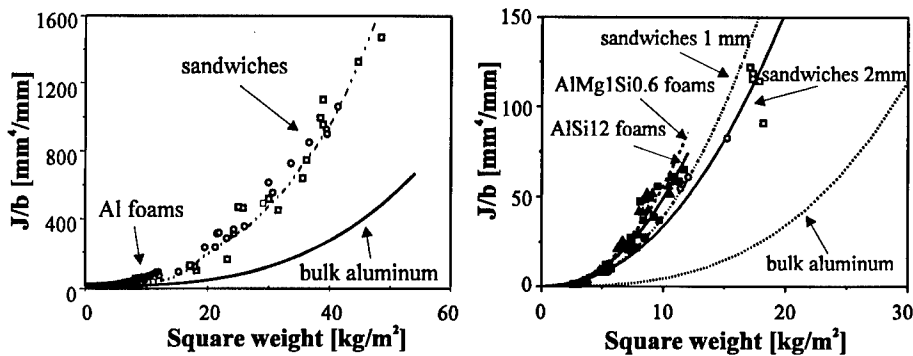


**Fig. 4** Moment of inertia normalized to the sample's width as a function of the square weight of various foamed panels and sandwiches (right: zoom of the diagram in the left).

## CONCLUSIONS

Bending stiffness of foamed aluminum panels and sandwiches was determined with respect to the thickness of the sample, cell-wall material and apparent density of the foam. It has been found that:

- the apparent density of the flat foamed samples is significantly affected by the surface skin and therefore cannot be used for the modelling of the elasticity modulus without taking the thickness of foamed sample into account
- the bending stiffness of the foamed panels is not significantly influenced by the choice of cell-wall material
- the square weight can be used as a parameter for the characterization of the foamed panels because it combines their weight, density and thickness
- real cross-sectional moment of inertia of the foamed panels and sandwiches can be calculated from their square weight supposing the relative density of the foam does not exceed 0.4.

## ACKNOWLEDGMENT

The financial support of SSVTS SR in the project ŠO/95/5305/035 and of MEPURA-Metallpulverges.m.b.H, Ranshofen, Austria is gratefully acknowledged.

## REFERENCES

1. F. Simančík, J. Jerz, J. Kováčik and P. Minár, *Kovove mater.* **35**, p. 265 (1997).
2. J. Kováčik and F. Simančík, *Scripta mater.*, to be published.

## HIGH CYCLE FATIGUE PROPERTIES OF ALUMINIUM FOAMS

B. E. ZETTL\*, S. E. STANZL-TSCHEGG\*, R. GRADINGER\*\*, H. P. DEGISCHER\*\*\*

\* Institute of Meteorology and Physics, University of Agricultural Sciences, AUSTRIA, (zettl@mail.boku.ac.at)

\*\* LKR-Centre of Competence on Light Metals, Ranshofen, AUSTRIA (office@lkr.co.at)

\*\*\* Institute of Material Science, Vienna University of Technology, AUSTRIA, (sek308@pop.tuwien.ac.at)

### ABSTRACT

Fatigue lifetime measurements have been performed on foamed Al-Mg-Si wrought alloys and Al-Si cast alloys in the high cycle range using an ultrasonic resonance testing method. The porous structure of the material is described by quantitative image analysis of optical micrographs and non destructively by X-ray computer tomography. The static mechanical properties as determined by tensile, compression and bending tests in earlier studies are used for material characterisation in this paper. The evaluation of the stress strain curves is specified for porous structures to obtain the stiffness and the plateau strength. The influence of the surface skin on the mechanical properties as well as on oscillation behaviour during lifetime measurements was studied.

### INTRODUCTION

Aluminium foams produced from powder metallurgical processes using prepared precursor material have a high potential for use in weight sensitive construction parts. The stiffness to weight ratio is the main criteria for material selection in light weight design. In the present work, the static mechanical properties and deformation behaviour have been determined with various tests.

Construction parts in transportation industry, for example, are subjected to a high number of varying stress amplitudes often. Therefore the fatigue properties must be known for reliable use of the material. Since load sequences of typical automotive components may consist of  $10^8$  cycles or more, the fatigue properties in the high cycle range are of special interest. The high frequency resonance testing technique is a time and energy saving method to determine the fatigue behaviour in the very high cycle regime.

Results of material tests of foamed metals have to be correlated to the composition as well as to the structure of the foam. Quantitative image analysis as well as X-ray computed tomography (CT) were applied to evaluate structure and cell geometry in this study.

### MATERIAL



Fig. 1: Image scan of optical micrograph of foamed AlMg1Si0.6 plate ( $\rho^*/\rho_s = 0.2$ ).

Three different types of Aluminium foams have been investigated: foamed AlMg0.6Si0.3 and AlMg1Si0.6 (Fig. 1) which are two different types of wrought alloys and AlSi12 cast alloy. Foams were produced by powder metallurgical production route [1] as rods with surface skin and 160 mm by length and 17 mm by diameter for lifetime measurements.

Figure 1 shows an example of the image-scan of the cross section of an AlMg1Si0.6 foamed plate. Different types of measurements were performed in order to describe the material properties. One was an

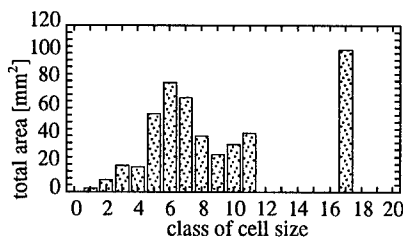


Fig.2: Classification of cell size as shown in Fig.1

image analysing system to characterize relative frequency of certain cell sizes, mass density mapping and the ratio of the sum of the cell area of cells of a defined size to the total cross section of the specimen [2]. The results of this procedure yielded local relative densities of 0.1 to 0.3. Cell areas were analysed and classified in 20 groups assuming circular shaped cells (classification in steps of 0.5 mm diameter). The summarized area values of all classes for the shown structure (Fig.1) is shown in figure 2.

Mechanical properties were determined by compression, tensile and bending tests [3]. Typical effects like buckling of cell walls or bending of cell edges e.g. cannot be characterized with the Young's modulus of elasticity only. An elastic stiffness parameter  $S(\epsilon)$  derived from unload/load loops during compression [3] is used to characterize the respond of the foam structure to load. The strength of the foams is described by the extrapolated plateau stress [1]. The strain  $\epsilon_{R_{p0}}$  at the extrapolated plateau stress  $R_{p0}$  characterizes the material's stiffness  $S_{R_{p0}}(\epsilon)$  is defined (for details see [1]). Both properties depend on the initial mass density of the foam by power laws.

In figure 3 the values for  $R_{p0}$  are plotted versus the relative mass density  $\rho^*/\rho_s$  of the undeformed foam. Comparing the  $R_{p0}$  data for different materials shows their dependence on the type of alloy (and heat treatment [1]). The stiffness  $S(\epsilon)$  does not clearly depend on the type of tested materials (Fig. 4).

### EXPERIMENT

A sine generator produces an electric vibration of 20 kHz frequency which is magnified and transformed into mechanical waves by a piezoelectric transducer (Fig. 5). The specimen is attached to this transformer via a magnifying piece (amplification transducer) and is excited to mechanical vibrations. The resulting longitudinal wave leads to tension-compression loading of the specimen with the mean stress equal to zero ( $R = -1$ ). If the system consisting of ultrasonic generator, transformer, horn and specimen is in resonance, vibration and thus load amplitudes become large enough to cause fracturing of the specimen. The vibration amplitude is maximum at the specimen ends; there the load amplitude of the standing wave

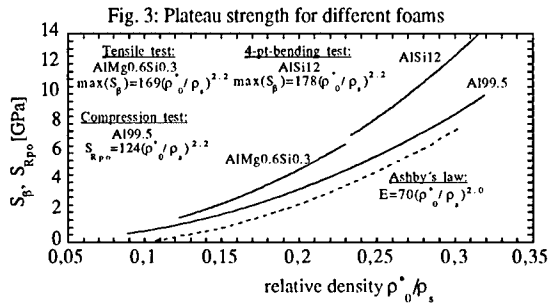
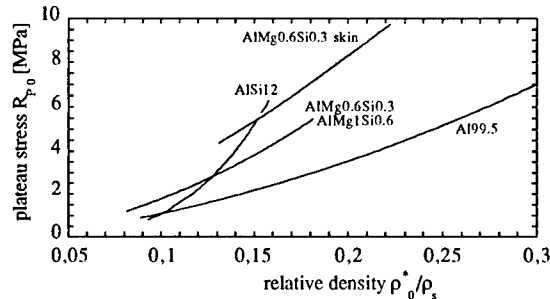


Fig. 3: Plateau strength for different foams

Fig. 4: Modulus of stiffness and elasticity for different foams

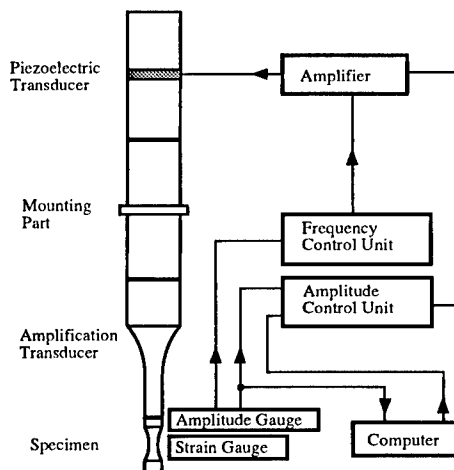


Fig. 5: Schematic of fatigue testing equipment

is zero. The load amplitude being effective in the specimen is controlled with an electromagnetic gauge, which detects the displacement amplitude at one of the two specimen ends. The strain amplitude in the specimen may be measured directly with strain gauges during the fatigue experiment. Details of the experimental procedure are published elsewhere [4],[5].

Besides the possibility to save time, the use of the ultrasonic resonance method makes possible a very advantageous way of energy transmission into the specimen. The material in the coupling area remains almost free of stress. The specimens may be adhered to a screw base without welding or machining. In addition loading is free of bending, as the specimens are fixed on one end only. Thus, thin-walled specimens can be loaded without buckling, which is not the case in conventional loading systems.

Specimens as shown in figure 6 were used for the measurements. The whole specimen consists of the foam part with surface skin, the glued screw base and a reflecting disc. As part of the generated standing wave is located in the solid material of the screw base and in the glued disc, the glued areas have to suffer some loading. The applied stress, however, is lower than the strength of the used adhesive. The length of the whole specimen is  $\lambda/2$ . This length is determined by the wave length  $\lambda_{Foam}$  in the foam specimen and  $\lambda_{Alu}$  of screw base and reflection disc.

The dots in figure 6 show the measured displacement distribution of the ultrasonic wave within the specimen. The drawn line represents the theoretically determined distribution. The distribution of the vibration amplitude in the foamed body of the specimen is:

$$A(l, t) = A_0(t) \cos(\pi l / \lambda_{Foam} - \delta) \quad (1) \quad \varepsilon = dA / dl \quad (2)$$

where  $A_0(t)$  is presenting the displacement maximum of the oscillation which is shifted by a distance  $\delta$  from the junction into the screw base. The strain  $\varepsilon$  is defined by equation (2).  $l_0$  is the length of the foamed body of the specimen

Measured and calculated values agree very well in the centre part of the specimen. Both, vibration node and strain maximum can be found there. The deviations at the specimen ends are caused by the displacement gauge geometry and the different magnetic properties of foam and solid material at the specimen ends. Two strain gauges are fixed in the centre of the specimen (strain maximum) in order to measure the strains during testing. The size of the strain gages is large enough ( $6 \times 6 \text{ mm}^2$ ) in order to determine the strain in an area which is larger than the size of a mean pore.

## RESULTS

### Lifetime measurements

Fatigue lifetime measurements were performed on the three different materials described above. The testing procedure was stopped either after  $10^9$  cycles or as soon as the resonance frequency changed by 50 Hz. Figures 7-9 show the lifetime data for the foamed aluminium-material. Specimens which did not fail within  $10^9$  cycles are marked with an arrow. These strain levels of survival are different for the tested materials. The highest strain level of AlMg1Si0.6 to withstand  $10^9$  load-cycles is  $0.35 \cdot 10^{-3}$  and the highest level where no specimen had failed is  $0.25 \cdot 10^{-3}$ . For

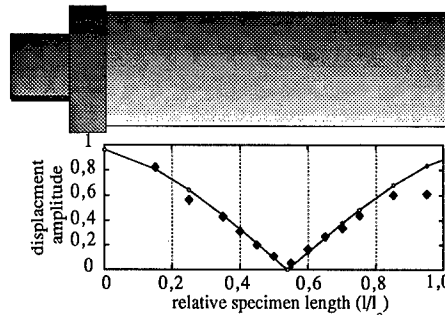


Fig. 6: Specimen geometry and comparison of the absolute value of calculated (line) and measured (dots) displacement amplitude along rel. specimen length ( $l/l_0$ ).

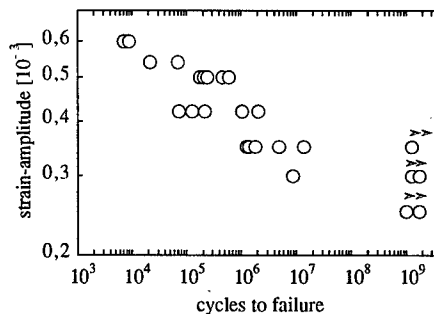


Fig. 7: Lifetimes of AlMg1Si0.6 foam with skin, at room temperature,  $R=-1$ , cycling frequency 20 kHz

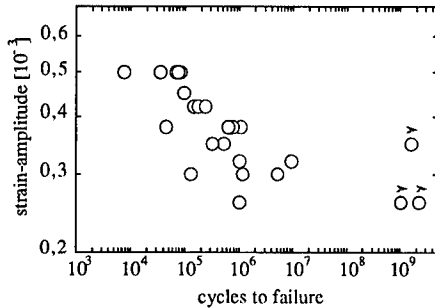


Fig. 8: Lifetimes of AlMg0.6Si0.3 foam with skin, at room temperature, R=-1, cycling frequency 20 kHz

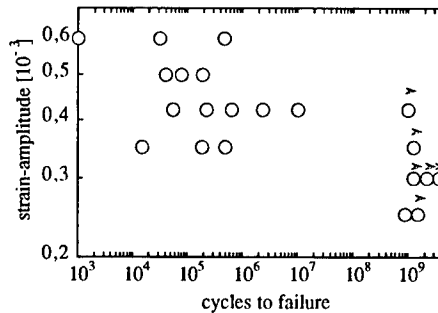


Fig. 9: Lifetimes of AlSi12 foam with skin, at room temperature, R=-1, cycling frequency 20 kHz

AlMg0.6Si0.3, the highest level with at least one survived specimen is  $0.35 \cdot 10^{-3}$ .

The highest withstand level of AlSi12 cast material is  $0.42 \cdot 10^{-3}$ . At the strain level of  $0.25 \cdot 10^{-3}$ , one specimen broke at nearly  $10^9$  cycles. This fractured specimen is the only one of all specimens where failure occurred between  $2 \cdot 10^7$  and  $10^9$  cycles. All other specimens either failed before  $2 \cdot 10^7$  cycles or not at all.

The most homogeneous lifetime data are observed for AlMg1Si0.6 (Fig. 7). The largest scatter of lifetimes about two decades is observed at the level of  $0.42 \cdot 10^{-3}$  (without considering unfailed specimens at lower load amplitudes). The range of scatter of AlSi12 cast material is larger at all load levels and maximum is 2.5 decades again at the same strain level of  $0.42 \cdot 10^{-3}$ . Scattering of the AlMg0.6Si0.3 material is in between.

#### Dynamic behaviour during lifetime measurement

The resonance frequency which is a characteristic value to describe the dynamic behaviour was observed during the testing procedure. The resonance frequency is determined by specimen length and material properties (modulus of elasticity, mass-density). Therefore variation of the resonance frequency points to a variation of material behaviour. Any decrease of resonance frequency at constant specimen-weight and volume e.g. indicates an decrease of stiffness.

All specimens show a decrease of frequency during the measuring process like the presented AlMg1Si0.6 specimens in figure 10.

The measuring procedure was stopped when the change of frequency was 50 Hz in comparison to the initial frequency. At this stage a crack at the skin of most specimens appears.

#### Measurement of modulus of elasticity

Due to the principle of the ultrasound-resonance-testing the modulus of elasticity can be measured with no additional effort. By moving a displacement measuring gauge along the length of a long specimen the position of the minimum of the displacement amplitude and thus the wavelength  $\lambda$  can be detected with high accuracy. Together with the mass density value  $\rho$  and frequency  $f$ , the modulus of elasticity is calculated according to the basic equation:

$$E = \lambda^2 f^2 \rho \quad (3)$$

In order to use the above equation the rod material has to be isotropic. Indeed foam may be approximated as isotropic material, as reported in literature [6]. In order to determine the stress-strain behaviour with a dynamic method, as used in this study, very low amplitude waves are applied in order to avoid inelastic effects. The modulus of elasticity then characterizes the stress-

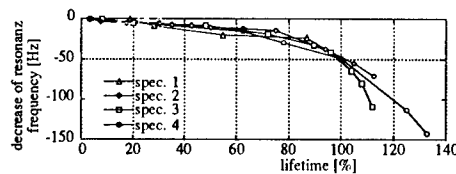


Fig. 10: During lifetime-measurements for all specimen a decrease of resonance-frequency was measured. The graph is showing data of four AlMg1Si0.6 specimens.

strain behaviour in the elastic region. Contrary to this, the stiffness  $S(\epsilon)$  has been determined statically from the slope of unload/load cycles in compression tests[3].

The value for  $E$  was measured for 19 specimens of the three different materials. All results are in the same range between 2.3 MPa and 5.2 MPa. Even if the values for AlMg0.6Si0.3 are a little bit lower no significant difference can be observed. The average value of the derived modulus of elasticity is  $E=3.9$  MPa. Figure 11 shows the measured values and also data from other authors. The power law fit for the experimental data is drawn through to the point of bulk aluminium. The derived equation is shown in the diagram.

Dynamic behaviour of specimen with removed skin

In order to investigate the influence of the skin on the vibration behaviour of pure foam several measurements were performed on foams with removed skin. Turning off the skin in steps of 0.1 mm from an AlSi12 specimen means a stepwise removal of the skin whose thickness is not perfectly constant along the circumference. Removing 0.3 mm of radius means to remove 50% of the skin-area. When 0.6 mm of the radius are removed, the skin is removed completely, and sound conduction through the skin is prevented anyway.

Removing the surface skin in steps of 0.1 mm leads to a decrease of the resonance frequency. The change of the resonance frequencies of three different specimens is shown in figure 12. The frequency is decreasing until 100% of the skin area are removed. Further removal shows only little effect on the vibration behaviour.

The displacement amplitude of the wave which passing through the pure foam can also be measured by using an electromagnetic gauge [4]. This amplitude at the free end of the specimen is also decreasing and becomes constant if the whole skin area is removed. Reductions of about 20- 40% were measured. Further reduction of the diameter only showed little effect on the displacement amplitude at the free end.

Removal of the surface skin leads to a reduction of the wavelength and modulus of elasticity. So far - without statistical confirmation - the value of the modulus of elasticity decreases by about 40- 60% in comparison to specimen with skin.

CT-measurements

Investigations of the cell structure at the place of fatigue crack initiation were performed using a medical X-ray computer tomograph [7]. In general, a large cell may be recognized below place of the surface skin where the fatigue crack appeared (Fig. 13). Since crack initiation did not always occur

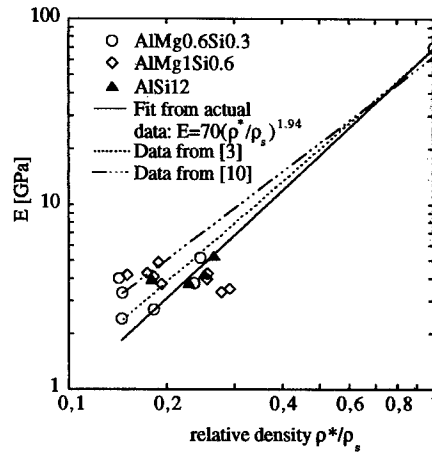


Fig. 11: Modulus of elasticity depending on density

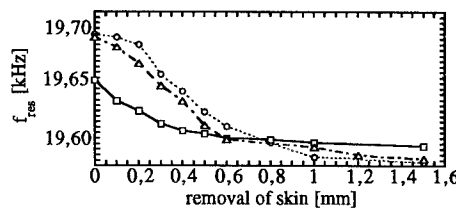


Fig. 12: Change of the resonance frequency by removal of skin



Fig. 13: CT images of two specimens which failed at low (right) and high (left) numbers of cycles (Markers indicate crack nucleation points).

at the place of highest stress always, but also approximately  $\pm 10$  mm aside, this indicates that the increase of local stress due to the local structure is not negligible. Figure 13 is showing the images of the cell structure at the crack initiation point of two AlMg0.6Si0.3 specimens which failed at the strain level of  $\epsilon=0.38 \cdot 10^{-3}$  after  $4 \cdot 10^4$  cycles (Fig. 13 left) and after  $1 \cdot 10^6$  cycles (Fig. 13 right). Measurements on the influence of the structure on the lifetime are not presented here.

## CONCLUSIONS

The surface skin of foamed materials does not only increase the static properties like  $R_{p0}$  (Fig. 3)[3] but also the modulus E and resonance frequency. Though resonance oscillation of a skinless specimen is possible, the vibration of a specimen with skin is dominated by the sound conduction within the skin layer. The foamed body of the specimen is excited to vibration.

Lifetime measurements are showing a bent SN-curve. The highest strain level, where at least one specimen has survived the testing procedure, is  $0.35 \cdot 10^{-3}$  for both AlMg1Si0.6 and AlMg0.6Si0.3, and  $0.42 \cdot 10^{-3}$  for AlSi12. The foamed AlMg1Si0.6 alloy is showing an endurance limit of  $0.25 \cdot 10^{-3}$ .

Specimens are failing before  $2 \cdot 10^7$  cycles or they are withstanding the applied load. If fracturing takes place, specimen damage can be noticed at early stages of lifetime. The resonance frequency decreases and thus indicates fractures of cell walls and edges. Microcracks grow at stress intensity factors equal or higher than the threshold value  $\Delta K_0$ . Minimum growth rates of about  $10^{-10}$  m/cycles ( $R=-1$ ) for comparable bulk materials (e.g. 6061 aluminium alloy) have been investigated [8]. If it is assumed that cracks are starting from existing defects of cell walls and one is growing constantly with a minimum rate up to a crack length of 2-3 mm, specimen failure must be finished within  $2 \cdot 10^7$ . Specimen showing an "infinite" lifetime ( $\geq 10^9$  cycles) obviously contain such defects, which, however, remain dormant or grow at undetectable rates [9].

It could be shown in this study, that the lifetimes of foamed Al-alloys are similar to that of bulk material for which the existence of  $\Delta K_0$  is proofed. This corresponding behaviour is suggesting some kind of threshold value for Al-foam similar to  $\Delta K_0$  for bulk materials. If the local stress intensity in the cell walls is higher than this threshold value due to large cell sizes or defects (small cracks, originating from the cooling process of the foam), cracks may propagate and specimen failure may occur within  $2 \cdot 10^7$  cycles.

CT images confirm that large cells below the surface skin are favouring short lifetimes. Besides damage of cell walls, large cells may lead to higher effective stresses in the surrounding cell walls assuming same thickness of the cell walls. Thus may result in shorter lifetimes.

## REFERENCES

1. H. P. Degischer, U. Galovsky, R. Gradinger, R. Kretz, F. Simancik in Metallschäume, edited by J. Banhart (Fraunhofer IFAM Symp. Metallschäume, MIT Bremen, 1997) pp. 79-90.
2. T. Klocker, H. P. Degischer, B. Kriszt, H. Knoblich, A. Falahati, Project sponsored by austrian federal ministry of science and transport, final report, (1997).
3. R. Gradinger, F. Simancik, H. P. Degischer in Int. Konf. ST-W&WP-BM-QM proceedings, Technical University Vienna (1997).
4. S. Stanzl, Ultrasonics 19, pp. 296- 272, 6 (1981).
5. S. Stanzl-Tschegg, H. R. Mayer, E. K. Tschegg, A. Beste, Int. J. Fatigue 15, pp. 311- 316, 4 (1993).
6. L. J. Gibson, M. F. Ashby, Cellular solids, Cambridge University Press, Cambridge, 1997, pp. 300- 302
7. A. Kottar, B. Kriszt, H. P. Degischer, Project sponsored by austrian federal ministry of science and transport, final report, (1997).
8. M. Papakyriakou, H.R. Mayer, S. E. Tschegg-Stanzl, M. Gröschl, Fatigue Fract. Engng. Mater. Struct. 18, p.4,477 (1995).
9. S. Suresh, Fatigue of materials, Cambridge University Press, Cambridge, 1991, pp. 202-216
10. M. Weber, PhD thesis, Technical University Clausthal, pp. 70-77, (1995).

## STRAIN RATE EFFECTS IN POROUS MATERIALS

J. LANKFORD, JR., K.A. DANNEMANN

Southwest Research Institute, 6220 Culebra Rd., San Antonio, TX 78238-5166

### ABSTRACT

The behavior of metal foams under rapid loading conditions is assessed. Dynamic loading experiments were conducted in our laboratory using a split Hopkinson pressure bar apparatus and a drop weight tester; strain rates ranged from  $45 \text{ s}^{-1}$  to  $1200 \text{ s}^{-1}$ . The implications of these experiments on open-cell, porous metals, and closed- and open-cell polymer foams are described. It is shown that there are two possible strain-rate dependent contributors to the impact resistance of cellular metals: (i) elastic-plastic resistance of the cellular metal "skeleton," and (ii) the gas pressure generated by gas flow within distorted open cells. A theoretical basis for these implications is presented.

### INTRODUCTION

In addition to thermal insulation and sound absorption applications, cellular metals are under consideration as potential energy absorbing structural components. The deformation capacity of these lightweight materials allows for significant energy absorption under blast or impact type loading corresponding to strain rates exceeding  $10^2 \text{ s}^{-1}$ .

A new class of porous metallic materials has emerged from recent process developments. However, the deformation behavior of these porous metals has not been investigated as extensively as elastomeric foams. Gibson and Ashby [1] have modeled the dependence of the mechanical behavior of metal foams upon the relevant material properties. However, this excellent work, which is the basis for much current experimentation, does not account for strain rate effects. The effects of intrinsic cell structure are addressed in more recent investigations [2] of the deformation behavior of porous aluminum, yet the effects of strain rate are not included.

The effects of strain rate on the compressive strength of elastomeric foams are well documented [3-6]. Strength increases are observed with increasing strain rate for polymer foams, as summarized by Gibson and Ashby [1], and are attributed to material properties, as well as viscous effects due to fluid flow through pores. The viscous contribution increases with decreasing cell size owing to increased flow tortuosity. Since few studies have been conducted to date on strain rate effects in cellular metals, investigations have been initiated in our laboratory to better understand the high rate deformation behavior of porous metals.

### EXPERIMENTAL

Open-cell aluminum (Al) foam, provided by Energy Research & Generation, Inc., was evaluated during initial investigations owing to the ready availability of this material. The 6101 Al foam had a relative density of 7% and contained approximately 16 cells per cm; the open-cell microstructure is shown in Figure 1. Solid material of the same composition was also tested for comparison.

Cylindrical test samples were electrodischarge machined from solid and cellular material. The samples measured 0.95 cm in diameter and 1.90 cm long. High strain rate (approximately  $1200 \text{ s}^{-1}$ ) compression tests were conducted at room temperature using a 1.25-cm diameter split Hopkinson pressure bar apparatus. A servo-controlled hydraulic test machine was used for low strain rate (approximately  $10^{-4}$  to  $10^{-3} \text{ s}^{-1}$ ) compression.

The compression response of elastomeric foams was previously investigated in our laboratory [6], using polyethylene (ETHAFOAM<sup>®</sup>) and polyurethane foam materials supplied by The Dow Chemical Company. In this case, high strain rate ( $40$ - $100 \text{ s}^{-1}$ ) tests were conducted using a gravity-

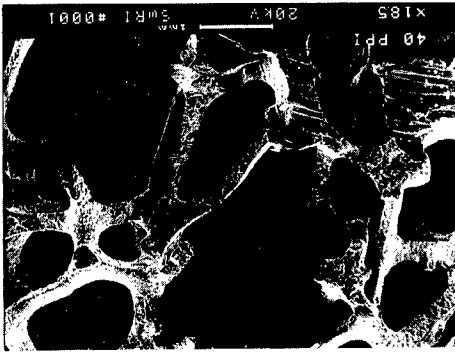


Figure 1. Open-cell structure:  
6101 Al,  $\rho/\rho_s = 0.07$ , 16 cells/cm.

operated drop tester instrumented with an accelerometer to monitor impact deceleration, and a slide-wire bridge to monitor head displacement.

## RESULTS

As expected, compression test results for solid 6101 Al reveal a weak dependence of compressive strength on strain rate, as shown in Figure 2. Any strain rate dependence is likewise negligible for the low density Al foam; minimal energy absorption was also observed (Figure 3).

The results for the cellular aluminum can be rationalized using the Gibson-Ashby [1] relationship for compressive strength controlled purely by plastic yielding within the cell walls.

$$\frac{\sigma_{pl}^*}{\sigma_y} = C(\rho/\rho_s)^{3/2} \quad (1)$$

where  $\sigma_{pl}^*$  is the critical compressive stress at collapse, and  $\sigma_y$  is the yield strength of the cell wall material. On this basis alone, there does not appear to be much chance for significant energy absorption enhancement due to higher loading rates.  $\sigma_y$  is the only obvious strain rate dependent parameter in the equation, and, as shown above, the yield strength dependence on strain rate for 6101 Al is weak.

In contrast, it is well known that the yield strength of most bulk polymers is also strain rate insensitive, yet the impact-absorbing capability of cellular variants of these materials is much in excess of their quasistatic capabilities. The reason for this lies in the details of the cell structure itself, as established in some earlier experiments [6] in our laboratory. Open-cell polyurethane foams with tortuous air pathways demonstrated the compressive stress-strain response shown in Figure 4, when tested over a wide range of strain rates. As the strain rate was increased from  $10^{-3} \text{ s}^{-1}$  to  $45 \text{ s}^{-1}$ , the energy-absorbing capability of the material, which is proportional to the area under the  $\sigma$ - $\epsilon$  curve, increased by approximately an order of magnitude. Subsequent experiments performed under a partial vacuum yielded lower strain rate-induced strengthening, proving that the effect is a consequence of the air pressure generated by flow through the porous foam structure. In the case of the 6101 Al foam tested above, the structure is so open (Figure 1) that air flow could not be a factor in the collapse of the material; hence, there was no influence of strain rate on strength.

Closed-cell polymeric foams [6] also display a strong strain rate strength dependence. For foamed polyethylene, the compressive yield strength and flow stress rose when the strain rate was

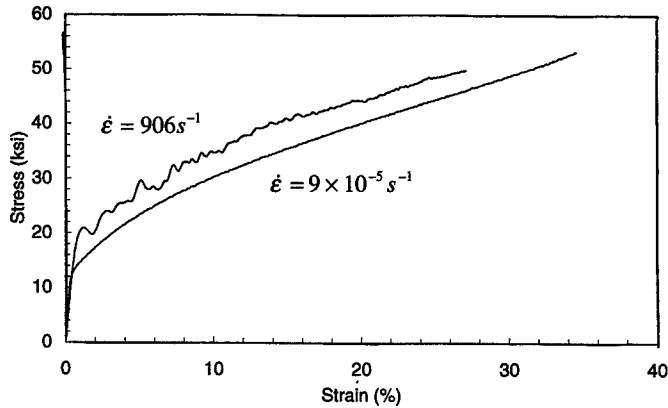


Figure 2. Static and dynamic compressive stress-strain response of bulk 6101-0 aluminum.

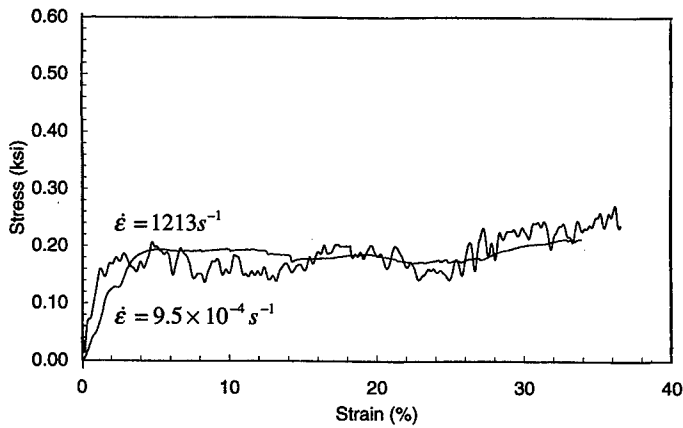


Figure 3. Static and dynamic compressive stress-strain response of open-cell 6101 Al foam.

increased from  $10^{-3} \text{ s}^{-1}$  to  $90 \text{ s}^{-1}$ . As shown in Figure 5, the area under the stress-strain curve increased more than 50%. The effect is less pronounced than for the open-cell polyurethane (Figure 4). The difference can be attributed to gas pressure buildup within already closed (hence, "preloaded") cells versus dynamic intercellular air flow in the open-cell foam.

## DISCUSSION

The results detailed above indicate that there are essentially two contributors to the impact resistance of cellular metals. The first is the possibly, but not necessarily, strain rate independent elastic-plastic resistance of the metallic foam "skeleton." Although the material itself will often be insensitive to the rate of deformation, collapse of the structure may involve sequential microscale

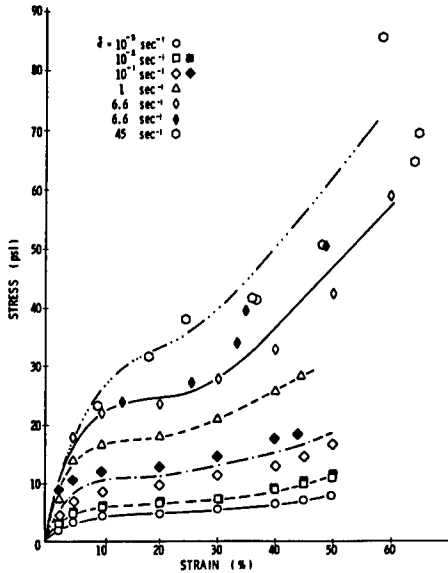


Figure 4. Strain rate dependence of stress-strain response of open-cell polyurethane, showing greatly increased energy absorption with increasing strain rate.

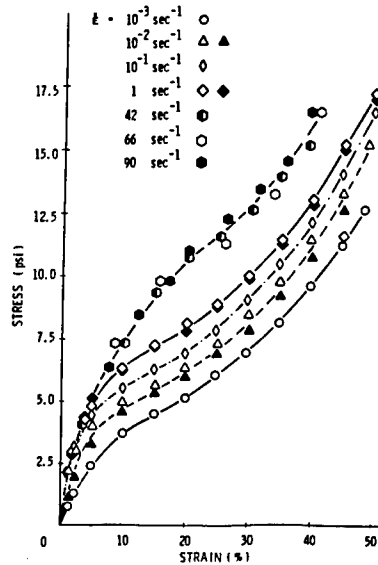


Figure 5. Strain rate dependence of stress-strain response of closed-cell polyethylene, showing increased energy absorption with increasing strain rate.

events leading to rate-dependence. This has been shown [7], for example, in rapidly loaded fiber-reinforced polymeric composites where structural collapse is loading rate-controlled through the time required for a kink band to propagate across the sample gage section.

In the case of cellular structures, localized plastic flow may cause analogous rate dependent structural breakdown. It has been shown [1] that a foam may yield plastically when the fully plastic moment of a cell wall is exceeded, giving large deformations via a plastic hinge effect. However, even when the foam is deforming in an overall elastic sense, local cell wall imperfections can significantly reduce the local stiffness [2] and lead to localized, premature plastic collapse. Cell wall strength is also an important parameter in cellular collapse, and can be optimized by controlling grain size and other metallurgical microscale parameters.

Plastic deformation of cell walls is most likely in open-cell metal foams with low aspect ratio cell walls (i.e., small cells). Macroscopic evidence of progressive failure is presented by Reddy *et al.* [8] for cellular metal structures simulated with metal rings. For porous metals with low relative density, simultaneous collapse of the structure is also possible owing to the high aspect ratio of the cell walls. These mechanisms are summarized in the schematic in Figure 6, which illustrates stress-strain curves for compressive deformation of open-cell porous metals of varying density (dotted lines represent higher strain rate deformation). Metallic foams with low relative densities (i.e., large pores) obviously exhibit minimal strain rate effect. The behavior follows the three-stage curve presented by Gibson and Ashby [1]. Buckling of the high-aspect ratio cell walls occurs following strain localization. The stress rises steeply when the cell walls come into contact during densification. For low density metal foams, the level of the plateau in the stress-strain curve is controlled almost solely by material instability. The contribution of intrinsic material properties to the deformation response increases with increasing relative density of the metal foams.

The second contributor to the compressive response of a cellular metal is strain rate dependent [6, 9], and is associated with airflow within distorted open cells. At high strain rates, viscous effects control the slope of the plateau region of the stress-strain curve. The effect of viscosity variation on the compressive deformation behavior of open-cell foams is depicted in the schematic of Figure 7, where increasing the viscosity of the fluid in an open-cell foam increases the strain rate effect. Tyler and Ashby [4], in fact, noted a transition to a linear strain rate dependence in open-cell polyurethane foams when the fluid (i.e., viscosity) was changed from air to a water-glycerine mixture. The connection between fluid velocity and cell structure strain rate dependence is not a simple one. However, it is clear that they are directly related in the sense that the higher strain rates associated with impact-type loadings will cause more rapid fluid flow in open-cell foams.

Gas pressure buildup in closed cells constitutes an essentially strain rate independent contributor to impact resistance. Tsai [10] has evaluated the situation of bulk longitudinal compression for closed-cell foams, whereby the dimension changes in only one direction while being constrained in the two mutually perpendicular directions. For closed-cell foams under small strains, the intracellular gas pressure increases until buckling of the cell structure is intensified. This accelerates gas pressure buildup, which then causes cell walls to rupture. The last is the critical event in the failure process, but not the end of effective energy absorption; subsequent ultimate failure is strain rate dependent, and controlled by viscous flow through the ruptured, hence open, cell system. Recently, the elastic-plastic analysis of Ozgur *et al.* [11] for crushing of gas filled, closed cell foams showed that internal gas pressure delays the onset of yielding in the cell walls during compressive loading. Concomitantly, collapse of the cell aggregate was postponed; rate effects were not investigated.

## CONCLUSIONS

Investigations conducted in our laboratory on open and closed-cell polymer foams, and open-cell aluminum foam indicate that there are two possible strain rate-dependent contributors to the impact resistance of cellular metals: (i) elastic-plastic resistance of the cellular metal "skeleton", and (ii) viscous effects due to airflow within open (or ruptured) cells. The first is possibly, but not necessarily, strain rate independent; the second contributor is strain rate dependent. The following critical parameters appear to control high rate energy absorption in metal foams: fluid viscosity, porous metal macrostructure (i.e., open-cell vs. closed-cell, cell size, relative density), and metallurgical properties (e.g., yield stress, flow stress).

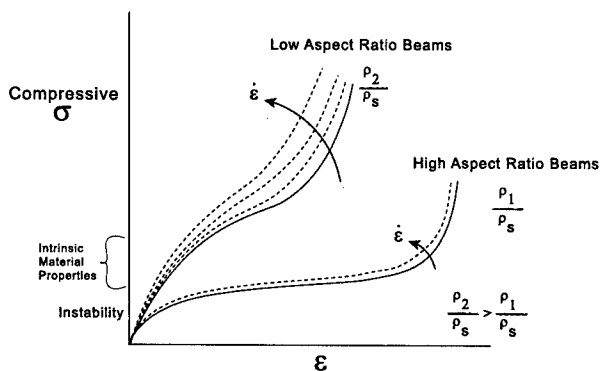


Figure 6. Schematic of strain rate effects on the stress-strain response of open-cell porous metals. Note the effect of density variation.

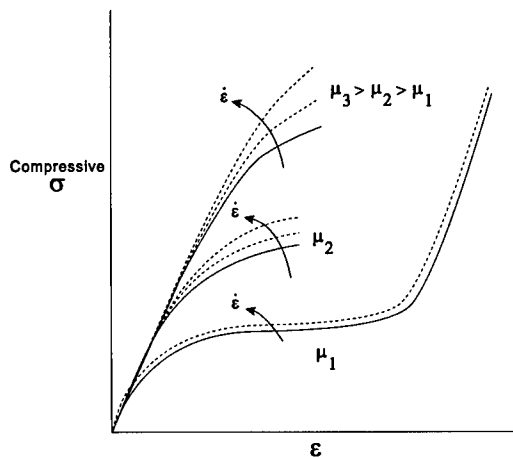


Figure 7. Schematic of strain rate effects on the stress-strain response of open-cell porous metals. Note the effect of increased fluid viscosity.

#### ACKNOWLEDGMENTS

This work was recently initiated under the sponsorship of the Office of Naval Research, Contract N00014-98-C-0126, monitored by Dr. Steven Fishman.

#### REFERENCES

1. L. J. Gibson and M. F. Ashby, *Cellular Solids: Structure and Properties*, 2<sup>nd</sup> edition, Pergamon Press, Oxford, 1997.
2. Y. Sugimara, J. Meyer, M. Y. He, H. Bart-Smith, J. Grenestedt, and A. G. Evans, *On the Mechanical Performance of Closed Cell Al Alloy Foams*, Proc. Ultralight Materials Conference, 1-33, July 1997.
3. J. Zhang and M. F. Ashby, CPGS Thesis, Engineering Depart., 1986.
4. C. J. Tyler and M. F. Ashby, Project Report, Cambridge University Engineering Dept., 1986.
5. J. A. Rinde and K. G. Hoge, *J. Appl. Polymer Sci.*, **15**, 1377, 1971.
6. A. Nagy, W. L. Ko, and U. S. Lindholm, *Mechanical Behavior of Foamed Materials Under Dynamic Compression*, *J. Cellular Plastics*, **10**, 1-8, 1974.
7. J. Lankford, *Compressive Failure of Fiber-Reinforced Composites: Buckling, Kinking, and the Role of the Interphase*, *Journal of Materials Science*, **30**, 4343-4348, 1995.
8. T. Y. Reddy, S. R. Reid, and R. Barr, *Int. J. Impact Engrg.*, **11**, No. 4, 463-480, 1991.
9. T. Liber and H. Epstein, *The Effect of Airflow on the Behavior of Foam as a Dynamic Element in Shock and Vibrations*, ASME Paper No. 69-VIBR-46, 1969.
10. J. T. Tsai, *The Compressive Deformation of Polymeric Foams*, *Polymer Engineering and Science*, **22**, 545-548, 1982.
11. M. Ozgur, R. L. Mullen, and G. Welsch, *Analysis of Closed Cell Metal Composites*, *Acta Mater.* **44**, 2115-2126, 1996.

---

## THE EFFECT OF PARENT METAL PROPERTIES ON THE PERFORMANCE OF LATTICE BLOCK MATERIAL™

M.L. Renauld\*, A.F. Giamei\*, M.S. Thompson\* and J. Priluck\*\*

\*Materials and Structures Technology Department, United Technologies Research Center, East Hartford, CT 06108

\*\* JAMCORP, 17 Jonspin Rd., Wilmington, MA, 01887

### ABSTRACT

Lattice Block Material™, or LBM™ is a unique lightweight structure consisting of repeated cells with an internal node connected to, in the most common configuration, 14 ligaments. In its metallic version, this product is available in a variety of castable metals including aluminum alloys, copper alloys, nickel alloys and steels. The relationship between LBM™ structural performance (strength and stiffness) and parent metal properties is investigated using compression tests in three primary orientations and 3-pt. bend tests. Analytical assessment of the LBM™ via finite element analysis shows reasonable agreement with experimental findings and provides predictions for LBM™ capabilities with different materials, unit cell sizes and ligament geometries.

### INTRODUCTION

There is continuing interest in structural weight reduction without an accompanying loss of density normalized mechanical properties, particularly in the aerospace industry. In pursuit of this goal, numerous structures such as sandwich panels with honeycomb or porous metal cores have been used or suggested [1-4]. A novel approach to low cost, lightweight metallic structure design and fabrication has been pursued by JAMCORP whereby repeating cells consisting of nodes and ligaments provide a uniform structure with density variation achievable via cell size modifications and ligament diameter changes. This product, termed Lattice Block Material™, can be tailored to a variety of applications not only through relative density changes, but also through the proper selection of parent metals, the choice of which currently includes iron, titanium, aluminum, nickel and cobalt base alloys. As this paper will show, the choice of parent metal and accompanying mechanical properties such as modulus, strength and ductility has a profound effect on the elastic and plastic deformation behavior of the LBM™ structure.

### EXPERIMENTAL PROCEDURE

Lattice Block Material™, as shown in Figure 1, was supplied by JAMCORP in a variety of geometrical configurations that included several unit cell sizes, defined by node

spacings of 0.64cm (0.25"), 1.27cm (0.5"), 1.91 cm (0.75") and 2.54cm (1.0"), with ligament diameters of 0.15cm (0.060"), 0.32cm (0.125") or 0.38cm (0.150"). Table 1 summarizes the five parent metal alloys used to fabricate the LBM™ samples.

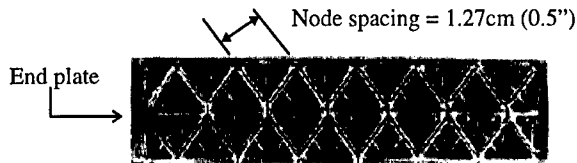


**Figure 1. Side view of 1.27cm (0.5") node spacing LBM™ block**

**Table 1  
Summary of Parent Metals**

Alloy Designation	Primary Constituent Element
A356	Aluminum
C95200	Copper
Hastelloy-X	Nickel
Stellite 6	Cobalt
17-4 PH Stainless Steel	Iron

Mechanical testing consisted of compression tests and 3-pt bend tests on LBM™ samples and tensile tests on fully dense parent metal specimens. All mechanical testing was performed in air at room temperature under a controlled crosshead displacement rate of 0.05 in/min for compression and tensile tests and 0.1 in/min for 3-pt bending tests. Compression samples were inserted between rigid parallel platens with sample deflection recorded by a deflectometer. Under 3-pt bend loading, flat steel plates were inserted between the round loading pins and LBM™ structure to distribute load over a small area. These plates measured 0.95cm (0.375") wide for samples with node spacings equal to 0.64cm (0.25") and 1.27cm (0.5") whereas 1.27cm (0.5") wide plates were used for 1.91cm (0.75") and 2.54 (1.0") node spacing samples. As with compression tests, a deflectometer was used to monitor the deflection of the center load pin relative to the lower support pins. Flat tensile specimens were cut from the fully dense end plates, shown in Figure 1, to determine parent metal properties for implementation in a finite element model. The tensile specimen gage sections measured from 0.17cm (0.065") to 0.38cm (0.150") thick and 0.38cm (0.150") to 0.64cm (0.250") wide. Strain was

measured by a 1.27cm (0.5") gage length extensometer mounted on each sample. Under all testing conditions, a load cell was used to measure force applied to the test specimen.

### ANALYTICAL APPROACH

A finite element model was built using Mentat II 2.3.1 and solved with MARC Ver. 6.2, both running on a Silicon Graphics workstation. Each ligament in the LBM™ structure was modeled as a single beam element with 7 degrees of freedom, 3 displacements ( $u, v, w$ ), 3 rotations ( $q_x, q_y, q_z$ ) and axial strain ( $d\bar{u}/ds$ ) which corresponds to MARC element #25. Compression tests were simulated by an LBM™ sample placed between two rigid surfaces, one of which is fixed and the other movable. To prevent the LBM™ block from sliding out from between the surfaces, an additional boundary condition is imposed. One node which contacts the fixed surface and is near the center of the structure is prevented from translating in either direction perpendicular to the plane of the fixed surface. Sample deformation is initiated by bringing the movable surface in contact with the LBM™, then translating the moving plate towards the fixed plate at a constant velocity. The predicted LBM™ response is essentially independent of this displacement rate since no material rate effects are built into the model. However, the rate must be slow enough to achieve a model solution at each time step. The total force supported by the LBM™ structure is the force applied to the moving surface and displacement is measured by travel distance of the movable surface from the point of LBM™ contact. The through-thickness compression model of a 2-ply LBM™ sample is shown in Figure 2.

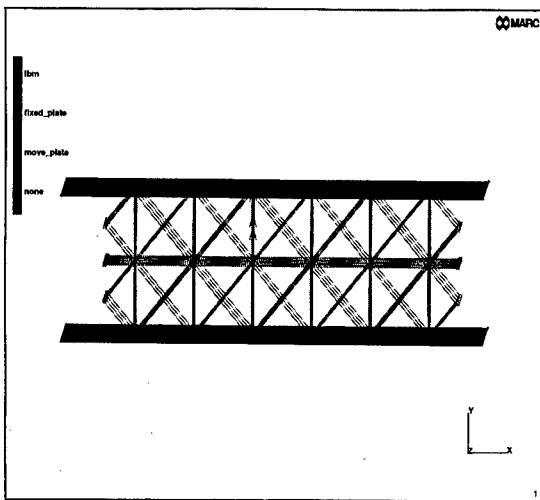
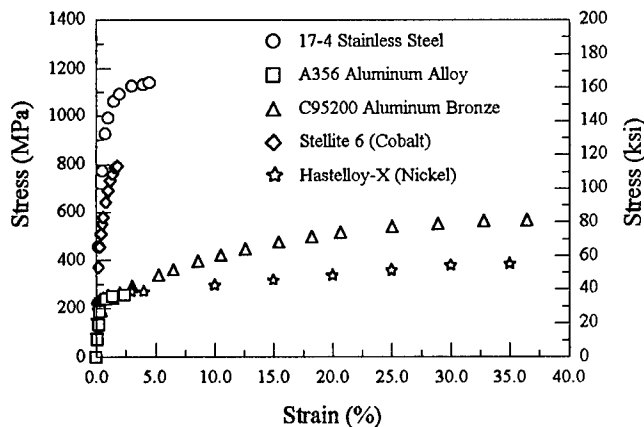


Figure 2. FEM of through-thickness (S) compression test on LBM™ sample.

## RESULTS

### Experimental

A uniaxial stress versus plastic strain curve is required for FEM simulations of inelastic material behavior. The average tensile stress-strain of 2-3 fully dense specimens per alloy are shown in Figure 3 wherein ductility differences are clearly shown among the low elongation materials, A356, Stellite 6 and 17-4 PH SS and high elongation alloys, Hastelloy X and C95200 Al-bronze. Additionally, a wide range of tensile strengths is observed, from 250 MPa for the A356 alloy to 1150 MPa for the stainless steel.



**Figure 3. Tensile stress-strain curves illustrating the range of strength and ductilities for the five alloys from which LBM™ samples were fabricated.**

The effects of these tensile properties are illustrated in the compression and bending traces of LBM™ as illustrated in Figures 4 and 5, respectively. In Figure 4, all four samples had the same nominal dimensions, unit cell size and ligament diameter. The only difference among the samples was the parent metal, either Al-bronze or A356 aluminum. The compression load-displacement curves have been converted to stress versus strain wherein stress is calculated by the total force applied to the specimen divided by the nominal specimen area and strain is measured as the compression platen displacement divided by the original specimen height. The higher strength and ductility of the Al-bronze samples are reflected by two distinct characteristics of the deformation curves, namely the higher maximum stress and the continued load support after maximum load. The ratio of the LBM™ strengths,  $LBM_{Al-bronze}^{TM}/LBM_{A356}^{TM} = 2.00$ , is nearly equal to the ratio of the parent metal strengths,  $\sigma_{uAl-bronze}/\sigma_{uA356} = 2.25$ . The load support after maximum load is much lower for the A356 LBM™ since beyond ~5% sample strain, ligament fracture occurred. In contrast, very few Al-bronze ligaments were

completely fractured after nearly 40% sample deformation, thereby allowing these samples to maintain load support after maximum load.

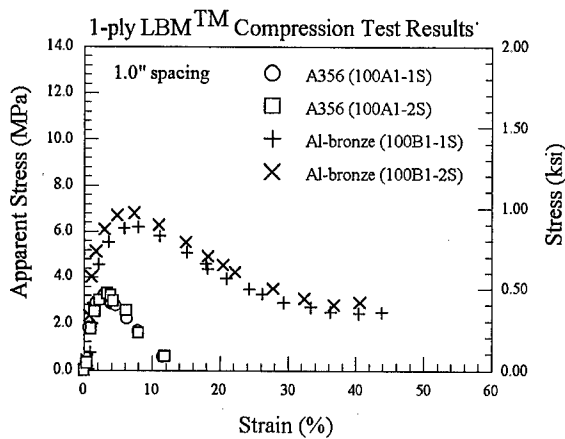


**Figure 4. The strength and inelastic deformation behavior of the LBM™ structure are directly related to tensile strength and ductility of the parent metal.**

Load-deflection curves from two bending tests are shown in Figure 5. The two samples were both 1-ply, 1.27cm (0.5") node spacing samples with 0.15cm (0.060") ligament diameters, but the ratio of the lower span distance to specimen height,  $l/h$ , was slightly different, 5 vs 6. The conversion of these traces to stress and strain is under consideration; therefore the results remain in terms of load and displacement. The maximum load supported by the stainless steel LBM™ is significantly more than the load supported by the Hastelloy-X LBM™, about 3.8 times as much. Similarly, the tensile strength of the 17-4 SS is about 3 times the tensile strength of Hastelloy-X. Tensile failure of stainless steel LBM™ ligaments causes an abrupt load drop as opposed to a gradual load decrease due to ligament yielding in the Hastelloy-X specimen.

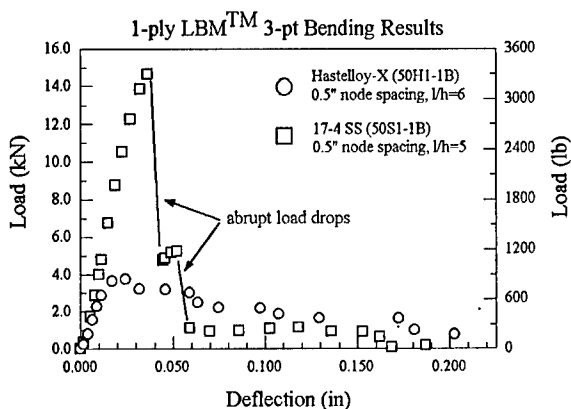


**Figure 5. The load-deflection curves from 3-pt bending of LBM™ structure can be qualitatively explained with parent metal tensile properties.**

### Computational

The finite element model predictions were compared with experimental data by modeling experimental test samples and comparing the predicted and experimental load-deflection curves. In general, the predicted LBM™ modulus under bending and compression is higher than the experimental stiffness and the maximum load is often slightly overpredicted. An example is presented in Figure 6 where the FEA response corresponds to the shaded curve and the experimental data are indicated by open circles. This A356 LBM™ sample is 2-ply, with 1.27cm (0.5") node spacing and 0.15cm (0.060") ligament diameter tested with a lower span to height ratio of 4. The elastic stiffness of the LBM™ structure is slightly underpredicted, although the greatest discrepancy in the elastic region is due an initial experimental deflection of about 0.051mm (0.002") with little load increase. The maximum load prediction from the FEM is slightly larger than the experimental observation, but the error is under 10%.

The main difference between the computational predictions and experimental results occurs after maximum sample load where the predicted load slowly decreases while the actual load drops quickly. In laboratory tests, the LBM™ ligaments fabricated from low ductility parent metals, such as the A356 specimen in Figure 6, begin to fracture after the peak load is achieved. However, the finite element model does not account for material separation and assumes that the ultimate material strength is maintained beyond the tensile failure strain. The analytical curve drops slowly due to ligament bending and the development of plastic hinges once the parent metal ultimate strength is reached.

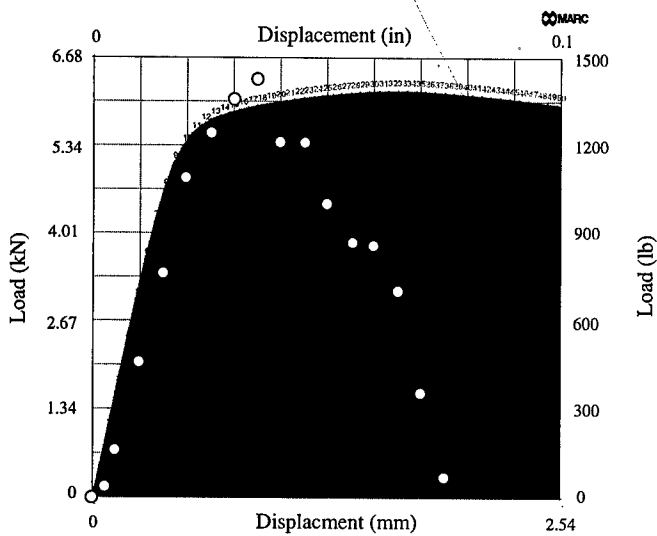


**Figure 6. Comparison of FEA predictions and experimental data for 3-pt bending of 2-ply, 1.27cm (0.5") spacing A356 aluminum LBM™.**

The finite element model was used to assess the effect of parent metal ultimate strength, ligament diameter and unit cell size on the 2-ply through-thickness compression properties of LBM™. Computations suggest that the effect of increasing parent metal strength is a linear increase in LBM™ strength (Figure 7). Hence for this loading condition, the optimum strength to weight ratio LBM™ should be made from a parent metal with an optimum strength to weight ratio. Preliminary predictions on the effects of ligament length and diameter suggest there may be an length to diameter ratio which optimizes the LBM™ performance for a given weight. Additional model predictions are aimed at identifying the optimal LBM™ geometrical configuration for a given loading condition.

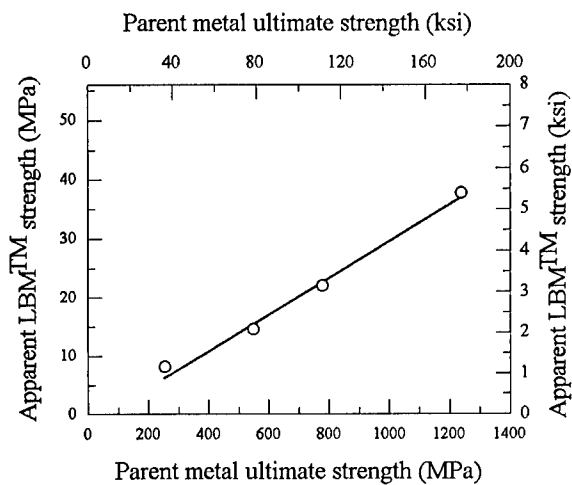


**Figure 7. FEA predictions of the effect of parent metal strength on the 2-ply through-thickness compressive strength of LBM™.**

#### SUMMARY

The parent metal ultimate strength and tensile ductility have been shown to exert significant influence on the deformation characteristics of LBM™ structures under compression and 3-pt bend loading. Finite element predictions for the stiffness and strength of LBM™ compare well with experimental results. Further predictions suggest that mechanical properties might be optimized for a given LBM™ weight through variations in unit cell size and ligament diameter.

#### ACKNOWLEDGMENTS

This work is supported by an ONR contract, Number N00014-95-C-0231, and a DARPA/ONR contract, Number N00014-96-C-0400, both of which are monitored by Dr. Steven G. Fishman. The authors also appreciate the mechanical test data generated by Corky Favrow and Al Ivaldi of UTRC's Mechanical Testing Group and photographic preparation by Joe Bracale and Roy Wong of UTRC's Materials Characterization Group. Recognition is also given to Phil Wettengel of Komtek (Worcester, MA) for supporting iron, nickel and cobalt based LBM™ efforts.

---

## REFERENCES

- [1] A.E. Simone and L.J. Gibson, "Efficient Structural Components using Porous Metals," *Materials Science and Engineering*, A229, 1997, pp. 55-62.
- [2] M. Burman and D. Zenkert, "Fatigue of Foam Core Sandwich Beams-1: Undamaged Specimens," *International Journal of Fatigue*, Vol. 19, No. 7, pp. 551-561.
- [3] M.F. Ashby, "The Mechanical Properties of Cellular Solids," *Metallurgical Transactions*, Vol. 14A, Sept. 1983, pp. 1755-1769.
- [4] L. J. Gibson and M.F. Ashby, Cellular Solids: Structure and Properties - Second Edition, Cambridge University Press, Cambridge, 1997.

---

**Part III**  
**Manufacture of Solid Foams**

---

## PRODUCTION METHODS FOR METALLIC FOAMS

J. BANHART, J. BAUMEISTER

Fraunhofer-Institute for Applied Materials Research (IFAM), Lesumer Heerstraße 36,  
28717 Bremen, Germany, ban@ifam.fhg.de

### ABSTRACT

The possibilities for making metallic foams or similar porous metal structures are reviewed. The various processes are classified according to the state of the starting metal - liquid, powdered, ionised. Liquid metal can be foamed directly by injecting gas, gas-releasing foaming agents or by producing supersaturated metal-gas solutions. Indirect methods include investment casting and usage of filler materials. Metal powders can also be used as starting materials for metallic foams: mixtures of such powders with foaming agents are compacted to foamable precursor materials that can be foamed in a second step. Instead of foaming agents inert gas can be directly entrapped in the precursor. Metal foams can also be made from metal powder slurries or by using polymer/powder mixtures. Finally, galvanic electro-deposition also allows to make highly porous metallic structures with open pores.

### INTRODUCTION

Cellular materials are widespread in everyday life and are used for cushioning, insulating, damping, constructing, filtering purposes and many other applications. Highly porous materials are known to have a high stiffness combined with a very low specific weight. For this reason cellular materials frequently occur in nature as constructional materials (e.g. woods and bones). The fact that even metals and metallic alloys can be produced as cellular solids or metal foams is not as well known as the possibility to foam more traditional engineering materials such as polymers, ceramics or glass. Metallic foams offer interesting perspectives due to the combination of properties which are related to the metallic character on the one and to the porous structure on the other hand.

In the past 40 years many attempts have been undertaken to foam metals or to produce porous metallic structures. In the present review some of the more important and successful procedures are described.

There is no clear-cut and generally accepted definition for the term "foam". First of all, one has to distinguish between liquid and solid foams. A liquid foam is a fine dispersion of gas bubbles in a liquid. Cooling down a liquid foam beneath the melting point of the respective material yields a frozen liquid foam which is then clearly a solid foam. What is generally meant in the context of metallic foams are in general solid metallic foams. One could restrict usage of the word "solid foam" to materials which originally were in the liquid state. However, customarily other porous structures such as sintered metal powders are often also called "foams" although they never were in a liquid state. So one often extends the usage of the word "foam" to porous metal structures which are

not actually foams, but resemble foams regarding their high porosity, the inter-connectivity of the solid material and their irregular structure.

## FOAMS MADE FROM METALLIC MELTS

A first group of foam making processes starts from the molten metal that is processed to a porous material by either foaming it directly, by using an indirect method via a polymer foam or by casting the liquid metal around solid filler materials which reserve space for the pores or which remain in the foam.

### Direct foaming of melts

Metallic melts can be foamed directly under certain circumstances by injecting gases into the liquid. Normally, the gas bubbles which are then formed in the metallic melt will tend to rise to its surface quickly due to the high buoyancy forces in the high-density liquid but this rise can be impeded by increasing the viscosity of the molten metal. This can be done by adding fine ceramic powders or alloying elements which form particles in the melt.

It should be noted that numerous attempts to foam liquid metals have been undertaken in the 60s and 70s (see e.g. Ref. 1), but apparently the processes then invented could not be sufficiently optimised to yield foams of a satisfactory quality and cost. In the past ten years, however, a number of new developments have taken place so that nowadays better production routes are available.

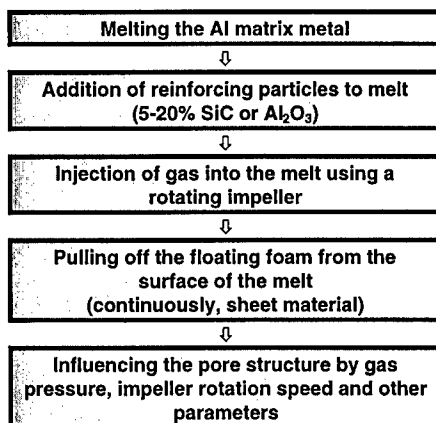


**Fig. 1: Direct foaming of melts (MMC foams)**

Currently there are two ways for directly foaming metallic melts. One line is being exploited by Cymat (originally by Alcan) in Canada and Hydro Aluminium in Norway<sup>2-5</sup> for foaming aluminium and aluminium alloys. According to this process that is depicted in schematical form in Fig. 1, silicon carbide, aluminium oxide or magnesium oxide particles are used to enhance the viscosity of the melt. Therefore, the first step consists of making an aluminium melt containing one of these substances. The problem to be solved resembles the one encountered in making ordinary MMCs, namely the problem of wetting the particles by the melt and of achieving a homogeneous distribution of the reinforcing particles<sup>6</sup>.

The liquid MMC melt is foamed in a second step by blowing gases (air, nitrogen, argon) into it using specially designed rotating impellers. These impellers have to produce very fine gas bubbles in the melt and distribute them homogeneously. The foam that is generated this way floats up to the surface of the liquid where it can be pulled off e.g.

by means of a conveyor band. Care has to be taken not to damage the foam structure by shearing the semi-solid foam too much. The resulting material is in principle as long as desired, as wide as the vessel containing the liquid metal allows it and typically 10 cm thick. The foamed material is either used in the state it comes out of the casting machine having a closed outer surface or is cut into the required shape after foaming. Due to the high content of ceramic particles, machining of the MMC-foams might be a problem. The advantage of the process is the ability of producing large volumes at a rather low cost and the low density that can be achieved. Porosities range from 80 to 97%. A possible disadvantage is the eventual necessity for cutting the foam and therefore opening the cells and the brittleness of the MMC foam due to the reinforcing particles contained in the cell walls. However, attempts for making shaped parts by casting the semi-liquid foam into moulds or by shaping the emerging foam with rolls have been undertaken<sup>7,8</sup> thus removing one of these disadvantages. Some properties of such metal foams have been investigated and are given in the literature<sup>9,10</sup>. MMC foams are probably the least expensive ones compared to other metallic foams.

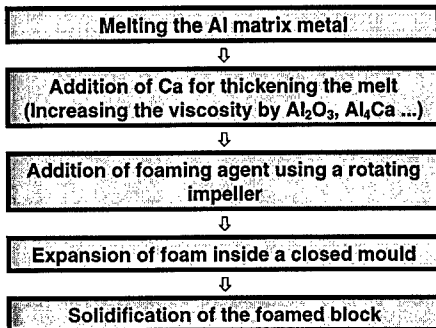


Fig. 2: Direct foaming of melts (ALPORAS-Process)

The second way for foaming melts directly is to add a foaming agent to the melt instead of blowing gas into it<sup>11,12</sup>. The foaming agent decomposes under the influence of heat and releases gas which then propels the foaming process. For the process that is currently in a state of a small-scale commercial exploitation at Shinko Wire in Japan, calcium is used to stabilise the melt (probably forming an  $Al_4Ca$  intermetallic) and titanium hydride  $TiH_2$  serves as the foaming agent releasing hydrogen gas when it is heated. The foamed aluminium is produced in batches of approximately 2000x1000x600 mm. Typical densities are 0.25 to 0.33 g/cm<sup>3</sup>. The blocks are cut into

sheets of the required thickness<sup>13</sup>, e.g. 5 mm to 250 mm, standard thickness 10 mm. The pore structure of the material - named ALPORAS - is rather uniform<sup>14</sup>. Mechanical<sup>14</sup> and sound absorption properties<sup>15</sup> have been measured. The material has been reported to be more expensive than the MMC foams described above.

#### Solid-gas eutectic solidification (Gasars)

A method that was developed some years ago in the Ukraine<sup>16</sup> exploits the fact that some liquid metals form a eutectic system with hydrogen gas. By solving hydrogen in these metals under high pressure (typically 50 atms) one first prepares a melt that is pore free with the hydrogen completely solved in the metal (see Fig. 3). If one then reduces temperature and pressure, one forces the melt to go through the two-phase regions. Beneath the eutectic temperature one arrives at a two-phase field corresponding to a solid plus the gas. If the process parameters - cooling rate and pressure profile - are chosen appropriately, the gas will accumulate in fine gas bubbles in the solid, thus forming a foam. The possibility of solidifying the liquid directionally offers the advantage of making foams with elongated pores. If the casting vessel is cylindrical,

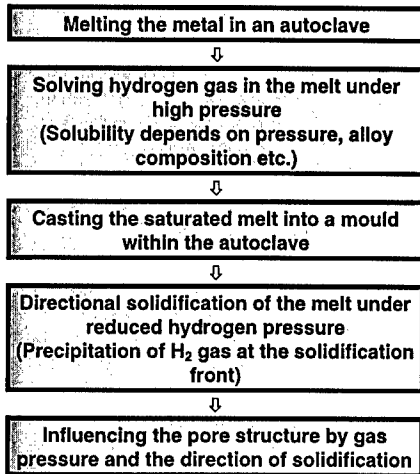


Fig. 3: Foaming metals by the Gasar process

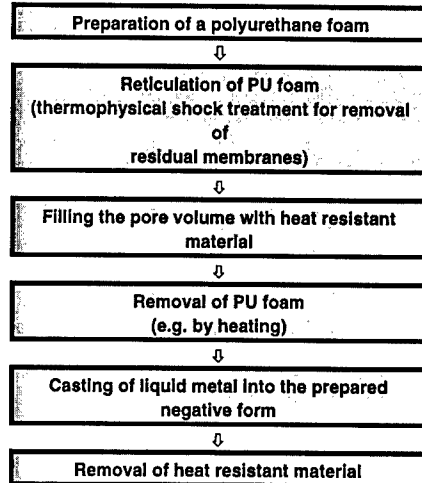


Fig. 4: Making metallic foams by investment casting

radial and axial pores can be made<sup>17</sup>. The maximum porosities that can be achieved by this process are not very high (5-75%) but metals with medium and high melting points such as copper and nickel can be foamed. The pore structure of such foams - called *gasars* - is somewhat problematic<sup>18,19</sup>, so that further improvements have to be awaited. The mechanical properties (compression and tension) of gasars have been characterised recently<sup>20,21</sup>.

#### Investment casting

Metal foams can also be fabricated without directly foaming the metal<sup>22-24</sup>. For this a polymer foam is used as a starting point (Fig. 4). The polymer foam is turned into a structure with open pores by manipulating the foaming process or by a reticulation treatment. The foam is then filled with a slurry of heat resistant material, e.g. a mixture of mullite, phenolic resin and calcium carbonate<sup>23</sup>. After drying the polymer is removed and molten metal is cast into the resulting open voids which exactly represent the original foam structure. After removal of the mould material (e.g. by pressurised water) a metallic foam is obtained that is an exact image of the original polymer foam. Fig. 5 shows a micrograph of such a foam that is being sold by ERG in California under the trade name DUOCEL. Various grades are available ranging from 2.5 to 16 pores per cm (10 to 40 ppi). Complex shaped parts can be fabricated by pre-forming the polymer foam. Prices have been reported to be high. Aluminium alloys are usually

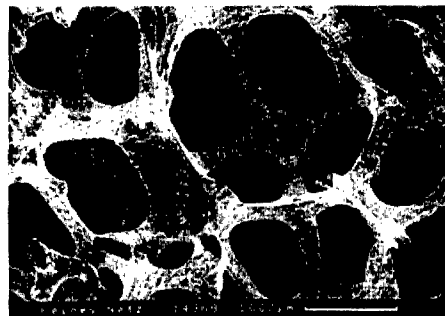
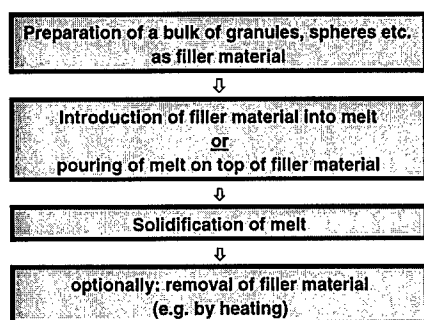


Fig. 5: SEM image of a metal foam made by investment casting (DUOCEL)

used but other metals can also be processed. The densities and foam morphologies are of course determined by the polymer foam. Porosities typically range from 80 to 97%.

### Syntactic foams using filler materials



**Fig. 6: Making metallic foams using filler materials**

Light-weight porous metals can be produced by casting around inorganic granules or hollow spheres of low density or by infiltrating such materials with a liquid melt (Fig. 6). A loose bulk of expanded clay granules, foamed glass spheres of aluminium oxide hollow spheres can be used for this<sup>25</sup>. The granules are then introduced into the melt or the melt is poured over the bulk of filler material. The heat capacity and conductivity of the granules is very low and therefore does not disturb the flow of the metal too much. Due to the high surface tension of the liquid metal wetting of the granules is a problem and in general the

interstices between the granules will not be filled completely. Creating a slight vacuum or an external pressure facilitates infiltration significantly. A wide range of metals can be processed this way including aluminium, magnesium, zinc, lead, tin etc. Parts of a predefined shape can be fabricated by designing a mould of the appropriate geometry. Sandwich panels have also been made<sup>26</sup>.

### FOAMS MADE FROM METAL POWDERS

Instead of the molten metal, metal powders can be used to make porous metallic structures. Again, there are several different methods which can be applied. In some of these processes the powders are processed into a compact precursor material prior to the actual foaming step, in others powders (or fibres, hollow spheres etc. which are considered to be powders here) are used for direct processing.

#### Fraunhofer Process

Foamed metals can be produced by a powder metallurgical method invented and patented<sup>27-29</sup> at Fraunhofer-Institute in Bremen, Germany .

The production process begins with the mixing of metal powders - elementary metals, alloys or powder blends - with a foaming agent, after which the mix is compacted to yield a dense, semi-finished product (Fig. 7). In principle, the compaction can be done by any technique that ensures that the foaming agent is embedded into the metal matrix without any residual open porosity.

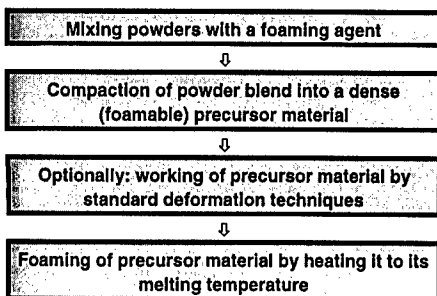


**Fig. 7: Powder metallurgical process for making foamed metals**



**Fig. 8: Lead foam made from metal powder (scale approx. 1:4)**

Examples for such compaction methods are uniaxial compression, extrusion or powder rolling<sup>26</sup>. Which compaction method is chosen depends on the required shape of the precursor material. However, extrusion seems to be the most economical method at the moment and is therefore the preferred method. Rectangular profiles with various cross sections are usually made. Thin sheets are then obtained by rolling.

Heat treatment at temperatures near the melting point of the matrix material is the next step. During this process the foaming agent, which is homogeneously distributed within the dense metallic matrix, decomposes. The released gas forces the compacted P/M material to expand thus forming its highly porous structure. Prior to foaming the precursor material can be processed into sheets, rods, profiles and other shapes etc. by conventional techniques like rolling, swaging or extrusion in order to improve the flow conditions during foaming inside moulds. The density of metal foams can be controlled by adjusting the content of foaming agent and several other foaming parameters such as temperatures and heating rates. If metal hydrides are used as foaming agents, a content of less than 1% is sufficient in most cases.

Although most application ideas are based on aluminium foams, the Fraunhofer method is not restricted to this metal: tin, zinc, brass, lead, and some other metals and alloys can also be foamed by choosing appropriate foaming agents and process parameters. The most common alloys for foaming, however, are pure aluminium, 2XXX alloys and 6XXX alloys. Casting alloys, such as AISi7 and AISi12, are also frequently used because of their low melting point and good foaming properties, while in principle virtually any aluminium alloy can be foamed by properly adjusting the process parameters. Fig. 8 shows a typical cross section of a P/M foam. One sees that the distribution of cell sizes and shapes is random which is typical for a foaming process.

Foaming a piece of precursor material in a furnace results in a lump of metal foam with an undefined shape unless the expansion is limited in certain directions. This is done by inserting the precursor material into a hollow mould and expanding it by heating. In this way near-net shaped parts can be prepared. Quite complicated parts can be manufactured by injecting the expanding foam into suitable moulds and allowing for final expansion there<sup>30</sup>.

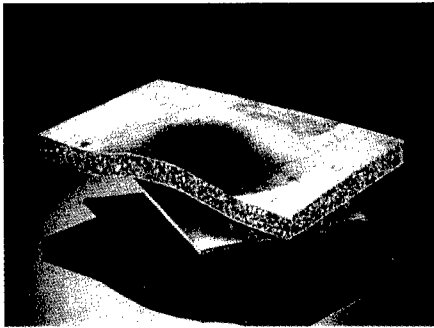


**Fig. 9: Composite structure made of an aluminium foam core and steel face sheets (size 250 x 250 x 10 mm<sup>3</sup>)**

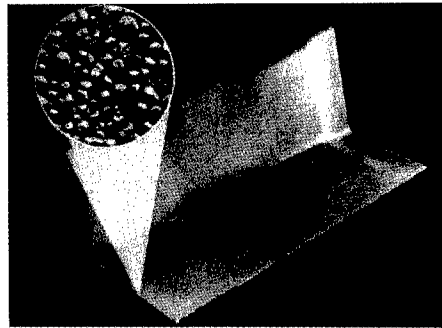


**Fig. 10: 3d-shaped sandwich of an aluminium foam with aluminium face sheets (width 1000mm, thickness 8 mm)**

Sandwich panels consisting of a foamed metal core and face sheets can be obtained by gluing the face sheets to a sheet of foam. Alternatively, if a pure metallic bonding is required, conventional sheets of metal - aluminium or steel - are roll-cladded to a sheet of foamable precursor material<sup>29</sup>. The resulting composite can be deformed in an optional step, e.g. by deep drawing. The final heat treatment then leads to sandwich structures such as the ones shown in Fig. 9 and 10. Aluminium foam can be combined with steel face sheets (Fig. 9) as well as with aluminium face sheets (Fig. 10). The large aluminium/aluminium foam part shown in Fig. 10 was a joint development of the German car maker Karmann and Fraunhofer-Institute for a concept car in which structural aluminium foam applications were demonstrated. The part is thought to replace the rear seat wall and has an enhanced stiffness at lower weight as compared to the conventional steel part.

Tubes can be filled with aluminium foam in various ways as shown in Fig. 11.

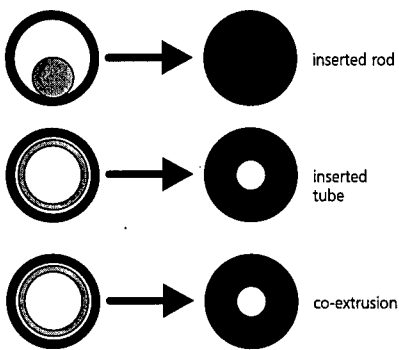


**Fig. 11: Methods for filling tubes with metal foam<sup>29</sup>**

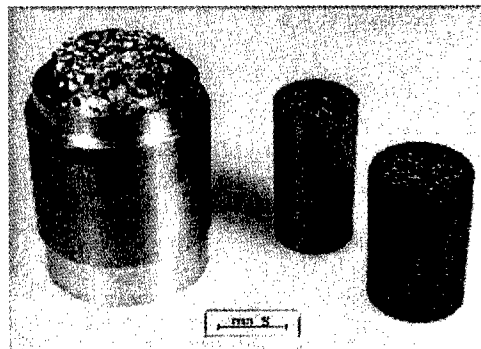


**Figure 12: Foam filled aluminium tubes. Foam: AISi12 alloy, tube: 6061 alloy**

The easiest way is to insert a rod of foamable precursor material into the tube to be filled and to place the tube into a furnace. The precursor material will start to foam and eventually fill the profile completely. The disadvantage of this method is, that only tubes with a significantly higher melting temperature as compared to the material to be foamed - e.g. steel tubes - can be used. If aluminium tubes are to be filled with foam the top of the tube will melt during foaming because it is not supported mechanically and the heat from the furnace can not be conducted into the precursor material. Thus a different way has to be chosen. One way is to insert a foamable tube into the tube to be filled. Then the foam will expand towards the centre of the tube. The foamable material is always in contact with the outer tube and therefore supports it. The expansion of the foam can be limited to a certain wall thickness by using a core in the centre of the tube. The third possibility is similar to the second but requires a co-extruded structure consisting of an outer tube of conventional aluminium and an inner tube of foamable precursor material. The two layers have a metallic bonding in contrast to the situation where the inner tube was merely inserted into the outer one. This bonding creates a better heat flow between the two tubes and therefore minimises the danger for the outer tube to be melted. Moreover, the metallic bonding between the foam and the outer tube will be better in this case as compared to the previous way, because between the inserted and the outer tube there are still oxide layers which partially prevent a metallic bonding even during foaming. Examples for foam-filled tubes are shown in Fig. 12.

More details of the Fraunhofer-process are given elsewhere<sup>31-33</sup>. Many mechanical and other physical properties have been characterised<sup>34-36</sup>. The process is now being extended to metals with higher melting points, e.g. iron and steel<sup>37-39</sup>. This extension of technology will introduce a wider scope of applications which make use of the high temperature resistance, extreme strength and other properties of these materials. Due to their excellent bio-compatibility, titanium foams could be used in prosthetical applications. However, these developments are just being worked out and are not yet in the advanced state-of-the-art of the aluminium foams.

### Gas Entrapment

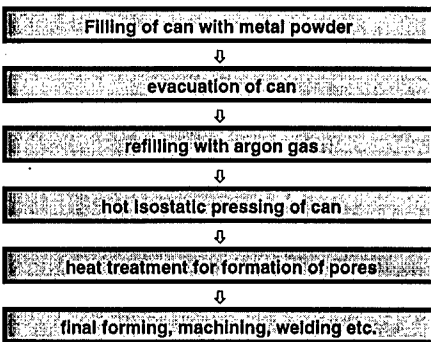
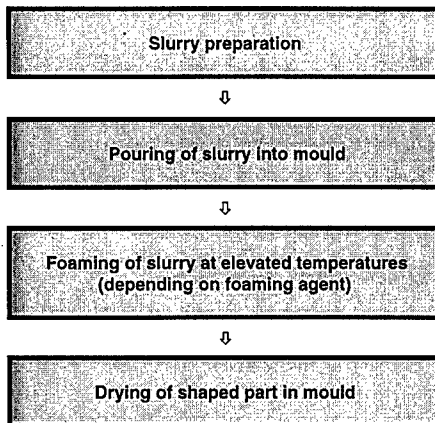
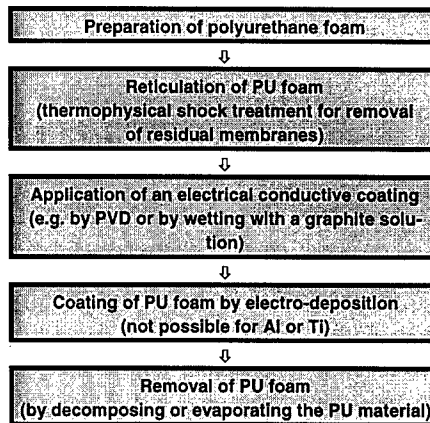


Fig. 13: Gas entrapment technique

Metals can be foamed without using a propelling agent by compressing powders to a precursor material and allowing gas to be entrapped in the metal structure during compaction<sup>40,41</sup> (see schematical representation in Fig. 13). Heating the precursor material then leads to an expansion of the metal due to the internal pressure created by the entrapped gas. The process has mainly been designed for making porous titanium structures. For this titanium powder is filled into a can that is then evacuated and refilled with argon gas. The filled can is densified by hot isostatic pressing, subsequently worked and finally foamed by means of an appropriate heat



**Fig. 14: Foaming of slurries**



**Fig. 15: Deposition technique for making metal foam**

treatment. Refinements and extensions of this process have been developed and properties of materials and components have been characterised<sup>42,43</sup>.

### Foaming of Slurries

Metallic foams can also be produced by preparing a slurry of metal powder mixed with a foaming agent (Fig. 14). The slurry is poured into a mould after mixing and dried there at elevated temperatures. The slurry becomes more viscous and starts to foam as gas begins to evolve. If sufficient stabilising measures have been taken the expanded slurry can be dried completely thus obtaining a metal foam. Such foams have been produced from aluminium powders using orthophosphoric acid with aluminium hydroxide or hydrochloric acid as a foaming agent<sup>44</sup>. Relative densities down to 7% have been achieved but there are problems with low strength<sup>45</sup> and cracks in the foamed material.

### Other techniques

There are many ways to make porous metallic products from metal powders, fibres or hollow spheres. The easiest way is to sinter loose powder fillings in a canister yielding a porous material with open porosity. Mixtures of metal powders and polymer binders can be extruded and then heat treated to produce porous parts<sup>46</sup>. This way porous materials with cylindrical pores can be produced. Reaction sintering of metal powder mixtures is also known to yield porous products.

Finally, hollow spheres made of titanium or steel, e.g., can be used to build highly porous structures by sintering<sup>47</sup>. Ordered and disordered arrangements can be realised. The density of such structures is extremely low with strengths that are still sufficient for many applications. By infiltrating the interstices between the hollow spheres the strength can be further increased.

---

## DEPOSITION TECHNIQUES

Deposition techniques start from the ionic state of metals (Fig. 15). The metal is galvanically deposited on a polymeric foam with open cells<sup>48-50</sup>. This process and the investment casting process therefore have in common that the actual foaming does not take place in the metallic state but with a polymer that is then replaced by a metal. Galvanic deposition on a polymer foam requires some electrical conductivity of the initial polymer foam. This is achieved by dipping the polymer foam into graphite solutions or by coating it with a thin conductive layer by metal vaporisation. After electroplating the polymer can be removed from the metal/polymer composite by thermal treatment. Foams of various grades can be fabricated ranging from 2 to 30 cells per cm (6 to 70 ppi). The preferred metal is nickel or a nickel-chrome alloy, but copper foams can also be fabricated.

Foams have been offered on a commercial basis under the name RETIMET (Dunlop Ltd., GB) and CELMET (Sumitomo, Japan, [46]). There is also a source in Belorussia<sup>50</sup>. Sheets with thicknesses between 2 and 10 mm are available with densities ranging from 0.2 to 0.5 g/cm<sup>3</sup>.

## SUMMARY

There is a large variety of methods to produce metallic foams or similar porous metal structures starting from liquid metal, powdered metal or from an electrolyte containing metal ions. Each process works for a selection of metals or alloys and yields foams of a typical morphology and density range. One therefore has the chance to tailor foam properties and to find a solution for one's specific application requirements.

The development of aluminium-based foams has been especially promoted by the request for certain structural light-weight applications so that the widest range of foams is available for this metal and its alloys. Various small-scale production facilities for aluminium foams are existent now in Japan, Canada, Slovakia, Austria and Germany. Some prototypes of aluminium foam parts have been developed and tested. However, it is not yet entirely clear in all cases whether the aluminium foam part can compete with the conventional part that it is supposed to replace both with respect to its physical and mechanical properties and to its economical performance.

The cost effectiveness of each process is different. It implies that only few methods are suitable for a high-volume mass production. Many of the methods will always be restricted to specialised applications where cost is not the most important parameter. Some of the processes for the production of aluminium foams - in particular the melt and the powder metallurgical processes - however, have the potential for mass production at reasonable costs. There seems to be a market for these materials provided that the unique properties of the metallic foam are fully exploited. This is the case when the foam has multiple functions, e.g. when its low weight in combination with its high-temperature resistance is desired.

## REFERENCES

- [1] L.M. Niebylski, C.P. Jarema, P.A. Immethun, US Patent 3 794 481 (1974)
- [2] I. Jin, L.D. Kenny, H. Sang, US Patent 4 973 358 (1990), PCT Patent WO 91/03578 (1991); PCT Patent WO 92/03582 (1992); US Patent 5 112 696 (1992)
- [3] M. Thomas and L.D. Kenny, PCT Patent WO 94/172218 (1994)
- [4] J.T. Wood, in: „*Metal Foams*“, Proc. Fraunhofer USA Metal Foam Symposium, 7.-8.10.1997, Stanton, Delaware. Eds.: J. Banhart and H. Eifert, MIT Verlag/Publishing Bremen (1998), p. 31
- [5] W. Ruch and B. Kirkevåg, International Patent Application PCT/NO90/00115 (1990); WO 91/01387 (1991)
- [6] D.J. Lloyd, A.D. McLeod, P.L. Morris, I. Jin, PCT Patent WO 91/19823 (1991)
- [7] L.D. Kenny and M. Thomas, PCT Patent WO 94/09931 (1994)
- [8] H. Sang, L.D. Kenny, I. Jin, PCT Patent WO 92/21457 (1992)
- [9] O. Prakash, H. Sang, J.D. Embury, *Mat. Sci. Eng.* **A199**, 195 (1995)
- [10] Product data sheets of Hydro Aluminium, Norway (1994)
- [11] S. Akiyama et al., European Patent Application EP 0 210803 A1 (1986), US Patent 4 713 277 (1987)
- [12] M. Itoh and T. Miyoshi, this symposium, R3.2
- [13] ALPORAS product information, Shinko Wire Co. Ltd., Japan (1998)
- [14] M. Otsuka, A. Kojima, M. Itoh, E. Ishii, in „*Science and Engineering of Light Metals*“ Proc. Conf. RASELM '91, Tokyo, Oct. 1991, Ed.: Japan Institute of Light Metals, p. 999 (1991)
- [15] E. Ishii, M. Itoh, Y. Morisawa, *Kobe Steel Engineering Reports*, **41**, 59 (1991), (in Japanese)
- [16] V.I. Shapovalov, US Patent 5 181 549 (1991); *MRS-Bulletin*, April 1994, p. 24-28; this symposium, R8.1
- [17] Y. Zheng, S. Sridhar, K.C. Russell, in „*Advances in Porous Materials*“, eds: S. Komareni et al., *MRS Society Bull.* Vol. **371**, p. 365, (1995)
- [18] A. Pattnaik, S.C. Sanday, C.L. Vold, H.I. Aaronson, *ibid.*, p. 371
- [19] J.M. Wolla and V. Provenzano, *ibid.*, p. 377
- [20] V. Provenzano, J. Wolla, P. Matic, A. Geltmacher, A. Kee, *ibid.*, p. 383
- [21] A.E. Simone and L.J. Gibson, *Acta Met.* **44**, 1437 (1996); *J. Mat. Sci.*, **32**, 451 (1997)
- [22] DUOCELL product information, ERG Inc., Oakland Ca., USA (1996)
- [23] Y. Yosida and C. Hayashi, Proc. Conf. Casting Science and Technology, Sept. 1990, p.103
- [24] I. Wagner et al., DGM Hauptversammlung 20.-23.5.1997, Braunschweig, Germany, (abstract)
- [25] W. Thiele, German Patent, 1 933 321 (1971); *Metals and Materials*, Aug. 1972, p. 349
- [26] M. Hartmann, R.F. Singer, in „*Metallschäume*“, Proc. Symp. Metal Foams, 6.-7.3.1997, Bremen, Germany. Ed.: J. Banhart, MIT-Verlag/Publishing Bremen (1997), p. 39, (in German); this symposium R5.5
- [27] J. Baumeister, German Patent 40 18 360 (1990); US Patent 5 151 246 (1992); European Patent EP 0460392A1 (1996)
- [28] J. Baumeister and H. Schrader, German Patent DE 41 01 630 (1991)
- [29] J. Baumeister, J. Banhart, M. Weber, German Patent DE 44 26 627 (1997)
- [30] F. Simancik, F. Schörghuber, this symposium, R3.7

- 
- [31] J. Banhart and P. Weigand, Proc. cited in [4], p. 15
- [32] J. Banhart, J. Baumeister, M. Weber, Proc. Euro. Conf. Advanced PM Materials (PM '95), Birmingham (UK), 23.-25. Oct. 1995, p. 201
- [33] F. Simancík, J. Kovácik, F. Schörghuber, Proc. cited in [26], p. 171
- [34] J. Banhart and J. Baumeister, J. Mat. Sci., in press, (1998)
- [35] H.P. Degischer, U. Galovski, R. Gradinger, R. Kretz, F. Simancík, Proc. cited in [26], p. 79, (in German)
- [36] C.J. Yu and J. Banhart, Proc. cited in [4], p.37
- [37] B. Kriszt, A. Falahati, H.P. Degischer, Proc. cited in [26], p. 59, (in German)
- [38] M. Weber, M. Knüwer, ibid., p. 73, (in German)
- [39] C.J. Yu, H. Eifert, M. Knüwer, M. Weber, this symposium, R3.4
- [40] R.L. Martin and R.J. Lederich, Metal Powder Report, Oct. 1992, p.30
- [41] M.W. Kearns, P.A. Blenkinshop, A.C. Barber, T.W. Farthing, Int. J. Powder Met. **24**, 59 (1988)
- [42] D.S. Shih et al., this symposium R7.3
- [43] this symposium, session R6
- [44] J.P. Drolet, Int. J. Powder Met., **13**, 223 (1977)
- [45] S.B. Kulkarni and P. Ramakrishnan, Int. J. Powder Met. **9**, 41 (1973)
- [46] L. Tuchinskiy and R. Loutfy, Proc. cited in [4], p. 23
- [47] K.M. Hurysz et al., this symposium, R5.3
- [48] Product data sheet of SEAC B.V., Netherlands (1986)
- [49] Product data sheet of Sumitomo Electric, Japan (1986)
- [50] Product data sheet of Ecosot, Belorussia (1996)

## ALUMINUM FOAM, "ALPORAS": THE PRODUCTION PROCESS, PROPERTIES AND APPLICATIONS

T. MIYOSHI\*, M. ITOH\*, S. AKIYAMA\*\*, A. KITAHARA\*\*

\*:Shinko Wire Company Ltd., New Tech. Prod. Div., Amagasaki, Japan

\*\* :Kyushu National Industrial Research Inst., Material Engineering Dept., Tosu, Japan

### ABSTRACT

The production of foamed aluminum has long been considered difficult to realize because of such problems as the low foamability of molten metal, the varying size of cellular structures, solidification shrinkage and so on. Recently these problems have been solved by a number of researches and some manufacturers produce foamed aluminum by their own methods. We have been employing a batch casting process and manufacturing foamed aluminum under the tradename ALPORAS® since 1986. This paper presents the manufacturing process, physical properties and some typical applications of ALPORAS.

### 1. INTRODUCTION

ALPORAS is an ultra-light weight material with a closed cell structure. We have been working on such a material for many years and have succeeded in its practical development. In particular, we have improved sound absorption and expanded the market of ALPORAS remarkably. Recently we have gotten better quality and larger sized blocks of aluminum foam by introducing a new manufacturing plant. These plants employ a batch casting process. We can control cell size and density according to the purpose with these new plants.

### 2. MANUFACTURING PROCESS OF ALUMINUM FOAM

The manufacturing process of the ALPORAS is a batch casting process (Fig.1). To make aluminum foam, it is necessary to stabilize bubbles in molten aluminum. The most important factor for stabilizing the bubbles in the molten aluminum is to increase its viscosity as shearing resistance acting on a fluid, and prevent the occurrence of bubble floatation. We use 1.5%Ca as thickening agent. Ca is added to molten aluminum at 680°C and stirred for 6 minutes in an ambient atmosphere. The thickened aluminum alloy is poured into a casting mold and stirred with an admixture of 1.6%TiH<sub>2</sub> as a blowing agent at 680°C. After stirring, the molten material is cured to expand and fill up the mold for about 15 minutes. Then, the foamed molten material is cooled to harden in the casting mold by fans. A cast ALPORAS block is 450mm wide, 2050mm long, 650mm high and weighs 160kg. After the aluminum foam block is removed from the casting mold, it is sliced into the plates with various kinds of thickness according to the purpose.

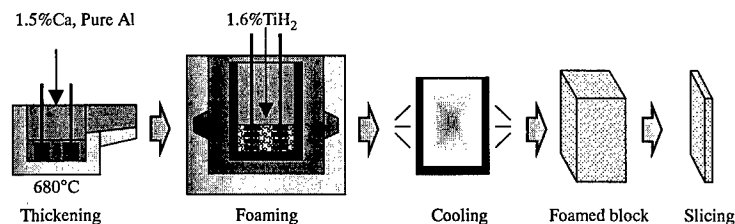


Fig.1 Manufacturing process of ALPORAS

## 2.1 THICKENING METHOD

For adjusting the viscosity of molten metal, there is a method to increase apparent viscosity by suspending and dispersing fine solid-phase particles. It can vary a thickening ratio over a wide range through the application of different solid-phase ratios. For fine solid-phase particles, ceramic particulate such as SiC, Si<sub>3</sub>N<sub>4</sub> and Al<sub>2</sub>O<sub>3</sub>, and the solid-phase of an alloy system in the solid-liquid zone are used for aluminum.

In these cases, however, it is difficult to control the temperature for keeping the solid-phase ratio at a constant value. Furthermore, it is reportedly known that several hours of agitation process is required for evenly wetting and suspending fine powder having a grain size less than 0.02 mm as in the case of SiC. In contrast, the solid phase of an oxide can be evenly dispersed by using an internal oxidation method such as agitation in an ambient atmosphere, blowing air and so on. Also, the addition and subsequent agitation of an element of high oxygen compatibility such as Ca and Mg, facilitate the progress of an oxidation process on and within the surface of molten metal, and can generate an oxide (i.e. CaO, MgO, Al<sub>2</sub>O<sub>3</sub>, CaAl<sub>2</sub>O<sub>4</sub> and so on) in the volume required for thickening the molten aluminum in a short time. This method utilizes chemical reaction within a solution and is capable of evenly wetting and dispersing fine solid-phase particles in a liquid.<sup>1,2)</sup> Fig.2 shows the change in stirring resistance due to the addition of Ca to molten aluminum.<sup>1)</sup> The thickening rate of pure molten aluminum does not increase so much. However, the addition of Ca increases the viscosity remarkably.

Fig.3 shows the effect of stirring resistance on porosity. When a stirring resistance is 0.25 kg-cm, bubbles easily float through the molten material and gas is dissipated from the surface of the molten material. So, the volume of each cell is small (Fig.4). At 0.45kg-cm, bubbles hardly float in the foaming molten material and gas pressure rises so high in the center of the molten material that the cell membranes collapse. Therefore, there is an appropriate stirring resistance for maximizing the foaming ratio.<sup>1)</sup>

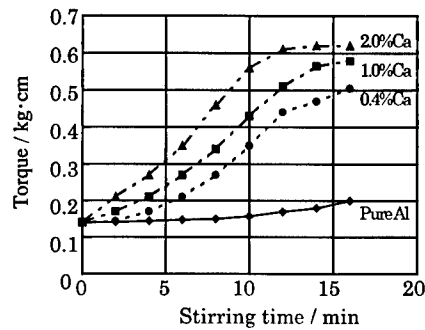


Fig.2 A change in stirring resistance due to the addition of Ca to molten Al<sup>1)</sup>

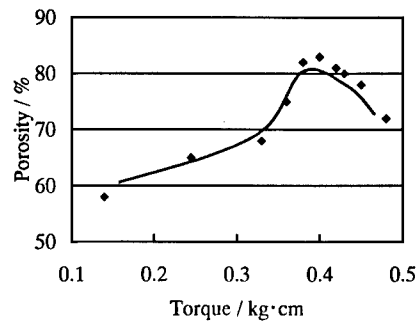


Fig.3 Effect of stirring resistance on porosity

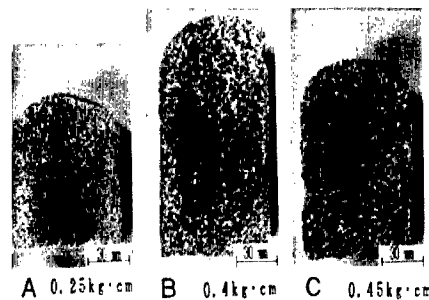


Fig.4 Effect of stirring resistance on foaming condition

## 2.2 FOAMING

Fig.5 shows hydrogen gas produced by the thermal decomposition reaction of the blowing agent,  $TiH_2$ , in molten aluminum.  $TiH_2$  is 1g and measured in atmospheric pressure. The volumetric yield of gaseous hydrogen from the decomposing  $TiH_2$  depends on the temperature: The higher the temperature, the more gaseous hydrogen is released from  $TiH_2$ . However, the higher the temperature, the faster the rate of releasing gaseous hydrogen. Most of the gaseous hydrogen bubbles that are released early float through the molten material and catch fire. Therefore, the useful blowing gas is that which is generated after admixing  $TiH_2$  and stirring.

## 3. CHARACTERISTICS

### 3.1 STRUCTURE

An internal structure of the aluminum foam is shown in Fig.6. The bubbles are no longer spherical and have polyhedron structure due to a high foaming ratio. Fig.7 shows the distribution of cell sizes for general type of ALPORAS. The cell sizes are distributed over a range of 1 mm to 13 mm and the mean cell size is 4.8 mm. We can control the cell size to some degree to meet the purpose of the material produced.

### 3.2 APPARENT DENSITY

Fig.8 shows examples of the distribution of the apparent density along the width direction of ALPORAS foamed block. The apparent density is high at the side of the block but gradually decrease towards the center. The apparent density of the product is between 0.18-0.24g/cc, which is approximately 13 times the volume of solid aluminum and is regarded as ultra-light. Also we can control the size to some degree to meet the intended purpose.

## 4. PROPERTIES

Fig.9 shows a compressive stress-strain curves of aluminum foam. The curve is reproducible as in the tension test. In this case,

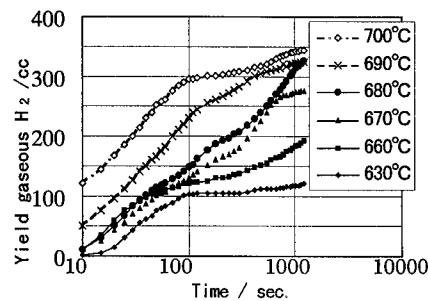


Fig.5 Hydrogen gas produced by the thermal decomposition of  $TiH_2$  in Al

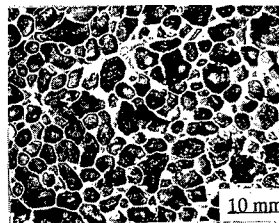


Fig.6 Internal structure of ALPORAS

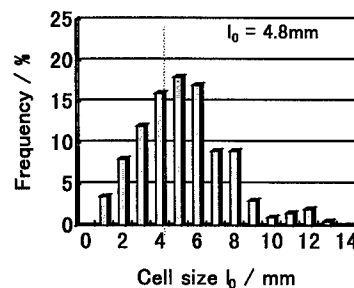


Fig.7 The cell size distribution of ALPORAS

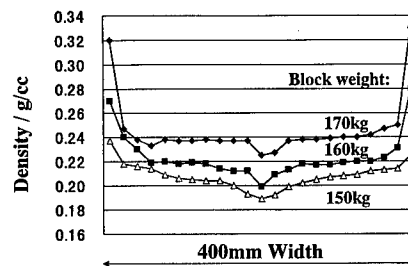


Fig.8 The distribution of the apparent density Along the width direction of blocks

however, the stress peak is followed by a plateau region, in which the flow stress is maintained at a nearly constant level. In the later stage of the plateau, the opposing cell walls begin to touch and the foams gradually collapse, resulting in the rapid increase in flow stress.<sup>3)</sup>

In Fig.10 of the tensile stress-strain curves, the stress sharply decreases after the yielding and the breaking force becomes very low. After the peak, cracks start to propagate perhaps from the corners of relatively large cells, leading to an unstable fracture.<sup>3)</sup>

Fig.11 shows the relationship between compressive strength and the porosity of the aluminum foam. With an increase in the porosity, the strength drops exponentially. The ratio of the drop further increases as the porosity exceeds 70%. This is because the spherical cells become polyhedron cells when the porosity exceeds 70% (Fig.12). This is one of the causes of stress concentration that occurs at the defects in the cell walls resulting from the growth and coalescence of bubbles. The tensile stress (Fig.13) and electrical resistance (Fig.14) also have a tendency similar to the compressive strength.

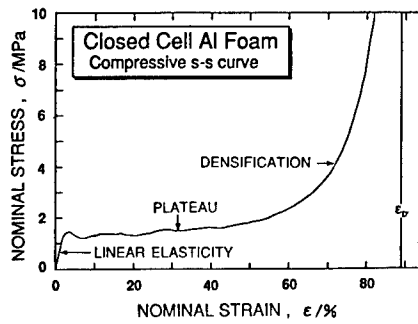


Fig.9 Compressive stress-strain curve

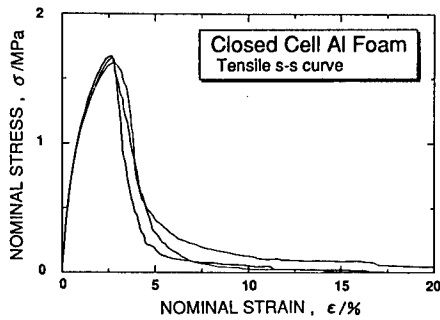


Fig.10 Tensile stress-strain curves

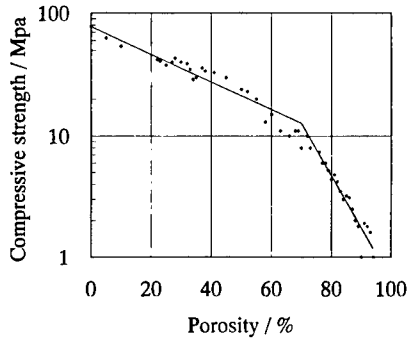


Fig.11 Compressive strength to the porosity

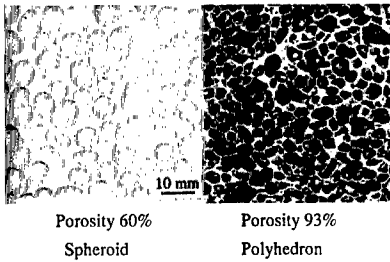


Fig.12 Structure of foamed aluminum

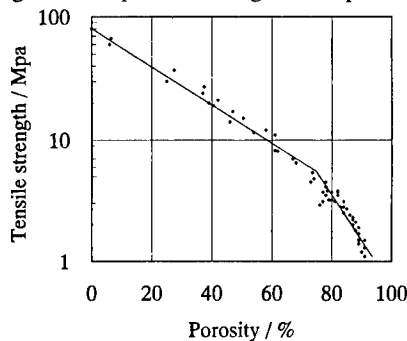


Fig.13 Tensile strength to the porosity

Fig.15 shows the sound absorbing coefficient of rolled ALPORAS measured by the reverberation chamber method in comparison with unrolled ALPORAS and a glass wool of 40 mm in thickness and 25 kg/m<sup>3</sup> in density.<sup>4)</sup> The rolled ALPORAS has such a large sound absorbing coefficient equivalent to the glass wool.

### 5. APPLICATIONS

Fig.16 shows an example of applications for sound absorbent. ALPORAS laid on the under-side of an elevated expressway for noise absorption. A cylindrically bent sound absorbing structure is laid on a noise reflecting surface of an elevated viaduct to absorb the vehicle noise, thus relieving the noise nuisance to the neighborhood residents. ALPORAS has a high impact absorbing function thanks to its substantial deformation capability under a low stress (Fig.9). It is used as an impact cushion for express rolling stocks and vehicles for saving drivers' life from collisions.

The aluminum foam has many other applications, including the double layer floor of a room where electronic equipment is arranged for office automation, filter material and microbiological incubation carriers.

### 6. CONCLUSIONS

ALPORAS is a closed cell type aluminum foam which is manufactured by a batch cast and thickened by Ca and blown by TiH<sub>2</sub>. The density of the general type is about 0.21 g/cc and its mean cell size is 4.8 mm in diameter. It has excellent sound absorption and shock absorption capabilities and its main application is sound absorbent.

### REFERENCES

- 1) K. Imagawa, H. Ueno, S. Akiyama, A. Kitahara and S. Nagata: Test Report of Agency of Industrial Science and Technology
- 2) H. Ueno and S. Akiyama: Suspension Viscosity
- 3) M. Ohtsuka, A. Kojima, M. Itoh and E. Ishii: Proc. Recent Advances in Science and Technologies of Light Metals (RASELM91), page 999
- 4) E. Ishii, M. Itoh and Y. Morisawa: Report in Kobe Steel Technical Bulletin 1991, Vol. 41, No.2

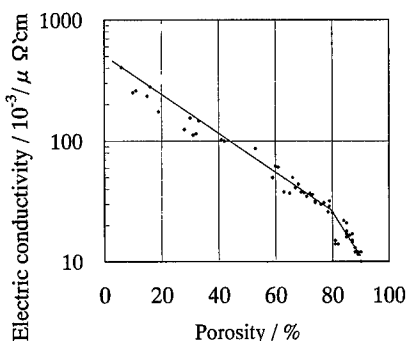


Fig.14 Effect of porosity of the foamed aluminum on electric conductivity

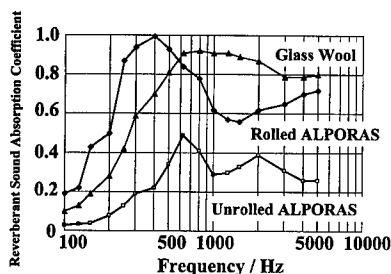


Fig.13 the sound absorbing coefficient of rolled ALPORAS

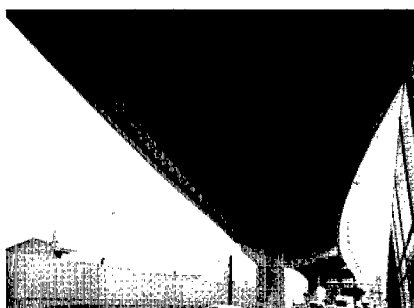


Fig.16 sound absorbing structure on the under-side of an elevated viaduct

---

## THE EFFECT OF OXIDE LAYERS ON GAS-GENERATING HYDRIDE PARTICLES DURING PRODUCTION OF ALUMINIUM FOAMS

V. GERGELY, T.W. CLYNE

Dept. of Materials Science and Metallurgy, University of Cambridge, Pembroke Street, Cambridge, CB2 3QZ, UK, twc10@cam.ac.uk

### ABSTRACT

Melt routes to metallic foam production offer attractions of low cost and the potential for good microstructural control. In situ gas generation may be preferable to external gas injection in terms of the important objective of generating a fine and uniform cell structure. The main difficulty with this approach has been that of ensuring that the gas-generating powder is suitably dispersed throughout the melt before the gas is released and the cells are formed.

In the present paper, procedures are outlined for preparation of powders for use in aluminium melts, where gas will be released only after a suitable delay, allowing the powders to first become well-dispersed in the melt and solidification to start. Pre-treatment of the foaming agent also facilitates a flexible production of castings with various porosity at the same processing conditions simply by varying the thickness of a diffusion barrier layer on the gas-releasing agent. The role of the melt viscosity history, as a function of a heat extraction rate from the solidifying melt and an alloy composition, on the final porosity of the castings is also briefly discussed.

### INTRODUCTION

A number of potential applications of metallic foams are being identified and renewed interest in these engineering materials is also reflected by several current research projects. One of the key issues for industrial exploitation of metallic foams is the development of cost-effective manufacturing strategies facilitating, preferably, net-shape production of foams with controlled porosity and cell size and minimised structural imperfection. Large volume production of metallic foams based on melt processing is potentially more attractive in terms of process economics in comparison with the powder route approach which, on the other hand, might allow closer control over the foam macrostructure.

In this study, the effects of some processing parameters on the final porosity and pore size of castings produced by in-situ gas-generation in aluminium alloy melts are examined. Particular attention is devoted to the possibility of controlling the onset and kinetics of gas evolution in the course of foam formation.

### EXPERIMENTAL PROCEDURES

#### Thermogravimetric Analysis of Titanium Hydride Powder

Thermogravimetric analysis (TGA) has been used to study the hydrogen release and oxidation kinetics of titanium hydride (TiH<sub>2</sub>) powder which was supplied by GoodFellow Cambridge Limited. The maximum particle size was claimed to be 150 µm. The oxidation of the powder (weight gain) was recorded at atmospheric pressure of air and the hydrogen release (weight loss) was monitored in argon, both under conditions of programmed heating in the temperature range of 25-1100 °C. The heating rate employed was 20 °C min<sup>-1</sup>. The hydrogen release measurements were also performed on thermally pre-oxidised titanium hydride powder. All experiments were carried out in STA-780 Series Thermal Analyser (Stanton Redcroft), using standard platinum crucibles, and Al<sub>2</sub>O<sub>3</sub> powder was used as a reference material. The amount of analysed powder was in the range of 16-18 mg.

## Production of Castings

### Foaming Agent Pre-treatment and Pelletisation

The titanium hydride powder was thermally oxidised in air before its incorporation into the melt. The thermal oxidation sequence of the powder placed in a ceramic crucible comprised heating of the hydride in air up to 400 °C (heating rate: 20 °C min<sup>-1</sup>) and a dwell at this temperature for 2, 4, 8, 24, 30 and 100 hours. Pre-oxidised powder was mixed with Al-12 wt% Si powder (~150 µm diameter) in the weight ratio of 1:8. This mixture was compacted into pellets with approx. dimensions of 5 mm in diameter and 4 mm in height, using a cold iso-static press.

### Melt Processing

A standard Al-7 wt% Si alloy was used for casting production and the melt processing was carried out in a salamander crucible of ~4 litres capacity. The charge of the alloy was induction melted and heated to about 660 °C. The power was switched off and melt stirring was initiated in the course of the alloy cooling at the melt temperature of 620 °C by raising the crucible support platform until a rotating stirrer was at a pre-selected depth within the melt. After 10 secs of stirring, the pellets containing the gas-generating pre-oxidised titanium hydride powder were introduced into the melt and the melt was stirred for a further 40 secs. A constant stirring speed of 900 rpm was used in all experiments.

In order to evaluate the effect of the amount of the foaming agent on the final casting porosity, two different quantities of the pre-oxidised TiH<sub>2</sub> powder, ~0.4 and 1.2 wt% of melt mass, were used for casting production. The melt size in this work was ~1 kg. The effect of the thermal history of the alloy solidification on the casting porosity was experimentally studied by allowing the melts to solidify with different heat extraction rates.

The casting production was designed in such a way that it allowed relatively straightforward identification of the effects of the most important processing variables on the final porosity of the castings. The porosity of castings produced via in-situ gas generation in Al-melts (thermal decomposition of the hydride and hydrogen evolution in the melt) depends on the melt viscosity history and on the gas release rate history. Both the melt viscosity history and the gas release rate history are function of other processing variables, summarised in Fig. 1. Some other processing variables not analysed in this paper (*eg* foaming agent addition melt temperature, melt stirring speed) were studied by Clyne and Chandra [1].

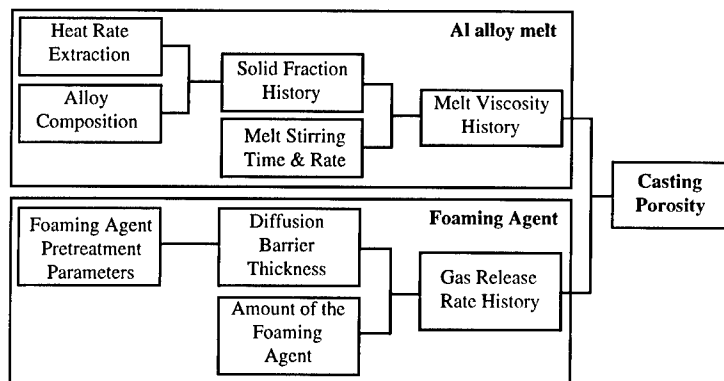


Fig. 1 Schematic illustration of the dependence of casting porosity on some processing variables, for in-situ gas generation.

## RESULTS

### Foaming Agent Gas Release Rates

#### Thermal Decomposition and Oxidation Kinetics of As-received TiH<sub>2</sub> Powder

The objective was to establish temperature/time combinations for oxidation pre-treatment of TiH<sub>2</sub> powder, in order to form an oxide layer (TiO<sub>2</sub>) on the metal hydride particles. Formation of a TiO<sub>2</sub> diffusion barrier layer on the TiH<sub>2</sub> particles could be the cheapest, simplest and probably the most efficient way to delay the decomposition reaction of the foaming agent in the course of melt processing, provided that it is possible to form a sufficiently thick oxide layer below the TiH<sub>2</sub> ignition temperature and below the temperature at which significant hydrogen evolution starts.

The TGA curve from as-received TiH<sub>2</sub> powder in argon is shown in Fig. 2. Significant weight loss, due to the thermal decomposition (hydrogen evolution) of the hydride, starts at about 500 °C (at a heating rate of 20 °C min<sup>-1</sup>). This result indicates that pre-oxidation of the powder has to be carried out below this temperature in order to minimise the loss of hydrogen from the powder.

The size, shape, and content of impurities in the metal are among the factors that influence the ignition temperature and the oxidation [2] of TiH<sub>2</sub> powder, giving rise to discrepancies in the reported data. The mean particles diameter of TiH<sub>2</sub> powder used in this study was around 20 µm, but the powder exhibited a big variation in particle size ranging from 0.5 µm to 600 µm. The morphology of the powder was angular [3].

A comprehensive study of TiH<sub>2</sub> oxidation was carried out by Lavrenko *et al* [2]. They reported that implantation of oxygen in TiH<sub>2</sub> starts at relatively low temperatures (247 °C) and is accompanied by the formation of a non-protective oxyhydride layer. During the later stages, titanium dioxide (rutile) is formed, and the reaction is limited by oxygen diffusion through the TiO<sub>2</sub> layer. The study of Gergely [3] shows that the oxidation kinetics of the hydride below its ignition temperature (~675 °C) is fairly slow. This indicates that the thickness of the oxide barrier layer at temperatures of interest (< 500 °C) can be well controlled, but only a relatively thin oxide layer (perhaps several tens nm), can be formed within a reasonable oxidation time.

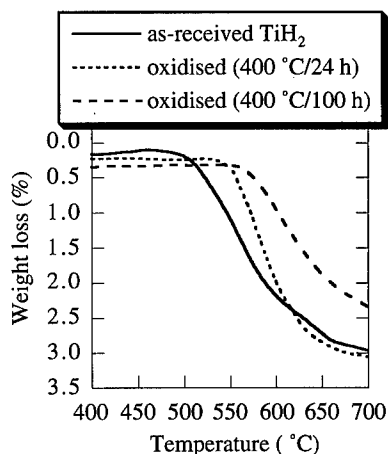


Fig. 2 Thermogravimetric curves for as-received and pre-oxidised TiH<sub>2</sub> powder recorded in argon. The heating rate was 20 °C min<sup>-1</sup>.

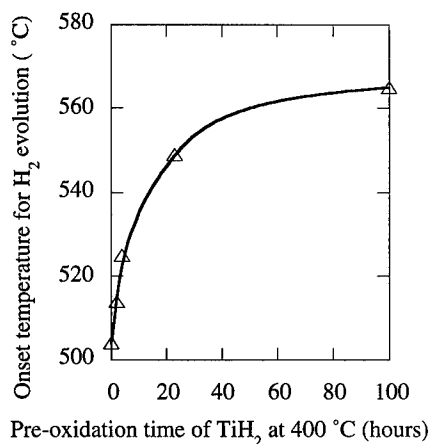


Fig. 3 Effect of pre-oxidation time of TiH<sub>2</sub> powder on the onset temperature of hydrogen evolution (data derived from TGA curves recorded in argon, heating rate was 20 °C min<sup>-1</sup>).

#### Effect of TiH<sub>2</sub> Pre-treatment on the Delay of Hydrogen Evolution

The beneficial effect of a TiO<sub>2</sub> film on Ti in preventing hydrogen absorption was reported by Fukuzuka *et al* [4]. It follows from this study that a thermally formed TiO<sub>2</sub> film acts as a barrier for hydrogen permeation, because of the small diffusion coefficient of hydrogen in the oxide. However, there is no report in the open literature about the effect of titanium hydride powder surface pre-oxidation on hydrogen evolution in the course of the hydride thermal loading. The aim of the TGA experiments was to explore the effect of oxide barrier layers (various thickness) on the decomposition rate of TiH<sub>2</sub> powder in argon, at a constant heating rate of 20 °C min<sup>-1</sup>. The thermogravimetric curves shown in Fig. 2 clearly demonstrate an effect of TiH<sub>2</sub> powder pre-oxidation in delaying hydrogen evolution. It can be inferred from the experimental curves that the onset of hydrogen release is shifted towards higher temperatures and postponed by several minutes in comparison with as-received TiH<sub>2</sub> powder, depending on the time of the hydride pre-oxidation. The beneficial effect of the diffusion barrier layer (TiO<sub>2</sub>) is summarised in Fig. 3 in terms of the onset temperatures of hydrogen evolution (derived from TGA curves) and the hydride pre-oxidation time. As seen in this figure, a plateau is reached as the oxidation times become prolonged. This may be explained by the fact that TiO<sub>2</sub> formation on the hydride is controlled by oxygen diffusion through the formed rutile layer and therefore the kinetics of the hydride oxidation decreases with increasing oxide thickness.

#### The Effect of Processing Variables on Casting Porosity

##### Role of Gas Evolution Control

Initial processing trials were focused on production of porous casting using as-received TiH<sub>2</sub> powder. It was soon realised that the as-received powder reacts rather too quickly on addition to molten Al-7Si alloy. In general, it is very difficult to control the foaming process and to produce aluminium foams with a reasonable and reproducible quality when as-received hydride is incorporated into the melt, no artificial melt viscosity increasing agent is used and no back pressure is applied in the course of foam formation. A section from a central part of the casting produced under such a condition is shown in Fig. 4a. It can be seen in this figure that this casting exhibits a big variation in pore size. Moreover, more detailed analysis of castings [3] which were produced using as-received TiH<sub>2</sub> powder has shown that these castings also exhibit big density variations between different regions of the casting.

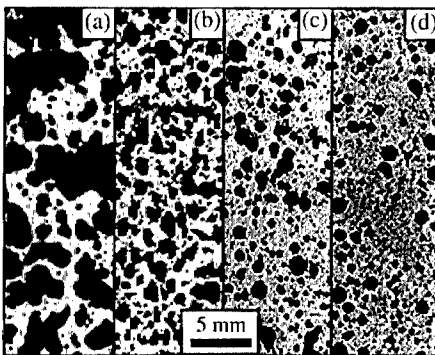


Fig. 4 Sections from Al-7Si castings showing the effect of TiH<sub>2</sub> prior-oxidation at 400 °C for various times ( $t_0$ ) on structure and porosity ( $P$ ). (a) as-received TiH<sub>2</sub>,  $P=55\%$ ; (b)  $t_0=2$  h,  $P=43\%$ ; (c)  $t_0=4$  h,  $P=34\%$ ; (d)  $t_0=30$  h,  $P=25\%$ .

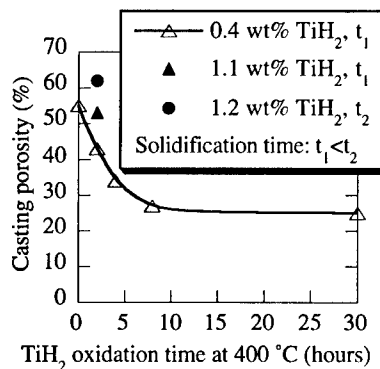
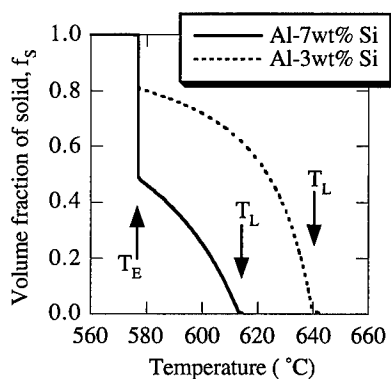


Fig. 5 Plot of the relationships between casting porosity (Al-7Si alloy), pre-oxidation time, melt viscosity history and the amount of foaming agent incorporated into the melt.

The sections from the castings which were produced using pre-oxidised  $\text{TiH}_2$  powder (400 °C for 2, 4 and 30 hours) are shown in Figs. 4b, c, and d. Two important results can be inferred from the sections. Firstly, the spread of pore size distribution is significantly lower in comparison with the section of the casting shown in Fig. 4a, which was produced at the same processing conditions except that the foaming agent had not been pre-treated. Secondly, the casting porosity can be efficiently controlled by varying the pre-oxidation time of the  $\text{TiH}_2$  powder. This is more explicitly demonstrated in Fig. 5, where the relationship between the hydride pre-oxidation time and the final casting porosity is plotted. These experimental results indicate that the onset (and probably also the kinetics) of hydrogen evolution can be controlled via coating of the foaming agent. This should result in further improvement of the structure of metallic foams produced by melt processing. Fig. 5 also shows that another processing variable controlling the casting porosity is the amount of the foaming agent incorporated into the melt.

#### Role of Melt Viscosity History

Melt viscosity history in the course of foam formation is one of the most important processing parameters controlling the bubble growth and impingement, cell wall thinning due to the Plateau border suction effect [5], cell coalescence and gravitational foam drainage. To predict the viscosity, we can assume the semi-solid metal to be a suspension of solid particles in liquid metal. This assumption is not valid for conventional castings, because a cohesive network of solid particles can start to develop at about 0.2 volume fraction of solid [6]. However, this is not the case for semi-solid metals during foam formation and therefore the suspension approach, as a first approximation, might be used to predict the viscosity of mushy metal. For viscosity prediction with higher solid fractions, the empirical Thomas equation [7] can be used. Solid fraction history in the course of an alloy solidification can be simulated by numerical modelling of solidification process, taking into consideration the heat flow, latent heat evolution and microsegregation phenomena. Such a model has been developed by Clyne [8] and has been applied in this work. Fig. 6 shows the effect of alloy composition and microsegregation on the solid fraction history at the same heat extraction rate from the melts. It can be inferred from this figure that even a relatively small change in the alloy composition can significantly alter the temperature/solid fraction relationship and this phenomena could be also utilised in the design of foam production. Fig. 7 shows the theoretical cooling curves for two different heat extraction



**Fig. 6** Prediction of solid fraction history as a function of melt temperature for Al-3Si and Al-7Si alloys, taking into account microsegregation (Scheil equation).

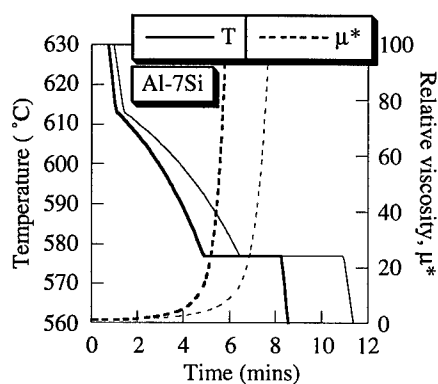


**Fig. 7** Theoretical cooling curves and viscosity history prediction for different heat extraction rates,  $Q$ . ( $Q = -2.4$  &  $-1.8 \text{ MW m}^{-3}$  refers to the thick & thin line respectively. Viscosity is relative to that of the liquid ( $\mu \approx 10^{-3} \text{ Pa s}$ ) and was calculated using the Thomas equation [7].)

rates and the associated viscosity history predictions for the Al-7Si alloy. Fig. 7 demonstrates that, by varying the heat extraction rate from the melt, we can efficiently control the viscosity history of semi-solid metals. Figs. 8a, b show sections from castings which were produced with the same processing parameters, except that the heat extraction rate from the melt in the course of melt solidification was higher in the case of casting (a). Comparison of these sections demonstrates that longer solidification time, and therefore longer bubble growth in a low viscosity environment, results in production of more porous solids and larger pores.

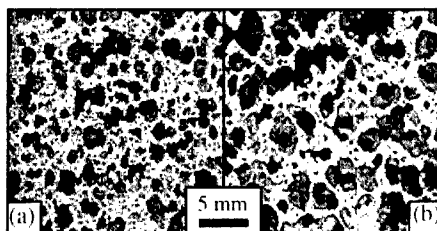


*Fig. 8 Sections from the Al-7Si castings produced at the same processing conditions (~1.2 wt% of TiH<sub>2</sub> powder prior-oxidised at 400 °C for 2 hours) except the heat extraction rate from the melt which was higher in the case of casting (a). Porosity levels are: (a) - P=53 %, (b) - P=62 %.*

## CONCLUSIONS

- 1) An optimum temperature for thermal oxidation of TiH<sub>2</sub> powder (~20 μm), in order to form a titanium oxide diffusion barrier layer, is about 400 °C. Oxidation of the hydride at this temperature only marginally depletes its hydrogen-releasing potential.
- 2) Pre-oxidation of the titanium hydride powder has at least two beneficial effects on foam production. Firstly, it postpones the onset of hydrogen evolution in the melt. This facilitates production of more homogeneous castings, because a more uniform dispersion of the hydride in the melt is achieved before the gas is released. Secondly, the porosity of castings, produced under the same processing conditions, can be flexibly designed by varying the oxide layer thickness on the powder.
- 3) In general, the porosity of castings, produced via in situ gas generation in Al-melts, can be controlled by regulating the following processing parameters:
  - (a) The onset of hydrogen evolution through varying the titanium oxide diffusion barrier layer thickness on the titanium hydride particles;
  - (b) Melt viscosity history, which is a function of the solid fraction history in the course of solidification. Solid fraction history depends on heat extraction rate from the melt, alloy composition and microsegregation phenomena;
  - (c) The amount of foaming agent incorporated into the melt.

## ACKNOWLEDGEMENTS

One of the authors (VG) is thankful to the CVCP of UK universities for Overseas Research Students Award and the Cambridge Overseas Trust for a scholarship. Additional funding was provided by the Department of Engineering through the Harvard MURI Prime Grant No. 00014-96-1-1028 and St John's College, University of Cambridge, UK.

## REFERENCES

1. T. W. Clyne, L. Chandra, Internal Report, University Cambridge, 1996.
2. V. A. Lavrenko, V. Zh. Shemet, L. A. Petrov, O. A. Teplov, S. K. Dolukhanyan, *Oxidation Metals* **33**, 177 (1990).
3. V. Gergely, CPGS thesis, University of Cambridge, 1997.
4. T. Fukuzuka, K. Shimogori, H. Satoh, F. Kamikubo in *Titanium '80*, edited by H. Kimura and O. Izumi (Proc. 4th Int. Conf. on Titanium, Kyoto, Japan, 1980), pp. 2783-2792.
5. J. J. Bikerman, *Foams*, (Springer-Verlag, New York, 1973), p. 337.
6. P. A. Joly, R. Mehrabian, *J. Mat. Sci.* **11**, 1393 (1976).
7. D. G. Thomas, *J. Colloid Sci.* **20**, 267 (1965).
8. T. W. Clyne, *Metal Sci.* **16**, 441 (1982).

---

## INVESTIGATION FOR THE SELECTION OF FOAMING AGENTS TO PRODUCE STEEL FOAMS

C.J. Yu\*, H.H. Eifert\*, M. Knuewer\*\*, M. Weber\*\*, J. Baumeister\*\*

\*Fraunhofer Resource Center Delaware, Newark, DE 19716

\*\*Fraunhofer Institute for Applied Materials Research, Bremen, Germany

### ABSTRACT

During earlier investigations conducted at the Fraunhofer Institute for Applied Materials Research (IFAM), concentrating on the metal foaming technology using the powder metallurgy process, it was shown that some steel alloys are foamable with Fraunhofer's patented powder technology approach. To further investigate the foamability of steel alloys, suitable foaming agents need to be identified and characterized. This article reports the finding of two metallic compounds used for steel foaming. The foaming behaviors of the selected foaming agents in the steel powder compacts are also evaluated in terms of different alloying elements.

### INTRODUCTION

A powder method for fabricating metallic foams was invented at the Fraunhofer Institute for Applied Materials Research (IFAM) [1]. This method allows for a direct near-net-shape fabrication of foamed parts with a relatively homogeneous pore structure. Metallic foams fabricated by this approach exhibit a close-cell microstructure with a higher mechanical strength compared with the open-cell foams. This type of microstructure is particularly attractive for applications in the field of lightweight construction and energy absorption. Although the initial investigations at Fraunhofer focused on the low melting point alloys including lead, tin, zinc and aluminum, the processing scheme allows for the foaming of high melting point alloys such as steel. Compared to the aluminum foam, steel foam will have advantages especially when the following properties are considered:

- increased mechanical strength and specific stiffness;
- increased melting temperature;
- reduced thermal conductivity;
- improved corrosion resistance.

These improvements in the steel foam properties are of interest for many structural applications. For example, use of steel foams for marine applications has the potential to reduce weight and to provide the necessary stability against fire and corrosion.

In a recent metal foam program sponsored by the Office of Naval Research, it was demonstrated by Fraunhofer that the foaming of steel with the powder metallurgical method is feasible. To process steel foams via a powder metallurgical method, a powdered foaming agent is mixed with an appropriate steel powder, and this mixture is then consolidated. Subsequent heating releases gas by decomposing the foaming agent at the melting point of the steel. Close-cell pores are formed during this process and stabilized by rapidly cooling and solidifying of the steel melt.

## EXPERIMENT

### Selection of foaming agents

The first step for the steel foam processing is to identify the suitable foaming agents for iron and steel alloys. These chemical compounds undergo thermal decomposition at high temperature to build up a sufficient gas pressure in the metal matrix before foaming starts. After melting the alloy, this gas pressure has to work against the atmospheric pressure, the metal surface tension and the hydrostatic pressure of the metal bath. Because of the elevated melting temperature of iron, only a few substances have a decomposition at the required temperature range. Two types of chemical compounds were considered: metal nitrides (generating  $N_2$ ) and metal carbonates (generating  $CO_2$ ). Differential thermal analyses were conducted on selected metal nitrides and carbonates. Two were found to show good decomposition temperatures to be used in steel foaming: strontium carbonate ( $SrCO_3$ ) and chromium nitride ( $Cr_3N$ ).

Chromium nitride and strontium carbonate exhibit nearly the same performance as foaming agent for the steel. Fig. 1 indicates a pore structure with more spherical and smoother cell walls obtained by using strontium carbonate. As a result, strontium carbonate was used as the primary foaming agent for steel.

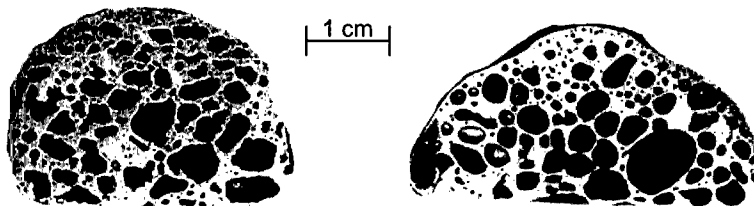


Fig. 1: Pore structure of foamed specimen with  $CrN$  (left) and  $SrCO_3$  (right)

### Effect of the amount of the foaming agent

The amount of the foaming agent (0.2 w.%) was first calculated with an estimated gas volume of  $80\text{ cm}^3$  for the selected sample size at a temperature of  $1250^\circ\text{C}$ . If the released gas were fully consumed to foam the specimen, the volume of the specimen will increase more than ten times. However, foaming experiments have shown that the attainable volume increase for this amount of foaming agent was about 150 % of the starting volume. This reduction in volume increase was investigated in further experiments. To establish an understanding of this low volume, experiments were conducted by varying the amount of  $SrCO_3$  foaming agent from 0.2 w.% to 1.0 w.%. Figure 2 shows the relationship of specimen density and foaming agent amount and the efficiency of the foaming gas release. Efficiency is defined as the ratio between the measured and the theoretical expansion. Fig. 2 also indicates that the reason for the low volume expansion is probably not due to the inefficient foaming gas release, but rather due to the limited foamability of the steel alloy. In addition, a large quantity of foaming

agent leads to a poor compaction behavior and reduced resultant density in the semi-finished specimen. The released gas escaped before foaming begins. Typical foamed specimens with 0.2 and 0.8 w.% foaming agent, respectively, are shown in Fig. 3.

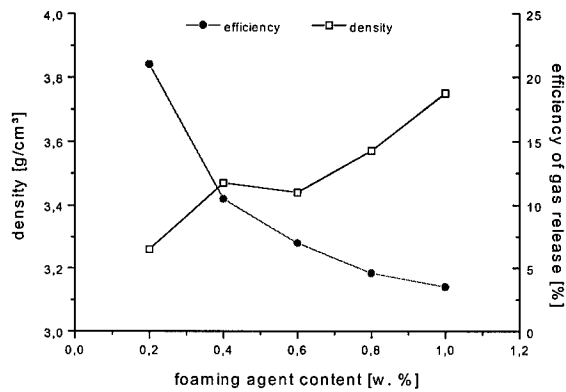


Fig. 2: Foaming agent content vs. steel foam density

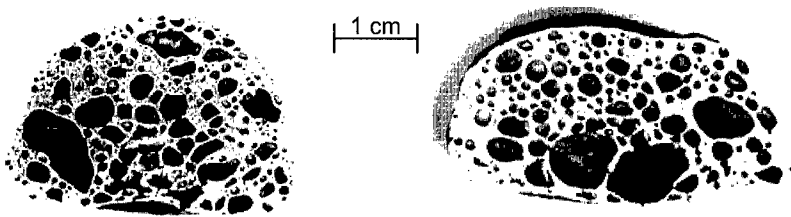


Fig. 3: Variation of the foaming agent amount; 0.2 w.% (left) and 0.8 w.% (right)

#### Effect of the amount of carbon

A series of alloying elements were added to the steel compact to assist in the steel foamability. Carbon was first identified as a favorable alloying element that could improve both the foamability and matrix strength. To significantly reduce the melting (and foaming) temperature, up to 4 w.% of carbon was added to the alloy. Nevertheless, it is known that the carbon content should be reduced to obtain an increase in matrix toughness. Fig. 4 shows the effect of carbon content (1 to 4 w.%) on foaming density, and demonstrates clearly that the best carbon content for increasing the foamability is between 2 and 3 w.%. Carbon contents of 1 w.% or 4 w.% showed no visible signs of foaming. However, we observed that a high carbon content (above 3 w.%) has the same effect on the compaction behavior as a high concentration of foaming agent. It is difficult to achieve both good compaction and a good foaming action. The difference in appearance between 2 and 3 w.% carbon, as shown in Fig. 5, is very small (both specimens are foamed with SrCO<sub>3</sub>).

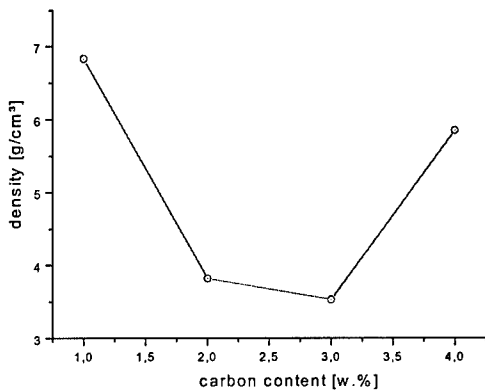


Fig. 4: Carbon content vs. steel foam density

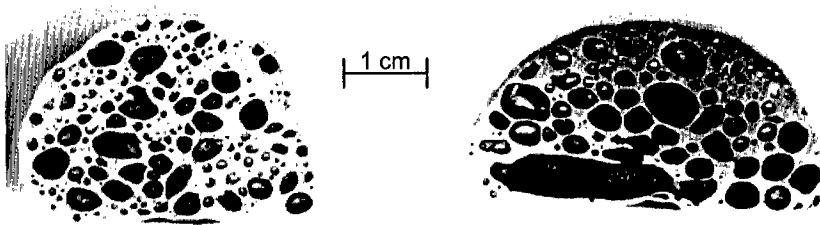


Fig. 5: effect of carbon content on microstructure of steel foam; 2 w.% (left) and 3 w.% (right)

#### Effect of phosphorous

The addition of phosphorous to a foamable iron-carbon alloy causes a further decrease of the melting temperature. The ternary iron-carbon-phosphorous eutectic temperature is at 950°C [2]. Phosphorous was added to a 2.5 w.% C and 0.2 w.% SrCO<sub>3</sub> foamable steel alloy in the form of FeP in the amounts 0.6, 1.2 and 1.8 w.% FeP. FeP was used because of problems associated with the high flammability of pure phosphorous. The effect of the phosphorous content is shown in Fig. 6.

The steel foam density was found to decrease significantly with the addition of phosphorous content greater than 1.2 w.% FeP. This is equivalent to adding 0.4 w.% of pure phosphorous. The pore structure of a foamed phosphorous-alloyed specimen is shown in Fig. 7. An irregular pore structure consisting of a few big and small pores was observed. This irregularity increases dramatically as the FeP amount increases.

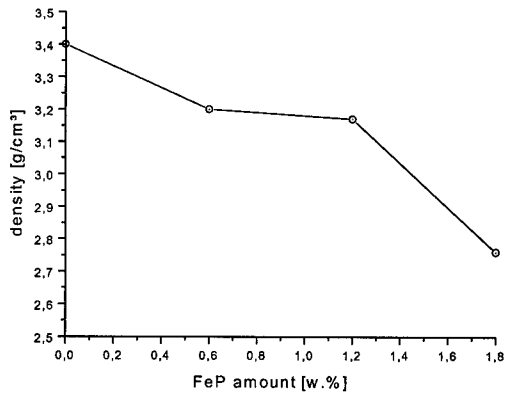


Fig. 6: Phosphorous (FeP) content vs. resultant density

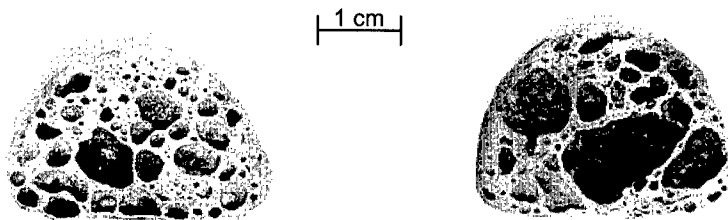


Fig. 7. Steel foam specimens with 0.6 w.% (left) and 1.8 w.% (right) FeP

#### Redox reaction for steel foaming

A redox reaction can be utilized for the foaming process instead of using decomposable substance such as metal nitrides and carbonates. The redox reaction between an oxide like silicon oxide and a reducing agent can produce a gaseous oxide that is usable as foaming gas. The alloying elements such as carbon can react with silicon oxide according to:



The CO-gas is available as a foaming agent for the steel alloy. In principle the lowest available density should be the same as the use of decomposable foaming agents. Experiments were conducted with various quantities of oxide/reducing agents. The result of these foaming experiments is shown in Fig. 8. The carbon content had the greatest effect in achieving the lowest foam density, whereas the silicon oxide content has either no or a negative effect on density. The lowest density reduction obtained was 3.14 g/cm<sup>3</sup> using fine SiO<sub>2</sub> powders.

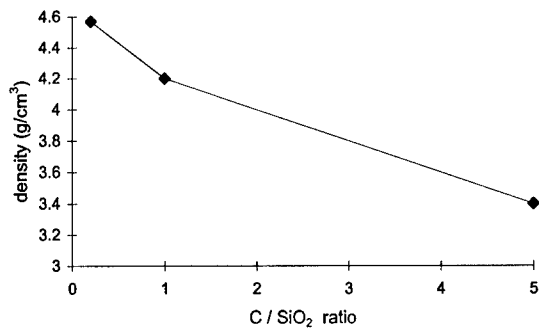


Fig. 8: Value of Density vs. C/SiO<sub>2</sub>-ratio

## SUMMARY

The use of strontium carbonate as a foaming agent produces the best pore structure among the foamed specimens. The latest investigations on steel foaming show that, with different foaming agents and alloying elements, a minimum density of approximately 3 g/cm<sup>3</sup> (equivalent to about 60% porosity) can be obtained. The addition of phosphorous leads to a further reduction of density to 2.75 g/cm<sup>3</sup>. This is equivalent to a porosity level of 65%. However, the density reduction with the addition of phosphorous is combined with an inhomogeneous and irregular pore structure. This inhomogeneity is possibly caused by a unsatisfactory compaction method. Compaction densities of less than 90% of the theoretical density were obtained. This suggests that the generated foaming gas emitted into the environment without foaming the specimen. Future investigations will focus on hot pressing and hot isostatic pressing (HIP) in order to achieve a higher foam porosity and a more homogeneous pore structure.

## ACKNOWLEDGEMENTS

This work was sponsored by the Office of Naval Research under Contract Number: N00014-97-C-0184. The authors would like to thank Dr. S.G. Fishman for his valuable support and guidance.

## REFERENCES

1. J. Baumeister and H. Schrader, "Method for Manufacturing Foamable Metal Bodies", U.S. Patent No. 5,151,246.
2. M. Weber, M. Knuever, W. Bleck and S. Feldhaus, "Entwicklung hochporoerer Stahlschaeme", Studiengesellschaft Stahlanwendung e.V., ISBN 3-930621-74-6.

## COMPLEX FOAMED ALUMINUM PARTS AS PERMANENT CORES IN ALUMINUM CASTINGS

F. SIMANČÍK \*, F. SCHOERGHUBER \*\*

\* Institute of Materials & Machine Mechanics, Račianska 75, SK-830 08 Bratislava 38,

Slovak Republic, e-mail: simancik@umms.savba.sk

\*\* Illichmann GmbH, A-4813 Altmünster, Austria

### ABSTRACT

The feasibility of complex shaped aluminum foam parts as permanent cores in aluminum castings has been investigated. The foamed samples were prepared by injection of the foam into sand molds. It turned out that sound castings can be produced if the foam core is properly preheated and/or surface treated before casting. The effect of the foam core on the performance of the casting was evaluated by in compression testing and by measuring structural damping. The gain in the related properties turned out to be much higher than the weight increase of the casting due to the presence of the core. The weight increase may be partially offset through a reduction of the wall-thickness of the shell.

### INTRODUCTION

A new injection-molding technique has recently been developed for the production of complex foamed aluminum parts with a density of 0.5-1.0 g.cm<sup>-3</sup> in various shapes and sizes [1]. The technique combines powder metallurgical and casting methods. The starting material is aluminum powder mixed with a foaming agent and continuously extruded into a compact foamable precursor. The precursor is then heated in a foaming chamber up to the melting temperature of the alloy. This leads to the formation of a liquid foam, which is injected in a controlled manner into the desired cavity. Metal or even sand molds can be used as a cavity, thus allowing cost effective large and small scale production and prototyping.

The foamed parts have a surface skin which improves their properties and gives them an appearance of normal aluminum castings (Fig. 1). However, this skin is relatively thin and sometimes contains small cracks, especially when the foam is made of aluminum casting alloys. Such foamed parts alone are therefore not suitable for highly loaded structural components, such as subframes, crossmembers, control arms etc. However, they could be effectively used instead of sand cores which are usually applied in various components to obtain weight-saving cavities. In this case the foam core will remain in the casting. Pouring aluminum around the foam improves the thickness and the properties of its outer skin, thus providing a unique possibility for the production of three dimensional sandwiches with isotropic core properties.

Some of the expected advantages of foam-cored castings are for example:

- Avoid costs of sand cores, sand removal and sand reclamation.
- Improve stiffness and crashworthiness of components.
- Accomplish internal casting configurations not feasible with sand cores.
- Accomplish completely closed lightweight sections in a casting
- Apply casting methods like squeeze casting, so far not accessible with sand cores.
- Improve noise, vibration and harshness performance.

The aim of this work is to

- Investigate the feasibility of aluminum foam parts as permanent cores in a casting.
- Determine the integrity of castings made with foam cores.

- Investigate if a reduction of the wall thickness of the shell would be possible.
- Determine the effects of foam cores on component performance.

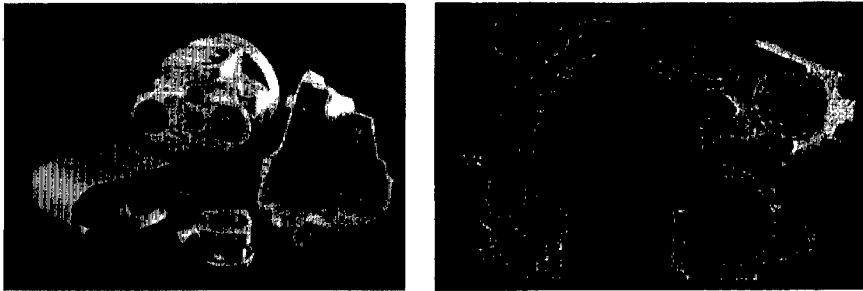


**Fig. 1** Various types of complex shaped aluminum foam parts.

## EXPERIMENTAL

The precursor for the foaming of core samples was made of two different aluminum alloys, the casting alloy AlSi12 and the wrought alloy AlMg1Si0.6. The samples with a density of 0.8-0.9g/cm<sup>3</sup> were prepared by injection of the foam into sand molds. Then they were inserted into an existing gravity die with conventional gating and risering (Fig. 2). The casting alloy AlSi9Cu3 at 740°C was used to cast the outer shell around the foam cores. Some of the cores were preheated at 400°C before casting. During the casting the mold was kept at its usual operating temperature. In order to improve the bonding between the shell and the core, some of the foam cores were surface treated by sand-blasting or coating with various diffusion supporting agents.

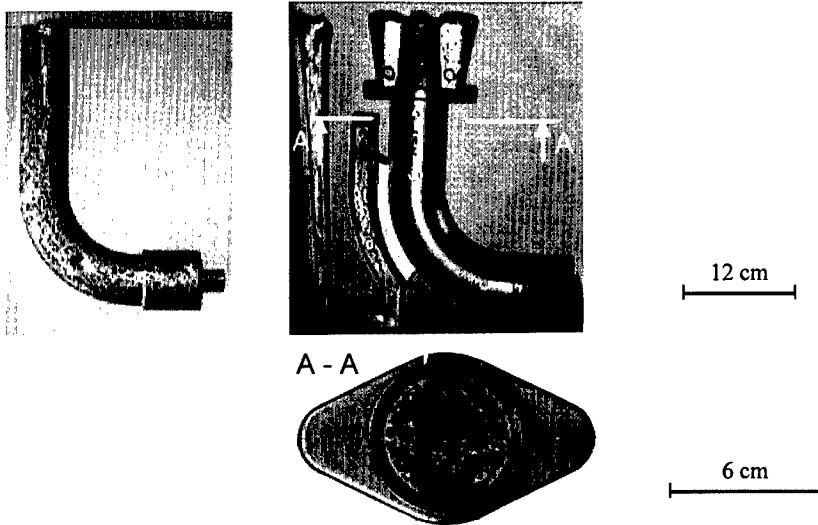


**Fig. 2** Foam-cored aluminum casting.

The foam-cored samples were visually and metallographically examined to determine the influence of technological parameters on the integrity of the casting and on the bonding between the core and the shell. The effect of the foam cores on the performance of the castings was tested by measuring the structural damping using the "impact hammer" method. The original hollow serial-production parts with identical shell geometry were also tested for comparison. The cylindrical samples with a diameter of 60 mm and a length of 13 mm were cut from the casting and were subjected to a compression load in the direction perpendicular to the main axis of the core.

## RESULTS AND DISCUSSION

None of the foam cores, neither cold nor preheated, have been melted during the pouring of the hot metal, neither have they been infiltrated. The skin of the core remained intact. A small gap could be detected between the shell and the cores prepared from wrought aluminum alloy. This is because of higher coefficient of thermal expansion of the core than of the shell (Fig. 3).

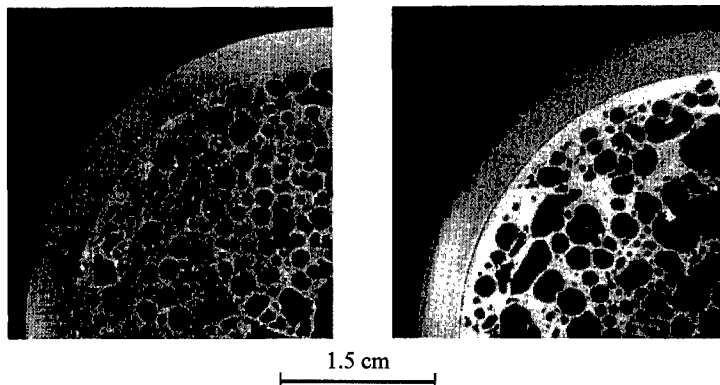


**Fig. 3** Aluminum casting with different foam cores:  
left - AlSi12-foam, right - AlMg1Si0.6-foam

When the foam cores were inserted at room temperature, cold shuts appeared in some regions of the castings, especially in those with lowest thickness of the shell. This problem had not been observed when the foam cores were preheated before casting. The preheating of the cores leads to a lower heat flow from the melt into the core, thus enabling considerable reduction of the wall thickness (Fig. 4) in comparison with usual sand cores which cannot be preheated. This is a very important, since it is obviously very desirable to offset the weight of the foam core through a reduction of the shell thickness.

Pouring liquid metal around the foam core will result in heating up and consequent expansion of the gas inside the pores. The expanding gas can cause porosity in the shell or even destroy the integrity of the casting because of gas bubbles (Fig. 5). This expansion of gases and the deterioration of the shell can be minimized by preheating the cores before insertion, because a gas inside the pores is already expanded.

Generally no bonding has developed between the core and the shell after casting because of the continuous aluminum oxide layer which prevents the core surface from reacting with the molten metal. There are two possible ways how to improve the bonding:

- a mechanical bonding can be established by the penetration of the liquid metal into the outer foam structure after opening the surface skin, e.g. by sand-blasting (Fig. 6a). This type of bonding leads to an increase in the weight of the casting of about 5%.
  - a metallurgical bonding can be achieved by coating the cores with various agents supporting diffusion through the aluminum oxide layer (Fig. 6b). Further research in this field is needed to find a suitable agent which will provide a good bonding between the shells and the cores, improving mechanical properties and corrosion resistance.
- It should be noted that the absence of bonding can sometimes improve structural damping of the part because of better energy dissipation at the separated interfaces.

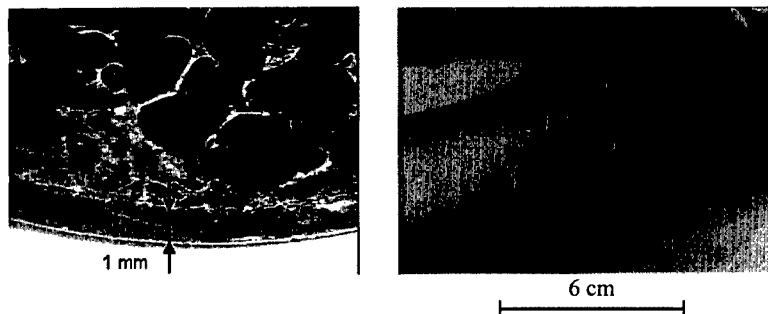


**Fig. 4** Effect of the preheating of the foam core on the casting integrity: left - preheated core (400 °C), right - cold core (room temperature).

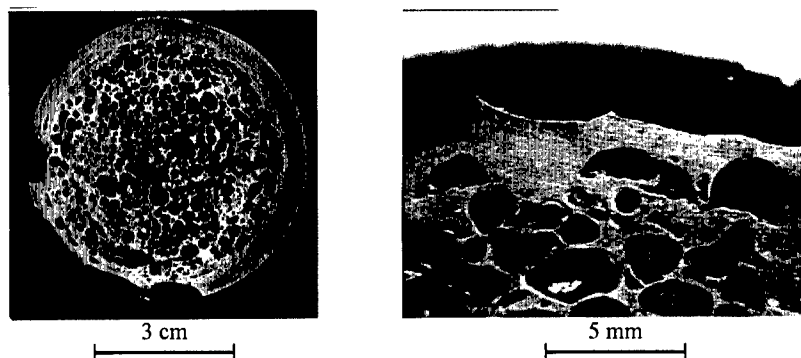


**Fig. 5** Effect of the expanding gases on the porosity of the shell.

The results from the testing of the aluminum castings containing foam cores are summarized in Fig. 7 and compared with the properties of the hollow parts. As can be seen, the effect of the foam core on the investigated properties is much higher than the relative increase of the weight of the casting. It can be anticipated, that the increase of the total weight of the component due to the presence of the foam core can be offset by a reduction of the shell thickness without a reduction of the gain in the properties.

Fig. 8 illustrates the performance of the foam core during compression load. In comparison with the hollow part, the foam-cored sample was able to withstand considerably higher deformation at higher stress levels even without the presence of any bonding between the core and the shell. This effect could be utilized for components where higher strength and energy absorption is an important issue.

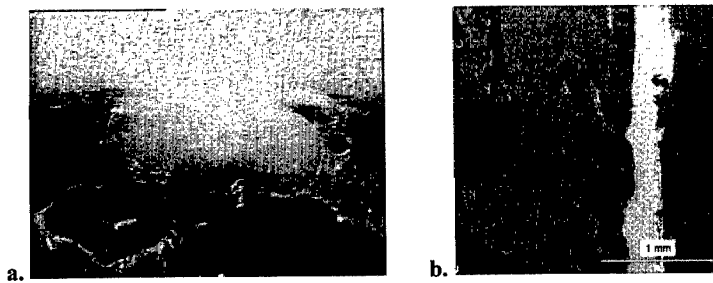


Fig. 6 Various types of bonding between the foam core and the shell:  
 a - mechanical bonding, b - metallurgical bonding.

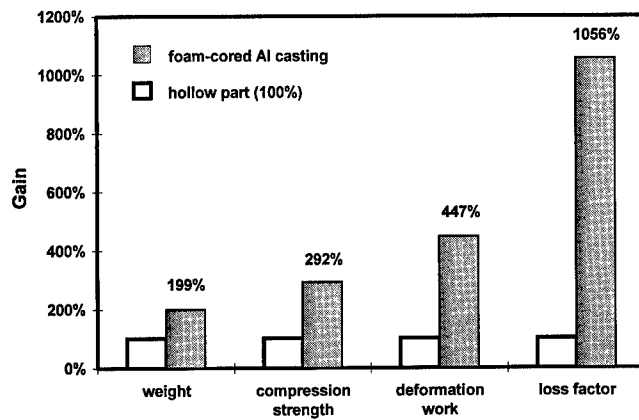
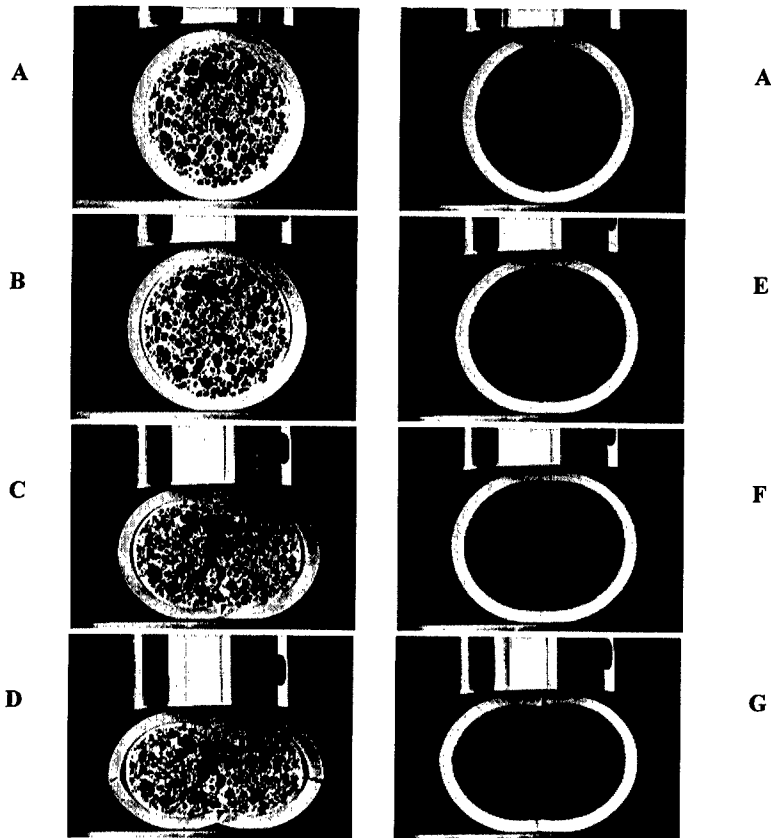
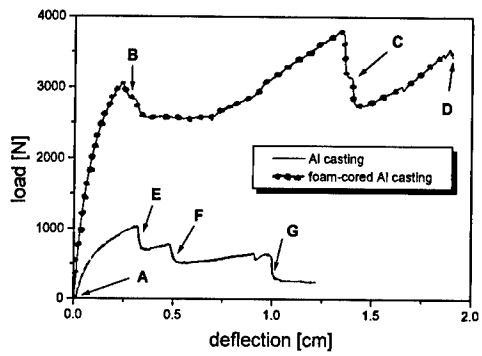


Fig. 7 The properties of the foam-cored casting in comparison with the hollow part.



**Fig. 8** Compression test of foam-cored casting in comparison with the hollow shell (sample geometry  $\phi$  60 x 13 mm, ram speed 1cm/min)

---

## CONCLUSIONS

It has been shown that complex shaped foams made of both cast and wrought aluminum alloys could replace sand cores in cast aluminum parts. Sound castings can be produced if the foam core is properly preheated and/or surface treated. The gain in the investigated properties is much higher than the weight increase due to the presence of the core. The weight increase may to some extent be offset by a reduction of the wall-thickness of the shell which is possible if a preheated foam core is used.

## ACKNOWLEDGMENTS

Authors gratefully acknowledge the financial support of Illichmann GmbH, Altmünster.

## REFERENCES

1. F. Simančík, J. Kováčik and F. Schoerghuber in Metallschäume, edited by J. Banhart (Proc. Symposium Metallschäume Bremen, 6.-7.3.1997) pp.171-176.

## JOINING OF ALUMINIUM STRUCTURES WITH ALUMINIUM FOAMS

J. Burzer, T. Bernard, H.W. Bergmann, University of Bayreuth, Institute for Materials Research,  
Department of Metallic Materials, Ludwig-Thoma-Strasse 36b, 95440 Bayreuth, Germany

### ABSTRACT

The aim of this work is the evaluation of new construction elements for applications in transportation industry which are based on new designs incorporating commonly applied aluminium structures and aluminium foams. The work includes the characterisation of the joining process, the joining mechanism and the mechanical properties of the joining zone. A testing method for the joints is developed which is based on a common tensile test in order to evaluate the influence of the main laser welding parameters on the toughness of the joints and to afford a comparison between laser beam welding and gluing process. The analysis of the joining mechanism is investigated with the help of metallographic studies. In addition, the energy absorption properties of aluminium hollows filled and joined with foam structures are characterised.

### INTRODUCTION

Due to the cellular structure of metallic foams, these materials have high specific stiffness values and energy absorption properties, making them suitable for applications requiring light-weight structures. The development and characterisation of aluminium foams is the subject of several research projects. Besides these investigations the development of processing technologies is necessary furthering the application of foamed metallic structures. In addition to gluing, laser welding is a viable technology for joining foams with semi-finished products, due to characteristics such as the keyhole effect and a minimal heat input. Thus, laser beam welding can be used to compensate for the existing lack of joining technologies.

### PRINCIPLES OF LASER WELDING

The principles of the laser welding process are well known [1]. In addition laser welding of aluminium alloys has been the subject of several research projects and is on the verge of industrial application [2]. Surface and key-hole welding mechanism are distinguished normally. Above a critical material dependent power density ( $10^6$  W/cm<sup>2</sup> for Al) the welding depth increases rapidly with the power density.

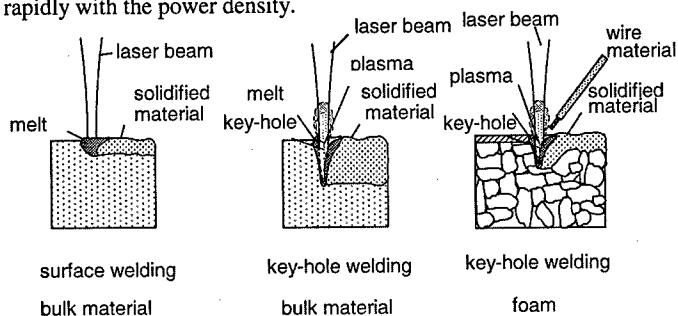


Figure 1: Welding mechanism during laser welding

In Figure 1 the two welding mechanisms and the laser welding of sheet-foam joints are shown. In the last case there is a need to supply additional material into the welding zone by a filler wire due to the porous structure of the foam lying beneath the sheet. Molten sheet material flows into the pores of the foam and without the addition of a filler wire, a groove at the surface of the seam could be created.

## EXPERIMENTAL SET UP

### Joining

The welding set up is shown in Figure 2. The filler wire is placed in front of the laser head (along the welding direction).

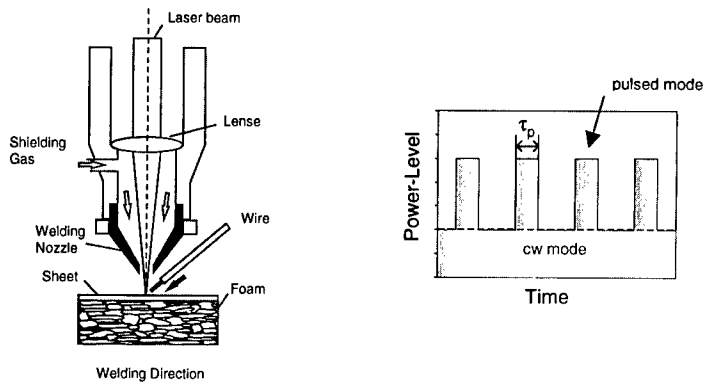


Figure 2: Laser welding set-up and process mode

All samples were welded using a Nd:YAG-Laser. This laser can be used in cw- or pulsed-mode. For this special welding task a mixture of the two modes was chosen (Figure 2). For Nd:YAG-lasers with a maximum power of 2 kW, the key hole effect can be realised more easily in the pulsed mode. The peculiarity of the key hole effect depends on the beam energy which is absorbed by the material in a single pulse. For investigating the effect of key hole welding on the toughness of the sheet-foam joints, two process parameters with different pulse time were chosen.

In order to compare welded and glued seams, a thermal curable two-component adhesive was used. The selection of the adhesive is based on experiences made in the aluminium car-body production. All samples were pickled before gluing. Due to the specific properties of the adhesive, a heat treatment of the samples was necessary after gluing.

### Materials

Table I shows the investigated materials. The sheet materials are aluminium alloys which are commonly used for aluminium car bodies. The choice of the filler material is based on previous investigations of laser welding of aluminium alloys [2]. The AlSi-alloy seems to be ideal for this application because of its good flow properties in the molten condition, which results in a good filling of the pores situated next to the aluminium sheet.

Table I: Investigated Materials

Foam Material		Bulk Material	Wire Material
0.5 g/cm <sup>3</sup>	0.35 g/cm <sup>3</sup>	2.7 g/cm <sup>3</sup>	2.7 g/cm <sup>3</sup>
pm - Al 99.5	sm - Al 99.5 + Al <sub>2</sub> O <sub>3</sub>	AlMgSi1	AlSi12
pm - AlMgSi	sm - AlMgSi + Al <sub>2</sub> O <sub>3</sub>	AlMg0.4Si1.2	
	sm - AlSi7Mg + SiC	AlMg4.5Mn	
		AlMgSi0.5	

### Testing Set-up

The toughness of the sheet-foam joints was evaluated using the set up shown in Figure 3. This evaluation is a modification of a German test-prescript DIN 50161 because of the lack of DIN-Norms and testing standarts for sheet-foam structures. The sheet was stripped from the fixed foam piece in a ZWICK Tensile Tester ZWICK 100 at a crosshead speed of 10 mm/min. For characterising the toughness of the glued joints, the common way of expressing the toughness, namely the maximum stress, was used. Due to difficulties in measuring the welded seam area, the toughness value of the welded joints was considered as a force related to the seam-length [3]. For a comparison between welding and gluing, the seam width was assumed to be 2 mm, which is a good approximation based on a number of measurements. For characterising the behaviour of foam-filled aluminium tubes, the tubes were filled with foam pieces of various diameters in order to investigate the influence of the filling quantity on the load-deflection-curve.

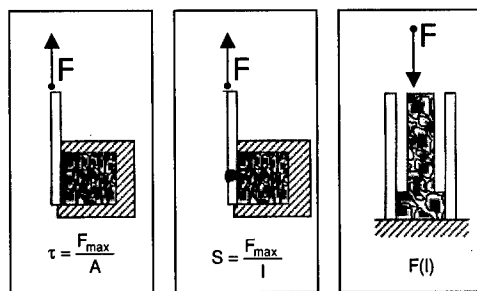


Figure 3: Set-up for toughness testing

## RESULTS

### Joining Mechanism

The toughness of the joint between the foam and sheet is important for promoting the transfer of loads in the structure and to best the energy absorption properties of the foamed material. Therefore an understanding of joining process is very important. The laser welding of foam structures and aluminium sheets is investigated in this work by metallographic examination of the weld zone and the influence of the laser parameters on the toughness of the joints.

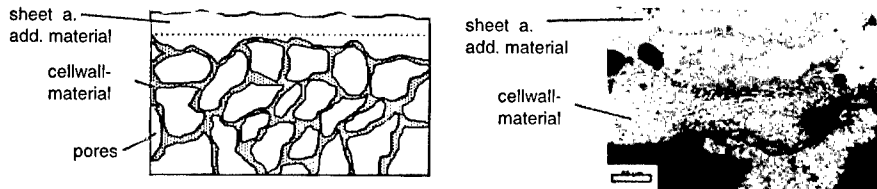


Figure 4: Joining mechanism of laser welded sheet foam joints

In Figure 4 a polished section of the joining zone is shown together with a schematic illustration of this area. It can be estimated that the connection of sheet and foam with laser welding is based on two principal mechanisms, a material related connection mechanism and a shape related connection mechanism. The heat input of the laser beam causes the melting of the parent sheet material and the underlying foam structure. After resolidification a metallic, material related connection is created. However this connection exists only between the molten sheet material and the molten material of several cell structures lying near the interface. Furthermore, the connection area is not identical with the area of the seam, but is related to the number and size of cell structures lying at the interface. The keyhole effect supports this connection mechanism. Because of the deep penetration of the laser beam, additional cells that are lying in close proximity to the sheet surface interface can be included in the joining zone. In addition the concentrated heat input of the laser beam is responsible for a minimal melting of foam structure outside the original joining zone. On the other hand, the molten material from the aluminium sheet and additional wire material flows into the pores of the foam structure during the welding process. This molten material partially fills the pores as shown in Figure 4. The additional material prevents the formation of a seam groove, and is responsible for the shape related connection mechanism. In the case of a thrust load the material filling the pores causes a blocking of the sheet and foam structure. Furthermore the experiments show that welding foams produced by the powder metallurgy method do not always require additional wire material, the formation of the groove in the seam surface being prevented by smaller pore sizes.

### Joining Toughness

The results for the influence of the laser parameters on the weld seam toughness are shown in Figure 5. The toughness values are shown for various amounts of filler material and different laser parameters, mainly the pulse-time  $\tau_{pulse}$ . The amount of additional material is changed by the speed of the wire, a higher speed resulting in more wire material in the seam. This is related to a change of the line energy of the laser welding process. The line energy is the amount of energy made available by the laser for the welding process. It depends generally on the laser power and the applied process speed. If these two parameters are constant, the line energy can be changed by varying the wire speed. For greater amounts of filler material more energy is required for melting the wire material and consequently is unavailable for melting the sheet or foam material. It is evident from the results shown in Figure 5 that increasing the interaction time of the laser beam and material ( $\tau_{pulse}$ ) results in higher values of the seam toughness. There is an increase of the toughness values for higher  $\tau_{pulse}$  up to 120 %. Improvements in the joint toughness for higher wire speeds is related to the observation that a greater amount of filler material causes a better shape-related connection of the sheet and foam structure because more molten material is flowing into the porous structure.

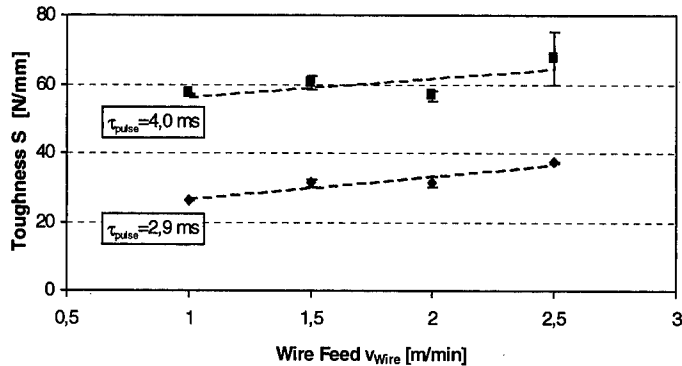


Figure 5: Influence of the laser process parameters on the toughness

For the comparison between welded and glued joints, the maximum load of the welded samples is correlated to an assumed area. The results of the comparison are shown in Figure 6. The toughness of the glued samples are independent of the sheet material and in all cases, are lower than the welded samples. This behaviour is caused by the missing material related joining mechanism and a lower effect of the shape related mechanism due to a non existing molten material in the case of the adhesive. However a higher average deviation of the results is obtained for the welded samples, most likely resulting from the different number of cell walls which are contained in the welded seam and which will have an important influence on the toughness.

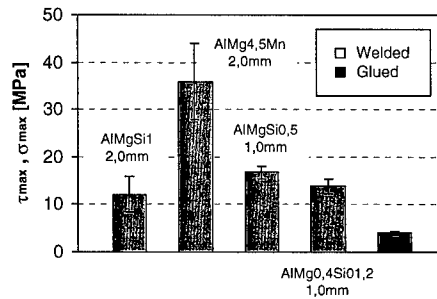


Figure 6: Comparison of laserwelding and gluing

### Aluminium tubes

The influence of foam-filled aluminium tubes is shown in Figure 7. Laser welding is used in this structure because if applied in automotive industry the foam body will need a fixation in the tube. In situ foaming in the tubes could cause problems because of the influence of the processing temperatures during the foaming process on the toughness of the heat treatable aluminium material of the tubes.

An important fact for the energy absorption characteristics of the tubes, which undergo circular buckling during compression, is the load difference of the initial and following load peaks. Filling the tubes with foams causes higher following peaks and therefore a higher efficiency in energy absorption. The 100 % and 80 % filled tubes show higher loads with 43 mm and 57 mm deflection, respectively. Due to the fact that this behaviour is undesirable for impact absorber, partially filled tubes seems to be right choice. However the specific energy absorption values, important for light weight structure, need to be improved in the future.

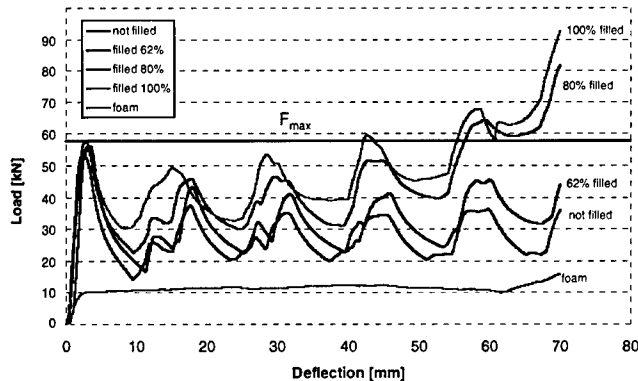


Figure 7: Load-Deflection curves of foam filled aluminium tubes

### Conclusions

The paper shows the application of laser welding for connecting aluminium sheets and aluminium hollows with foam structures. The connection is based on two principle mechanisms, a shape-related and a material-related mechanism. The toughness of the joints depends on the interaction time of the laser beam and sample material, the amount of additional wire material and the sheet material. The toughness of welded joints is higher than the toughness of glued samples. Filling of aluminium tubes with foam could improve the energy absorption behaviour. The laser welding process is suitable for manufacturing sandwich structures with foam cores or foam-filled aluminium hollows, as shown in Figure 8.

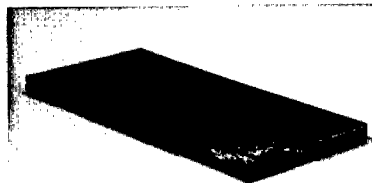


Figure 8: Laser welded aluminium-sandwich

### Acknowledgements

The authors wish to thank the companies AUDI AG, Daimler Benz AG, Linde AG, VAW Aluminium AG, Mepura for their support of this study. The investigations of this topic are supported by the Bavarian Research Foundation within the framework of FORLAS II. Furthermore the authors wish to thank Mrs. Jackie Uhm for the correction of the paper.

### References

1. Verein Deutscher Ingenieure, *Schweißen mit CO<sub>2</sub>-Hochleistungslasern*, edited by VDI-Verlag, Düsseldorf, 1987
2. H. Waldmann, R. Plank, K. Lauterwald, in H.W. Bergmann, *Proceedings of the 4<sup>th</sup> International Conference on Sheet Metal She Met '96*, edited by H.J.J. Klas, B. Shirvani, U.P. Singh, M. Geiger (Twente, 1996), p. 349-360
3. J. Burzer, H.W. Bergmann, in *Metallschäume*, edited by J. Barnhart (MIT-Verlag, Bremen, 1997) p. 163-170

---

## Lyophilic Liquid Porosimetry and a New Liquid Autoporosimeter

I. Tyomkin

TRI/Princeton, Princeton, New Jersey, USA

**Abstract.** Lyophilic liquid porosimetry determines the volumes of different size pores by measuring the amount of liquid in these pores, thus, providing pore volume distribution (PVD) data for porous structures. Any liquid that wets the sample may be used. This opens unique opportunities for porous structure evaluation. It provides realistic PVD analysis when the liquid of interest changes the porous structure. It determines uptake/drainage hysteresis of real liquids. It allows direct measurements of uptake and retention capillary pressures with different amounts of liquid in a sample. Lyophilic liquid porosimetry determines liquid/solid contact angles of different size pores within the sample. It can also be used for PVD analysis of both soft, brittle materials and porous metal materials.

Cellular materials are either open, closed or mixed cell porous structures. In applications these pores may fill with liquids (i.e. resins) or gases. Usually, these materials are heteroporous, having a variety of shapes and pore sizes. All of these pores contribute differently to the total performance of the material. Some of these pores are more effective, while others may be useless, harmful, too expensive, etc. For example, in cellular materials used in structural applications, the smallest pores may have too much solid wall per unit volume and, therefore, may be too expensive, while the largest pores could potentially create weak spots, causing cracks. The development of high tech materials should be based on the optimization of the most effective pores, while minimizing useless pores and eliminating harmful pores.

There are different methods of pore size distribution (PSD) analysis. Specialized analytical methods measure different parameters of the porous structure, they are pore volume distribution (PVD), pore surface area distribution (PSAD), pore throat distribution (PTD), pore permeability distribution (PPD), etc.

PVD of open pore structures can be measured by liquid porosimetry. This method determines the volumes of different size pores by measuring the amount of liquid in these pores. There is a lyophobic and a lyophilic liquid porosimetry. In lyophobic liquid porosimetry, a non-wetting liquid is forced into pores by external pressure, this constitutes an advancing mode. After this, external pressure can be released and the capillary pressure pushes liquid out of the pores; this is a receding mode. Here, the most common technique is *mercury intrusion porosimetry*. Unfortunately, mercury porosimetry applies high pressures, which may deform or break a sample. It also has a tough lyophobicity requirement for solid/liquid interface, and can not be used for many porous metal samples, because they form amalgams. Mercury is toxic and therefore is not desirable in laboratories. It has many other disadvantages [1].

In lyophilic liquid porosimetry (or simply "*liquid porosimetry*"), the capillary pressure spontaneously pulls a wetting liquid into the pores (advancing mode). When external pressure is applied, the liquid in the pores is pushed out (receding mode). Capillary and external pressures control the filling/drainage of pores [2-4]. If capillary pressure is higher, the pore is

filled with liquid. If the external pressure is higher, it drains the pore. The radius  $R$  of filled/drained pore is defined by the Laplace equation; thus  $R$  is an equivalent radius of cylindrical pore, having the same capillary pressure:

$$R = \frac{2\gamma \cos \theta}{\Delta P} \quad (1)$$

Here  $\gamma$  is surface tension,  $\theta$  is contact angle (advancing for filling and receding for drainage),  $\Delta P$  is external pressure.

The basic principle of lyophilic liquid porosimetry is illustrated in Fig. 1.

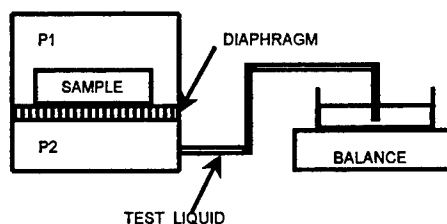


Fig. 1. Lyophilic liquid porosimetry principle.

The specimen is placed on a porous diaphragm. The external pressure may originate either by hydrostatic head (balance reservoir is lower than sample), or air pressure in the chamber, or combination of two. When the external pressure is increased/decreased, the liquid drains/fills pores according to equation (1). The amount of displaced liquid is monitored by an analytical balance.

Liquid porosimetry can use any liquid that wets a sample - water, aqueous solutions, organic liquids and solutions. Liquid porosimetry eliminates the tough hydrophobicity requirement of mercury porosimetry for solid/liquid interface and can be used for a wide variety of materials. This opens additional opportunities not available in mercury porosimetry. Liquid porosimetry can provide realistic PVD analysis when the liquid of interest changes the porous structure. It allows direct measurements of uptake and retention capillary pressures with different amounts of liquid of interest in the sample. It determines liquid uptake/drainage hysteresis. Liquid porosimetry can also determine liquid/solid contact angles of different size pores within the sample. It can evaluate PVD of a sample surface, of an interlayer between 2 layers, warp and fill yarn in the fabric, etc. It can predict partitioning of liquid of interest between 2 specimen in contact. Unlike mercury porosimetry, there is much less stress on the sample in lyophilic porosimetry, and this allows PVD analysis of soft and brittle materials. Liquid porosimetry can be used for the analysis of a wide variety of materials such as: porous metals, sintered materials, composite reinforcements, soils, woven and nonwoven fibrous materials, papers, etc.

The TRI/AUTOPOROSIMETER is based on years of experience in liquid porosimetry analysis. This is a sophisticated, computerized, precision quality instrument for measurement of volume, contact angle and other characteristics of different size pores from 1 to 1000

microns in a wide variety of materials. It consists of a test chamber, air pumping system, pore volume measuring system, sample thickness monitoring system, temperature monitoring system, 5 channel analog data acquisition system, solenoid valves operating system with I/O board and solid state relays, an analytical balance, etc. The software includes experiment control software, data treatment software, and supporting software.

The test chamber design allows for sample handling not available in mercury porosimeters: sample compression to a required thickness or with chosen load, studies of sample thickness changes during sorption/desorption, etc. A special option allows studies of sample structure under high compression loads up to 150 atm. Other options are available on request.

Liquid porosimetry experiments can be performed in advancing and/or receding mode. Fig. 2 shows typical experimental data for a single mode. The data is presented in the form of two PVD curves. The cumulative curve presents pore volume distribution as a sum of the volumes of pores starting from the smallest pores. The derivative curve presents the volumes of individual groups of different size pores. Here the abscissa is the equivalent radius of the pores, however, it may be capillary pressure or other parameters. The ordinate may have different units (fig. 2).

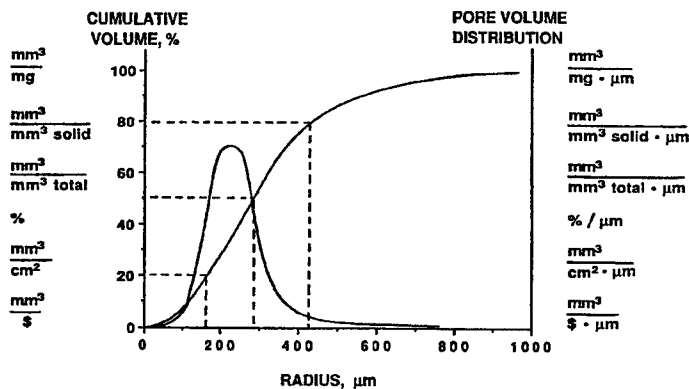


Fig.2. Cumulative and differential PVD.

The PVD analysis does not relate to the pore numbers because it is based on the measurement of the volume of liquid located in all pores of the same size. A recalculation of the volume of pores into a number of pores may be but rather should not be performed because recalculated pore numbers usually carry a lot of error due to assumptions (cylindrical capillary of chosen radius and length, etc.) and provide information that has little practical sense.

If mercury porosimetry is applicable for a sample, then PVD data both from liquid and mercury porosimetry are closely related (fig. 3). The PVD curves difference for water with TX-100 surfactant and mercury in fig. 3 is within the tested specimen property variance.

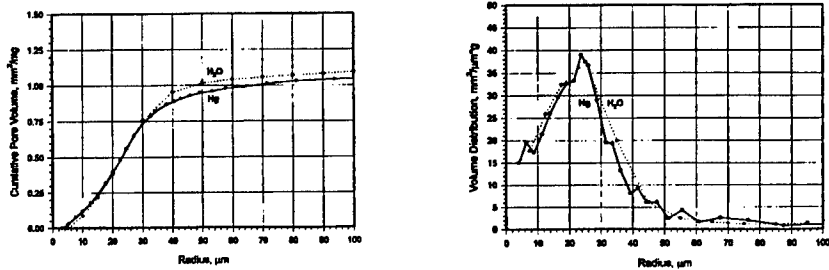


Fig 3. Water with TX-100 surfactant and mercury intrusion PVD data for a sintered polymer material.

The PVD curve may have one or more peaks. Fig. 4 shows the PVD of sintered stainless steel 100 micron porous plate (manufacturer's rating). Fig 5 shows bimodal distribution typical for woven fabrics. The larger pore size peak represents pores between yarns; the smaller pore size peak represent pores between single fibers in the yarns.

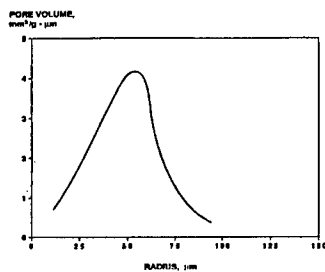


Fig. 4. PVD of a stainless steel sintered plate.

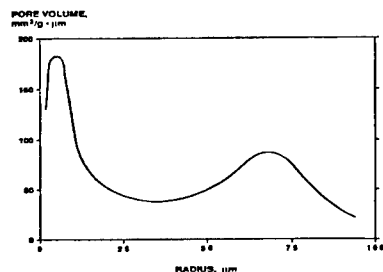


Fig. 5. PVD of a woven fabric.

Absorbed liquid may cause swelling of the solid, this may result in changes in the porous structure. The change can be determined by comparing PVD data for the liquid of interest with data for a non-swelling liquid. Fig. 6 compares data for a nonwoven pad of cotton fibers tested with hexadecane (non-swelling liquid) and aqueous TX-100 (surfactant) solution. Water causes swelling of cellulose fibers resulting in increased pore sizes (the PVD curve shifts towards the larger pores) and an increase in the total pore volume.

The porous structure of a deformable material would be affected by compression. Thiae compression can be accomplished by compression of the sample to a fixed thickness or by placing loads on the sample. Fig. 7 shows changes in the porous structure of a nonwoven fibrous material at compression to different fixed thickness from 6.2 to 1.4 millimeters. The compression shifts the plot of cumulative volume (CV %) vs. pore size (R, microns) towards the smaller pore sizes.

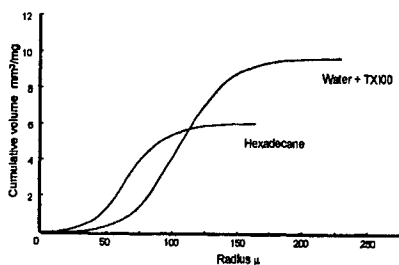


Fig. 6. Cotton pad. PVD with hexadecane and water with TX-100.

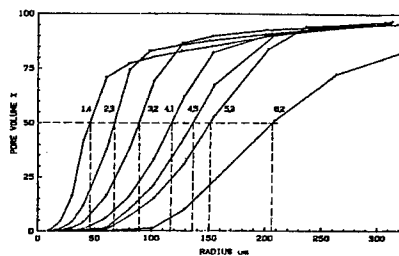


Fig. 7. PVD for polymer pad at compression from 6.2 to 1.4 mm.

#### Summary.

Lyophilic liquid porosimetry analyzes porous structures using liquids that may be in contact with the material in actual applications. It provides real world information on the properties and performance of materials. Most of this information is unique to this technique.

The TRI/Autoporosimeter provides high accuracy data and can be used for product development, quality control, applied and theoretical research.

#### Acknowledgement:

This work was sponsored by a group of participating companies who support the *Interaction of Fluids with Porous Materials* Core Technology Project at TRI/Princeton.

#### References:

1. D.N. Winslow, in *Surface and Colloid Science*, Vol. 13, edited by Egon Matijevic and Robert Good. (Plenum Press, New York and London, 1984), pp. 259-282.
2. B. Miller and I. Tyomkin, *Journal of Colloid Interface Science*, No. 162, pp. 163-170 (1994).
3. Yu. M Vol'fkovich, V.E. Sosenkin, E. I. Shkol'nikov, and V. S. Bagotskii, *Dokl. Akad. Nauk USSR*, 232, 603 (1977); Soviet Patent No. 543,852, *Byul. Izobor.*, No. 3 (1977).
4. A. A. Burgeni, C. Kapur, *Textile Res. J.*, No. 55, pp. 356-366 (1967).

---

## EDDY CURRENT CHARACTERIZATION OF METAL FOAMS

K.P. DHARMASENA, H. N. G. WADLEY

Intelligent Processing of Materials Laboratory, University of Virginia, Charlottesville, VA 22903

### ABSTRACT

Cellular materials are characterized by their relative density, pore shape and orientation, the average cell size, and the degree of pore interconnectivity which all depend upon the method and conditions used for processing. This has created an interest in non-invasive sensor techniques to characterize the foam structure. Multifrequency electrical impedance measurements were performed using an eddy current technique on open cell aluminum foam with systematically varied relative densities and pore sizes. The impedance was dominated at all frequencies by the amount of metal contained within a probed volume of foam and the tortuosity of the current path. At low frequency, the impedance data were found to be relatively insensitive to pore size variations enabling an independent measure of the relative density. At high frequency, the data indicated a strong dependence on the cell size.

### INTRODUCTION

Present day metal foams are produced by liquid-phase (melt foaming) and solid-phase (powder metallurgical) methods [1,2]. The porous metal structure may be characterized by the porosity (relative density), the average pore size, pore shape, the pore orientation and the degree of pore interconnectivity (open cell vs. closed cell foams). Within each class of foams, the pore structure is determined by the processing conditions. The wide range of relative densities and pore sizes in most metal foams has created a need for a non-invasive characterization technique to assess foam structure after processing and a sensor for structure control during the foaming process. In this study, an eddy current sensor technique is used to explore the possibility of characterizing open cell metal foams by systematic investigation of the effects of relative density and pore size on the measured electrical impedance response. Eddy current sensing has been traditionally been used as a nondestructive test method for crack detection, characterization of flaws, and as a measurement technique for electrical conductivity and magnetic permeability of metals and alloys. In recent years, an interest has developed in the application of these sensors for materials processes such as hot isostatic pressing (thickness and density measurements) and semiconductor crystal growth (solid-liquid interface characterization) [3-7].

### EDDY CURRENT SENSOR PRINCIPLE

The physical basis for all eddy current sensor concepts is electromagnetic induction. A schematic arrangement of a eddy current sensor - test sample arrangement is shown in Fig. 1. The eddy currents can be induced in a conducting sample by the changing magnetic flux of a nearby coil excited with an alternating current. The induced currents depend upon the distance between the coil and sample, the detailed geometries of the coil and sample, the magnitude of the current and its excitation frequency, and the sample's electromagnetic properties (electrical conductivity and magnetic permeability). The eddy currents create their own secondary electromagnetic fields which then interact with the primary field imposed by the excitation current, thereby altering the coil impedance. Often, the perturbations of the electromagnetic field are measured with a second (pickup) coil resulting in a transfer impedance measurement.

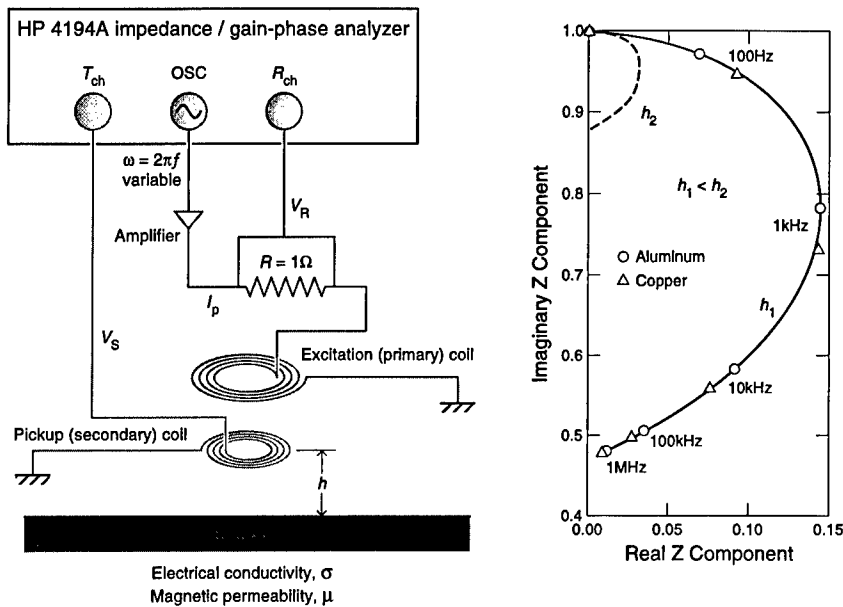


Figure 1. Eddy current sensor principle for a two-coil sensor and a characteristic impedance plane diagram.

For a two-coil arrangement, the primary coil of the sensor is connected to a variable frequency oscillator with optional power amplification (Fig. 1). The transfer impedance is obtained from the ratio of the induced voltage in the secondary coil ( $V_s$ ) to the current flow through the primary coil ( $I_p$ ). The primary current can be continuously monitored by measuring the voltage drop across a known resistor ( $R$ ). The ratio  $V_s:V_R$  defines a sensor gain ( $G$ ), and the difference in phase between the primary and secondary coils,  $\phi = \phi_s - \phi_p$ , a measured phase. Multifrequency gain and phase measurements made with and without the sample enable the computation of the real (in-phase) and imaginary (out of phase) parts of the normalized (complex) impedance. The two components are typically plotted against each other to obtain a characteristic comma shaped impedance plane diagram. Fig. 1 shows the computed multifrequency impedance plane curves for two sample-sensor separation distances,  $h_1$  and  $h_2$ . The open triangles and open circles represent the frequency data points for copper and aluminum respectively. The effect of decreasing the electrical conductivity of the sample is indicated by a shifting of frequency data points in a counterclockwise direction along the impedance curve. The effect of increasing the sample-sensor separation,  $h$ , results in a shrinkage of the impedance curve towards the empty coil measurement,  $0 + j1$ .

The selection of the test frequency determines the penetration depth of fields into a sample. It is often characterized by an exponential decay of a plane wave field's penetration into a planar test material. The depth of penetration is inversely proportional to the square root of the product of frequency, electrical conductivity and magnetic permeability. Thus lower frequency measurements enable features of the sample's interior beneath the sensor to be probed while higher frequency measurements interrogate those closer to the sample surface.

---

## SENSOR DESIGN AND MEASUREMENT METHODOLOGY

The eddy current sensor arrangement (schematically shown in Fig. 1) consisted of two "pancake-type" coils, spirally wound within grooves machined on the bottom face of two 31.5 mm diameter x 2.5mm thick ceramic disks. Four turns of evenly spaced 30AWG platinum wire were wound radially on one disk from a starting diameter of 11 mm up to a diameter of 26 mm for the primary (excitation) coil. The secondary (pickup) coil consisted of four turns wound on the second disk from a starting diameter of 9 mm up to 24 mm. The two disks were placed within a ceramic housing and retained securely with a threaded ceramic lock ring. When assembled, the secondary coil was located 2.5 mm above the bottom of the housing and 2.5 mm below the primary coil.

A Hewlett Packard Impedance/Gain-Phase Analyzer was used to supply a variable frequency signal to the primary coil of the sensor. This signal was amplified with a Bryston amplifier to enhance the field strength. The voltage drop across a low inductance, 1 ohm resistor was recorded in the reference channel of the analyzer operating in the gain-phase mode. The induced voltage in the secondary coil was measured in the test channel of the analyzer. The analyzer was programmed to record the ratios of the two voltages and the relative phase of the two signals at 75 logarithmically spaced frequencies between 1 kHz - 1 MHz. Gain and phase measurements were first obtained without the samples to normalize the impedance calculations.

## TEST SAMPLES

Open-cell aluminum (Duocel<sup>®</sup>) foams produced by ERG Materials and Aerospace Corporation were used for this investigation. Duocel<sup>®</sup> is manufactured by the directional solidification of a superheated metal [8]. The resulting material has a structure of open, dodecahedral-shaped cells connected by continuous, solid metal ligaments. Since the Duocel<sup>®</sup> foam is produced with independently variable porosity from 5 to 40 pores per inch and independently variable density from 3 to 12 percent, 12 different samples representative of the full range of densities and pore sizes were selected. 102 mm x 102 mm x 102 mm size samples were obtained for eddy current and laser-ultrasonic measurements. These consisted of 6101-T6 aluminum alloy samples of nominally 4%, 8% and 12% relative densities (+/- 2%) with inverse pore sizes of 5 pores per inch (ppi), 10 ppi, 20 ppi and 40 ppi.

## EXPERIMENTAL RESULTS

Impedance measurements were first made with a solid aluminum sample to provide a reference impedance curve. This was followed by measurements with each of the twelve Duocel<sup>®</sup> foam samples by placing the two-coil eddy current sensor on the open faces of the cellular foam samples.

Fig. 2 shows the comparison of normalized impedance curves for a solid aluminum sample with a porous aluminum foam having a relative density of 4.9% and inverse pore size of 5 ppi over a frequency range of 1 kHz - 1 MHz. It is evident from the difference in shapes and sizes of the two impedance curves that the porosity has a marked effect on the eddy current sensor response. For the solid aluminum sample (which is highly conductive), the chosen frequency range of 1 kHz - 1 MHz traces only the bottom half of the characteristic comma shaped curve. The knee of the impedance curve where the real component (which represents resistive losses) is a maximum, occurs below the lowest test frequency of 1 kHz. In contrast, with the foamed aluminum sample, the impedance locus traces the comma shaped curve more fully and the knee occurs around 12 kHz. The shifting of frequency data points in the counterclockwise direction is

indicative of a much lower “apparent” electrical conductivity of the aluminum foam compared with the solid aluminum sample. This phenomenon can be attributed to the fact that in the porous sample, the current flow occurs along a more tortuous path and is also influenced by the limited cross-section of metal (e.g. ligament diameter) available for conduction thus increasing its resistivity relative to a reference solid aluminum sample.

The second contrast between the two curves is the relative size difference. In conventional eddy current measurements, a shrinkage in the size of the impedance curve is associated with an increasing sample to sensor separation (commonly referred to as the “lift-off” effect). As the sample is moved away from the sensor (or vice versa) the flux linkage between the sensor and sample progressively diminishes and the impedance approaches a measurement representing an empty coil value (which is  $0+j1$  in the normalized impedance plane). However, in our experiments, the sensor housing was in contact with the top surface of both the solid aluminum and foam samples (with the pickup coil located 2.5 mm away from the surface). The observation of the size difference between the two curves can be attributed to the pickup coil’s sensitivity to an apparent “lift-off” phenomenon since the “effective” sample-sensor distance is strongly influenced by the fraction of nonconducting air within the foam.

When comparing the impedance components at different frequencies, it is evident that the normalized imaginary component for the foam is consistently higher than the solid aluminum at all test frequencies. In fact, the data points for the solid aluminum represents a lower bound curve. The degree of shifting of the imaginary component away from the solid aluminum is a measure of the porosity of the sample and hence the imaginary impedance vs. frequency plots is used for comparisons of effects varying densities and cell sizes.

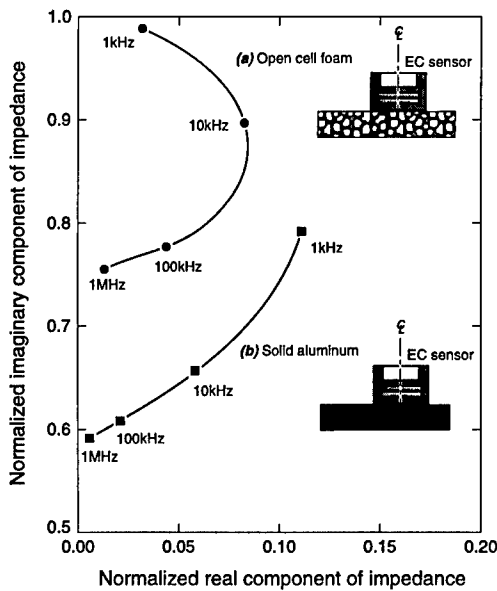


Figure 2. Comparison of normalized impedance curve for an open-cell foam (with relative density of 4.9% and inverse cell size of 5 pores per inch) with solid aluminum.

Fig. 3 shows the effect of varying the relative density on the sensor's impedance for an inverse pore size of 20 ppi. It clearly indicates that the eddy current sensor is sensitive to sample density variations. The most porous sample with a relative density of 3.8% shows the highest imaginary impedance values at all test frequencies reflective of a lower "apparent" electrical conductivity. A monotonically decreasing trend in imaginary impedance component is observed with increasing sample density. Similar trends were also seen with the samples having inverse pore sizes of 5, 10 and 40 ppi (not shown here).

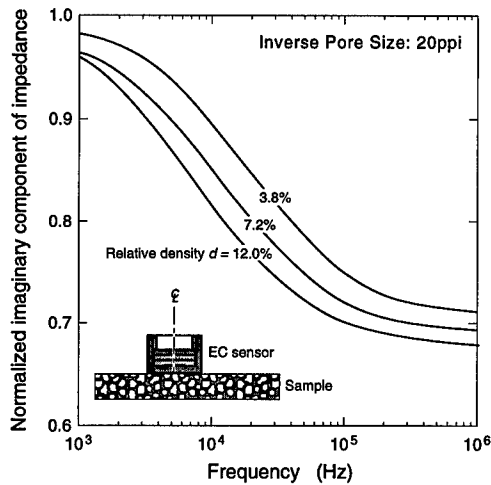


Figure 3. The effect of variation of relative density on the impedance response for an inverse pore size of 20 ppi.

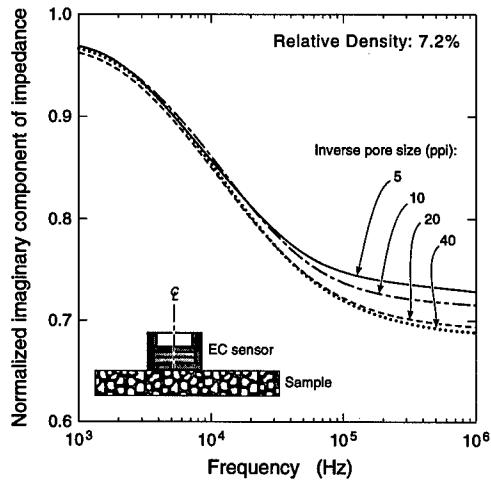


Figure 4. The effect of variation of inverse pore size on the impedance response for a relative density of 7.2%.

In contrast, Fig. 4 shows the effects of different cell sizes for a given density. It is observed that for a constant density value for all four samples, the impedance response is relatively insensitive to the pore size at low frequencies (1 kHz -10 kHz range), while showing a stronger effect at high frequencies. This observation suggests that eddy current measurements at low frequencies are more influenced by the sample density since the flux penetrates deeper in to the sample providing a bulk property measurement. At higher frequencies, the flux is concentrated at the surface of the sample resulting in an increased influence of the individual cell sizes on the sensor response.

#### SUMMARY

A study has been conducted to investigate the feasibility of using eddy currents to characterize the structure of metal foams. Work to date has focused on open-cell aluminum foam samples. The study revealed that the eddy current sensor technique is sensitive to both relative density and pore size of metal foams. Multifrequency electrical impedance measurements in the low frequency range show relative insensitivity to pore size variations enabling independent measurements of the relative density of the foam. High frequency data will enable the determination of the cell sizes closer to the surface.

#### ACKNOWLEDGMENTS

This work has been performed as a part of the research of the Multidisciplinary University Research Initiative (MURI) program on Ultralight Metals Structures conducted by a consortium that includes Harvard University, the Massachusetts Institute of Technology, the University of Virginia and Cambridge University. The consortium work has been supported by DARPA, under a ONR grant monitored by Dr. Steven Fishman. The authors wish to thank Bryan Leyda, ERG Materials and Aerospace Corporation for useful discussions.

#### REFERENCES

1. V. Shapovalov, MRS Bulletin, 24-28 (1994).
2. G.J. Davies and S. Zhen, J. Materials Science, 18, 1899-1911 (1983).
3. A.H. Kahn, M.L. Mester and H.N.G. Wadley, in Intelligent Processing of Materials, edited by H.N.G. Wadley and W.E. Eckhart, Jr. (TMS, Warrendale, 1990), pp. 293-316.
4. K.P. Dharmasena and H.N.G. Wadley, in Review of Progress in QNDE, Vol 10A, edited by D.O. Thompson and D.E. Chimenti (Plenum Press, New York, 1990), pp. 1111-1118.
5. K.P. Dharmasena and H.N.G. Wadley, J. Crystal Growth, 130, 553-566 (1993).
6. K.P. Dharmasena and H.N.G. Wadley, J. Crystal Growth, 172, 303-312 (1997).
7. K.P. Dharmasena and H.N.G. Wadley, J. Crystal Growth, 172, 337-349 (1997).
8. Duocel<sup>®</sup> Data Sheet, ERG Inc.

---

**Part IV**  
**Other Foam Materials and Processes**

## APPLICATIONS FOR SILICA-BASED AEROGEL PRODUCTS ON AN INDUSTRIAL SCALE

M. Schmidt, F. Schwertfeger  
Hoechst Research & Technology Deutschland GmbH & Co. KG  
Building G864, D-65926 Frankfurt/Main, Germany

### ABSTRACT

Aerogels, nanoporous lightweight materials, were discovered more than 60 years ago. The supercritical manufacturing process and expensive raw materials typically used to produce aerogels prohibited commercialization on an industrial scale. Recently a commercially attractive ambient pressure production process was developed which will allow broader commercialization of silica-aerogel products.

Some aerogel products for insulation applications and their preparation are described. Sound insulation properties including a remarkable absorption in the difficult low frequency range was found. In the case of insulation plates performance depends on binder and can be positively influenced by choosing the right binding material.

### INTRODUCTION

Aerogels, nanoporous lightweight materials, were discovered more than 60 years ago. During the years a lot of potential applications were described. But the traditionally practiced supercritical production process and normally used expensive raw materials prevented a production in an industrial scale due to cost reasons.

Among the potential applications, the field of thermal insulation is the most significant [1]. While cooler regions use lots of energy for heating in winter, air conditioning systems are heavily used in tropical countries. The consequence is that large quantities of fossil fuels are burned in the domestic sector, both reducing natural energy resources and producing considerable environmental pollution.

This balance can only be improved by means of alternative energy sources and by more effective thermal insulation. The aim is to reduce thermal losses by very good insulation. Besides ecological aspects there is an enormous potential in energy cost savings. It is not surprising, therefore, that the market volume for thermal insulation reaches about 10 billion DM (5.6 billion \$) for western Europe.

Recently we developed a commercially attractive ambient pressure production process for silica aerogels [2]. Table I shows some properties of these aerogels.

Table I: Some properties of silica aerogels

particle size	up to some millimeters
particle density	$\approx 120 - 150 \text{ kg/m}^3$
bulk density	$\approx 30 - 80 \text{ kg/m}^3$ (depending on particle size distribution)
thermal conductivity of a particle	$\approx 15 \text{ mW/m}\cdot\text{K}$
porosity	$> 90\%$
pore radius	$\approx 10 \text{ nm}$

specific surface	up to 1000 m <sup>2</sup> /g
water resistance	durably hydrophobic up to 250°C (in air)
temperature stability	up to 600°C (above sintering occurs)

## PREPARATION OF AEROGEL AS INSULATION MATERIAL

In some applications aerogels can be used as loose bulk material, but for the majority of applications we anticipate a bound form such as aerogel containing plate or structural part. For this purpose many different binding materials or binding systems can be considered.

In general, the binding materials can be subdivided into dry and wet systems. Included among dry systems are thermoplastic polymers as particles and fibers, though particle foams can also be considered. Wet system solutions include dispersions, suspensions, foams or melting.

Depending on which properties of the composite in addition to a good thermal insulation are desired or to influence the processing it is possible to add additives to the binding systems like surfactants, flame retarding agents, infrared opacifiers, fungicides and softener. For reasons of mechanical stability fibers can be added or the plate can be laminated with foils, fleeces or wovens.

## EXAMPLES OF PRODUCTS CONTAINING AEROGEL AND THEIR PROPERTIES

### Insulation with aerogel as bulk material

The simplest example of an aerogel containing product is as bulk material under ambient conditions. To optimize the thermal insulation performance the volume fraction of aerogel should be maximized. The achievable volume fraction depends on the particle size distribution of the aerogel particles used. In practice volume fractions between 60% and 70% should be achievable. In our experiments the size of the particles was in the range of 0.5 - 2 mm. Assuming a thermal conductivity for the aerogel of  $\lambda_{AE} = 15$  mW/m·K and for air of  $\lambda_{Air} = 26$  mW/m·K, the resulting thermal conductivity of the bulk is in the range of  $\lambda_{Bulk} = 17 - 19$  mW/m·K.

As a measure for the sound insulation performance the coefficient of sound absorption  $\alpha$  was determined with Kundt's tube. Figure 2 shows coefficient of sound absorption for different heights of an aerogel particle layer as function of frequency.

### Insulation with aerogel bound by a thermoplastic polymer

An example of a dry binding system is the used of polyvinylbutyrale (PVB) particles as a binder. This thermoplastic polymer has a remarkable low thermal conductivity of  $\lambda_{PVB} = 26$  mW/m·K.

Though mixing small PVB particles with aerogel particles and pressing the mixture at temperatures in the range of the melting point of the polymer, a plate can be formed. Figure 3 shows the thermal conductivity of such a plate as function of volume fraction aerogel.

The curve shows the result of a simulation [3]. Comparing it with measurements for different compositions of a plate a good correlation is shown. For aerogel content of  $c_{AE} \geq 90$  Vol.%, values of thermal conductivity in the range of  $\lambda_{PVB/AE} \leq 25$  mW/m·K can be realized. The stability of composites is reduced with increasing content of aerogel, but composites with an aerogel content up to  $c_{AE} \approx 95$  Vol.% can be handled in a technical environment. Though the

addition of some volume percent fibers or foil scraps to the polymer/aerogel mixture the stability can be improved without a significant deterioration of insulation performance.

In addition to the thermal properties, the elastomechanic properties of a composite can be influenced by adding aerogel.

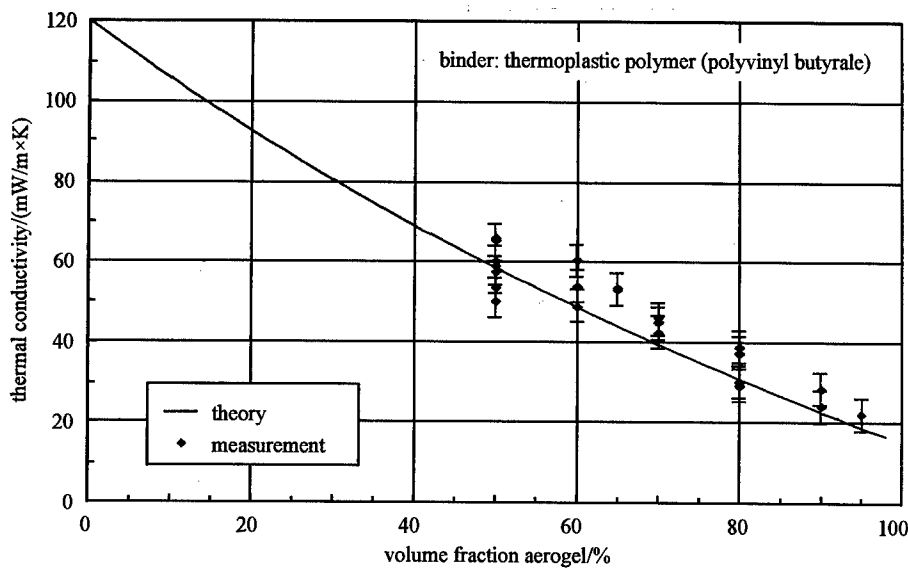


Fig. 1 Thermal conductivity of an insulation plate bound with polyvinylbutyral as function of volume fraction aerogel

#### Insulation with aerogel bound by a dispersion

An example of a liquid binding system is dispersion. In this field, experiments with aqueous vinylacetate/ethene dispersions were conducted.

The dispersion is added to a certain amount of aerogel particles, then the mixture is pressed to a plate. The plate is then dried and the dispersion particles build up a polymer film which connects the aerogel particles. Figure 2 shows the thermal conductivity of such a plate as function of volume fraction aerogel.

The curve shows the result of a simulation [2]. Comparing it with measurements for different compositions of a plate a good agreement can be stated. For aerogel contents of  $c_{AE} \geq 90$  Vol.% values of thermal conductivity in the range of  $\lambda_{PVB/AE} \leq 25$  mW/m·K can be realized.

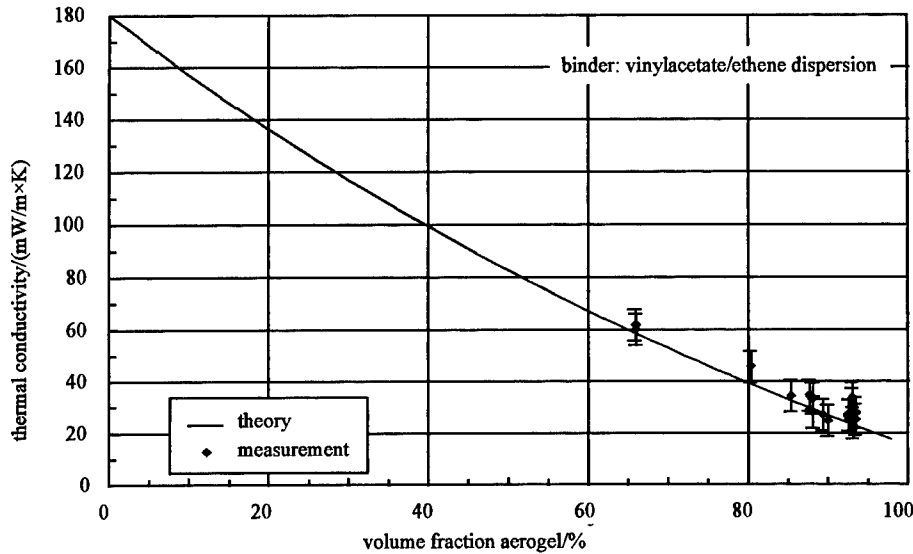


Fig. 2: Thermal conductivity of an insulation plate bound with a dispersion as function of volume fraction aerogel

#### Combination of thermal and acoustic insulation

Figure 3 shows the sound absorption of different aerogel containing products compared with traditional insulation materials. The measurements with a sample thickness of 20 mm were done with Kundt's tube.

Expanded polystyrene (EPS) and extruded polystyrene (XPS) only show a poor sound absorption performance and are not suitable for sound insulation. The values for mineral wool, which shows acceptable sound absorption at high frequencies, decrease clearly at frequencies below 800 Hz. The aerogel bulk material and in particular the dispersion bound aerogel plate show here a dramatically improved sound insulation. In contrast, the values for the PVB-bound plate discussed previously are in the range of the values of EPS/XPS and are therefore unsuitable for sound insulation applications.

Figure 3 shows also the coefficient of thermal transmission  $k$  for the different materials. The coefficient of thermal transmission can be calculated from the thermal conductivity of the material  $\lambda$ , its thickness  $s$  and the coefficients of heat transmission on the inner side  $\alpha_i$  respectively on the outer side  $\alpha_o$  by equation 1. For the sake of simplicity the coefficients of heat transmission are assumed to infinity.

$$\frac{1}{k} = \left( \frac{1}{\alpha_i} + \frac{s}{\lambda} + \frac{1}{\alpha_o} \right). \quad (1)$$

The values for the traditional materials are in the range between 1.8 and 2.0 W/m<sup>2</sup>·K. The values of aerogel containing products are significantly lower between 0.9 and 1.2 W/m<sup>2</sup>·K.

These measurements show how the choice of the binder can influence the acoustic performance of an aerogel containing product. This can be made nearly independent of the thermal insulation performance.

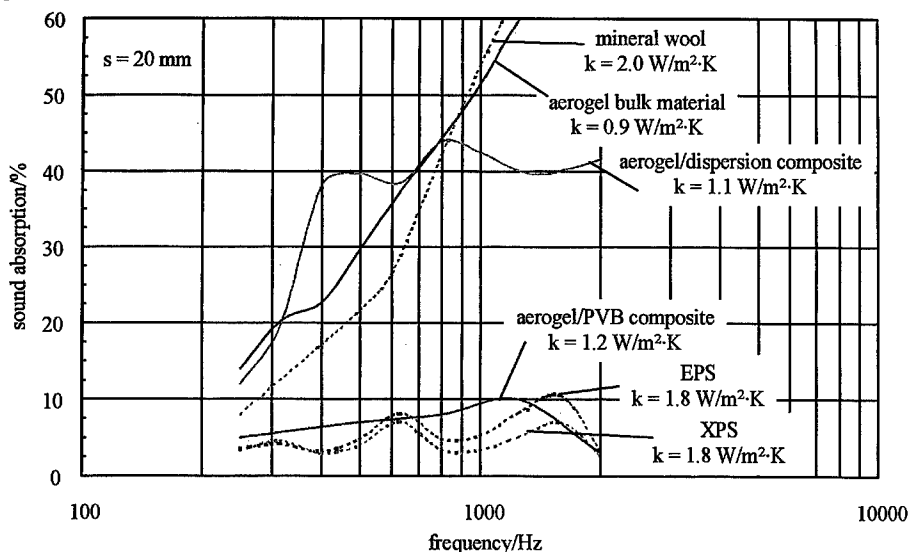


Fig. 3: Sound absorption as function of frequency and coefficient of thermal resistance for aerogel bulk material and aerogel containing composites compared with EPS and XPS

#### Elastomechanic properties of aerogel bulk material and aerogel containing composites

To determine elastomechanic properties compression tests were done. Figure 4 shows the compressive strain as function of compression for aerogel bulk material and two aerogel/epoxy resin composites compared with a XPS sample.

The curve for the bulk material shows a very elastic behavior. It was possible to reach compressions up to 80% without significant particle destruction. This is an astonishing fact since the particles are rather fragile at shearing stress.

The aerogel/epoxy resin composite with the higher amount of aerogel ( $c_{vol,AE} = 85,2\%$ ) was a little bit stiffer but shows a similar behavior. The aerogel/epoxy resin composite with the lower amount of aerogel ( $c_{vol,AE} = 79,8\%$ ) shows elastomechanic behavior typical for elastomers. A destruction of the sample occurred at compression values in the range of 80%.

The curve of the XPS sample shows a relatively steep increase of the compressive strain for compressions up to 8%. Beyond the values remain constant. This can be explained with the occurrence of cracks due to stress in the material.

With  $\lambda = 27.9 \text{ mW/m}\cdot\text{K}$  or  $\lambda = 34.9 \text{ mW/m}\cdot\text{K}$  the thermal conductivity of the aerogel/epoxy resin composites is slightly below the value of the XPS sample ( $\lambda = 35 \text{ mW/m}\cdot\text{K}$ ).

These measurements show how the choice of the binder can influence the elastomechanic performance of an aerogel containing product. The elastomechanic behavior can be varied over a wide range without a dramatic loss in thermal insulation.

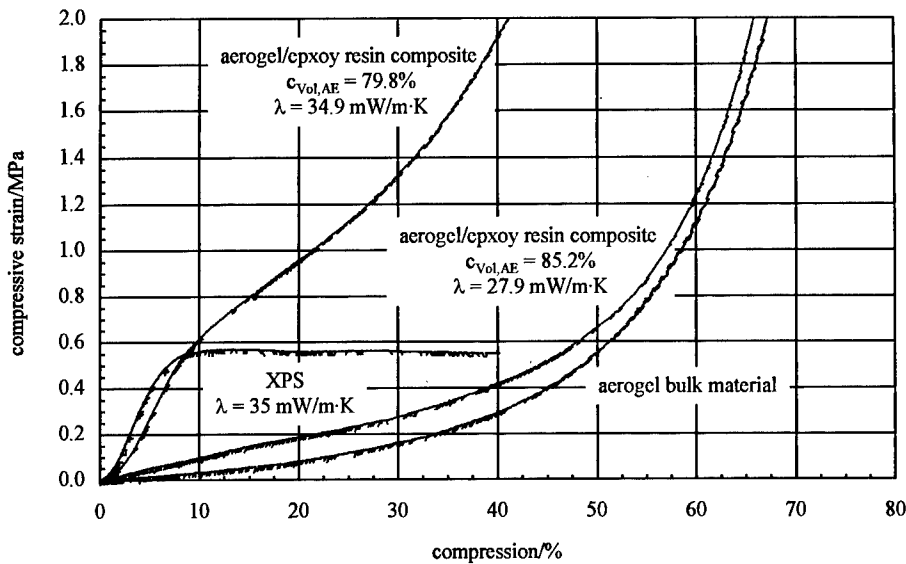


Fig. 4: Compressive strain as function of compression for aerogel bulk material and aerogel containing composites compared with XPS

#### SUMMARY

There are different ways to use aerogels for insulation applications and properties of an aerogel product strongly depend on the preparation. In thermal insulation aerogel products show outstanding performance compared to traditional materials.

Acoustic insulation performance in the normally difficult to handle low frequency range was good.

The elastomechanic behavior can be varied over a wide range without a dramatic loss in thermal insulation. An insulation plate with the stability of an XPS plate was easy to manufacture.

#### REFERENCES

- [1] M. Schmidt, F. Schwertfeger, *J. Non-Cryst. Solids* (1998), in press
- [2] F. Schwertfeger, D. Frank, M. Schmidt, *J. Non-Cryst. Solids* (1998), in press
- [3] Z. Hashin, S. Shtrikman, *J. App. Phys.* **33**, p. 3125 (1962)

## STRUCTURAL GRAPHITIC CARBON FOAMS

Kristen M. Kearns<sup>1</sup>, David P. Anderson<sup>2</sup>, and Heather J. Anderson<sup>1</sup>

<sup>1</sup> Air Force Laboratory, Materials and Manufacturing Directorate, 2941 P St. Ste. 1,  
Wright-Patterson Air Force Base, Ohio 45433-7750, kearnskm@ml.wpafb.af.mil

<sup>2</sup> University of Dayton Research Institute, 300 College Park Avenue,  
Dayton, Ohio 45469-0168, andersdp@ml.wpafb.af.mil

### ABSTRACT

Graphitic carbon foams are a unique material form with very high structural and thermal properties at a light weight. A process has been developed to produce microcellular, open-celled graphitic foams. The process includes heating a mesophase pitch preform above the pitch melting temperature in a pressurized reactor. At the appropriate time, the pressure is released, the gas nucleates bubbles, and these bubbles grow forming the pitch into the foam structure. The resultant foamed pitch is then stabilized in an oxygen environment. At this point a rigid structure exists with some mechanical integrity. The foam is then carbonized to 800°C followed by a graphitization to 2700°C.

The shear action from the growing bubbles aligns the graphitic planes along the foam struts to provide the ideal structure for good mechanical properties. Some of these properties have been characterized for some of the foam materials. It is known that variations of the blowing temperature, blowing pressure and saturation time result in foams of variously sized with mostly open pores; however, the mechanism of bubble nucleation is not known. Therefore foams were blown with various gases to begin to determine the nucleation method. These gases are comprised of a variety of molecular weights as well as a range of various solubility levels. By examining the resultant structures of the foam, differences were noted to develop an explanation of the foaming mechanism.

### INTRODUCTION

Structural composites are based on disconnected carbon fibers integrated in some type of matrix. The strength and stiffness of commercial carbon fibers are due to the graphitic morphology that originates from the melt spinning of the precursor pitch. If an interconnected network of struts could be produced which possessed a similar morphology to the carbon fiber, a new generation of composite reinforcement could emerge. Foams are an example of such materials, the open-cell structure being the desired architecture. Microcellular, open-cell foams can be produced from anisotropic pitch with graphitic planes aligned along the struts. The process sequence includes blowing, stabilizing, carbonizing, then graphitizing the foam, similar to the process for manufacturing pitch-based carbon fibers. A foam could be blown into a mold for net-shape composites or co-processed with fibers for anisotropic reinforcements. Model graphitic foams were predicted [1] to have a compression modulus of approximately 2 GPa with a density of about 0.1 g/cm<sup>3</sup>. Not many other foams or core materials have a density and compression modulus near these values.

The original process for fabricating microcellular foams was developed by Colton and Suh [2]. They demonstrated that microcellular foams could be produced from amorphous polymers by saturating the polymer with a gas, then heating above the glass transition temperature. The

pressure of the gas against the now soft polymer resulted in a foam of uniformly distributed pores. Dutta, *et al.* [3] modified this process by saturating with nitrogen in the melt to get better solubility of nitrogen into the pitch. In this process, the solubility of nitrogen into the pitch is critical to foam fabrication. The molten pitch was saturated with nitrogen gas and held for 10 minutes before dropping the pressure and temperature suddenly.

The current method of fabricating microcellular foams is a variation of both the Suh and Dutta work. It includes a slight initial pressurization before the pitch is heated and a further pressurization at the final temperature. For this process pressure, temperature and time are the controllable parameters and can be varied to produce foams with various magnitudes and types (closed or open) of porosity. However, the mechanism that produces the foam is not well understood. Therefore, various gases were used to blow foams to determine their effect on the cellular structure

## EXPERIMENT

### Materials

Foams were processed from AR pitch manufactured by Mitsubishi Gas Chemical Co. The pitch is produced by the catalytic polymerization of naphthalene and supplied in a pellet form. Manufacturing data claims the softening temperature is 239°C and the material is 100 percent anisotropic. The glass transition temperature occurs over a temperature range of 230 to 260°C. The blowing gases were all obtained in gas cylinders from their manufacturers and used without further purification. The four blowing gases examined to date were helium, nitrogen, argon and carbon dioxide.

### Processing

The pitch pellet was jet-milled into particles of an average size of 1-3  $\mu\text{m}$  and pressed into a 57-mm-diameter cylinder ~5 mm thick. The pitch disk was then placed in a Parr pressure reactor and heated (under a slight gas pressure) at 3°C/min to the desired final temperature. When the disk reached the final temperature additional gas was added to obtain the final desired pressure and the entire system was held at these conditions for a predetermined amount of time. The pressure was abruptly vented to the atmosphere. Further processing was required to transform it from a pitch into a carbonaceous foam. After blowing, the foam was removed from the reactor and placed in a 150 to 180°C oven to oxygen stabilize the pitch. When a weight gain of approximately 7 percent had been reached (except the helium foams which never did stabilize, samples were carbonized with a 60°C/hour heating rate to 850°C in a nitrogen environment.

### Characterization

Physical evaluations included weights and dimensional measurements. Dimensional measurements were used to calculate volumetric changes during foam blowing. These measurements were taken after disk fabrication, after foaming, and after carbonization to give a non-destructive indication of any differences produced by the various gases and processing steps. The completely processed foams were examined under both fluorescent optical and scanning electron microscopy (SEM) and measurements of the pore size, pore shape, and amount of open porosity were made. The foam bulk densities and porosities were measured using the Archimedes

displacement method of ASTM C 373-72. These averages and the other measurements for each process parameter level were then plotted for each process parameter.

### Design of Experiment

A 2<sup>4</sup> half factorial design of experiment was performed to look at the effect of four process parameters: the initial pressure, final temperature, final pressure, and the length of the hold time at the final conditions. This was performed with each of the four blowing gases: helium, nitrogen, argon, and carbon dioxide. Table 1 provides the experimental values for each parameter and Table 2 the conditions of each experimental run.

Table 1  
Experimental Parameters

Initial Pressure (P <sub>i</sub> ):	Low (-)	High (+)
Final Temperature (T <sub>f</sub> ):	Low (-)	High (+)
Final Pressure (P <sub>f</sub> ):	Low (-)	High (+)
Hold Duration (t):	Short (-)	Long (+)

Table 2  
Experimental Run Conditions

Sample #	P <sub>i</sub>	T <sub>f</sub>	P <sub>f</sub>	t
1	+	+	+	+
2	-	+	+	-
3	+	-	+	-
4	-	-	+	+
5	+	+	-	-
6	-	+	-	+
7	+	-	-	+
8	-	-	-	-

## RESULTS

### Noninteractive Gases

The effects of the processing parameters on the volume expansion data are shown in Figure 1. The porosity data followed the expansion data directly and the bulk density was inversely related, but are not shown.

The first thing to note is that “final” pressure has little effect. The hold duration also did not have a large influence. The “initial” pressure shows a molecular mass effect of the gases; the larger mass produced more expansion at higher pressure while smaller masses (progressively) expanding less. At higher temperatures the lightweight gases expand more than at the lower temperatures, while the heavier gas (argon) expanded the same independent of temperature.

The gas penetrates the interstitial spaces between particles in the disk preform during the initial pressurization and heat-up (~1-1/2 hours). At the higher temperature, either more spaces may be sealed off trapping more gas or, more likely, the lower viscosity of the pitch offers less resistance to deformation when the pressure is reduced.

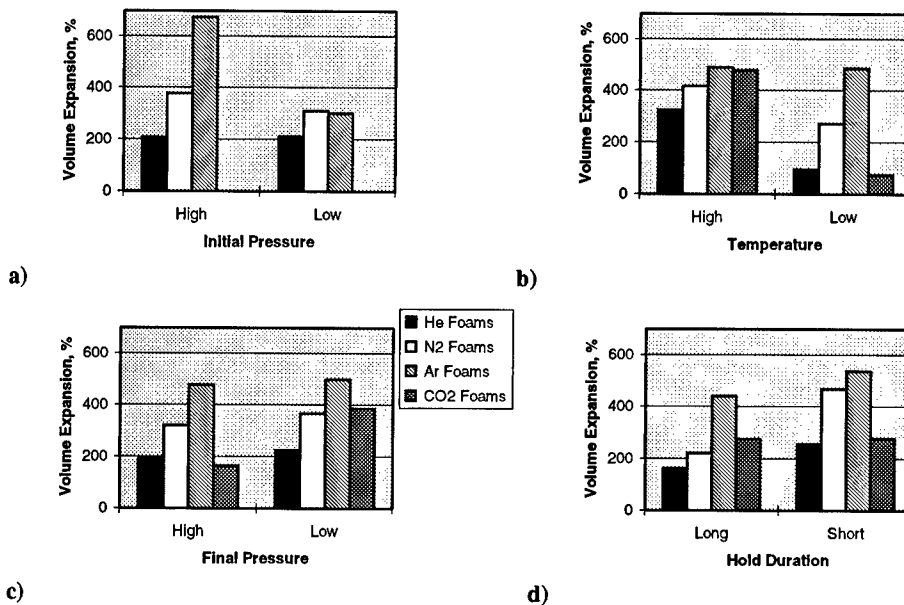


Figure 1. Average volumetric expansion for a) initial pressure, b) final temperature, c) final pressure, and d) hold time.

When the pressure is released several things occur:

Gas molecules which can escape from the spaces do so.

Gases that cannot escape cause the pitch to foam.

Spaces that have connections large enough for the gases to flow between will coalesce into single bubbles.

Eventually the foam expands to the point where the gas can escape to the outside rather than continuing to foam the pitch.

Because the spaces containing the foaming gas are already sealed off before the application of the final pressure, this parameter does not have an effect and the hold time is also irrelevant. The lower pitch viscosity at higher temperatures offers less resistance to expansion, so the volume increases more for the smaller molecules; it is harder for the larger molecules to escape so the temperature has less effect. Likewise at higher pressures the large molecules expand to their fullest extent, while the smaller gas molecules expand only until they can escape, regardless of the pressure which ends the foam expansion. A simple calculation of the volume expansion of the gases at the processing conditions shows that if full expansion occurs at the lower pressure to give 300% volume expansion, then the higher pressure would expand 750% which is very close to that observed for argon.

The helium blown foam does not produce an open-cell structure because it can more easily escape as the foam expands. The closed-cell foam that is produced is difficult to stabilize for further processing.

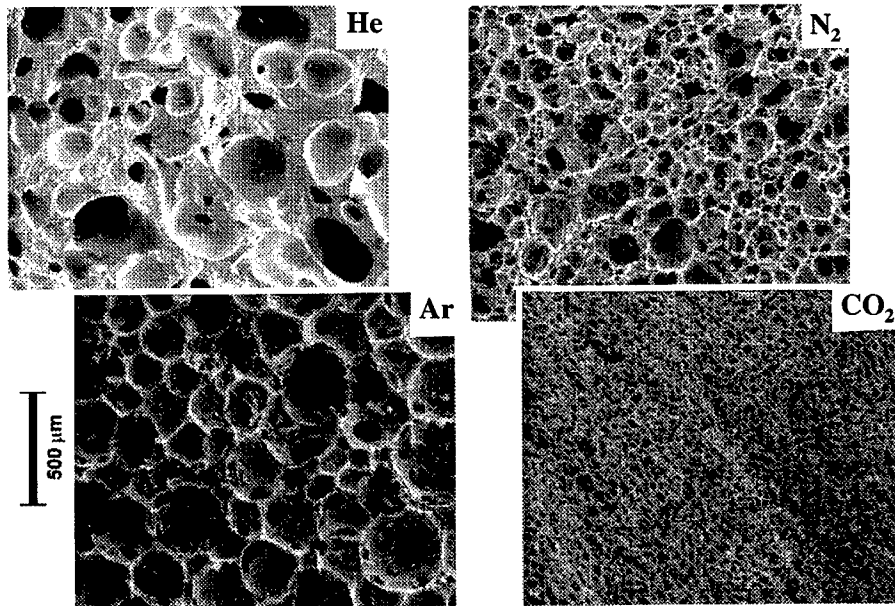


Figure 2. Typical SEMs of foam samples by blowing gas produced at the lower temperature, short hold duration, and higher pressures.

Typical SEMs of the foams are shown in Figure 2. Most notable is the closed-cell structure of the helium foam. The cell sizes are plotted as functions of processing parameters in Figure 3 except for the argon foams. Data have not yet been collected for the argon foams but a cursory examination indicate they are slightly larger than the corresponding nitrogen foam cells.

The cells of the helium blown foams appear much larger than those formed from nitrogen blowing. This is consistent with the explanation of the gas in the pitch either blowing a foam with coalesced bubbles or escapes. The amount of gas in any given final bubble will be dependent on how much coalescence occurs; helium should be subject to the most coalescence. Also when expanding, the helium can escape easier, because of its small size leaving closed cells. Since argon is larger than He or N<sub>2</sub>, it cannot easily escape and so it continues to expand the pitch longer. This also is indicated by the overall higher porosity of the argon foam.

#### Interactive Gas (CO<sub>2</sub>)

Initial gas pressure was not included in the CO<sub>2</sub> foam study, because there was insufficient pressure to achieve the highest final pressure. Therefore, an initial pressure was chosen to give the desired final pressure. The major observation from the CO<sub>2</sub> foams is the very small cell sizes at the lower temperature (largest change for all the gases). This also corresponds to a significantly larger volume expansion as well. The SEM of Figure 2 also shows the very small cell size of the carbon dioxide foams compared to the other gases at lower processing temperatures. Whether these results are from an increased amount of gas initially available at the higher temperature or the lower pitch viscosity is not known. The pressure effect is also opposite from what was expected from the noninteractive gases (higher pressure gave less expansion).

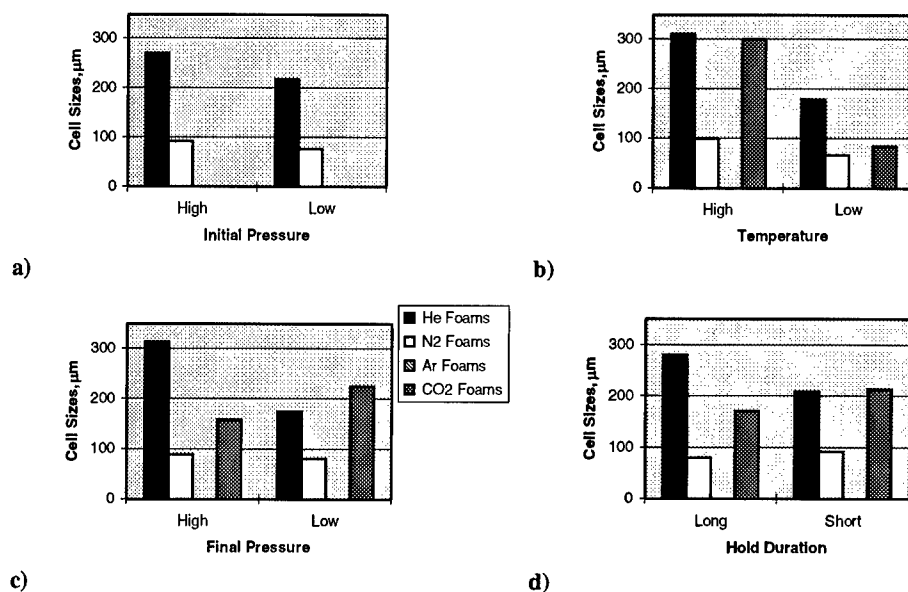


Figure 3. Average foam cell size for a) initial pressure, b) final temperature, c) final pressure, and d) hold time.

## CONCLUSIONS

The helium molecule being very small produces a closed-cell structure possibly due to its ability to escape the pitch more rapidly than the other gases. The larger argon molecules expand the pitch more and produce larger, more open cells than nitrogen. The higher temperature gives more expansion probably from the lower pitch viscosity. More expansion occurs at higher pressure probably due to more gas being available to expand the pitch. The CO<sub>2</sub> foams cannot be easily explained in the same fashion and need to be studied in more detail. Further efforts will concentrate on determining the mechanism in which these foams are being produced

## ACKNOWLEDGEMENTS

This work was partially supported by the U. S. Air Force under Contract Number F33615-95-D-5029.

## REFERENCES

1. R. B. Hall and J.W. Hager, 21<sup>st</sup> Biennial Conference on Carbon Extended Abstracts, 100 (1993).
2. J. S. Colton and N. P. Suh, *Polymer Engineering and Science*, **27** (7) 485 (1987); **27** (7) 493 (1987); **27** (7) 500 (1987).
3. D. Dutta, C. S. Hill and D. P. Anderson in *Novel Forms of Carbon II* edited by C. L. Renschler, D. M. Cox, J. J. Pouch, and Y. Achiba (Mater. Res. Soc. Proc. **349**, San Francisco, CA, 1994) pp. 61-66.

## STEEL AND TITANIUM HOLLOW SPHERE FOAMS

K.M. HURYSZ\*, J.L. CLARK\*, A. R. NAGEL\*, C.U. HARDWICKE\*\*, K.J. LEE\*,  
J.K. COCHRAN\*, T.H. SANDERS, JR.\*

\*Georgia Institute of Technology, Materials Science and Engineering, Atlanta, GA 30332-0245

\*\* Physical Metallurgy Laboratory, General Electric Corporation, Schenectady, NY 12301

### ABSTRACT

Metal hollow sphere foams are fabricated by bonding millimeter sized metal alloy hollow spheres at points of contact. The spheres are formed as powder shells from slurries. For stainless steel spheres, the starting powder is a mixture of iron and chromium oxide. Thermal treatment in hydrogen reduces the oxides to Fe/Cr alloys with less than 2% porosity in sphere walls. The nominal composition is close to that of 405 stainless. Carburization in CO/CO<sub>2</sub> atmosphere followed by heat treatment produces foams of either 410 or 420 type stainless steels depending on carbon content. Compressive stress-strain behavior was measured on point contact bonded stainless foams both before and after carburization. Hardness measurements on steel sphere walls were used to estimate the yield strength. Relative strengths of the foams were positioned between open and closed cell models. This was encouraging because bonding in the foams was less than optimum and the hollow sphere walls contained defects. As processing improves, strengths should increase. To produce titanium alloy spheres, the starting powder is titanium alloy hydride. Thermal treatment in an inert atmosphere decomposes the hydride and sinters the titanium powder in the sphere walls to greater than 96% relative density. Both titanium and Ti-6V-4V spheres and foams have been produced. Oxygen contents are a concern for titanium compositions and processing is being altered to reduce oxygen levels to increase ductility.

### INTRODUCTION

This paper concentrates on processing of steel and titanium foams as potential high strength structures. They are discussed in two separate sections because thermochemical processing of the two are considerably different. Interest is growing in the development of economical, low density, high strength metal foams. In both the aerospace and automotive industries, the need for both weight and cost reduction without compromising quality has become a dominant driver. Foams for stiffening, energy absorption, and foam core construction are increasing in use. However, current foams have limitations based on both thermal and mechanical considerations. For foams which have acceptable properties, significant density reductions are desired without sacrificing properties. In automotive applications which require energy absorption, polymer foams are the currently the only apparent economical alternative. The superior properties of metals would enhance foam properties and create new uses if economical metal foams were available. For next generation foams, the designer must achieve more mass efficient foam architectures and the maximum material properties allowed by foam processing.

#### Mechanics of Foams

The two basic architectures used to describe foams; open cell and closed cell, result in characteristic thermal and mechanical behavior. In open cell foams, the porosity is continuous and material resides in pore interstices forming a strut-like structure. The material in closed cell foams is located in the cell walls. Gibson and Ashby [1] derived the relation for foam elastic modulus as:

$$E^*/E_s \propto G^*/G_s \propto C_1 \phi^2 (\rho^*/\rho_s)^2 + C_2 (1-\phi) (\rho^*/\rho_s) \quad (1)$$

where  $E^*$  and  $E_s$  are the Young's Modulus of the foam and bulk solid, respectively,  $G^*$  and  $G_s$  are the shear modulus of the foam and bulk solid, respectively,  $\rho^*$  and  $\rho_s$  are the density of the foam and the solid, respectively, and  $\phi$  is the volume fraction of the solid residing in cell edges. For a pure open cell foam,  $\phi$  is unity because no material is present in the cell wall. The elastic constants for open cell foams are modeled to be proportional to relative density squared and  $C_1$  is close to unity [1] so that modulus of open cell structures is,

$$E^* = E_s(\rho^*/\rho_s)^2 \quad (2)$$

If all of the material is distributed in the cell faces, as in an ideal closed cell foam,  $\phi = 0$  and the elastic constants are linearly related to the density. Values for the closed cell constant  $C_2$  for upper limit modulus are 0.5 for the Hashin limit [2] and 0.35 for the Kelvin solid [3]. Thus, closed cell foam modulus may be as high as,

$$E^* = 0.5 E_s (\rho^*/\rho_s) \quad (3)$$

For tensile and compressive strengths of foams, Gibson and Ashby [1] also derived an equation for the ultimate strength of brittle foams and the yield strength of plastic foams,

$$\sigma^*/\sigma_s = C_3\phi(\rho^*/\rho_s)^{3/2} + C_4(1-\phi)(\rho^*/\rho_s) \quad (4)$$

where  $\sigma$  is strength,  $C_3$  is 0.3 [1] and  $C_4$  is 0.35 [4]. The strength of open cell structures is,

$$\sigma^* = 0.3 \sigma_s (\rho^*/\rho_s)^{3/2} \quad (5)$$

while that for a closed cell foam has the form,

$$\sigma^* = 0.35 \sigma_s (\rho^*/\rho_s) \quad (6)$$

Obviously, at the same density, closed cell foams are projected to be stronger and stiffer than open cell structures by factors of 5 and 7, respectively, at 6% density and a factor of 2.5 at 20% density. However, the properties of the solid in the foam are as critical as the architecture because it is not unusual for solid properties of the foam material to be lower than expected for engineering metals by a considerable factor due to processing related defects or composition limitations. For example, the solid yield stress,  $\sigma_s$ , for aluminum/5%calcium in *ALPORAS* foam from Shinko Wire was estimated from hardness to be 130 MPa [4] and that of an Al(Si) subeutectic alloy in *ALULIGHT* foam from Fraunhofer was 250 MPa [4]. Producing solid yield strengths in the 400-500 MPa range typical of an engineering aluminum would improve foam strengths as much as would maximizing morphological perfection.

Ultimately, in designing with foams, a desired stiffness will be specified at a minimum density. When steel and titanium are considered, analyses such those presented in Figure 1 emphasize the need to develop foams from higher strength alloys. Figure 1 was constructed by assuming  $\sigma_s$  midrange values of 1575 MPa for stainless steel, 864 MPa for Ti-6Al-4V, and 385 MPa for aluminum. These values were selected as ones that should be achievable in foam structures. These plots were constructed from 5 to 50% relative density for each alloy. The

obvious conclusion is that at a particular density, steel and titanium should achieve higher strengths assuming foams can be manufactured at a sufficiently low density. When stiffness is considered, foam architecture becomes more important than material because the specific stiffness of the engineering metals are so similar, Figure 2, and the importance of producing a closed cell structure is amplified. These conclusions provide the basis for developing steel and titanium hollow sphere foams. It is assumed that the point contact bonded hollow sphere structure is a quasi-closed cell structure with properties conforming to the closed cell models.

### Hollow Sphere Technology

A process has been developed that forms uniform thin-wall hollow spheres and after sintering, they can be bonded at points of contact into foams. This technology was originally developed for the formation of ceramic structures [5,6] and is now being applied to metals using brittle powder precursors which can subsequently be converted to alloys. Monosized ( $\pm 4\%$ ) thin-walled spherical shells are formed when slurries containing constituent powders and polymer dispersants are injected through the outer jet of a coaxial nozzle. As illustrated in Figure 3, gas passing through an inner jet forms bubbles [7]. Sphere diameter can be varied between 1 and 6 mm through the control of process parameters. Wall thickness is typically 100  $\mu\text{m}$  and can be varied from  $\sim 40$  to 200  $\mu\text{m}$ . Slurry exits the nozzle in the form of a hollow cylinder that closes due to surface tension and hydrostatic forces, forming a hollow sphere. The sphere hardens in flight as the liquid component of the slurry evaporates. If high vapor pressure liquid, ie. acetone, is used, evaporation is rapid. Dry, polymer-bonded powder shells with reasonable handling strength result. After forming, the spheres are sintered to densify and further strengthen the walls. The process forms spheres at rates of 3,000 to 15,000 spheres/min with typical production rates of 2 to 7 kg/hr from a single nozzle. Ceramic hollow sphere foams have been fabricated with density as low as 5% of theoretical.

### STAINLESS STEEL FOAMS

The objective of this work was to demonstrate that it is feasible to fabricate stainless steel hollow sphere foams and characterize initial mechanical properties of these foams. Iron and chromium oxide powders were batched as 88.2 wt.%  $\text{Fe}_2\text{O}_3$  and 11.8 wt.%  $\text{Cr}_2\text{O}_3$  so that upon reduction, an 88%Fe/12%Cr stainless steel alloy would result. This is the composition of AISI

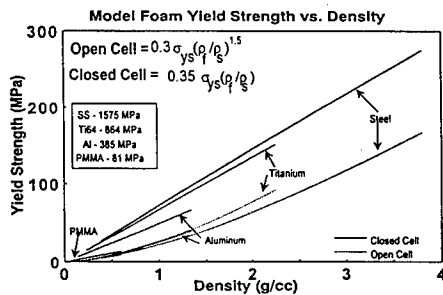


Figure 1. Projected Yield Strengths For Open and Closed Cell Foams from Engineering Alloys.

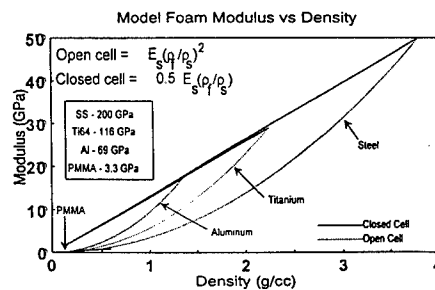


Figure 2. Projected Stiffness For Open and Closed Cell Foams from Engineering Alloys.

410 and 420 stainless steels, without considering carbon or trace alloying elements such as Al and Si. If the foams are carburized to the correct levels and properly heat treated, bulk properties similar to these steels should result. This composition without carbon is also similar to AISI 405 stainless steel except for minor impurities.

#### Experimental Procedure

Typically, powders with average particle size of ~3-5  $\mu\text{m}$  are needed to produce slurries with the required rheology for hollow sphere fabrication. Using  $\text{Fe}_2\text{O}_3$  and  $\text{Cr}_2\text{O}_3$  powders in this particle size range, hollow spheres were formed from acetone based slurries dispersed with low molecular weight poly-methylmethacrylate (PMMA) as the dispersant and binder. The as-formed (green) oxide hollow spheres were reduced in hydrogen at one atmosphere at 1300°C for 6, 12, 15, and 24 hours. In one method of processing, prior to reduction, the "green" oxide spheres were fired in air at 1350°C to increase sphere strength for ease of handling. A more detailed description of the fabrication of stainless steel hollow spheres has been reported by A. Nagel, et al. [8,9]

Foam structures were formed by two methods. In the first method, no bond phase was added and loose beds of green or air-fired oxide spheres were reduced with hydrogen at 1300°C in alumina crucibles 3.75 cm in height and 2.5 cm in diameter. Diffusion bonds formed between the point contacts of spheres thus forming foam structures. In the second method, larger foam structures approximately 10 cm long and 6 cm in diameter were also constructed using a bond phase. Air fired oxide spheres were lightly coated with an aqueous bonding slurry of  $\text{Fe}_2\text{O}_3$  and  $\text{Cr}_2\text{O}_3$  powders employing an organic binder. The spheres were then packed into a mold and air dried. The bonding slurry formed bond fillets at the points of contact between spheres. The bonded oxide foam was reduced in hydrogen.

The metallic foams were carburized using mixtures of CO and  $\text{CO}_2$  at 1000°C and forced air cooled from the carburization temperature using a high velocity fan. They were subsequently sub-zero cooled in liquid nitrogen and annealed at 250°C for 1 hour in air.

Microhardness was evaluated with indents in sphere wall cross sections using a LECO 400F microhardness tester. Stress/strain behavior of bonded foam, right circular cylinders 1.6 cm in diameter by 2.0 cm in length was tested under compression using a screw test frame with a 5000 lb. load limit. Sample ends were cut parallel with a diamond blade. The sectioned end pieces were mounted and polished to examine the microstructure and measure microhardness.

#### Microstructure of 88%Fe-12%Cr Foams from Direct Oxide Reduction

The oxide foams were reduced completely in flowing hydrogen at 1350°C at all times. Porosity and grain size measured on the cross sections of spheres reduced for 24 hours indicated porosity to be less than 2% and an average grain size of approximately 60  $\mu\text{m}$ , typically 30-50% of the sphere wall thickness. After six hours of reduction, porosity in the 12-14% range was present in sphere walls, Figure 3. For foams bonded by reducing loose beds of green spheres, sphere/sphere diffusion bonds with contact diameters of 100-200  $\mu\text{m}$  were formed, Figure 4. However, the number of bonds per sphere was significantly less than for foams formed with a slurry bond phase. In diffusion bonded cases, approximately 50% of the closely adjacent spheres were not bonded whereas using slurry bonding, even relatively large sphere to sphere gaps were spanned. For slurry bonding, the average number of bonds per sphere would be equal to the coordination number of ~7.5 for random beds of monosized spheres

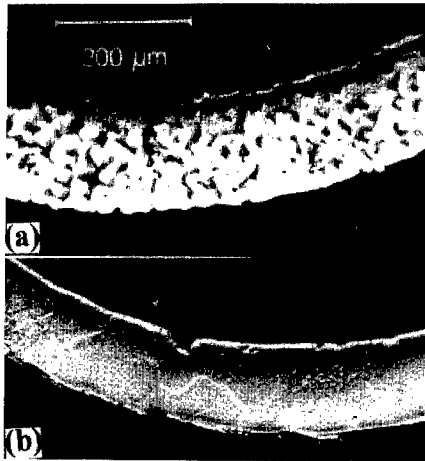


Figure 3. Microstructure of  $\text{Fe}_{0.88}\text{Cr}_{0.12}$  Sphere Walls Reduced in  $\text{H}_2$  (a) 6 hours and (b) 24 hours.



Figure 4. Point Contact Diffusion Bonds between  $\text{Fe}_{0.88}\text{Cr}_{0.12}$  Spheres Reduced in  $\text{H}_2$  for 24 hours.

#### Carburization of Stainless Steel Foams

Steel hollow spheres reduced for 12 hours were carburized for 30 minutes at  $1000^\circ\text{C}$  using ten different ratios of  $\text{CO}$  to  $\text{CO}_2$  ranging from 0.34 to infinity. For spheres not carburized, a hardness of  $\sim 100$  Hv was obtained and at higher  $P_{\text{CO}}/P_{\text{CO}_2}$  ratios, Vickers hardness as high as 625 was measured. The microstructure of the carburized foams were martensitic and this structure was found in all spheres with hardness over 400 Hv.

#### Mechanical Testing of Foams

A set of diffusion bonded foam cylinders (no bond phase added) was reduced for 12 hours. The density of the three foams varied from 13 to 20% relative density. This group of foams was not carburized and the average hardness of the sphere walls was approximately 100 Hv. During compressive loading of the non-carburized, the deformation appeared to be uniformly distributed across the length of the cylinder. Planar buckling did not occur. Photographs of a foam prior to loading and after compressively straining to 70% are shown in Figure 5. Compressive engineering stress-strain curves for the three foams in this group are shown in Figure 6. The stress-strain test for the 19% foam was stopped manually and was not due to foam failure.

The engineering stress-strain curve of a carburized foam was also measured, Figure 7. The hardness of this foam was approximately 625 Hv. From visual observation, the behavior of this foam under compression varied greatly from the non-carburized foams. The initial foam was a tapered cylinder, unlike the non-carburized foams. When the foam was compressed, individual spheres were observed to eject from the sides due to insufficient bonding and the foam appeared to fail at the larger diameter end. A maximum compressive strength of 5000 psi was measured.

The engineering stress-strain data were used to compare the measured properties of the foams to theoretical predictions, Figure 8. Relative strength of closed cell foams is calculated from Equation [6], upper line Figure 8, and that of open cell foams is calculated from Equation [5], lower line. In the case of the non-carburized foams, the properties of 405 stainless can be

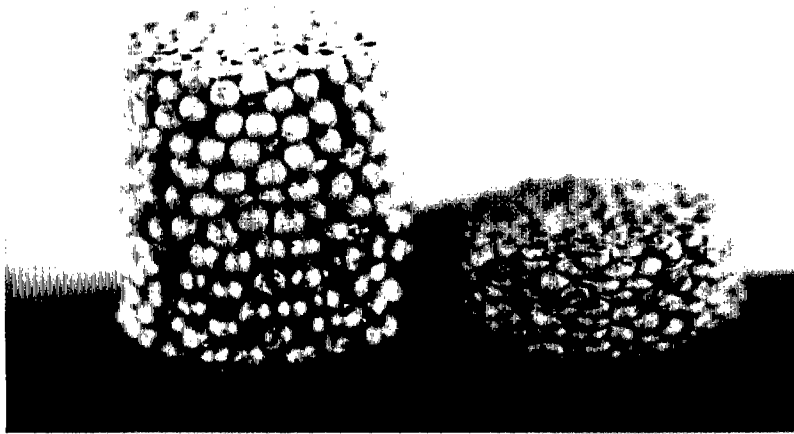


Figure 5. Non-Carburized  $Fe_{0.88}Cr_{0.12}$  Foams Before and After 70% Compressive Deformation.

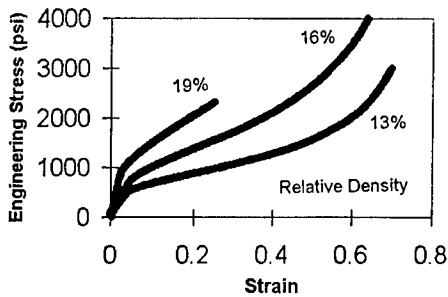


Figure 6. Compressive Engineering Stress-Strain Curves for Non-carburized  $Fe_{0.88}Cr_{0.12}$  Foams.

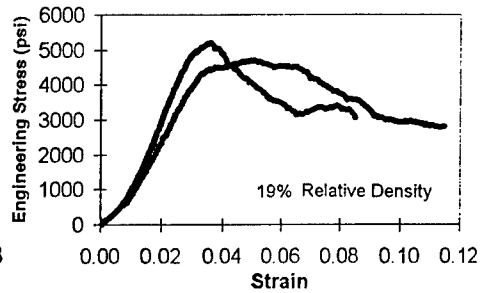


Figure 7. Engineering Stress-Strain Curve of  $Fe_{0.88}Cr_{0.12}$  Carburized Foams.

used as a reference. A yield value of 40 ksi, reported for annealed 405 stainless steel of 81 HRB (150 Hv) [10], was used to calculate the relative yield strength of the three non-carburized foams, solid black triangles, Figure 8. Yield stresses for the non-carburized steel foams,  $\sigma^*$ , were 600, 800, and 950 psi for the 13%, 16%, and 19% relative density foams, respectively. The ultimate tensile strength of 420 stainless steel in a quenched and lightly annealed (250°C) state is 190-220 ksi,  $\sigma_{ts}$  [10]. The solid black square is the relative failure strength of the carburized foam using 190 ksi for  $\sigma_{ts}$  and 5100 psi for  $\sigma^*$ . These relative strengths of the hollow sphere stainless steel foams are close to the projections for open cell foams. However, the measured microhardness of the non-carburized foams was approximately 100 Hv. This suggests that the properties of the foam wall material are less than that of 405 stainless steel. The open triangles, Figure 8, assume a bulk yield stress of 30 ksi for  $\sigma_s$  based on the lower hardness values. Also, the carburized foam

failed at the larger diameter end. The diameter at this end was 10% larger than the average diameter of the foam and a corrected relative density for the carburized foam was calculated to be 16%. This point is represented by the open square. Based on this analysis, the relative strength of the hollow sphere foams are midway between projections for open and closed cell foams.

Examination of the microstructure of all four foams showed a large degree of porosity. In the case of the carburized foam, there appeared to be interconnecting porosity. This porosity resulted in a reduced cross sectional area and thus lower measured properties. It is also likely that poor bonding between spheres in the foams compromised strength of all the foams and in the case of the carburized sample, the loss of individual sphere under loading confirms this. These first metallic foams constructed of hollow stainless steel spheres are promising. The assumptions used for bulk values show that the foams exceeded the predicted properties of open celled foams and may be closer to closed cell character than projected here due to porosity effects.

#### Scale-Up of Stainless Steel Foams

The success of producing small size stainless steel hollow sphere foams resulted in efforts to scale-up to larger size foams. In this stage, firing of iron/chromium oxide structures in hydrogen resulted in cracking of the foam structure. The large volume changes associated with the reduction process may be the cause of the cracking. To test this hypothesis, expansion as a function of temperature was determined using a dilatometer. Atmospheres of hydrogen, argon, and air were used to study the expansion of powder samples during firing. This measured the extent of expansion, determined the temperature range of major size changes, and the effect of atmosphere and firing profile on the expansion. The most desirable result of the analysis would be to determine the appropriate atmosphere and firing profile that would eliminate the expansion of the samples altogether.

Dilatometer studies were conducted on  $\text{Fe}_2\text{O}_3$ ,  $\text{Cr}_2\text{O}_3$ , and  $88\text{Fe}_2\text{O}_3/12\text{Cr}_2\text{O}_3$  powders that were pressed into pellets of approximately 6 mm in thickness. The samples were heated in the dilatometer to  $1450^\circ\text{C}$  at  $2^\circ\text{C}/\text{min}$  in an atmosphere of  $4\%\text{H}_2/\text{Ar}$ . The resultant traces, Figure 9, show that  $\text{Fe}_2\text{O}_3$  undergoes ~7% linear expansion early in the firing process at around  $400\text{-}600^\circ\text{C}$ . Other traces were made of the  $88\text{Fe}_2\text{O}_3/12\text{Cr}_2\text{O}_3$  mix in air and argon and no expansion resulted in either air or argon below  $900^\circ\text{C}$ . Thus, it was concluded that the expansion is due to intermediate phases produced in the reduction of  $\text{Fe}_2\text{O}_3$  to Fe. Specifically, the hydrogen in the reducing atmosphere reacts to create one or more of the reaction paths outlined below.

	% Vol. Change	% Lin. Change
$\text{Fe}_2\text{O}_3 + 3\text{H}_2 \rightarrow 2\text{Fe} + 3\text{H}_2\text{O}$	-34	-11
$3\text{Fe}_2\text{O}_3 + \text{H}_2 \rightarrow 2\text{Fe}_3\text{O}_4 + \text{H}_2\text{O}$	1	0.3
$\text{Fe}_3\text{O}_4 + \text{H}_2 \rightarrow 3\text{FeO} + \text{H}_2\text{O}$	-9	-3
$\text{FeO} + \text{H}_2 \rightarrow \text{Fe} + \text{H}_2\text{O}$	-27	-9
$\text{Fe}_2\text{O}_3 + \text{H}_2 \rightarrow \text{Fe}(\text{OH})_2 + \text{FeO}$	23	7.7
$\text{Fe}(\text{OH})_2 \rightarrow \text{FeO} + \text{H}_2$	-40	-13

For each reaction, an associated volume change was calculated from reactant and product densities. By comparing calculated linear change and the experimental linear change the deleterious reaction path was tentatively identified as formation of an iron hydroxide intermediary.

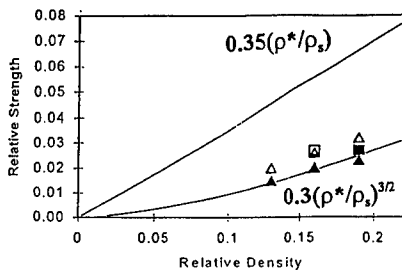


Figure 8. Relative Strength of  $\text{Fe}_{0.88}\text{Cr}_{0.12}$  Hollow Sphere Foams Compared to Open/Closed Cell Models

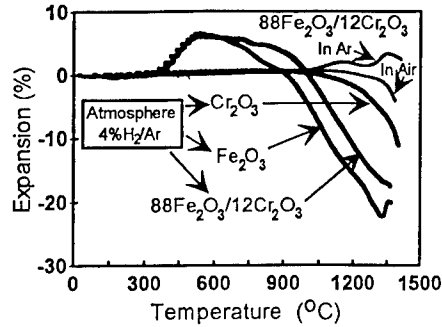


Figure 9. Dilatometric Analysis of Iron and Chromium Oxide in Hydrogen, Argon, and Air.

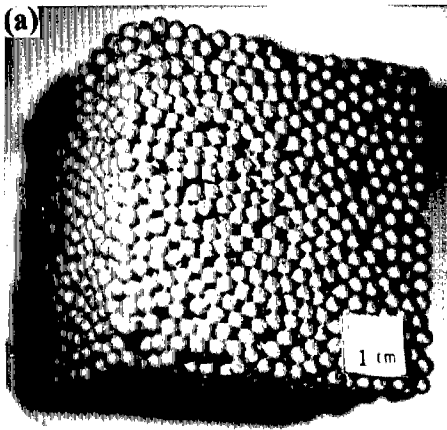


Figure 10. Hollow Sphere,  $\text{Fe}_{0.88}\text{Cr}_{0.12}\text{O}_{1.5}$ , Foam Cube Sintered at  $1350^\circ\text{C}$ , (a) Edge Length of 5 cm and (b) Point Contact Bonds.

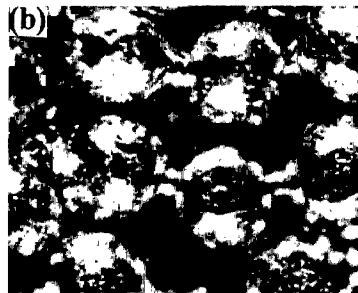
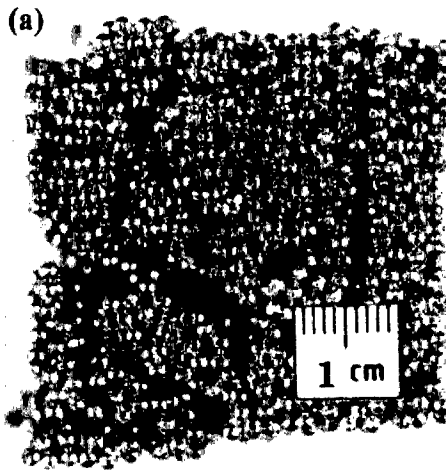


Figure 11. Stainless Steel Hollow Sphere Foam,  $\text{Fe}_{0.88}\text{Cr}_{0.12}$ , (a) Edge Length = 3.5 cm, Density = 1.5 g/cc, (b) Point Contact Bonds.

To test this, the  $88\text{Fe}_2\text{O}_3/12\text{Cr}_2\text{O}_3$  mix was held at  $550^\circ\text{C}$  in  $\text{H}_2$  for one hour, cooled to room temperature. XRD was unable to confirm these compounds and the expansion reaction has not been identified.

However, as can be seen by comparing the bonded oxide foam in Figure. 10 with the reduced stainless steel foam in Figure. 11, the low temperature cracking is in qualitative agreement with the 7% expansion from the hydroxide. If hydroxide cracking can be eliminated, successful fabrication of large size steel foams should follow. If the reaction could be suppressed, the expansion would not occur and cracking would not follow. This may be achieved by introducing hydrogen later in the firing process. At this point another reaction path would be more favorable and no hydroxide phase would be produced. If the reaction could not be suppressed, the firing profile may be adjusted by slow heating such that the expansion would be uniform throughout. Thus, stresses would be minimized between the internal and external structures eliminating cracks. Both approaches are being investigated.

## TITANIUM HOLLOW SPHERES

Titanium hydride hollow spheres fabricated from  $\text{TiH}_2$  powders are heat treated to decompose the hydride and sinter the titanium in the shell wall to high density. Early in this program, Ti-6Al-4V foams were fabricated from Ti-6Al-4V hydride [11]. These foams were brittle due to the combined effect of aluminum and interstitial oxygen impurities reducing ductility. To improve ductility, processing has been altered to reduce oxygen pickup and composition has been changed to pure Ti, which is more oxygen tolerant, by fabricating balloons from  $\text{TiH}_2$  rather than the hydride Ti-6Al-4V alloy. For acetone slurries containing Ti-6Al-4V hydride, poly-methyl methacrylate (PMMA) was used as the dispersant to produce low viscosity at relatively high solids contents. When acetone slurries of  $\text{TiH}_2$  were prepared, PMMA did not provide dispersion. A polyester/polyamine copolymer (PS3 from ICI) was identified which provided good dispersion and was shown to operate with an electrosteric stabilization mechanism [12, 13]. Unfortunately, although PS3 provided good dispersion, it was shown to produce significant changes in drying behavior such that free falling slurry shells collapsed on landing or were distorted with dimples, indents, and excessive holes. Silane coupling agents were identified as a possible dispersant with might not alter drying rates. Thus, rheological, electrophoretic mobility, and drying studies were conducted on  $\text{TiH}_2$  acetone slurries dispersed with silane coupling agents. This is reported below.

### Experimental Procedure

In this investigation, titanium hydride powder was dry ball milled in hermetic polyethylene jars with steel balls for 64 hours to produce powders with a 1-10  $\mu\text{m}$  diameter particle size range and a 6  $\mu\text{m}$  average particle size. The containers were backfilled with argon before milling to reduce powder exposure to contaminant gases such as oxygen and nitrogen.

Titanium hydride powder to be treated with the coupling agent was mixed with a 5% solution of Dow Corning 6020 polysilane (ethylene diaminepropyl trimethoxysilane) in methanol to provide a concentration of 0.25 to 1.00 weight % silane based on powder weight. Hydride slurries were prepared by dissolving polymeric dispersants and binders in acetone and subsequently adding the powder. Elvacite 2008 and 2041 grade PMMA and PS3, supplied by ICI, Inc., were used as dispersants and binders. Each dispersion was milled overnight to ensure thorough mixing and deagglomeration. Slurry viscosity was measured using a Brookfield LV type viscometer. Zeta potential was evaluated with a Coulter 440SX electrophoretic mobility unit.

### Slurry Rheology and Stability

The suitability of slurry for use in the hollow sphere foam technique is dictated by the solids loading and degree of dispersion, the influence of polymer additives on the evaporation of acetone from the formed spheres, and the minimization of impurities soluble in the metal lattice that serve to embrittle the foam. Poorly dispersed slurries will not process smoothly and those containing excess acetone do not have enough time to dry. The rheology effect of the three dispersants tested here on  $TiH_2$ /acetone slurries, Figure 12, shows high viscosity at low solids content when using PMMA only as the dispersant. Thus, PMMA did not provide dispersion but it is added as the binder and adverse interactions between the dispersant and PMMA are to be avoided. Addition of PS3 copolymer or 6020 silane provided good dispersion with viscosities of  $\sim 100$  mPa.sec for a solids content in the 48-50 v/o. Differences in the effect of PS3 and 6020 may be due to differences in  $TiH_2$  particle size.

Zeta potential measurements of titanium hydride with several dispersing agents in acetone, Figure 13, provided some understanding.  $TiH_2$  had a large negative surface charge in pure acetone (-110 mV). When PMMA was added, the potential remained negative but decreased to less than -10 mV at PMMA concentrations needed to serve as a binder. Dispersion of  $TiH_2$  with PS3 was maximized at 1.0 wt% polymer and generally exhibited a more negative zeta potential than PMMA. It is believed the larger absolute charge provided by PS3, even in the presence of PMMA, is sufficient to provide an electrostatic dispersion component which when combined with steric stabilization resulted in stable dispersions due to electrosteric stabilization.

Silane treatment chemisorbs as a monolayer on surfaces and in the case of  $TiH_2$ , silane adsorption provided reversal in surface charge from negative to positive due to the amine component of the silane. At 1 w/o silane, PMMA addition reduced the potential to the +20 mV range but this was sufficient to provide stable dispersion with silane /PMMA combinations. Zeta potentials are measured at low solids loading ( $\sim 0.1$  w/o) and at 0.25 w/o silane, PMMA apparently competes with silane for the  $TiH_2$  surface and reverses the surface charge to negative. At the high solids loading of hollow sphere slurries, adequate dispersion of  $TiH_2$  slurry treated with 0.25 and 1.00 wt% silane was achieved at both half-monolayer (1.88 wt%) and monolayer (3.75 wt%) coverage with PMMA. PMMA is known to similarly disperse  $Al_2O_3$ ,  $ZrO_2$ , and  $TiO_2$ , each having a positive surface charge in acetone and to not disperse  $SiO_2$  which has a negatively charged surface. Thus, with the silane induced charge reversal, PMMA is expected to have an adsorption isotherm similar to adsorption on other positive surfaces. This will have to be confirmed.

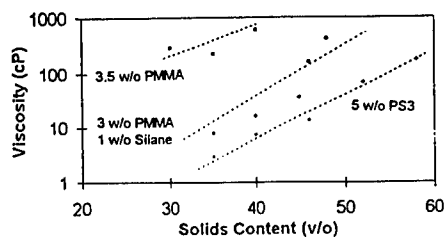


Figure 12. Dependence of  $TiH_2$ / Acetone Slurry Viscosity on Binder and Dispersant Additives.

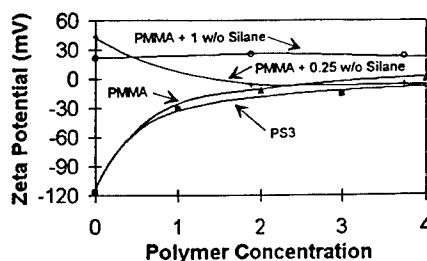


Figure 13. Zeta Potential of  $TiH_2$  in Acetone Modified with Dispersing Agents.

A negative surface charge is expected on  $TiH_2$  powder is since hydrogen vacancies exist in titanium hydride and the reported surface potentials measured for  $H_2$  chemisorbed on the transition metals are all negative [14]. This is confirmed by the inability of anionic surfactants to stabilize titanium hydride slurries as well as negative zeta potential measurements.

#### Evaporation Behavior of Titanium Hydride Slurries

Acetone evaporation rate were measure as a function of time for 35 v/o  $TiH_2$ /acetone slurries with additions of combinations of PMMA, PS3, and 6020 Silane, Figure 14. It is possible to theorize why slurries prepared with PS3 do not harden rapidly into rigid shells like those prepared with PMMA or PMMA with silane dispersion. When the curves are extrapolated to zero time, during the critical initial drying stage, acetone is evaporating from the slurry dispersed with PS3 at rates approaching that of pure acetone. For the slurries containing solely PMMA and PMMA with the aminosilane coupling agent, a significantly lower evaporation rate is observed early in the process. This lower evaporation rate can be attributed to the rapid formation of a polymer skin. This skin becomes the rate limiting step to evaporation and slows the process enough to maintain a stiff, tack free PMMA stabilizing surface. Slurries dispersed with PMMA thus require a longer total drying time but a stable, supporting polymer shell is maintained from early in the drying process until complete evaporation occurs. Addition of even small quantities of PS3 increases the initial evaporation rate significantly, is assumed to prevent a continuous PMMA shell that acts as a barrier to transport, and results in hollow sphere collapse on landing.

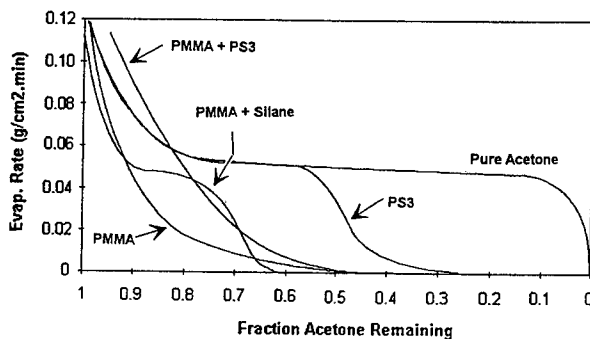


Figure 14. Acetone Evaporation Rates for 35 v/o  $TiH_2$ /Acetone Slurries with Additions of PMMA, PS3, and 6020 Silane.

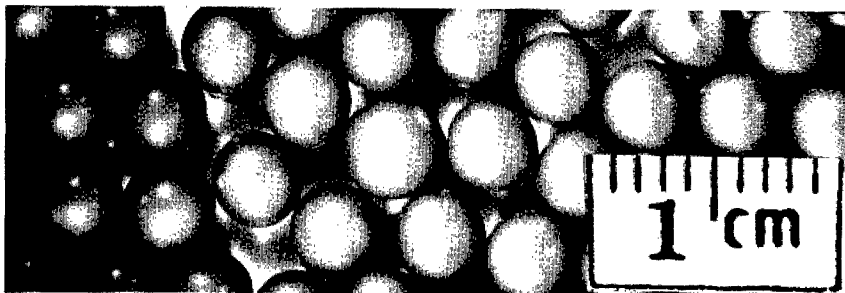


Figure 15.  $TiH_2$  Hollow Spheres Fabricated with Silane Dispersion in Acetone/PMMA Solution.

To demonstrate that silane dispersion of  $TiH_2$  is usable in hollow sphere formation, slurries have been prepared with  $TiH_2$  treated with 0.25 to 1.00 w/o silane and dispersed in acetone/PMMA solutions. The spheres formed well from the coaxial nozzle and drying in free flight was not noticeably different from slurries using only PMMA as the dispersant and binder. As can be seen in Figure. 15, as-formed  $TiH_2$  sphere surfaces were smooth and relatively defect free. Wall thickness for this batch of sphere was very good and density of the resulting sintered Ti shells was 1.0 g/cc. Foams fabricated from these spheres would have a bulk density of 0.65 g/cc or 14% relative density.

## CONCLUSIONS

Stainless steel hollow spheres have been fabricated from iron and chromium oxide powders and converted to dense Fe/Cr alloys by hydrogen reduction. The nominal composition is close to that of 405 stainless and carburization in CO/ $CO_2$  atmosphere followed by heat treatment produces foams of either 410 or 420 type stainless steels depending on carbon content. Compressive stress-strain behavior on point contact bonded stainless steel foams demonstrated that relative strengths of the foams were positioned between open and closed cell models. This was encouraging because bonding in the foams was less than optimum and the hollow sphere walls contained defects. As processing improves, strengths should increase. To produce titanium alloy spheres, the starting powder is titanium alloy hydride. Thermal treatment in an inert atmosphere decomposes the hydride and sinters the titanium powder in the sphere walls to greater than 96% relative density. Oxygen contents are a concern for titanium compositions and processing is being altered to reduce oxygen levels to increase ductility. Rheology and electrophoretic mobility studies demonstrated that polyaminosilane effectively disperses titanium hydride in acetone. The silane chemisorbs on the hydride reversing the surface charge from negative to positive and, even in the presence of poly-methylmethacrylate, provides sufficient charge to provide electrosteric stabilization. Unlike the polyester/polyamine dispersant, PS3, the silane coupling agent does not alter drying behavior of high solids content, acetone/PMMA based dispersions.

## ACKNOWLEDGMENTS

This work was supported by United Technologies Research Laboratories under Defense Advanced Research Projects Agency Contract N00014-96C-0400 and by the Office of Naval Research under Grant N00014-97-1-0492.

## REFERENCES

1. L. Gibson, M. Ashby, Cellular Solids: Structures and Properties, 2<sup>nd</sup> Ed., Cambridge University Press, Cambridge, UK, 1997.
2. Z. Hashin and S. Shtrikman, *J. Mech. Phys. Solids*, **11** (1963) 127-140.
3. A. Kraynik, *J. Appl. Mech.*, to be published.
4. Y. Sugimura, J. Meyer, M.Y. He, H. Bart-Smith, J. Grenstedt, A.G. Evans, "On the Mechanical Performance of Closed Cell Al Alloy Foams, *Acta Materialia*, **45**, (1997), 5245-5259.
5. L.B. Torobin, "Method for Making Hollow Porous Microspheres", U.S. Patent 4671909, 9 Jun 87.
6. J.K. Cochran, "Methods for Producing Fiber Reinforced Microspheres Made From Disperse Particle Compositions", U.S. Patent 4867931, 19 Sep 89.

- 
7. L. B. Torobin, "Hollow Microspheres Made From Dispersed Particle Compositions and Their Production", U.S. Patent 4777154, 11 Oct 88.
  8. A.R. Nagel, C. Uslu, K.J. Lee, J. K. Cochran, T. H. Sanders, "Steel Closed Cell Foams from Direct Oxide Reduction", Synthesis/Processing of Light Weight Metallic Materials II, Edited by Malcolm Ward-Close, TMS, Warrendale, PA, pp 395-406, September, 1997.
  9. A.R. Nagle, K.M. Hurysz, K.J. Lee, J. K. Cochran, and T.H. Sanders, "Closed Cell Steel Foams: Fabrication and Mechanical Testing", Metallurgical and Materials Transactions A, Submitted February 23, 1998.
  10. Stainless Steels, American Society for Metals, 1994.
  11. C.U. Hardwicke, K.J. Lee, T.H. Sanders, J. K. Cochran, "Ti-6Al-4V Hollow Sphere Foams", Proceedings of Synthesis of Light Weight Metallic Materials, II, Edited by Malcolm Ward-Close, TMS, Warrendale, PA, pp 289-300, Feb. 1997
  12. C.U. Hardwicke, J.K. Cochran, and T.H. Sanders, "Rheological Properties of Concentrated, Nonaqueous Titanium Hydride Suspensions", Colloids and Surfaces A: Physicochemical and Engineering Aspects, Submitted, February 19, 1998
  13. C.U. Hardwicke, "Processing and Properties of Ti-6Al-4V Hollow Sphere Foams From Hydride Powder", PhD Dissertation, Georgia Institute of Technology, Atlanta, GA, August, 1997.
  14. W. M. Mueller, "Titanium Hydrides", in Metal Hydrides, W. M. Mueller, J. P. Blackledge and G. G. Libowitz (ed.), Academic Press, 336-382, 1968.

## NOVEL HOLLOW POWDER POROUS STRUCTURES

David J. Sypeck, Phillip A. Parrish and Haydn N.G. Wadley  
University of Virginia, School of Engineering and Applied Science, Department of Materials  
Science and Engineering, Charlottesville, VA 22903

### ABSTRACT

Recent finite element calculations [1] indicate that structures constructed from partially compacted hollow spheres exhibit a greater stiffness and strength than many other cellular structures at comparable density. It has been observed that gas atomization of metallic powders often leads to entrapment of the flow field gas [2]. The resulting hollow powders are an unwanted by-product in the sense that they lead to porosity and future sites of defect in solid parts. Here a method is developed to separate the hollow powders according to their size, shape and density. They are then consolidated to a porous structure. Examples of this are given for both a titanium alloy and a nickel-base superalloy. The compressive mechanical properties are measured and compared to those of other porous structures.

### INTRODUCTION

Porous structures based upon hollow metallic spheres with thin walls, strong interparticle bonds and a close packed arrangement [3] are a new class of cellular materials whose modulus and strength are predicted to exceed those of many other cellular materials [1]. As load bearing structures, their cell geometry is attractive in the sense that each cell can be of uniform size, shape, wall thickness and ligament with those adjacent. This morphology contrasts sharply with that of many cellular solids where cells are abnormally shaped, cell walls can be curved or broken and excess material aggregates at nodes. A group of cells with high aspect ratios then work collectively to cause large localized deformations which propagate and lead to a significant knockdown in weight specific mechanical properties [4]. The cell shapes of the hollow sphere structures on the other hand, resist bending and buckling, and are responsible for the greater predicted stiffnesses and strengths compared with many other cellular structures of comparable density. Furthermore, controllable amounts of open and closed porosity can be achieved creating multifunction opportunities for this class of materials.

Researchers have demonstrated methods for producing hollow metallic shells using double wall capillary apparatus [5]. Variants of the method for the casting of ceramic slurries are under development [6]. However, these double wall capillary methods are limited to comparatively large diameter shells owing to difficulties in the machining of small capillary tubes and maintaining them unobstructed. Furthermore, selection of materials for parts in contact (e.g. capillary tubes, crucible, etc.) with the molten shell material is problematic if reactive metals are involved (e.g. titanium alloys). Cleanliness can also be an issue especially when reducing an oxide slurry to create a metal sphere [6]. Processes currently envisioned may also be costly.

It has been observed that gas filled hollow powders are a common by-product of gas atomization [2]. During the atomization process, high velocity gas jets are used to break apart a thin stream of molten material into many small droplets which then rapidly solidify to a powder. The mechanism(s) by which hollow powders are formed remains controversial. One explanation envisions the molten material encircling, closing off and trapping the gas inside [2]. Consider a spherical liquid droplet in a uniform velocity gas flow. Bag formation occurs when the Weber number,  $We = \rho_{\infty} V_{\infty}^2 D_s / \sigma$ , is in the range  $12 < We \leq 50$  [7] where  $\rho_{\infty}$  and  $V_{\infty}$  are the density and velocity (relative to the droplet) of the gas flow,  $D_s$  and  $\sigma$  are the diameter and surface

tension of the drop. Suppose  $\sigma = 1480$  dyn/cm and  $\sigma = 1760$  dyn/cm for elemental Ti and Ni at their melting points [8],  $\rho_\infty = 1.78$  kg/m<sup>3</sup> for Ar at sea level [8] and  $D_s = 1$  mm. Then bag formation is anticipated when  $100 < V_\infty \leq 204$  m/s for Ti and  $109 < V_\infty \leq 222$  m/s for Ni. It is reasonable that these subsonic velocities could be seen by the drop in an atomization plume. This appears to be an important factor if one seeks to produce large numbers of gas atomized hollow powders rather than prevent them. In this paper we develop a method to separate the hollow powders from other gas atomization products, present a way to consolidate them to a porous structure, measure their compression behavior and compare these properties with other porous materials.

## SEPARATION THEORY

Sedimentation, elutriation and density gradient methods have all been used for separating powders according to their size, shape and density [9,10]. Such methods might be used to recover hollow metallic powders from other gas atomization products (e.g. solid powder, flake, etc.). Consider the levitation of a sphere in a uniform vertical flow, Fig. 1. The gravitational force,  $F_g$ , buoyancy force,  $F_b$ , and drag force,  $F_d$ , are simply related;

$$F_g = \pi D_s^3 \rho_s g / 6 \quad (1)$$

$$F_b = \pi D_s^3 \rho_\infty g / 6 \quad (2)$$

$$F_d = C_D \pi D_s^2 \rho_\infty V_\infty^2 / 8 \quad (3)$$

where  $D_s$  is the sphere diameter,  $\rho_s$  and  $\rho_\infty$  are the sphere and fluid densities,  $g$  is the acceleration of gravity,  $C_D$  is the sphere drag coefficient (a shape sensitive parameter) and  $V_\infty$  is the fluid free-stream velocity [11]. The drag coefficient depends on the sphere Reynolds number,  $Re_s = \rho_\infty V_\infty D_s / \mu_\infty$ , where  $\mu_\infty$  is the fluid viscosity. When  $Re_s \leq 1$  (i.e. Stokes flow regime),  $C_D \sim 24/Re_s$ , when  $1 < Re_s \leq 400$ ,  $C_D \sim 24/Re_s^{0.646}$ , when  $400 < Re_s \leq 3 \times 10^5$ ,  $C_D \sim 0.5$  [11]. For the fluid in motion, Equations (1), (2) and (3) find the velocity required to lift the sphere:

$$V_\infty > \sqrt{\frac{4D_s(\rho_s - \rho_\infty)g}{3\rho_\infty C_D}} \quad (4)$$

To prevent unsteady turbulent flow and avoid excessive mixing, the flow Reynolds number,  $Re_\infty = \rho_\infty \bar{V}_\infty D / \mu_\infty$ , should be kept low. Here,  $\bar{V}_\infty$  is the mean flow velocity and  $D$  is a characteristic length. For a circular pipe of inner diameter  $D$ , laminar flow is always expected when  $Re_\infty < 2300$ . For higher Reynolds numbers, the amount of viscous damping may not be sufficient to quell disturbances and random flow fluctuations (i.e. turbulence) can appear [11].

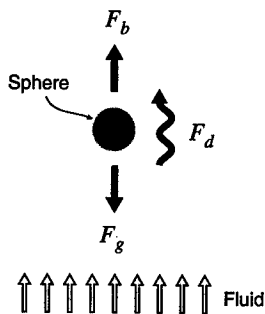
## SEPARATION

To evaluate the separation methodology, two different argon atomized metallic powders were obtained from Crucible Research (Pittsburgh, PA) [12]. One was a Ti-6.2Al-3.9V (wt.%) alloy (Ti-6Al-4V) sieved at -14/+35 mesh (i.e. particle diameters varied from 500  $\mu$ m to 1.4 mm). The

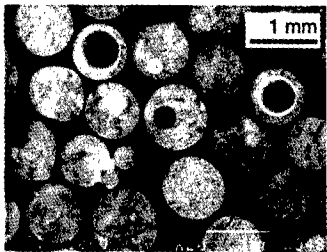
other was a Ni-21.3Cr-8.8Mo-3.9Nb-0.13Al-0.19Ti (wt.%) nickel-base superalloy (Ni 625) sieved at -10/+45 mesh (i.e. 355  $\mu\text{m}$  to 2 mm). Both contained solid, porous and hollow powders along with flake. The powders were generally spherical and often had satellites attached to them.

Flake and powders heavily laden with satellites are undesirable in the sense that they add much weight to a hollow sphere structure but with little mechanical advantage. By noting that spherical powders roll more readily, a collection of predominantly spherical powders was obtained by repeatedly placing powders on an inclined surface and agitating. To extract the hollow powders, two approaches were investigated. Using a static fluid approach, 4.5 g of sodium metatungstate ( $3\text{Na}_2\text{WO}_4 \cdot 9\text{WO}_3 \cdot \text{H}_2\text{O}$ ) per 1 ml of distilled  $\text{H}_2\text{O}$  were combined to produce a true fluid having a density of  $2.9 \text{ g/cm}^3$  [10]. Spherical Ti-6Al-4V powders were placed into the heavy fluid and agitated such that hollow powders having densities less than  $2.9 \text{ g/cm}^3$  floated to the surface. Using a dynamic fluid approach, spherical Ni 625 powders were sieved at -10/+20 mesh (i.e. 850  $\mu\text{m}$  to 2 mm) to obtain a distribution of large, visible, easily handled powders, Fig. 1. These were placed in a vertical elutriation apparatus, Fig. 1, and the mean flow velocity was varied from 25 cm/s to 50 cm/s in 5 cm/s increments. The elutriation column was 1.00 m high and its inner diameter was 1.27 cm (0.50 in). Excessive turbulence was suppressed by keeping the flow Reynolds number low,  $3517 \leq Re_\infty \leq 7034$ . The size, shape and density of the recovered powders could be systematically controlled by varying the mean flow velocity, Fig. 2. Powders recovered for  $\bar{V}_\infty \leq 30 \text{ cm/s}$  were all hollow and kept for consolidation.

a) Sphere equilibrium



b) Predominantly spherical Ni 625 powder (-10/+20 mesh)



c) Elutriation apparatus

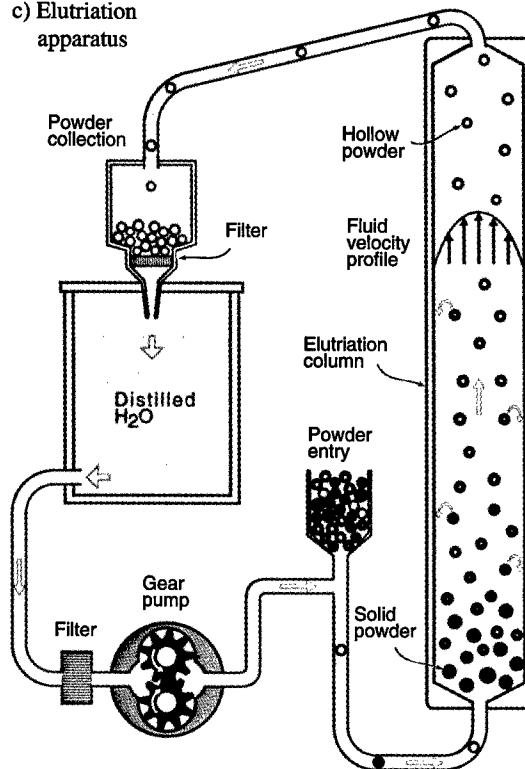


Figure 1. Sphere equilibrium, predominantly spherical Ni 625 powder, elutriation apparatus.

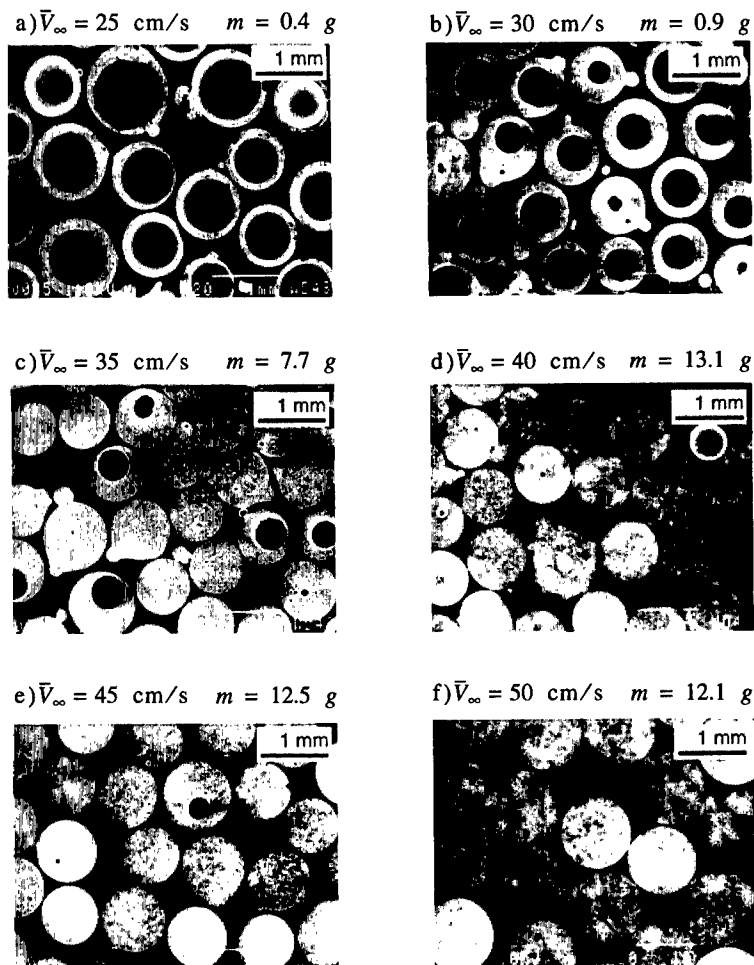


Figure 2. Separated Ni 625 and the mass,  $m$ , recovered. For  $\bar{V}_\infty > 50$  cm/s,  $m = 7.7$  g.

#### CONSOLIDATION AND MECHANICAL TESTING

Hollow Ti-6Al-4V and Ni 625 powders were sealed in evacuated,  $P < 5 \times 10^{-7}$  torr, cylindrical quartz canisters and sintered. For Ti-6Al-4V, this occurred at 1000°C for 24 hr while for Ni 625, this occurred at 1300°C for 24 hr. Cooling was in furnace. The Ti-6Al-4V sample was cylindrical with a 6.8 mm diameter, 4.0 mm height and 1.2 g/cm<sup>3</sup> density. The two Ni 625 samples were also cylindrical but with 10.0 mm and 9.6 mm diameters, 12.7 mm and 12.8 mm heights and 2.7 g/cm<sup>3</sup> and 3.1 g/cm<sup>3</sup> densities. One of these (possibly located in a furnace hot spot) had cells which were strongly bonded while the other had cells which were weakly bonded, Fig. 3.

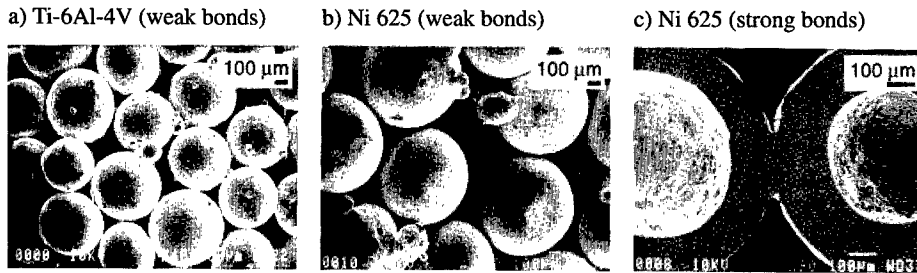


Figure 3. Hollow powder porous structures after consolidation.

Samples were room temperature compression tested at a constant crosshead displacement rate of 0.001 mm/s using a screw driven electromechanical testing machine equipped with stainless steel compression platens. For the weakly bonded Ti-6Al-4V and Ni 625 samples, cells regularly broke away and fell to the compression platens during testing. Thus, failure through cell ligament shearing led to upper strengths of just 6.2 MPa and 6.4 MPa, Fig. 4. For the strongly bonded Ni 625 sample, the ligaments remained intact and a bi-linear stress-strain behavior was observed but with no well defined upper yield. The unloading modulus was about 5.2 GPa.

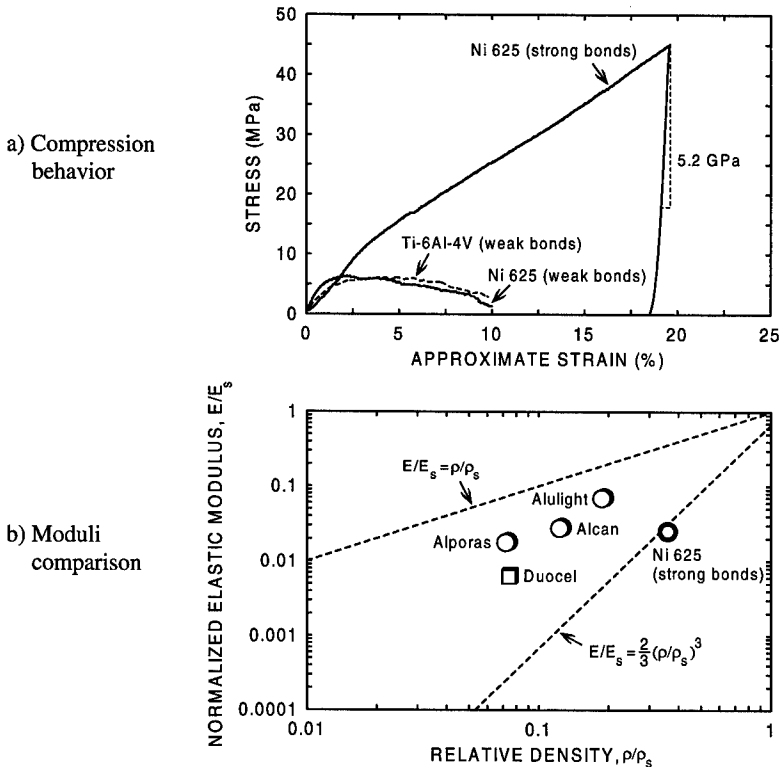


Figure 4. Compression behavior and moduli comparison.

## CONCLUSIONS

Hollow gas atomized metallic powders have been separated based on their size, shape and density. The elutriation method can be used to obtain tight distributions of very spherical powder, to remove non-spherical powders, those laden with satellites or those containing porosity. Control over hollow powder wall thickness can also be gained. Upon sintering, hollow powder porous structures were created. A strong ligament between cells was essential for good mechanical properties. The relative modulus of the well bonded Ni 625 hollow powder structure was comparable to that of honeycomb in-plane. A well defined upper yield strength was not observed which could lead to many interesting applications. Potential advantages of the gas atomized Ti-6Al-4V and Ni 625 hollow powder structures include small grain sizes, high temperature load carry capability and the ability to be heat treated. Furthermore, complex-shaped components with very high internal porosity are possible. This could occur by packing high gas pressure filled spheres in a desired geometry or mold followed by heating and expansion in a reduced pressure environment. The lower the external pressure, the higher will be the porosity.

## ACKNOWLEDGEMENTS

We wish to thank W.H. Shoup of the UVA Chemistry Department for his generous help with quartz sample encapsulation. Also, C.F. Yolton and B.J. McTiernan of Crucible Research for providing the powder. This work has been supported by the DARPA/ONR URI at Harvard (N00014-96-I-1028, program managers, S. Wax and S. Fishman).

## REFERENCES

1. J.L. Grenestedt, *Int. J. Solids Structures*, in press (1998).
2. B.H. Rabin, G.R. Smolik and G.E. Korth, *Mat. Sci. and Eng.* **A124**, 1 (1990).
3. B. Norris and F.J. Gojny, U.S. Patent No. 4,925,740 (15 May 1990).
4. H. Bart-Smith, A.-F. Bastawros, D.R. Mumm, A.G. Evans, D.J. Sypeck and H.N.G. Wadley, *Acta mater.*, in press (1998).
5. J.M. Beggs, T.G. Wang and D.D. Elleman, U.S. Patent No. 4,344,787 (17 Aug 1982).
6. N. Baxter, C. Uslu, K.J. Lee, T.H. Sanders and J.K. Cochran, in *Synthesis/Processing of Light Weight Metallic Materials II*, edited by M. Ward-Close (TMS, Warrendale, PA, 1997), pp. 417-430.
7. M. Pilch and C.A. Erdman, *Int. J. Multiphase Flow*, **13**(6), 741 (1987).
8. *Handbook of Chemistry and Physics*, 63rd ed. (CRC Press, Inc., Boca Raton, FL, 1982).
9. G.H. Gessinger, *Powder Metallurgy of Superalloys*, (Butterworths, London, 1984), p.43.
10. R. Kamps, B. Plewinsky, M. Miehe and K. Wetz, U.S. Patent No. 4,557,718 (10 Dec 1985).
11. R.W. Fox and A.T. McDonald, *Introduction To Fluid Mechanics*, 4th ed. (Wiley, New York, 1992).
12. C.F. Yolton and J.H. Moll, U.S. Patent No. 4,544,404 (1 Oct 1985).

---

## FABRICATION AND PROPERTIES OF SYNTACTIC MAGNESIUM FOAMS

M. HARTMANN, K. REINDEL, R. F. SINGER

Department of Material Science, University of Erlangen, Erlangen, GERMANY

### ABSTRACT

Syntactic magnesium foams which consist of thin-walled hollow alumina spheres embedded in a magnesium matrix were fabricated by infiltrating a three-dimensional array of hollow spheres with a magnesium melt by using a gas pressure-assisted casting technique.

The resulting composite contains closed cells of homogeneous and isotropic morphology. The densities of the syntactic magnesium foams were between 1.0 and 1.4 g/cm<sup>3</sup>. The densities were controlled by variations in the bulk density of the hollow spheres with the volume fraction of spheres kept constant at approximately 63 %.

Compressive deformation characteristics of the composites were evaluated with respect to the influence of matrix strength and sphere wall thickness on characteristic variables such as compressive strength, plateau stress and energy absorption efficiency. Differences in the strength of the magnesium-based matrix materials investigated (cp-Mg, AM20, AM50, AZ91) had little influence on the compressive strength of the syntactic foam. However, an increasing relative wall thickness of the hollow ceramic spheres led to a significant strength enhancement. In all cases the ratio between compressive and plateau strength rose with increasing composite strength resulting in decreasing energy absorption efficiency.

### INTRODUCTION

Weight reduction and enhancement of impact protection are some of the primary driving forces in the automotive industry. Metal foams represent a new class of low density structural materials which offer the potential to reduce weight and to absorb impact energy efficiently.

There is a wide range of methods to fabricate metallic foams, most of them being based on the introduction of gas bubbles into a molten metal prior to solidification via an external source or from gas evolution from chemical decomposition [1]. As these foaming techniques depend upon solidification of a foamed liquid metal, the pore size and distribution is difficult to control resulting in the solidified foams often having a wide variety of porosity characteristics.

An alternative method for manufacturing low density cellular solids utilizes a second hollow phase which is introduced into a matrix. The resulting three-phase composite is termed a "syntactic foam". Syntactic metal foams have been produced by liquid metal infiltration of hollow ceramic microsphere arrays. The technique has been applied to aluminum [2, 3] and to titanium [4] matrices. With this process the distribution and size of the porosity can be set exactly since the structure is independent of matrix solidification.

The objectives of this study are to fabricate high quality, low density syntactic metal foams using magnesium, the lightest commonly used structural metal, as the matrix component and to evaluate the effect of matrix strength and hollow sphere morphology on the compressive deformation characteristics of the composites.

## EXPERIMENTAL PROCEDURE

The hollow sintered alumina spheres used in this study were supplied by an outside vendor. These spheres were produced by a patented powder slurry technique [5]. Four different sphere types with varying physical properties were investigated. The spheres were of two diameter sizes, 2.8 and 3.7 mm, with standard deviations of less than 7 % for each sphere type. Average wall thicknesses for the 2.8 mm diameter spheres were either 133 or 181  $\mu\text{m}$ . For the 3.7 mm diameter spheres, the average wall thicknesses were found to be 115 or 150  $\mu\text{m}$  respectively. Considerable fluctuations were measured within the wall thicknesses of the single spheres resulting in standard deviations ranging from 40 to 60 %. The corresponding average sphere densities were 0.55 or 0.78  $\text{g/cm}^3$  for the 3.7 mm diameter spheres, and 0.81 or 1.14  $\text{g/cm}^3$  for the 2.8 mm diameter spheres. To remove hollow ceramic spheres with defects such as cracks and holes, a vacuum assisted sedimentation process was applied prior to infiltration.

In order to fabricate the syntactic magnesium foams, an infiltration casting technique was developed. The principle of this process is based on low pressure die casting and the single steps are illustrated in Fig. 1. Hollow ceramic spheres were charged into a steel mold and subjected to vibration to achieve dense packing. During the infiltration casting process, liquid magnesium is forced into the evacuated mold by applying an Argon gas pressure. The magnesium matrix alloys used were cp-Mg, AM20, AM50 and AZ91. Unless specified otherwise, the infiltration process parameters were kept constant (melt temperature: 700  $^{\circ}\text{C}$ , minimum die temperature: 400  $^{\circ}\text{C}$ , vacuum: 0.1 bar, infiltration pressure: 0.5 bar, infiltration time: 2 min).

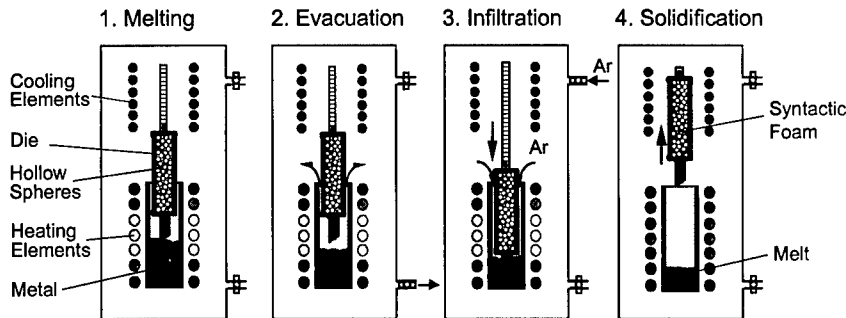


Fig. 1: Schematic of the infiltration casting process used to fabricate syntactic metal foams.

Rectangular bars 120 mm in length were fabricated. They were machined on all sides to yield six rectangular samples of 30 mm in height and 20 mm in width, giving an aspect ratio of 1.5.

Uniaxial compression tests were carried out in an Instron 4505 testing machine between two unlubricated hardened steel plates with an initial strain rate of  $5.5 \cdot 10^{-3}/\text{s}$ . The strain was determined using cross head displacement. All specimens were tested in the as-cast condition and the density of the samples was measured geometrically.

In order to evaluate the mechanical properties of the magnesium matrix with no spheres, matrix alloys were cast into rectangular bars using the above process. From these castings, cylinders 10 mm in diameter and 15 mm in height were machined for compression tests according to ASTM Standard E9-89a.

## RESULTS AND DISCUSSION

### Infiltration Quality

Using appropriate process parameters syntactic magnesium foams with closed-cell structure were successfully fabricated by the infiltration casting process described, i.e. the narrow spaces between the hollow spheres were completely filled with metal (Fig. 2). Pore size and shape correspond to the morphology of the hollow spheres. Thus, the cell structure of the composite is homogeneous and isotropic for randomly packed spheres of fairly equal diameter. In work reported elsewhere [6], metallurgically-bonded sandwich structures with dense facesheets have also been fabricated using an essentially similar approach.

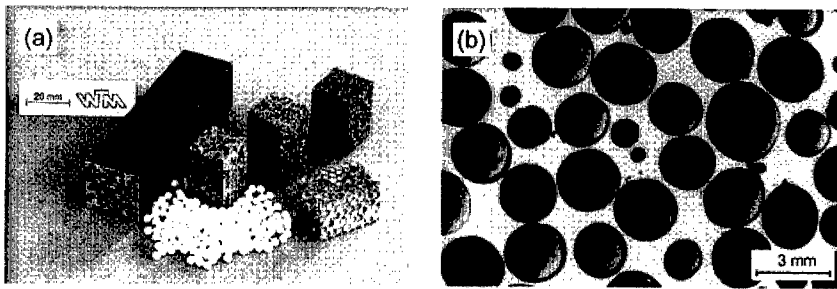


Fig. 2: (a) Syntactic magnesium foams in the as-cast and machined conditions.  
(b) Closed spherical cell structure of a syntactic magnesium foam revealing the thin walls of the hollow ceramic spheres.

The composite density in the present study varied between 1.0 and 1.4 g/cm<sup>3</sup> depending on the components used. It could be reasonably well predicted by a rule of mixtures approach assuming no macro- or microporosity was present and setting the volume fraction of spheres to 63 % for all specimens in accordance to independent earlier experiments. The porosity of the syntactic foams, i.e. the volume of the sphere interior divided by the volume of the sample, ranged from 42 to 52 %.

In order to achieve high infiltration quality, process parameters must be controlled carefully. Fig. 3 displays the influence of infiltration pressure on composite density as an indication for infiltration quality. Under the above named conditions, a low pressure around 0.5 bar is optimal for complete die filling without the melt penetrating into the inner cavity of the spheres. The resulting composite density is almost constant along the casting length and is in fair agreement with the calculated density. Deviations in density are probably due to inaccuracies in measuring the sphere density, the sphere volume fraction, microporosity within the matrix and incomplete infiltration in the contact area between two spheres. An example of incomplete infiltration between two spheres is shown in Fig. 3c).

Applying higher-than-optimal infiltration pressures lead to magnesium penetration of the sintered sphere wall material. The SEM micrograph in Fig. 3 documents the phenomenon of sphere wall penetration, showing a solidified droplet of magnesium on the inner side of the wall. When such penetration occurs, the cellular structure is destroyed giving high composite densities. As shown in Fig. 3, a density gradient exists along the casting length indicating that metalostatic pressure and thermal conditions favor sphere penetration in the lower part of the mold. Even an infiltration pressure of 2.9 bar does not result in a complete infiltration of the spheres as gas is entrapped within the spheres.

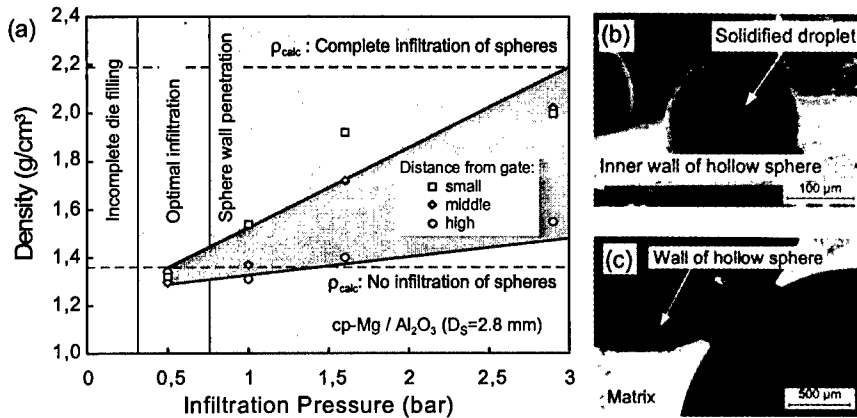


Fig. 3: a) Effect of infiltration pressure on density of the composites. Infiltration pressure is limited by penetration of the melt into the internal cavities of the spheres due to open porosity in the sintered ceramic walls. b) SEM micrograph showing solidified magnesium droplet on the inner side of the hollow sphere. c) Optical micrograph showing incomplete infiltration in regions of sphere to sphere contact.

### Compressive Properties

Fig. 4a) shows a compressive stress-strain curve for a syntactic magnesium foam. At the beginning of the collapse plateau, the stress-strain curve is characterized by the appearance of a peak stress with subsequent minor fluctuations of the stress. This is due to a deformation mechanism which is predominantly characterized by a progressive brittle failure of spheres along local planes of maximum shear stress in conjunction with plastic yielding and fracture of the matrix as shown in Fig. 4b). As a result of the narrow cell size distribution, the plateau stress remains virtually constant up to strains of 55 to 65 %.

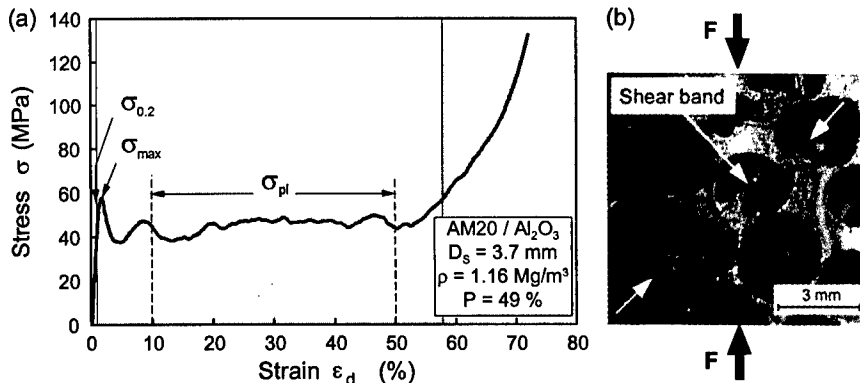


Fig. 4: a) Compressive stress-strain curve for a syntactic magnesium foam. b) Photograph showing strain localization in a shear band.

To evaluate the influence of the mechanical properties of the matrix and the hollow sphere morphology on the compression behavior of the composites, 0.2 %-yield, plateau, and compressive strength ( $\sigma_{0.2}$ ,  $\sigma_{pl}$ ,  $\sigma_{max}$ ), were determined for each compression test. 0.2 % offset yield strength and compressive strength were measured according to ASTM Standard E 9-89a, while the plateau stress was defined as the average stress between the strains of 10 % and 50 %.

The effect of hollow sphere morphology on these values is shown in Fig. 5a). Hollow sphere morphology is expressed by normalized sphere cross sectional area, assuming the load carrying area of the spheres is the relevant parameter of influence. A significant strength enhancement is attained by use of thick-walled hollow spheres. A linear relationship between strength and normalized sphere cross-sectional area appears to hold for the examined range of conditions. The slope of the plateau stress line seems to be significantly lower than the slope of the 0.2 %-yield and compressive strength lines. This is a reflection of the fact that the stress drop, observed after the first localized shear bands are initiated, becomes greater with increasing relative wall thickness. This may be due to the loss of the higher load carrying contribution from the thick-walled spheres after initial sphere collapse occurs.

Energy absorption capacity was determined by measuring the area below the stress-strain curve. It is directly related to the plateau strength. The highest energy absorption capacity found was for the thick-walled hollow spheres. The specific energy absorption capacity was observed to remain almost unaltered for the different spheres, reaching around 18.5 J/g at 50 % strain. The energy absorption efficiency defined as the actual absorbed energy divided by the ideal absorbed energy at the same strain for rigid ideal-plastic material behavior, reaches typical medium values of about 75 % at 55 to 65 % strain for the cp-Mg / alumina hollow sphere composites.

Concerning the influence of the matrix strength a linear increase in compressive strength of the composite with increasing compressive strength of the matrix alloy is observed as shown in Fig. 5b). The enhancement of composite strength with matrix strength is very weak. The slope of the regression line in Fig. 5b) is only 0.09. Assuming that a rule of mixture relationship holds, the increase of composite strength should be proportional to the volume fraction of the matrix. The latter has been determined experimentally to be 0.37, i.e. much larger than 0.09. It seems that there are two effects contributing to the small slope of the regression line. First, the actual area fraction of the matrix in a shear band can be very low, e.g. in case of close packed areas as low as 0.093. Second, there may be a decline in the matrix strength contribution due to decreasing ductility of higher strength matrices, allowing for propagation of sphere wall cracks into the matrix. A complete discussion of the effect of matrix strength on composite strength is beyond the scope of this paper.

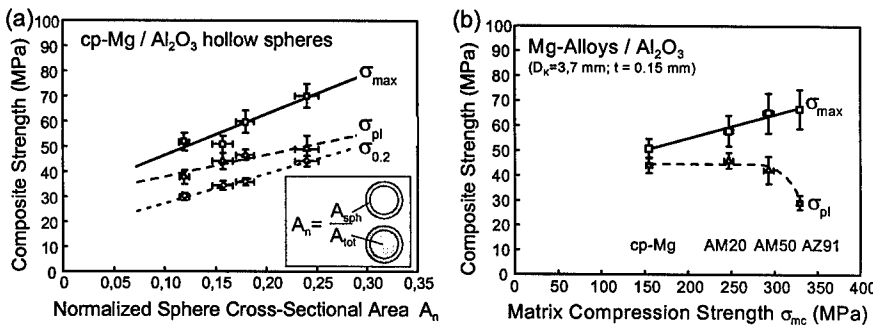


Fig. 5: Effect of hollow sphere morphology (a) and matrix compressive strength (b) on composite strength under compression.

In contrast to the compressive strength the plateau strength remains almost constant as the matrix strength increases, but drops significantly for the AZ91 matrix. This drop may be associated with the brittleness of the AZ91 matrix, leading to the propagation of sphere wall cracks into the matrix and a consequent loss of foam integrity. From the increasing ratio of compressive to plateau stress with respect to increasing matrix compressive strength, the average energy absorption efficiency decreases from 78 % for the cp-Mg matrix to 55 % for the AZ91 matrix.

## CONCLUSIONS AND OUTLOOK

Syntactic magnesium foams having homogeneous, isotropic cell structures were reproducibly fabricated by a non-isothermal infiltration casting technique using a preheated die filled via gas pressure. Process parameters must be controlled carefully if open porosity exists in the ceramic shells of the hollow spheres to avoid sphere wall penetration by the melt. This problem may be solved in the future by sintering the spheres at higher temperatures or for longer times to achieve impermeable sphere walls. On this basis an up-scaling to conditions as in low pressure die casting facilities seems to be possible.

Compressive stress-strain deformation of the syntactic magnesium foams indicate a large potential for kinetic energy absorption applications. Physical density, compressive strength and plateau strength values are significantly higher than for most conventional aluminum foams. Thus, the present materials are of particular advantage if high energy absorption is required in a limited volume.

The experimental data shows that syntactic magnesium foams can be designed for various load-carrying and energy absorption needs. For energy absorption applications, low relative wall thickness in conjunction with low matrix strength are needed to minimize an undesirable stress maximum prior to the plateau stress. If compressive strength is the primary design parameter, high strength matrix alloys and thick-walled hollow spheres offer the highest potential.

## ACKNOWLEDGMENTS

The authors would like to acknowledge the Deutsche Forschungsgemeinschaft for their support of this research.

## REFERENCES

1. G. J. Davies and Shu Zhen, *J. Mat. Science* **18**, pp. 1899-1911(1983).
2. W. J. Drury, S. A. Rickles, T. H. Sanders, Jr., J. K. Cochran, in Light-Weight Alloys for Aerospace Applications, edited by E. W. Lee, E. H. Chia and N. J. Kim (The Minerals, Metals & Materials Society, 1989), pp. 311-322.
3. S. P. Rawal, B. R. Lanning, M. S. Misra, in Metal Matrix Composites, edited by A. Miravete (Proc. of the 9th Int. Conf. on Composite Materials (ICCM/9), Madrid, 1993), pp. 203-210.
4. B. R. Lanning, S. P. Rawal, M. S. Misra, in Advanced Metal Matrix Composites for Elevated Temperatures, edited by M. N. Gungor et al. (Conf. Proc., Cincinnati, Ohio, USA, 1991), pp. 79-83.
5. L. B. Torobin, U.S. Patent No. 4 671 909 (9 June 1987).
6. M. Hartmann, R. F. Singer, in Metallschäume, edited by J. Banhart (Conf. Proc., Verlag MIT, Bremen, 1997), pp. 39-57.

---

## Porous Al Alloys by Local Melting and Diffusion of Metal Powders

N. WANG, E. A. STARKE, Jr., H. N.G. WADLEY  
Department of Materials Science and Engineering  
University of Virginia, Charlottesville, VA 22903

### ABSTRACT

A novel method exploiting local melt and diffusion induced porosity is described for producing porous Al alloys. Aluminum powder and zinc powder were blended and cold-compacted to a near net shape. A porous Al-Zn alloy component was then formed by annealing the material above the melting point of zinc but below the solidus temperature of the alloy. Pores were generated by the diffusion of molten Zn into the solid Al grains. The pore structure is shown to be determined by the volume fraction, distribution, and size of the Zn powders in the powder mixture, and by time and temperature of the annealing heat treatment. The pores can be further expanded by incorporating small amounts of titanium hydride into the powder blend and conducting the annealing treatment above the decomposition temperature of the titanium hydride ( $T > 447^{\circ}\text{C}$ ). Porosity levels of 45 vol.% have been achieved to date. This processing approach appears amenable to the production of sandwich panels with a gradient porosity core and fully dense face sheets, and is applicable to other solid solution systems.

### INTRODUCTION

Porous metals are emerging as a new class of engineering material that offer unusual combinations of physical and mechanical properties. Significant applications appear to exist in fields where structural weight saving and improvements in impact resistance (mechanical energy absorption), noise and vibration damping, fire resistance, and thermal conduction, are demanded. The properties of porous metals depend primarily on the characteristics of the pore structure, including the volume fraction of pores, pore size, shape, distribution and morphology (i.e. open/closed cell). The pore structure is determined by the manufacturing process. There are many processes available to produce porous metals, using a variety of casting, vapor deposition, and powder metallurgy techniques [1-3]. For light weight structures, functionally graded distributions of porosity appear to be very useful. In particular, the development of plate-like materials with low density porous cores and dense aluminum alloy face-sheets appears to be important for aerospace structures [4].

Here, we explore a diffusional process for synthesizing porous aluminum alloys. As a general rule, the diffusion rate of the two different types of atoms in a binary alloy system is not the same. The element with the lower melting point often diffuses faster [5,6]. This results in a difference in mass transfer during thermal exposure, i.e., the material with higher melting point gains in mass and expands, while the material with lower melting point loses mass and shrinks. Pores can be formed by such non-equivalence in mass transfer. In binary aluminum alloy systems, zinc has the greatest solid solubility in aluminum (a maximum of 83.1 wt.% or 66.4 at.%) and a considerably lower melting point ( $419.6^{\circ}\text{C}$ ) relative to that of aluminum ( $660.5^{\circ}\text{C}$ ). Thus, a mixture of Zn and Al powders might be anticipated to become porous when significant interdiffusion is allowed.

To explore this idea, a mixture of aluminum and zinc powders was cold-compacted and then annealed to promote the non-equivalent mass transfer between Al and Zn powders. When

annealed above the melting point of zinc, the diffusional flux of zinc into aluminum becomes so predominant that pores are created at the locations initially occupied by zinc grains. Effects of the content, distribution, and size of zinc powders in the mixture on the formation of pores, as well as the use of titanium hydrides, were studied.

## PROCESS AND EXPERIMENTS

The basic process to produce porous Al-Zn alloys consists of three steps. First, aluminum powder and zinc powder (or zinc combined with titanium hydride powder) were mixed in various proportions; then cold-compacted to a given shape (cylinder-shaped  $\phi 32 \times 12$  mm in this study) at a pressure of 150 MPa; and thereafter annealed above the melting point of zinc, but below the solidus temperature of the alloy. Table I gives the conditions tested to date.

Table I Compositions and annealing treatment conditions

Alloy	Powder		Composition (wt.%)			Heat Treatment (annealing)
	Al	Size( $\mu$ m)	Al	Zn	TiH <sub>2</sub> ( $\sim 10\mu$ m)	
1	44-420	<840	bal	20.0	-	(1) 378°C / 24-48hours (2) 418°C / 24-48hours (3) 450°C / 20-72hours (4) 510°C / 20-90hours  * samples were wrapped with aluminum foil during annealing.
2	44-420	<840	bal	20.0	1.0	
3	44-420	<840	bal	50.0	-	
4	44-420	<140	bal	50.0	-	
5	44-420	<840	bal	50.0	2.0	
6	44-420	<840	bal	66.6	-	
7	44-420	<840	bal	66.6	2.0	
8	44-420	<840	bal	73.0	-	
9	44-420	<840	bal	73.0	2.0	

The percent porosity was determined by metallographic measurement of the area of pores. Microstructures of the alloy matrix around pores were highlighted using dilute Keller's reagent.

## RESULTS AND DISCUSSION

Figure 1 shows scanning electron micrographs of the porous alloy containing 20 wt.% zinc. The annealing treatments were varied by varying temperature and hold time. Pores surrounded by zinc-rich zones were clearly visible following annealing at 450°C for 48 hours, See Figure 1 (a). Zinc diffused more uniformly throughout the matrix during annealing at 510°C for 90 hours, See Figure 1 (b). No pores were observed when the alloy was annealed at 378°C for 60 hours.

Larger volumes of pores were generated by increasing the Zn content. Figure 2 shows the porous structure for an alloy containing 73 wt.% zinc. With annealing at 450°C for 48 hours, approximately 30 vol.% porosity was produced, See Figure 2 (a). The porosity level was further increased to approximately 45 vol.% by incorporating titanium hydride into the powder mixture, as shown in figure 2 (b). The effect of the addition of gas-releasing agent (TiH<sub>2</sub>) on pore expansion is illustrated in Figure 3. The pores formed by diffusion of molten zinc into aluminum grains provided empty spaces for gas release, and the releasing gas from dissolution of titanium hydride created pressure to expand the pores during annealing. The observation of eutectoid Al-Zn phases and TiAl-type phases at the boundary of pores in a Al-Zn solid solution indicated the predominant diffusion of zinc into aluminum and dissolution of titanium hydride.

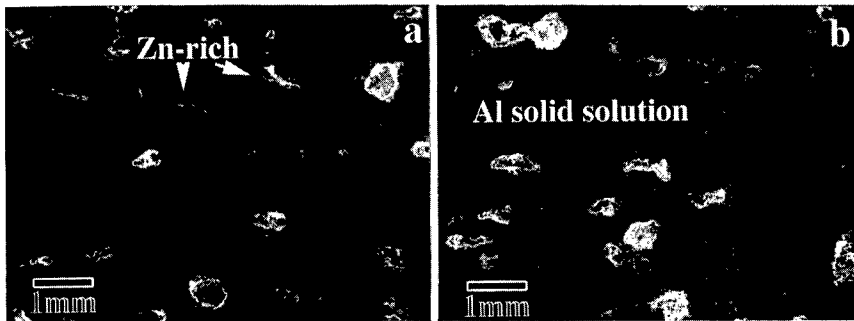


Figure 1 Scanning electron micrographs of the porous alloy containing 20 wt.% of zinc. (a) annealed at 450°C for 48 hours, (b) annealed at 510°C for 90 hours.

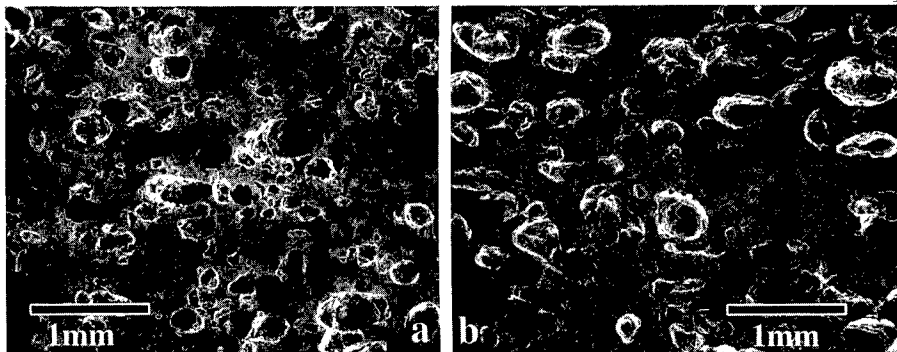


Figure 2 Porous structure for an alloy containing 73 wt.% zinc without (a) and with (b) titanium hydride. All annealed at 450°C for 48 hours.

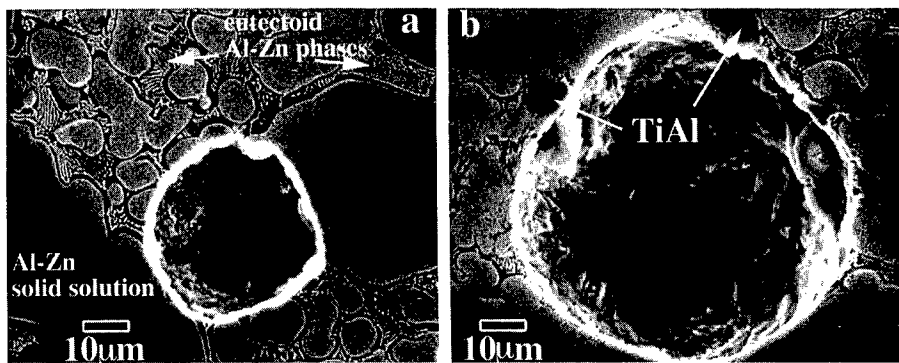


Figure 3 Typical micrographs showing a) a pore formed by diffusion of zinc into aluminum grains, b) expanded by the pressure of the releasing gas from dissolution of titanium hydride, following annealing at 450°C for 48 hours.

Figure 4 gives the pore size versus the size of zinc powder and the addition of titanium hydride. The pore size was found to be closely related to the size of zinc powder. The addition of titanium hydride enlarged the pore size to some extent.

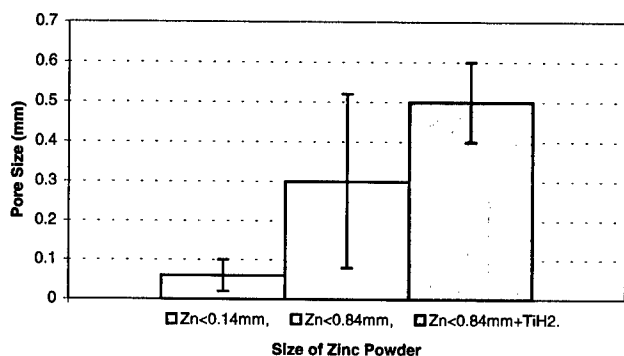


Figure 4 The pore size vs. the size of zinc powder and the addition of titanium hydride.

The distribution of pores in the porous Al-Zn alloy produced was found to correspond to the distribution of zinc powders in the powder mixture. The homogeneously distributed zinc powders produced homogeneously distributed pores in the alloy, and the unevenly distributed zinc powders resulted in unevenly distributed pores, as shown in Figure 5. However, if the annealing temperature was higher than the solidus temperature of the nominal composition of the alloy, such correspondence was destroyed, and both porosity and pore size decreased.

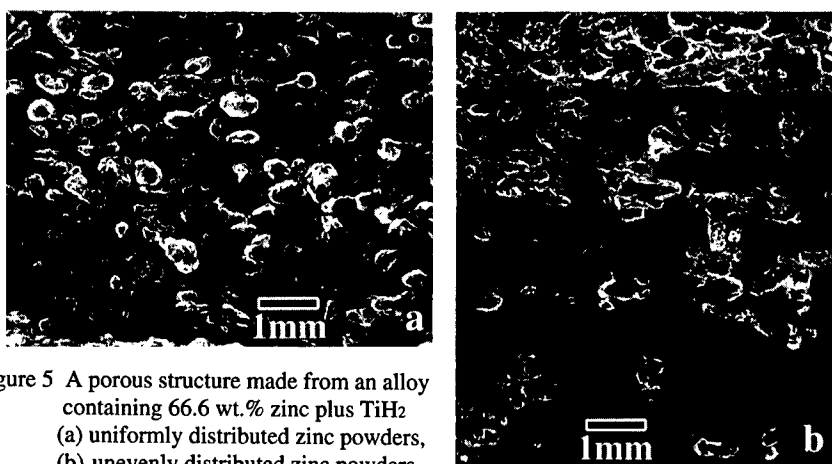


Figure 5 A porous structure made from an alloy containing 66.6 wt.% zinc plus TiH<sub>2</sub>  
 (a) uniformly distributed zinc powders,  
 (b) unevenly distributed zinc powders.

Figure 6 shows the general trend of the effect of zinc content on porosity. Porosity increased with increasing zinc content. It is believed that the porosity could be continuously increased by increasing the zinc content up to 83.1 wt.%, which is the maximum solubility of zinc in aluminum. The further increment in porosity by adding titanium hydride was found to be more significant at higher zinc content. This was attributed to the dissolution of larger amounts of titanium hydride, which was combined with zinc powders, at higher zinc content.

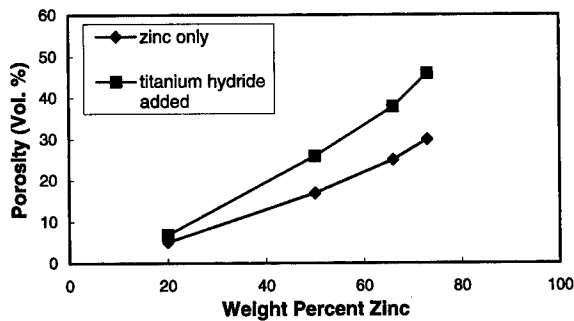


Figure 6 The porosity vs. the content of zinc for alloys annealed at 450°C/48h.

This technique is applicable to other solid solution systems for which the components have great solubility and difference in melting point. It has the potential for direct manufacture of complex shaped or sandwich structures with controllable pore distributions.

## SUMMARY

A new transient liquid phase diffusional process to produce porous Al alloys has been described and demonstrated using a model Al-Zn system. The pore structure formed by this method is primarily determined by the content, size, and distribution of zinc powders in the press-shaped aluminum and zinc powder mixture. When the annealing temperature was above the melting point of zinc, but below the solidus temperature of the alloy, the zinc powders melted and diffused into the still solid aluminum grains. Pores were created at the locations occupied initially by zinc. The addition of titanium hydride aided pore expansion, thus increasing the porosity. A porous Al-Zn alloy with porosity level of 45 vol.% has been achieved. The principles of the technique can be extended to other binary metal-metal or metal-alloy systems.

## ACKNOWLEDGMENTS

This work has been performed as part of the research of the Multidisciplinary University Research Initiative (MURI) program on Ultralight Metal Structures. The authors wish to thank Dr. Dana Elzey, Dr. Philip Parrish and other colleagues for helpful discussions. The consortium's work has been supported by DARPA/DSO under contract N00014-96-I-1028, monitored by Steve Wax (DARPA) and Steve Fishman of the Office of Naval Research.

---

## REFERENCES

1. G.J. Davies and Shu Zhen, "Review: Metallic foams: their production, properties and applications", *Journal of Materials Science*, 18 (1983), 1899-1911.
2. V. Shapovalov, "Porous Metals", *MRS Bulletin*, April 1994, 24-28.
3. J. Banhart, J. Baumeister and M. Weber, "Damping properties of aluminum foams", *Materials Science and Engineering*, A205 (1996), 221-228.
4. M.F. Ashby, *Materials Selection in Mechanical Design*, (Pergamon, Oxford 1992), 5-55.
5. Stanislaw Mrowec, *Defects and Diffusion in Solids*, (Elsevier Scientific Publishing Company, 1980), 209-213.
6. Paul Shewmon, *Diffusion in Solids*, (TMS, 1989), 132-137.

---

**Part V**  
**Hice-Based Materials**

## DEVELOPMENT AND SCALE-UP OF THE LOW DENSITY CORE PROCESS FOR Ti-64

D. S. SCHWARTZ, D. S. SHIH, R. J. LEDERICH, R. L. MARTIN, AND D. A. DEUSER  
The Boeing Company, St. Louis, MO 63166-0516

### ABSTRACT

The Low Density Core (LDC) process is a method for making metallic structures with solid surfaces covering a porous core. The development of the LDC process for making Ti-64 sheet based structures is described. Sheets  $\sim 2000 \times 1200 \times 4 \text{ mm}^3$  have been made with  $\sim 40 \text{ vol. \%}$  core porosity levels, and several forming techniques have been demonstrated. The LDC billet breakdown and forming behavior was found to be similar to conventional Ti-64 processes, so LDC Ti-64 sheet has the advantage that it can be fabricated into structures using well-established methods.

### INTRODUCTION

The aerospace industry has a continuing need for low-cost methods to fabricate metallic structures with very high stiffness-to-weight ratios. Traditionally, honeycomb construction has been used, but a need exists for lower-cost, more buckling and crippling resistant structures. One promising alternative is metal structure made using the Low Density Core (LDC) process, which is a method for manufacturing complex thin gauge parts with solid outer surfaces enclosing a porous core. In this paper, an overview of the LDC process and its development will be given.

### BACKGROUND

The LDC process is the name given to a powder metallurgy-based manufacturing process developed at Boeing [1] based on an entrapped gas technique devised by Kearns et al. [2]. Powder of the desired alloy is packed into a specially designed can, which is outgassed and then charged with 300 - 500 kPa (absolute) of Ar gas. The gas pressure is sealed into the canister, and then hot isostatically pressed (HIPed) at carefully selected pressure and temperature conditions. The HIPing process fully consolidates the metal powder. The high pressures involved in HIPing, typically  $> 100 \text{ MPa}$ , compress the entrapped gas into a volume several hundred times less than it initially occupied. Metallography shows that the porosity level at this stage is  $\sim 2\%$ . The consolidated, gas containing billet is then hot-worked using conventional techniques such as hot-rolling, hot-pressing or extrusion, into a near-net final shape. The part is subjected to an expansion annealing treatment in a vacuum or flowing Ar environment. Typically, the part is annealed at  $> 0.6T_m$  for 6 - 24 hours. At the elevated annealing temperature, the material is soft, and the entrapped gas pressure is high enough to expand the surrounding material. Expansion continues until equilibrium is reached between the gas pressure and the constraint of the surrounding material. The result is a material containing  $\sim 20 - 40 \text{ vol. \%}$  of largely unconnected 10 - 100  $\mu\text{m}$  diameter pores. A unique feature of the process being developed at Boeing is that the entire hot-working and expansion process is conducted with the original HIP canister in place, and the walls of the canister serve as solid face sheets covering the porous inner core in the final product. The as-HIPed material can be readily hot-worked, and unique thin-gauge porous-cored Ti-64 sheet can be produced (Fig. 1). The limit on how thin LDC sheet can be made is not yet known, but it is thought to be in the 2 - 3 mm range. Due to the importance of Ti-6Al-4V to the aerospace industry, this alloy was used to demonstrate the LDC fabrication

process. However, the processes described are applicable to other metallic materials, e.g. Ni- and Cu-based alloys.

#### POWDER SELECTION

It was found that the morphology and purity of the Ti-64 powders used in the process had a large effect on the final product. Several different types of Ti-64 powder were examined in the development of the process. These included blended elemental powders (BEP), pre-alloyed hydride-dehydride powder (HDHP), and pre-alloyed plasma rotating electrode powder (PREP). The BEP was procured from Micron Metals, Salt Lake City, Utah, and the HDHP and PREP were procured from Starmet Corp., Concord, Massachusetts. The BEP is a low-cost blend of Ti sponge fines and pre-alloyed Al-V powder. The blended powders react during the HIPing process to form the target Ti-64 alloy. Although the BEP generally resulted in high quality,

uniformly porous material, the relatively low purity of this product (in particular, oxygen levels > 3000 wppm) is thought to be a major factor in causing a face sheet delamination problem. HDHP is higher purity than BEP, but the hydride-dehydride method of powder making produces powder with a jagged, irregular shape, which does not result in suitable entrapment of the gas charge during HIP consolidation. Good gas entrapment appears to require powder that packs densely and uniformly, with small interstitial volume between the powder particles. The PREP is purer than BEP or HDHP and has a more spherical morphology, which packs tightly (packing density ~ 65%) into a nearly close-packed arrangement. These factors combine to make LDC products manufactured with PREP significantly better than BEP and HDHP in terms of both higher porosity levels and reduced face sheet delamination. The superior performance of the PREP outweighed its higher cost, and PREP was chosen for Boeing's development and scale up efforts.

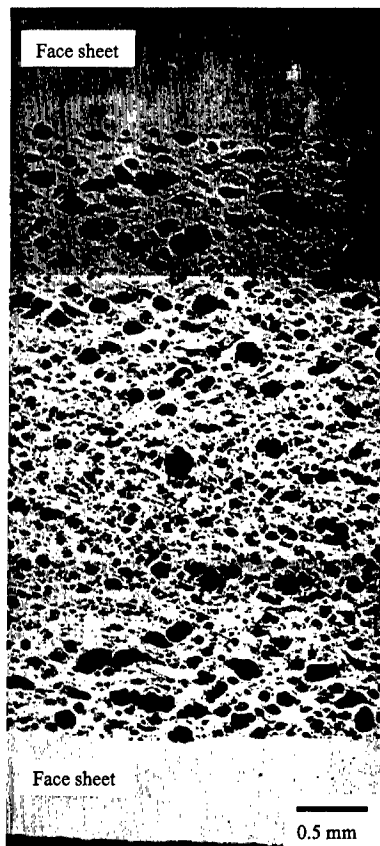


Figure 1. Cross section of LDC Ti-64 sheet manufactured with PREP.

#### CANISTER DESIGN AND HOT ISOSTATIC PRESSING

A unique feature of the LDC process is the incorporation of parts of the HIP canister into the final product. The primary HIP canister design used in this program consisted of a ~ 500 x 500 x 50 mm<sup>3</sup> Ti-64 parallelepiped. This design was chosen so that the canister could be directly hot-rolled after HIPing, with no additional shaping of the canister. The 500 x 500 mm<sup>2</sup> can surfaces are kept on the powder compact after HIPing; after hot rolling, these surfaces form thin face sheets sandwiching the porous core material. The basic



Figure 2. Edge view of hot brake-formed LDC Ti-64, showing severe cracking through the core.

HIP process consists of 1) packing the canister with PREP Ti-64, 2) outgassing the powders at 300°C to  $< 10^{-2}$  Pa, 3) backfilling the canister with 300 - 500 kPa Ar, 4) sealing the pressurized canister, and 5) HIPing the canister. After examining a variety of HIP schedules, 1100°C/6h/103MPa was identified as optimal and was used for most of this study.

#### BILLET BREAKDOWN

After HIP consolidation, the LDC billet can be handled similarly to conventional Ti-64. Hot rolling in air and forging in a vacuum hot press were both found to be viable methods for breaking down the LDC billet into sheet material. Hot rolling is the less expensive of the two, so most of the development effort centered on this method. Large scale rolling was performed in a commercial 2-high rolling mill at Lawrence Aviation Industries, Port Jefferson, New York. The as-HIPed 500 x 500 x 50 mm<sup>3</sup> LDC billets were cross-rolled at 900°C. The largest LDC sheet produced to date is ~ 2000 x 1200 x 4 mm<sup>3</sup>. The quality of the rollings was improved significantly by packing the billet in a steel envelop prior to rolling, which reduces oxygen pick up and generally improves the homogeneity of the sheet surface.



Figure 3. Corrugated LDC Ti-64 sheet made by drape forming (scale marker in inches).

#### SHEET FORMING

LDC sheet was formed using three established methods for conventional Ti-64: hot brake forming, isothermal die forming and superplastic forming. Hot brake forming is a very low cost, high strain rate bending technique performed in air on preheated material. LDC sheet was not formable using this technique; core cracking followed by face sheet delamination occurred in every trial, even when the workpiece was heated as high as ~ 1000°C (Fig. 2). Isothermal die forming was successful at bending LDC sheet to 90°, with a bending radius of ~ 10 mm. Drape forming, i.e. superplastic

forming with a sacrificial driver sheet, was also successful. A complex corrugated shape with a series of tight 90° bends was formed at B. F. Goodrich Aerospace, Chula Vista, CA (Fig. 3). In general, hot formability of LDC Ti-64 sheet was found to be good, provided the forming is done isothermally and at relatively low strain rates.

#### FORMATION OF POROSITY

The ideal gas law can be used to predict the amount of porosity to expect for a given gas pressure, expansion anneal temperature, and initial gas volume. After the powder filled canister is charged with Ar gas and sealed, the number of gas molecules is fixed, assuming no leakage. Therefore, the initial gas pressure, volume and temperature ( $P_0$ ,  $V_0$ , and  $T_0$  respectively) can be equated to  $P$ ,  $V$ , and  $T$  at any other condition simply by:

$$\frac{P_0 V_0}{T_0} = \frac{P_1 V_1}{T_1} \quad (1)$$

The volume fraction ( $X$ ) of gas in the canister is:

$$X = \frac{V_{GAS}}{V_{GAS} + V_{METAL}} = \left( 1 + \frac{V_{METAL}}{V_{GAS}} \right)^{-1} \quad (2)$$

where  $V_{GAS}$  is the gas volume at the particular pressure and temperature conditions, and  $V_{METAL}$  is the volume of metal in the canister, which is fixed. The volume fraction of gas in the HIP canister before consolidation is determined by the packing density of the powder ( $D$ ), i.e. the gas simply fills the interstitial spaces in the powder filled can. This allows the volume ratio of the metal to the initial gas volume ( $V_0$ ) to be expressed as:

$$\frac{V_{METAL}}{V_0} = \frac{D}{1-D} \quad (3)$$

Putting equations 1 and 3 into equation 2 gives an expression for the expected volume fraction of gas in the can at any temperature and pressure:

$$X_1 = \left( 1 + \frac{D}{1-D} \frac{P_1 T_0}{P_0 T_1} \right)^{-1} \quad (4)$$

However, this formulation assumes that the entrapped gas expands at the temperature  $T_1$  until it is in equilibrium with the external pressure,  $P_1$ . In fact, gas entrapped in a pore expands until it is in equilibrium with the resistance to deformation of the constraining material. If the gas pressure inside a pore causes the tangential stress around a pore to exceed the material yield stress, the pore will expand; it will stop expanding when the internal pressure is balanced by the tangential stress. If we assume the pores are spherical and non-interacting, the tangential stress due to internal pressure  $P_1$  is  $\frac{1}{2}P_1$  [3]. Therefore, when  $P_1 \approx 2\sigma$ , the gas will stop expanding. Putting this result into equation 3 gives the final expression for the expected gas porosity volume fraction:

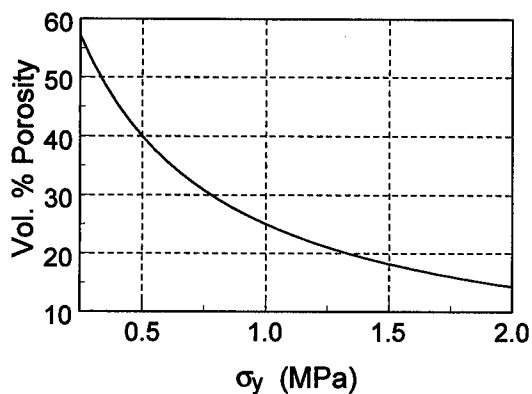


Figure 4. Predicted volume % porosity in Ti-64, as a function of yield stress for 304 kPa initial gas pressure, expanded at 920°C.

$$X_1 = \left( 1 + \frac{D}{1-D} \frac{2\sigma_y T_0}{P_0 T_1} \right)^{-1} \quad (5)$$

Using equation 5, the expected vol. % porosity is plotted in Fig. 4 as a function of the yield stress of Ti-64. Actual values were used for the packing density ( $D = 0.65$ ), initial gas pressure ( $P_0 = 304$  kPa), initial temperature ( $T_0 = 293$ K), and expansion temperature ( $T_1 = 1193$ K). The value of  $\sigma_y$  at the expansion temperature is not well known, being very strain rate and purity level dependent [4]. It is known to lie in the range 0.25 - 2.0 MPa, so this range was used for the

plot in Fig. 4. The PREP powder used in this program was relatively pure, so  $\sigma_y$  for this material should be at the low end of the range, and the measured values of 35 - 40 vol. % porosity in our LDC material are consistent with the analysis resulting in equation 5. Equation 5 shows that to achieve more porosity one should decrease the packing density, increase the initial gas pressure, reduce the initial gas temperature, increase the expansion temperature and/or reduce the yield stress of the material at the expansion temperature. Due to practical concerns, there are stringent limits on all these parameters. Low packing densities can lead to can failures resulting from large volume changes during HIPing. Higher gas pressure can lead to leakage and an "orange peel" surface roughness effect. 304 kPa (absolute) was settled on as a safe initial gas pressure. For Ti-64, expansion temperatures above the  $\beta$ -transus temperature (1000°C) will cause the material to transform to an undesirable fully Widmanstätten microstructure. The ideal expansion anneal temperature is ~ 920°C, which produces a more practical fine grained, equiaxed  $\alpha +$  transformed  $\beta$  microstructure.

#### CONCLUSIONS

The LDC process has been successfully demonstrated to be viable for producing thin gauge sheet with a ~ 40 vol. % porous core. The ideal gas law can be used to predict the porosity levels attainable for a given set of process parameters, although the accuracy of the prediction is limited by uncertainty in the value of the elevated temperature yield stress. The LDC sheet can be formed into complex shapes using conventional isothermal forming techniques. LDC material shows promise for aerospace applications and is being actively developed by the Boeing Company.

#### ACKNOWLEDGEMENTS

The authors are grateful for support from DARPA and ONR for the work presented here (contract no. N00014-95-2-0007, program monitors: Drs. R. Crowe, S. Fishman, and S. Wax).

---

#### REFERENCES

1. R. L. Martin, Integral Porous-Core Metal Bodies and in situ Method of Manufacture Thereof, U. S. Patent No. 5 564 064 (8 October, 1996).
2. M. W. Kearns, P. A. Blenkinsop, A. C. Barber, T. W. Farthing, *Int. J. Powder Res.* **24**, p. 59 (1988)
3. S. P. Timoshenko, J. N. Goodier, Theory of Elasticity, 3<sup>rd</sup> ed., (McGraw-Hill, New York, 1970) pp. 392-395.
4. T. L. Mackay, S. M. L. Sastry, C. F. Yolton, Tech. Rep. AFWAL-TR-80-4038, (Air Force Res. Lab., 1980).

## SUPERPLASTIC FOAMING OF TITANIUM AND Ti-6Al-4V

D.C. DUNAND\*, J. TEISEN#

\* Department of Materials Science and Engineering, Northwestern University, Evanston, IL 60208, USA, dunand@nwu.edu.

# Department of Materials, Swiss Federal Institute of Technology (ETH), Zürich, Switzerland.

### ABSTRACT

Solid-state foaming of metals can be achieved by hot-isostatic pressing of powders in presence of argon followed by expansion of the resulting high-pressure argon bubbles at ambient pressure and elevated temperature. This foaming technique was first demonstrated by Kearns et al. [1] for Ti-6Al-4V, but is limited by its low creep rate and ductility, which lead to early cell wall fracture. We address these issues by performing the foaming step under superplastic conditions. Rather than using microstructural superplasticity (requiring fine grains which are difficult to achieve in porous powder-metallurgy materials), we used transformation superplasticity, which occurs at all grain sizes by biasing with a deviatoric stress (from the pore pressure) of internal stresses (from the allotropic mismatch during thermal cycling about the allotropic temperature range). As compared to control experiments performed under isothermal creep conditions, superplastic foaming under temperature cycling of unalloyed titanium and alloyed Ti-6Al-4V led to a significantly higher pore volume fraction and higher foaming rate.

### INTRODUCTION

Liquid state foaming of titanium (e.g. by gas injection, incorporation of hollow spheres, infiltration of lost preforms or gas-solid eutectic solidification) is nearly impossible because of the high melting point and reactivity of titanium. Similarly, electrolytic deposition and metal sputtering are exceedingly difficult to achieve without contamination. For titanium and its alloys, solid processing is thus the most practical fabrication route. Sintering of loose powders gives only low porosity levels and low foam strength; sintering of short wires is very expensive because of the difficulty of drawing fine titanium wires; and slurry foaming is undesirable due to contamination from the suspending medium.

An simple approach to titanium foam processing was demonstrated by Kearns et al. [1] with Ti-6Al-4V and is schematically depicted in Fig. 1. First, metal powders are consolidated by Hot Isostatic Pressing (HIP) in the presence of argon gas, resulting in a billet with isolated high-pressure argon bubbles. Second, the billet is annealed at ambient pressure and elevated temperature, so that the pressurized bubbles expand by creep of the surrounding matrix. As compared to polymer foaming, this process is limited by the slow creep deformation of the metal and by the fracture of pore walls, because of the high strength and limited ductility of the metal. As pore walls fracture, adjacent bubbles become connected to each other and to the sample surface where the pressurized gas responsible for foaming escapes.

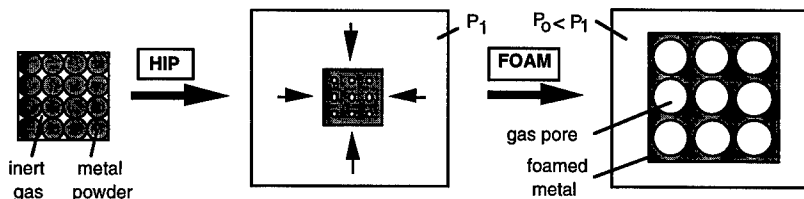


Figure 1: Schematic of foaming process, where powders are first compacted in the presence of argon and the resulting high-pressure argon bubbles are then expanded under creep or superplastic conditions.

In the present paper, we demonstrate that the problems of slow deformation rates and premature wall rupture can be alleviated by using superplastic titanium which deforms rapidly and can attain very high tensile ductility under uni- and multiaxial stress conditions [2], thus allowing much more extensive pore dilatation and final porosity. Typically, superplasticity occurs by grain-boundary sliding in fine-grain materials. This so-called *microstructural superplasticity* cannot be achieved in pure titanium because of rapid grain growth above the critical value of 10  $\mu\text{m}$ , but is easily achievable in bulk Ti-6Al-4V because the duplex structure prevents grain growth at the deformation temperature. However, the fine grain size necessary for microstructural superplasticity in Ti-6Al-4V is achieved by a complex thermomechanical treatment (rolling and annealing) which cannot be performed on powders, so that HIPed materials are typically incapable of superplastic deformation without subsequent thermomechanical treatment. Such a treatment would however be very problematic in the argon-containing porous preforms described above, because of pore elongation and linkage during rolling, limiting the subsequent pore expansion. Another possible superplastic mechanism in allotropic materials such as titanium and Ti-6Al-4V is *transformation superplasticity*. Because this type of superplasticity does not require fine grains, it is applicable to both pure titanium and Ti-6Al-4V after powder compaction and without thermomechanical treatment. The mechanism relies on internal mismatch stresses produced by the density difference between the two allotropic phases coexisting during transformation. These mismatch stresses or strains are biased in the direction of an externally applied stress, resulting in a net strain increment in the biasing direction, which can be accumulated upon multiple cycling up to very large values in excess of 100% without fracture or cavitation. Transformation superplasticity has been reported in titanium [3-6], Ti-6Al-4V [2, 6, 7] and many other allotropic metals, as reviewed in Refs. [8, 9]. The present paper demonstrates that titanium foamed under transformation superplasticity conditions exhibits higher final porosities and higher foaming rates than in the original isothermal process of Kearns et al. [1] where deformation occurs by creep.

## EXPERIMENT

Spherical powders of commercial-purity titanium (CP-Ti) and Ti-6Al-4V (from Nuclear Metals, Concord, MA) were used with median size of about 130  $\mu\text{m}$  and mesh size of -80 and -100, respectively. Powders were packed to about 70% density and encapsulated in an evacuated steel can which was back-filled with argon at a pressure of 3.3 bar. The powders were densified by HIP at 890°C and 100 MPa for 125 minutes at UltraClad (Andover, MA).

Cubic samples with about 6 mm edges were cut from the billets by electro-discharge machining, polished with SiC paper and encapsulated in quartz tubes evacuated to  $10^{-5}$  torr together with a tantalum foil getter. In isothermal annealing experiments, these capsules were introduced in a furnace held at temperatures of 903°C or 960°C for CP-Ti and 923°C and 960°C for Ti-6Al-4V, and annealed from 15 min. to 24 h. before being water quenched. Thermal cycling experiments were performed in a graphite furnace with a cycle period of 4 minutes between 830°C and 980°C, a temperature range spanning the allotropic temperature range of both CP-Ti (nominally at 882°C, but most probably higher and wider because of oxygen content) and that of Ti-6Al-4V [10]. Cycling was performed on vacuum-encapsulated specimens with cover gas in the furnace, as well as on non-encapsulated specimens with the furnace evacuated (10-30 mtorr). Despite being placed within a thin titanium foil getter cage, the latter specimens exhibited a thin black surface layer which was found by x-ray diffraction to be titanium carbide resulting from degassing of the heating elements.

After annealing, the surface of the specimens was lightly polished to remove contamination and density measurements were performed by the Archimedes method in distilled water on samples impregnated with vacuum grease to prevent water infiltration of open porosity. The relative density error due to mass and temperature error was estimated as 0.75 %. Metallographic samples were cut in half with a low-speed diamond saw along one of the cube face diagonals, mounted in epoxy at room temperature, ground on 500 to 4000 grit SiC paper and polished with 0.3- $\mu\text{m}$   $\text{Al}_2\text{O}_3$ . To minimize pore wall deformation during metallography, the porous samples were vacuum infiltrated at regular intervals during polishing with epoxy resin which filled all pores connected to the surface. The samples were etched by a modified version of Kroll's reagent (25% HF, 25%  $\text{HNO}_3$  and 50%  $\text{H}_2\text{O}$ ).

## RESULTS

Figure 2(a) shows average sample porosity as a function of annealing time for CP-Ti foamed isothermally at 903° and 960°C or under cycling conditions from 830°C to 980°C. In all cases, cycled samples show the fastest rate of foaming and the highest terminal porosity after 24 h. Figure 2(b) is the equivalent plot for Ti-6Al-4V. No significant difference was found between encapsulated and non-encapsulated samples.

Initial pores in the HIP billets retained the general shape of the gap between powders in the original preforms and were thus non-spherical, as also reported in Ref. [1]. Their sizes were  $6\pm 3$   $\mu\text{m}$  for CP-Ti and  $17\pm 9$   $\mu\text{m}$  for Ti-6Al-4V, and the initial porosity was 0.55%. Matrix grain size was about 50  $\mu\text{m}$  for CP-Ti, much larger than the maximum value of 10  $\mu\text{m}$  for fine-grain superplasticity. The Ti-6Al-4V matrix exhibited a typical as-cast structure [11], consisting of transformed  $\beta$  grains containing acicular  $\alpha$  plates up to 100  $\mu\text{m}$  in length.

Figures 3(a-b) show the pore structure in CP-Ti after foaming for 5 h. under isothermal creeping conditions and thermal cycling superplastic conditions, respectively. In both cases, pores are rounded and have a diameter of up to 200  $\mu\text{m}$  (many of the smaller pores result from the metallographic plane intersecting far from the equatorial plane of the pore). Pore coalescence is much more pronounced in the isothermally-foamed sample (arrows in Fig. 3(a)) than for the cycled sample which exhibits many examples of thin pore walls (arrows in Fig. 3(b)). The matrix shows colonies of serrated  $\alpha$  grains typical of CP-Ti annealed in the  $\beta$  field and gas-cooled [11].

Figures 4(a-b) show the microstructure of Ti-6Al-4V after foaming for 5 h. under isothermal and cycling conditions, respectively. Individual spherical metal particles (marked with "P" in Figs. 4(a-b)) are connected by thin walls (arrows) and separated by non-spherical pores. Both the average pore volume and overall porosity are noticeably smaller than for the equivalent CP-Ti samples (Figs. 3(a-b)). The matrix consists of coarsened  $\alpha$  plates separated by intergranular  $\beta$ , typical of  $\beta$ -annealed Ti-6Al-4V [11].

## DISCUSSION

### Isothermal Foaming Kinetics

While isothermal experiments by Kearns et al. [1] resulted in terminal porosities for Ti-6Al-4V somewhat higher than for our isothermal experiments (32% vs. 27%), their samples were annealed much longer (46 h. vs. 24 h.) and at much higher temperatures (1240°C vs. 960°C, leading to faceted cubic pores): this illustrates that the large increase (by a factor 33) in initial argon pressure utilized in the present study leads to significantly faster foaming kinetics with only limited decrease in terminal porosity. Terminal porosities for CP-Ti are similar to those for Ti-6Al-4V, as expected from the similar creep rupture strains for these materials. The kinetics of isothermal foaming (Figs. 2(a-b)) are however much slower for Ti-6Al-4V, as expected from its higher creep strength. Mass conservation gives the maximal final porosity  $f_2$  after complete foaming as:

$$f_2 = \frac{r}{r + f_1^{-1} - 1} \quad (1)$$

where  $f_1$  is the initial porosity and  $r=(p_1T_2)/(p_2T_1)$  is the ratio of the pore volumes after and before expansion, assuming that the ideal gas law holds. With the present experimental conditions ( $f_1=0.3$ ,  $p_1 = 3.3$  atm and  $T_1/T_2=300/1233$ ) and assuming that an upper bound value for the final pore pressure is  $p_2=1$  atm, Eq. (1) predicts a maximal porosity of 85%. The observed terminal porosities are lower most probably because of pore wall rupture and escape of the pressurized argon from the foam: open porosity was indeed present as evidenced by a slow absorption of water during density measurement of ungreased samples foamed between 5 h and 24 h. The inherent ductility of the wall material primarily dictates the extent of deformation before pore walls rupture and foaming stops. Other effects reducing the total achievable porosity include non-uniform spatial distribution of pores, non-uniform size distribution of powders (and thus pores), non-spherical shape of pores, external specimen surfaces (which were indeed found to become rough as a result of individual pore bulging), and friction between the specimen and its supporting surface.

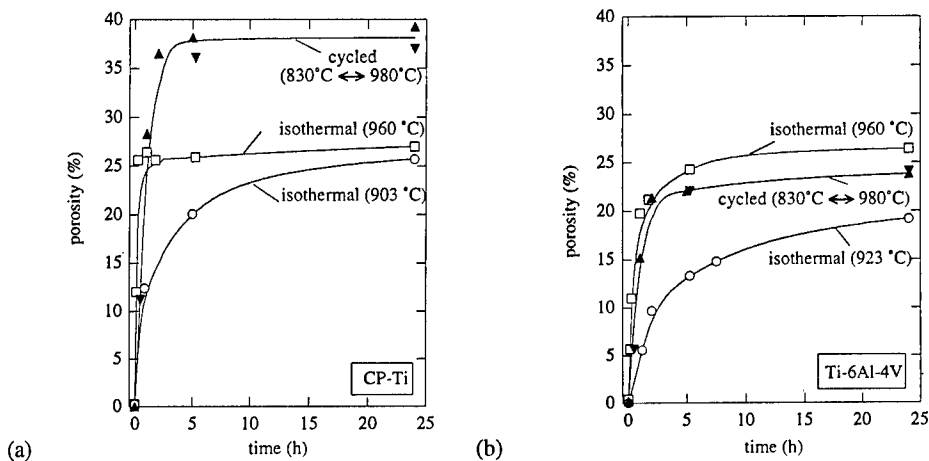


Fig. 2: Porosity as a function of time for isothermal and cyclic experiments (a) CP-Ti and (b) Ti-6Al-4V (symbol ▼ is for encapsulated samples; ▲ is for non-encapsulated samples).



Fig. 3a: CP-Ti isothermally annealed at 960°C for 5.25 h.

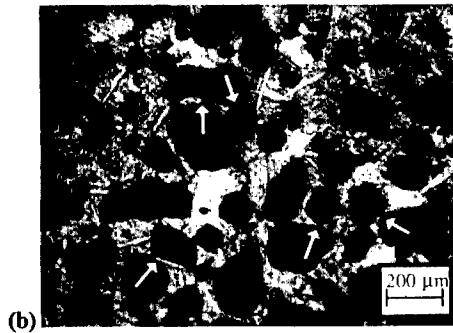


Fig. 3b: CP-Ti thermally cycled between 830°C and 980°C for 5 h.

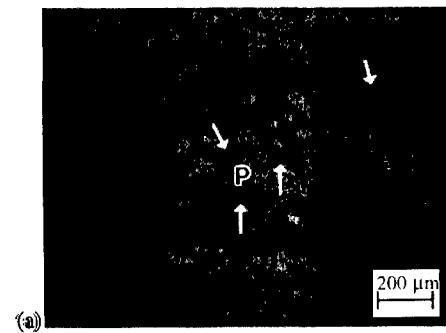


Fig. 4a: Ti-6Al-4V isothermally annealed at 960°C for 5.25 h.

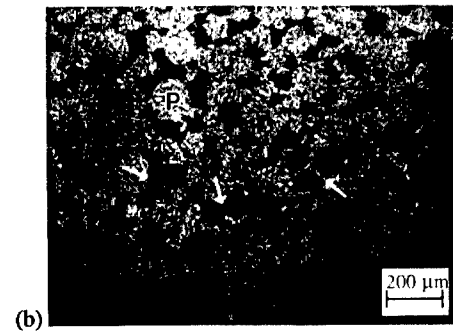


Fig. 4b: Ti-6Al-4V thermally cycled between 830°C and 980°C for 5 h.

### Superplastic Foaming Kinetics

Neglecting the small pressure variation ( $\pm 6\%$  due to the cyclic temperature), cycling experiments can be compared directly to isothermal experiments carried out at the same equivalent temperature, defined as the temperature for isothermal creep where the diffusion coefficient is the same as the time-averaged diffusion coefficient of the cycling temperature creep [2, 5]. Using lattice activation energies given in Ref. [12] for  $\alpha$ -Ti and  $\beta$ -Ti, the effective temperatures are found to be  $903^\circ$  for CP-Ti and  $923^\circ\text{C}$  for Ti-6Al-4V. Figures 2(a-b) show that for both materials the kinetics of foaming is significantly faster under cycling conditions than under isothermal conditions at the corresponding effective temperature. Furthermore, the terminal porosity after 24 h. is also much higher for the cycled samples. This clearly demonstrates that foaming under transformation superplasticity conditions leads to faster deformation rates and larger strains to fracture than under creep conditions, as also observed for bulk CP-Ti and Ti-6Al-4V subjected to uniaxial and multiaxial tests [2, 6, 7]. Even when the cycling experiments are compared to isothermal experiments at  $960^\circ\text{C}$  (much above the effective temperature and near the maximum cycling temperature of  $980^\circ\text{C}$ ), foaming kinetics and terminal porosities are higher for the cycled samples in CP-Ti and comparable in Ti-6Al-4V. Modeling of the foaming kinetics under both isothermal and cyclic conditions will be presented in later publications.

While superplastic foaming kinetics are similar for both materials at short times, the terminal porosity is much lower for Ti-6Al-4V than for CP-Ti. This difference can be explained by differences in pore shapes, as discussed in the following paragraph.

### Pore Microstructure

For CP-Ti, initial pores in the HIP preform are somewhat rounded and become more spherical as deformation proceeds, so that a large amount of material is available for deformation in the pore walls. Then, superplastic deformation of the cell walls is indeed expected to lead to significantly larger overall pore size and porosity than under creep conditions. Also, as expected, pore rupture is extensive in the isothermal specimens (arrows in Fig. 3(a)), while the superplastic sample shows intact pore walls less than  $10\ \mu\text{m}$  in thickness (arrows in Fig. 3(b)).

For Ti-6Al-4V, initial pores in the HIP preform are strongly cusped and retain the shape of the original gap between spherical metal powder. After foaming, most powders are still recognizable in their original shape (marked with "P" in Figs. 4(a-b)). The pore walls contain relatively little material and thus fracture earlier than for CP-Ti, resulting in smaller average porosities. The increased deformation rate and ductility imparted by superplastic conditions lead to little improvement in average porosity (Fig. 2(b)), because little material is available for superplastic deformation in the pore walls. The microstructure of foamed Ti-6Al-4V is similar to that of lightly sintered powders and the terminal porosity (27%) is less than the initial porosity of the powder preform (30%). The foam strength is however expected to be higher than that of a sintered preform of equivalent porosity, because the wall thickness is more uniform.

### CONCLUSIONS

1. Solid-state foaming by creep expansion at constant temperature of inert gas bubbles, as first demonstrated by Kearns et al. [1] in Ti-6Al-4V, was studied in both CP-Ti and Ti-6Al-4V. Foaming is more rapid and more extensive in CP-Ti than in Ti-6Al-4V below  $923^\circ\text{C}$ , because of the reduced creep strength and the increased pore spheroidization in CP-Ti.
2. We demonstrated that superplasticity can be used in both CP-Ti and Ti-6Al-4V (i) to accelerate the foaming kinetics, because of the reduced strength of superplastic materials, and (ii) to increase the maximum attainable porosity, because of the increased ductility of superplastic materials.
3. Microstructural superplasticity is impractical for foaming, because fine grains are difficult to produce in porous preforms without thermomechanical treatment, and impossible to maintain in CP-Ti because of rapid grain growth. We thus used transformation superplasticity which results from the biasing by a deviatoric stress (from the bubble pressure) of isotropic stresses

- (from the volume mismatch between allotropic phases produced during thermal cycling about the allotropic range).
4. While transformation superplasticity has been observed in bulk titanium and titanium alloys, the present study is, to the best of our knowledge, the first report of the application of this deformation mechanism to foaming of metals and to deformation of microscopic features (cell walls).

#### ACKNOWLEDGMENTS

The work summarized in this paper was performed at the Department of Materials Science and Engineering of the Massachusetts Institute of Technology where D.C.D. was the AMAX Associate Professor of Materials Engineering and J.T. was an Exchange Undergraduate Student. D.C.D. acknowledges the financial support AMAX in the form of a Endowed Career Development Chair.

#### REFERENCES

1. M.W. Kearns, P.A. Blenkinsop, A.C. Barber, and T.W. Farthing, *Intern. J. Powder Metall.* **24**, p. 59 (1988).
2. D.C. Dunand and S. Myojin, *Mater. Sci. Eng.* **230**, p. 25 (1997).
3. G.W. Greenwood and R.H. Johnson, *Proc. Roy. Soc. Lond.* **283A**, p. 403 (1965).
4. C. Chaix and A. Lasalmonie, *Res Mech.* **2**, p. 241 (1981).
5. D.C. Dunand and C.M. Bedell, *Acta Mater.* **44**, p. 1063 (1996).
6. N. Furushiro, H. Kuramoto, Y. Takayama, and S. Hori, *Trans. ISIJ* **27**, p. 725 (1987).
7. D. Leriche, E. Gautier, and A. Simon, in *Sixth World Conference on Titanium* (1988), p. 163.
8. T.G. Nieh, J. Wadsworth, and O.D. Sherby, *Superplasticity in Metals and Ceramics*, Cambridge, 1997, pp. 213-216.
9. D.C. Dunand, in *International Conference on Thermomechanical Processing of Steels and Other Materials*, edited by T. Chandra and T. Sakai (TMS, Warrendale, 1997), p. 1821.
10. W. Szliniarz and G. Smolka, *J. Mater. Proc. Tech.* p. 413 (1995).
11. *Metals Handbook: Metallography and Microstructures*, ASM, Metals Park, OH, 1985, pp. 464-468.
12. H.J. Frost and M.F. Ashby, *Deformation-Mechanism Maps: The Plasticity and Creep of Metals and Ceramics*, Pergamon Press, 1982, p. 44.

---

## ELASTIC PROPERTIES OF LOW DENSITY CORE (LDC) Ti-6Al-4V SANDWICH CORES

D. T. QUEHEILLALT, H. N. G. WADLEY, D. S. SCHWARTZ<sup>†</sup>

IPM Laboratory, University of Virginia, Charlottesville, VA 22903, dtq2j@virginia.edu

<sup>†</sup>The Boeing Company, St. Louis, MO 63166-0516

### ABSTRACT

Lightweight, structurally efficient low density core (LDC) sandwich structures can be produced by entrapping argon gas within a finely dispersed distribution of pores in a microstructure and using a high temperature anneal to cause pore growth by gas expansion. This results in a porous microstructure with a relative density as low as ~0.70. Laser ultrasonic methods have been used to measure the longitudinal and shear wave velocities and hence the elastic properties of LDC Ti-6Al-4V cores prior to, and after gas expansion treatments of up to 48 hr at 920°C. The data was compared with several analytical models for predicting the volume fraction of porosity dependent elastic properties of porous materials.

### INTRODUCTION

Cellular or foamed solids made from polymers, ceramics or metals possess combinations of electrical, mechanical and thermal properties that ideally suit them to a growing list of applications. For example, their high energy absorption characteristics make them well suited to absorbing the energy of impacts, their good acoustic damping characteristics result in excellent sound control, the high thermal insulation behavior of closed cell foams suits them to fire resistance applications, the very high surface area of open cell foams makes them ideal heat transfer structures and their high specific moduli and strengths make them well suited for numerous lightweight aerospace structures [1].

Lightweight metal sandwich structures (typically consisting of a honeycomb glued, brazed or diffusion bonded between two face sheets) are more structurally efficient than semi-monocoque, stringer-stiffened plates and shells [2,3]. However, honeycomb structures of this construction have infrequently found applications in primary load-carrying structures, due to their high manufacturing costs. An interest has therefore developed in new processing technologies for the low cost manufacture of structurally efficient low density cored sandwich structures. Many approaches are currently used to make ultralight metal foams [4-8]. Here, we explore an extension of a novel powder metallurgy (P/M) technique first proposed by Kearns et al. [7] and Martin et al. [8] for the production of lightweight porous cored metal sandwich structures.

Low density core (LDC) sandwich structures can be produced by starting with a Ti-6Al-4V powder compact in a Ti-6Al-4V canister. The powder compact is hot vacuum outgassed, pre-preserved with argon (to a pressure between 2 and 7 atm.) and consolidated by hot isostatic pressing (HIPing). The HIP can strongly diffusion bonds to the porous core resulting in an integrally bonded structure. These consolidated samples are then hot-forged and/or hot-rolled to create a plate consisting of a core with finely dispersed distribution of pores containing high pressure argon gas and thin, fully dense face sheets. The small pores in these as-processed structures can then be reexpanded using a high temperature annealing cycle in which the hydrostatic pressure of the entrapped argon gas induces flow of the matrix material. This process results in a low density (40 - 50% porosity) porous cored sandwich structure with an overall relative density of about 0.7.

At the present time, little is known about the relationships between the expansion process, the resulting distribution and morphologies of the pores sizes and the elastic properties of these LDC structures. Here we use a laser ultrasonic (LU) technique to measure the longitudinal and shear wave velocities and hence the elastic moduli of LDC Ti-6Al-4V in the as-processed state and after expansion treatments of up to 48 hrs at 920°C. The porosity content and morphologies were evaluated and the laser ultrasonically determined elastic properties were compared with an analytical model for the pore volume fraction dependence of the elastic properties.

## BACKGROUND

The propagation of high frequency elastic waves (ultrasound) in isotropic polycrystalline bodies is directly related to the (dynamic) elastic moduli of the body. The linear elastic behavior of isotropic bodies can be fully described by two independent elastic stiffness constants [9]. In the long wavelength limit, the longitudinal ( $v_l$ ) and shear ( $v_s$ ) wave velocities can be expressed in terms of the low frequency limit (static) elastic constants and the density:

$$v_l = \sqrt{\frac{K + (4/3)G}{\rho}}, \quad (1)$$

$$v_s = \sqrt{\frac{G}{\rho}}. \quad (2)$$

where  $K$  is the bulk modulus,  $G$  is the shear modulus and  $\rho$  is the density. Both elastic moduli can be determined from measurement of the longitudinal and shear wave velocities provided  $\rho$  is known. Once two of the elastic constants of an isotropic body are known, other elastic constants such as Young's modulus ( $E$ ) and Poisson's ratio ( $\nu$ ), can be evaluated from well known analytical relationships (i.e.  $E = 9KG/(3K + G)$  and  $\nu = E/2G - 1$ ) [10].

The elastic moduli of bodies are dependent on the volume fraction of porosity ( $V_p$ ) within the body. A number of analytical models for the dependence, upon relative density ( $\rho^*/\rho_0 = 1 - V_p$ ), of the elastic moduli have been developed [11]. Many of these models were originally developed for two-solid phase systems and adapted to porous materials by assuming the density and elastic stiffness of the second phase tends to zero. Budiansky [12] used a self consistent approach to analyze a body containing randomly distributed spherical pores. In his model, the porosity dependence of the bulk modulus ( $K$ ) and the shear modulus ( $G$ ) are represented by

$$K = K_0 \left[ 1 - \frac{3V_p(1-\nu)}{2(1-\nu)} \right] \quad (3)$$

$$G = G_0 \left[ 1 - 15V_p \left( \frac{1-\nu}{7-5\nu} \right) \right] \quad (4)$$

where:  $\nu = \nu_0(1 - V_p)$ , and  $K_0$  and  $G_0$  are the bulk and shear moduli and  $\nu_0$  is Poisson's ratio for the fully dense material. Typical properties for fully dense isotropic polycrystalline Ti-6Al-4V used were:  $K_0 = 120$  GPa,  $E_0 = 114$  GPa,  $G_0 = 42.5$  GPa,  $\nu_0 = 0.342$  and  $\rho_0 = 4.42$  g/cm<sup>3</sup> [13].

## EXPERIMENTAL

### Sample preparation

Porous Ti-6Al-4V cores produced by the LDC method were provided by the Boeing Company (St. Louis, MO) for characterization of the porosity dependent elastic properties. A Ti-6Al-4V HIP canister had been filled with blended elemental (CP Ti and Al-V alloy) powders, vacuum outgassed and re-pressurized with 5 atm. of argon gas. The powder compact was HIPed at 1150°C for 4 hours at a pressure of ~103 MPa. The resultant structure was machined to remove the HIP canister leaving only the porous core. Samples were subsequently machined  $10 \times 10 \times 20 \text{ mm}^3$  and examined in the as-HIPed state and expanded at 920°C for 0.5, 1, 2, 4, 6, 12, 24, 36 and 48 hours. A vacuum of  $\sim 10^{-6}$  torr was established in the furnace chamber prior to annealing. The samples were heated at a rate of 10°C/min to 920°C, held for the proper time and furnace cooled. This resulted in samples with relative densities ranging from 0.70 to 0.98.

### Laser ultrasonic sensing

The ultrasonic time-of-flight (TOF) between precisely positioned source and receiver points was measured using a laser ultrasonic system. A ~10 ns duration *Q*-switched Nd:YAG laser pulse was used as the ultrasonic source. The energy per pulse was ~10 mJ and the roughly Gaussian beam of the multimode pulse was focused to an approximate circular spot of 1 mm diameter. Thus, the source power density was ~125 MW/cm<sup>2</sup>. In addition, a glass slide and propylene glycol couplant was used to enhance the acoustic signal strength [14].

The ultrasonic receiver was a Mach-Zehnder heterodyne laser interferometer, which responded to the sample's out-of-plane (normal) surface displacement associated with wavefront arrivals at the receiver point [15]. It was powered by a 5mW HeNe laser which produced a continuous Gaussian beam of 632.8 nm wavelength focused to a circular spot ~100 μm diameter. The interferometer had a displacement sensitivity of 0.4 Å/mV and exhibited linear output for displacements up to about 300 Å. For the experiments reported here, maximum surface displacements were on the order of 200 Å. The signal from the interferometer was bandpass filtered between 10 kHz and 10 MHz and recorded with a digital oscilloscope at 2 ns intervals using 8-bit analog-to-digital conversion. To improve the signal-to-noise ratio, each waveform used for a TOF measurement was the average of ~25 pulses collected at a pulse repetition rate of 20 Hz. A fast photodiode identified the origination time for the ultrasonic signals.

## RESULTS AND DISCUSSION

### Elastic properties

The longitudinal ( $v_l$ ) and shear ( $v_s$ ) wave velocities were evaluated by dividing the known ultrasonic propagation distance by the respective time-of-flight ( $\text{TOF}_l$ ,  $\text{TOF}_s$ ). Measurements were made in several directions and the relative differences in the velocity measurements were less than ±1%. Therefore, the velocities and subsequent elastic properties are assumed to be isotropic in nature. Figure 1 shows the measured longitudinal wave, Fig. 1a, and shear wave, Fig. 1b, velocity data and the relative density of each corresponding sample. The laser ultrasonic data indicates a decrease in both the longitudinal and shear wave velocities with decreasing relative density. Also shown in Fig. 1 is the density dependent longitudinal and shear wave velocities for porous Ti-6Al-4V evaluated from Eqn. (1) - (4) and the measured density. Both the longitudinal and shear wave velocity data are in good agreement with the Budiansky model.

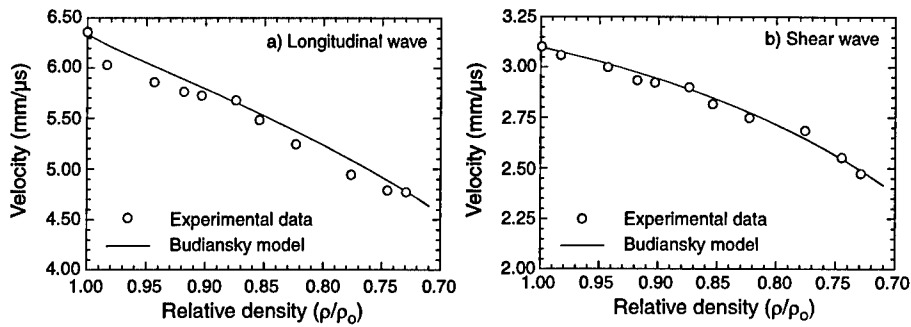


Figure 1 Experimentally determined longitudinal (a) and shear wave (b) velocities as a function of density together with Budiansky's model prediction for Ti-6Al-4V porous cores.

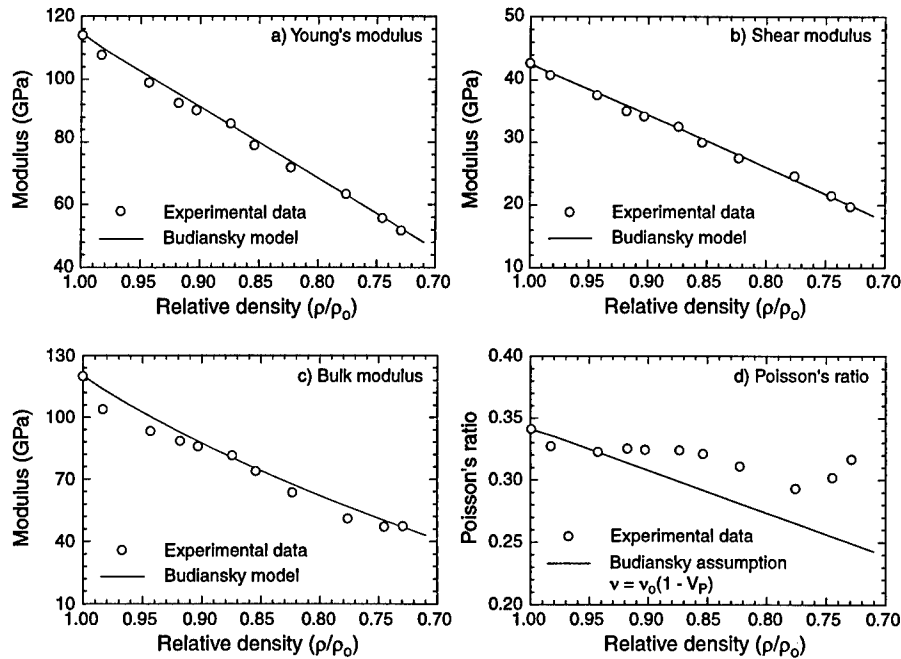


Figure 2 Experimentally determined and model predicted elastic properties for a) Young's modulus ( $E$ ), b) the shear modulus ( $G$ ), c) the bulk modulus ( $K$ ), and d) Poisson's ratio ( $\nu$ ) as a function of relative density for Ti-6Al-4V porous cores.

Figure 2 shows the experimentally determined Young's modulus (E), the shear modulus (G), the bulk modulus (K), and Poisson's ratio ( $\nu$ ) along with the model predicted density dependence for porous Ti-6Al-4V, evaluated from Eqn. (3) and (4). The laser ultrasonically determined moduli exhibited a decrease with decreasing relative density. However, Poisson's ratio exhibited little or no dependence on the relative density. Budiansky's model shows excellent agreement with the data for E, G, and K. Figure 2d shows Poisson's ratio and Budiansky's assumption  $\nu = \nu_0(1 - V_p)$  where  $\nu_0$  is Poisson's ratio for fully dense Ti-6Al-4V and  $V_p$  is the volume fraction of porosity. The variability between the experimental data are not that surprising, since  $\nu$  is a small quantity dependent on the differences of the other elastic properties and hence quite sensitive to small deviations in them [11].

#### Microstructural analysis

Figure 3 shows scanning electron micrographs for the as-HIPed and annealed at 920°C for 24 hours. The as-rolled microstructure, Fig. 3a, shows a relatively uniform distribution of pores of varying sizes and morphologies. Although a majority of the pores were spherical in nature with an average diameter of  $\sim 1 - 5 \mu\text{m}$ , some of the pores had large aspect ratios, up to 3:1, with random orientations. The  $\alpha$ -phase average grain size was measured using a modified Hilliard circle technique for duplex microstructures. The microstructure consisted of primarily equiaxed  $\alpha$ -phase grains, 10  $\mu\text{m}$  diameter, with a fine dispersion of  $\beta$ -phase at the grain boundaries and an intergranular Widmånstatten structure. The microstructure after annealing at 920°C for 24 hr, Fig. 3b, shows a wide distribution of pore sizes and morphologies,  $\sim 1 - 20 \mu\text{m}$  in diameter. The microstructure consisted of primarily equiaxed  $\alpha$ -phase grains, 20  $\mu\text{m}$  diameter, with a fine dispersion of  $\beta$  colonies primarily at the grain boundaries.

Standard X-ray diffraction (XRD) patterns were acquired using a SCINTAG Inc. XDS 2000 (Cupertino, CA) X-ray diffractometer. Ti-6Al-4V (PREP) powder, -140 MESH, from Crucible Materials Inc. (Concord, MA) was used to obtain a diffraction pattern for a random oriented powder sample. The X-ray diffraction patterns indicate both the as-HIPed and the expanded microstructures were similar in nature with the random oriented powder sample. Consistent with no preferred grain orientation or texture evolution during processing.

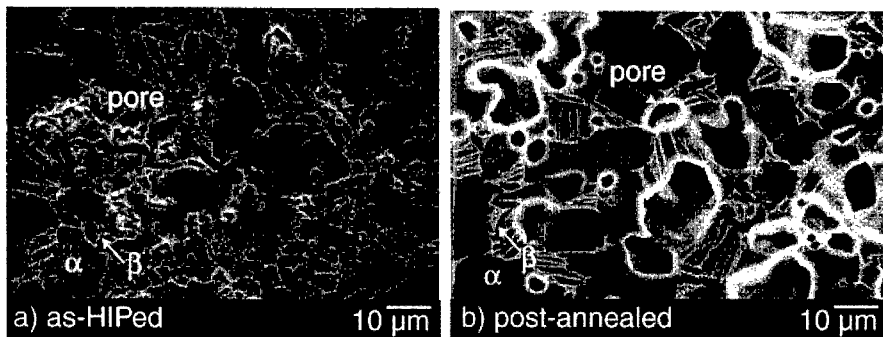


Figure 3 Scanning electron micrographs of typical cross sections of a) the as-HIPed and b) the annealed at 920°C for 24 hr microstructures.

## CONCLUSIONS

A laser ultrasonic technique has been used to measure the longitudinal and shear wave velocities and hence the elastic properties of LDC Ti-6Al-4V in the as-rolled state and after expansion at 920°C for up to 48 hours. The pore content and their morphologies were evaluated metallographically and the laser ultrasonically determined elastic properties (E, K, G and  $\nu$ ) were successfully compared with Budiansky's model for the pore volume fraction dependence of the elastic properties. Therefore, by using a combination of laser ultrasonically determined elastic properties and pore volume fraction dependent models, one can accurately predict the elastic properties of these porous cores as a function of the relative density aiding in the development of lightweight structurally efficient sandwich structures.

## ACKNOWLEDGEMENTS

This work has been performed as part of the research of the Multidisciplinary University Research Initiative (MURI) program on Ultralight Metal Structures conducted by a consortium of Universities consisting of Harvard University, the Massachusetts Institute of Technology, the University of Virginia and Cambridge University led by Anthony Evans of Harvard University. We are grateful for the many helpful discussions with our colleagues in these organizations. The consortium's work has been supported by DARPA/DSO under contract N00014-96-I-1028 monitored by Steve Wax (DARPA) and Steve Fishman of the Office of Naval Research.

## REFERENCES

1. L. J. Gibson and M. F. Ashby, *Cellular Solids: Structure and Properties*, 2nd Ed. (Cambridge University Press, Cambridge, UK 1997).
2. M. F. Ashby, *Materials Selection in Mechanical Design*, (Pergamon, Oxford 1992).
3. F. R. Shanley, *Weight-Strength Analysis of Aircraft Structures*, (Dover, New York 1960).
4. S. Akiyama, H. Ueno, K. Imagawa, A. Akira, S. Nagata, K. Morimoto, T. Nishikawa and M. Itoh, U.S. Patent No. 4,713,277 (15 December 1987).
5. J. Baumeister and H. Schrader, U.S. Patent No. 5,151,246 (29 September 1992).
6. V. I. Shapovalov and A. G. Timchenko, *Fizika Metall.* **76** 335 (1993).
7. M. W. Kearns, P. A. Blenkinsop, A. C. Barber and T. W. Farthing, *Proceeding of the Sixth World Conference on Titanium*, (Cannes, France, 1988) pp. 667-672.
8. R. L. Martin and R. J. Lederich, *Advances in Powder Metallurgy: Proceeding of the 1991 Powder Metallurgy Conference and Exposition*, (Powder Metallurgy Industries Federation, Princeton, 1991) pp. 361-370.
9. B. A. Auld, *Acoustic Fields and Waves in Solids*, (Kreiger, Malabar, FL 1990).
10. R. L. Bisplinghoff, J. W. Mar and T. H. H. Pian, *Statics of Deformable Solids*, (Dover, New York 1965).
11. R. W. Rice, *Treatise on Materials Science and Technology*, Vol. 11, edited by R. K. MacCrone, (Academic Press, New York 1977).
12. B. Budiansky, *J. Mech. Phys. Solids* **13** 223 (1965).
13. *Metals Handbook*, Vol. 2, *Properties and Selection: Nonferrous Alloys and Special-Purpose Materials*, (ASM International, Metals Park, OH 1990).
14. C. B. Scruby and L. E. Drain, *Laser Ultrasonics: Techniques and Applications*, (Hilger, New York 1990).
15. J. P. Monchalán, *IEEE Trans. Ultrason. Ferroelectr. Freq. Control*, **UFFC-33** (5) 485 (1986).
16. G. F. Vander Voort, *Metallography: Principles and Practice*, (McGraw-Hill, New York 1984).

---

## IN-SITU SENSING OF THE EXPANSION OF LOW DENSITY CORE (LDC) Ti-6Al-4V SANDWICH STRUCTURES

D. T. QUEHEILLALT, B. W. CHOI, H. N. G. WADLEY, D. S. SCHWARTZ<sup>†</sup>

IPM Laboratory, University of Virginia, Charlottesville, VA 22903, dtq2j@virginia.edu

<sup>†</sup>The Boeing Company, St. Louis, MO 63166-0516

### ABSTRACT

A combination multifrequency eddy current and laser ultrasonic sensors have been used to measure the pore expansion kinetics and elastic moduli evolution during the annealing of low density core (LDC) Ti-6Al-4V sandwich structures. The LDC samples were heated to 920°C and held there for up to 12 hr. The eddy current sensor measured the sample thickness (i.e. relative density) and revealed that the samples began to expand early during heating and was nearly complete after 4 hr at 920°C. The laser ultrasonic sensor measurements indicated a concomitant decrease in the elastic moduli with the reduction in relative density. The combination of an eddy current and laser ultrasonic sensor is therefore able to measure both the density and the elastic moduli independently during the annealing stage of LDC Ti-6Al-4V sandwich structure processing providing a simple method for directly controlling the parameters most critical to aerospace applications of these new materials.

### INTRODUCTION

Many approaches have been developed to manufacture ultralight metal foams [1-5]. Here, we explore an extension of a novel powder metallurgy technique first proposed by Kearns et al. [4] and Martin et al. [5] for the production of low density core (LDC) Ti-6Al-4V sandwich structures. During the manufacture of these sandwich structures, high pressure argon gas is entrapped in a finely dispersed distribution of pores. These structures are expanded via a high temperature annealing cycle in which the hydrostatic pressure of the entrapped argon gas overcomes the flow stress of the matrix resulting in a porous cored structure. The relative density and elastic properties are both directly governed by the porous core structure, and before this new class of materials can be introduced into service, methods need to be developed for their control.

Intelligent Processing of Materials (IPM) methodologies based upon process simulation, and sensor-based control are beginning to be used for controlling the processing of many high performance materials [6]. IPM process simulation seeks to combine process models for a material's response to processing stimuli (e.g. pressure, temperature, etc.) with characteristics of the process equipment to predict the evolution of a materials performance defining microstructure/composition variables. When appropriate non-invasive sensors are used to measure key attributes of the material (i.e. phase content, grain size, pore content, etc.) during the process, IPM controllers can be used to execute novel model-based feedback control schemes that result in materials with goal state combinations of properties [7,8].

At the present time, little is known about the kinetics of the expansion process or the relations between the distribution and morphology of pores and the elastic properties of these LDC structures. Here, we show that the expansion kinetics and the elastic properties can be measured using a combination of eddy current and laser ultrasonic sensors. By using this pair of sensors, the physical expansion and the time-of-flight of ultrasonic waves can be simultaneously measured. The expansion and time-of-flight (TOF) data can be analyzed to independently determine the density and elastic moduli during the annealing of LDC Ti-6Al-4V sandwich structures.

## EXPERIMENTAL PROCEDURES

### Eddy current sensing

Eddy current (EC) sensors are based upon the electromagnetic induction of (eddy) currents in conducting samples. Since the magnitude of the currents depends on the distance from the source of the electromagnetic field, EC sensors can be used to measure the distance between the (known) location of a sensor and the sample surface [9]. The high temperature sensor design used here was based on a pair of spirally wound, 30 AWG platinum primary (driving) and secondary (pickup) coils [10]. In order to avoid changes in the sensor's response upon heating/cooling, grooves (the same size as the wire diameter) were machined at the bottom end of two alumina disks to constrain the movement of these coils. The eddy current sensor components were assembled in an alumina housing and retained securely in place with a ceramic threaded locking ring, Fig. 1. A small hole (3mm) was drilled through the center of each sensor to allow laser access to the sample.

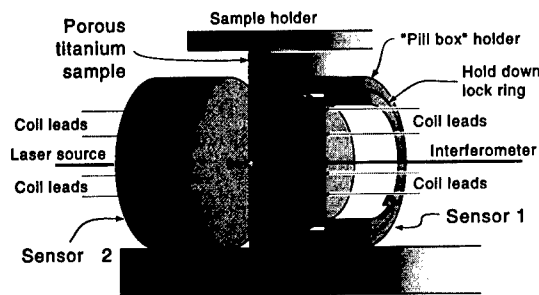


Figure 1 A schematic of the cross-sectional view of the probe type eddy current and laser ultrasonic sensor.

Multifrequency impedance measurements were performed using an impedance/gain-phase analyzer. A RF power amplifier was used to increase the primary current and thus to enhance the voltage signal monitored across a  $1\Omega$  precision resistor in the primary test circuit. An attenuator was used in the line to the test channel to prevent overloading of the secondary coil signal. The multifrequency measurement was automated via a personal computer in conjunction with a program installed in the impedance analyzer. The program on the analyzer recorded test and reference channel voltages for 51 logarithmically spaced frequencies between 50 kHz and 5 MHz. It then calculated the gain and phase angle difference and the normalized impedance components at each frequency.

### Laser ultrasonic sensing

The ultrasonic TOF's between precisely positioned source and receiver points was measured using a laser ultrasonic system [11]. A  $\sim 10$  ns duration  $Q$ -switched Nd:YAG laser pulse was used as the ultrasonic source. The energy per pulse was  $\sim 10$  mJ and the roughly Gaussian beam of the multimode pulse was focused to an approximate circular spot of 1 mm diameter. The source power density was  $\sim 125$  MW/cm<sup>2</sup>.

The ultrasonic receiver was a Mach-Zehnder heterodyne laser interferometer which responded to the out-of-plane (normal) surface displacement associated with wavefront arrivals [12]. It was powered by a 5 mW HeNe laser which produced a 632.8-nm wavelength continuous Gaussian beam focused to a circular spot  $\sim 100$   $\mu$ m in diameter. The signal from the interferometer was bandpass filtered between 10 kHz and 10 MHz and recorded with a precision digital oscilloscope at a 2 ns sampling interval using 8-bit analog-to-digital conversion. To improve the signal-to-noise ratio average waveforms from  $\sim 10$  pulses (with a pulse repetition rate of 20 Hz were collected). A fast photodiode identified the origination time for the ultrasonic signals.

### Sample preparation and test methodology

Low density core Ti-6Al-4V sandwich panels were prepared by the Boeing Company, St. Louis, MO. A Ti-6Al-4V HIP canister was filled with Ti-6Al-4V PREP powder. The can was hot vacuum outgassed and pressurized with 3 atm. (0.3 MPa) argon. The gas charged powder compact was HIPed at 1040°C for 6 hours at a pressure of 103 MPa. After HIPing, the sample was hot-rolled in air at 900°C to a final thickness of ~3.3 mm. The rolling process typically consisted of 40 cross-rolled passes. This process resulted in relatively uniform structure with integrally bonded solid face sheets that were  $300 \pm 10 \mu\text{m}$  thick.

Rectangular ( $3 \times 5 \text{ cm}^2$ ) samples were machined from the sandwich structure for the expansion tests. The samples were lightly ground on both sides to remove oxide scale. One surface was diamond polished to a  $6 \mu\text{m}$  finish to create a reflective surface for the laser interferometer. The samples were then ultrasonically cleaned, placed in the eddy current/laser ultrasonic sensor and the entire assembly inserted into a tube furnace. A vacuum of  $\sim 10^{-6}$  torr was established in the chamber and the temperature was brought up to 100°C and held for 12 hours to drive off residual water entrapped in the sample or sensor. The samples were then heated at a rate of 10°C/min. to 920°C, and held for ~12 hr at this temperature and furnace cooled.

## RESULTS AND ANALYSIS

### Eddy current sensing

Figure 2 shows the samples expansion (a) and the concomitant density decrease (b) as a function of process time. It is clear that expansion began during the heating phase of the cycle and continued during the anneal cycle. It appears that after ~4 hr most of the expansion rate was close to zero. Two expansion tests were conducted, and both sets of data were in good agreement. Also shown in Fig. 2a is the relative contribution due to the temperature dependent coefficient of linear thermal expansion to the samples total expansion [13]. It is clear that the coefficient of linear thermal expansion contribution was small compared with the samples total expansion. Figure 2b shows the density as a function of process time calculated from the expansion data. Also shown in Fig. 2b is the relative decrease in density calculated from the temperature dependent coefficient of thermal expansion. The as-rolled sample had an initial density (face sheets + porous core) of  $4.32 \text{ g/cm}^3$  (~0.98 relative density). After the annealing cycle the overall density was  $\sim 3.60 \text{ g/cm}^3$  (a relative density of 0.83).

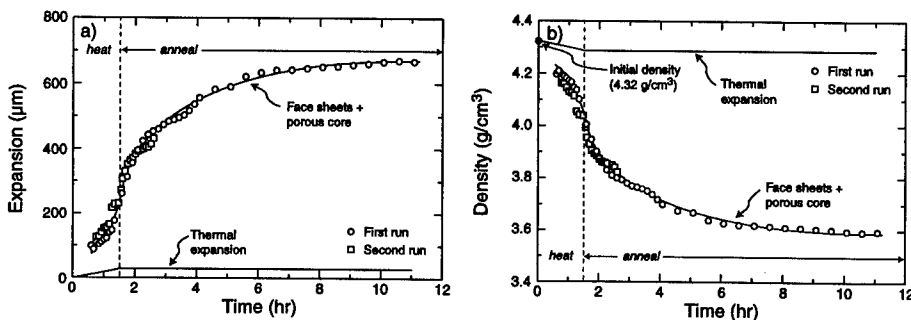


Figure 2 Eddy current response for a) the expansion and b) the density evolution during expansion of Ti-6Al-4V LDC sandwich structures.

### Laser ultrasonic sensing

Figure 3 shows the evolution of the time-of-flight for the longitudinal (a) and shear (b) waves as a function of process time. Like the eddy current data of Fig. 2, the longitudinal and shear wave TOF's began to increase during heating and continued to increase during the anneal for about 3 hours. The TOF data for both expansion tests show good agreement with each other. Also shown in Fig. 3 is the relative contribution of the face sheets to the total TOF. The increase in TOF is a result of three processes; the temperature dependent softening of the elastic moduli, the density dependent velocity of ultrasound and the pore volume fraction dependence of the elastic moduli.

The longitudinal and shear wave velocities (not shown here) were calculated by dividing the samples thickness (Fig. 2a) by the TOF data (Fig. 3). Once the ultrasonic velocities and the density were known, the elastic moduli could be evaluated. Figure 4 shows the evolution of the Young's (Fig. 4a) and shear (Fig. 4b) moduli as a function of process time. Again there was a decrease in both the Young's and the shear moduli during heating and this continued during the anneal. The temperature dependence of the elastic moduli for fully dense Ti-6Al-4V was previously determined [14]. Figure 4 shows the contribution of the temperature dependent moduli to the total moduli decrease. It is clear that the temperature dependent softening of the elastic moduli contributes a significant portion to the overall decrease in elastic moduli.

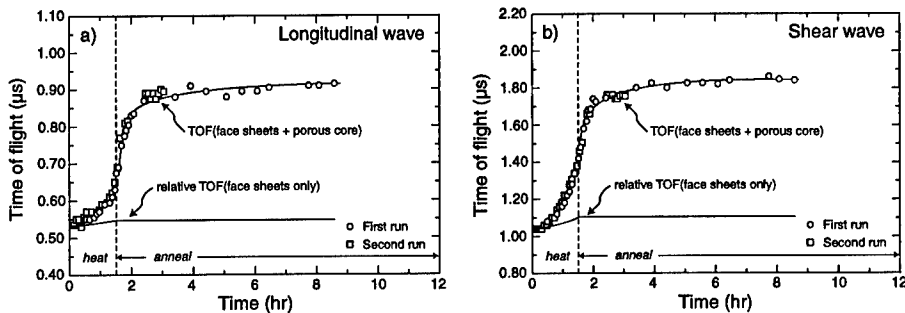


Figure 3 Laser ultrasonic response for the longitudinal and the shear wave time-of-flight evolution during expansion of Ti-6Al-4V LDC sandwich structures.

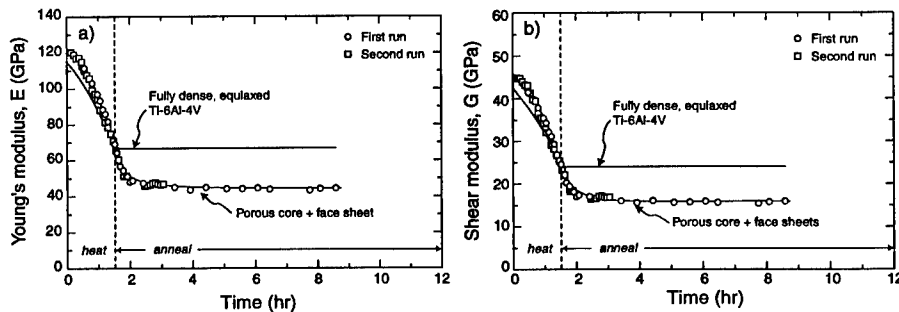


Figure 4 The a) Young's modulus (E) and b) shear modulus (G) evolution calculated from the eddy current measured expansion and the laser ultrasonically measured longitudinal and shear wave velocity data.

### Microstructural and XRD analysis

Figure 5 shows scanning electron micrographs of the as-rolled and post-annealed microstructures. In the as-rolled sample, Fig. 5a, the heavily deformed microstructure was fine grained (lamellar spacing:  $\alpha$ -phase  $\sim 5 \mu\text{m}$ ,  $\beta$ -phase  $< 5 \mu\text{m}$ ) and contained pores with pore sizes ranging from 1 to 50  $\mu\text{m}$  and morphologies that varied from spherical to pancake shaped; the latter predominantly elongated in the rolling plane. In the expanded sample, Fig. 5b, the microstructure had recrystallized to a fine (11  $\mu\text{m}$  diameter) equiaxed structure with a relatively uniform distribution of semi-spherical pores ranging from 5 to 200  $\mu\text{m}$  in diameter.

Figure 6 shows X-ray diffraction (XRD) patterns for a) randomly oriented Ti-6Al-4V powder and b) the post-annealed microstructure (normal to the rolling plane). Ti-6Al-4V PREP powder (-140 MESH) was used to obtain a diffraction pattern for the random oriented powder sample. The XRD pattern of Fig. 6b shows an increase in the relative amounts of the basal (0002) peak of the h.c.p.  $\alpha$ -phase, indicating some degree of preferred grain orientation (texture) with respect to the powder sample, Fig. 6a. The cross-rolling of Ti-6Al-4V tends to align the basal (0002) or "c" axis of the  $\alpha$ -phase normal to the rolling plane resulting in an elastically anisotropic structure due to the fact that Young's modulus parallel to the "c" axis ( $E_{33} = \sim 145 \text{ GPa}$ ) is larger than Young's modulus perpendicular to the "c" axis ( $E_{11} = \sim 100 \text{ GPa}$ ) [15,16]. This anisotropic affect can be seen during the early heating stage of Fig. 4.

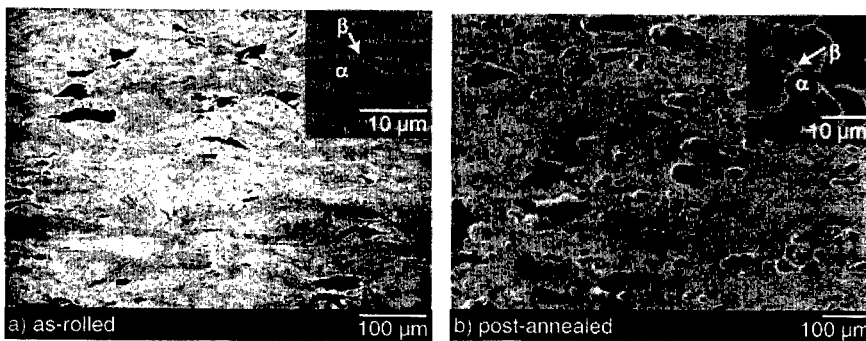


Figure 5 Scanning electron micrographs of the cross section of a) the as-rolled microstructure and b) the post-annealed microstructure of Ti-6Al-4V LDC sandwich structures. High magnification micrographs of the  $\alpha/\beta$  structure are shown in the inserts.

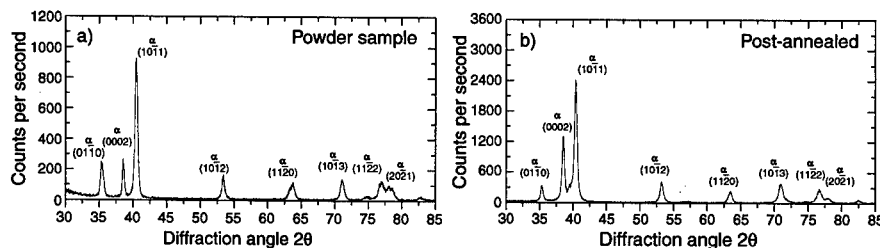


Figure 6 X-ray diffraction (XRD) patterns for a) Ti-6Al-4V random powder and b) the post annealed microstructure.

## CONCLUSIONS

Eddy current and laser ultrasonic sensors have been used to independently measure the density and the elastic moduli (E and G) as a function of time during the expansion of low density core (LDC) Ti-6Al-4V sandwich structures. It was found that the initial LDC structure began to expand during heating, went through a maximum rate at  $\sim 685^{\circ}\text{C}$  and was nearly complete after a four hour hold at  $920^{\circ}\text{C}$ . During expansion there was also a concomitant decrease in the elastic moduli that correlated directly with the evolution of the porous microstructure. These results provide a good starting point for the development of a micro-mechanics based model for predicting the expansion kinetics of LDC Ti-6Al-4V sandwich structures and design of a furnace control system for the expansion step of the LDC process.

## ACKNOWLEDGEMENTS

This work has been performed as part of the research of the Multidisciplinary University Research Initiative (MURI) program on Ultralight Metal Structures conducted by a consortium of Universities consisting of Harvard University, the Massachusetts Institute of Technology, the University of Virginia and Cambridge University led by Anthony Evans of Harvard University. We are grateful for the many helpful discussions with our colleagues in these organizations. The consortium's work has been supported by DARPA/DSO under contract N00014-96-I-1028 monitored by Steve Wax (DARPA) and Steve Fishman (ONR).

## REFERENCES

1. S. Akiyama, H. Ueno, K. Imagawa, A. Akira, S. Nagata, K. Morimoto, T. Nishikawa and M. Itoh, U.S. Patent No. 4,713,277 (15 December 1987).
2. J. Baumeister and H. Schrader, U.S. Patent No. 5,151,246 (29 September 1992).
3. V. I. Shapovalov and A. G. Timchenko, *Fizika Metall.* **76** 335 (1993).
4. M. W. Kearns, P. A. Blenkinsop, A. C. Barber and T. W. Farthing, *Proceeding of the Sixth World Conference on Titanium*, (Cannes, France, 1988) pp. 667-672.
5. R. L. Martin and R. J. Lederich, *Advances in Powder Metallurgy: Proceeding of the 1991 Powder Metallurgy Conference and Exposition*, (Powder Metallurgy Industries Federation, Princeton, 1991) pp. 361-370.
6. H. N. G. Wadley and R. Vancheeswaran, *JOM* **50** (1) 19 (1998).
7. D. G. Meyer and H. N. G. Wadley, *Metall. Trans. B* **24**, 289 (1989).
8. R. Vancheeswaran, D. G. Meyer and H. N. G. Wadley, *Acta Mater.* **45** (10) 4001 (1997).
9. K. P. Dharmasena and H. N. G. Wadley, *Rev. Prog. QNDE*, edited by D. O. Thompson and D. E. Chimenti (Plenum Press, New York, 1991) pp. 1111-1118.
10. H. L. Libby, *Introduction to Electromagnetic Nondestructive Test Methods*, (Wiley, New York, 1971).
11. C. B. Scruby and L. E. Drain, *Laser Ultrasonics: Techniques and Applications*, (Hilger, New York 1990).
12. J. P. Monchalain, *IEEE Trans. Ultrason. Ferroelectr. Freq. Control* **UFFC-33** (5), 485 (1986).
13. Y. S. Touloukian, R. K. Kirby, R. E. Taylor and T. Y. R. Lee, *Thermophysical Properties of Matter: Thermal Expansion of Non Metallic Solids*, **12**, (IFI/Plenum, New York, 1975).
14. D.T. Queheillalt, B.W. Choi, R. Vancheeswaran, H.N.G. Wadley, D. S. Schwartz, submitted *Acta Mater.* 1998.
15. E. W. Collings, *The Physical Metallurgy of Titanium Alloys*, (ASM, Metals Park, OH 1984).
16. H. M. Flower, *High Performance Materials in Aerospace*, (Chapman Hall, London, 1995).

---

## PROCESS MODELING OF Ti-6Al-4V SPM MATERIALS

S.S. Ahmed \*, G. Huang \*, H. Gegel \*, D. Barker \*\*

\*UES Software Inc., 4401 Dayton-Xenia Rd., Dayton, OH 45432, shatil@engineer.com

\*\* UES Inc., 4401 Dayton-Xenia Rd., Dayton, OH 45432

### ABSTRACT

Structural Porous Metals (SPM) was specifically designed to offer large weight reductions in structural applications. The pores of gas are incorporated into the SPM during hot isostatic pressing. Since the gas in the pores are at high pressure and are closed isolated pores, SPM can be processed by standard methods such as rolling or forging without collapsing the gas pores. The objective of this paper is to show that the combination of computer simulation and intrinsic workability modeling provide a rapid and cost-effective way, for understanding the process and selecting the process parameters. This paper explains how SPM material data and developed material density updating scheme can be used in conjunction with the existing theory and FEM model.

### INTRODUCTION

Process modeling for microstructure and shape optimization is required to achieve both engineering and manufacturing functional objectives. Since the rheological behavior of this new class of alloys is envisioned to have both plastic and fluid behavior, a new technique was developed that takes these two factors into account.

Development of a finite element method (FEM) forming simulation capability for Structural Porous Metal (SPM) was the goal of this research and to achieve it we had to understand the material behavior of this novel material under different processing conditions. The SPM is a sandwich material with low density core (LDC) material at the center and solid face sheets on two sides. Simulation of material flow for the face sheets is not difficult with the existing commercial FEM software, but to predict the flow behavior of LDC by using the FEM model was difficult due to the presence of high pressure gas pores. Unlike the traditional powder metallurgy (P/M) systems the densification is not unrestricted, but dependent on the internal gas pressure of the pores. Using this concept to account for the incompressibility of the gas contained in workpiece material, the current model of porous material in a commercial FEA package ANTARES[1] has been extended to be able to simulate material flow of SPM. This paper has used data from sub-scale rolling of SPM[2] and compression test data dependent on thermo-mechanical history[3] performed at the Air Force Research Laboratory (ARFL), Wright Patterson Air Force Base, OH.

In the process of implementing the SPM model into existing FEA application, Dynamic Material Model (DMM) Processing Map for Ti-6Al-4V SPM alloy was also developed. The processing map was developed for the purpose of defining the proper processing parameters of temperature and strain rate. DMM processing maps are very useful in explaining the process behavior and the simulation results. They define the stable processing range in processing space where the workpiece material is not sensitive to the temperature, effective strain-rate, and effective strain path, and the variance in microstructure parameters and mechanical properties is small and nearly constant. In addition, in the stable processing range the slope of the resulting mechanical properties with respect to temperature or effective strain-rate is very small.

## THEORY

The implementation of the SPM model in an existing FEA application is described in this section. The general constitutive equation in FEM formulation is given by:

$$\boldsymbol{\sigma}^* = 2\mu\dot{\boldsymbol{\epsilon}} + \mathbf{m}\lambda\mathbf{m}^T\dot{\boldsymbol{\epsilon}} \quad (1)$$

where  $\boldsymbol{\sigma}^*$  is the stress vector

$\dot{\boldsymbol{\epsilon}}$  is the strain rate vector

$\mathbf{m} = [1 \ 1 \ 1 \ 0 \ 0 \ 0]^T$  for 3D models

$\mathbf{m} = [1 \ 1 \ 1 \ 0]^T$  for 2D plane strain or axi-symmetric models

$\mu$  and  $\lambda$  are equivalent to Lamé's Constants for the linear elastic material, and will be functions of temperature, strain, strain rate, relative density and flow stress in general. From the existing general expression for the stresses induced in the powder material[4],  $\mu$  and  $\lambda$  can be given by:

$$\mu = \frac{Y_R}{2\dot{\epsilon}_p A} \quad (2)$$

$$\lambda = \frac{Y_R}{3\dot{\epsilon}_p (3-A)} \quad (3)$$

where  $Y_R$  is the yield stress which is dependent on relative density,  $\dot{\epsilon}_p$  is the effective strain rate, and  $A$  is a parameter dependent on Poisson's Ratio  $\nu$  which is again dependent on relative density  $R$ .  $A$  is given by:

$$A = 2(1+\nu) \quad (4)$$

The velocity field in the FEM is approximated as:

$$\mathbf{u} = \mathbf{N}^T \mathbf{v} \quad (5)$$

where  $\mathbf{v}$  is the nodal velocity and  $\mathbf{N}$  is the shape function matrix. By differentiating Eq.(5), it gives:

$$\dot{\boldsymbol{\epsilon}} = \mathbf{B}\mathbf{v} \quad (6)$$

where  $\mathbf{B}$  is the strain rate matrix. Therefore after substituting  $\dot{\boldsymbol{\epsilon}}$  from Eq.(6), Eq.(1) changes to:

$$\boldsymbol{\sigma}^* = (2\mu + \mathbf{m}\lambda\mathbf{m}^T)\mathbf{B}\mathbf{v} \quad (7)$$

To incorporate the SPM behavior into the above FEM model, it is assumed that the total stress for SPM will be additive of the general stress  $\boldsymbol{\sigma}^*$  and the pressure inside the pores. But initially the material is at equilibrium, so the stress due to pressure will be the change in pressure  $\Delta p$ .

$$\boldsymbol{\sigma} = \boldsymbol{\sigma}^* + \mathbf{m}\Delta p \quad (8)$$

If  $p_0$  and  $p$  are the initial and current gas pressure respectively then  $\Delta p$  can be written as:

$$\Delta p = -(p - p_0) \quad (9)$$

From the Ideal Gas Law:

$$\frac{p v_p}{T} = \frac{p_0 v_{p0}}{T_0} \quad (10)$$

where  $v_p$  and  $v_{p0}$  are the initial and current volume of pores and  $T$  and  $T_0$  are the initial and current temperatures. If  $R$  and  $R_0$  are the initial and current relative density and  $v$  and  $v_0$  are the total initial and current volumes, then volume of gas pores and total volume can be related by,

$$\frac{v_p}{v_{p0}} = \frac{(1-R)v}{(1-R_0)v_0} \quad (11)$$

Substituting the value of  $p$  from Eq.(10) and using the relation in Eq.(11), into Eq.(9), it gives:

$$\Delta p = -p_0 \left( \frac{(1-R)v_0 T}{(1-R_0)v T_0} - 1 \right) \quad (12)$$

Volumetric strain  $\varepsilon_v$  can be defined as:

$$\varepsilon_v = \ln \left( \frac{v}{v_0} \right) \quad (13)$$

Eq.(13) can be solved for  $v/v_0$  and substituted in Eq.(12) to give:

$$\Delta p = -p_0 \left( \frac{(1-R)T}{(1-R_0)T_0 e^{\varepsilon_v}} - 1 \right) \quad (14)$$

The general constitutive equation for SPM is thus developed from Eq.(14) and Eq.(8), as:

$$\sigma = \sigma^* - m p_0 \left( \frac{(1-R)T}{(1-R_0)T_0 e^{\varepsilon_v}} - 1 \right) \quad (15)$$

## SIMULATIONS AND RESULTS

Using the above explained theory, two finite element simulations were run. Their setup, results, and observations are discussed below.

### *Upsetting or Compression Simulation of LDC*

#### Setup

Upsetting or compression test results were available for Ti-6Al-4V on LDC material of the SPM specimens[3]. So to validate the simulation results a 2-dimensional axisymmetric model was created with matching experimental parameters, which are:

- Size: 0.252 in. diameter and 0.375 in. height
- Initial Temperature: 1382 F
- Initial Gas Pressure: 15ksi and 15000ksi
- Initial Relative Density: 91%
- Deformation Stroke: 0.1875 in

Shear Friction Coefficient : 0.0

Analysis Type: Stess ( mechanical )

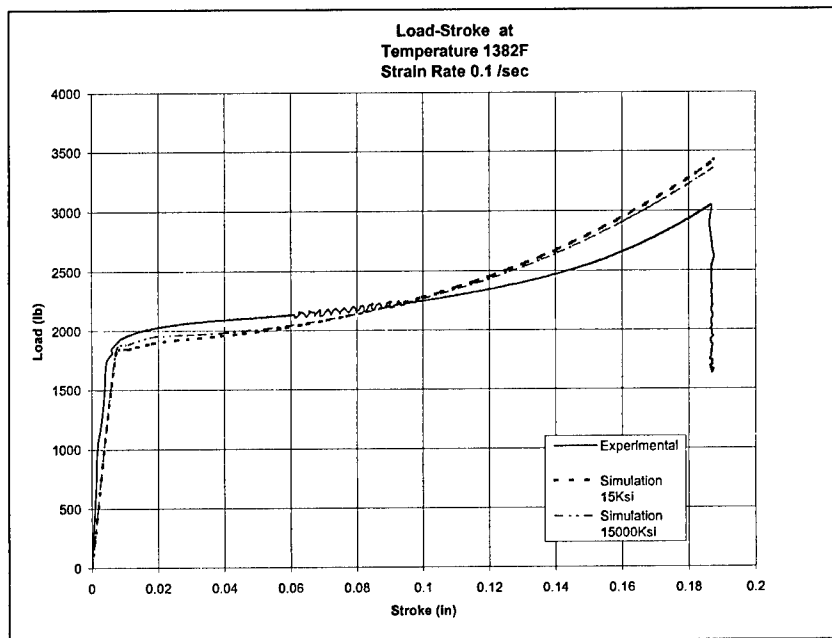
Ram Velocity:  $v_{ram} = \dot{\epsilon} l_0 e^{-\dot{\epsilon} t}$ , where  $\dot{\epsilon} = 0.1 \text{sec}^{-1}$ ,  $l_0 = 0.375 \text{in.}$ , and  $t$  is time in sec.

Exponential function is used for the ram velocity to model the constant strain rate  $0.1 \text{sec}^{-1}$  for the process. This was necessary as the experimental result was available for  $0.1 \text{sec}^{-1}$  strain rate.

### Results

The simulation result is compared with the load-stroke curve obtained from experimental data which is displayed in Figure.1.

Figure.1



### Observation and Discussion

Load-Stroke curves for experimental and simulation data in Figure.1 are within maximum 10% variation, which may be due to the fact that the simulation has used the relationship proposed by Zhadannovich[5] between the Poisson's Ratio  $\nu$  and relative density  $R$ , which states that:

$$\nu = 0.5R^n \quad (16)$$

The value of the exponent  $n$  has been experimentally determined as approximately 2 for aluminium and ferrous powders by Kuhn[6]. For modeling purpose  $n \cong 2$  was used for SPM, which is not yet experimentally verified.

To see the effect of internal pressure in the compressed billet, another simulation was run with internal gas pressure as 15000 ksi keeping all other parameters same as before and it was observed that the final relative density reduced from 97% to 95%. Which shows the usefulness of simulation in determining the effect of internal pressure on densification. The load curve also varied by initially going higher and then falling down (Figure.1). But as the initial relative density was already about 91% the variance is not that substantial, with lower initial relative density the variance increases.

### ***Rolling Simulation of SPM***

#### **Setup**

A 2-dimensional plane strain rolling model was setup with two phase material, to take into account the dense face sheet and LDC material. The roll speed and dimensions of workpiece and the rolls were matched with the sub-scale rolling of SPM performed at MPL[2].

- Thickness: 0.015 in. face sheet and 0.253 in. LDC
- Initial Temperature: 1562 F (workpiece), 75 F (roller)
- Initial Gas Pressure: 15000 psi
- Initial Relative Density: 91%
- Roll Diameter: 8 in
- Roll Speed: 33.4 rpm
- Roll Bite: 0.913 in
- Analysis Type: Coupled ( mechanical and thermal )

A Dynamic Material Model (DMM) Processing Map[6] was developed for Ti-6Al-4V SPM with 91% relative density to provide a framework for understanding the deformation process and this map is given in (Figure.2). This map was constructed from the material stability information, which is contained in a set of compression tests done as a function of constant temperature, constant effective strain-rate, and deformation time[3].

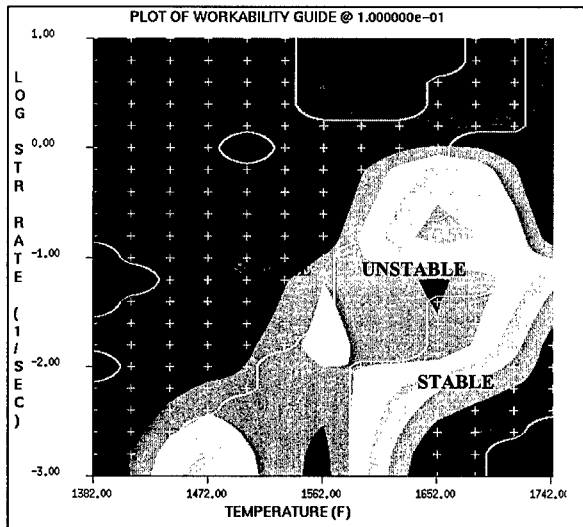


**Figure.2**  
DMM Processing Map  
for Ti-6Al-4V SPM 91%  
Relative Density

## Results

The rolling simulation results show the relative density contour (Figure.3) and the strain-rate contour (Figure.4) at certain time steps.

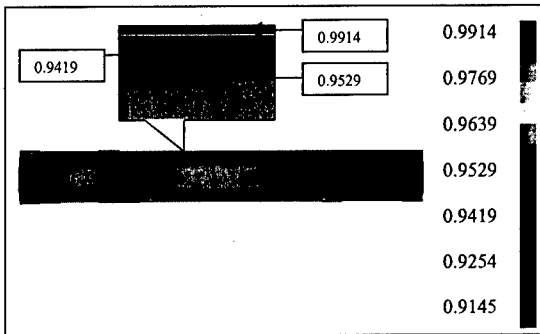


Figure.3  
Relative Density Contour at  
time 0.149 sec

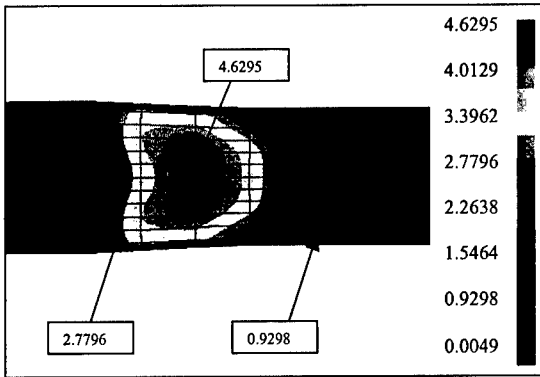


Figure.4  
Strain-Rate Contour ( $\text{sec}^{-1}$ )  
at time 0.1 sec

## Observation and Discussion

As mentioned above the initial parameters for the rolling simulation were chosen as per the actual sub-scale rolling of Ti-6Al-4V SPM [2]. From the results of the simulation it was found that the strain rate for the process was in the order of  $10^1 \text{ sec}^{-1}$ , the strain was about 0.1 and the temperature was in the range of 1562 F. Once these parameters are known from the simulation and based on the DMM map in (Figure.2), it is seen that the rolling process is being operated near the boundary of unstable processing conditions. This statement can also be rationalized by considering that the formation of gas blister while actual rolling was avoided with 91% Ti-6Al-4V because, it was necessary to establish a balance between the mechanical stability of the matrix material and the mechanical stability of the gas pores. To achieve this balance, the SPM material should be subjected to processing parameters, which cause the stability for the forming process to lie on the boundary of the stable region, where the deformation process is bimodal in the sense of stability. When the processing parameters of temperature and strain-rate lie on this

---

boundary, the flow stress of the continuous matrix material is approximately equal to the pressure in the gas pores, and this condition will result in a stable material flow process.

## CONCLUSION

The theory of incorporating the SPM material flow in an existing FEM model was presented, and two simulation models with Ti-6Al-4V SPM as the workpiece material were discussed. In the compression model it was shown that the described theory for simulating LDC of SPM material conforms reasonably well with the experimental results, and the effect of internal pressure on load and relative density was also discussed. In the rolling model it was shown that with the aid of computer modeling along with a DMM processing map, the process parameters can be chosen such that processing difficulties of the SPM workpiece material can be avoided. Future research will concentrate on overcoming the difficulties of two phase automatic mesh generation so that the Finite Element Model can be extended to simulating 3-dimensional complex geometry. An empirical relationship has to be determined between the Poisson's Ratio, the relative density, and initial pressure.

## ACKNOWLEDGEMENTS

The authors would like to acknowledge support from McDonnell Douglas Aerospace(Boeing) and ARPA for support of this study through the cooperative agreement no. N00014-95-2-0007.

## REFERENCES

1. ANTARES™, Commercially available FEA Application for Bulk Forming, UES Software Inc., Dayton, Ohio.
2. D. Barker, UES Inc., (private communication), regarding Test Rolling of SPM cans at WPAFB, 1997.
3. D. Barker, UES Inc., (private communication), regarding Compression Testing of LDC at WPAFB, 1997.
4. A. Chaudhary, and S. Doraivelu, Processing Science Research to Develop Fundamental Analytical, Physical, and Material Modeling Techniques for Difficult-to-Process Materials, (Report No. WL-TR-91-4018 Materials Directorate, Wright Laboratory, WPAFB, Ohio, 1990) p. F-29
5. G.M. Zhadannovich, Theory of Compacting of Metal Powders, translated from Teoriz Pressovaniya Metzlichaskikli Poroshkov, by the Foreign Technology Division, WPAFB, Ohio. U.S.A. (Translation No. FTD-HC-23-775-70, June, 1971), p. 1-262.
6. H.A. Kuhn, Deformation Process of Sintered Powder Metal, Powder Metallurgy Processing: New Techniques and Analysis, (Academic Press, New York, 1978), p. 99.
7. H.L. Gegel, Synthesis of Atomistics and Continuum Modeling, edited by R.J. Arsenault, J.R. Beeler, Jr., and D.M. Esterling, (Computer Simulation in Material Science, ASM International, 1988), p.291-344.

---

## THE INFLUENCE OF INTERNAL PORE PRESSURE DURING ROLL FORMING OF STRUCTURALLY POROUS METALS

D.M. ELZEY, H.N.G. WADLEY

Department of Materials Science and Engineering, University of Virginia, Charlottesville, VA 22903

### ABSTRACT

Structurally porous metal sandwich panels consisting of dense face sheets and porous cores of controlled relative density can be manufactured by trapping inert gas during hot isostatic pressing and modifying its distribution via subsequent thermo-mechanical forming. At high pressures, the internal gas is expected to influence the forming response. This paper describes a model for the roll forming of a porous metal panel and its use to explore the effects of internal pore pressure upon rolling response. It is shown that for gas pressures below about half the yield strength of the fully dense matrix material, there is essentially no influence on the forming response. Only in the case of very high initial pore pressures or at relative densities approaching full theoretical does a noticeable effect arise. In this case, a limiting upper density is attainable which depends on the specific rolling conditions and geometry.

### INTRODUCTION

Lightweight sandwich panels consisting of honeycomb or porous cores bonded between stiff face sheets have high structural efficiency in applications where high bending and buckling resistance are needed, such as the wing skins and floor panels of aircraft, the hulls of some ships and high-performance skis [1]. Metallic sandwich panels, such as those obtained by bonding aluminum or titanium face sheets to a honeycomb core of the same alloy, may offer an alternative to conventional (polymer and polymer composite) sandwich panels for many applications, especially at elevated temperatures. However, the high cost of manufacturing these systems has limited their application and stimulated interest in the development of lower cost alternatives.

One approach to titanium sandwich panel manufacture is based on an entrapped gas processing method [2]. In this approach, titanium powder is sealed inside a titanium canister under a significant (several atmospheres) pressure of an inert gas such as argon. This canister is then consolidated by hot isostatic pressing to a relative density of about 98%. The high pressure of gas-filled pores in this structure inhibit full pore closure. These pores then remain during the thermo-mechanical forming of a panel by either hot forging or rolling. When this structure is finally annealed, the pores expand creating a component with fully dense face sheets (derived from the original can) and a core with a relative density as low as 50%.

The subsequent mechanical performance of these low-density core (LDC) panels depends significantly on the core's density, the relative thickness of the core and face sheet, and the quality of the face sheet/core interface. The core density and the core and face sheet thicknesses are a complicated function of the initial can thickness and gas pressure, the initial powder size distribution, the material properties of the can and powder, and the processing conditions used for consolidation, subsequent hot deformation and the final annealing treatment. As efforts continue to deduce the best process sequence [3], interest is growing in the development of predictive models that relate the core density to process conditions. These models are needed to understand the conflicting dependencies of key product attributes such as porosity content on the method and conditions used for processing. The high levels of porosity in these materials results in significant plastic compressibility which precludes the use of standard results from most forming analyses, which

are based on the assumption of plastic incompressibility [4]. The classical (slab) analysis [5] has recently been extended to investigate the deformation encountered during rolling of a plastically compressible sandwich panel [6]. Here, a further modification is introduced to allow the influence of internal pore pressure on the rolling response to be investigated.

### ROLL FORMING ANALYSIS

We analyze a model sandwich structure consisting of a porous core stiffened with fully dense face sheets subjected to flat rolling conditions, as shown in Fig. 1. Our approach is to extend the classical (slab) rolling analysis of Orowan [7] and Bland and Ford [8] for incompressible plastic solids to the case of plastically compressible materials, such as metallic foams. The analysis seeks to calculate the roll separation force,  $F_R$ , the roll pressure distribution,  $p(x_1)$ , the stresses and the partitioning of strains both between the face sheet and core, and between deviatoric and dilatational deformations for arbitrary roll reductions. The face sheets are assumed to be perfectly bonded to the core, thus requiring strain compatibility at the face sheet-core interface, i.e.  $\dot{\epsilon}_{1C} = \dot{\epsilon}_{1F}$ , where subscripts 'C' and 'F' refer to the core and face sheet, respectively.

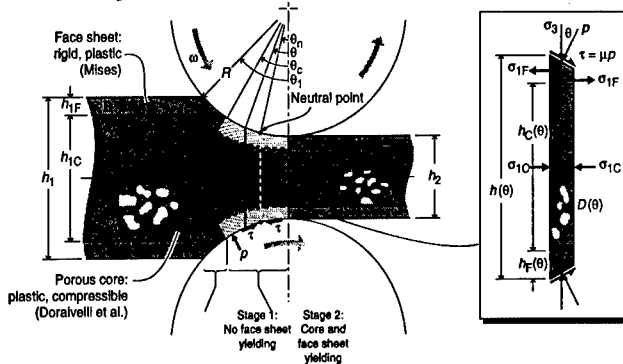


**Figure 1** Schematic of the roll forming process applied to a low density core metal sandwich panel.

The classical analysis considers a thin slice (or "slab") of material in the  $x_2$ - $x_3$  plane, of differential thickness,  $dx_1$ , and located at an angle,  $\theta$ : a balance of forces in the longitudinal direction leads to (Fig. 1)

$$\frac{d\sigma_1}{d\theta} = \frac{2Rp(\sin\theta \pm \mu \cos\theta) - 2R\sigma_1 \sin\theta}{h_2 + 2R(1 - \cos\theta)} \quad (1)$$

where  $\sigma_1$  is the stress in the rolling (longitudinal) direction,  $h_2$  is the roll gap height at the exit,  $p$  is the roll pressure and  $\mu$  is the coefficient of friction, which is assumed constant throughout the roll gap. The sign of the friction term depends on the location of the differential slice with respect to the neutral point: on the exit side ( $\theta < \theta_n$ ), the term is positive while on the entry side ( $\theta > \theta_n$ ), the term is negative. The roll pressure,  $p$ , is related to the vertical stress,  $\sigma_3$ , by  $p = \sigma_3 / (1 \pm \mu \tan\theta)$ . Equation (1) embodies the classical approach to rolling analysis and applies to both incompressible and compressible solids.

Equation (1) gives one relation for the three unknown (principal) stresses. For the case of a plastically deforming medium, the yield criterion affords a second relation. A third equation is obtained from the plane strain condition,  $\dot{\epsilon}_2 = 0$ . The sandwich panel is taken to deform plastically, but due to the presence of porosity, compressibility must be included. An effective yield cri-

terion for the sandwich is obtained by considering the face sheets as a Mises material and the porous core as yielding according to the potential of Doraivelu *et al* [9]. The rolling solution for the effective medium will yield the overall stresses,  $\sigma_1$  and  $\sigma_3$ , and strains  $\epsilon_1$  and  $\epsilon_3$ , which can then be used to deduce the average stresses and strains in the face sheet and the core. For plane strain conditions ( $\dot{\epsilon}_2 = 0$ ), the face sheets then yield when  $\sigma_{1F} - \sigma_{3F} = \pm(2/\sqrt{3})\sigma_0$  is satisfied. The core yields plastically when the potential,  $\Phi$ , given by

$$\Phi = (2 + D^2)J_2' + \frac{(1 - D^2)}{3}J_1^2 - (D\sigma_0)^2 = 0, \quad (2)$$

is satisfied. Here,  $J_1 = \sigma_1 + \sigma_2 + \sigma_3$ , is the first invariant of the stress tensor,

$J_2' = [(\sigma_1 - \sigma_2)^2 + (\sigma_2 - \sigma_3)^2 + (\sigma_3 - \sigma_1)^2]/6$  is the second invariant of the deviator tensor, and  $D$  is the relative density. Equation (3) defines a surface (ellipsoid) in principal stress space representing all states of stress resulting in plastic yielding at a given density. As  $D$  increases, the yield surface expands, in analogy with the strain hardening of plastic solids. As  $D \rightarrow 1$ , the Doraivelu-potential allows the Mises yield criterion for an incompressible, plastic solid to be recovered.

Consider a small region (slice) of the composite sandwich which is subjected to overall principal stresses,  $\sigma_3$  (normal to the face sheets), and lateral stresses,  $\sigma_1$  and  $\sigma_2$  ( $\sigma_1, \sigma_3$ ). Since the lateral stresses within the constituents must also be in equilibrium with the lateral stress acting on the sandwich, a force balance in the lateral ( $x_1$ ) direction gives  $\sigma_{1C}f_C + \sigma_{1F}f_F = \sigma_1$  in which  $f_C$  and  $f_F$  are the core and face sheet volume fractions. Substituting in expressions for the lateral component stresses,  $\sigma_{1F}$  and  $\sigma_{1C}$ , [from the Mises criterion and (2)] results in an effective yield criterion for the sandwich panel

$$\frac{(2D^2 + D^4)\sigma_3 \pm 2\sqrt{(-4 + 3D^4 + D^6)\sigma_3^2 + (4D^2 - D^6)\sigma_0^2}}{4 - D^2} \cdot f_C + \left(\sigma_3 \pm \frac{2}{\sqrt{3}}\sigma_0\right) \cdot f_F = \sigma_1 \quad (3)$$

in which the applied principal stress,  $\sigma_3$  ( $= \sigma_{3C} = \sigma_{3F}$ ), has been introduced.

Expressing Equation (3) as a potential,  $\Phi^*$ , allows an associated flow rule to be obtained by assuming normality of strain increments

$$d\epsilon_i = \Lambda \frac{\partial}{\partial \sigma_i} \Phi^* \quad (4)$$

where the subscript '*i*' refers to principal strain increments and stresses, and  $\Lambda$  is a density-dependent scalar. The overall lateral strain increments can be determined by substituting the effective yield potential for the sandwich panel (3) into (4). The cumulative lateral strain is obtained numerically by integrating (summing) the strain increments,  $\epsilon_1(x_1) = \int d\epsilon_1(x_1)$ .

Implementation of the analysis begins by numerically solving the ODE given by (1) for the lateral stress,  $\sigma_1$ . Initially, the core is assumed to have a constant density,  $D(\theta_1) = D_0$  and (1) is solved assuming the applied strain increment,  $d\epsilon_3$ , is small enough such that the error in neglecting a change in density is acceptably small. This finite difference procedure is continued as successive increments in roll angle,  $\theta$ , are applied.

Once the macroscopic stresses,  $\sigma_1$  and  $\sigma_3$ , are obtained from (1) and (3) for the prescribed strain, Eqn. (2) and the Mises criterion can be used to obtain the lateral stresses in the core and face sheet. The relative density in the core depends on the core strains according to  $D(\theta) = D_0[1 - (\epsilon_1(\theta) + \epsilon_3(\theta))]$ .

In addition to the roll radius,  $R$ , and the starting plate thickness,  $h_1$ , the reduction (or final thickness,  $h_2$ ), the coefficient of friction,  $\mu$ , and the distribution of relative density,  $D(\theta)$ , must be

given as input. However,  $D(\theta)$  is not known for the steady-state problem, in which the leading edge of the plate has passed between the rolls and is some distance from the roll gap exit. Initially, the density is known only for the plate prior to entering the roll gap, where  $D$  is a constant,  $D = D_0$ . To circumvent this problem, a transient solution is developed in which the distribution of relative density is determined as the plate proceeds into the roll gap.

Large reductions are usually achieved during rolling by the application of a sequence of smaller reductions. The rolling model allows the evolution of core density, roll pressure distribution, etc. to be predicted for multiple-pass roll schedules.

#### INFLUENCE OF PORE PRESSURE

The process used to manufacture LDC titanium sandwich panels relies on high internal gas pressure within the pores to expand the mechanically worked preform during an annealing heat treatment. Densification of the core during rolling leads to increased gas pressure within the voids (assuming diffusion of the gas into the metallic matrix can be neglected) and if sufficiently high, can be expected to affect the deformation behavior of the (porous) preform. An initial gas pressure of 1 MPa at a starting density of 0.6 increases to 30 MPa at a relative density of 0.99, or roughly 100 MPa if the temperature is also raised to 1200 K. Another possible effect of increased pore pressures during rolling is the observed tendency for face sheet blistering (face sheet debonds from the porous core) [3]. Depending on the permeability of the porous core, gas pressure may build at the core-face sheet interface and provide the driving force for interfacial debond crack growth. The influence of pore pressure on rolling is explored by extending the analysis briefly presented above to include internal pore pressure.

The Doraivelu potential is modified by adding an internal pressure ( $p$ ) to the hydrostatic stress. The modified potential for the case of plane strain becomes

$$\Phi_g = (2 - D^2 - D^4)\eta p_0^2 + (-2 + D^2 + D^4)\eta p_0(\sigma_1 + \sigma_3) + \frac{1}{4}(-D^4(\sigma_1 + \sigma_3)^2 - 4D^2(\sigma_0^2 + \sigma_1\sigma_3) + 4(\sigma_1^2 + \sigma_3^2)) \quad (5)$$

where for an ideal gas,  $\eta(D) = (1 - D_0)/D_0 \cdot D/(1 - D)$  and  $p_0$  is the initial pore pressure. The pore pressure after some densification is given by  $p = \eta(D)p_0$ . Figure 2 illustrates the predicted influence of increasing initial pressure and densification. Increasing initial pore pressure translates the yield locus in the direction of compressive hydrostatic stress. This results in a lowering of the tensile mean stress to cause yielding and an increase in resistance to yielding in hydrostatic compression. An increase in density has a similar effect in translating the yield locus to higher compressive mean stress (since increasing the density increases the pore pressure), but also results in an isotropic expansion of the elliptical yield locus due to densification hardening.

As seen in Fig. 2(a), the yield locus may become detached from the stress axes for sufficiently high initial gas pressures, indicating that compressive stresses must be applied to prevent plastic yielding. Even though the yield locus may enclose the stress-free state initially, increased pressure due to densification during rolling can lead to detachment of the yield locus from the stress-free state (though this is not indicated for the conditions shown in Fig. 2(b)). A given material point (differential slice) experiences an increasing hydrostatic compressive stress during rolling, which reaches a maximum at the neutral point. Beyond the neutral point, the mean stress decreases monotonically (since in the absence of front or back tension, the longitudinal stress ( $\sigma_1$ ) must be zero at the exit). The low exit mean stress may not be sufficient to maintain the compressed state achieved during the roll pass, leading to a volume expansion (decrease in density). The translation of the yield locus shown in Fig. 2(b) (e.g. for  $D = 0.9$ ) also indicates a volume expansion as the

material point approaches the roll gap exit since, if normality of the plastic strain vector is assumed, then  $d\epsilon_1 \geq |d\epsilon_3|$ , so that  $dD < 0$ .

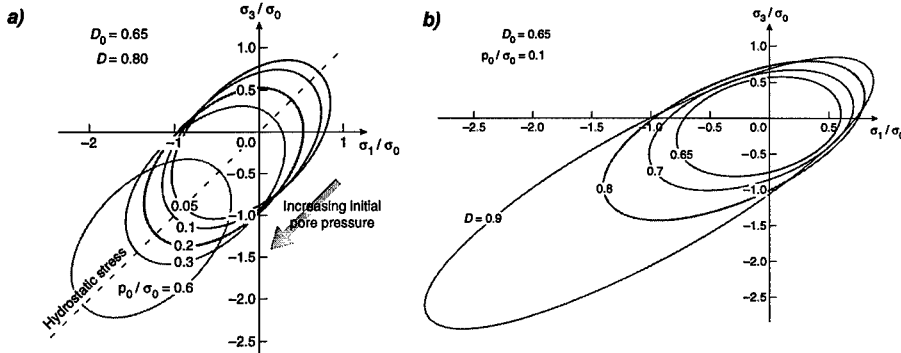


**Figure 2** (a) Increasing the starting relative pore pressure causes the yield locus to shift in the direction of higher hydrostatic compressive yield strength. (b) During rolling, densification results in both isotropic hardening and translation of the yield locus (due to increasing gas pressure).

Substituting the modified potential (5) into the rolling analysis allows the influence of initial pore pressure ( $p_0$ ), specified at a given density ( $D_0$ ), to be investigated. Figure 3 shows the dependence of the densification efficiency,  $\eta_D$ , defined as

$$\eta_D = \frac{\Delta D / D_0}{\Delta h / h_0}, \tag{6}$$

on the initial pore pressure and relative density. In this expression,  $\Delta D$  and  $\Delta h$  represent changes in density and thickness from their initial values,  $D_0$  and  $h_0$ . It can be seen that for  $p_0/\sigma_0 < 0.4$ , the densification efficiency is negligibly affected by pore pressure. Beyond this however, the densification efficiency drops off due to the effect of high internal gas pressure causing increasing incompressibility.

While Fig. 3 indicates no significant influence of pore pressure on densification during rolling for relative pore pressures below about  $p_0/\sigma_0 = 0.4$ , the roll contact pressure and rolling force are significantly increased. The density decrease which may occur near the roll gap exit is analogous to the expansion of a compressible (supersonic) gas through a converging nozzle. Expansion is most likely under rolling conditions which maximize the stress state triaxiality, e.g. large roll diameter and high roll/workpiece friction coefficient. The effects of increased incompressibility and expansion will also be enhanced when rolling at elevated temperatures since the flow stress of the alloy matrix is reduced, resulting in higher relative pore pressures.

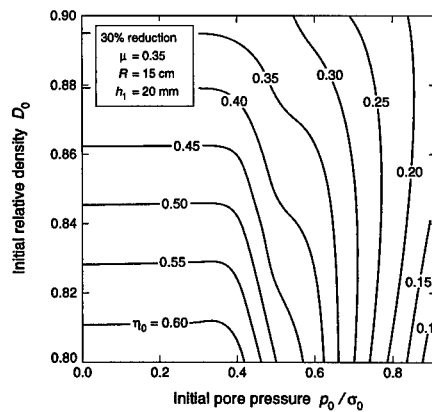


**Figure 3** Contours showing the effect of pore pressure in decreasing the densification efficiency for relative pressures beyond  $p_0/\sigma_0 = 0.4$ .

## SUMMARY

The classical (slab) model for flat rolling has been extended to include plastic compressibility. The rolling of face sheet-stiffened, porous core sandwich panels has been analyzed by introducing an effective (homogeneous), but anisotropic, density-dependent yield potential and assuming normality of plastic strain increments. Application of a plastic potential for the porous core which reduces to the Mises yield criterion when the relative density approaches one, allows the original (incompressible) rolling result to be recovered at full density. A modification of the plastic potential describing the core's yield behavior to include the effect of internal pore pressure was also introduced. The model allows prediction of the distribution of normal pressure, core relative density, and face sheet thickness as a function of applied reduction, initial core density, core volume fraction and initial gas pressure. It was found that pore pressure can be expected to have a significant effect on roll forming behavior for initial pore pressures exceeding about half the flow strength of the fully dense matrix. These conditions are more likely met when rolling at elevated temperature.

## ACKNOWLEDGEMENTS

The authors wish to express their thanks to Dr. D.S. Schwartz for helping to define the problem and to Prof. N.A. Fleck for helpful discussions. Financial support through the Ultralight Metal Structures MURI Program (Contract No. N00014-96-1-1028, program monitors, Steve Wax (DARPA) and Steve Fishman (ONR)) is gratefully acknowledged.

## REFERENCES

1. L.J. Gibson and M.F. Ashby, Cellular Solids: Structure and Properties, (Pergamon Press Oxford, 1997), p.345.
2. M.W. Kearns, P.A. Blenkinsop, A.C. Barber, and T.W. Farthing, *Int. J. Powd. Met.* **24**(1), 59 (1988).
3. D.S. Schwartz and D. Shih (private communication).
4. R. Hill, The Mathematical Theory of Plasticity, (Clarendon Press, Oxford, 1950).
5. E.M. Mielnik, Metalworking Science and Engineering, (McGraw Hill, New York, 1991), p.222.
6. D.M. Elzey, presented at the Ultralight Metal Structures MURI Review, Charlottesville, VA, 1997 (unpublished).
7. E. Orowan, *Proc. Inst. Mech. Engrs.* **150**, 140 (1943).
8. D.R. Bland and H. Ford, *Proc. Inst. Mech. Engrs.* **159** 144 (1948).
9. S.M. Doraivelu, H.L. Gegel, J.S. Gunasekera, J.C. Malas, J.T. Morgan and J.F. Thomas, Jr., *Int. J. Mech. Sci.* **26**(9/10), 527 (1984).

---

**Part VI**  
**Application and Design Principles**

## Parameters of Construction for Applications of Metal Foams

R. Neugebauer, Th. Hipke  
Fraunhofer Institute for Machine Tools and Forming Technologies, Chemnitz, Germany

### ABSTRACT

This article will present characteristics that have great importance for the industrial use of metal foam structures. In detail, these are

- Design criteria for detachable joint connections
- Investigation of the thermal behavior of sandwich composites

### INTRODUCTION

Foamed parts must be bonded to other components in order to be able to use them. In practice, it is not possible to limit applications to merely foaming out parts, whereby the framework construction can receive the connection elements (links). Therefore, the assembly of foamed parts requires a search for suitable detachable joint connections and to quantify the durability of them. To reach this goal, the connection pull-out strength is to be determined for the widest variety of links.

Because of the required higher processing accuracies, the thermal behavior of components is becoming more and more important for practical applications. This also applies to sandwich composite materials with metal foam. Of particular interest is the interrelationship between thermal deformations and the structure of the sandwich plate. Factors such as cover sheet material and thickness, plate thickness and foam density play an important roll in this relationship.

### EXPERIMENT and RESULTS

#### Design criteria for detachable joint connections

First, to investigate joint connections, suitable links were researched and selected. Here, the tested links were limited to the standard products of known manufacturers, or to standard DIN elements. There is no need to use special links at this stage because the available connection elements cover such a wide range of suitable geometries.

A list of the possible types of fastening methods is shown in Table I.

Table I: The links used and their possible types of fastening methods

	Foam into place	Adhesive bonding	Screw	Press into place
Hexagon head screw DIN 933	X	X	X	
Wood screw DIN 571	X		X	
Sheet metal screw DIN ISO 1471 Form C	X		X	
Hexagon nut DIN 934 and DIN 6331	X	X		
Castle nut DIN 935	X	X		
Knurled nut DIN 466	X	X		
Round nut DIN 82013	X	X		X
Recoil threaded insert			X	
Threaded inserts "SonicLok" and "Ensaf" (the Kerb-Konus company)	X	X		

Depending on the standard part geometry various joining processes are possible as a connection method. In addition to the known processes of adhesive bonding, screwing in and pressing into place, the process of foaming into place, can also be used. The tests carried out to determine the pull-out strength of foamed-in links are the subject of later investigations.

The following additional variables were also considered:

- Alloy (cast alloy AISi12 and wrought alloy AlMg1Si0.6)
- Plate density (0.5, 0.7, 0.9 and 1.1 g/cm<sup>3</sup>)
- Diameter of the links
- For screws: thread reach

Foamed plates of the dimensions 300mm x 300mm x 50mm were supplied as test samples.

These plates were each cut into 6 strips, thus allowing them to be laterally inserted into the tension testing machine (type WPM-ZDM 300) when they were tested and the links were subsequently pulled out.

Screws were twisted into the nut-shaped parts. The screws, as well as the screw-shaped links, were gripped in tongs while the foam strips were held by a blankholder on the bottom crosshead of the testing machine.

The pull-out process is started with the top crosshead being hydraulically raised with the tongs. When this happens, a tensile force acts upon the connection. Further lifting of the top crosshead causes an increase in action force. The dependence of the force on the path can be directly output from a connected computer system in the form of a force-path diagram and saved (Figure 1). In this way, it was possible to determine the maximum force at which the connection fails.

For the wood and sheet metal screws, as well as the recoil inserts, a core diameter is predrilled so that is slightly less than the normal core diameters used in steel machining operations. For the joining process of adhesive bonding, the links were fixed with a metal adhesive. Here, a core hole, that guaranteed a minimum adhesive thickness of 1 mm, is drilled.

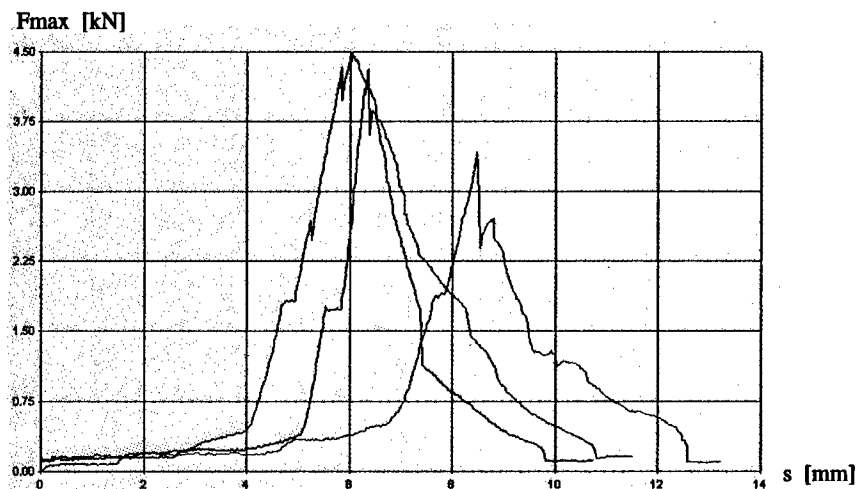


Figure 1: Force-path progression when three of the same types of links are pulled out (M6 hexagon head nut bonded in place)

The failure behavior depends on the type of connection. The rise of force is very steep for bonded connections. The steepness of the curve reflects the elasticity of all the involved test

constituents, such as the tension testing machine, the tongs, the link and the foam strips. In the case of high densities, the links came free after the adhesive layer failed, while the lower densities, it was the foam structure that gave way. For links that are screwed in, the force-path diagram shows a large area of plastic deformation before the maximum force is reached. Here also, the pulling out take place in several stages - and always interrupted by the cell walls hooking into each other.

It can be seen that to a certain degree extremely high loads can be transmitted, and the suitability of the links varies greatly. Figure 2 shows that screwed connections can transmit significantly lower forces than bonded ones. At this relatively low foam density of 0.7 g/cm<sup>3</sup>, the pores are fairly large, with some having open cell walls, and the adhesive accumulates in the entire area of the connection. This results in the creation of a completely new material that also exhibits a large effective surface area, in turn resulting in good distribution of force. Of the adhesively bonded connections, the hexagon head screw achieved the highest values because, at 20 mm, it also has the greatest connection length. At the other end is the hexagon nut, with a joint length of 6 mm, which has an effect in lower transmittable forces. The existence of undercuts or knurls is generally an advantage because they act as an additional closure form for the link in the adhesive zone.

Inserted links were not listed because the transmitted forces, at 1 kN, are insignificant.

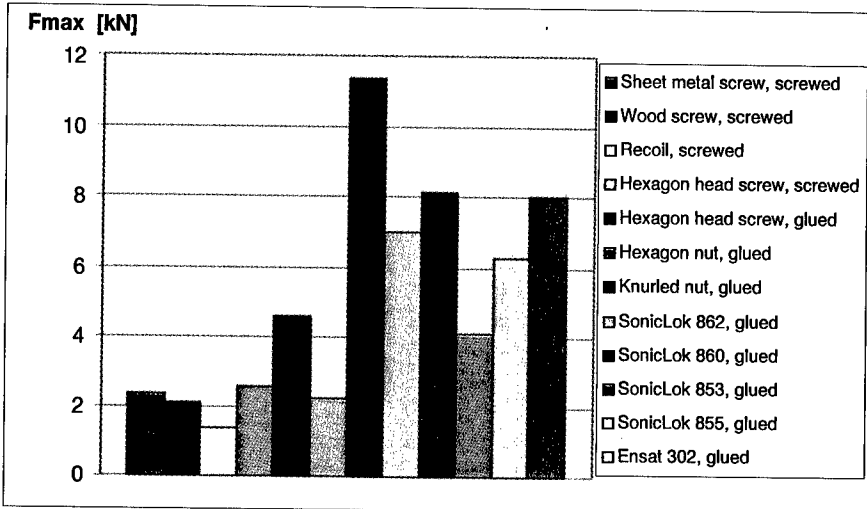


Figure 2: Maximum forces for various links at diameter M6 and a foam density of 0.7 g/cm<sup>3</sup>

At higher densities, the superiority of adhesively bonded connections is no longer apparent. The adhesive cannot penetrate the pore structure because the drilled walls are almost completely closed. Screwed connections, on the other hand, find sufficient material to form a threaded form capable of bearing loads.

The influence of the parameters density on the maximum force is shown only with the example of the screwed in M6 recoil threaded inserts (Figure 3). The force rises as density increases. The precise values are almost follow a straight line for which the function is specified. A polynomial formulation of the 2nd degree at least supplies similar values in the density range of 0.4 to 1.2 g/cm<sup>3</sup>.

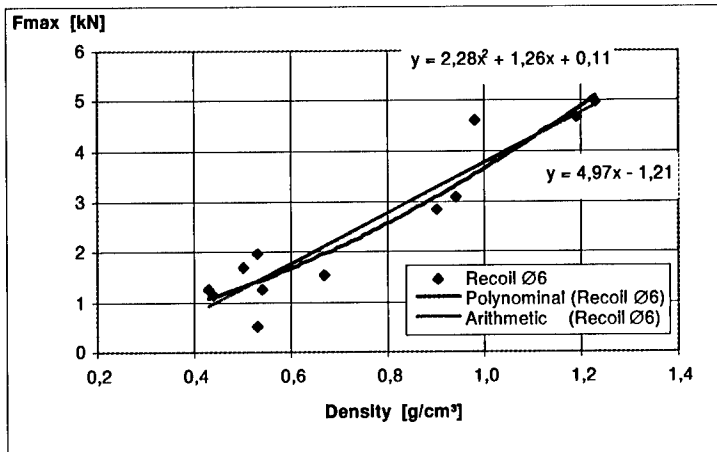


Figure 3: Influence of density on the maximum force for a screwed in M6 recoil threaded insert

#### Investigation of the thermal behavior of sandwich composites

Foamed plates of the dimensions 400mm x 300mm x height were used as test samples, whereby various plate height were used. The following variables were considered:

- Cover sheet material (steel or aluminum)
- Cover sheet thickness (1 and 2mm)
- Plate density (0.5, 0.7 and 0.9 g/cm³)
- Plate height (10, 25 and 40mm)

The tests were performed in the thermal cell of the Fraunhofer Institute. The test configuration is shown in Figure 4. The plates were clamped down on one side. They were heated with a heating mat placed on the top cover plate, and this mat creates a temperature of approx. 75°.

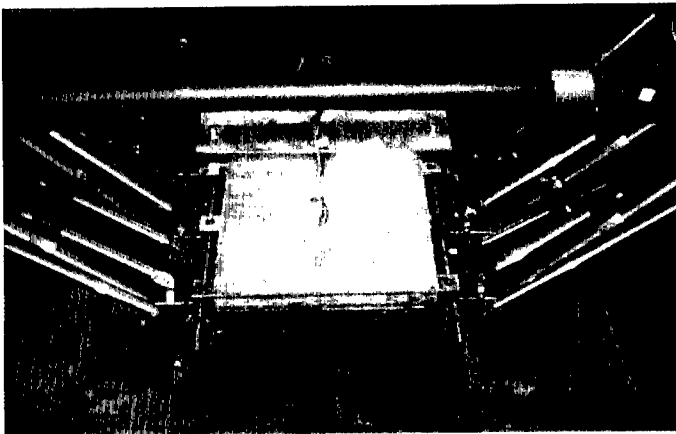


Figure 4: Test configuration for determining thermal deformations of sandwich plates (shown without heating mat)

Three path sensors were placed at 6 positions over extension arms, and recorded deformations of the respective position in the x-, y- and z-direction. The temperature was determined with two sensors on the bottom of the plate and two sensors on the top. The thermal cell guaranteed a constant ambient temperature of 20°C during the test. Hardly any thermal strain is shown in the measuring rods. The temperature progression during the heating-up phase shows that the temperature of the top is higher than that of the bottom. However, the temperature difference is less than anticipated; i.e., the insulation effect of the foam is rather slight. The temperature gradient for all plates, regardless of plate thickness and density, 3.5 to 4 K. Because the geometric expansions are known, the thermal deformations in the resulting linear expansion coefficients can be calculated. All plates exhibit very good agreement in expansion in the x- and z-direction (Figure 5).

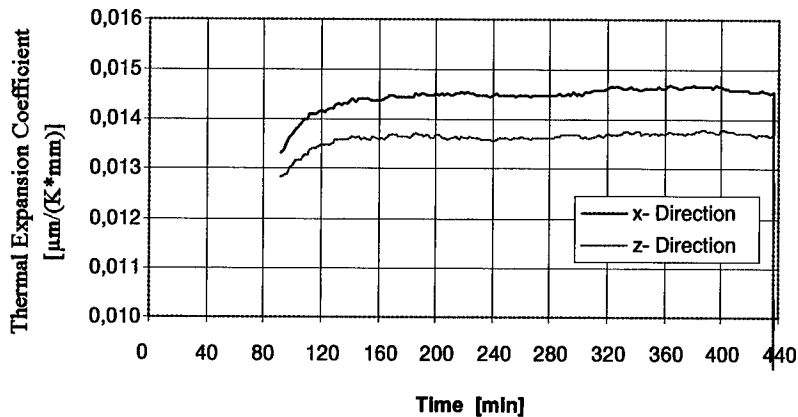


Figure 5: Linear expansion coefficient of a sandwich plate (steel cover plate; thickness 1mm; height 25mm)

The expansion coefficient of the aluminum-clad foam plates are, depending on design, within a range of 0.020 to 0.024  $\mu\text{m}/(\text{K}\cdot\text{mm})$ . These values are slightly larger than those of the alloy AlSi12 (0.0199 to 0.0206  $\mu\text{m}/(\text{K}\cdot\text{mm})$ ) which was used as foam material. The cover sheets have an expansion coefficient of 0.0235  $\mu\text{m}/(\text{K}\cdot\text{mm})$ . This means that the influence of the cover sheet on the overall expansion is dominant.

The lower expansion coefficient of steel (0.012  $\mu\text{m}/\text{K}\cdot\text{mm}$ ) also reduces the resulting strain of the sandwich plate (Figure 6). Here, the cover sheet apparently has a stronger influence. The expansion coefficients of the plates with a steel cover sheet were between 0.0105 and 0.014  $\mu\text{m}/(\text{K}\cdot\text{mm})$ .

If the density is used as a variable quantity, it can be said that at higher densities the expansion coefficient goes down slightly. This is a contradiction of the assumption that, with a higher density, the influence of the foam over the entire expansion increases and the overall expansion coefficient thus becomes larger. This requires further investigation.

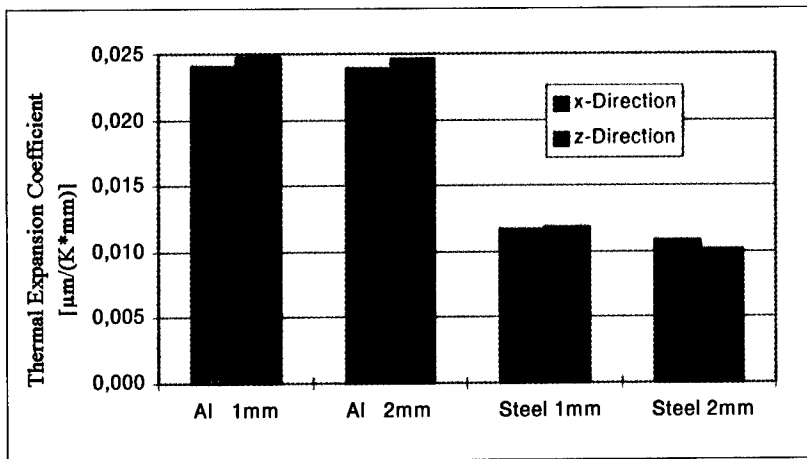


Figure 6: Expansion coefficients depending on cover sheet parameters (density 0.65g/cm<sup>3</sup>; height 25mm)

## CONCLUSIONS

It was shown that links in metal foam are fully capable of transmitting high forces, with the result that joints need not always be positioned in solid zones. In the lower density range, adhesively bonded connections are clearly superior to screwed ones. At higher densities, i.e. 1.0 g/cm<sup>3</sup>, both methods perform approximately the same and, depending on the design, can transmit tensile forces up to 20 kN. For all connections longer joints are advantageous. Undercuts and knurls are required especially for bonded connections.

In the investigation of sandwich plates regarding thermally-caused strain, it was determined that the linear expansion coefficient of the entire plate largely depends on the expansion coefficient of the cover sheet. Thus, for the foam material AlSi12 and aluminum cover sheets, a coefficient of 0.020 to 0.024 µm/(K\*mm) can be anticipated, and when steel cover sheet are used, a coefficient of 0.0105 to 0.014 µm/(K\*mm) is to be expected.

## REFERENCES

1. H. von Hagen; J. Baumeister; D. Nicklas; M. Paschen; M. Weber: Sandwiches with steel cover sheet and foamed aluminium. (Dresdner Leichtbausymposium, June 1997)
2. N. Sedliaková; F. Simancik; J. Kovácik; P. Minár: Joining of aluminium foams. (Symposium Metallschäume, Bremen 1997)
3. R. Neugebauer; F. Wieland; H. Lang: Die Maschine - dima (1996) H 1/2, S. 40-43
4. R. Neugebauer; T. Hipke; F. Wieland: Die Maschine - dima (1998) H 3

---

## Lightweight Products with Metal Foam - Properties and Methods of Processing

R. Neugebauer, Institutsleiter FhG IWU, Chemnitz

H. Bräunlich, U. Wagner, Abteilung Umformtechnologien, FhG IWU, Chemnitz

### ABSTRACT

The aim of future production technology is the economic application of lightweight components with improved property profiles.

Demands for weight reduction made by both the automotive industry and the machine-building industry can be met through selective utilization of metal foam composite structures. To that end, basic investigations into material behavior and the machineability of metal foam composites are necessary.

The presentation will submit an overview of the properties and processing parameters of selected composites based on an analysis of industrial requirements. The development of analytical models of the process mechanics will contribute to the creation of preconditions for a numerical simulation of selected processes. Innovative applications and the potential for future use of metal foam composites in lightweight construction will be shown as well.

Finally, results from projects of the *Fraunhofer-Institut für Werkzeugmaschinen und Umformtechnik* together with industrial companies in Saxony will be presented.

### INTRODUCTION

Up to now, foamed metals with more than 50% porosity have scarcely been applied in industry. Their multi-faceted properties are entirely different from the problem of producing reproducible metal foams. To date, neither generally applicable mechanical properties or corrosion behavior nor any profound experience regarding the processing of foamed metals has been available. Great variations in mechanical parameters suggest that, rather than having a discrete value, there needs to be a range of strength for a certain density; this behavior aggravates both metal forming and cutting.

The lightweight material metal foam is, in addition, faced with materials which have already been successfully applied in lightweight construction, for instance plastic and ceramic foams as well as composites such as SMC or BMC and natural products.

Metal foams may be used in the automotive industry (underbody, engine hood, trunk deck, sun roof, stiffener of fenders or under-run fenders of trucks. They may also be used for partial or complete "space-frame" approaches. Other applications can be found in machines (tables, frames) and their periphery (elements of handling systems). Open-pore metal foams may be used for heat exchangers and air filters.

However, alternative materials are already being successfully applied in the above mentioned products (plastic foam hood insulation, engine encapsulation, ceramic foam in chemical processing, SMC-fenders, frames of sunroofs).

This situation strongly calls for the identification and publication of generally applicable properties and processing guidelines for metal foams and metal foam composites.

## EXPERIMENT

The following investigations will be described:

- Determination of mechanical properties of metal foams with different kinds of load.
- Determination of basic parameters for the processing of metal foam composites.
- Modeling of components made from metal foam or including metal foam.

The materials of Al99.5, AlSi12, AlMgSi with foam densities of 0.4; 0.75 and 1.0  $\text{g/cm}^3$  respectively were tested. The cover sheets of the sandwich composites were steel or aluminum alloy. Furthermore, foamed steel tubes were tested.

## RESULTS

### Mechanical properties of metal foams with different kinds of load

**Tensile test:** All samples showed the brittle behavior typical of metal foams. In figure 1 two specimens are illustrated. Figure 2 depicts the fracture caused by a tensile load. It can be clearly seen that the metal foam initially fails at the areas of lower local density.

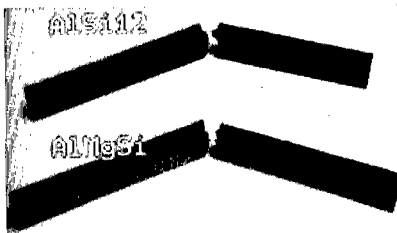


Figure 1: Tensile test samples



Figure 2: Failure behavior in fracture area

Figure 3 presents the tensile strengths established for different foam densities. Furthermore, Young's Modulus was determined. A dependence of the foam density can be observed. The strongly varying values can be traced back to the inhomogeneous pore structure.

Figure 4 depicts Young's Modulus dependent on foam density.

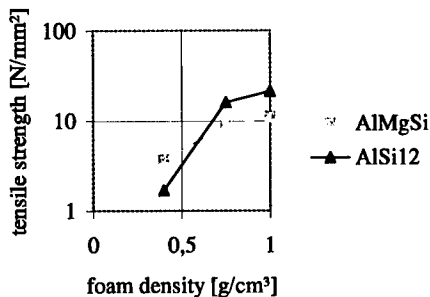


Figure 3:  
Tensile strength dependent on foam density

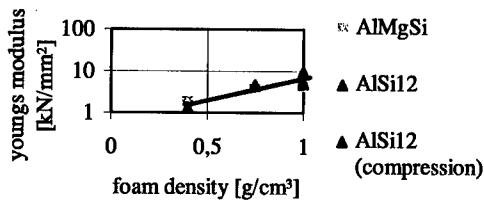


Figure 4: Young's Modulus dependent on foam density

**Compression test:** Here, yield strength and compressive strength were tested at a degree of upsetting of 45%. Samples of all test materials at degrees of upsetting of 15%, 30% and 45% are illustrated in figure 5. The determined yield strengths as a function of the foam density are shown in figure 6.

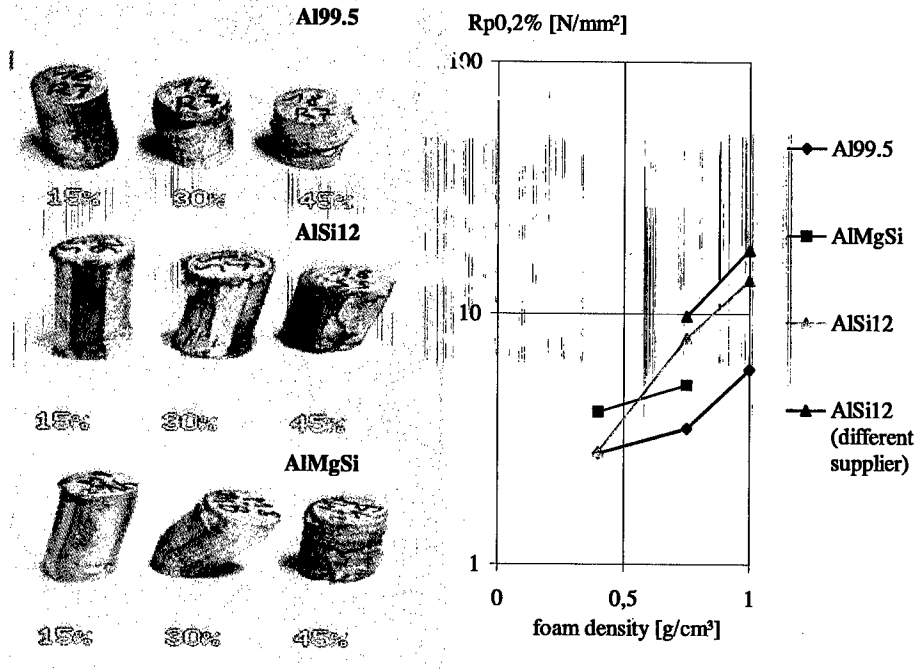


Figure 5: Foam samples of different degrees of upsetting

Figure 6: Yield strength dependent on foam density

Table I depicts the compressive strength of the test materials at a degree of upsetting of 45% for the foam densities of 0.45, 0.7 and 1 g/cm<sup>3</sup>. Figure 7 shows the compressive strength of different materials dependent on foam density.

material	Foam density [g/cm <sup>3</sup> ]	compression strength [N/mm <sup>2</sup> ]
Al99.5	0,4	7
	0,7	11
	1,0	35
AlSi12	0,4	5
	0,7	20
	1,0	50
AlMgSi	0,4	13
	0,7	22
	1,0	-

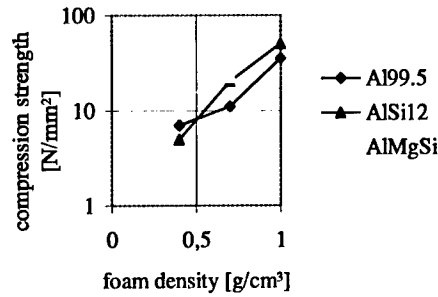


Table I: Compressive strengths of foam materials

Figure 7: Compressive strength dependent on foam density

**V-bending of metal foams and metal foam composite structures**

A form-constrained V-bending was carried out. In the test, failure of the metal foam occurred in the bending radius at the tensile side that faces the die after about 25% of the bending path. Only the exterior layer of the inner radius remained undamaged. A progressive forming of a metal foam composite structure with AlSi12-core and steel cover sheets resulted in the foam being detached from the inner cover sheet at the bending leg. A composite featuring the same foam core but with aluminum cover sheets showed an identical result.

Maximum bending forces of about 30 kN could be reached with the bending of composites having Al99.5 foam core and steel or aluminum cover sheets. Due to the impact of the forming force the thickness of the composite was considerably reduced in the bending radius. Seen from the outside, however, the cohesion of the composite appeared to be maintained. Figures 8 and 9 show the results of the V-bending tests for various composites.

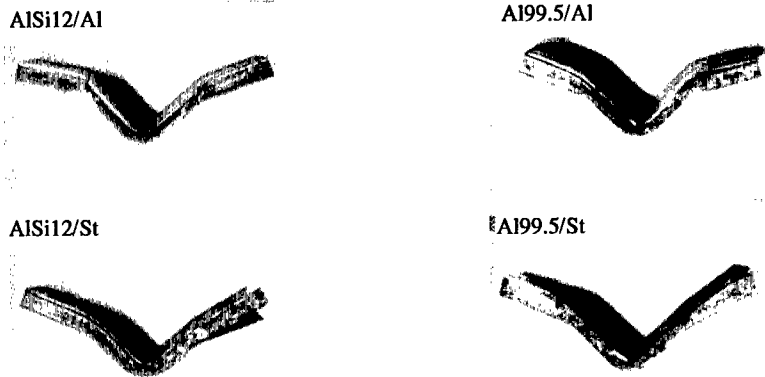


Figure 8: Metal foam composite with AlSi12 foam core and Al- or St cover sheet

Figure 9: Metal foam composite with Al99.5 foam core and Al- or St cover sheet

Basic parameters for manufacturing metal foam composite structures

■ Forming

When forming under tensile stress, buckling tests with a hemispheric punch ( $d = 100 \text{ mm}$ ) were carried out. The blank holder force was kept at a constant  $20 \text{ kN}$ . Lubrication was carried out with Teflon foil between punch and sheet.

Tests were carried out on the usual metal foams and composite structures with foam densities of  $0.8; 1.0$  and  $1.2 \text{ g/cm}^3$ . Buckling depths between  $5$  and  $12 \text{ mm}$  could be reached for the foam sheets and the sandwich composites. Here, drawing forces were between  $0.5$  and  $3.9 \text{ kN}$ .

The results lead to the conclusion that formability under tensile load is considerably limited. An impact of density cannot be observed. The locally very irregular porous structure results in considerable scattering of the achievable buckling depths thus exceeding. the impact of the material density.

Different causes of failure could be observed during the tests.

- Causes of failure - sandwich

1 generation of grooves at the upper cover sheet

- already initialized after a small change of shape
- progresses up to generation of cracks in the cover sheet
- increased tensile stress as compared to bottom side

2 fracture of foam core (middle of sample)

- correlation to generation of grooves in cover sheet

3 delamination of cover sheet at the bottom side of the sandwich (middle of sample at punch side)

- crack formation in foam core
- exterior areas are not yet in full contact with the punch
- stress distribution over cross section

4 delamination of both cover sheets at various places in the sandwich

Figures 10 and 11 illustrate different causes of failure.

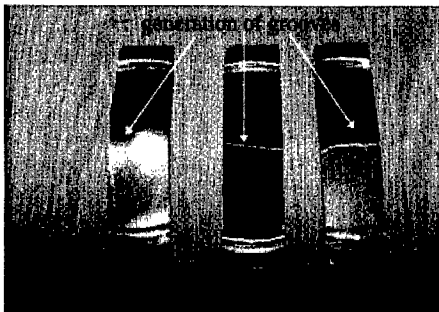


Figure 10: Failure case 1 sandwich composite

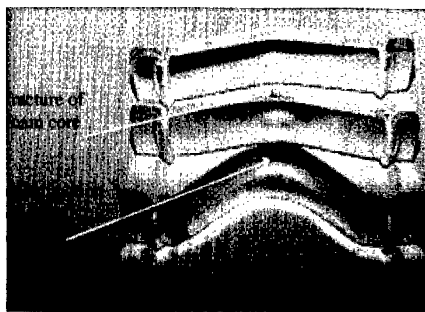


Figure 11: Failure case 2 and 3 sandwich composite

## ■ Cutting

### Water jet cutting

The investigations were aimed at a determination of process parameters and process limits for the machining of aluminum foam alloys.

The phenomena which occur during the interaction of water jet and material are little known as they cannot be directly observed.

On the first impact of the water jet the surface of the workpiece is loaded shock-like due to a fluid dash. Each individual zone of the porous material which comes into contact with the jet in the course of the cutting process is exposed to this single shock load. This leads to considerable tension peaks within the material structure of the individual webs, causing initial damage of the material.

In figure 12, this state is illustrated for the machining of AlMgSi foam at a density of  $1.0 \text{ g/cm}^3$  and in figure 13 it is illustrated for the machining at a density of  $0,4 \text{ g/cm}^3$ . Machining grooves can still be detected under these conditions however, resulting in reduced trailing.



Figure 12: density  $1,0 \text{ g/cm}^3$



Figure 13: density  $0,4 \text{ g/cm}^3$

The cutting tests for aluminum foam samples by means of water jet proved the assumption that - as opposed to the machining of solid aluminum - the cutting result is mainly influenced by porosity (homogeneity and size). The impact of the material thickness to be cut is similar to that of the solid material. In random tests, it was identified that the parameters of jet generation (length and diameter of focus), and of the abrasive material (flow, size and type), and also the hydraulic parameters (pressure, diameter of jet) do not have a major influence. When cutting porous structure, the variation of feed rate as a machining parameter had an impact on the quality of the cut edges, in particular at the side of the jet exit (widening and formation of grooves). The cutting quality achieved met the requirements of roughing).

Cutting the aluminum foam samples was easily possible for a maximum material thickness of 50 mm (at a density of  $0.4$  to  $0.5 \text{ g/cm}^3$ ) and by ensuring that the above mentioned conditions were observed at a feed speed between 50 mm/min and 100 mm/min. With decreasing material thickness (minimum of 8 mm) feed rates of up to 400 mm/min could be achieved at constant quality.

### Modeling of components made from or including metal foam

The investigation into the structural parts may determine the theoretical potential by which the parts can be reduced in weight, if foamed sandwich-like materials or hollow parts are applied instead of steel or investment casting parts. Due to mass reduction, either the load of the drive is decreased (possible reduction in drive size) or else higher dynamics are achieved.

Basically, it has to be observed that a general replacement of previously non-foamed components with foamed components of the same outward appearance is barely possible.

---

Here, the foamed structures are either foamed hollow parts or sandwich parts. Their mass was evaluated correspondingly. Individual parts were modeled as standard as well as hollow parts with a wall thickness of 0.5 mm.

Masses were determined for each individual part and for three different degrees of density (0.4, 0.75, 1.1 g/cm<sup>3</sup>).

In further tests on load carrying capability, a corresponding density had to be assigned to the individual part by means of calculation or testing. The choice of the material density to be used - which should be as low as possible - depends on the individual case of application.

Therefore, before foaming technology is applied the individual case of application has to be closely examined. A general application of foamed elements instead of traditional parts cannot be recommended.

When evaluating individual parts with regard to their producibility as foamed hollow parts or as sandwich parts, the foamability is of greatest concern, irrespective of the costs of producing the hollow part.

Good foamability is guaranteed, when

1. there is enough space left between adjacent walls
2. the contour is simple (flow behavior of foam).

An increase in the dynamics of the entire device depends on mass reduction and on the vibration behavior of the components. Foamed components show good damping capability.

Calculations were carried out for the mass reduction for an entire handling device with these parts being used. The calculation shows that a total reduction of 495 kg can be achieved when producing the aforementioned parts as foamed hollow parts. Thus, handling may be carried out more dynamically, accelerating or decelerating at a greater rate.

## CONCLUSIONS

A broad application of metal foam as a lightweight material currently faces difficulties in the reproducibility of metal foams, in the determination of generally applicable mechanical parameters, in the processing of foamed metals and in the description of the corrosion behavior. Competition from other lightweight materials strongly calls for the aforementioned challenges to be met.

The investigations lead to the following conclusions:

- description of scatter bands for material parameters is required, since values diverge at constant foam density due to inhomogeneous porosity
- formability of foamed samples and composite structures is severely limited under tensile stress and the impact of density is concealed by the inhomogeneous porosity
- cutting (water jet cutting) well possible
- there is a considerable potential for mass reduction when using foamed metals for highly-loaded dynamic components

The focus of future investigations has to be the modification of material testing methods, investigations into the processing of composite structures with foamable material, and the development and optimization of low-cost production methods for composite components in different areas of industry. To achieve these goals it is necessary to intensify cooperation between metal foam producer, research institute and industrial user.

---

## REFERENCES

1. Banhart, J. and Baumeister J. and Weber, M, Der Konstrukteur **10**(1994).
2. Shapovalov, V, MRS Bulletin, April 1994.
3. Banhart, J and Baumeister, J and Weber, M, VDI-Berichte **1021**.
4. Thornton, P.H and Magee, C.L., Metallurgical Transactions, **64**(1975).
5. Davies, G.J. and Shu Zhen, Journal of Materials Science, **18**(1983).
6. Baumeister, J. and Banhart, J. and Weber, M., VDI-Berichte **1151**.

---

**Part VII**  
**Gasar Materials**

## FORMATION OF ORDERED GAS-SOLID STRUCTURES VIA SOLIDIFICATION IN METAL-HYDROGEN SYSTEMS

V.I. SHAPOVALOV

State Metallurgical Academy of Ukraine,  
Sandia National Laboratories, PO Box 5800-1134, Albuquerque, NM 87123

### ABSTRACT

This work contains theoretical discussions concerning the large amount of previously published experimental data related to gas eutectic transformations in metal-hydrogen systems. Theories of pore nucleation and growth in these gas-solid materials will be presented and related to observed morphologies and structures. This work is intended to be helpful to theorists that work with metal-hydrogen systems, and experimentalists engaged in manufacturing technology development of these ordered gas-solid structures.

### INTRODUCTION

The work discussed here resulted from research conducted into the behavior of metal-hydrogen (M-H) systems at high temperatures and pressures conducted primarily at the State Metallurgical Academy of Ukraine starting in 1969. Additional work on other materials began in 1994 at Sandia National Laboratories in Albuquerque, NM and in 1995 at Naval Research Laboratory in Washington, D.C. In these studies, phase diagrams were constructed for systems displaying gas eutectic equilibria, including: Al-H, Be-H, Cr-H, Cu-H, Fe-H, Mg-H, Mn-H, Mo-H, Ni-H, Ti-H, W-H, Fe-C-H, alloy 625-H, alloy 718-H, alloy PH13-8Mo-H, and alloy ASTM-F75-H [1-7].

Simultaneous formation of solid metal and (hydrogen) gas from the liquid occurs in M-H alloys having gas-eutectic compositions. This reaction was named a gas eutectic reaction. An ordered combination of phases, termed "gasarite," may arise from such a gas eutectic reaction. It is comprised of a polycrystalline solid matrix and continuous oriented ellipsoidal pores filled with hydrogen, shown in Fig. 1(a).

The gasarite forms at solidification velocities ranging from 0.05 to 5 mm/s. Its morphological characteristics are largely determined by the hydrogen content and the gas pressure over the solidifying melt. Short-range order of pores, with a coordination number of about 6 is typically observed in a plane normal to the direction of solidification.

A few general observations about gasarite structures are: 1) the pore size distribution is dependent on gasarite formation conditions, and is non-uniform because concurrent growth of large and small pores is possible; 2) as the solidification front advances, the average pore diameter is increased and neighboring pores may periodically coalesce; 3) no branching of pores is ever observed to occur; 4) a pore may have periodic necks over its length; 5) pore growth arrest and nucleation of new pores may occur all through the solidification; and 6) no gasarite pores are nucleated on the mold surface. A non-porous metal skin 0.05-5 mm thick forms first.

The principal morphological parameters of gasarite are the average pore diameter  $d$ , the average pore length  $L$ , the average pore aspect ratio  $g=L/d$ , the void fraction  $P$ , and the pore area density  $n$  defined as pore number per  $1 \text{ cm}^2$  of a section normal to pore direction. These characteristics were found to have following variation ranges:

$d$	$L$	$g$	$P$	$n$
10 $\mu\text{m}$ to 10 mm	100 $\mu\text{m}$ to 30 cm	1 to 300	0.05 to 0.75	1 to $10^5 \text{ cm}^{-2}$

*Gasar* is the name coined for a material whose structure includes gasarite [1]. The word is an acronym of Russian expression meaning "gas-reinforced." Figure 1(b) depicts structural features of gasars. Diverse pore morphologies and/or alternating porous and non-porous layers can be produced by tailoring the process variables, such as hydrogen pressure, inert gas pressure, solidification velocity and pouring temperature [2].

In what follows, an attempt is made to explain mechanisms of phase nucleation and growth in gas eutectic reaction on the basis of experimental data.

#### PORE NUCLEATION

It is believed that nucleation of a gaseous phase in a liquid is heterogeneous, i.e. occurs on existing discontinuities in the liquid bulk or at the liquid/solid interface. The discontinuities may vary in nature, like:

- gas bubbles entrained from the atmosphere during melt pouring or stirring,
- bubbles formed in passing a gas through the melt,
- small bubbles caused by cavitation,
- small pits on the surface of high-melting particles suspended in the melt,
- small pits on the mold walls,
- regions where the liquid does not contact the solidification front.

The following is an explanation of pore nucleation in gasarite, shown in Fig. 2. A non-porous skin forms directly after pouring the melt into the mold. As the skin grows, the liquid ahead of the solidification front becomes increasingly supersaturated with hydrogen. Microscopic pits are always present on the surface of a growing solid due to the very nature of solidification. A pit may have such a curvature that the liquid will lose contact with the solidification front. A

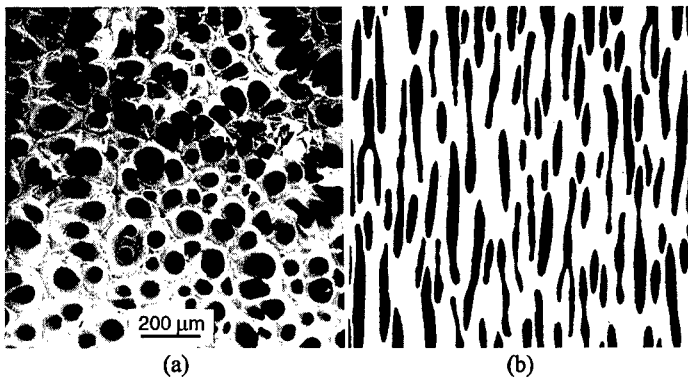


Figure 1. Gasarite. (a) Typical gasarite structure. Fracture surface normal to pore direction. 50x. (b) Schematic of typical gasarite features shown sectioned along pore direction.

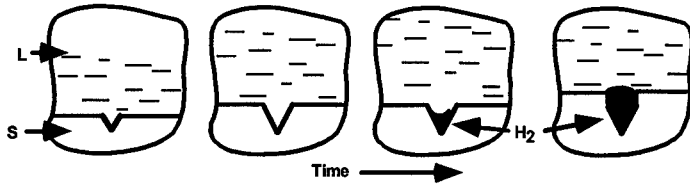


Figure 2. Gas nucleation at the solidification front in gas eutectic reaction.

cavern filled with hydrogen and metal vapor will form here. Should the cavern size be greater than or equal to certain critical radius  $R_0$ , a hydrogen bubble capable of growth will nucleate. The radius  $R_0$  can be estimated assuming that the surface energy of a bubble is equal to its bulk energy,

$$pV = \sigma S \quad (1)$$

where  $p = p_{\text{cap}} + p_{\text{hydr}} + p_{\text{ch}}$  is the pressure within the bubble,  $p_{\text{cap}}$  the capillary pressure,  $p_{\text{hydr}}$  the hydrostatic pressure,  $p_{\text{ch}}$  the gas pressure in the chamber,  $V$  the bubble volume,  $\sigma$  the average of the specific surface energies of the gas:liquid and the gas:solid interface,  $S$  the total area of bubble contact with the melt and the solid. Assuming a spherical bubble, one gets from (1),

$$(4/3)\pi R_0^3 p = 4\pi R_0^2 \sigma \quad (2)$$

On rearrangement,

$$pR_0 = 3\sigma \quad (3)$$

Hence the pressure dependency of the critical radius is,

$$R_0 = 3\sigma/p \quad (4)$$

Taking into account that the bubble is not spherical and the specific surface energies are different, we obtain,

$$R_0 = (\sigma_{\text{GL}}K_L + \sigma_{\text{GS}}K_S)/K_V p, \quad (5)$$

where  $\sigma_{\text{GL}}$  is the surface energy at the gas:liquid interface,  $\sigma_{\text{GS}}$  is the surface energy at the gas:solid interface,  $K_L$  and  $K_S$  the coefficients accounting for the relative areas of the gas:liquid and the gas:solid interface,  $K_V$  the proportionality factor used in the equation for the volume of a non-spherical bubble,  $V = K_V R_0^3$ . It is seen from Eqs. (4) and (5) that increasing the pressure will appreciably reduce  $R_0$ . Thus ever smaller discontinuities at the solidification front will be able to act as gaseous phase nuclei. To put it differently, increasing  $p$  will increase the number of hydrogen gas nuclei. This behavior is indeed observed in reality. The gas pressure above the solidifying melt is the major parameter that determines the number of pores per unit area in a plane normal to the growth of a gasaritic structure. One also can assume that the bubbles originate on high-melting particles floating in the melt ahead of the solidification front. The bubbles are next engulfed by the advancing front and the gas eutectic reaction sets in [6].

Let us consider this case: a buoyancy force  $F_A = (4/3)\pi R^3 d$  ( $R$  being the bubble radius,  $d$  the specific weight of the liquid) will act on any bubble, inducing it to rise in the melt. According to the Stoke's law, the velocity of the bubble's upward motion,

$$v = 2R^2 d / 9\eta \quad (6)$$

where  $\eta$  is the viscosity of the liquid. In experiments on Cu-H alloys, the gasarite forms in the solidification velocity range of 0.05 to 5 mm/s. At its maximum velocity of 5 mm/s, the solidification front thus can engulf bubbles about 100  $\mu\text{m}$  in size. These estimates support the idea [8] that hydrogen bubble nucleation may take place ahead of the solidification front. Furthermore, the above comments about the influence of pressure on nucleation at the solidification front also hold for the nucleation on suspended particles.

Two mechanisms of gas nucleation in gas eutectic reactions have thus been suggested. The question of how large their relative contributions are is highly important for scientific and practical purposes. To answer it, carefully planned experimentation on reasonably pure melts is needed.

## GASARITE GROWTH

Following an initial familiarization with the gasar process, an analogy is commonly drawn with gas evolution observed when the cap is removed from a container with a carbonated beverage. This approach is wrong, for the gasar process involves distinctly different phenomena.

When a bottle of soda water is opened the pressure in the liquid drops abruptly, allowing evolution of dissolved gas. Figure 3(a) depicts the progress of evolution. There are gas release sites - small pits filled with carbon dioxide - on the inner surface of the bottle. The gas dissolved in the liquid tends to migrate to these sites. As the gas volume at a site is increased, a bubble comes into being. The bubble grows and eventually is released from the site to rise to the surface. Some gas remains in the pit and acts on as a gas evolution site. This process is repeated as long as there is some degree of supersaturation in the liquid. A major part of the gas may also be evolved directly from the liquid surface without forming bubbles. Also note that boiling of a liquid is a similar process, except that the cavities are filled with vapor, rather than carbon dioxide.

In the gasar process, solid metal precipitates from the liquid simultaneously with gas, shown in Fig. 3(b). No decrease in pressure is necessary for this to happen. Moreover, increasing pressure is commonly needed to produce an ordered structure.

The suggestion [9] that the pore growth proceeds through a mechanism described earlier cannot be accepted either. The idea was that the advancing solidification front "stretches" gas bubbles already present in the liquid.

One should not overlook, however, that a diameter down to 10  $\mu\text{m}$  is sufficient for a bubble to rise fast enough not to be engulfed by the solidification front. Note that gasars may have pores 10 mm and more in diameter. A bubble as large as that will rise very rapidly, at about 100 mm/s.

One should also keep in mind that a crystalline solid grows concurrently with the gas in any gas eutectic reaction. However, the same phenomenological effect is seen in experiments involved combinations of non-interacting items like oil drops in solidifying boric acid, which preclude diffusion phenomena[9].

Steady-state growth in which all process variables are constant should result in a structure comprised of a non-porous matrix containing regular cylindrical channelways. In this situation the

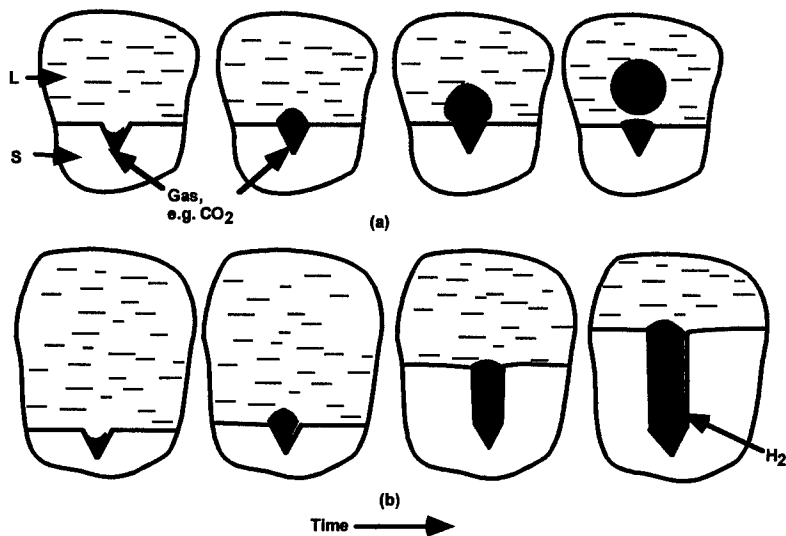


Figure 3. Gas evolution as opposed to gas eutectic reaction. (a) Bubbling in a liquid that boils or is supersaturated with a gas. Examples: boiling, carbon dioxide evolution from soda water. (b) Concurrent growth of a gaseous and a solid phase in gas eutectic reaction.

growth of the solid and the gas is sustained through transverse diffusion of hydrogen ahead of the solidification front. This process is possible due to hydrogen concentration gradients developing as expected from the M-H phase diagram, shown in Fig. 4. Hydrogen diffuses in the liquid along the solidification front, providing both solidification of the metal and growth of the gas channelways.

Hydrogen diffusivity in metals is high enough to allow rather long spacings between gas channelway axes (up to 10 mm), so diffusional self-adjustment of structure hardly plays any significant part in gasars. For this reason, it is not supercooling, but rather nucleation conditions and pressure in solidification that determine structural characteristics of a gasar as contrasted to a solid-solid eutectic.

Even under constant external conditions, however, the gasar structure departs from ideal, as has been found from numerous experiments. Growth arrest, coarsening, non-uniform size and irregular shape of pores were observed, shown in Fig. 1(b). For practical purposes, it is highly important to understand these phenomena.

#### Pore Growth Arrest

Multiple nucleation of the gaseous phase at the solidification front is believed to be among the causes of channelway growth arrest. Hydrogen concentration in the liquid ahead of the growing gas-eutectic colony is non-uniform, see Fig. 4. The supersaturation with hydrogen is at its highest at points lying farthest from the gas channelways ( $C_1$  in Fig. 4). When an active gas-liberation site originates here, it will attract a rapid influx of hydrogen that may be followed by emergence of a new pore. Should that happen, the growth of neighboring pores will slow down or stop.

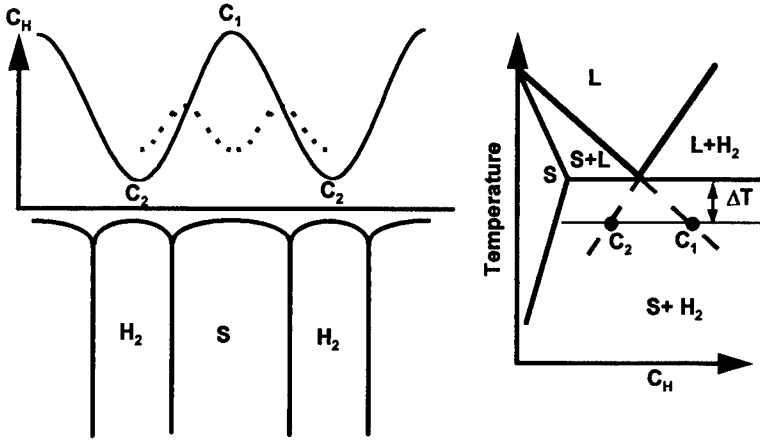


Figure 4. Hydrogen concentration distribution in a liquid ahead of the gas eutectic reaction front (left) and a portion of metal-hydrogen phase diagram near eutectic point (right).

Another cause of pore growth arrest is conceivably a unique mode of heat removal from the solidification front. In formation of a gas-solid structure, thermal radiation into gas channelways can contribute to transfer of heat from the front alongside with the common heat transfer processes observed for non-porous alloys, see Fig. 5.

The melt above a bubble becomes thereby supercooled, and a solid dome forms above the bubble, locally terminating the growth of gaseous phase. This happens only when the gas channelway is long enough. The amount of radiant energy absorbed by a channelway can be written as:

$$Q = \Sigma A(T_0/T_i)^4 \quad (i = 1, 2, \dots, n) \quad (7)$$

where  $n$  is the number of beam reflection events in a pore,  $A$  the proportionality factor depending on the channelway wall surface texture,  $T_0$  the temperature of emitting melt,  $T_i$  the temperature of walls at the  $i$ th reflection point.

The number of reflection events  $n$  is inversely proportional to the diameter and directly proportional to the length of the channelway. The minimum surface temperature of channelway walls (at its bottom) declines as the channelway grows. Therefore, the growth arrest is to be anticipated for channelways with a certain aspect ratio. This conclusion is generally corroborated by experiment, although in some cases abnormally long or short pores develop.

Yet another cause of growth arrest is constituted by gas pressure decline in a pore. As a pore grows, the average temperature  $T$  of the gas contained in it decreases, so the hydrogen pressure will be diminished in accordance with the Boyle's law,

$$p = (N/V)kT, \quad (8)$$

where  $N$  is the amount of gaseous substance in the pore,  $V$  the pore volume, and  $k$  the Boltzmann constant. For this reason, the gas growth will slow down and the liquid at the liquid:gas interface will freeze. This is confirmed by the fact that at the onset of gasar formation, when the temperature gradient is high, the pores are shorter than at later stages. Notably, this fact also

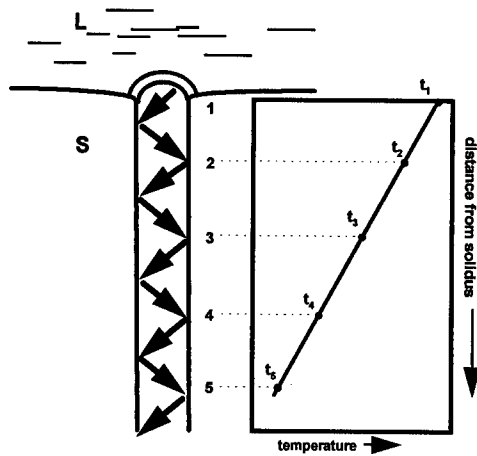


Figure 5. Schematic description of melt thermal radiation into a pore.

favors the two preceding hypotheses. All three mechanisms are believed to contribute to pore growth arrest in varying degrees.

#### Pore Coarsening

Two ways in which coarsening may develop during gas eutectic growth are deemed possible. First, as mentioned above, a pore may be terminated for some reason. A new pore may or may not subsequently be nucleated. If not, the neighboring pores will consume the hydrogen that otherwise would have been used for continued growth of the extinct pore. In consequence of this, the diameters of the neighboring pores will increase while the total number of pores will be decreased, shown in Fig. 6(a). This phenomenon may be termed wedging. It is observed mainly in low-porosity gasars (up to 30%).

The second possibility for pore coarsening is as follows. At higher void fractions exceeding 40 %, pore coalescence becomes prominent. If a hexagonal arrangement of pores is assumed, the void fraction  $P$  will be determined by the pore diameter  $D$  and the ligament thickness  $x$  according to,

$$P = \sqrt{3}\pi D^2 / 6(D + x) \quad (9)$$

Clearly, the pore spacing is relatively small at void fractions exceeding 40 %. Hence, the appreciable statistical possibility of contact between growing pores, shown in Fig. 6(b). Following a contact, the tips of the two pores will coalesce to form a wider tip advancing to continue the growth of one larger pore that replaces the two smaller ones. Repeated coalescence is possible that leads to progressive coarsening of the structure. This mechanism is especially important for M-H systems where hydrogen solubility differs greatly for the liquid and the solid metal ( $M = \text{Fe}$  or  $\text{Ni}$ ).

### Changes in Pore Diameter

These phenomena manifest themselves in pores having increasing or decreasing diameter or a wavy wall profile. Some flaring pores may result from wedging and coalescence (Fig. 6), while massive flaring is associated with monotonously decreasing pressure in solidification. Flaring pores are not infrequently observed at an initial stage of gasar growth, directly after nucleation of first pores.

Some tapered pores may result from wedging, shown in Fig. 6(a). They appear in great numbers when the solidification pressure is increased. Corrugated pores result from periodical variation of gas pressure above the solidifying gasar. The wider portions of a pore correspond to lower pressures, and the narrower portions to higher pressures. Internal pressure fluctuations within a pore also may cause repeated widening and narrowing. They take place when the volume rate of gas formation is greater than that of the solid. The tip of a growing pore in this situation will bulge to a diameter exceeding that of the channelway. A bubble is eventually detached from the channelway and rises to the surface, shown in Fig. 7. This cycle may be repeated many times. The pressure in the pore is increased as the bubble expands, but drops once the bubble is released. The increasing internal pressure has the same effect as decreasing the pressure above the melt. Consequently, the pore diameter will increase during the bubble expansion and decrease following the bubble release.

### Pore Orientation

The growth velocity vector is always normal to the solidification front at the pore initiation site. Therefore, any misalignment of pores is associated with local nonplanar areas of the solidification front, shown in Fig. 8.

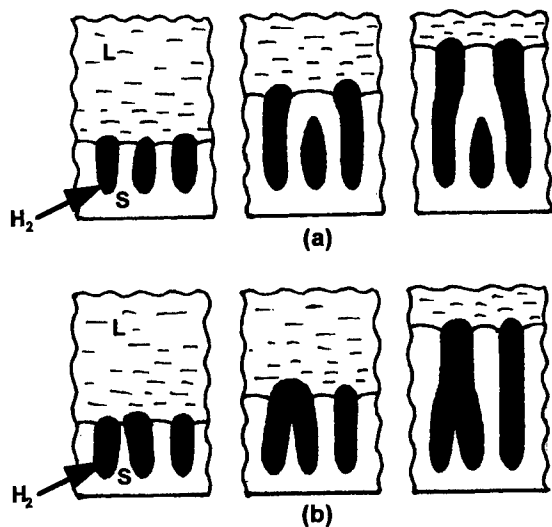


Figure 6. Pore coarsening by wedging (a) and coalescence (b).

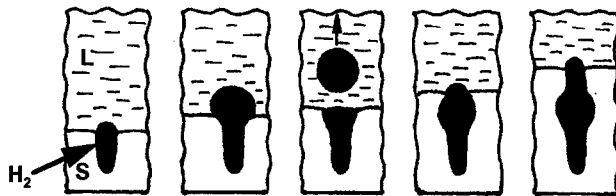


Figure 7. Mechanism of widening and narrowing of a growing pore.

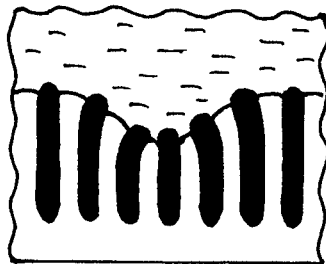


Figure 8. Pore orientation changes caused by a non-planarity of the solidification front.

## CONCLUSIONS

1. The gaseous phase nucleation in formation of ordered gas-solid structures may occur at the solidification front or on high-melting particles suspended in the liquid ahead of the front. The first mechanism would seem more viable.
2. The critical radius of bubble nuclei is shown to hyperbolically decrease with pressure. The bubble nucleation rate is increased accordingly.
3. Gasar pore formation follows a mechanism distinct from that of evolution of gas in carbonated beverages or bubbling in a boiling liquid. Furthermore, the ellipsoidal pore growth cannot be ascribed to stretching of gas bubbles by the advancing solidification front.
4. The gasar pore growth proceeds by hydrogen transverse diffusion ahead of the solidification front and concurrent advancement of the solid and the gaseous phase into the melt. When the growth rates of the two phases are equal, an "ideal" structure including cylindrical channelways in a non-porous matrix should form.
5. Unlike in solid-solid eutectics, the gasarite pore spacing is determined not only by diffusional self-adjustment. Rather, it is a function of the nucleation conditions and the solidification pressure.
6. A pore may be terminated by any of the following causes:
  - nucleation of a new pore in a space between the growing pores,
  - supplementary removal of heat from the bubble tip via thermal radiation into the channelway, and
  - pressure reduction in the pore due to the gas average temperature declining as the pore extends.
7. Pore coarsening in growth of a gas eutectic may be caused by wedging or pore coalescence. Wedging is mainly observed at low void fractions, and coalescence at high void fractions.

8. Some conical pores result from wedging, while widespread formation is due to pressure changes in solidification.
9. Corrugated pores may form due to periodical changes of pressure above the melt. Similar effects are caused by repeated detachment of bubbles from the solidification front.
10. Pore orientation in gasarite is determined by the shape of the solidification front, because the growth vector direction of a pore is always normal to the front at its location.

#### ACKNOWLEDGMENTS

The author would like to thank Michael Maguire for discussion of results and regular assistance, Frank Zanner and William Hammetter for their efforts allowing the author to work at and with Sandia National Laboratories, Virgil Provenzano and Bhakta Rath (Navel Research Laboratory) for oversight of joint gasar work, Raymond Decker (former president of ASM International) for helping with the interchange with American scientists and technicians, and Hideo Nakajima (Osaka University, Japan) for oversight of joint gasar work and discussion of results.

#### REFERENCES

1. V.I. Shapovalov, Influence of hydrogen on structure and properties of iron-carbon alloys, Metallurgiya Publishing House, Moscow, 1982, pp. 10- 235 (In Russian).
2. V.I. Shapovalov, US Patent 5,181,549 (26 January, 1993).
3. V.I. Shapovalov V.I., MRS Bull., 4, p.24, 19 (1994).
4. M.D. Baldwin, M.C. Maguire, and F.J. Zanner, in Proceedings of the 1997 International symposium on Liquid metal Processing and Casting, Santa Fe, New Mexico, February 16-19, 1997, edited by A. Mithell and P. Auburtin, pp. 417-426.
5. A. Pattnaik, S.C. Sanday, C.S. Vold, and H.I. Aaronson H.I., in Advances in Porous Materials, edited by S.Komarneni, D.M. Smith, and J.S. Beck (Mat. Res. Soc. Symp. Proc., Vol. 371, Pittsburg, PA 1995, pp. 371-376)
6. J.M. Wolla and V.Provenzano, *ibid.*, pp.377-382.
7. V. Provenzano, J.M. Wolla, P. Matic, A. Geltmacher, and A. Kee, *ibid.*, pp. 383-389.
8. Y. Zheng, S. Sridhar, and K.C. Russel, *ibid.*, pp. 365-370.
9. Chernov A.A., Modern Crystallography 111. Crystal Growth, Springer Verlag, Berlin, Heidelberg, New York, Tokyo, 1984, p.p. 123-127.

## GASAR POROUS METALS PROCESS CONTROL

J.M. Apprill\*, D.R. Poirier\*, M.C. Maguire\*\*, T.C. Gutsch\*\*\*

\*M.S.E. Department, University of Arizona, Tucson, AZ 85721, apprill@u.arizona.edu

\*\*Sandia National Laboratories, P.O. Box 5800, M/S #1134, Albuquerque, NM 87185

\*\*\*California State University, Chico, CA

### ABSTRACT

GASAR porous metals are produced by melting under a partial pressure of hydrogen and then casting into a mold that ensures directional solidification. Hydrogen is driven out of solution and usually grows as quasi-cylindrical pores normal to the solidification front. Experiments with pure nickel have been carried out under processing conditions of varying  $H_2$  partial pressure, total pressure ( $H_2 + Ar$ ), and superheat. An analysis that considers heterogeneous bubble nucleation was developed that identifies processing conditions in which hydrogen bubbles are stable in the liquid before solidification. It is hypothesized that these conditions lead to low porosity because these bubbles float out of the melt and "escape" the advancing solidification front. Experimental data are shown to support this hypothesis.

### INTRODUCTION

A common cause of porosity in many cast metals, particularly aluminum alloys, is due to the decreased solubility of hydrogen in the solid metal as opposed to the liquid. During solidification hydrogen is partitioned from the solid into the liquid. Eventually, the liquid becomes supersaturated with hydrogen, hydrogen bubbles are formed, and can subsequently be trapped in the advancing solidification front.

While this porosity is very undesirable in most cast metals, the GASAR process exploits this phenomenon as a method to produce porous metals. In the GASAR process, the metal is purposely melted under a  $H_2(g)$  partial pressure. After saturating the melt with hydrogen, it is directionally solidified, and the rejected hydrogen grows as quasi-cylindrical pores in the direction of the solidification front. The result is an anisotropic porous material with cylindrical pores oriented in the solidification direction.

The purpose of these experiments with Ni were to characterize the effects of  $H_2$  partial pressure, total pressure ( $H_2 + Ar$ ), and superheat on volume percent porosity of the final GASAR samples.

### EXPERIMENT

The experiments were performed on 99.99% pure electrolytic nickel. The furnace is a bottom-pour induction melting furnace housed in an ASME certified pressure vessel rated for 54 atm maximum pressure, shown in Fig. 1. The top cover of the furnace contains an actuator for the crucible stopper rod, and penetration ports for a viewing camera and an optical pyrometer. The main body of the furnace houses the crucible, and contains ports for the induction coil leads and the vacuum line. The bottom cover contains a cylindrical mold with a water cooled copper chill plate at the base to promote directional solidification.

Standard operating procedure consists of placing a metal charge in place in the crucible. The chamber is then sealed, vacuum evacuated and the charge is melted by the induction coils. The liquid metal is taken to the appropriate superheat temperature, and  $H_2(g)$  and  $Ar(g)$  are added to the furnace. After an appropriate time to ensure equilibration of the melt with the atmosphere, the metal is tapped by lifting the stopper rod. Solidification commences when the metal reaches the water cooled copper chill plate at the bottom of the mold.

The hydrogen content in the samples is controlled by the furnace atmosphere, a mixture of  $H_2(g)$  and  $Ar(g)$ . By changing the partial pressure of  $H_2(g)$ , different contents of hydrogen in the melt are obtained. In order to insure correct hydrogen content, the molten metal is held at the desired partial

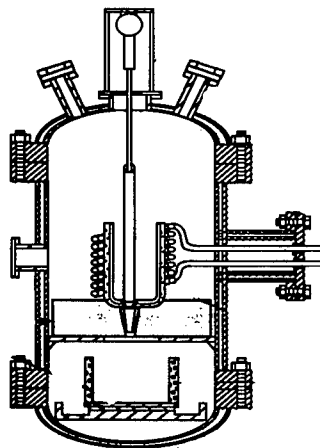


Fig. 1: Sandia GASAR furnace

pressures and superheat for 300 seconds, while the melt is being stirred by the electromagnetic forces created by the induction coils.

A three variable factorial designed experiment was conducted.  $H_2(g)$  partial pressure was studied at 2 and 10 atm;  $Ar(g)$  partial pressure was studied at 0 and 10 atm; and superheat was studied at 50 °C and 150 °C above the melting point. Since  $Ar(g)$  has no appreciable solubility in Ni, it was used as an experimental variable in order to vary the total pressure in the furnace atmosphere. Total pressure is the sum of the  $H_2(g)$  partial pressure and the  $Ar(g)$  partial pressure. One observation per treatment was observed for a total of  $2^3 = 8$  experiments. In addition to this, two observations at the processing conditions of 6 atm  $H_2(g)$ , 5 atm  $Ar(g)$ , and 100 °C superheat were studied to give some measure of process variability. The limited number of experiments were due to the slow turn around times for the furnace. The measured response in these experiments was volume percent porosity.

The cast GASAR ingots were 250 cm in diameter and 10 to 15 cm in length depending on the porosity formation. The ingots were halved, and a 5 cm x 5 cm x 1 cm section was taken from the location near the center of the ingot, approximately 1 cm from the surface contacting the chill plate. The density of these samples was determined by weighing them in air and in water and applying Archimedes' principle. Volume percent porosity was calculated by comparing the GASAR density to the density of pure nickel.

## THEORY

### Bubble Formation Due to Liquid Cooling

When the liquid metal is held at the given processing conditions of  $H_2(g)$  partial pressure,  $Ar(g)$  partial pressure, and superheat for 300 seconds prior to casting, this corresponds to a given hydrogen content in the liquid metal and is given by Sievert's Law:

$$\ln X_{H,l} = \frac{-A}{T} + B + \frac{1}{2} \ln P_{H_2} \quad (1)$$

where  $X_{H,l}$  is the mole fraction of hydrogen in Ni(l), T is the temperature of Ni(l),  $P_{H_2}$  is the partial pressure of hydrogen at the Ni(l) /  $H_2(g)$  interface, and A and B are constants where  $A = 3081$  and  $B = -5.14$  [1].

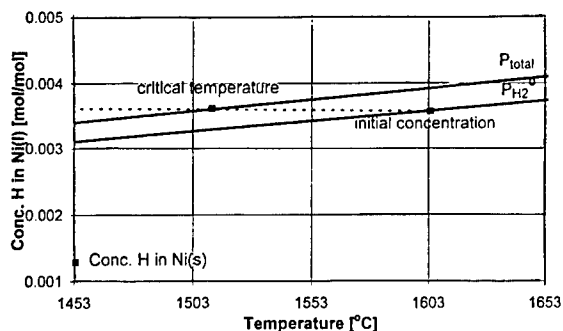


Fig. 2: Concentration of hydrogen in Ni(l) as a function of temperature for the processing conditions: 10 atm  $H_2(g)$ ; 2 atm  $Ar(g)$ ; 150 °C superheat.

Figure 2 is a plot of  $X_{H,l}$  as a function of T at two values for  $H_2(g)$  partial pressure. The first value,  $P_{H_2}^0$ , is the given processing condition which the Ni(l) was exposed to for 300 seconds prior to casting. The second value,  $P_{total}$ , is the  $H_2(g)$  partial pressure which is equal to the total pressure in the furnace atmosphere.  $P_{total}$  is the sum of the  $H_2(g)$  and the  $Ar(g)$  partial pressures in the furnace atmosphere.

When the Ni(l) is cast, it falls onto the water cooled Cu chill plate in the mold below. As the liquid cools, its solubility for hydrogen decreases and hydrogen attempts to come out of solution at a pressure  $P_{H_2}^0$ . However, hydrogen can only come out of solution at  $P_{H_2}^0$  at the top of the melt, which is

solidifying from the bottom up. Therefore the liquid becomes supersaturated with hydrogen. The liquid continues to cool until at the critical temperature the hydrogen can come out of solution at a pressure of  $P_{total}$ . Therefore the critical temperature is the temperature at which the  $H_2(g)$  partial pressure is equal to the external pressure and can drive back the atmosphere to form a bubble.

#### Nucleation of Bubbles on Pits and Cracks of Non-Wetted Inclusions

The above discussion takes no account of how the hydrogen will leave the melt once the critical temperature has been reached. There is ample evidence that considers that bubble nucleation occurs on pits and cracks of non-wetted inclusions in the melt [2-8]. Consider a conical pit in an  $Al_2O_3(s)$  inclusion in the Ni(l) melt under vacuum (Fig. 3).

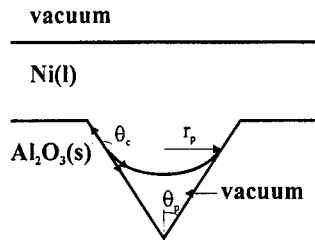


Fig. 3: Conical Cavity

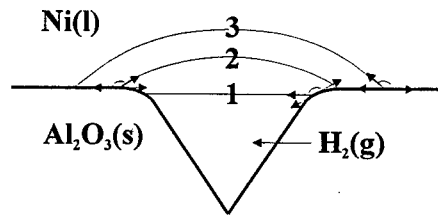


Fig. 4: A growing bubble nucleus

The pressure drop across the curved meniscus is given by Laplace's equation:

$$\Delta P = P_{concave} - P_{convex} = \frac{2\gamma}{r} \quad (2)$$

where  $P_{concave}$  is the pressure on the concave side of the meniscus, in this case it is equal to the pressure of Ni(l) at the meniscus;  $P_{convex}$  is the pressure on the convex side of the meniscus, in this case it is zero;  $r$  is the radius of curvature, and  $\gamma$  is the Ni(l) surface energy which is  $1.81 \text{ Jm}^{-2}$  [9]. For this geometry, one can relate the pressure drop across the meniscus to the size of the conical pit by the following equation:

$$\Delta P = P_{concave} - P_{convex} = \frac{-2\gamma \cos(\theta_c - \theta_p)}{r_p} \quad (3)$$

where  $\theta_c$  is the contact angle of Ni(l) on  $Al_2O_3(s)$  which is  $140^\circ$  [9],  $\theta_p$  is equal to one half the angle of the conical pit, and  $r_p$  is the radius of the conical pit at the level of the meniscus. Substituting values of  $10^\circ$  for  $\theta_p$  and  $2.3 \text{ atm}$  for  $\Delta P$ , one can solve Eq. 3 for  $r_p$  equal to  $10 \mu\text{m}$ . Therefore, if an  $Al_2O_3(s)$  inclusion with a conical pit half angle of  $10^\circ$  existed in the Ni(l) at a depth which caused a hydrostatic pressure of  $2.3 \text{ atm}$ , then the Ni(l) would penetrate the conical pit until the radius of its meniscus was  $10 \mu\text{m}$ .

It is therefore shown that when Ni is melt under vacuum, the bottoms of pits and cracks of non-wetted inclusions will not be wet by the melt and will exist as "pockets" of vacuum in the liquid. When  $H_2(g)$  and  $Ar(g)$  are added to the furnace, hydrogen will go into solution with the liquid, diffuse to these "pockets" and come out of solution to exist as  $H_2(g)$  again. The "pocket" is now a bubble nucleus. The  $H_2(g)$  pressure in this nucleus is given by Sievert's Law (Eq. 1) and, during the 300 second saturation period, it becomes equal to the  $H_2(g)$  partial pressure in the furnace.  $Ar(g)$  won't diffuse to these pockets because it has limited solubility in the liquid.

It should be noted that the prominent feature of these bubble nuclei is their concave liquid/gas interface with respect to the liquid phase. This allows the gaseous phase to exist at a pressure below that of the liquid, as shown by Eq. 2. In order for the nucleus to form a bubble (with a convex interface with respect to the liquid phase) the pressure in the nucleus must increase to a value greater than the pressure in the liquid.

As stated earlier, when the Ni(l) cools, it becomes supersaturated with hydrogen. In the Ni(l) adjacent to the nuclei, hydrogen comes out of solution to exist as H<sub>2</sub>(g) in a nucleus. This increases the pressure in the nucleus and causes it to grow until the meniscus reaches the top of the conical pit. From here, it is useful to follow Pugachev's [10] discussion of a bubble detaching from a capillary during the Maximum Pressure Method to measure surface tension. If one assumes the opening of a conical pit (or the tip of a capillary) has rounded edges, then further increase in the pressure in the nucleus will be utilized to straighten the meniscus. It should be noted that the contact angle is independent of the surface geometry, and is the same on a curved surface as on a flat surface [11]. When the pressure in the nucleus equals the pressure in the liquid, the interface will become planar (position 1 of Fig. 4). On further increase in pressure, a small bubble will begin to form and the three phase interface will move over the rounded part of the opening. This corresponds to the maximum pressure in the nuclei because the interface is convex with respect to the liquid phase, and the radius of curvature is at a minimum (position 2 of Fig. 4). From here, any further increase in the volume of the bubble due to hydrogen diffusing from the supersaturated liquid will result in an increase in the radius of curvature (position 3 of Fig. 4). This also leads to a subsequent decrease in the equilibrium pressure in the nucleus as given by Laplace's equation (Eq. 2). Therefore, bubble growth will occur rapidly and will either detach or engulf the inclusion. If one assumes that the critical point of bubble formation to be when the meniscus is flat and the pressure in the nucleus is equal to the pressure in the liquid, then the analysis in the previous section is correct.

#### Hydrogen Solubility in the Solid Metal

Hydrogen solubility in Ni(s) is given by Sievert's Law, but with different constants:

$$\ln X_{H,s} = \frac{-A'}{T} + B' + \frac{1}{2} \ln P_{H_2} \quad (4)$$

where X<sub>H,s</sub> is the mole fraction of hydrogen in Ni(s), T is the temperature of Ni(s), P<sub>H<sub>2</sub></sub> is the partial pressure of hydrogen at the H<sub>2</sub>(g) / Ni(s) interface, and A' = 1967, B' = -6.77 [1]. One must examine hydrogen solubility in the solid at the solidification front, since this is where porosity develops. Consider Fig. 5 which shows a pore full of H<sub>2</sub>(g) growing with the solidification front. The pressure drop across this curved interface can be ignored because the radius of curvature is large. There must be a mechanical equilibrium between the pressure in the pore and the pressure in the liquid. If one neglects hydrostatic pressure, the pressure in the pore must be equal to the pressure in the furnace atmosphere. The hydrogen solubility in the solid at the solidification front is therefore given by:

$$X_{H,s} = \sqrt{P_{total}} \exp\left(\frac{-A'}{T_m} + B'\right) \quad (5)$$

where P<sub>total</sub> is the total pressure in the furnace atmosphere, and T<sub>m</sub> is the melting point of nickel, which is the temperature of Ni(s) at the solidification front. It should be noted that the melting point of the nickel with hydrogen in solution is within 1°C of the melting point of pure nickel [12].

#### Solubility Diagrams

Consider Fig. 2 again, which is the representative diagram for a sample processed with a large percentage of H<sub>2</sub>(g) in the furnace atmosphere and/or a large superheat. In this case, the critical point is reached at a temperature in excess of the melting point. Therefore bubbles will form in the liquid well ahead of the solidification front and it is hypothesized that these bubbles float out of the melt and are not trapped as porosity in the solid. These processing conditions will be termed "bubble forming".

Figure 6a is representative of processing conditions with a very low percentage of H<sub>2</sub>(g) in the furnace atmosphere and a low superheat. In this case, the liquid reaches the melting point before the

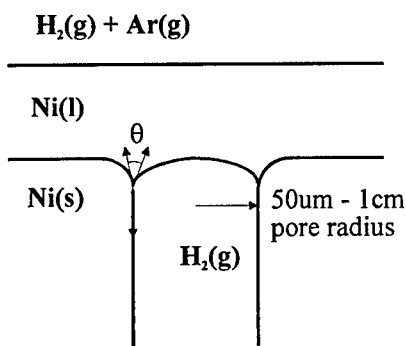


Fig.5: A pore growing with the solidification front.

critical temperature, and the hydrogen concentration in the liquid does not exceed the hydrogen solubility in the solid. Therefore, as the solidification front advances, hydrogen goes from liquid solution to solid solution and no porosity develops. These processing conditions are termed "pore free" conditions. Figure 6b is representative of processing conditions with a moderate percentage of H<sub>2</sub>(g) in the furnace atmosphere and a moderate to low superheat. In this case, the liquid reaches the melting point before the critical temperature, but the hydrogen content in the liquid exceeds the hydrogen solubility in the solid. Therefore, hydrogen is rejected by the advancing solid, thus supersaturating the liquid ahead of the solidification front. Bubbles form in the supersaturated liquid and are subsequently caught by the advancing solidification front to become pores. These processing conditions are termed "pore forming" conditions.

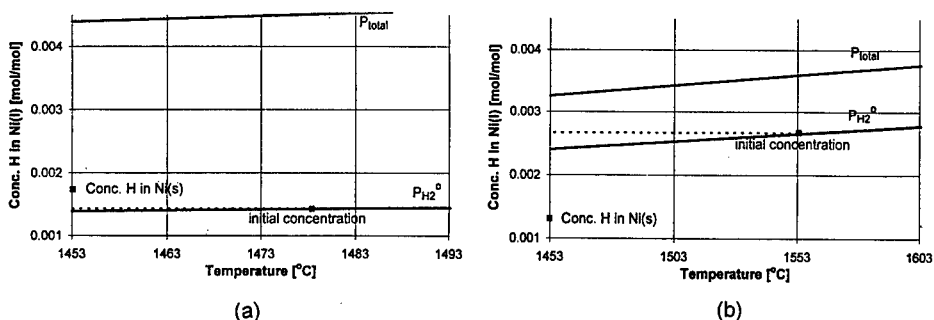


Figure 6: Solubility diagrams for a) 2 atm H<sub>2</sub>(g), 18 atm Ar(g), 25 °C superheat; b) 6 atm H<sub>2</sub>(g), 5 atm Ar(g), 100 °C superheat.

## RESULTS

Table 1 lists the processing conditions, measured porosity, and calculated porosity for each experiment. No experiments were performed with pore free processing conditions. However, the two experiments which approached pore free conditions were #3 and #7. These samples contained very low porosity, as expected.

Table 1 reveals that the samples processed under bubble forming conditions are characterized by low porosity. As stated earlier, it is believed that bubbles formed in these samples float out of the melt and are not captured as porosity. During these experiments, the mold camera recorded the solidifying melt "bubbling" and "spitting". This was not observed with the non-bubble forming conditions. Nonetheless, cylindrical pores are formed with the bubble forming compositions, so some bubbles are trapped in the solid.

Experiment	H <sub>2</sub> (g) p.p. [atm]	Ar(g) p.p. [atm]	Superheat [°C]	Processing Conditions	Porosity [vol.%]	Predicted Porosity
1	6	5	150	Pore forming	52.9	58.4
2	10	0	50	Bubble forming	9.2	
3	2	10	150	Pore forming	6.4	22.9
4	2	0	150	Bubble forming	14.1	
5	10	10	150	Pore forming	42.0	51.0
6	6	5	100	Pore forming	54.7	58.4
7	2	10	50	Pore forming	16.9	14.5
8	2	0	50	Borderline	63.0	83.5
9	10	10	50	Pore forming	54.6	46.6
10	10	0	150	Bubble forming	13.5	

Table 1: Experimental Results

During pore forming conditions, it is believed that all the bubbles formed are caught by the solidification front and become pores. If so, then a simplistic model based on the ideal gas law can be used to calculate volume percent porosity in the final casting:

$$\text{Volume\% Porosity} = \frac{(X_{H,l} - X_{H,s})RT_m}{(X_{H,l} - X_{H,s})RT_m + (P_{\text{total}} \cdot M / \rho_s)} \quad (6)$$

where  $X_{H,l}$  and  $X_{H,s}$  are the hydrogen concentrations in the liquid and solid at the solidification front (Fig. 6b),  $T_m$  is the melting point of Ni,  $P_{\text{total}}$  is the total pressure in the furnace atmosphere, and  $M$  and  $\rho_s$  are the molar mass and density of Ni(s) respectively. By examining Table 1, it is apparent that this simple model does a reasonable job of predicting volume percent porosity in the pore forming samples. It should be noted that experiment #8 was a borderline case between bubble forming and pore forming conditions, in which the critical temperature was very close to the melting point. Due to the large porosity in this sample, it is believed to be pore forming.

## CONCLUSION

Experiments were performed with nickel and the effects of the processing conditions  $H_2(g)$  partial pressure, total pressure, and superheat on volume percent porosity were studied. The following conclusions can be drawn:

1. In the GASAR process, a large percentage of  $H_2(g)$  in the furnace atmosphere and/or a large superheat create conditions in which  $H_2(g)$  bubbles form in the cooling Ni(l) well ahead of the advancing solidification front. This is undesirable for process control because these bubbles float out of the melt and are not incorporated into the final porosity.
2. The  $H_2(g)$  bubbles are most likely nucleated on pits and cracks of non-wetted inclusions in the melt. It can be shown that when the pressure in the nuclei is equal to the pressure in the surrounding liquid, bubble formation occurs.
3. Experiments with a moderate percentage of  $H_2(g)$  in the furnace atmosphere and a moderate to low superheat create conditions in which bubbles are not expected to float out of the melt. In these cases, volume percent porosity can be predicted reasonably well with a simple model based on the ideal gas law.
4. It is hypothesized that processing conditions with a very small percentage of hydrogen in the furnace atmosphere and a low superheat would produce pore free castings.

## ACKNOWLEDGMENTS

Special thanks go to Mark Miszkil for his tireless help conducting GASAR experiments. This work was supported by the United States Department of Energy under contract DE-AC04-94AL85000. Sandia is a multiprogram laboratory operated by Sandia Corporation, a Lockheed Martin Company, for the United States Department of Energy.

## REFERENCES

1. E.A. Brandes, G.B. Brook, *Smithells Metals Reference Book*, 7<sup>th</sup> Ed., Butterworth-Heinemann, Boston, 1992, pp. 12-3.
2. S. Tiwari, J. Beech, *Metal Science*, pp. 356-362 (1978).
3. G. Laslaz, P. Laty, *Trans. AFS* **99**, pp. 83-90 (1991).
4. P. Mohanty, F. Samuel, J. Gruzleski, *Met. Trans.* **24A**, pp. 1845-56 (1993).
5. S. Sridhar, K.C. Russell, *J. Mater. Synthesis and Processing* **3**, pp. 215-222 (1995).
6. H. Fredriksson, I. Svensson, *Met. Trans.* **7B**, pp. 599-606 (1976).
7. H. Shahani, H. Fredriksson, *Scand. J. Metallurgy* **14**, pp. 316-320 (1985).
8. K. Brondyke, P. Hess, *Trans. AIME* **230**, pp. 1542-46 (1964).
9. B.V. Tsarevskii, S.I. Popel in *The Role of Surface Phenomena in Metallurgy*, edited by V.N. Eremenko (Consultants Bureau Enterprises Inc., N.Y., 1963), pp. 96-101.
10. P.P. Pugachev in *Surface Phenomena in Metallurgical Processes*, edited by A.I. Belyaev (Consultants Bureau Enterprises Inc., N.Y., 1965), pp. 152-65.
11. J. Israelachvili, *Intermolecular and Surface Forces*, 2<sup>nd</sup> Ed., Academic Press, N.Y., 1992, pp. 319-321.
12. Y. Zheng, MSc Thesis, Dept. of Mater. Sci. Engr., M.I.T., 1995.

## THE EFFECT OF GASAR PROCESSING PARAMETERS ON POROSITY AND PROPERTIES IN ALUMINUM ALLOY

C.J. Paradies\*, A. Tobin\* and Jeff Wolla\*\*

\*Northrop Grumman Corporation, AS&T, M/S A01-26, Bethpage, NY 11714

\*\*Naval Research Laboratory, Washington, DC 20375

### ABSTRACT

The GASAR process involves the dissolution of hydrogen in a molten metal or alloy by controlling the hydrogen pressure and the temperature in a high pressure chamber. The difference between the hydrogen solubility in the melt and the solid is used to control the growth of hydrogen pores within the solidifying structure. Designed experiments have been performed to determine the relative effects of the saturation pressure, temperature, casting pressure, mold temperature and cooling rate on the total porosity, pore size, distribution and shape in pure nickel and aluminum alloys. The shape and distribution of pores was found to depend upon the structure of the primary solid during pore nucleation and growth. Reducing the casting pressure had the strongest effect on increasing the total porosity and pore size.

### INTRODUCTION

The GASAR process developed by V. Shapovalov [1] leads to the formation of pore structures in the solid by controlling the solidification of liquid metals with significant quantities of dissolved hydrogen in solution. The difference between the solubility of hydrogen in the liquid at high temperature and elevated hydrogen pressures and the solid during solidification at lower temperature and pressure causes hydrogen induced pore development. The temperature, pressure and composition phase diagram determines the amount of hydrogen that is available to form pores. The kinetics of the rate of nucleation, solidification and outgassing of hydrogen fixes the volume fraction of porosity that remain within the metal after solidification is complete.

Lightweight structures with special thermal, acoustic and energy absorption characteristics have been cast in nickel, copper, aluminum, iron and magnesium and their alloys using the GASAR process [1,2]. An understanding of the effects of the process control parameters on the total porosity and pore size, shape and distribution of pores is being developed. Some preliminary experiments were designed and conducted at Naval Research Laboratory and at Sandia National Laboratory to evaluate the effects of process control parameters on the pore structures developed during casting.

### EXPERIMENTAL PROCEDURES

A laboratory scale apparatus was located at the Naval Research Laboratory (NRL) and a scaled-up facility was utilized for nickel GASARs at Sandia National Laboratory. In the facility at NRL, an aluminum alloy was melted in a crucible, held at a hydrogen saturation pressure and temperature for a fixed period of time and then poured into a 22.6 mm diameter x 140mm long BN-coated stainless steel mold attached to a copper chill. The various processing parameters

used to design the experiments conducted at NRL are listed in Table 1. Seventy experiments were conducted to evaluate effects of the process variables on the formation of porosity. The casting pressure was achieved by venting a portion of the gas and then using a vacuum pump, when necessary. An experimental design based on Taguchi methods was developed to investigate the relative importance of some of the control parameters. From this initial set of experiments, a new sequence of experiments was performed to determine the conditions most suitable for producing porosity in aluminum alloys. The solidification rate was controlled by either pouring the alloy directly onto an exposed copper chill or by interposing a disk of fiberfrax felt between the copper chill and the melt. In addition to porosity, the effect of the processing conditions on pore size and shape was evaluated.

Table 1: Processing Parameters for the Experiments at the Naval Research Laboratory.

Alloys:	A357	AA6061	AA2090	AA2195
Saturation T:	690 - 966 °C			
Saturation time:	15 - 90 minutes			
Total Pressure:	45 - 280 psig			
HYDROGEN Pressure:	45 - 221 psig			
Mold:	insulated	non-insulated	preheated	
Chill:	copper	copper + fiberfrax	steel	
Casting Pressure:	-14 to 200 psig			
Sequence:	vent & pour		pour & vent	

The experiments performed at Sandia used 99.9998% pure nickel. The alloy was melted in an induction furnace and was poured onto a copper chill by raising a stopper rod. A camera was positioned to observe the molten nickel as it solidified. The control parameters and the procedure were similar to the experiments conducted at NRL; however, the solidification pressure was the same as the total pressure during saturation of the hydrogen in the melt. Eleven experiments were conducted using nickel, as shown in Table 2.

Table 2: Control Parameters & Results of the nickel GASAR Experiments Conducted at Sandia.

Exp	Control Parameters			Porosity Specimen				Pore Size	
	$\Delta T$	$P_{H_2}$	$P_{Ar}$	1	2	3	Ave.	diameter	shape
	(C)	(atm)	(atm)	(%)	(%)	(%)	(%)	(mm)	
1	100	6	5	19	17	17	18	small	elong.
2	50	10	0	9	5	6	7	small	elong.
3	150	2	10	6			6	small	elong.
4	150	2	0	14	7	10	11	small	elong.
5	150	10	10	42	21	20	28	large	elong.
6	100	6	5	55	23	49	42	large	elong.
7	50	2	10	17	16	15	16	small	elong.
8	50	2	0	63			63	large	elong.
9	50	10	10	55	43	43	47	small	elong.
10	150	10	0	14			14	large	elong.
11	100	6	5	53	44	40	46	medium	elong.

## RESULTS

The ingots cast at Sandia National Laboratory showed elongated pores. The total porosity, pore size and shape depended upon the processing conditions, as summarized in Table 2. The size ranges used in Table 2 correspond to the following diameters: small < 2 mm, medium < 5 mm, large  $\geq 5$  mm. The smallest pores had a mean diameter of 95  $\mu\text{m}$  and aspect ratio of 4.3. The largest pores had diameters as large as 9 mm, and extended to nearly the length of the casting. Typical pore structures are shown in Figure 1. Etching of the nickel did not reveal the underlying columnar-dendritic structure, because the nickel was too pure; however, dendrites exposed by the redistribution of melt toward the end of solidification showed a columnar-dendritic structure of the solid nickel. Although the rates of solidification and thermal gradients within the melt were not measured, it was assumed that they corresponded to the factors that influenced the thermal history of the melt: the pouring temperature, the ratio of hydrogen to argon and the total pressure. Bubbles were observed evolving from the surface of the castings during solidification. More gas was observed escaping during the casting of Heats 2, 4, 8 and 10 than during the other heats.

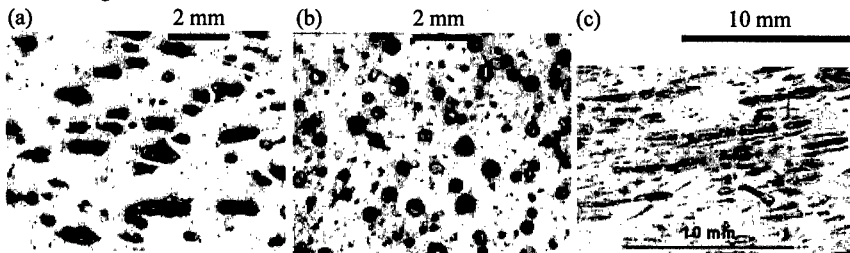


Figure 1 Micro structure of Nickel GASAR for heat 7 in (a) the elongated direction, (b) the transverse direction and (c) Heat 9 in the elongated direction.

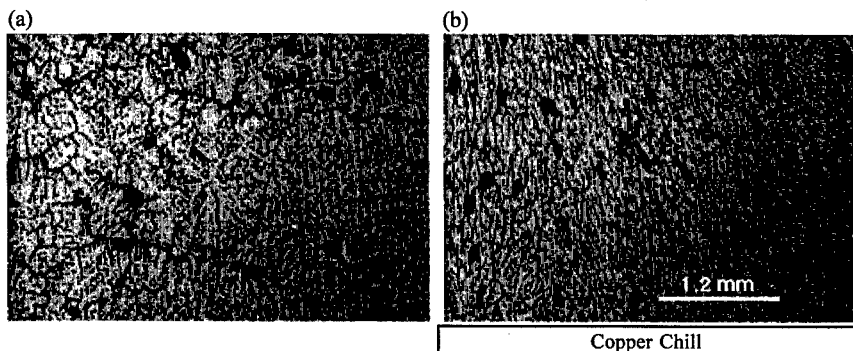


Figure 2: Images of the microstructures of GASAR processed samples for an A357 alloy with (a) equiaxed grains and spheroidal pores and (b) columnar-dendritic grains and elongated pores.

Pore structures observed in Al alloy ingots were often spheroidal or irregular. These pores were distributed in the regions between the grains or sub-grain boundaries of the equiaxed dendrites, Figure 2 (a). Some elongated pores were found between the columnar dendrites that were growing in the columnar zone of the casting, Figure 2b. Therefore, pore sizes and shapes were very dependent upon the primary solid structure. Figure 3 indicates that the total porosity also depends upon the solidification pressure. As the solidification pressure increases both the pore size and total porosity decrease. The outlined area in Figure 4 shows the tips of primary aluminum dendrites protruding into a pore. The region between the dendrite tips is eutectic.

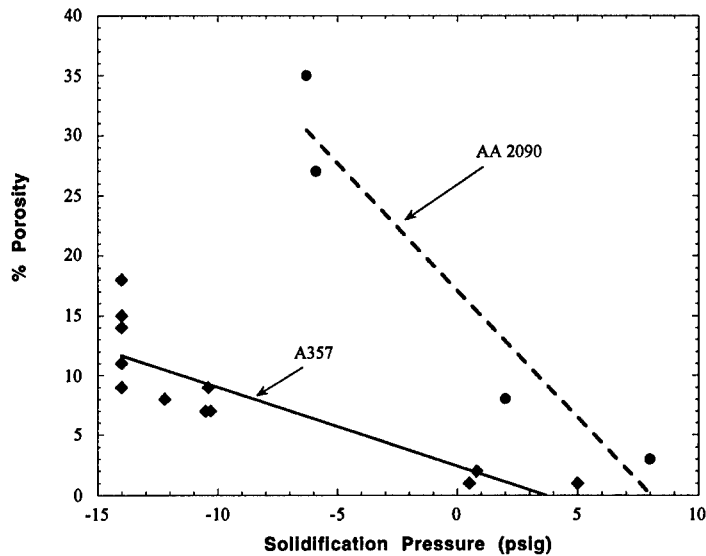


Figure 3 Effect of the solidification pressure on the total porosity for A357 and AA2090.

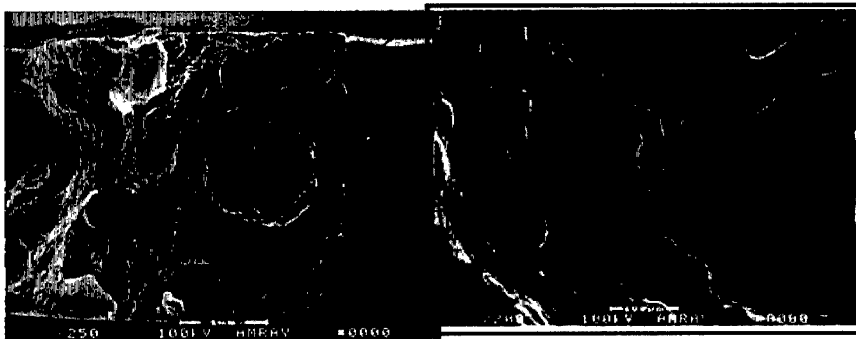


Figure 4: SEM Images of a pore from the fractured region of a tensile specimen. The area outlined is magnified further to reveal inner pore surface in the image to the right.

---

## DISCUSSION

The size and shape of the pores appear to be distributed between the primary, solid phases, indicating that either the pores nucleate in the interdendritic regions or that they eventually move to these locations during solidification. The pores impinge upon the preexisting solid phase causing the melt to be pushed away from the dendrites. The irregular shape of the pores in AA2090 samples might be caused by nucleation and growth of the pores later during the process of solidification. Alternatively, the presence of lithium and copper in the alloy AA2090 might cause a decrease in the surface tension. A lower surface tension would reduce the hydrogen pressure within the pores required to force the melt from around the primary dendrite tips. The pores could then exhibit the irregular, interdendritic and nonspherical shapes observed. Significant elongation of the pores was only observed in the AA2195 (Weldalite) specimen. A region of elongated pores was found in the region of the casting where the primary dendrites exhibited columnar-dendritic growth. This was the only aluminum alloy that exhibited both a large columnar-dendritic region and a comparatively high total porosity. The elongation of the pores is attributed to the shape of the primary dendrites and the interdendritic channels that the hydrogen pore displaced.

Elongation of pores was observed in all of the nickel experiments. The pores appear to impinge upon the solid in the radial direction; therefore, the pores grow into the melt in the direction of the solidification by diffusion of the hydrogen from the solidifying interface. The solidification pressure, the concentration of hydrogen at the interface, the distance to the pores and the rate of advance of the dendrites play a part in determining the growth rate of the pores. Because the pressure within the pore must balance the external pressure, the metalostatic pressure and the surface tension forces acting on the pore, the solidification pressure is critical. As the solidification pressure increases, more hydrogen must diffuse to the pore to maintain its volume and the pore will grow more slowly.

To maximize the total porosity, a pressure sufficient to keep the pores from growing faster than the dendrites is required. Otherwise, a bubble will either grow to block the columnar dendrites surrounding it, increasing its radius or a portion of the pore will detach and float to the surface of the melt. Evidence for both of these mechanisms of pore evolution were observed in experiments with supersaturations of hydrogen. The diameter of the pores with hydrogen supersaturations, heats 2, 4 and 10, grew with distance from the chill, vigorous effervescence was observed at the melt surface and the total porosity was much less than predicted from the phase diagram[3]. The diameter of the pores in unsaturated melts did not increase as much with distance from the chill. The bubbles that were observed escaping from unsaturated melts provide some evidence for the detachment mechanism. Nucleation in the liquid was possible for the supersaturated melts, but bubbles were also observed evolving from melts that were unsaturated but near the nickel-hydrogen eutectic, indicating that bubbles were originating at the melt-solid interface, perhaps as the pores grew faster than the columnar dendrites.

The slight curvature of the pores visible in Figure 1 (c) is evidence that growth of the pores are coupled to the growth of the columnar dendrites. Curvature was most apparent for the pores growing near the mold walls. Near the copper chill and the central portion of the casting the

---

curvature was not observed. It is well known that the growth direction of dendrites is influenced by thermal gradients. It was apparent in the Al alloy micrographs that heat transfer to the initially cold walls influenced the direction of growth of the dendrites and pores during the early stages of solidification. Preheating of the mold eliminated this. The same process must have occurred during the casting of nickel, and the pores followed the direction of growth of the columnar dendrites.

Small diameter pores with low aspect ratios were observed in specimens cut from billets with hydrogen concentrations in the melt that were far from the metal-hydrogen eutectic. The low concentrations of hydrogen in the melt caused the total porosity to remain low, as predicted by the phase diagram. To explain the lower aspect ratio for the heats with comparatively low concentrations it is necessary to examine the competition between pore growth and dendritic growth. If the pores grow at a slower rate than the advancing dendrites, the dendrites would impinge eventually upon one another, causing the extinction of the pores. This extinction mechanism could account for the low aspect ratios observed for these heats. Coupled, steady-state growth occurred only when the external pressure caused the rate of advance of the pores to be the same as the rate of advance of the columnar dendrites. Heats 6, 8, 9 and 11 were nearly at these conditions, and some of the pores in these heats were observed to extend through the length of the billet. These conditions maximized the porosity in the ingot.

## CONCLUSIONS

Decreasing the casting pressure increases the pore size and total porosity. Total porosity, pore size and pore shape also depend upon the temperature-composition-pressure phase diagram for the metal-hydrogen system, the rate of solidification, the temperature gradient and the process sequence, but these parameters are interactive and require additional experiments to evaluate their significance. Pore shape depends upon the microstructure of the primary solid phase; elongated pores are associated with cellular or cellular-dendritic growth.

## ACKNOWLEDGEMENTS

The authors would like to acknowledge the researchers and technicians at Sandia National Laboratory for producing the nickel heats and the financial support of DARPA/ONR Agreement No. N00014-97-2-0001.

## REFERENCES

1. V.I. Shapovalov, "Porous Metals," *MRS Bulletin*, pp.24-28, April (1998).
2. V.I. Shapovalov, "Method for Manufacturing Porous Articles," *United States Patent*, No. 5,181,549 January (1993).
3. J. Apprill, M. Maguire and T. Gutsch, "Pore/Bubble Stability in GASAR Porous Metals Processing," *Porous and Cellular Materials: for Structural Applications*, Proceedings of the MRS Spring Meeting, MRS (1998).

---

## CHARACTERIZATION OF POROUS GASAR ALUMINUM

R. J. Bonenberger<sup>1</sup>, A. J. Kee<sup>2</sup>, R. K. Everett<sup>3</sup>, and P. Matic<sup>3</sup>

<sup>1</sup> FM Technologies, Inc., 10529-B Braddock Rd., Fairfax, VA 22032

<sup>2</sup> Geo-Centers, Inc., P.O. Box 441340, Fort Washington, MD 20749

<sup>3</sup> Naval Research Laboratory, Code 6382, 4555 Overlook Ave., SW, Washington, DC 20375

### ABSTRACT

Experimental and numerical analyses were performed on porous aluminum samples to evaluate microstructure and mechanical properties. Experiments consisted of tensile tests on dog-bone specimens containing 9 to 17% porosity, which were instrumented with axial and transverse extensometers. Properties measured included Young's modulus, Poisson's ratio, proportional limit, 0.2% offset yield strength, and ultimate tensile strength. Results indicated that Young's modulus and all strengths decreased with increasing porosity, but Poisson's ratio remained constant with porosity. For the numerical simulations, 3-D, mesoscale, multilayer models were constructed to evaluate the effects of pore morphology and interactions on material properties. The models allowed systematic spatial positioning of the pore within the cell and the ability to form solid zones. Pore arrangement, the effect of constraint, and gradients on the stress state were investigated. By using different combinations of hex cells as building blocks, several complicated microstructural arrangements were simulated.

### INTRODUCTION

An accepted practice in the fabrication of metals is to avoid the presence of porosity. The common belief is that porous materials exhibit properties that are inferior to the solid samples. Recent research concerning porous metals fabricated with the GASAR process, however, has challenged this axiom. This process, developed by Shapovalov [1,2], consists of a gas-solid eutectic reaction in which hydrogen is allowed to diffuse into the molten metal. Upon solidification, a distribution of pores remains in the material. The pores can range in shape from spherical to elongated and can be either continuous or closed, depending on process variables such as hydrogen pressure, heat removal direction and rate, and alloy composition. Therefore, such materials have the ability for properties to be tailored for optimum use in specific applications.

Prior experimental [3] and numerical [4,5] investigations of a porous copper GASAR metal have shown a retention or enhancement of yield strength with respect to solid copper for porosity levels up to 25%. The observed strength behavior is attributed to pore morphology (size, shape, and spacing) and transverse constraint. Unit cell finite element models determined that optimal parameters for increased strength were higher constraint due to pore free zones, lower pore aspect ratio, higher pore spacing, and higher pore offset [6]. The present research is focused on analyzing GASAR aluminum alloys planned for use in structural applications. Experiments on an aluminum-iron (Al-Fe) alloy are used to quantify variations in mechanical properties as a function of amount of porosity. Hexagonal mesoscale finite element models are developed to quantify the interactions between microstructural features and to determine their effects on bulk material constitutive response.

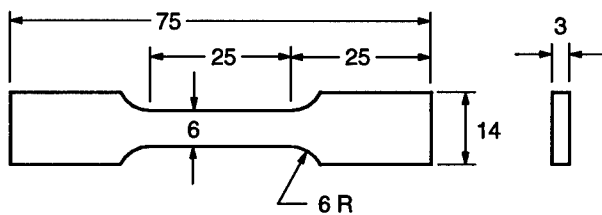
## EXPERIMENTAL METHOD

The material investigated was an aluminum-iron alloy produced at the Dnepropetrovsk Metallurgy Institute in the Ukraine by V. Shapovalov and associates. The density of the alloy was measured as  $2748 \text{ kg/m}^3$ , which is slightly higher than the density for pure aluminum ( $2700 \text{ kg/m}^3$ ) due to the iron additions. From the measured density, the iron content was estimated to be approximately 2.7%. This value agrees with a recent paper by Shapovalov that listed iron contents between 1 and 8% [1]. The material samples had a bulk porosity ranging from 13.5 to 16.5%. Examination of the microstructure revealed a collection of spherical pores randomly distributed throughout the material and ranging in size from 0.25 to 2.0 mm. No evidence of significant pore clustering or ordering was observed.

To obtain more accurate estimates of local porosity values, slabs were cut from the bulk samples with a high-speed circular saw containing a diamond cutting wheel. The slabs were then milled to a rectangular shape and measured using micrometers to a resolution of 0.0125 mm. The average values from five measurements of the slab dimensions were used to calculate the volume. The mass of the slab was obtained with a digital, analytical balance to a resolution of 0.001 g. Porosity values for each slab were determined by comparing the calculated density to that measured for the solid alloy. This technique produced local porosities ranging from 9 to 17%, which is slightly larger than the bulk porosity range.

Tensile specimens were machined from each of the slabs and tested to obtain mechanical properties. The geometry employed, shown in Figure 1, was a rectangular, dog-bone shape patterned after the current ASTM standard [7]. The overall dimensions were 75 mm long, 14 mm wide, and 3 mm thick. The specimen contained a central section 25 mm in length that was reduced to approximately 1/2 of the total specimen width. This region acts to localize the deformation and to prevent fracture in the grip sections. Fillets of radii 6 mm provide a uniform transition between the reduced section and the grip area. The small profile is advantageous because it allows the maximum number of specimens from limited quantities of material. Instrumentation on the specimens consisted of axial and transverse extensometers attached to the reduced section.

Loading of the specimens occurred in two phases. The first phase consisted of loading/unloading several times below the proportional limit to determine elastic properties (i.e. Young's modulus and Poisson's ratio). In the second phase, the specimens were loaded in tension into the plastic regime until failure to investigate flow and fracture behavior. Properties measured included proportional limit, 0.2% offset yield strength, and ultimate tensile strength.



• all dimensions are mm

Figure 1 - Geometry of the rectangular test specimens

In addition, the specimens were periodically unloaded and reloaded during this phase to monitor the change in elastic properties. Load and displacement data were collected during the entire test by a PC-based data acquisition system and stored as an ASCII file on a hard disk. The data file was imported into a commercial spreadsheet program for further analysis.

## EXPERIMENTAL RESULTS

A total of 10 experiments were performed to determine mechanical property data for the Al-Fe alloy over the porosity range from 9 to 17%. The first specimen was loaded monotonically to failure and only provided the constitutive behavior and strength data. The remaining 9 specimens were subjected to the two-phase loading process and gave the above information as well as elastic property data. All tests were conducted at room temperature on a servo-hydraulic universal test machine with a capacity of 245 kN. The phase 1 loading was performed under load control at a rate of 7.4 N/sec to a level of 222 N. The phase 2 loading was completed using displacement control at a rate of 0.125 mm/min until failure.

Trends were established for both elastic property and strength data as a function of the amount of porosity in the sample. Results for Young's modulus are shown in Figure 2. The symbols represent the average value of multiple tests on a single specimen for determining the property. The vertical bars around each data point indicate the range of values measured during the multiple loading/unloading cycles, which was less than  $\pm 3\%$  for all cases. From the figure, Young's modulus exhibited a decrease from 62.3 to 51.2 GPa as porosity increased from 9 to 17%. Scatter in the data was present but not excessive. The dashed line in the figure represents the result of a regression analysis on the data. Since the correlation coefficient is only 0.8267, it is unlikely that the Young's modulus-porosity relation can be characterized as linear. However,  $R^2$  will be utilized as a "goodness of fit" measure throughout the remainder of this paper.

The variation of Poisson's ratio with porosity is given in Figure 3. Unlike the results for Young's modulus, Poisson's ratio appeared to be insensitive to the amount of porosity. The values ranged from 0.211 to 0.331 with no clear trends in the data. The variation between

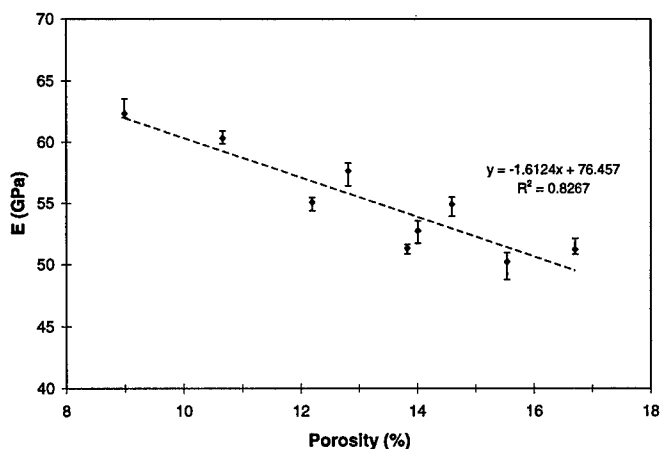


Figure 2 - Variation of Young's modulus with porosity in the elastic region

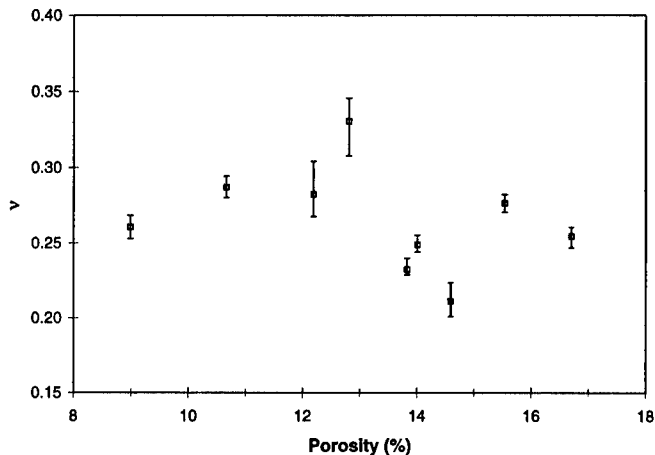


Figure 3 - Variation of Poisson's ratio with porosity in the elastic region

multiple measurements on a single specimen was as much as  $\pm 8\%$ , and the data scatter among different specimens was appreciable. These observations are not unusual considering the small, transverse deformations that must be monitored when determining Poisson's ratio. In addition, large differences in Poisson's ratio were observed among specimens with similar levels of porosity. The same effect was present in the Young's modulus data, but to a lesser extent. This behavior is attributed to differences in the pore morphology between specimens. Because of the absence of a clear trend in the data, no curve fit was performed on the Poisson's ratio information.

All of the strength data, namely proportional limit, 0.2% offset yield strength, and ultimate tensile strength, are presented in Figure 4. Each of these measures experienced a decrease with increasing levels of porosity. The proportional limit exhibited a decrease of 20% with a large amount of scatter. The yield strength experienced a decrease of 24% and much less scatter than for the proportional limit. The ultimate tensile strength exhibited the greatest decrease of 41% over the range of porosities investigated. Scatter was comparable to that of the yield strength data. The dashed lines in the figure are the result of linear regression on each of the data sets. The  $R^2$  value was very poor for the proportional limit data (0.3122) and was about equal for the yield strength and ultimate tensile strength data (0.7681-0.7674). One interesting observation is the large disparity between the proportional limit and the 0.2% offset yield strength. For many metals, these two quantities are approximately equal. For the porous Al-Fe alloy, the proportional limit is approximately 33% of the magnitude of the yield strength. This behavior is probably due to micro-yielding in the vicinity of the pores, which produces a nonlinear stress-strain response. As the stress increases, so does the amount of micro-yielding until, finally, plastic flow initiates on the macroscale. The macroscopic flow coincides with the 0.2% offset yield strength. Therefore, it is important to specify the exact parameter used to define the yield point for porous materials.

The constitutive response for all specimens during plastic loading until failure is presented in Figure 5. The nearly vertical lines on the stress-strain curves in the plastic region represent the unloading/reloading cycles performed to monitor the change in elastic properties

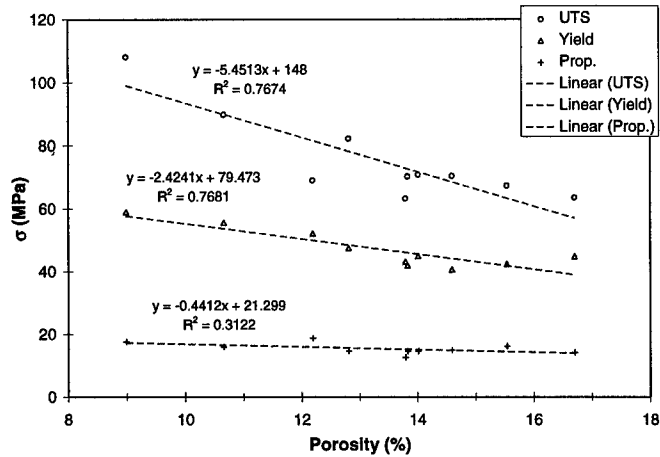


Figure 4- Variation of proportional limit, yield, and ultimate tensile strengths with porosity

during deformation. As seen from the figure, there is a consistent decrease in the strain hardening behavior as porosity increases from 9 to 14%. From 14 to 17%, however, the flow response seems to collapse onto a single curve. No clear trends were observed for the strains at fracture due to the non-uniform nature of the microstructure, which causes failure at the weakest location in the specimen. In all cases, the strain at maximum load was less than 4% which represents a substantial decrease in ductility in comparison to most non-porous, annealed aluminum alloys.

For all of the unloading/reloading cycles in the plastic region, measurements of Young's

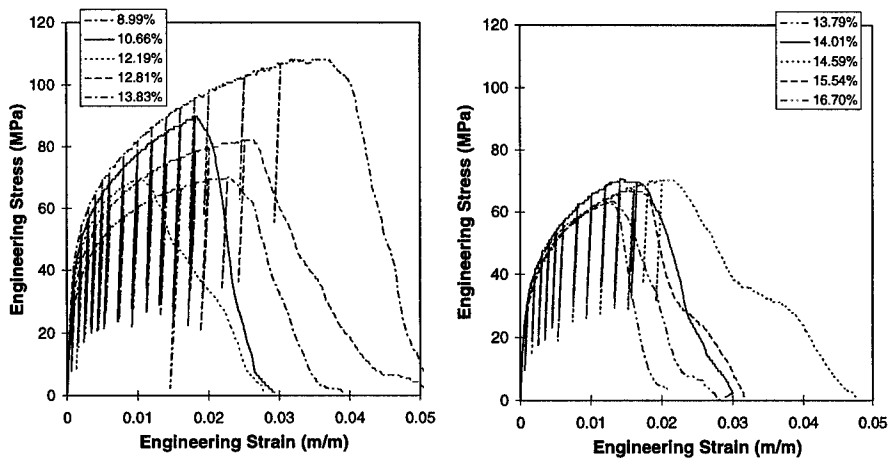


Figure 5 - Stress-strain response of specimens until failure

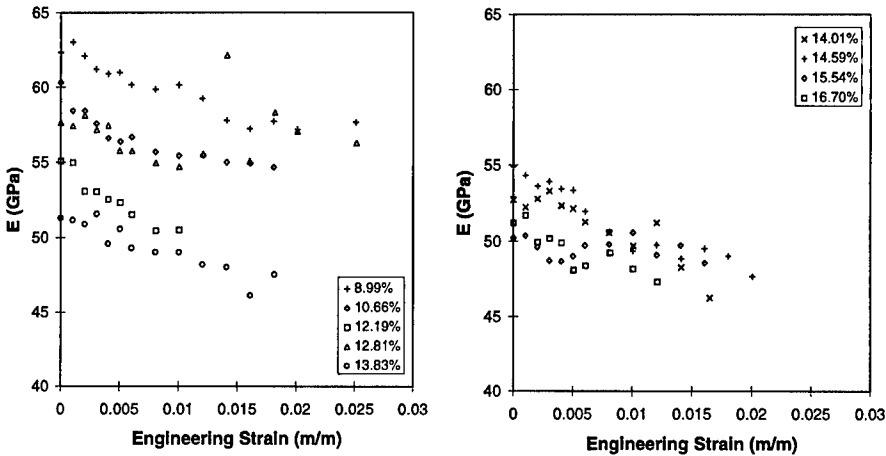


Figure 6- Variation of Young's modulus with strain during tensile tests

modulus and Poisson's ratio were made to investigate trends in these properties throughout the deformation. The results for Young's modulus are presented in Figure 6, and the data for Poisson's ratio are given in Figure 7. The values shown were determined during the reloading portion of the cycle only, as an attempt to minimize scatter in the data. However, significant scatter remains in both data sets that makes quantification of any changes in the properties nearly impossible. Nevertheless, there is a clear decreasing trend in Young's modulus and an increasing trend in Poisson's ratio with increasing strain. This behavior agrees qualitatively with the response of solid metals under similar loading conditions [8].

Normally accepted practice is to characterize the properties of porous materials with

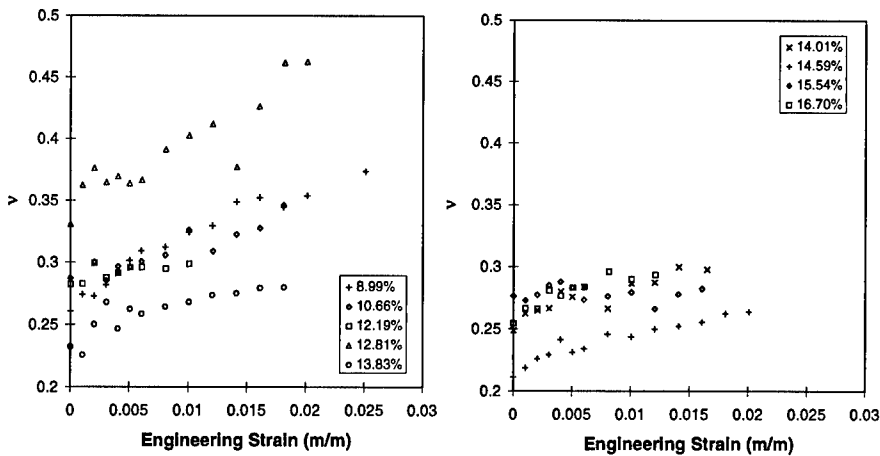


Figure 7 - Variation of Poisson's ratio with strain during tensile tests

respect to porosity or volume fraction. Considering porosity alone, however, is not sufficient to fully describe pore morphology in terms of pore sizes, shapes, and spatial arrangements. This fact becomes more significant for porous materials containing non-uniform microstructures, such as clusters of pores or pore-free zones. Therefore, alternate methods of describing such materials must be employed.

One alternate metric is the concept of nearest-neighbor distance (NND). This idea was originally developed for describing the behavior of particulate- and fiber-reinforced composite materials, but the theory can be easily transferred to porous materials by treating the pore as a particle with zero stiffness and mechanical properties. The underlying premise for the NND concept is that features in the microstructure are most likely to be affected by their nearest neighbors. In a porous material, the NND between pores is a function of the size, shape, and spatial distribution of the pores. Estimates of mean NNDs can be obtained in either 2- or 3-dimensions by constructing unit cell models with random orientations, thereby producing a distribution of NNDs. These distances compare favorably to similar values from computer-generated random patterns and are generally much smaller than separations predicted using periodic models. Under the assumption of spherical pores distributed randomly throughout the material, which is consistent with the pore morphology observed in this material, volume fraction or porosity can be determined from measurements of NND. Note, however, that it is not possible to calculate NND from measurements of porosity. An extensive review of the NND theory and its applicability to mechanical property predictions for composite materials has recently been completed [9], which contains further details for the interested reader.

Based upon the previous discussion, the strength data from Figure 4 were re-plotted vs. NND normalized by the mean pore diameter, and the results are shown in Figure 8. In this case, the proportional limit, yield, and ultimate tensile strengths all increase with increasing NND. These trends agree with the observation that NND is inversely related to porosity. A closer comparison between Figure 4 and Figure 8 reveals that the goodness of fit, as measured by the  $R^2$  values, is significantly higher when the strength data is shown vs. normalized NND

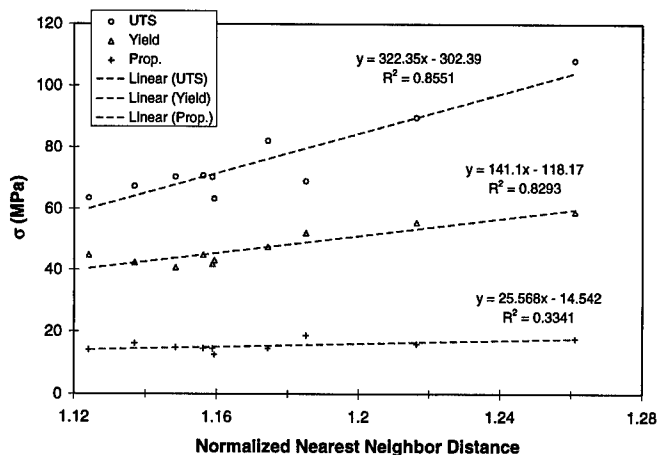


Figure 8 - Variation of proportional limit, yield, and ultimate tensile strengths with normalized nearest-neighbor distance

than when presented vs. porosity. This observation further demonstrates that NND, rather than porosity, is a more useful metric for describing mechanical properties of these porous materials. It should be noted that Young's modulus can also be plotted vs. normalized NND rather than vs. porosity. However, the improvement in  $R^2$  is not as dramatic due to the relative structural insensitivity of Young's modulus, and the results are not included in this paper.

### FINITE ELEMENT MODELING

Finite element models were generated using ABAQUS/Explicit (Version 5.6) [10,11]. Type CPS8R eight-noded, constant strain elements were used to construct the representative hexagonal unit cell building blocks. The representative solid hexagon contained 108 elements and 183 nodes, and the representative hexagon with a pore contained 72 elements and 144 nodes. The models were constructed with 7 hexagons on a layer. Figure 9 shows several example pore arrangements in a model. Each model contained three layers for a total of 21 hexagons. A maximum of 21 pores is possible in this test configuration. Finite element models representing a layer of hexagons with and without pores are shown in Figures 10(a) and 10(b). A representative finite element model containing all three layers is given in Figure 10(c).

The porous GASAR alloy used in the finite element models was Al A356. This material was modeled as an isotropic elastic-plastic material. The elastic modulus was 72,400 MPa, and Poisson's ratio was 0.33. The plastic behavior of the alloy followed a von Mises yield behavior. Uniaxial yield stress was 147.5 MPa, and uniaxial yield strain was 0.0021. Strain hardening behavior is presented in Figure 11. Twenty hexagonal models with various pore configurations were loaded linear-elastically in uniaxial tension to quantify an optimal pore microstructure. Pore configurations for eight of the cases are shown schematically in Figure 9.

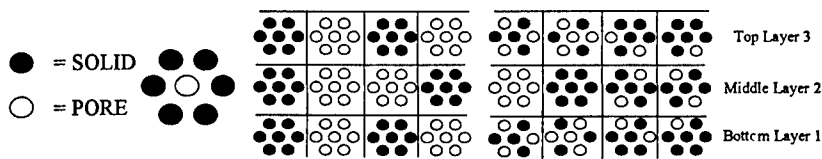


Figure 9 - Hexagonal test pore configurations

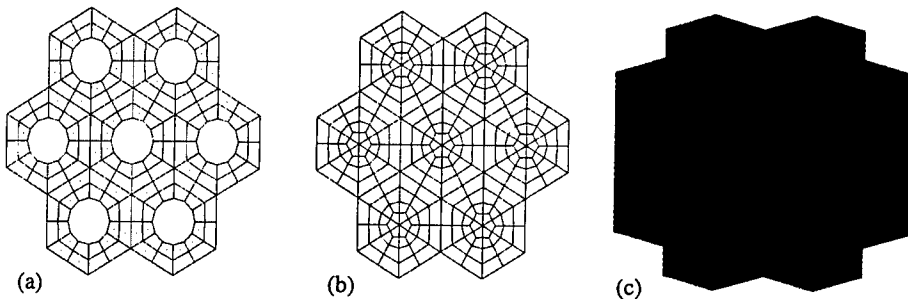


Figure 10 - Finite element models showing a) hexagons with pores, b) hexagons without pores, and c) three layers

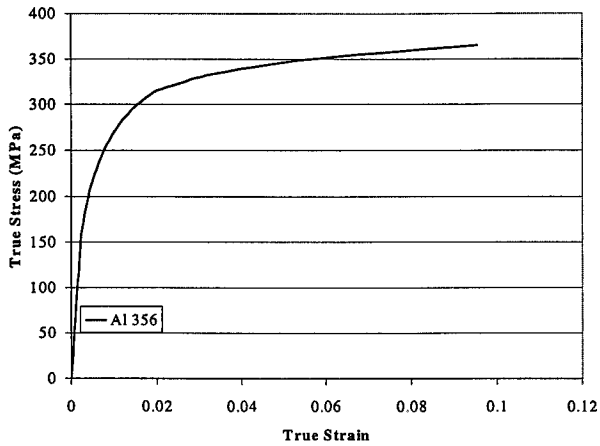


Figure 11 - Al A356 elastic-plastic material curve

### FINITE ELEMENT RESULTS

Elastic finite element simulations were performed to compare the relative bulk stiffness of each test pore configuration. Normalized load vs. normalized displacement plots were generated to assess each configuration. The results are compared to the case of a solid, hexagonal model and are presented in Figure 12. The four test configurations exhibiting highest bulk stiffness due to pore arrangement are shown in Figure 13.

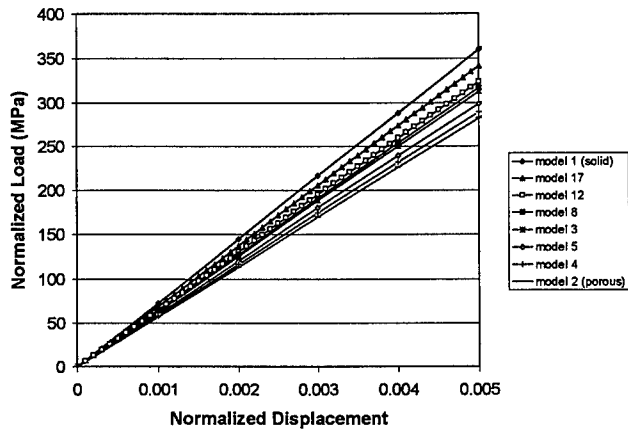


Figure 12 - Normalized load vs. normalized displacement comparison of representative elastic bulk stiffness results

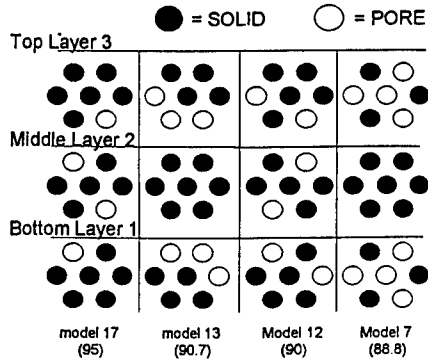


Figure 13 - Top four pore configurations for highest bulk stiffness

The relative importance of the pore free zones is shown in these models. Pore free zones provide a high level of constraint between the pores, which results in a higher bulk stiffness. Also, pore free zones affect the path along which fracture can occur between pores. The best pore configuration was model 17 which shows a decrease of 5% in modulus. Note that this decrease is only slightly greater than the porosity level of 4.3%, if modulus is assumed to vary linearly with porosity. The other pore configurations showed a greater decrease in modulus that was larger than the volume porosity level.

The effect of porosity vs. percent normalized load is shown in Figure 14. For a given volume porosity, or maximum area porosity, there are differences in bulk stiffness at the same porosity level. In Figure 15(a), the effect of pore configuration at a given volume porosity of 10.8% is shown. The examples demonstrate that bulk stiffness changes by 3-5% due to variations in offset, pore free zones, spacing, and aspect ratio for a given volume porosity.

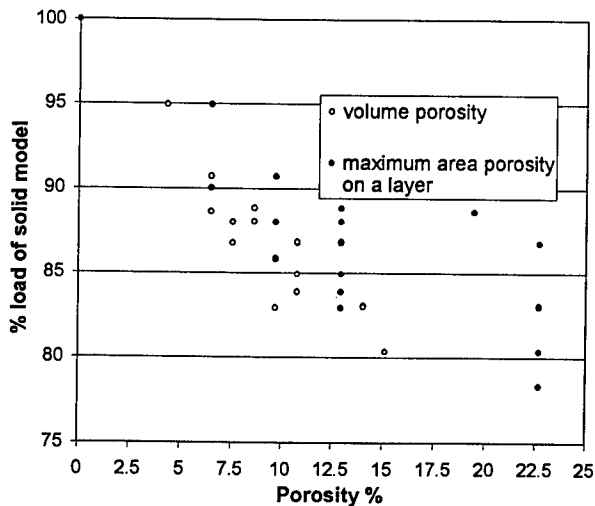


Figure 14 - Volume porosity and maximum porosity on a layer vs. % normalized load.

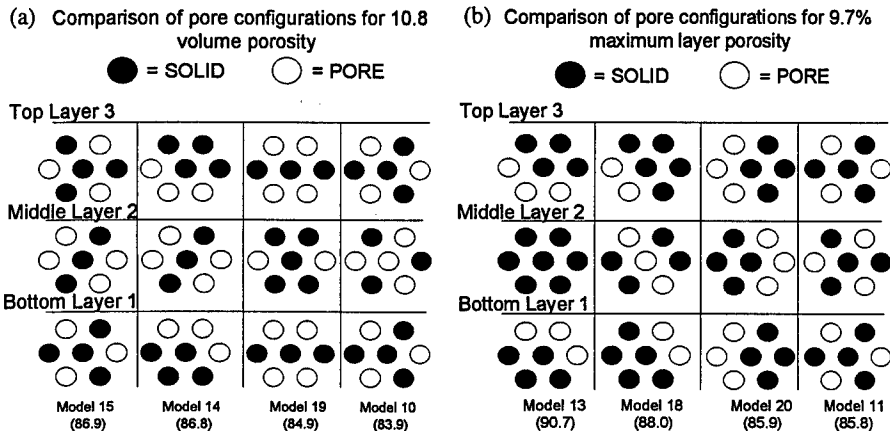


Figure 15 - a) Percent load vs. maximum volume porosity b) percent load vs. maximum layer porosity

In Figure 15(b), the effect of pore configuration at a given maximum layer porosity of 9.7% is shown. These models have larger pore free zones than those in Figure 15(a), which provide higher constraint levels between the pores and contribute to higher bulk stiffness. These models demonstrate the important role of pore free zones on the bulk properties of porous metals.

## CONCLUSION

Experiments were performed on samples of a GASAR aluminum-iron alloy to quantify trends in mechanical properties in relation to level of porosity. Rectangular, dog-bone specimens were subjected to tensile loading in both elastic and plastic regions to allow measurements of Young's modulus, Poisson's ratio, proportional limit, 0.2% offset yield strength, and ultimate tensile strength. Porosity levels from 9 to 17% were investigated. Over this range, it was observed that Young's modulus decreased by 18% but that Poisson's ratio remained generally constant. All of the strength measurements exhibited decreasing trends with increasing amounts of porosity, that ranged from 20% for proportional limit, 24% for yield strength, and 41% for ultimate tensile strength. For a given sample, it was also observed that Young's modulus decreased and Poisson's ratio increased with increasing plastic strain, but the results were hard to quantify due to scatter in the data. Finally, the concept of nearest-neighbor distance was introduced as an alternate parameter for describing pore morphology, and it was shown that strength data experienced a better fit to this new parameter than to porosity.

The mesoscale finite element models verify that pore configuration has an effect on bulk stiffness. The relative importance of the pore free zones was shown to be a significant parameter. The best pore configurations exhibit a decrease in modulus slightly below the volume porosity. The capability to incorporate pore free zones, pore spacing, pore offset, and pore aspect ratio into a model facilitates the investigation of many different pore configurations to determine an optimal arrangement. The best cases need to be incorporated into a larger model to evaluate the effects of more complicated pore configurations.

---

## ACKNOWLEDGMENTS

The authors would like to thank Dr. Virgil Provenzano of the Naval Research Laboratory and Dr. Donald Shih of Boeing for providing the porous Al-Fe material used in the experiments. Thanks are also due to Mr. Kenneth Killian for machining the test specimens. Research funding was supplied by the Defense Advanced Research Projects Agency, under the direction of Dr. C. Robert Crowe and Dr. Steven Wax, and supervised by Dr. Steven Fishman of the Office of Naval Research (contract #: N0001497WX21071). Funding was also provided by ONR through the NRL basic research program.

## REFERENCES

1. V. I. Shapovalov and A. G. Timchenko, *Phys. Met. and Metall.* **76** (3), 335-337 (1993).
2. V. I. Schapovlov, *MRS Bull.* **19** (4), 24-28 (1994).
3. J. M. Wolla and V. Provenzano in *Advances in Porous Materials*, edited by S. Komarneni, D. Smith, and J. Beck (Mater. Res. Soc. Proc. **371**, Pittsburgh, PA, 1995) pp. 377-382.
4. A. Kee and P. Matic, *Mater. Sci. Engr.* **A224**, 85-95 (1995).
5. A. Kee, P. Matic, and J. Wolla, *Mater. Sci. Engr.* **A230**, 14-24 (1997).
6. A. Kee and P. Matic, in *ABAQUS User's Conf. Proc.* (Hibbitt, Karlsson, & Sorensen, Pawtucket, RI, 1996) pp. 403-417.
7. ASTM E8, in *Annual Book of ASTM Standards, v. 3.01* (ASTM, Philadelphia, PA, 1993) pp. 130-149.
8. J. F. Bell, in *Handbuch der Physik, v. 6, Mechanics of Solids I*, edited by S. Flügge and C. Truesdell (Springer-Verlag, New York, NY, 1973) pp. 92-97; 147-148.
9. R. K. Everett, Ph.D. dissertation, University of Maryland, 1996.
10. *ABAQUS/Explicit User Manuals: Ver. 5.6* (Hibbitt, Karlsson, & Sorensen, Pawtucket, RI, 1996).
11. *ABAQUS/Post Manual: Ver. 5.6* (Hibbitt, Karlsson, & Sorensen, Pawtucket, RI, 1996).

## METALLOGRAPHIC STUDY OF GASAR POROUS MAGNESIUM

Chanman Park and Steven R. Nutt  
University of Southern California, Department of Materials Science, Los Angeles, CA.

### ABSTRACT

One of the promising techniques for making porous metals is the so-called GASAR process. In principle, the process affords considerable control over pore size, shape, and distribution. However, in practice, the pore microstructure is difficult to control, and a clearer understanding of microstructural evolution would be helpful. In this study, we undertake a detailed microstructural study of a porous Mg and AZ31 Mg alloy synthesized by the GASAR process. Microscopic studies demonstrated the presence of different pore size ranges. The pore distribution depended on the distance from the chill end of ingots. TEM observations revealed apparent crack lines (gas tracks) near the pores and ternary intermetallic phases in the alloy.

### INTRODUCTION

Recently, porous metals and ceramics have been made by a GASAR process that is a novel solid-gas eutectic solidification process. The GASAR process was developed by Shapovalov at the Dnepropetrovsk Metallurgical Institute (DMI) in the Ukraine [1]. A liquid metal saturated with hydrogen in a metal-hydrogen system is cooled through the eutectic point. The solidification of the metal and nucleation of pores occur simultaneously at the eutectic point, and pores develop from the diffusion of gaseous hydrogen out of the melt as it freezes.[1]

The purpose of the present work was to investigate the microstructure of GASAR Mg and AZ31 Mg alloy. The intent was to explore the microstructural features in the vicinity of pores to gain better understanding of the mechanisms involved in pore formation, which in turn would suggest improvements in processing methods.

### EXPERIMENTAL PROCEDURES

GASAR Mg and AZ31 Mg alloy specimens were supplied by NRL (Naval Research Lab). Cylindrical specimens 8 cm long by 2 cm were sectioned longitudinally and transversely. First, each sample was cut 2.5 cm from the "chill end" of the mold (sample #1). The chill end of the mold was the first to contact the cooling sink. The solidification front originated at this end and moved through the sample along its length. Following the first cut, a second cut was made 3.5 cm from the cooled end (sample #2), then 5 cm from the cooled end (sample #3), and finally 6 cm from the cooled end (sample #4). Fig. 1 shows the sectioning of sample.

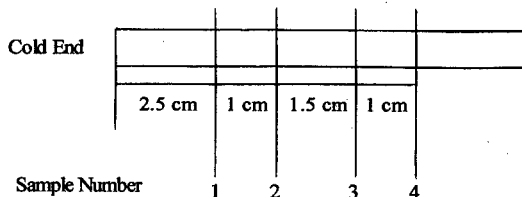
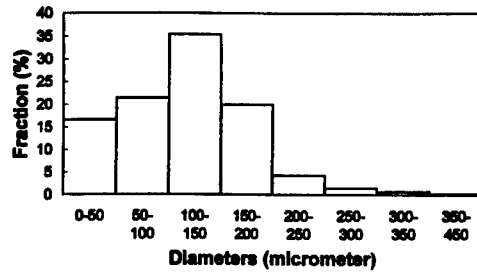
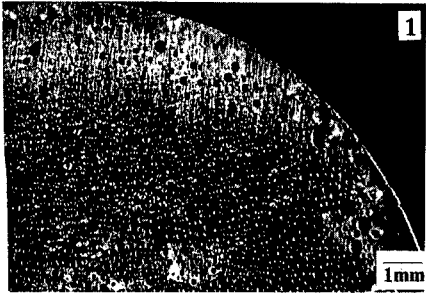
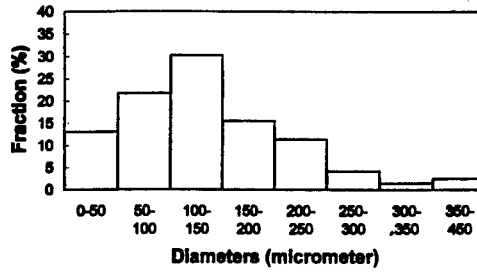
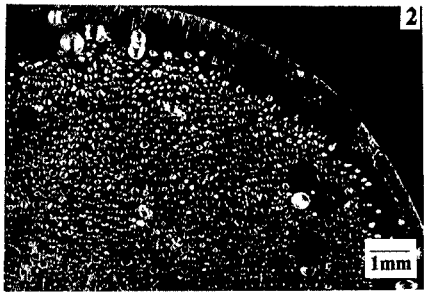


Fig. 1 Sectioning of samples

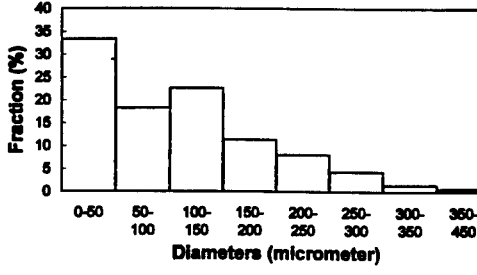
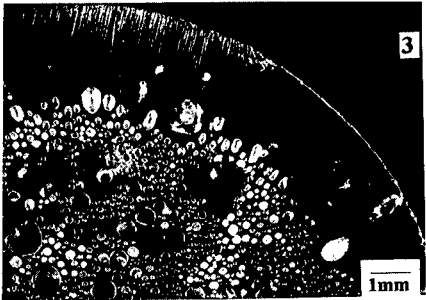
A total of four cuts were made using a low-speed diamond saw, resulting in five pieces.



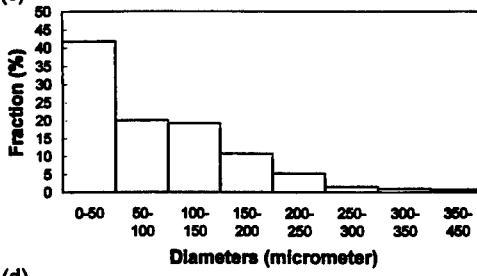
(a)



(b)



(c)



(d)

Fig.2 Picture of transverse section and fraction of pore diameters  
 (a) Sample number 1 (b) Sample number 2 (c) Sample number 3 (d) Sample number 4

Afterwards, sample edges were beveled to remove rough edges and facilitate polishing. Glycol was used exclusively to disperse the diamond polishing abrasives. After each polishing step, samples were cleaned ultrasonically in ethanol for 5 min. Samples were examined by conventional metallography and TEM. TEM samples were prepared by ion milling.

## RESULTS

### A) Porosity and Pore Size Distribution

Mg and AZ31 Mg alloy exhibited different pore structures and sizes. In each material, porosity and pore size varied with distance from the chill end (sample number). Mg exhibited more uniform porosity than AZ31. Figs. 2 shows the pore distributions in Mg.

#### a) Porous Mg

Near the chill end, the pore distribution is fairly uniform except in the peripheral region, where the sample is almost pore-free (Fig. 2(a)). The distribution of pore sizes is shown in the accompanying histogram, which shows that most of the pores are under 200  $\mu\text{m}$ . The pores are roughly cylindrical and extend up to 2.5 cm along the cylinder axis. As the distance from the chill end increases, the pore distribution becomes less uniform. Fig. 2(b) shows sample #2 (3.5 cm from the chill end). The peripheral region (1 mm thick) is virtually pore-free, while the core region exhibits a few large spherical pores over 500  $\mu\text{m}$  in diameter. The distribution of pore sizes is similar to sample 1, although there are more large pores (over 200  $\mu\text{m}$ ). Sample #3 confirms the trend, as shown in Fig. 2(c). The pore distribution is highly non-uniform, and the pore-free annulus is  $\sim 2.5$  mm thick. Numerous micropores ( $>10$   $\mu\text{m}$ ) were observed, although the 16 large pores accounted for much of the pore volume and were distributed throughout the cross-section. The shape of the pores varied with radial position. Near the center, pores were cylindrical less than 1.5 cm in length, while beyond the mid-radius, the pores ranged from spherical to radially elongated. Finally, at 6 cm from the chill end, the pore distribution was dominated by large radial elliptical pores in peripheral regions, accompanied by micropores ( $>10$   $\mu\text{m}$ ), shown in Fig. 2(d). The core region showed cylindrical pores, although much shorter in length than in previous samples.

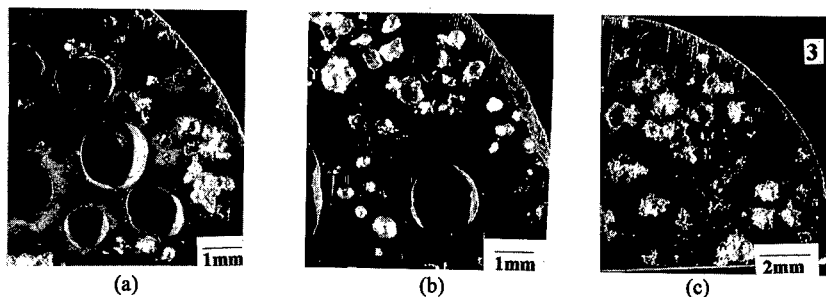


Fig. 3. Pictures of transverse section of AZ31 Mg alloy.

(a) Sample number 1 (b) Sample number 2 (c) Sample number 3

#### b) Porous AZ31

The pore distribution in AZ31 was coarser than in pure Mg, as shown in Fig. 3, taken 2.5 cm from the chill end. The pore sizes ranged from 10  $\mu\text{m}$  to 2 mm in diameter, although most were in the range of 0.1-0.5 mm in diameter. The largest pores were cylindrical and less than 1 cm in length, while the small pores tended to exhibit irregular shapes. With increasing distance from the chill end, the pore distribution became less uniform and more bimodal, with few large pores, and

numerous much smaller pores. Irregular pore shapes can result from exposure of grown-out dendrites. [2]

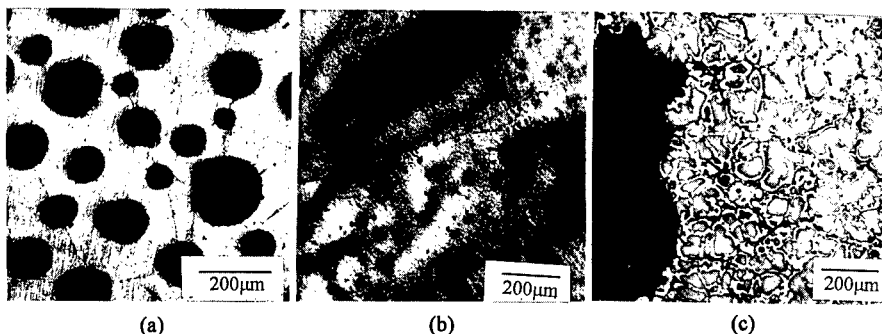


Fig. 4. Micrographs showing (a) pores in porous Mg, (b) micropores in porous Mg, and (c) porous AZ31 Mg alloy.

## B) Microstructure

### 1) Porous Mg

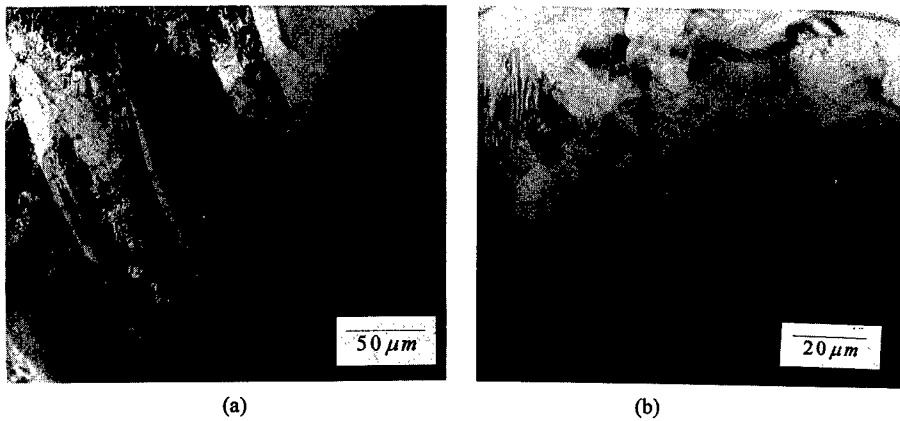
The micrographs of porous Mg specimens are shown in Fig. 4(a). The transverse sections of the porous specimens reveal that several pores are contained within each grain and that the grain boundaries run from one pore to the next. Simone showed similar micrographs of porous copper specimens made by the GASAR process [3]. However, porous Mg shows micropores (e.g., sample 4), which appear both intragranularly and along grain boundaries, as shown in Fig. 4(b).

### 2) Porous AZ31

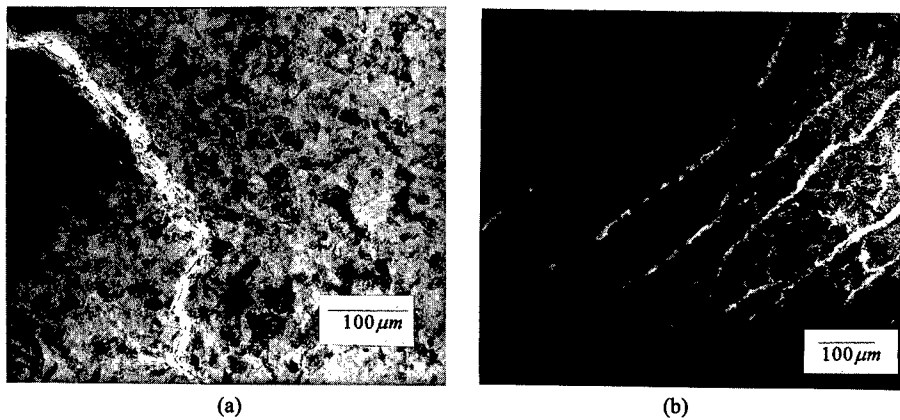
Optical micrographs reveal the metallurgical structure of AZ31. Fig. 4(c) shows a dendritic structure typical of sand-cast or gravity-die-cast Mg alloys such as AZ91 or AZ80 [4, 5]. The dendrites are  $\alpha$ -Mg with intergranular  $\beta$ - $Mg_{17}Al_{12}$ . In the cast state, the  $\beta$ -phase  $Mg_{17}Al_{12}$  appears in alloys containing more than 2% aluminum[5]. The grain size is fairly large in comparison with the coarse grains in die castings. However, the microstructure close to the pores shows much smaller grain sizes (less than 50  $\mu m$ ), also confirmed by TEM observations, as discussed below.

TEM analysis was performed on AZ31 porous samples, and attention was focused on two areas - the dense annular peripheral area and regions immediately adjacent to pores. The peripheral region exhibited extensive deformation and twinning, as shown in Fig. 5(a). [6, 7] From electron diffraction pattern and x-ray spectral analysis, this phase is  $Mg_{17}Al_{12}$ . However, the microstructures are different near the pores. The grain size is smaller and twinning is absent, as shown in Fig. 5(b). The small grain size is attributed to the pressure near the pores, which is relatively higher in the core region than in peripheral regions.

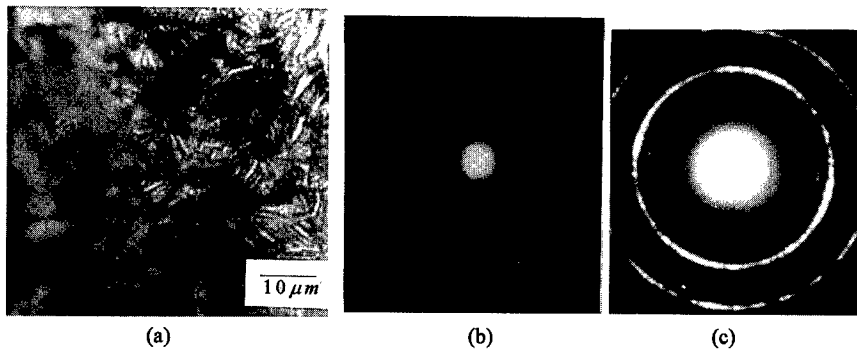
Two interesting results should be noted. First, apparent cracks, possibly "gas tracks," exist near the pores. The features are  $\sim 800 \mu m$  long by 10  $\mu m$  across. Some areas show a rather large crack, and the grain size in the adjoining material is small (Fig. 6(a)). Other areas, such as Fig. 6(b), exhibit a vein-like network of fine parallel cracks, with fine grain sizes (less than 5  $\mu m$ ). The boundary between coarse- and fine-grain regions is shown in Fig. 7(a). EDS spectral analysis shows substantial oxygen content in the fine-grain area. Electron diffraction and EDS analysis led to identification of the coarse- and fine-grain phase as  $Mg_{17}Al_{12}$ . The typical SAD ring pattern is shown in Fig. 7(b) and (c), where the spottiness of the rings arises from the small grain size [7]. Secondly, there exist two ternary intermetallic phases within the alloy, identified by diffraction and EDS as  $Mg_{32}(Zn,Al)_{49}$  and  $Mg_5Zn_2Al_2$ . Fig. 8 shows a region of both ternary intermetallic



(a) (b)  
 Fig.5 TEM Pictures: (a) Peripheral region (b) Near the pores



(a) (b)  
 Fig.6 TEM Pictures: (a) Large gas track (b) Vein-like network of fine gas track



(a) (b) (c)  
 Fig.7 TEM Pictures: (a) The boundary between coarse- and fine-grain regions (b) SAD ring pattern for coarse-grain regions (c) SAD ring pattern for fine-grain regions

phases. The small dark area is  $Mg_{32}((Zn,Al)_{49})$ , while the large grain is  $Mg_5Zn_2Al_2$ . The ternary  $Mg_5Zn_2Al_2$  phase is first formed by peritectic reaction between the  $Mg_{32}((Zn,Al)_{49})$  phase, the  $Mg_{17}Al_{12}$  phase, and liquid at 393°C. The  $Mg_5Zn_2Al_2$  phase crystallizes directly from liquid within a relatively narrow range of compositions [8].



Fig. 8 The ternary intermetallic phases  $Mg_{32}((Zn,Al)_{49})$  and  $Mg_5Zn_2Al_2$ .

## CONCLUSION

Microscopic studies of GASAR process Mg ingots have demonstrated the presence of different pore size ranges. The pore distribution depends on the distance from the cold end of ingots. Porous Mg shows more uniform pore size distribution than the porous AZ31 Mg alloy. TEM observations revealed different microstructures in the predominantly solid area and the regions near the pores. Also, TEM revealed two interesting facts: one is the crack lines (gas marks) near the pores and the other is the ternary phases in the sample.

## ACKNOWLEDGMENTS

The authors are grateful to the Northrop-Grumman Corp. and to the TRW Foundation for financial support of this work.

## REFERENCES

1. Vladimir I. Shapovalov, *MRS Bull.* **19** (4), 24 (1994).
2. A. Patinaik, S. C. Sanday, C. L. Vold and H. I. Aaronson, *MRS Symp. Proc.* **371**, 371 (1995).
3. A. E. Simone and L. J. Gibson, *Acta Mater.* **44** (4), 1437-1447 (1996).
4. W. P. Sequeira, M. T. Murray, G. L. Dunlop and D. H. StJohn, in *Automotive Alloys*, edited by Subodh K. Das (TMS, Pennsylvania, 1997), p. 169-183.
5. I. J. Polmear, *Light Alloys; Metallurgy of the Light Metals*, (Edward Arnold Publishers, London, 1981) p. 138.
6. S. E. Ion, F. J. Humphreys and S. H. White, *Acta Metall.* **30**, 1909 (1982)
7. G. Thomas and M. J. Goringe, *Transmission Electron Microscopy of Materials*, (John Wiley & Sons Publishers, New York, 1979) p. 92.
8. *ASM Metals Reference Book; A handbook of data about metals and metalworking*, (American Society for Metals Publishers, Ohio, 1981) p. 406.

## AUTHOR INDEX

- Ahmed, S.S., 249  
Akiyama, S., 133  
Anderson, David P., 185  
Anderson, Heather J., 185  
Apprill, J.M., 291
- Banhart, J., 121  
Baranda, P.S., 83  
Barker, D., 249  
Bart-Smith, H., 71  
Bastawros, A-F., 71  
Baumeister, J., 121, 145  
Bergmann, H.W., 159  
Bernard, T., 159  
Bleck, W., 59  
Bonnenberger, R.J., 303  
Bonhomme, J., 83  
Bräunlich, H., 271  
Burzer, J., 159
- Choi, B.W., 243  
Clark, J.L., 191  
Clyne, T.W., 139  
Cochran, J.K., 191
- Dannemann, K.A., 103  
Degischer, H.F., 97  
Deuser, D.A., 225  
Dharmasena, K.P., 171  
Dunand, D.C., 231
- Eifert, H.H., 145  
Elzey, D.M., 257  
Evans, A.G., 71  
Everett, R.K., 303
- Gegel, H., 249  
Gergely, V., 139  
Giamei, A.F., 109  
Gibson, L.J., 53  
Goods, S.H., 15  
Gradinger, R., 97  
Greil, Peter, 21  
Grenstedt, Joachim L., 3  
Gutsch, T.C., 291
- Han, Heung Nam, 33  
Hardwicke, C.U., 191  
Hartmann, M., 211  
Hipke, Th., 265  
Huang, G., 249  
Huang, J.S., 27  
Huryz, K.M., 191  
Hutchinson, John W., 39
- Itoh, M., 133
- Jacobson, L.A., 65
- Kearns, Kristen M., 185  
Kee, A.J., 303  
Kim, Hyoung Seop, 33  
Kitahara, A., 133  
Knuewer, M., 145  
Kováčik, J., 91
- Lankford, Jr., J., 103  
Lederich, R.J., 225  
Lee, Dong Nyung, 33  
Lee, K.J., 191  
Lin, J.Y., 27
- Maguire, M.C., 291  
Margevicius, R.W., 65  
Martin, R.L., 225  
Matic, P., 303  
Miller, Ronald E., 39  
Mináriková, N., 91  
Miyoshi, T., 133  
Mumm, D.R., 71
- Nagel, A.R., 191  
Neugebauer, R., 265, 271  
Neuschwanger, C.L., 15  
Nutt, Steven R., 315
- Oh, Kyu Hwan, 33
- Paradies, C.J., 297  
Park, Chanman, 315  
Parrish, Phillip A., 205  
Poirier, D.R., 291  
Priluck, J., 109
- Queheillalt, D.T., 237, 243
- Reindel, K., 211  
Renauld, M.L., 109
- Saenz, E., 83  
Sanders, Jr., T.H., 191  
Sanders, W., 53  
Schmidt, M., 179  
Schneider, Thomas, 21  
Schober, Georg, 21  
Schoerghuber, F., 151  
Schwartz, D.S., 225, 237, 243  
Schwertfeger, F., 179  
Shapovalov, V.I., 281  
Shih, D.S., 225  
Simančík, F., 91, 151  
Singer, R.F., 211  
Stanek, P.W., 65  
Stanzi-Tschegg, S.E., 97  
Starke, Jr., E.A., 217  
Sypeck, David J., 71, 205

---

Teisen, J., 231  
Thompson, M.S., 109  
Tobin, A., 297  
Tyomkin, I., 165

von Hagen, H., 59

Wadley, Haydn N.G., 71, 171, 205,  
217, 237, 243, 257

Wagner, U., 271

Wang, N., 217  
Wanner, A., 45  
Weber, M., 145  
Whinnery, L.L., 15  
Wolla, Jeff, 297

Yu, C.J., 145

Zettl, B.E., 97

## SUBJECT INDEX

- A357, 297
- AA2090, 297
- AA2195, 297
- aerated autoclaved concrete, 21
- aerogels, 179
- Al filler, 15
- AlSi<sub>7</sub>Mg, 83
- aluminum, 83
  - alloy, 297
  - castings, 151
  - foam, 53, 59, 65, 83, 97, 133, 139, 159, 171
- anisotropic, 45
- automated porosimeter, 165
- batch casting process, 133
- bending properties, 91
- beryllium, 65
- Brinell hardness of sintered porous copper, 33
- cell
  - morphologies, 71
  - structure, 53, 83
  - wall fracture, 231
- cellular, 71
- materials, 171
- solids, 3
- ceramics, 45
- closed cell, 3
- collapse stress, 15
- complex shaped aluminum foam parts, 151
- compression testing, 151
- compressive
  - deformation characteristics, 211
  - strength, 21, 53, 103
- construction parameters, 265
- continuum plasticity, 39
- deformation
  - modes, 71
  - of porous metal rings, 33
- densification, 257
- detachable joints, 265
- diffusion, 217
- dynamic loading, 103
- eddy current, 171, 243
- effective elastic moduli, 45
- elastic
  - moduli, 243
  - properties, 45, 237
- electrical conductivity, 171
- electrodeposition, 121
- elongated pores, 297
- elutriation, 205
- energy absorption, 145, 159
- entrapped gas, 225
- expansion kinetics, 243
- experimental and numerical analyses, 303
- fabrication, 211
- FEM, 249
- finite elements, 39
  - analysis, 21, 109
- foam(s), 27, 83
  - core, 151
  - thickness, 59
- foamed
  - aluminum, 133
  - metals, 39
  - panels, 91
- foaming agents, 121
- formation of porosity, 225
- forming, 257, 271
- gas
  - atomization, 205
  - pressure-assisted casting technique, 211
- GASAR, 281, 291, 297
  - process, 315
- gasarite, 281
- gluing, 159
- graphitic carbon foams, 185
- high
  - cycle fatigue, 27
  - properties, 97
  - rate deformation, 103
- hollow powders, 205
- hot isostatic pressing, 225
- hydride particles, 139
- hydrogen, 291, 297
  - porosity, 297
- hydrostatic stress, 257
- imperfections, 3
- indentation, 39
- injection-molding technique, 151
- insulation, 171
- joining mechanism, 159
- laser
  - ultrasonic, 243
  - methods, 237
  - welding, 159
- Lattice Block Material (LBM)<sup>TM</sup>, 109
- lightweight, 185
  - products, 271
  - structure, 109, 145

liquid metal, 121  
 low(-)  
   cycle fatigue, 27  
   density core, 225, 237  
 machining, 271  
 macrocrack, 27  
 manufacturing process, 133  
 mechanical  
   properties, 3, 59, 65, 97, 271  
   testing, 109  
 mesoscale, 303  
 metal(-), 133  
   foam, 171, 271  
   hydrogen, 281  
   powders, 121  
 metallic foams, 121, 257  
 Mg alloy (AZ31) synthesized, 315  
 microcellular foams, 185  
 microstructural, 315  
 modeling, 249, 271  
 models, 53  
 modulus, 15, 297  
   of elasticity, 91  
 moments of inertia, 91  
 multiaxial Weibull theory, 21  
 multilayer models, 303  
  
 nanoporous, 171  
 nickel(-), 291  
   base superalloy, 205  
  
 open-cell foams, 185  
  
 phase transformation, 231  
 plasma spraying, 45  
 plastic compressibility, 39  
 plateau strength, 97  
 Poisson's ratio, 303  
 polyurethane, 15  
 pore size distribution, 165  
 porosimetry, 165  
 porosity, 139  
   distribution, 21  
 porous, 297  
   Al alloys, 217  
   building materials, 21  
   GASAR aluminum, 303  
   materials, 165  
   metal(s), 103  
   sandwich panels, 257  
   pure Mg, 315  
   structures, 205  
 powder, 191  
   metallurgy, 145  
 processing, 257  
 properties, 211  
 proportional limit, 303  
  
 pullout strength, 265  
  
 relative density, 171  
 ring compression of porous metals, 33  
 rolling, 257  
  
 sample density, 59  
 sandwich, 91  
   plates, 265  
   structures, 237  
 shear properties, 83  
 sheet forming, 225  
 silica, 171  
 sintering, 45  
 slurries, 191  
 solidification, 281  
 solid-state foaming, 231  
 spinel, 45  
 SPM, 249  
 steel, 191  
   foam, 145  
 stiffness(es), 3, 97, 109  
 strain rate effects, 103  
 strength, 109  
   parameters, 59  
 stress intensity range, 27  
 structural, 185  
   damping, 151  
   porous metal, 249  
 structures, 281  
 superplasticity, 231  
 surface strain mapping, 71  
 syntactic magnesium foams, 211  
  
 tensile tests, 303  
 testing methods, 59  
 thermal-expansion coefficient, 265  
 Ti-6Al-4V, 225, 231, 237, 243, 249  
 TiO<sub>2</sub> diffusion barrier layer, 139  
 titanium, 231  
   alloy, 205  
   hollow sphere foams, 191  
  
 ultimate tensile strength, 303  
 uniaxial, biaxial and triaxial  
   densification, 65  
  
 viscous effects, 103  
  
 x-ray computed tomography, 71, 97  
  
 yield(ing), 71  
   criteria for the porous metals, 33  
   locus, 257  
   strength, 303  
 Young's modulus, 53, 303